



S. A. Morse

# **Basalts and Phase Diagrams**

An Introduction to the Quantitative Use of  
Phase Diagrams in Igneous Petrology

With 241 Figures

Springer-Verlag  
New York Heidelberg Berlin

*S. A. Morse*  
Department of Geology and Geography  
University of Massachusetts  
Amherst, Massachusetts 01003  
USA

Library of Congress Cataloging in Publication Data

Morse, S. A., 1931–

Basalts and phase diagrams

Bibliography: p.

Includes index.

1. Basalt. 2. Phase diagrams. 3. Rocks, Igneous.

I. Title

QE462.B3M67

552'.26'028

80-12429

All rights reserved.

No part of this book may be translated or reproduced in any form without written permission of Springer-Verlag.

The use of general descriptive names, trade names, trademarks, etc., in this publication, even if the former are not especially identified, is not to be taken as a sign that such names, as understood by the Trade Marks and Merchandise Marks Act, may accordingly be used freely by anyone.

© 1980 by Springer-Verlag New York Inc.

Softcover reprint of the hardcover 1st edition 1980

9 8 7 6 5 4 3 2 1

ISBN-13: 978-1-4612-6083-7  
DOI: 10.1007/978-1-4612-6081-3

e-ISBN-13: 978-1-4612-6081-3

*For Dorothy*

# Preface

The science of igneous petrology is founded on astute observation of rocks, guided by the rigorous principles of physical chemistry. It is, perhaps, the wedding of fallible observation with rigorous theory that makes this such a delicious science. In view of this, it is appropriate to study rocks and phase diagrams hand in hand. Good books on petrography abound, but there are few introductory books on phase diagrams, and none that illustrate in detail the quantitative analysis of fractional and equilibrium crystallization and melting, the four limiting processes capable of rigorous discussion. This book is an attempt to remedy the deficiency.

Basalts underlie some 70 percent of the earth's surface and represent the most abundant magma type on both the earth and the moon. It is therefore fitting to address their origin in some detail. As it happens, most of the interesting principles of phase equilibrium diagrams as applied to igneous rocks can be illustrated with basalts. I have therefore tied the exposition of phase diagrams to the larger story, still unfolding, of the origin and fate of the basaltic magma. In so doing, one neglects many interesting rocks, but their origins can be studied using the principles developed here.

This book was begun with undergraduate students in mind, and continued with graduate students in mind. The early parts of the chapters are elementary and the later parts are more advanced. Thus the later pages of some chapters contain discussions of non-binary or non-ternary solid solution, Gibbs free energy diagrams, and use of the lever rule with fractional crystallization and melting. The later chapters themselves tend to contain more advanced material, such as an introduction to Schreinemaker's rules (Chapter 16). On the other hand, the material in the chapters on high

pressure and volatile components presumes no special prior knowledge and can be interwoven with the earlier chapters on low pressure equilibria if that is desired. Some of the principles treated in the book serve the needs of metamorphic petrology, too, as a prelude to that study.

For many years, the gem of textbooks on igneous petrology has been Bowen's *The Evolution of the Igneous Rocks* (1928). No advanced student will want to miss exposure to this treatise of genius, or for that matter to its distinguished successor, subtitled *Fiftieth Anniversary Perspectives*, edited by H. S. Yoder, Jr. (1979). However, even Bowen dwelt but briefly on the mechanics of how phase diagrams may be used to full advantage, and indeed, many of his best discourses on the matter came only later (e.g., Bowen and Schairer, 1935; Bowen, 1941; Tuttle and Bowen, 1958). When I was a student, the elegant use of phase diagrams was a closet specialty practiced by a few brilliant experimentalists and just as few clever teachers. When I began to teach, I resolved to do my best to give away their secrets, so here they are.

I am much indebted to JOHN LYONS, who started me out on the right foot, and to many other tutors and colleagues, particularly HATTEN YODER, the late FRANK SCHAIRER, DONALD LINDSLEY, IKUO KUSHIRO, DEAN PRESNALL, and PETER WYLLIE. Their help and encouragement have been of great value. I would like to be able to say they bear equal blame for any shortcomings of this book, but regrettably that is not the case.

Pelham, Massachusetts  
April, 1980

S.A. MORSE

# Contents

<b>1. Introduction</b>	
Basalt Problems	1
Phase Diagrams as Models of Rocks	4
<b>2. Mineralogy and Chemistry of Basalts</b>	
Mineralogy	7
Chemistry	9
The CIPW Norm	10
The Basalt Tetrahedron: A Model for Basalt Study	12
Petrographic Characteristics	17
Other Types of Norm Calculation	18
<b>3. Crystals and Melts</b>	
Introduction	21
Definitions	22
Water: A Familiar but Bad Example	23
The Phenomena of Melting and Crystallization	27
Supercooling and Superheating	28
Melting as a Function of Pressure	28
Solutions: Solid and Liquid	29
<b>4. The Phase Rule as a Tool</b>	
Introduction	31
Systems, Components, Phases, Variables, Equilibrium	31
The Phase Rule and Variance	35

<b>5. Diopside and Anorthite: Supposedly a Binary Eutectic System</b>	
Introduction	37
Preparation and Melting of Diopside (Di)	37
Preparation and Melting of Anorthite (An)	39
Preparation of Di-An Mixtures	40
<i>T-X</i> Plots: Liquidus and Solidus	40
Diopside-Anorthite as a Binary System	42
Variance in Di-An	43
The Lever Rule	46
Nature of the Eutectic: Isothermal Melting and Crystallization	47
Analysis of Crystallization and Melting	48
Fractional Crystallization and Melting	50
Complications	52
Binary Solid Solutions in General	52
Non-binary Solid Solution: The Role of Al in Pyroxene	53
A Relevant Graphical Treatment	54
Petrologic Consequences	57
Summary of Basic Principles	57
<i>G-X</i> Diagrams	58
<b>6. Plagioclase: The System An-Ab</b>	
Introduction	61
Preparation and Melting of Albite	62
Liquidus and Solidus	63
Variance	64
Lever Rule	64
Equilibrium Crystallization	65
Fractional Crystallization	67
Equilibrium Melting	68
Fractional Melting	68
Assimilation	69
The Lever Rule with Fractional Crystallization and Melting	71
<i>G-X</i> Diagrams	73
<b>7. Diopside-Albite: A Complex System</b>	
Introduction	77
Pseudobinary <i>T-X</i> Diagram	78
Components and Liquid Trends	79
Petrologic Considerations	83
<b>8. Diopside-Anorthite-Albite</b>	
Introduction	85
Properties of Triangles	86
Deduction of the Ternary <i>T-X</i> Projection	87
The Experimental Ternary Diagram	90
Equilibrium Crystallization	91
Fractional Crystallization	104
Rock Paths (ISC Paths)	112

Contents	xi
Equilibrium Melting	114
Fractional Melting	114
Complications Due to Non-ternary Nature	117
Summary of Basic Principles	118
Lever Rule with Fractional Crystallization and Melting	120
Derivation of Fractionation and Equilibrium Paths	123
Equilibrium Paths	126
<b>9. Forsterite-Diopside-Anorthite: A Basaltic Analog</b>	
Introduction	129
Preparation and Melting of Forsterite	130
Two Sidelines: Forsterite-Diopside and Forsterite-Anorthite	130
Treatment of Fo-Di-An as a Ternary System	133
Fractional Crystallization	138
Equilibrium Melting	140
Fractional Melting	140
Discussion of Melting	143
Effects of Non-ternary Nature	144
Summary	145
Addendum: The Spinel + Liquid Field	146
<b>10. Incongruent Melting: The System Forsterite-Silica</b>	
Introduction	151
Incongruent Melting of Enstatite	152
Equilibrium Crystallization Paths	154
Fractional Crystallization	156
Melting	156
Summary	157
<i>G-X</i> Diagrams	159
<b>11. Forsterite-Anorthite-Silica: Incongruent Melting in a Ternary System</b>	
Introduction	161
Binary Joins	162
Primary Phase Regions	162
Cotectic Crystallization	163
Equilibrium Crystallization	164
Fractional Crystallization	171
Equilibrium Melting	174
Fractional Melting	174
Application to Basalts and Related Rocks	176
<b>12. Forsterite-Diopside-Silica: Pyroxenes and Their Reactions</b>	
Introduction	181
Bounding Joins	182
Ternary Compounds: Olivine and Pyroxenes	182
The Ternary System	184
Equilibrium Crystallization	186

Summary of Equilibrium Crystallization	196
Fractional Crystallization	196
Summary of Fractional Crystallization	199
Fractional Melting	200
Diopside-Rich Compositions	202
Nature of the Diopside-Pigeonite Boundary	206
The Diopside Field	207
Application to Basalts and “Granites”	212
<i>G-X</i> Diagrams for Systems with Maxima or Minima	213
<b>13. Layered Intrusions: A First Glance</b>	
Introduction	217
Layered Intrusions	217
Kiglapait Intrusion	220
Skaergaard Intrusion	223
Stillwater Complex	227
Muskox Intrusion	230
The Pigeonite Field in Fo-Di-An-SiO <sub>2</sub>	237
Accumulate Theory	239
<b>14. Nepheline-Silica and the Rest of the Basalt Tetrahedron</b>	
Introduction	243
Nepheline-Silica	243
The Thermal Barrier in More Complex Systems	247
The Critical Plane as a Model System	251
The Rest of the Basalt Tetrahedron	253
<b>15. Potassium: Petrogeny’s Residua System and Ternary Feldspars</b>	
Introduction	255
Sanidine: The System Kalsilite-Silica	256
Albite-Orthoclase	258
Residua System, Ne-Ks-SiO <sub>2</sub>	262
Introduction to Ternary Feldspars	279
Complex Crystallization of Solid Solutions	284
<i>G-X</i> Diagrams for the Albite-Orthoclase Join	288
<b>16. Iron and Oxygen</b>	
Introduction	295
Iron in Silicates	296
Fayalite	296
The Fo-Fa Series	298
Olivine Melting, Revisited	300
Fayalite and Its Oxidation	303
Oxygen in Melts	305
Oxygen Fugacity and the Concept of the Oxygen Buffer	306
Olivine Melting: A <i>T</i> - <i>f</i> <sub>O<sub>2</sub></sub> Analysis	308
Richardson’s Rule	322

<b>17. Iron-Bearing Olivines and Pyroxenes</b>	
Introduction	325
The System MgO-FeO-SiO <sub>2</sub>	325
Oxygen Content of Iron Silicate Liquids	327
The System Olivine-Anorthite-Silica	328
<i>T</i> - <i>f</i> <sub>O<sub>2</sub></sub> Relations in Mg-Fe-Si-O	331
Role of Oxygen Fugacity in Complex Systems	338
The Pyroxene Quadrilateral	339
<b>18. The Effects of High Pressure</b>	
Introduction	345
High Pressure Apparatus	346
Representations of Melting Curves	350
Diopside	350
Anorthite	351
Diopside-Anorthite	353
Albite	354
Plagioclase	355
Diopside-Anorthite-Albite	356
Forsterite	357
Forsterite-Diopside-Anorthite	358
Silica	360
Forsterite-Silica	361
Forsterite-Anorthite-Silica	364
Forsterite-Diopside-Silica	365
Nepheline-Silica	365
Kalsilite-Silica	369
Alkali Feldspar	371
Fayalite, and Olivine Solutions	371
Fe-SiO <sub>2</sub> -O	373
MgO-FeO-SiO <sub>2</sub>	378
Summary	378
<b>19. Effects of Volatiles at High Pressure</b>	
Introduction	381
Forsterite-H <sub>2</sub> O	383
SiO <sub>2</sub> -H <sub>2</sub> O	385
Enstatite-H <sub>2</sub> O	389
Forsterite-Plagioclase-Silica-H <sub>2</sub> O	389
Forsterite-Diopside-Silica-H <sub>2</sub> O	390
Albite-H <sub>2</sub> O	394
Albite-Orthoclase-H <sub>2</sub> O	395
Diopside-H <sub>2</sub> O	398
Diopside-CO <sub>2</sub> -H <sub>2</sub> O	398
Phlogopite-H <sub>2</sub> O	398
General <i>P</i> - <i>T</i> - <i>X</i> Relations for the Model System A-H <sub>2</sub> O	399
Summary	402
<i>G</i> - <i>X</i> Diagrams for Ab-Or-H <sub>2</sub> O	403

<b>20. Some Applications to Basalt Magma Genesis</b>	
Mineral Facies of the Upper Mantle	405
Mineral Facies of Basalt at Pressures	408
Melting at a Cusp for Abyssal Tholeiites	409
Effect of Pressure on Silica Saturation	412
Wet Versus Dry Melting	413
Carbon Dioxide and the ZIVC Reaction	418
Peridotite-CO <sub>2</sub> -H <sub>2</sub> O Solids	420
Summary and Comment	422
<b>Appendix 1: Chemical Calculations</b>	
Appendix 1A: <i>CIPW</i> Norm Calculation Procedures	427
Appendix 1B: Cation and Oxygen Units	434
<b>Appendix 2: The System, MgO-FeO-SiO<sub>2</sub></b>	
Introduction	437
A Series of Isothermal Planes	437
Three-Phase Triangles and Three-Phase Boundaries	445
Courses of Crystallization	447
Fractional Crystallization	457
Notes on Appendix 2	459
<b>References</b>	<b>461</b>
<b>Author Index</b>	<b>473</b>
<b>Subject Index</b>	<b>477</b>

# List of Symbols<sup>1</sup>

<i>a</i>	Activity	$F_s$	Fraction solid
Ab	Albite (NaAlSi <sub>3</sub> O <sub>8</sub> )	<i>G</i>	Gibbs free energy or Gas
An	Anorthite (CaAl <sub>2</sub> Si <sub>2</sub> O <sub>8</sub> )	<i>H</i>	Enthalpy
BC	Bulk composition	ILC	Instantaneous liquid composition
<i>c</i>	Number of components	ISC	Instantaneous solid composition
CAMS	The system CaO-Al <sub>2</sub> O <sub>3</sub> -MgO-SiO <sub>2</sub>	Jd	Jadeite (NaAlSi <sub>2</sub> O <sub>6</sub> )
CaTs	Ca-Tschermak's molecule (CaAl <sub>2</sub> SiO <sub>6</sub> )	kbar	Kilobars
CIPW	Cross, Iddings, Pirsson, Washington	Ks	Kalsilite (KAlSiO <sub>4</sub> )
Cr	Cristobalite (SiO <sub>2</sub> )	<i>L, l</i>	Liquid
Di	Diopside (CaMgSi <sub>2</sub> O <sub>6</sub> )	Lc	Leucite (KAlSi <sub>2</sub> O <sub>6</sub> )
<i>E</i>	Internal energy	M	Maximum or Magnetite (Fe <sub>3</sub> O <sub>4</sub> )
En	Enstatite (MgSiO <sub>3</sub> )	m	Minimum
FE	Fictive extract	$\mu$	Chemical potential
Fa	Fayalite (Fe <sub>2</sub> SiO <sub>4</sub> )	MW	Magnetite-wüstite
$F_L$	Fraction liquid	<i>N</i>	Mole fraction
FMQ	Fayalite-magnetite-quartz	<i>n</i>	Number of moles
Fo	Forsterite (Mg <sub>2</sub> SiO <sub>4</sub> )	Ne	Nepheline (NaAlSiO <sub>4</sub> )
$f_{O_2}$	Oxygen fugacity	Or	Orthoclase (KAlSi <sub>3</sub> O <sub>8</sub> )

<sup>1</sup>See also Table 2.3

<i>P</i>	Pressure	ss	Solid solution
<i>P<sub>aq</sub></i>	Pressure of aqueous fluid	<i>T</i>	Temperature
<i>P<sub>T</sub></i>	Total pressure	<i>T<sub>c</sub></i>	Critical temperature
Pig	Pigeonite	TLC	Total liquid composition
Pr	Protoenstatite	Tr	Tridymite (SiO <sub>2</sub> )
$\phi$	Number of phases	TSC	Total solid composition
Q	Quartz (SiO <sub>2</sub> )	<i>V</i>	Volume or Vapor
<i>S</i>	Entropy or Singular point	<i>W</i>	Variance
S	Solid (also Silica)	<i>W</i>	Wüstite (Fe <sub>1-x</sub> O)
Sa	Sanidine (KAlSi <sub>3</sub> O <sub>8</sub> )	<i>W<sub>p</sub></i>	Variance, constant pressure
Sp	Spinel (MgAl <sub>2</sub> O <sub>4</sub> )	<i>X</i>	Composition or Mole fraction

## Chapter 1

# Introduction

## Basalt Problems

Basalt is the lava which pours out of Kilauea in Hawaii, which formed the island of Surtsey, off Iceland, and which appears to underlie the thin layer of sediments over most of the ocean floor. The name is applied to the solid rock, the lava, and to the magma<sup>1</sup> which, on eruption, becomes lava. What do we know of these materials? We may know the composition of the rock, and even of the lava at various stages of eruption, from chemical analyses. Seismic evidence tells us that earthquakes from 50–60 km deep precede Hawaiian eruptions; this is far beneath the Mohorovičić discontinuity, and we can reasonably infer that the earthquakes are related to movement of magma in the upper mantle. The source of magma is therefore evidently the mantle. The temperature of the lava at eruption can be measured, and commonly falls in the range 1150–1250°C. It would seem that we know a great deal about basalt.

But what do we not know about basalt? We do not really know the depth of magma generation, for the seismic events do not necessarily report the genesis of magma. We do not know the exact composition or temperature of generation, since both of these are altered on passage to the surface. We do not know what is melted to form the original magma. We do not know what crystals form in transit, and of these, which are left behind and which are floated upward. We do not know what forces impel the magma to the surface. We do not know what processes of melting or crystallization

<sup>1</sup>A Greek word suggesting the consistency of paste.

produce the variety of basalt magma compositions which we see. We do not understand the sources of heat required to generate basalt magma, although we suppose that it must ultimately come from the decay of radioactive elements, perhaps aided by tidal friction (Shaw, 1970). In particular, we do not understand how heat is concentrated within the mantle. We do not even know very well the chemical changes which take place during crystallization at the surface, although recent studies in Hawaii have greatly improved our knowledge of at least one specific batch of magma. In short, we still have only a general idea of the origin of basalt magma, the progenitor of the most common igneous rock type at the surface of the crust. These problems are multiplied further in the case of plutonic (gabbroic) rocks which we can never observe in the process of formation.

What we do know of basalt genesis comes from a wide variety of studies: geochemical, geophysical, and petrological. Of petrological questions, the chief ones are: what *rock* is melted or partly melted in the mantle to form the relatively uniform magma which we classify as basalt, and what *processes* can work on such a magma to produce the suites of differentiated rocks which are associated with basalt? The role of experimental petrology has been to place limits on the answers to these questions, to identify parents and processes which are capable of producing what we see, and to shelve those which appear not to work.

There is no single, sharply defined basalt problem. There is a range of problems having to do, first, with the source of magma, and second, with what the magma may become. These two threads of basalt study are inextricably entwined, for the question of the fate of magmas may or may not be resolved at the instant of origin. In this book we shall keep both melting within the mantle and crystallization of the resulting magmas in view, and we shall find, as we go, a number of working hypotheses which deserve to be considered concurrently.

For many petrologists, the heart of the basalt problem lies in the eruption, often from the same vent, of tholeiitic basalts at one time and alkali basalts at another time.<sup>2</sup> To many petrologists, "alkali basalt" signifies, first and foremost, silica undersaturation with respect to alkalis, and "tholeiite" signifies silica oversaturation. We shall use these connotations in a model of basalts in the next chapter. There is no dispute among field workers that tholeiitic basalts most commonly carry interstitial quartz or micropegmatite, or both, when well-crystallized. It is also commonly observed that silica-saturated rocks such as dacite are found associated with tholeiitic basalts. Since the interstitial materials on the one hand and dacitic or rhyolitic rocks on the other hand have much the same composition, a genetic sequence tholeiite→rhyolite may reasonably be inferred. Similarly, alkali basalts never carry interstitial quartz or micropegmatite, but may carry interstitial

<sup>2</sup>These names and the classification of basalts are discussed somewhat more fully in the next chapter.

microsyenite or an undersaturated mineral such as a feldspathoid, commonly nepheline. They are commonly associated in the field with such silica-undersaturated rocks as trachyte and phonolite. Hence no great intuitive leap is required to deduce the genetic sequence alkali basalt→phonolite.

A genetic sequence might be implemented in a variety of ways; we shall commonly be concerned in this book with *fractional crystallization* as a means of achieving a genetic sequence. This mechanism is one suggested by the internal evidence of the rocks, for if, as textures indicate, an interstitial residuum (of, say, micropegmatite or microsyenite) represents a late-solidified fraction of liquid (i.e. magma), it is but a small step to infer that separation of all the other crystals from this small fraction of magma would yield an appropriately advanced rock, such as rhyolite or trachyte. Other mechanisms (for example, volatile transfer of ions) have been proposed for implementing genetic sequence, but none are so firmly grounded in direct evidence as fractional crystallization. On the other hand, it would be a grave error to suppose that fractional crystallization is the *only* process causing variation in magmas.

Basalts other than alkali basalt and tholeiite are well known. Among these are high-alumina basalts,<sup>3</sup> which occur in abundance on the ocean floor, and to a lesser extent elsewhere. High-alumina basalts of the ocean floor have been called oceanic tholeiites or abyssal tholeiites.<sup>4</sup> They form a chemically distinct group in their low content of "volatile" elements such as Rb, U, and Th. High-alumina basalts in general appear to be high in the components of plagioclase feldspar, even when glassy, hence apparently not mechanically enriched in plagioclase crystals. There is also, very likely, a class of basalts intermediate between alkali basalt and tholeiite, as defined above, which are neither oversaturated nor undersaturated with respect to silica, and which belong to a genetic sequence culminating in trachyte, itself neither oversaturated nor undersaturated. But for present purposes we may treat these other types of basalt as bothersome diversions from a simple model, and illustrate many valid points in terms of arbitrarily defined alkali basalt and tholeiite.

The implied genetic sequences of these latter two types pose a fundamental question: do the two magma types have a common or diverse origin? If common, is there a common parent magma, or a common parental mantle rock? If diverse, what are the diverse parent magmas or rocks? These questions are depicted more clearly in Figure 1.1, where they are presented as a set of five propositions. Those in the left-hand column concern the mantle rock which is partially melted to produce magma. In (1), a single mantle rock XY produces, by different or temporally distinct processes, both tholeiite and alkali basalt magmas. In (2), each magma type arises

<sup>3</sup>Kuno, 1960.

<sup>4</sup>Engel and others, 1965; Gast, 1965.

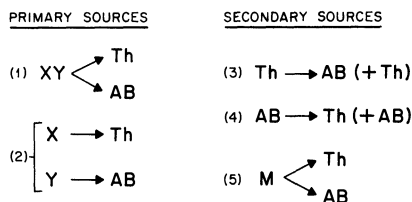


**Figure 1.1.** Five propositions on the origin of tholeiite (Th) and alkali basalt (AB) magmas. The left-hand column represents the primary solid sources (mantle rocks X and Y); the right-hand column represents secondary, magmatic sources. M is an undefined parent magma.

from a different rock, X or Y. In (3), a primary tholeiite magma (from (1) or (2)) differentiates to produce alkali basalt magma as well as tholeiitic liquids. In (4), a primary alkali basalt magma produces tholeiite (as well as alkali basaltic) magma. In (5), an unknown common parent magma differentiates by two processes to produce both alkali basalt and tholeiite magmas.<sup>5</sup>

In this book, we shall not attempt to arrive at a firm decision in favor of a single one of these propositions, but instead we shall inquire how to evaluate the various propositions by means of phase diagrams. Other important methods of evaluation, such as studies of minor element distribution, are largely beyond the scope of this book, but in regard to minor elements it should be pointed out that the principles of phase diagrams usually apply to minor as well as major elements.<sup>6</sup> The experimental study of basaltic minerals and their phase relations is, in any event, a fundamental and powerful means of evaluating hypotheses of basalt origin.

## Phase Diagrams as Models of Rocks

At one time there was quite an uproar over the application of phase diagrams to natural rocks, some claiming that since the natural rocks are obviously more complicated than synthetic systems, the phase diagrams are simplistic and misleading. We may now cheerfully relegate the uproar to the history and philosophy of science, and say we are sophisticated

<sup>5</sup>Some of these propositions can be identified with their proponents. (1) was advocated by Fennor (1913), and later by Yoder and Tilley (1962). (2) is essentially the two-magma idea of Kennedy and Anderson (1938) and Kuno (1959). (3) has been proposed by Macdonald (1949) and Tilley (1950). (4) was proposed by Bailey and others (1924), Bowen (1928, p. 78), and Tomita (1935). (5) invokes a hypothetical parent magma, neither alkali basalt nor tholeiite, which, until identified, might better be ignored.

<sup>6</sup>This is true insofar as minor elements reside in discrete, thermodynamically stable sites in the crystal structure. It ceases to be rigorously true when minor elements reside in defects in the crystal structure.

enough to have a word which should long ago have disarmed the combatants: phase diagrams are *models* of natural rocks. We should not hesitate to confess that they are simplistic, but if we are conscious of using them as models, they need not be misleading. As models they can help us to understand the ground rules of the game, the purpose of which is to discover rock forming processes which are inaccessible to direct view.

In order for phase diagrams to serve as instructive models, they must deal initially with relatively few chemical elements, each of which is present in a state of high purity; in other words, the models with which we work should be chemically simple. If this were not so, we should quickly be presented with experimental results, due to impurities or complexities, which we could not interpret in any straightforward way. This is simply to say that we wish our experiments to be controlled, so that we may change one variable at a time and discover the result of changing that variable. Once a few fundamental principles are discovered, we may make more and more complicated models, till they approach natural rocks themselves.

Experiments on natural rocks may provide even better models than those on synthetic systems, but even these experiments generate models rather than duplicating natural processes, because we cannot *a priori* define, let alone control, all the variables of the natural process. If we could, our work would be done. The interpretation of experiments on natural rocks is risky, and impossible without the principles furnished by synthetic systems in which all the variables may be controlled.

This book treats a limited number of experimental systems, and shows how they may be brought to bear on the problems of basalts. The emphasis is on the application of phase diagrams to both petrologic problems and experimental problems. We shall see that they may be used both qualitatively and quantitatively, as guides to research and guides to rock genesis. Although the theme is basalt genesis, the principles encountered are applicable over the field of igneous petrology in general.

We shall be concerned, in each system studied, with both crystallization and melting phenomena, since basalt magmas must be approached both from the standpoint of what they may become (residual liquids produced by fractional crystallization) and from the standpoint of how they originate (partial or complete melting of mantle rocks).

Each experimental system discussed is to be regarded as a model which illustrates some principle of basalt genesis. At appropriate points, imperfections in the models will be discussed, and complications due to crystal compositions lying outside the model system will be stressed. Many of these complications furnish guides to further research, some of which has yet to be undertaken.

On occasion, it will be fruitful to deduce phase diagrams from incomplete data, using both geologic and phase-rule horse sense. This practice is a very common exercise for the experimentalist, for it produces and tests hypotheses related to current research, and often points the way to rewarding future

research. Indeed, the facility with which an experimentalist may generate model phase diagrams when faced with mineralogical problems often bewilders and annoys the field geologist, when in fact a development of such talents would benefit the latter and greatly enhance communication between field and laboratory worker.

Our discussion of basalt origin will be selective, not comprehensive; no thorough review of the problems will be attempted, and certain threads will be followed for their amenability to treatment by phase diagrams, to the neglect of other threads equally important to basalt genesis.

We begin by a brief discussion of basalts, in Chapter 2, followed by discussions of some pertinent physical chemistry in Chapters 3 and 4. With Chapter 5 begins a systematic exposition of phase diagrams, their experimental background, and their interpretation.

## Chapter 2

# Mineralogy and Chemistry of Basalts

## Mineralogy

When basaltic lava is abruptly quenched, it solidifies to glass. When slowly cooled, it crystallizes, more or less completely, to an assemblage of minerals. We may speak of the mineralogy of basalts in terms of these minerals (*modal* composition), and of the chemistry of basalts both in terms of elements (or oxides) and the *potential* minerals which might form if the lava were slowly cooled (*normative* composition). The calculation of normative minerals is discussed below, but first we may consider the actual minerals found in well-crystallized basalts.

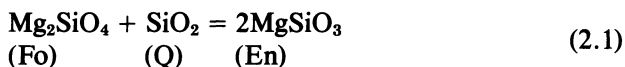
The two essential minerals of greatest importance are plagioclase and pyroxene, since these make up perhaps 80% of many basalts. Indeed, for a starting model, we should not be far off base to consider plagioclase and pyroxene alone for ideas of basalt crystallization; this is precisely what we shall do in Chapters 5 to 8. The plagioclase involved is an intermediate member of the An-Ab series, and Bowen (1928) showed that a composition very near An<sub>50</sub> occurs most frequently in basalts. The pyroxene is chiefly calcic, that is, a member of the augite series, usually more magnesian than ferrous-rich ( $Mg/(Mg + Fe) > 0.5$ ), and commonly not very far from diopside, although it ranges to subcalcic augite. Calcium-poor pyroxene, generally hypersthene, may or may not be present, depending on the abundance of silica relative to other constituents. Ca-poor pyroxene is a critical mineral in basalt classification, its presence signifying tholeiitic basalt, and its absence usually implying alkali basalt.

Olivine is another critical mineral in basalt classification. In alkali basalt,

it is commonly present instead of Ca-poor pyroxene. In olivine tholeiites, it is present in company with Ca-poor pyroxene.

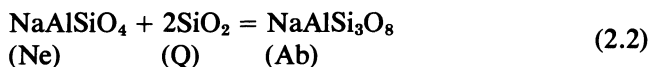
By adding olivine, our basalt model has grown to four minerals: plagioclase, two pyroxenes, and olivine. These four minerals make a model which is indeed a close analog of natural basalts. The only ubiquitous mineral which we have left out so far is Fe-Ti oxide, usually titaniferous magnetite, perhaps in company with ilmenite, although more oxidized varieties occur. We shall find that consideration of these non-silicates of cations which can easily be oxidized requires a special type of experimental and theoretical treatment, in which the availability of oxygen must be controlled or specified in some way.

Other minerals which occur in basalts, and which play an important role in classification when they occur, are quartz and nepheline. Quartz commonly occurs in company with Ca-poor pyroxene. Olivine may occur, but if so it is usually mantled by a more siliceous mineral, usually Ca-poor pyroxene, for magnesian olivine is not stable in the presence of excess silica, because of the reaction



Rocks which carry quartz are *silica-oversaturated* rocks, and rocks which carry Ca-poor pyroxene instead of quartz could be described as *silica-saturated* rocks.

Nepheline occurs in some rocks lacking Ca-poor pyroxene; its presence is due to a deficiency of silica required to form feldspar. Were such silica available, nepheline would react to form the albite component of plagioclase by the reaction



The presence of nepheline (or another feldspathoid) therefore clearly signifies a state of *silica-undersaturation*, i.e. an amount of silica too small for the continual formation of feldspar throughout the crystallization history of the rocks. Nepheline is accompanied by olivine, this being the most silica-poor Fe-Mg silicate in common basaltic rocks. Nepheline-bearing basalts lie at the opposite end of a spectrum from quartz-bearing basalts; the spectrum consists of the sequence

Basanite (Ne-bearing)	critically undersaturated
Alkali basalt	critically undersaturated
Olivine tholeiite	undersaturated
Hypersthene basalt	saturated
Tholeiite (Q-bearing)	oversaturated

## Chemistry

Table 2.1 lists the average chemical composition of crustal rocks, as estimated by Ronov and Yaroshevsky (1969), expressed as weight, atom, and volume percent. This table, however approximate it may be, leaves no doubt that the earth's crust is dominated by oxygen, and that in terms of weight of atoms, silicon runs a strong second. The volume percent column reflects the small ionic radius of silicon and the large radii of Ca Na, and K relative to Si.

Table 2.2 gives the chemical composition of the average basalt, as estimated from the data of Chayes (1972), and stated in the usual format of weight percent of oxides. Again, silicon and oxygen dominate the analysis (as  $\text{SiO}_2$ , near 50% in all basalts),  $\text{Al}_2\text{O}_3$  is next in abundance, and CaO, MgO, and FeO are closely similar, averaging a little less than 10%. Other oxides are almost always below the 5% level, and until one has inspected many basalt analyses, they all tend to look about the same, despite important differences which do exist. There is a way of treating chemical analyses, however, in such a way as to bring out important differences which are not manifest on simple inspection. This treatment is the norm calculation.

**Table 2.1** Chemical Composition of the Earth's Crust (Oceanic and Continental), as Estimated by Ronov and Yaroshevsky (1969, p.55).

As Oxides, Wt %		As Atoms (8 most abundant)				
		Wt. %	Atom %	Radius*	Volume %	
$\text{SiO}_2$	57.60	O	46.84	66.98	1.30	90.62
$\text{Al}_2\text{O}_3$	15.30	Si	26.92	21.93	.34	.53
$\text{Fe}_2\text{O}_3$	2.53	Al	8.10	6.87	.56	.74
FeO	4.27	Fe	5.09	2.08	.86	.82
MnO	0.16	Ca	5.00	2.86	1.15	2.68
MgO	3.88	Mg	2.34	2.20	.80	.69
CaO	6.99	Na	2.14	2.13	1.10	1.74
$\text{Na}_2\text{O}$	2.88	K	1.94	1.13	1.46	2.17
$\text{K}_2\text{O}$	2.34					
$\text{TiO}_2$	0.84					
$\text{P}_2\text{O}_5$	0.22					
$\text{H}_2\text{O}^+$	1.37					
$\text{CO}_2$	1.40					

\*After Whittaker and Muntus (1970); in Å.

**Table 2.2** Chemical Composition of Cenozoic Basalt, as Estimated from the Data of Chayes (1972). The Figures Represent the Average of 2413 Individual Chemical Analyses.

SiO <sub>2</sub>	47.65
Al <sub>2</sub> O <sub>3</sub>	15.28
Fe <sub>2</sub> O <sub>3</sub>	3.57
FeO	7.54
MgO	7.52
CaO	9.91
Na <sub>2</sub> O	2.98
K <sub>2</sub> O	1.23
TiO <sub>2</sub>	2.14
P <sub>2</sub> O <sub>5</sub>	.44
H <sub>2</sub> O	1.51
<b>Total</b>	<b>99.77</b>

Note: The norm of this analysis is presented in Table 2.4.

## The CIPW Norm

The norm calculation is an arbitrary formula for casting a chemical analysis of a rock into potential minerals which could form if the rock crystallized completely under idealized conditions. Many different formulas have been proposed, some with a view to enabling further calculations (e.g. the molecular norms of Niggli, 1936, and Eskola, 1954), and some with a view to representing more exactly the actual mineralogy of the rock (metamorphic norms: see Barth, 1962, p. 337–343). For many purposes, however, the CIPW<sup>1</sup> norm is quite adequate,<sup>2</sup> and preferable because of the large catalog of CIPW norms available for comparison, e.g. Washington's (1917) Tables. The calculation has great utility in discussing fine-grained or glassy rocks whose actual mineralogy is obscure or non-existent, and it provides an important link between natural rocks and experimental systems which are defined by their chemistry alone.

The CIPW norm is a weight norm, that is, the final result is expressed as weight percent of the various *normative minerals*, or potential minerals implied by the chemical analysis. With common basaltic rocks, these

<sup>1</sup>Named for its inventors, Cross, Iddings, Pirsson, and Washington (1903).

<sup>2</sup>Or superior; see Chayes (1963).

minerals are the feldspars, pyroxenes, olivine, ilmenite, magnetite, apatite, and sometimes nepheline or quartz. The first three groups, which are solid solutions, are calculated in terms of their end members, so that one may recalculate the *normative feldspar composition* as percentages of An,<sup>3</sup> Ab, and Or, or the *normative pyroxene compositions* in terms of Wo, En, and Fs, or the *normative olivine composition* in terms of Fo and Fa.

One may rant on at some length about the method and purpose of the norm calculation, but no amount of ranting is so instructive as the performance of a few calculations. The calculation is easily done with a slide rule or pocket calculator, and three or four examples should suffice to show what the norm calculation is all about.<sup>4</sup> A simplified calculation procedure, adequate for most basaltic rocks, is given in Appendix I, along with a shorthand form which facilitates the calculation. A single example is given below to suggest the general outline of the calculation, using Chayes' average basalt from Table 2.2.

In order to calculate mineral formulae from a weight percent analysis,

<sup>3</sup>A list of common normative minerals and their abbreviations is given in Table 2.3.

<sup>4</sup>The norm calculation is in principle simple to program for a digital computer, and this is in itself an instructive exercise. However, an accurate and complete CIPW norm program is tedious to write, and it is wise practice to obtain a tried and true program if possible.

**Table 2.3** Common Normative Mineral Molecules in the CIPW Norm.

		Salic Group
	Quartz ( <i>q</i> )	SiO <sub>2</sub>
	Orthoclase ( <i>or</i> )	K <sub>2</sub> O·Al <sub>2</sub> O <sub>3</sub> ·6SiO <sub>2</sub>
	Albite ( <i>ab</i> )	Na <sub>2</sub> O·Al <sub>2</sub> O <sub>3</sub> ·6SiO <sub>2</sub>
	Anorthite ( <i>an</i> )	CaO·Al <sub>2</sub> O <sub>3</sub> ·2SiO <sub>2</sub>
	Leucite ( <i>lc</i> )	K <sub>2</sub> O·Al <sub>2</sub> O <sub>3</sub> ·4SiO <sub>2</sub>
	Nepheline ( <i>ne</i> )	Na <sub>2</sub> O·Al <sub>2</sub> O <sub>3</sub> ·2SiO <sub>2</sub>
	Kalsilite ( <i>ks</i> )	K <sub>2</sub> O·Al <sub>2</sub> O <sub>3</sub> ·2SiO <sub>2</sub>
		Femic Group
	Diopside ( <i>di</i> )	CaO·(Mg,Fe)O·2SiO <sub>2</sub>
	Wollastonite ( <i>wo</i> )	CaO·SiO <sub>2</sub>
Hypersthene ( <i>hy</i> )	[ Enstatite ( <i>en</i> )	MgO·SiO <sub>2</sub> ]
	[ Ferrosilite ( <i>fs</i> )	FeO·SiO <sub>2</sub> ]
	Olivine ( <i>ol</i> )	2(Mg,Fe)O·SiO <sub>2</sub>
	Forsterite ( <i>fo</i> )	2MgO·SiO <sub>2</sub>
	Fayalite ( <i>fa</i> )	2FeO·SiO <sub>2</sub>
	Magnetite ( <i>mt</i> )	FeO·Fe <sub>2</sub> O <sub>3</sub>
	Ilmenite ( <i>il</i> )	FeO·TiO <sub>2</sub>
	Apatite ( <i>ap</i> )	3(3CaO·P <sub>2</sub> O <sub>5</sub> )·CaF <sub>2</sub>

Note: Diopside may be calculated into its *wo*, *en*, *fs* components. Hypersthene, if present, is always calculated in addition to these.

the analysis must first be recast into molecular proportions (Table 2.4). This is done by dividing the weight percent of each oxide by the rounded molecular weight of that oxide. The molecular proportions are then used up in a standard order, first by assigning all  $P_2O_5$  to apatite, using an appropriate amount of CaO to yield an arbitrary apatite formula. Then  $TiO_2$  is used to form ilmenite,  $FeO \cdot TiO_2$ , with an equal amount of FeO, and so on. A debit ledger enables one to keep track of the amounts of CaO, FeO, etc. used. The calculation proceeds in routine fashion through hypersthene (Hy), at which point a summation is made of all silica used. If the original molecular proportion of silica is in excess of that used, the rock is oversaturated, and the excess silica is reported as quartz in the norm. If the original amount is less than that used, some or all of the MgO, FeO assigned to hypersthene must be recalculated to the less siliceous mineral olivine. If, when all hypersthene is thus converted to olivine, too much silica has still been used, some or all of the  $Na_2O$ ,  $Al_2O_3$  assigned to albite must be recalculated to the less siliceous mineral nepheline, and the rock is silica-undersaturated. If, as rarely happens, too much silica has still been used, orthoclase must be converted to leucite. When the appropriate silica balance has been achieved, the molecular amounts for each normative mineral are multiplied by the molecular weight of the mineral to achieve a weight percent norm.  $H_2O$  and other volatiles are ignored in the calculation, and simply added on at the end to see if the summation approximates that of the original chemical analysis, which it should if no errors have been made.

A few trial norm calculations should be made in order to appreciate the chemical mineralogy which underlies the norm scheme. It is best to begin with an oversaturated tholeiite, which is the simplest calculation, then proceed to an olivine-hypersthene tholeiite, and finally to a nepheline-normative alkali basalt. Several chemical analyses from each of these groups are listed in Appendix I for convenience. Good sources of analyses for further practice can be found in Yoder and Tilley (1962) and Macdonald and Katsura (1964).<sup>5</sup>

## The Basalt Tetrahedron: A Model for Basalt Study

Yoder and Tilley (1962) have devised a scheme for classifying basaltic rocks by their CIPW norms, using a "basalt tetrahedron." The basalt tetrahedron (Figures 2.1 and 2.2) is simply the quaternary system forsterite-diopside-nepheline-quartz, a group of minerals which serves, to a first approximation, as a model of basalts. Plagioclase is represented by albite, which lies on the line nepheline (Ne)-quartz (Q) by virtue of reaction 2.2. Pyroxene is represented by diopside, at one corner of the tetrahedron, and enstatite, which lies between forsterite (Fo) and quartz by virtue of reaction 2.1.

<sup>5</sup>The budding petrographer may have the dubious pleasure of discovering some errors in the CIPW norms of one of these tables.

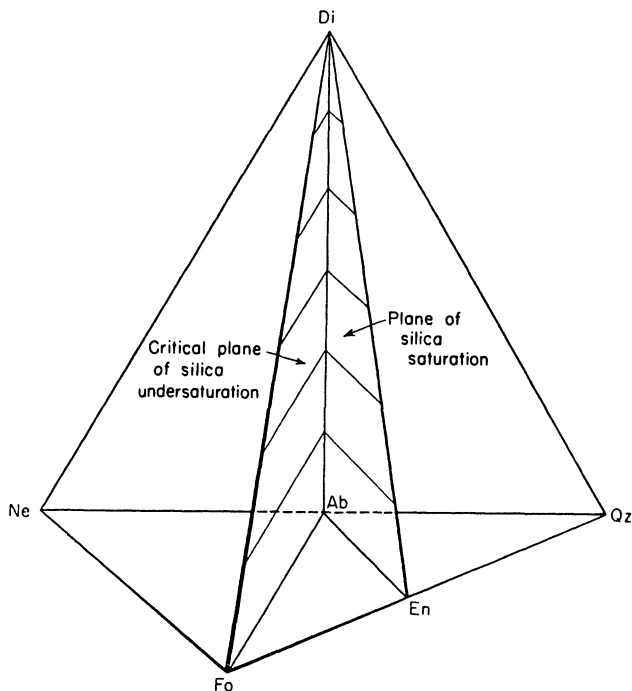


**Figure 2.1.** The fundamental basalt tetrahedron of Yoder and Tilley (1962), the system Di-Fo-Ne-Qz, showing the plane of silica saturation Di-En-Ab, and the critical plane of silica undersaturation Di-Fo-Ab. Although iron-free, the system accounts for the major phases of basalts. (Reproduced by permission.)

Olivine is represented by the forsterite corner, quartz by the quartz corner, and feldspathoid by the nepheline corner of the tetrahedron. As sketched in Figure 2.1, the tetrahedron is cut by two planes, one a critical plane of silica undersaturation (Fo-Di-Ab) which separates the region of critically undersaturated rocks toward nepheline from the region of undersaturated and saturated rocks toward quartz. Those rocks falling exactly in the critical plane Fo-Di-Ab could be called critically undersaturated rocks in terms of their CIPW norm. The other plane of importance is the plane of silica saturation (En-Di-Ab), which separates the region of silica-undersaturated rocks toward the critical plane from the region of silica-oversaturated rocks toward quartz.

Figure 2.2 is the generalized basalt tetrahedron of Yoder and Tilley, so-called because plagioclase, olivine, augite, and hypersthene in general are substituted for the pure end members albite, forsterite, diopside, and hypersthene. This implies consideration of FeO in addition to the oxides Na<sub>2</sub>O, Al<sub>2</sub>O<sub>3</sub>, CaO, MgO, and SiO<sub>2</sub> required to form the fundamental tetrahedron of Figure 2.1, and also requires CaO and Al<sub>2</sub>O<sub>3</sub> to be projected in such a way as to furnish anorthite. The generalized tetrahedron offers a convenient means of summarizing the essential characteristics of basaltic

**Table 2.4** Example of a Norm Calculation, Using the Average Basalt of Table 2.2.

Oxide	Wt. %	Mol. Wt.	Mol. No. <sup>a</sup>	Subtractions	Calculations
SiO <sub>2</sub>	<u>47.65</u>	60	<u>794-794 = 0</u>		<i>Mg, Fe</i>
Al <sub>2</sub> O <sub>3</sub>	<u>15.28</u>	102	<u>149-13-48 = 88-88 = 0</u>		188+56 = 244
Fe <sub>2</sub> O <sub>3</sub>	<u>3.57</u>	160	<u>22-22 = 0</u>		188/2.44 = 77%
FeO	<u>7.54</u>	72	<u>105-22-27 = 56-18 = 38-38 = 0</u>		<i>hy, ol</i>
MnO	—	71	—		2S = 188
MgO	<u>7.52</u>	40	<u>188-61 = 127-127 = 0</u>		x = 23
CaO	<u>9.91</u>	56	<u>177-10-88 = 79-79 = 0</u>		M = 165
Na <sub>2</sub> O	<u>2.98</u>	62	<u>48-48 = 0</u>		y = 142
K <sub>2</sub> O	<u>1.23</u>	94	<u>13-13 = 0</u>		
P <sub>2</sub> O <sub>5</sub>	<u>.44</u>	142	<u>3-3 = 0</u>		
TiO <sub>2</sub>	<u>2.14</u>	80	<u>27-27 = 0</u>		
Rest	<u>1.51</u>		(“Rest” = H <sub>2</sub> O etc)		Analysis sum <u>99.77</u>

Normative Minerals

I	II	III	IV
	SiO <sub>2</sub> Used	Mol. Wt/ 1000	Weight Norm <sup>b</sup>
<i>ap</i> (P+[CaO = 3.33P])	—	.336	<i>ap</i> <u>1.00</u>
<i>mt</i> (Fe''' + Fe')	—	.232	<i>mt</i> <u>5.10</u>

<i>il</i> (Ti+Fe <sup>2+</sup> )	27	27	—	.152	<i>il</i>	<u>4.10</u>
<i>or</i> (K+Al)	13	13	(6K)	.556	<i>or</i>	<u>7.23</u>
<i>ab</i> (Na+Al)	48	48	(6Na)	.524	<i>ab</i>	<u>25.15</u>
<i>an</i> (Al+Ca)	88	88	(2Ca)	.278	<i>an</i>	<u>24.46</u>
Σ MgO + FeO left = 244, % MgO = 77						
<i>di</i> (Ca+MgFe)	<i>wo</i>	<u>79</u>	(2Ca)	158	(for Σ <i>di</i> )	<u>9.16</u>
	79	<i>en</i>		.100		<u>6.10</u>
		<i>fs</i>		.132	<i>di</i>	<u>17.64</u>
<i>hy</i> (Mg+Fe)	<i>en</i>	<u>18</u>	Σ SiO <sub>2</sub> = 700	.100		<u>1.80</u>
	23	<i>fs</i>	(1Mg)	.132	<i>hy</i>	<u>2.46</u>
		<i>fo</i>	(.5Mg)	.140		
			(.5Fe)	.204		
	142	<i>fa</i>	(2Na)	.284	<i>ol</i>	<u>11.03</u>
<i>ne</i> (Na+Al)			(1Si)	.060	<i>ne</i>	—
<i>q</i> (Si)			Σ SiO <sub>2</sub> = 794		<i>q</i>	—
					Rest	<u>1.51</u>
					Σ	<u>99.68</u>

Total feldspar 56.84

An/Plag = 49.3

<sup>a</sup>10<sup>8</sup> Wt. %/Mol. Wt.  
<sup>b</sup>Mol.No. of first oxide in Col.I × Col.III

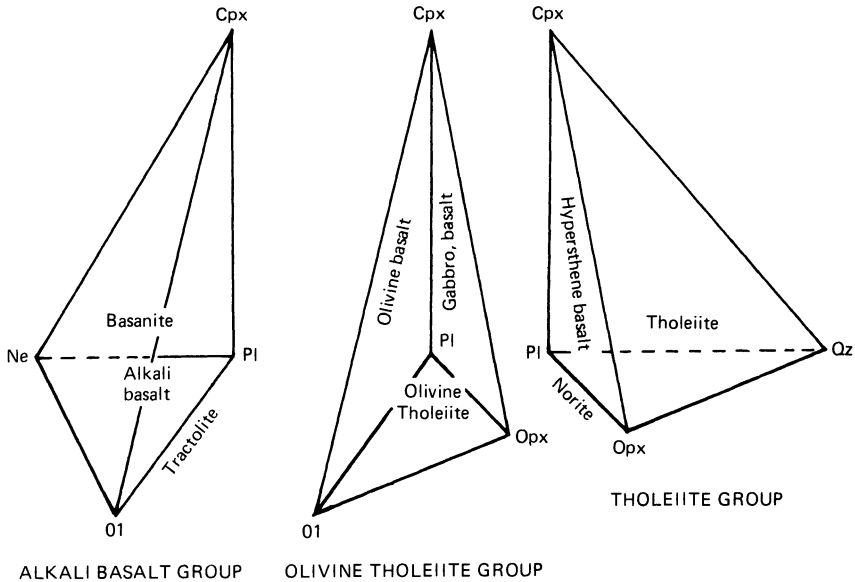


**Figure 2.2.** The basalt tetrahedron generalized to admit iron members of Di and Fo corners (i.e. olivine in general instead of the end member Fo, etc.), and An, and exploded to show nomenclature of major basalt types based on their normative composition.

rocks in terms of their chemistry. The positions of the rock names inserted in the expanded tetrahedron of Figure 2.2 reflect the salient mineral and chemical features of the rocks, which can be summarized as follows:

There are five unique groups of basalt, based on their normative composition. Three of these occupy volumes in the tetrahedron, and the other two lie on the planes of saturation and critical undersaturation. They are:

1. *Tholeiite* (oversaturated): normative *quartz* and *hypersthene* (region to the right of the plane of silica saturation).
2. *Hypersthene basalt* (also tholeiite, saturated): normative *hypersthene* (on plane of silica saturation—has just enough  $\text{SiO}_2$  to make hypersthene, but not enough for free quartz).
3. *Olivine tholeiite* (undersaturated): normative *hypersthene* and *olivine* (region to the left of the plane of silica saturation).
4. *Olivine basalt*: normative *olivine* (on the critical plane of silica undersaturation—not enough  $\text{SiO}_2$  to make hypersthene).
5. *Alkali basalt*: normative *olivine* and *nepheline* (region to the left of the critical plane of silica undersaturation).

Note that saturation with respect to silica does not depend on silica percentage alone, but on the ratio of silica to alkalis, etc. In calculating

the norm of a rock high in alkalis, silica is used to make *or* and *ab*, so there may not be enough left over for *hy* or even olivine, in which case the norm shows *ne* and represents alkali basalt. The same silica percentage with low alkalis could be an olivine tholeiite or even tholeiite.

Similar nomenclature applies to plutonic rocks if the word *gabbro* is substituted for basalt.

## Petrographic Characteristics

1. Tholeiite: *Augite* (or subcalcic augite), *plagioclase* (commonly labradorite), and *iron oxides* are essential minerals. Olivine is minor or absent. *Interstitial acid residuum* (glass or quartz-feldspar intergrowth) is *characteristic*. Hypersthene is present or "occult" in the augite. Olivine, if present, generally shows reaction to Hy where in contact with groundmass (= liquid).

These remarks apply to all the tholeiites (Groups 1–3 above); the olivine percentage generally rises toward the critical plane of silica undersaturation.

2. Alkali basalt: *Nepheline* is present well within the volume, but generally absent near the critical plane. Pyroxene is high in CaO. No hypersthene occurs. *Plagioclase* near An<sub>50</sub>, commonly zoned to oligoclase. Olivine both as phenocrysts *and* in groundmass. *Characteristically holocrystalline*, without the interstitial residuum common in tholeiite.

The basalt tetrahedron is a model, and it does not satisfy all the characteristics of natural basalts. In particular, it ignores apatite and Fe-Ti oxides. Moreover, it formalizes the silicate minerals by means of the artificial CIPW norm. In spite of this, it is a useful conceptual model for beginning the study of basalt, and many of its apparent shortcomings can be systematically eliminated by expanding the model after the fashion of Figure 2.2. We shall find in particular that the region around the critical plane is very instructive, since it generates some important hypotheses about the relationships of alkali basalt and tholeiite.

The basalt tetrahedron will be used in this book as a framework on which to hang ideas about basalt, and as a checklist with which to keep track of a systematic examination of phase diagrams. The phase diagrams which we will examine will concern those two- and three-mineral assemblages in the tetrahedron, and a few others (such as An-Ab) which lie contiguous to the tetrahedron.

Other models can of course be constructed for the examination of basalt. The basalt tetrahedron of Yoder and Tilley is a part of the 5-component system Na<sub>2</sub>O-CaO-Al<sub>2</sub>O<sub>3</sub>-MgO-SiO<sub>2</sub>. The omission of Na<sub>2</sub>O from this system

permits a tetrahedral representation of the remainder, "CAMS", which contains the basaltic minerals diopside, enstatite, and anorthite, as well as important related compounds such as wollastonite, quartz, spinel, and the aluminous, pyroxene-like compound known as calcium-Tschermak's molecule. We shall find occasion to refer to this system in later chapters, where its utility will be demonstrated.

## Other Types of Norm Calculation

The CIPW norm is stated in weight units, and is convenient for comparing, in general terms, rock analyses and phase diagrams that are plotted in weight units. The latter are inappropriate, however, when strictly quantitative comparisons are desired, because the iron end members of femic molecules are heavier than the magnesian end members, and therefore do not plot at the same point in a diagram expressed in weight units. The problem is overcome by use of another type of norm, such as the cation or oxygen norm. Each of these uses the same combining conventions as the CIPW norm, but each is expressed in a different way.

The cation norm, sometimes called the molecular norm, is calculated from oxides stated in terms of one cation. Thus for example,  $\text{Na}_2\text{O}$  is calculated as  $2\text{NaO}_{1/2}$ , and the weight percentage is divided by 31 rather

**Table 2.5** Comparison of CIPW and Cation Norms, Gough Island Alkali Olivine Basalt of Barth (1962; Table III-9).

Oxide	Wt. %	CIPW Norm		Cation Norm	
$\text{SiO}_2$	49.10	<i>ap</i>	1.34	Ap	1.18
$\text{TiO}_2$	3.59	<i>mt</i>	4.18	Mt	3.04
$\text{Al}_2\text{O}_3$	16.21	<i>il</i>	6.84	Il	5.06
$\text{Fe}_2\text{O}_3$	2.87	<i>or</i>	16.12	Or	16.59
FeO	6.84	<i>ab</i>	25.68	Ab	27.00
MnO	0.05	<i>an</i>	20.29	An	20.42
MgO	5.04	<i>di</i>	16.25	Di	16.42
CaO	8.90	<i>ol</i>	6.60	Ol	7.26
$\text{Na}_2\text{O}$	3.53	<i>ne</i>	2.27	Ne	3.04
$\text{K}_2\text{O}$	2.76	Rest	<u>0.47</u>		<u>--</u>
$\text{P}_2\text{O}_5$	0.54	Sum	100.04		100.01
$\text{H}_2\text{O}$	<u>0.47</u>	An	0.44		0.43
Sum	99.90	Fsp	62.09		64.01

than 62. Similarly, the oxygen norm is calculated from oxides states in terms of one oxygen. Thus  $\text{Na}_2\text{O}$  is divided by 62, but  $\text{SiO}_2$  is divided by 30 rather than 60, to yield units of  $\text{Si}_{1/2}\text{O}$ . Further descriptions are given in Appendix 1. The symbols of the cation norm are rendered “Ap”, etc., to distinguish them from the CIPW “ap”, etc.

Cation norms are useful for comparing chemical analyses of natural rocks to phase diagrams plotted in cation units. Oxygen norms are rarely used, but diagrams plotted in oxygen units are especially useful for plotting *modal* (volume) analyses of rocks, since oxygen accounts for most of the volume of rock-forming silicate minerals.

The qualitative characteristics (such as the presence of *ne* and *Ne*) of CIPW, cation, and oxygen norms will always be the same, because the same CIPW combining conventions are used in each. The CIPW and cation norms of an alkali olivine basalt are compared in Table 2.5.

## Chapter 3

# Crystals and Melts

### Introduction

It might be supposed that crystals and melts are so familiar that their properties would be self-evident. Our familiarity is, however, based largely on the crystal ice and the melt water, and the substance  $\text{H}_2\text{O}$  has such unusual properties that we would be seriously misled if we used this as a model for silicates, as we shall see below. The phenomena of melting and crystallization are as yet only imperfectly understood, and it is only recently that much attention has been paid to the atomic organization of liquids which turns out to have much importance for melting theory.

The classic treatise on crystals and melts is the 1903 work of Tammann, *Kristallisieren und Schmelzen* (Crystallization and Melting). This remarkable work is still of fundamental importance to students of the subject, and one finds reference to it in many research papers in the current literature. Tammann's work was developed without consideration of the atomic arrangement of matter which we call structure, and the modern treatise which gives the structure of crystals and liquids their appropriate emphasis is the book *Melting and Crystal Structure* by Ubbelohde (1965, 1979), already a classic, and a fascinating and readable work to which the serious student is commended.

## Definitions

A *crystal* is a region of matter characterized by periodicity. More precisely, it is a regular arrangement of atoms which occupy sites in the mathematical construct called a *lattice*. A crystal is said to have *structure*, a term which describes the combination of lattice sites, which are imaginary, with atoms, which are real. Most of us are accustomed to ascribing further characteristics to crystals. Among these are a definite chemical composition, which is to say that the crystal has a homogeneous distribution of atom species, ideally in a fixed proportion throughout the crystal, so that once a *unit cell* is defined as the smallest and simplest repeat unit required to reproduce the crystal by the operations of symmetry, we can suppose that every other unit cell is identical to the first. As a concept, this is helpful, but we must recall that it will not do for zoned crystals. In any event, the concept of definite chemical composition rightly demands that there be severe constraints on the kind and variety of atom species present in the crystal.

Under the term crystal we also comprehend a morphological meaning: a polyhedral form bounded by plane faces, or what is called a euhedral crystal. We shall ordinarily be concerned in this book with the structural definition of crystals and not the morphological one. The general designation solid (S) will be taken to imply the crystalline state, structurally defined.

A *liquid* is not so easy to define as a crystal, surprising as it may seem. Without doubt it is a substance of very low rigidity compared to the crystalline form of the same substance: it is a fluid. Also without doubt its component atoms are more highly disordered than those of a crystal, but it is a grave mistake to suppose that the atom positions in a liquid are random, because there is a certain degree of short range order, or in other words some measure of structure, although disorder increases with temperature. The chemical composition of a liquid is subject to far fewer constraints than that of a crystal, hence wide compositional variability is a characteristic of liquids in general, although liquid composition may be constrained artificially in experiments. In terms of compressibility, liquids lie between gases and solids, separated from each of these by orders of magnitude under certain conditions of temperature and pressure.

It is convenient to describe a liquid near its freezing point (or the beginning of its freezing range) as a *melt*. Since in this book we are concerned largely with equilibria between crystals and liquids, our liquids are best considered melts, whether natural magmas or synthetic liquids. Melts, since they lie by our definition near the freezing point, are those liquids whose structure is most ordered, and about whose structure we are most concerned. Melts and crystals are both referred to as *condensed phases*, in contrast to the vapor state.

As melts are superheated (i.e. heated above their equilibrium with crystals) they pass into liquids in the more general sense, and finally pass into the *vapor* (or *gaseous*) state. A vapor has the unique property of filling

its container, hence is in principle easier to define than a liquid. It is, like liquid, a fluid, but one in which the atoms are more dispersed and more disordered. It is more compressible, less rigid, and less dense than liquid. At temperatures and pressures below a certain value called the *critical point*, vapor and liquid form an interface with each other. At a given pressure below the critical point, a liquid passes into a vapor (boils) at a fixed value of temperature. Above the pressure of the critical point, liquid passes continuously into vapor with rising temperature, by becoming more and more disordered and less and less dense, so that the distinction between liquid and vapor fades above the critical point. Critical points involving the merged identity of liquid and vapor are of no importance<sup>1</sup> in petrologic systems without a volatile component, because the vapor pressure of silicate liquids is very small. Such critical points may be of interest, however, when a volatile component such as water is present.

In principle, critical phenomena between solid and liquid states of matter are possible, but they have not been conclusively demonstrated to exist,<sup>2</sup> and they need not concern us further.

## Water: A Familiar but Bad Example

It is pertinent to discuss briefly the states of matter of the compound H<sub>2</sub>O, and to point out how unusual this compound is relative to the silicates with which we shall be chiefly concerned.

The most obvious difference between H<sub>2</sub>O and silicates is that the former is liquid at room temperature, and is relatively close to its freezing point over the earth's surface. A more subtle difference, and one which is the source of much initial confusion among students of silicates, is that ice shows a negative change of volume on melting under normal conditions, so that ice floats in the sea and in cocktails, and the milk left too long on the winter doorstep extrudes its creamy top and cap from the neck of the bottle. That is, ice is less dense than water. This is true of remarkably few substances, among which are the elements Ga, Sb, and Bi. For all known rock-forming materials, the reverse is true, crystals being denser than their pure liquids, although there is some doubt about the relative densities of plagioclase feldspar and the complex liquids which are basaltic magmas.

Liquid water has a very low viscosity, resulting in hydrodynamic properties familiar to all. Silicate liquids, on the other hand, are very viscous; the melts used in glassmaking are more fluid than most silicate liquids, and many melts, for example feldspar liquids, cannot be poured because they are so viscous. Natural basalt lava may flow rather freely, of course, as

<sup>1</sup>Extraterrestrial petrology is excluded from this remark.

<sup>2</sup>See Ubbelohde (1965, p. 19–24) for discussion.

motion pictures of Kilauea and other eruptions show, but much of the hydrodynamic behavior of erupting lava is determined by small quantities of water vapor and other volatiles which diminish viscosity. The stiffness of silicate liquids and the fluidity of water are directly related to the differences in ordering of the two liquid structures. Water consists almost totally of individual molecules of  $\text{H}_2\text{O}$ , which, having only weak polarity and attraction for each other, are rarely hooked together. Silicate liquids, on the other hand, are dominated by  $(\text{SiO}_4)^{-4}$  tetrahedral groups, which have a relatively strong affinity for each other (by sharing corners) and for cations, so that there is a rather high degree of polymerization in silicate liquids which has a profound effect on their physical properties and their ability to nucleate on freezing.

Water, like most metals, freezes readily into crystals, and in ordinary circumstances cannot be quenched to a glass, because the molecules are so mobile that they very quickly arrange themselves in the pattern of the crystal once nucleation has begun. Silicate liquids, on the other hand, tend to be easily quenched to the glassy state, their molecules being so tangled up in such a sticky medium that they may require a relatively long time (hours, days, or months) to form crystal nuclei from which crystal growth may proceed. Moreover, crystal growth is slow once begun, because of slow diffusion rates in viscous silicate liquids. The reluctance of silicate liquids to nucleate in the laboratory is probably not accurately indicative of most natural events, since a natural magma is usually under a flow regime rather than a static regime, and a flow regime greatly increases the number and variety of sites favorable for nucleation. In static laboratory experiments, the ability to quench silicate liquids to glass is of fundamental utility, since this provides a *post facto* test for the presence of liquid at the temperature of the experiment, and allows interpretation of textural relations between crystals and "liquid" (now glass).

In summary, water is very different from silicate liquids in its low freezing point, its negative change of volume on melting, its viscosity, its degree of polymerization, its ease of nucleation and unquenchability. Water, however, is capable of dissolving in silicate liquids to an appreciable degree, and it is not surprising, in view of its unusual and contrasting properties, that even small amounts of water produce drastic changes in the behavior of silicate melts, as discussed in Chapter 19.

It is appropriate at this point to introduce the phase diagram for water, which summarizes some of the things we have said about volume change on melting and the critical point, and which contains some surprises at high pressure which ought to be common knowledge among students of the earth.

Figure 3.1 is the phase diagram for water, drawn approximately to scale, for low pressures. Ignoring for present purposes the finer points of phase diagrams which occupy most of this book, we can view Figure 3.1 simply

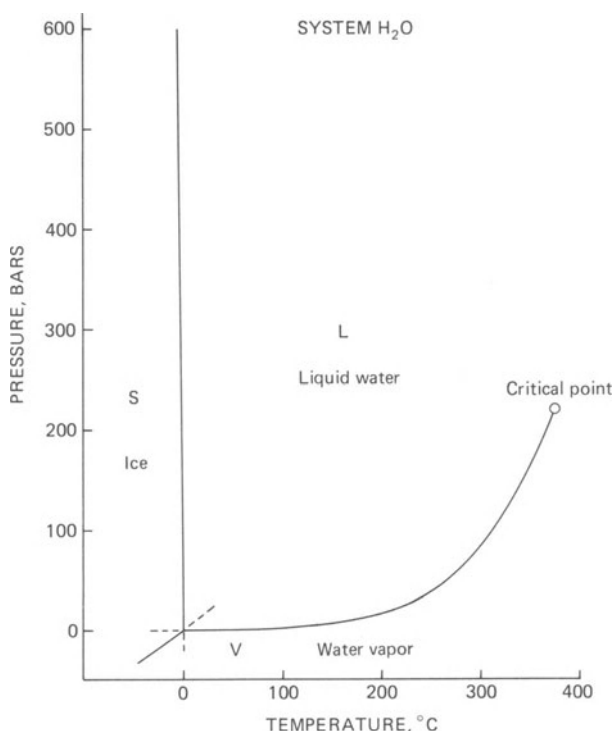


**Figure 3.1.** Part of the phase diagram for water, approximately to scale. The zero point of the Celsius temperature scale is on the S/L curve at one atmosphere in air (system H<sub>2</sub>O-air).

as a map, in two-dimensional pressure-temperature space, of the regions where ice, liquid, and vapor are stable. Ice is stable in the left portion of the diagram, at low temperatures, and its stability field is bounded by a line which is the *melting curve*, denoting equilibrium with liquid, and another line, the *sublimation curve*, denoting equilibrium with vapor. To the right of the melting curve, the field of liquid extends, at low pressures, to the *boiling point curve*, which denotes equilibrium of water and vapor. To the right of the sublimation curve, the field of vapor extends outward indefinitely and upward to the boiling point curve. The three curves separating regions of different states of matter intersect in a triple point, a unique point in  $P$ - $T$  space (i.e., having a single value of pressure and a single value of temperature), where all three states of matter coexist. Since we shall rarely be concerned with all three states of matter for single compounds of petrologic interest, we shall rarely encounter this sort of triple point, although triple points involving solid and liquid states of matter (3 solids, or 2 solids and one liquid) are common and important in petrology.

The melting curve, or *S-L* curve, is of special interest, as it has a negative slope, which results from the decrease of volume on melting discussed above. A decrease of volume on melting implies that pressure favors the liquid state (it being the denser), hence the negative slope.

Another feature of interest in Figure 3.1 is the critical point at 221 bars,<sup>3</sup> 373° C, where the separate identities of liquid and vapor merge and become indistinguishable. The liquid near this temperature is quite different in its properties from the melt near the melting curve, even though one may be changed continuously into the other.

Figure 3.2 shows the phase diagram for water at high pressures as well as low. This reveals seven different crystalline modifications (polymorphs) of ice, each of which has its own field of stability in *P-T* space. The negative melting curve of ice<sub>I</sub> terminates at a triple point with ice<sub>III</sub> and liquid, and no other form of ice has a negative melting curve, so this unusual aspect of water disappears above about 2 kbar pressure. Since

<sup>3</sup>One bar is close to one atmosphere of pressure (0.987 atm).

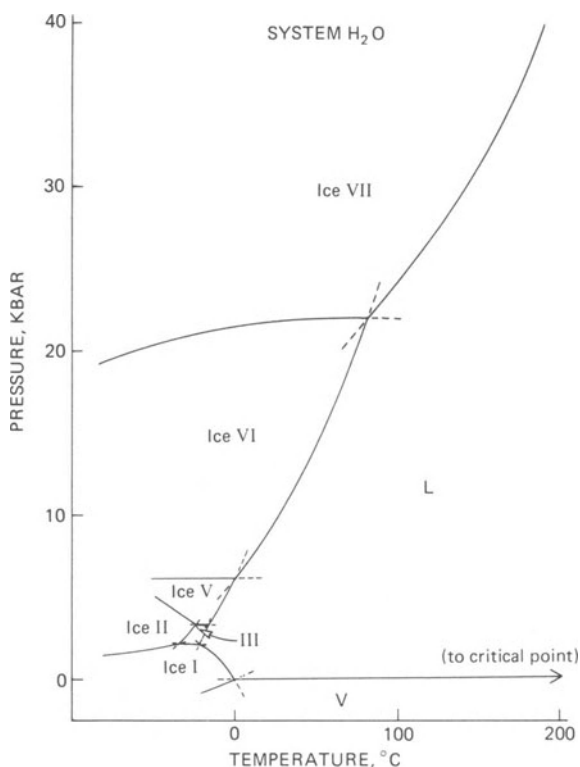


**Figure 3.2.** Phase diagram for water at high pressures, after Bridgman (references listed in Clark, 1966, p. 372). Ice IV is a metastable phase occurring in the *P-T* region of Ice V.

pressure favors the denser phase, and the higher polymorphs of ice melt with an increase in volume, the solid phase is favored, and higher and higher temperatures are required to melt ice at very high pressures. Note that at about 24 kbar, the melting point of ice<sub>VII</sub> is the same as the *boiling* point of water at atmospheric pressure!

## The Phenomena of Melting and Crystallization

The change from the solid to the liquid state involves a large jump in randomness of atom positions, from somewhere near non-random (ordered) in the crystal to highly random (disordered) in the liquid. The ordering of atoms or ions into specific sites in a crystal is, however, perfect only at 0° K, and from absolute zero to the melting temperature, disorder increases, sometimes in discrete jumps implying phase transformations, and sometimes smoothly. The underlying cause of disorder is the thermal motion of atoms, which increases smoothly with temperature above 0° K. The phenomenon of melting, then, is one of a discontinuous jump in disorder accompanying a change from solid to liquid state. The “disorder” of which we speak is of several kinds, both in crystal and liquid states. Among these are positional disorder, which relates simply to the mutual positions of atoms, as in crystal structure sites or in the liquid, and orientational disorder, which relates to the orientation of units of the structure such as molecules or polymers.<sup>4</sup>

That melts retain some degree of order, i.e. structure, is shown by a wide variety of indirect evidence, but also more directly by X-ray diffraction studies, which in some cases have demonstrated a quasi-crystalline structure in the melt, even to the degree of implying the existence of unit cells much like those of the crystal (Ubbelohde, 1965, p. 91). The structure of silicate melts is undoubtedly a matter of much importance to petrology, although little quantitative work has been done as yet. Effects related to melt structure are discussed briefly in Chapter 6, in connection with the melting of albite.

The changes which occur in the vicinity of the melting point in both crystals and melts are collectively referred to as *premonitory phenomena*.<sup>5</sup> In crystals, these phenomena can be related to vibrational disorder and to defects in the crystal structure. In melts, pre-freezing effects have been described by Ubbelohde (1965) as involving the formation of aggregates or clusters (perhaps “polymers” would be appropriate in silicates) which may serve as nuclei for spontaneous crystallization. The sum of these effects is such as to diminish the difference between solid and liquid states near the melting point.

<sup>4</sup>For a discussion of disorder and melting, see Ubbelohde (1965), Chapter 5.

<sup>5</sup>Ubbelohde (1965), p. 4; Chapters 11 and 12.

## Supercooling and Superheating

It is common knowledge that water can be supercooled, by slow abstraction of heat in the absence of impurities or motion, to temperatures well below the freezing point. The same is probably true of most silicate liquids, and supercooling is a quite general phenomenon in melts. Supercooling results from the fact that the nucleation of a crystal is a random process, requiring the accidental arrangement, in the melt, of atoms in the pattern of the crystal structure, after which a crystal nucleus may grow at a great rate. The presence of foreign particles or dislocations due to motion in the melt merely increases the probability of nucleation by affording a sort of substrate upon which atoms may become ordered. If such hetero-nuclei<sup>6</sup> are present in experimental work, supercooling is extremely difficult to achieve. With careful experimental control, however, it is found that a wide range of substances, including pure metals, halides, and molecular liquids, can be supercooled to about 80% of their Kelvin melting temperature. The recurrence of values around 80% suggests that this represents a fundamental limit of supercooling. Supercooling of this sort of magnitude is probably extremely rare in natural silicate melts, because of the presence of hetero-nuclei and shearing motion in the magma, and in fact it is a fair question whether any appreciable supercooling ever occurs in magmas. In experimental work, however, especially with viscous melts, supercooling may be a serious hindrance to experimental success.

Superheating of crystals above their melting temperature is a rare phenomenon, and usually amounts to only a fraction of a degree when it occurs. However, in crystals which melt to very viscous liquids, such as quartz or albite, superheating of as much as 300° has been reported. This emphasizes the fact that melting and crystallization are rate processes, and when a viscous melt with a high degree of structure is involved, rates of disordering and diffusion may become infinitesimally slow.

## Melting as a Function of Pressure

Most solid compounds, with the notable exception of ice<sub>f</sub> and a few others, have positive volume changes on melting, and therefore have positive melting curves in  $P$ - $T$  space, by the Clausius Clapeyron equation

$$\frac{\bar{S}_f}{(\bar{V}_L - \bar{V}_S)} = \frac{dP}{dT} \quad (3.1)$$

in which  $\bar{S}_f$  is the molar entropy of fusion, always positive, and  $\bar{V}_L$  and  $\bar{V}_S$  are the molar volumes of liquid and solid, respectively, their difference

<sup>6</sup>Ubbelohde (1965), p. 284.

being usually positive. It is then the normal expectation for silicate minerals to have positive melting curves, which they do in all known cases, in the absence of volatile components, at low to intermediate pressures.

The introduction of water to anhydrous silicate systems produces negative melting curves, because water dissolves in the melt to a greater extent than in the crystal, stabilizing the melt at a lower temperature as more pressure is applied to the vapor phase, by LeChatelier's principle. This is a most important effect for petrology because of the general availability of H<sub>2</sub>O in the earth's crust, and parts of the mantle, and because of the very large temperature differences between dry and hydrous melting curves for the same crystal. The effect on a number of silicate systems is discussed in Chapter 19.

## **Solutions: Solid and Liquid**

It is common experience that liquids are likely to be solutions, and natural magmas are no exception; they are in fact complex solutions of large numbers of components, of which only about ten are major. Most of the melts of interest to our present purpose will be solutions.

Most naturally occurring minerals are also solutions, called solid or crystalline solutions, of two or more end members which are stable in their pure state only in the absence of suitable contaminants, or at 0° K. The extent of solid solution is very limited in many minerals, and complete between end members in many others, for example in plagioclase feldspar at high temperatures. Except in rare cases, we shall be dealing with natural and synthetic crystals which show solid solution toward other compositions to a degree which should not be ignored, although we shall find it helpful to ignore this phenomenon temporarily, in some cases, to simplify presentation of chemical principles.

## Chapter 4

# The Phase Rule as a Tool

### Introduction

Phase diagrams are both constructed and interpreted in accordance with certain principles of physical chemistry embodied in what is known as the Gibbs phase rule. A working knowledge of the phase rule is essential for the effective use of phase diagrams. Such a working knowledge is very simple to acquire, since the phase rule is a very simple statement about the relationships of three variables. Like many rules, the phase rule conceals in its simplicity a very subtle, brilliant, and powerful chain of logical reasoning, and it is possible, perhaps even desirable for advanced students, to analyze phase diagrams from first principles without using the rule as a crutch. We shall use the phase rule as a tool, however, and the purpose of this chapter is to provide some fundamental definitions and a very rudimentary sketch of the principles upon which the phase rule rests. As we shall develop and use it, the phase rule is a part of what is called classical thermodynamics, the counterpart of which is statistical mechanics.

### Systems, Components, Phases, Variables, Equilibrium

A *system* may be defined as an assemblage of material bodies interacting among themselves. As generally used, the term implies that matter cannot be exchanged with the system's surroundings, a condition which is often explicitly stated by use of the term *closed system*. Heat can be exchanged

with the surroundings, so the temperature of the system may be externally controlled. Pressure may be applied to the system, and its volume thereby adjusted, again without the exchange of matter. A system may also be described as an arbitrarily chosen small part of the universe. Most of our systems will be made up from and described in terms of a few selected chemical compounds, such as for example diopside and anorthite, but the term system can also apply to a small region of the mantle undergoing melting, or to a magma flowing through a fissure, or any chosen part of such a magma.

An *open system* is a system which may undergo interchange of matter with its surroundings, usually limited interchange, so that the amount of one component, such as water vapor, may be controlled externally while the amounts of all other components remain fixed at their initial values. A container sealed by an osmotic membrane is a good example of such an open system, and a sealed capsule of platinum at high temperatures is a good example of such a membrane with respect to hydrogen, which diffuses easily through hot platinum. As a counter-example, a similarly-filled gold capsule under the same conditions is essentially a closed system, gold being impermeable to hydrogen, or very nearly so for most practical purposes.

A *component* of a system is a chemical constituent whose quantity may be independently and arbitrarily varied. In a closed system, the amounts of the various components are chosen at some initial time, and left unchanged during the process of interest. The simplest sort of component is an atom of a given chemical species, and the components of a system may, if necessary or convenient, be described and controlled in terms of masses of elements. If the expected chemical reactions so warrant, more complicated constituents, such as the metal oxides usually reported in a chemical analysis, may be chosen, or even constituents such as mineral formulae. Thus one and the same system could be described in terms of the four components Ca, Mg, Si, O, or the three components CaO, MgO, SiO<sub>2</sub>, or the two components CaSiO<sub>3</sub> and MgSiO<sub>3</sub>, or the single component Ca-MgSi<sub>2</sub>O<sub>6</sub>. Systems are described by the number (*c*) and identity of their components, for example, as follows:

The *unary* (*c* = 1) system CaMgSi<sub>2</sub>O<sub>6</sub>

The *binary* (*c* = 2) system CaSiO<sub>3</sub> – MgSiO<sub>3</sub>

The *ternary* (*c* = 3) system CaO – MgO – SiO<sub>2</sub>

The *quaternary* (*c* = 4) system Ca-Mg-Si-O

The choice of components is a matter of experience. It is mandatory to choose the smallest number, hence the most complicated identity, of components until experimental or theoretical experience dictates otherwise. It develops, for example, that choice of the single component CaAl<sub>2</sub>Si<sub>2</sub>O<sub>8</sub>

is often adequate for discussing the melting of pure anorthite, whereas in discussing accurately the melting of mixtures of diopside and anorthite the two components diopside and anorthite will not suffice, because diopside is not pure  $\text{CaMgSi}_2\text{O}_6$  in the presence of Al, and both crystals and melts must be discussed in terms of at least a ternary system, as discussed in Chapter 5.

A *phase* may be described as a homogeneous, mechanically separable part of a system. Phases are separated from one another by interfaces. Each mineral or crystal species or glass is a phase (*S*), each magma or liquid or melt is a phase (*L*), each vapor is a phase (*V*). In a system of many phases, many of these may be solid, but commonly only one (or zero) is a liquid, and only one (or zero) a gas. A system may be partly described by the number ( $\phi$ ) and identity of its phases. In the phase diagram for water at low pressure (Figure 3.1) each phase is a different state of matter, but as Figure 3.2 illustrates, there are numerous phases of ice which are all members of the solid state. The mistake of equating phases with states of matter must be avoided.

The criterion of mechanical separability is a potentially troublesome part of the definition of phase. The criterion means separability *in principle*, such as could be ascertained with a microscope. For example, it is quite feasible to separate the pyroxene and plagioclase from one another in a coarse gabbro, and in principle it is also possible to separate them in a very fine-grained basalt, although one would prefer to avoid such a task. But how good a microscope should one use to deduce separability? One may see fine exsolution lamellae in pyroxene, and conclude that these should be counted as a phase separate from the host pyroxene, but how about the different types of layers in a mixed-layer silicate (Zen, 1963), or the different domains in a feldspar crystal? Such subdivisions may reach such a small scale that chemical reactions with the external environment “ignore” the separate parts and respond only to the bulk crystal, although chemical reactions between or among the various subdivisions may still be imagined. In rare cases, therefore, the definition of a phase must be determined by experience, or at least theory, and tailored to the scale of the questions being asked.

*Variables* or *parameters* of state are quantities used to describe the state of a system. These fall into two classes, extensive and intensive. *Extensive* variables are those which depend on the size (mass) of the system or its parts, such as

Masses of phases (or of the system)

Volume of the system

Entropy (*S*) of the system

Enthalpy (*H*) of the system

*Intensive* variables are those which are *independent* of mass, such as

Temperature ( $T$ )

Pressure ( $P$ )

Concentrations of the components ( $X$ )

The object of the phase rule is to discover the minimum number of independent statements which must be made about intensive and extensive variables in order to describe the system completely. The phase rule applies only to systems in *chemical equilibrium*, which may be described as a state of no observable change in the masses of the various reactants and products, or a state in which chemical reactions proceed with equal rate in either direction. Chemical equilibrium also implies thermal and pressure equilibrium, so we should expect the system to be isothermal and isobaric at equilibrium. This definition excludes *local equilibrium*, which is a useful concept for dealing with systems in a chemical or thermal gradient, for example. The zoning of a crystal of feldspar represents a kind of local equilibrium.

It is useful to identify two kinds of chemical equilibrium. We shall most often be concerned with *stable* equilibrium, a state which represents the lowest free energy of the system under the specified  $P$  and  $T$ . Another kind, *metastable* equilibrium, represents a supposedly transient state of affairs wherein the system has not achieved the lowest free energy state, but looks and acts as though it were at equilibrium over the time scale of observation. This time scale may be indefinitely long, and for example, all igneous and metamorphic hand specimens of rocks are at metastable equilibrium, at room temperature, because the chemical reactions which should continue in cooling simply do not proceed at a finite rate near room temperature. If it were not for this fact, we could never observe the properties of minerals at high temperature which in fact are quenched in by prohibitively slow reaction rates. Other examples of metastable equilibrium are supercooled melts, and glass quenched from the liquid state. In most phase diagrams, solid lines denote stable equilibrium, and when produced beyond an intersection such as a triple point, are dashed to denote metastable equilibrium. A few examples of such *metastable extensions* are shown in the upper part of Figure 3.2, and at the triple point in Figure 3.1. The metastable extension denotes the fact that, at least in principle, reactions can be made to run just outside the true field of stability of the reactants. For example, supercooled liquid and vapor can coexist at metastable equilibrium in the field of ice, near the triple point. We shall not be greatly concerned with such phenomena in the context of this book, but the metastable state is important in much experimental work, and in the interpretation of natural rocks.

## The Phase Rule and Variance

Statements about components, phases, and variables may be marshalled into a formula known as the phase rule which gives the number of additional statements which must be made to define the system completely. It can be shown that, in a system at equilibrium, the number of variables which can be *independently* varied (without disturbing the equilibrium) is equal to the number of components in the system, plus two. The reasoning goes briefly like this. An equation describing the internal energy  $E$  of a system can be written

$$dE = TdS - PdV + \mu_a dn_a + \dots + \mu_k dn_k \quad (4.1)$$

where  $T$  is absolute temperature,  $S$  is entropy,  $P$  is pressure,  $V$  is volume,  $\mu$  is the chemical potential, or the partial free energy per mole of a component,  $n$  is the number of moles (i.e. amount), and  $a \dots k$  are each components of the system. Readers not familiar with chemical thermodynamics should not throw up their hands in horror, for what we propose to show does not require an understanding of all these terms. At equilibrium, by definition, entropy, volume, and amounts of components may not change, so their differentials equal zero:  $dS = 0$ ,  $dV = 0$ ,  $dn_i = 0$ . Therefore at equilibrium, equation (4.1) integrates to

$$E = TS - PV + \mu_a n_a + \dots + \mu_k n_k \quad (4.2)$$

We see now, merely as a book-keeping exercise, that the energy of the system depends upon two terms,  $TS$  and  $PV$ , and *as many other terms*  $\mu_i n_i$  as there are components. Hence the energy of the system, which is to say the state of the system, is completely described by  $c + 2$  independent variables.

These  $c + 2$  variables could all be extensive, such as the masses of phases, or partly extensive and partly intensive, such as  $T$  and  $P$ . If they all happened to be extensive, then specifying the number and identity of each phase present would serve to describe the system, or in other words we should need to make  $\phi$  statements, one for each phase, in order to describe the system. This condition of description can be written

$$\phi = c + 2 \quad (4.3)$$

and interpreted as meaning "when the number of phases equals the number of components plus two, the system is uniquely defined in terms of its intensive variables." In other words, there is only one temperature, one pressure, and one concentration of components in some phase when  $\phi = c + 2$  identifiable phases are present in the system. A corollary of this is that  $c + 2$  gives the maximum number of phases which can coexist at equilibrium.

If by chance some of the  $c + 2$  variables needed to describe the system

were *intensive* variables, then of course  $\phi < c + 2$ , i.e. the number of phases present is less than  $c + 2$ , and a certain number of intensive variables must be specified to describe the system completely. Let  $W$  be this number of intensive variables to be specified, and then

$$W = c + 2 - \phi \quad (4.4)$$

which is the Gibbs phase rule.  $W$  is an integer commonly called the variance, and is also commonly denoted  $F$ , for *degrees of freedom*.

We can now see that for completeness, equation (4.3) should read

$$\phi \leq c + 2 \quad (4.5)$$

with the variance  $W$  giving the difference when the inequality applies.

We identify with  $W$  the intensive variables  $P$ ,  $T$ , and  $X$ . As an example, suppose  $W = c + 2 - \phi = 1$ ; the system is said to be *univariant*, and a *single* statement, either about pressure, or about temperature, or about the concentrations of components, suffices to describe the system completely. This is true whether  $c = 1$  and  $\phi = 2$ , or whether  $c = 19$  and  $\phi = 20$ . Suppose  $W = 2$ ; the system is *divariant*, and two statements, one each about two of the variables  $P$ ,  $T$ ,  $X$ , are required to describe the system completely, and so on.

The example chosen in equation (4.3) is one in which  $W = 0$ , and such a system with  $\phi = c + 2$  is *invariant*, a state which is very informative because for any particular set of  $\phi$  phases, it is unique.

The phase rule is thus a shorthand way of assessing the maximum number of intensive parameters which can change independently of each other without decreasing the number of coexisting phases in the system. The nature and utility of the phase rule becomes clearer with its actual application in the succeeding chapters.

## Chapter 5

# Diopside and Anorthite: Supposedly a Binary Eutectic System

### Introduction

This chapter introduces the study of phase equilibrium diagrams as models of natural rocks. The system to be described is simple, yet it furnishes a neat example of what may go wrong with a model when a mineral chooses not to have the idealized composition you so hopefully expected it would. This complication, fortunately, increases rather than decreases the relevance of the model system to natural basalts.

This is a longish chapter, because it must cope with the basic principles of phase diagrams in the course of describing a single example. If it occasionally seems that we are straying rather far from basalts, it need only be recalled that a flanking maneuver is sometimes more productive than a frontal assault.

### Preparation and Melting of Diopside (Di)

Diopside is one of the easiest minerals to synthesize accurately, i.e. with correct composition, so easy in fact that the melting point of pure synthetic diopside is used as a calibration point (1391.5° C) in the Geophysical Laboratory temperature scale.<sup>1</sup>

<sup>1</sup>Temperature scales in silicate research are discussed by Sosman (1952). Despite the use of diopside as a calibrant, it actually has a small melting range (Kushiro, 1972), and the figure 1391.5°C refers to the upper limit of the range.

The ideal formula for diopside is  $\text{CaMgSi}_2\text{O}_6$ ; stated in oxides, convenient for experimental work,  $\text{CaO} \cdot \text{MgO} \cdot 2\text{SiO}_2$ . Each of these oxides may be obtained in a state of high purity. One uses reagent grade  $\text{CaCO}_3$  (calcite) as a source of CaO. MgO may be obtained commercially in high purity, although Mg metal may be even purer, and this may be oxidized in acid to form MgO, which is the mineral periclase. Many schemes have been used to obtain pure  $\text{SiO}_2$ . One of the simplest, probably as good as any, is to crush and mill optical grade quartz crystal in steel, and remove the contaminating steel magnetically and with acid. This quartz contains fluid inclusions, and is not yet pure  $\text{SiO}_2$  in its most reactive form, so one converts it to cristobalite by heating in a platinum crucible at  $1500^\circ\text{C}$  or higher for a number of hours (the tridymite/cristobalite transformation occurs at about  $1470^\circ\text{C}$ ). Complete conversion to cristobalite is seldom achieved short of several days, as found by Yoder and Schairer in 1968 (verbal communication), but the material is probably adequate for most purposes after a few hours of heating. One must temper the desire for complete conversion with the reality of heating platinum crucibles at these temperatures: whiskers of platinum will form in time on the surface of the charge, and one will be weighing a very heavy contaminant into one's silicate mixture. Schairer was also fond of pointing out that the quartz must lie *loosely* in the crucible (don't breathe on it!), or the volume changes on heating through the high-low quartz and high quartz-tridymite transformations will deform the crucible severely.

Given the suitable, desiccated starting materials, one simply mixes in a platinum crucible appropriate weights of  $\text{CaCO}_3$ , MgO, and  $\text{SiO}_2$  to form diopside (a 10-gm yield is convenient). Enough  $\text{CaCO}_3$  must be weighed in to yield the appropriate amount of CaO; the  $\text{CO}_2$  will escape on heating. The crucible with its charge is placed in a ceramic-lined, platinum-wound furnace and heated to around  $1500^\circ\text{C}$  for several hours, overnight for example. The charge is quenched by setting the crucible in a pan of water, the resultant glass is broken and knocked out onto a paper by hammering the crucible,<sup>2</sup> the glass is crushed in a steel mortar to mix it, tramp steel is removed with a magnet, and the charge is returned to the crucible and melted again. A few fusions suffice to produce a homogeneous glass. Homogeneity is checked by examining an immersion mount of a bit of the crushed glass under the microscope; the glass particles should all have the same refractive index and be free of any inclusions of undissolved material.

Once a pure, homogeneous diopside glass is obtained, it can be crystallized readily by holding it at  $1200\text{--}1300^\circ\text{C}$  overnight, or several times overnight if desired for better crystallinity. The resulting crystals are extremely small (usually much less than  $10\ \mu\text{m}$  in length), but give sharp X-ray peaks. They can be used in melting experiments by the quenching method (or by differential thermal analysis, which measures a discontinuity

<sup>2</sup>Hammering is not necessary if  $\text{Pt}_{95}\text{Au}_5$  is used, as the melt does not wet this alloy.

in temperature rise with constant application of heat, thus indicating the latent heat absorbed on melting). The quenching method<sup>3</sup> utilizes the fact that most silicate liquids can be converted to a glass by abrupt cooling (quenching). In the quenching method, a small amount (such as 10 mg) of crystalline diopside is wrapped in an envelope of platinum foil and suspended in a vertical-tube furnace by a fine platinum wire. A thermocouple is suspended beside the envelope, furnishing the temperature of the experiment. After heating at constant temperature for an hour or so, an electric current is applied to melt the platinum suspension wire, and the platinum envelope with its diopside charge falls into a dish of mercury, cooling to nearly room temperature in a few seconds. When examined under the microscope, the charge will be seen to consist of diopside crystals if the temperature was below the melting temperature, or of glass if above. With careful measurement of temperatures, runs at 1390° C yield crystals, and runs at 1393° C yield glass, indicating a melting point of  $1391.5 \pm 1.5^\circ \text{C}$ . Few silicate melting points can be determined so closely by this method; an uncertainty of  $\pm 3^\circ \text{C}$  to  $\pm 10^\circ \text{C}$  is more normal. Diopside has given consistent results and its melting point is now used routinely (along with NaCl, 800.5° C) for the calibration of thermocouples used in experimental work.

## Preparation and Melting of Anorthite (An)

Anorthite,  $\text{CaAl}_2\text{Si}_2\text{O}_8$  or  $\text{CaO} \cdot \text{Al}_2\text{O}_3 \cdot 2\text{SiO}_2$ , can also be synthesized readily. The sources of CaO and  $\text{SiO}_2$  have already been discussed in connection with diopside. Alumina,  $\text{Al}_2\text{O}_3$ , can be obtained commercially in high purity. Once again, the CaO is weighed in as  $\text{CaCO}_3$  with allowance for the escape of  $\text{CO}_2$ . The problems of synthesis are somewhat greater in this case, since  $\text{Al}_2\text{O}_3$ , better known as the mineral corundum or the gems ruby and sapphire, is highly refractory and doesn't dissolve easily in a silicate melt. The possibility of melting the  $\text{Al}_2\text{O}_3$  itself is precluded in ordinary work by its high melting point (2072° C), which is in excess of that of the platinum (1770° C) used as both container and furnace winding. At least three fusions at about 1600° C are made, each separated by a quench and rough crush of the glass, before the mixture is examined for homogeneity. After this, fusions are separated by finer crushing in a steel mortar, with magnetic removal of tramp steel, and are continued until no corundum grains remain and the glass has a homogeneous refractive index. The melting point of anorthite, determined by the quenching method, is taken as 1553° C, since it demonstrably lies between 1550 and 1555° C. There is some doubt that this compound melts (congruently) to a liquid of its own

<sup>3</sup>A description of the quenching method is given by Osborn and Schairer (1941).

composition at a single value of temperature. Corundum has been observed in the glass quenched from temperatures near the assumed melting point, and anorthite may in fact melt to corundum and a more lime-silicate-rich liquid over a small interval. The difficulty of thermal control and measurement at these high temperatures renders a precise answer to this question elusive.

## Preparation of Di-An Mixtures

It might be supposed that homogeneous glasses with compositions between pure Di and pure An would be made by melting weighed mixtures of the pure end-member glasses. For tactical reasons, however, a better approach is to make each composition from scratch, in 10 gm. batches, using the same starting materials as for the pure compounds, i.e.  $\text{CaCO}_3$ ,  $\text{MgO}$ ,  $\text{Al}_2\text{O}_3$ , and  $\text{SiO}_2$ . The principal reason for this is that the addition of almost anything ( $\text{MgO}$  in this case) facilitates the dissolution of  $\text{Al}_2\text{O}_3$  into the silicate melt, so it is easier to make a homogeneous glass of  $\text{Di}_{10} \text{An}_{90}$  composition than a glass of  $\text{An}_{100}$  composition. The ease of dissolution of  $\text{Al}_2\text{O}_3$  can be ascribed to the lower viscosity of the liquid when  $\text{MgO}$  is present. Pure diopside liquid is so runny that it can be poured, while silicate liquids rich in alumina are stiff as a board. It is to be presumed that liquids of lower viscosity tend to make better solvents, since they can carry away the solute components more rapidly.

Most silicate glasses are in like manner made directly to their composition from oxide mixes rather than from end-member compounds, for similar reasons. Alkalies, however, are usually added as disilicates to minimize alkali loss by volatilization.

For the study of a system such as Diopside-Anorthite, it is customary to prepare compositions at 10% intervals by weight. Additional compositions may be prepared at a later time if more precise experimental data are needed.

## T-X Plots: Liquidus and Solidus

The experimental study of a system such as Di-An proceeds by a determination of the beginning of melting (first appearance of glass in quenched runs) and end of melting (last appearance of crystals in quenched runs) for a series of compositions, determined by the quenching method described above under *Preparation and melting of diopside*. The information obtained from a series of experiments is best appreciated in graphical form, such as a graph of temperature versus composition, or  $T$ - $X$  plot. The ordinate is

conventionally temperature in degrees Celsius, and the abscissa, composition. In our examples,  $X$  will denote composition in weight percent, simply because weights are the experimentally convenient measures of amounts. Composition could be stated in other terms, for example molecular percent or mole fraction, which is the useful form for thermodynamic and crystal chemical calculations.

A typical  $T$ - $X$  plot (see Fig. 5.1) of a binary (two-component) silicate system consists of symbols or labels depicting solid, solid plus liquid, or liquid states at the termination of each run, and a collection of curves

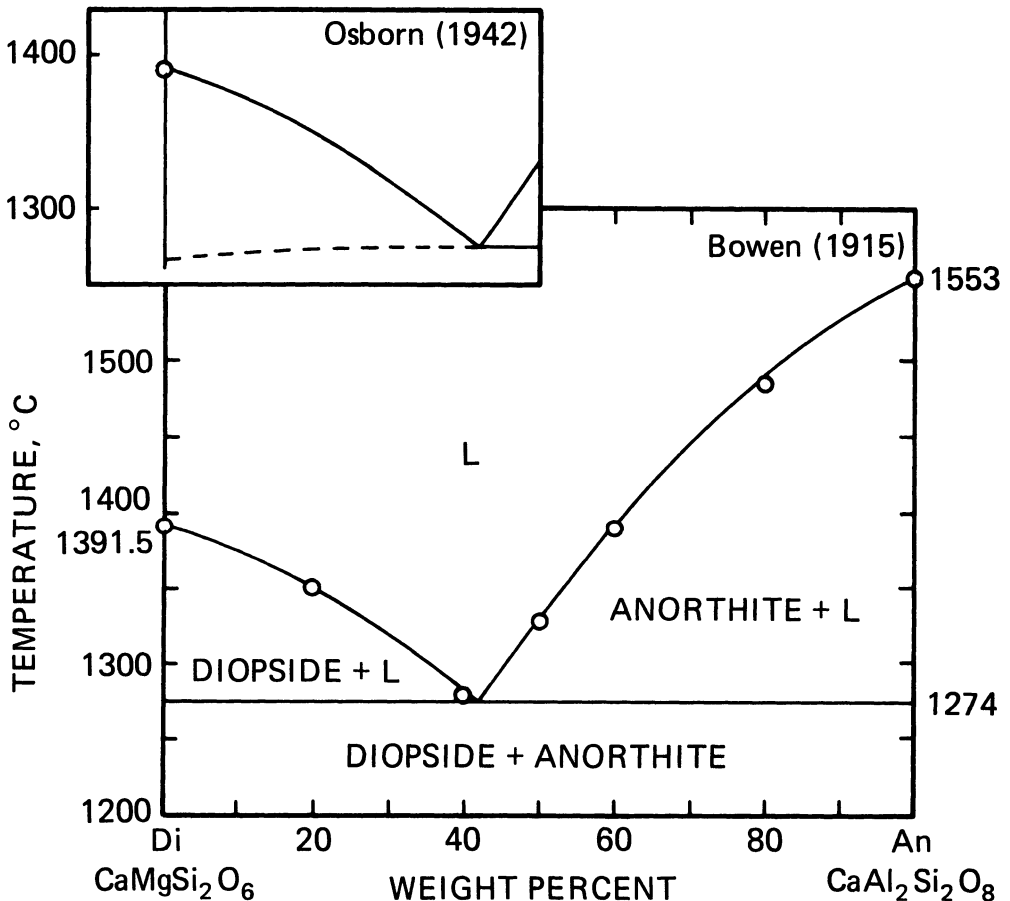


**Figure 5.1.** Phase equilibrium diagram of the system diopside-anorthite, after Bowen (1915), with inset after Osborn (1942). Experimental points defining the liquidus curves are circled. The Bowen diagram assumes a binary eutectic system. The Osborn diagram reflects the discovery that the system is not binary for diopside-rich compositions. This is because Al enters diopside crystals, as discussed later in the chapter.

marking the boundaries between regions of solid (S), solid plus liquid, and liquid (L).<sup>4</sup> These curves have special names, and properties which are very useful. The curve separating the liquid region from the solid plus liquid region is termed the *liquidus*, best remembered as the *curve which at any temperature gives the composition of the liquid in equilibrium with a specified solid*. The curve separating the solid plus liquid region from the solid region is termed the *solidus* or beginning-of-melting curve. If the solid consists strictly of crystals of end member composition, such as pure Di and pure An, the solidus is a *straight, isothermal line*, and the compositions of crystals lie at either end of the line. If solid solution occurs, and the system is strictly binary, the solidus is a *curve which at any temperature gives the composition of the crystals in equilibrium with a specified liquid*. The case where solid solution occurs is discussed more fully in Chapter 6.

## Diopside-Anorthite as a Binary System

On earth, the minerals diopside and anorthite occur with compositions very close to the ideal end members only in metamorphic rocks. In igneous rocks, formed at higher temperatures, they contain various “impurities”, or more realistically, show solid solution toward other components. It should not then surprise us if the crystals formed in high-temperature laboratory experiments showed compositions other than end-member compositions. This is the case with the system Di-An. There is evidence that the system is not strictly binary, in other words that solid solution does not involve only the two components, and we shall consider this problem at the end of this chapter. For the moment, let us pretend that the system is binary, and that all crystals are pure diopside or pure anorthite. In this way, we can illustrate some important principles of phase diagrams and igneous rocks.

The system Diopside-Anorthite has been studied at 1 atm pressure by Bowen (1915) and Osborn (1942). The  $T$ - $X$  plot, or equilibrium diagram, or phase diagram, essentially as determined by Bowen, is shown in Fig. 5.1. Small circles are shown at the melting points of the end members, diopside and anorthite, and at the final melting points of Di-An mixtures at several intervals along the  $X$  axis. These circles represent the midpoint between the two experimental runs bracketing the final melting point. For example, if a run quenched from 1352°C shows glass only, and a run quenched from 1348°C shows glass with a small amount of diopside crystals, the final melting point for the mixture (in this case  $\text{Di}_{80}\text{An}_{20}$ ) is plotted at 1350°C.

<sup>4</sup>A complete plot would also show a vapor ( $V$ ) region. However, the vapor pressure of silicates and silicate liquids is so low that the vapor state is usually ignored.  $T$ - $X$  diagrams are assumed to represent a pressure of 1 atm unless otherwise stated.

The collection of small circles showing the final melting points defines the liquidus curves. Above these curves the system consists only of liquid. It is clear from the shape of the liquidus curves that they will intersect somewhere near a composition of  $\text{Di}_{58}\text{An}_{42}$  and a temperature somewhere near  $1274^\circ\text{C}$ . The lowering of liquidus temperatures away from end members is a common phenomenon in silicate systems and one familiar to chemists under the title of *freezing point depression*. Either end member may be considered an ‘‘impurity’’ which, when added to the other, causes lowering of the final melting point (or first freezing point, depending on the point of view).

It is to be noted that none of the mixtures studied *within* the system melts at a single temperature, but that all show a melting *range* beginning (in this case) somewhere near  $1274^\circ\text{C}$  and terminating at the liquidus curve. The same is true of virtually all rocks, which crystallize or melt completely over a range of temperature rather than at a point. This apparently innocent fact is one of fundamental importance in petrology, for it accounts for the possibility of magmas changing their composition by removal of crystals, or fractional crystallization, about which we shall have much to say.

The horizontal line at  $1274^\circ\text{C}$  lies through the beginning of melting of each composition studied. In Bowen’s work, these all fell at the same temperature, within experimental error. The horizontal line is an *isotherm*, and it is also the solidus for the system in the sense that it locates the boundary between the fields of solid ( $S$ ) and solid + liquid ( $S + L$ ).

The point marked by the intersection of the two liquidus curves and the solidus ( $\text{Di}_{58}\text{An}_{42}$ ;  $1274^\circ\text{C}$ ) is termed the *eutectic*<sup>5</sup>; it lies at the one and only composition within the system which has a true melting point rather than a melting interval. The diagram of Fig. 5.1 is one of a *binary eutectic system*. The eutectic is an important phenomenon which we shall consider in more detail below.

## Variance in Di-An

We continue to assume that Di and An are pure compounds, and that the system is binary.

The phase rule may be stated as

$$W = c + 2 - \phi$$

We recall that the 2 signifies intensive parameters not dependent on the masses of things in the system; we may identify among these parameters

<sup>5</sup>Guthrie (1884) coined this term to signify the lowest-melting point in a system. Strictly speaking, this point in this system implies the coexistence of Di, An,  $L$ , and vapor which occurs at a single value of pressure well below 1 atm. Because of the low vapor pressure of silicate liquids, this strict definition is usually ignored.

temperature ( $T$ ), and pressure ( $P$ ). The phase rule reminds us that if we wish to describe the system completely, we shall need to make  $c + 2 - \phi$  statements about independent parameters. However, as long as we are considering experiments made at constant pressure (isobaric conditions), we are holding one variable ( $P$ ) fixed, and we need make only  $c + 1 - \phi$  statements to describe the system. Any other arbitrary restriction, such as on  $T$  (an isothermal restriction), would have the same effect. We may then rewrite the phase rule for isobaric conditions:

$$W_p = c + 1 - \phi$$

in which the subscript  $p$  reminds us that the variance is reduced by one because of an isobaric restriction. For present purposes, the constant pressure is 1 atm, since the experiments were performed at atmospheric pressure, i.e., with no pressure control.

We now need to evaluate  $c$ , and then  $\phi$ , in order to evaluate the variance. We have already decided that the system Di-An is binary ( $c = 2$ ), but let us consider some alternatives for the moment. The system contains only the elements Ca, Al, Mg, Si, and O, so at worst it would have to be described in 5 components (quinary system). If we believe that the cations are almost always bound to oxygens in melts and crystals, we could use as components CaO, Al<sub>2</sub>O<sub>3</sub>, MgO, and SiO<sub>2</sub> ( $c = 4$ , quaternary system). If we believed that the liquids and crystals can be described as mixtures of CaSiO<sub>3</sub>, MgSiO<sub>3</sub>, and Al<sub>2</sub>SiO<sub>5</sub> (an unlikely eventuality), we could describe the system as ternary ( $c = 3$ ). Another ternary alternative will be described at the end of this chapter. Finally, if we believe that the crystals and liquids can be described in terms of pure Di (CaMgSi<sub>2</sub>O<sub>6</sub>), pure An (CaAl<sub>2</sub>Si<sub>2</sub>O<sub>8</sub>) and liquid solutions or solid mixtures of these, we are justified in calling the system binary, as we shall now do. Hence we shall use the phase rule statement  $W_p = 3 - \phi$ .

As for  $\phi$ , the experiments, summarized in the phase diagram (Fig. 5.1), describe the phases for us. As the figure suggests, above the liquidus curves, there is but a single phase,  $L$ , and  $W_p = 3 - 1 = 2$ ; this is a *divariant region*.<sup>6</sup> Such a region is often described as having *two degrees of freedom*, and it is interesting to note that, under the restriction of constant pressure, this region is a *two dimensional field* in the phase diagram. Saying that  $W_p = 2$  is equivalent to saying that we must make two statements, one for each dimension, to know where we are in that part of the phase diagram labelled  $L$ . We must specify the temperature and the chosen *bulk compo-*

<sup>6</sup>Strictly speaking, it is an isobarically divariant region. If  $P$  is allowed to vary,  $W = c + 2 - \phi = 4 - \phi$  and the region of  $\phi = 1$  is truly trivariant. Whenever  $W_p$  is written, it must be remembered that the variance is under *restriction* and is always one less than the unrestricted variance  $W$ . This understanding will be assumed in the following pages.

sition<sup>7</sup> of the system in order to plot a point in the  $L$  field, for example 1500°C and  $\text{Di}_{50}\text{An}_{50}$ .

On either of the liquidus curves in Fig. 5.1, there are two phases, either  $\text{Di} + L$  or  $\text{An} + L$ , depending on the curve. In this case  $W_p = 3 - 2 = 1$ , and the system is *univariant* for any point on either of the liquidus curves. It is interesting to note that, with the restriction of constant pressure, univariance corresponds to a *one* dimensional line. Saying that  $W_p = 1$  is equivalent to saying that we need make only one statement (about one dimension) to plot a point in the  $S - L$  part of the phase diagram. For example, given the identity of the phases as  $\text{An} + L$ , one need only specify the temperature as 1328°C to be informed from the phase diagram that a liquid of composition  $\text{Di}_{50}\text{An}_{50}$  coexists with crystals of pure An. (One learns nothing of the *bulk* composition, which could lie anywhere between  $\text{Di}_{50}\text{An}_{50}$  and  $\text{Di}_{10}\text{An}_{100}$ , but that is immaterial as far as chemical reactions at equilibrium are concerned.) Alternatively one could specify the composition of the liquid in equilibrium with crystals of pure An as  $\text{Di}_{50}\text{An}_{50}$ , and learn from the diagram that the temperature for such a situation is 1328°C.

There is a unique point, the eutectic, in the diagram of Fig. 5.1 at which the two liquidus curves intersect at the solidus. Since the liquidus curves specify equilibrium between  $\text{Di} + L$  on the one hand and  $\text{An} + L$  on the other hand, the eutectic apparently involves an equilibrium among all three,  $\text{Di} + \text{An} + L$ . Here and only here,  $\phi = 3$ , and  $W_p = 3 - 3 = 0$ ; the eutectic is an *invariant point*. Notice again the correspondence between variance and dimensions, both being zero in this case.<sup>8</sup> Saying that the variance is zero is a most informative statement, since nothing further need be said to learn from the phase diagram that the temperature is 1274°C, and that the liquid has the composition  $\text{Di}_{58}\text{An}_{42}$  and coexists with pure Di crystals and pure An crystals.

The regions between the liquidus and solidus curves are convenient places for labels, and for plotting bulk compositions at specified temperatures, but no phases lie within them. They may each contain an infinite number of horizontal (isothermal) *tie lines* connecting points on the liquidus with the appropriate ordinate, in other words, tying liquids of appropriate composition to the (unchanging) compositions of the crystals with which they coexist. On any of these tie lines can be plotted a bulk composition. The tie lines and bulk compositions are usually omitted in phase diagrams except during graphical analysis, which is described below.

<sup>7</sup>“Bulk composition” is a term used to describe any chosen mixture within a system for purposes of discussion; it is so called to help distinguish the total composition from the individual compositions of crystals or liquids. It is very important to remember that the system is defined by the bulk composition chosen, which may not change during any single process or experiment.

<sup>8</sup>The true eutectic (see footnote 5, above) involves  $\text{Di} + \text{An} + L + V$ ,  $\phi = 4$ , and is truly invariant, i.e.  $W = 4 - 4 = 0$ .

Below the solidus is a region where crystals of Di and crystals of An coexist (in proportions dependent on the bulk composition). Here  $\phi = 2$ , and it is clear that  $W_p = 3 - 2 = 1$ . However, if we ask what must be specified to plot a point in this field, it appears that both  $T$  and a bulk composition  $X$  are required, and this suggests that  $W_p = 2$ . This dilemma may be resolved by saying that we know of no reactions between Di and An in this region, and therefore that criteria of chemical equilibrium are irrelevant, hence we need not concern ourselves with variance here. This is not a totally satisfactory way out, but it is perhaps sufficient for present purposes.

### The Lever Rule

When crystals coexist with liquid in a binary system, it is possible (except when liquid is at a eutectic) to know the relative percentages of each ( $S$  and  $L$  is  $l/(s + l)$ ); similarly the fraction of  $s/(s + l)$ , and the sum of  $s$  and  $l$  is permits the quantitative use of phase diagrams in the analysis of crystallization and melting. The treatment of relative percentages is a simple graphical procedure based on the *lever rule* or *rule of moments*. This rule is best described by a sketch, Fig. 5.2, of a lever sitting on a fulcrum. The fulcrum is labelled BC for "bulk composition" and the ends of the lever are labelled  $S$  for the position of the solid (or crystal) and  $L$  for the position of the liquid. Lever lengths are labelled  $s$  and  $l$ . In the illustration it is clear that  $l$  outweighs  $s$  because of occupying a longer arm of the lever. Quantitatively, the fraction of the total mass of the system represented by  $L$  is  $l/(s + l)$ ; similarly the fraction of  $s/(s + l)$ , and the sum of  $s$  and  $l$  is 1. To convert fraction to percentage only requires multiplication of the fraction by 100. For example, if  $l = 9$  (in arbitrary units of length—millimeters are convenient), and  $s = 3$ , the fraction of  $L$  is  $9/12 = .75$ , or 75%, and the fraction of  $S$  is  $3/12 = .25$ , or 25%. We shall frequently use the symbol  $F_L$ , for *fraction of liquid remaining* (or produced).

The only problem with the lever rule lies in knowing which side of the bulk composition fulcrum to label  $l$  and which to label  $s$ . This problem is

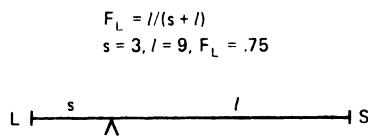
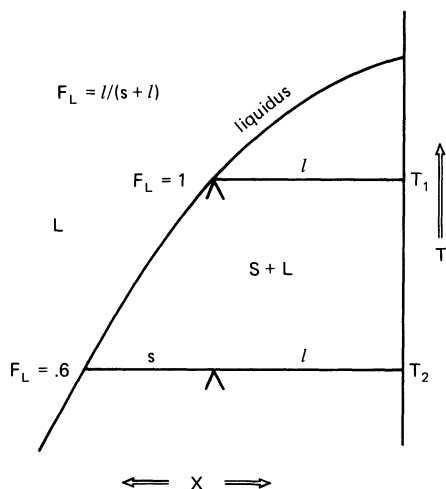


Figure 5.2. Principle of the lever rule.



**Figure 5.3.** Example of the lever rule.

easily solved by a commonsense analysis. If the fulcrum lies *at* the liquidus (see Fig. 5.3) at a certain temperature  $T_1$ , the bulk composition is practically in the liquid field and the entire lever is represented by  $l$  (to the right of the fulcrum), and  $s = 0$ . At a lower temperature ( $T_2$  in Fig. 5.3), the proportion of crystals has, logically, increased, and the end of the lever labelled  $s$  has grown while  $l$  remains the same length. The  $l$  end of the lever is always the end *away* from the liquidus curve with respect to the fulcrum, and the  $s$  end is always away from the crystal composition (the ordinate in this case).

The accurate application of the lever rule requires that a phase diagram be redrawn from the original data on a much larger scale than that of a textbook page, but a semiquantitative treatment with small scale drawings will serve to illustrate most of our points. This comment does suggest that experimental petrologists would perform a useful service by fitting curves to their data by numerical methods and expressing these fits analytically, so that the lever rule might be applied by computation.

## Nature of the Eutectic: Isothermal Melting and Crystallization

If one pursues the lever rule of Fig. 5.3 in the context of the  $An + L$  field of Di-An (Fig. 5.1), one quickly discovers that, since  $L$  has fixed length, there is some liquid left at a temperature of  $1274^\circ$ , when the liquid has just reached the eutectic composition, no matter where the original bulk composition lay. We also know, from the fact that  $W_p = 0$  at the eutectic, that neither temperature, nor the composition of the liquid, nor the compositions of crystals of Di or crystals of An may change as long as the liquid remains

at E. Furthermore, we comprehend from the diagrams that a minute decrement of temperature below  $1274^{\circ}$  results in solid Di + An only, without liquid. It is apparent that an unusual event occurs at E, namely the isothermal crystallization of liquid to yield a completely solid mass of Di and An crystals. The lever rule is of no use while the liquid is at E, the ratio of crystals to liquid being no longer a function of  $T$ , but only of time, dictated by the rate of heat loss from the system. The reaction at E is  $L = S + \text{cals}$  (calories) on crystallization and  $S + \text{cals} = L$  on melting. Furthermore, since the liquid does not change composition, it must produce (on crystallization) Di and An in exactly its own ratio, i.e. 58:42, so the isothermal, eutectic crystallization of 1 g of liquid yields .58 g of Di crystals and .42 g of An crystals. Melting consumes crystals in these proportions to yield the eutectic liquid.

Although isothermal crystallization of rocks is probably rare in nature, isothermal melting may be common at the sources of magmas in the mantle. In either event, the process should be kept in mind, since the heat to be removed (or added) is only the latent heat of crystallization (or fusion), and not the heat required to change the temperature of the body as well.

## Analysis of Crystallization and Melting

We are now sufficiently prepared with concepts and jargon to proceed to the *denouement* of any experimental system, a complete analysis of the course of crystallization (or melting) of any selected bulk composition. We begin with crystallization, using Fig. 5.4, which is again the system diopside-anorthite with some graphical constructions and a doubled scale of temperature.

Choosing  $\text{Di}_{40}\text{An}_{60}$  as a bulk composition, we imagine a liquid of this composition at temperature  $T_1$ . There is one phase,  $L$ , and  $W_p = 3 - 1 = 2$ . As the liquid is cooled, nothing happens except for some ordering of atoms in the liquid until the An +  $L$  liquidus curve is reached at  $T_2$ . At this moment, the first few crystals of An begin to form;  $\phi = 2$ , and  $W_p = 3 - 2$  equals 1. After an infinitesimal drop in temperature, the liquid has a composition of nearly  $\text{Di}_{40}\text{An}_{60}$ , but is shifted slightly to the left of this, by an amount corresponding to the mass of An crystals which have formed. Cooling is continued, and more crystals of An form as a result. If we take stock of the situation at  $T_3$ , we deduce from the diagram that the weight of An crystals formed by this time is given by  $s_3/(s_3 + l_3)$ , or about 20%. At this point the liquid, having yielded so much pure An, is correspondingly poorer in An and richer in Di, with a composition of about  $\text{Di}_{50}\text{An}_{50}$ . Continued cooling, as before, enriches the liquid in Di by the crystallization of An, and as before, further crystallization of An requires both heat loss

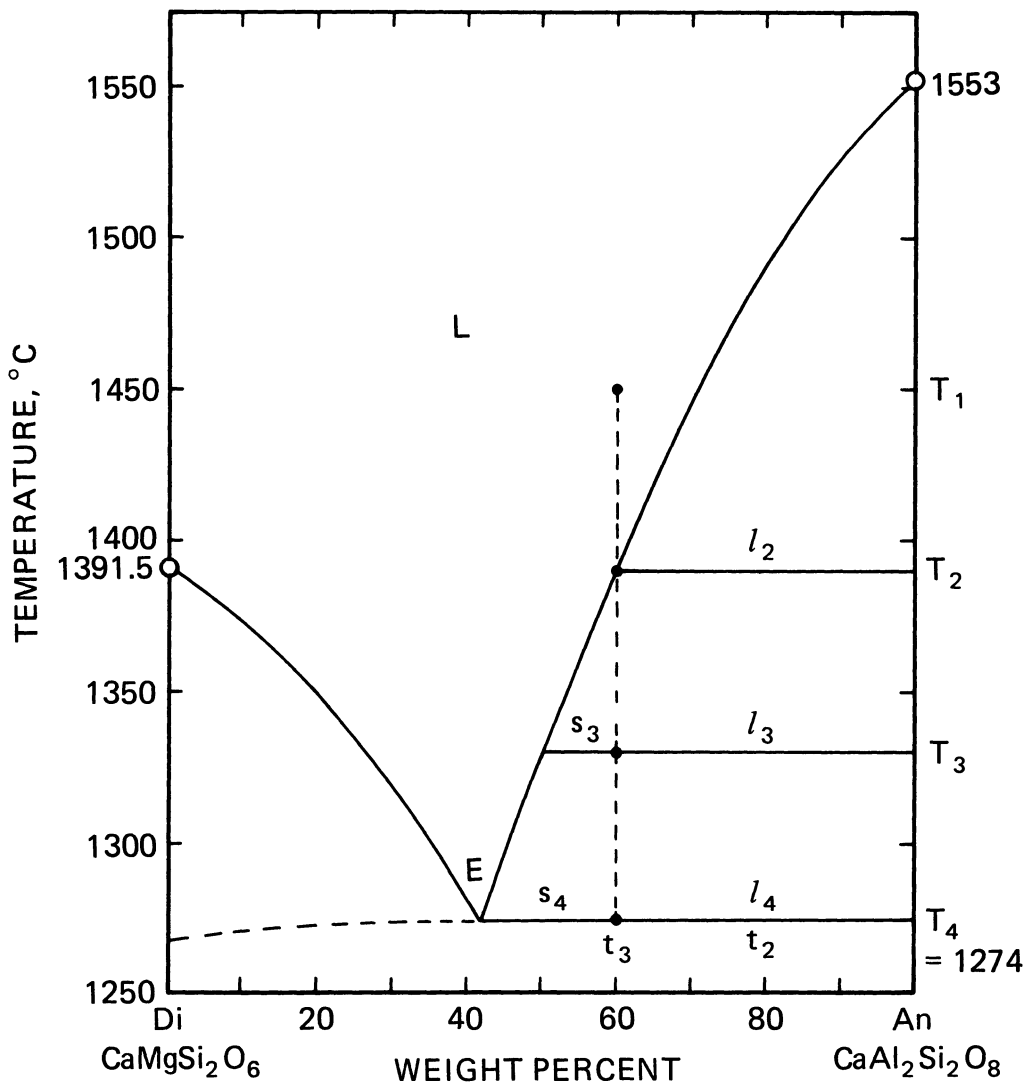


Figure 5.4. The system diopside-anorthite redrawn with an expanded temperature scale. Base of diagram measures 10 cm.

and temperature drop. The slope of the liquidus at any point is the resultant of a horizontal vector away from An and a vertical vector downward.

Eventually, cooling of the liquid with its charge of An crystals, accompanied by further crystallization of An, brings the liquid to  $T_4$  and the eutectic composition. The instant before the temperature reaches  $T_4$ , the amount of An which has crystallized is given by  $s_4/(s_4 + l_4)$ , or about 31%.

At the instant when the liquid reaches the eutectic E and temperature  $T_4$ , crystals of Di begin to form for the first time. With continued removal of heat, the temperature remains at  $T_4$  while the liquid of composition E produces crystals of Di and An in the ratio of E (58:42) until it is used up, at which moment the entire mass is solid, and the temperature drops with further removal of heat.

We now turn our attention to the history of the solids produced by this entire process. The bulk composition having been chosen as  $\text{Di}_{40}\text{An}_{60}$ , it is clear that the entire crystallization process should yield 40% Di, 60% An by the time the liquid is used up. During the cooling from  $T_2$  to  $T_4$ , the *total solid composition* (TSC) lay on the An ordinate. While the liquid lay at the eutectic, at temperature  $T_4$ , crystallization of Di as well as An gradually moved the TSC away from An, along the isotherm  $T_4$ , as a function of time ( $t$ ). There was a time  $t_2$  when the TSC was  $\text{Di}_{20}\text{An}_{80}$ , for example, although we cannot know when that was from the phase diagram. Eventually there was a time  $t_3$  when the TSC reached  $\text{Di}_{40}\text{An}_{60}$ , the bulk composition, and it was at this moment that the last of the liquid disappeared.

The same principles apply to crystallization initially in the Di field, as for example that of a bulk composition  $\text{Di}_{80}\text{An}_{20}$ . An initially homogeneous liquid of this composition will, on cooling, first produce crystals of diopside and consequently move toward An down the Di + L liquidus curve till it reaches E. At E, isothermal crystallization of Di and An crystals will ensue until the liquid is gone and the Di:An ratio of the solids reaches 80:20.

Complete equilibrium melting in such a system as Di-An follows the reverse path of complete equilibrium crystallization. A mixture of crystals of Di and An, say in the ratio 40:60 will, when heated to  $T_4$  (Fig. 5.4), begin to melt with the production of a eutectic liquid of composition E. Crystals will melt in the ratio Di:An 58:42 until all the Di is gone; the lever rule shows that 69% of the mass can be melted in this way without a change of either liquid composition or temperature. With continued input of heat, the liquid dissolves An crystals and hence becomes richer in An, moving along the liquidus curve as the temperature rises. At  $T_3$ , the percentage of liquid is 80%, as it was on crystallization, and at  $T_2$ , the last An crystal is taken into solution and the liquid may be heated without further chemical reaction.

## Fractional Crystallization and Melting

The crystallization and melting processes described above are *equilibrium* processes, in which all of the crystals present remain in perfect equilibrium with the liquid. We may imagine another process, perfect *fractional* crystallization in which crystals are removed from equilibrium with the liquid as soon as they are formed. This process has a comparatively minor effect in a binary eutectic system, but is of much importance in many other types

of systems. In the crystallization of Di-An, using the example of Fig. 5.4, removal of An crystals from the main body of liquid, perhaps by settling or floating, has no new effect on the composition of the liquid during its trip down the An + L liquidus curve. The only effect of perfect fractionation of An is to hide An crystals from view, so that if we could sample the liquid at any temperature we should see only a trace of An crystals, and we might think the liquid had always had the bulk composition of its liquidus composition at the moment of sampling. After the liquid has reached the eutectic E, removal of Di and An crystals will of course have no effect on the composition of the liquid, and both the liquid and the rock which it produces will have the eutectic composition. Probably the only geologically meaningful application of this fractional crystallization process is that liquids or rocks appearing to have eutectic compositions may have started out with bulk compositions far from the eutectic, only to have lost crystals continuously or intermittently during crystallization.

For the process of fractional crystallization in general, it is convenient to define the *instantaneous solid composition* (ISC) as the composition of the solid being crystallized from the liquid at any moment. In the example just given, the ISC consists simply of An crystals at first. When the liquid reaches point E, the ISC jumps discontinuously from An to E, the eutectic ratio of diopside and anorthite. We shall occasionally refer to such jumps in the ISC as "rock hops," and it should be emphasized that such discontinuities in the ISC path can occur *only* with fractional crystallization. In equilibrium crystallization, the ISC is identical to the TSC, and the TSC path must be continuous in *all* processes.

Perfect fractional melting is a process in which liquid is continuously removed from the crystals as soon as it is formed. Using the example of  $\text{Di}_{40}\text{An}_{60}$  as a solid starting mixture, perfect fractional melting will yield liquid of composition  $\text{Di}_{58}\text{An}_{42}$ , at isothermal conditions, as long as any diopside crystals remain. During this time, the TSC moves from  $\text{Di}_{40}\text{An}_{60}$  to  $\text{Di}_0\text{An}_{100}$ , which is precisely the reverse of the crystallization process while the liquid is at E. As soon as the last crystal of diopside is converted to liquid, however, the remaining solid mass consists only of An crystals. *No further melting* can take place until the temperature rises from  $1274^\circ\text{C}$  to  $1553^\circ\text{C}$ , the melting point of pure An, at which point all the An melts isothermally. In this latter part of the process, fractional melting is strikingly unlike equilibrium melting, since there is a large temperature interval over which no liquid is generated. Under equilibrium conditions, the entire original bulk composition would have been melted at about  $1387^\circ$ , whereas fractional melting leaves a substantial crystalline residuum of pure An which is far more refractory than the initial bulk composition. This is a geologically important consequence, since it implies that fractional melting even under isothermal conditions in the mantle may leave behind crystalline residua which are unlikely to melt again unless a very large amount of heating occurs.

The temperature gap in fractional melting is of further interest in phase equilibria because it emphasizes the fact that, in equilibrium melting, An crystals dissolve in the liquid at temperatures far below their own melting point.

For fractional melting in general, it will be convenient to define the *instantaneous liquid composition* (ILC) as the composition of the liquid being formed, at any instant, from the crystals. The ILC is precisely analogous to the ISC; in the example at hand, it originates at E and, after a hiatus in melting, jumps discontinuously to An. The *total liquid composition* (TLC) is the sum over all ILC's produced during a melting process, and it must equal the bulk composition of the system at the end of melting. Thus in the present example, the TLC begins at E and, with the eventual addition of liquid An, moves toward An until it reaches the bulk composition. We never speak of the TLC in connection with any process except fractional melting, for in all other processes the TLC simply equals liquid, *L*. Similarly, the ILC is confined to fractional melting; in all equilibrium processes and in fractional crystallization,  $ILC = TLC = L$ . To recapitulate the behavior of the four kinds of *paths* in crystallization and melting, the TSC, TLC and *L* paths are always continuous; ISC and ILC paths may be discontinuous, providing us with rock hops and liquid hops.

## Complications

It is now time to face the fact that Di-An is not a truly binary system. This is true largely because Di is not a pure compound of composition  $\text{CaMgSi}_2\text{O}_6$  in the presence of certain impurities, in this instance  $\text{Al}_2\text{O}_3$ . Before enlarging on this statement, however, it is appropriate to make some general remarks on limited solid solubility.

## Binary Solid Solutions in General

Many binary eutectic phase diagrams are known to have the form shown in Fig. 5.5, in which the compounds A and B exist in the pure state only at their respective melting points. At all lower temperatures, the solid phase  $A_{ss}$  is a limited solid solution (subscript ss) toward B, and the solid phase  $B_{ss}$  is a limited solid solution toward A. The mutual solubilities of solid A and solid B increase with falling temperature from the melting points of pure A and pure B, reaching maxima at the eutectic temperature. The curves which give the composition of  $A_{ss}$  in equilibrium with liquid and the composition of  $B_{ss}$  in equilibrium with liquid are the *solidus* curves. Below the temperature of the eutectic,  $T_e$ , the mutual solubilities of A and B

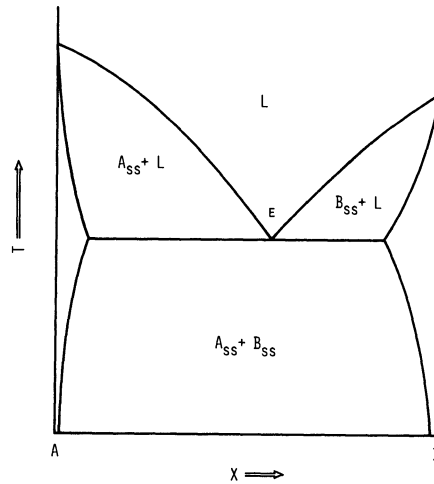


**Figure 5.5.** Idealized binary eutectic system.

commonly *decrease*, presumably reaching zero at  $0^{\circ}\text{K}$ . The curves which give the composition, at any temperature, of  $A_{ss}$  and  $B_{ss}$  in equilibrium with each other are part of a curve termed a *solvus*. The region between these limbs of the solvus is often referred to as a *miscibility gap*. The solvus curve in this case is intersected by a beginning-of-melting isotherm, but a solvus may be wholly within the solid field or, rarely in silicate systems, wholly within the liquid field.

We shall not dwell further on the properties of solvi at this juncture, except to point out that some degree of mutual solubility between solid end members of a binary system is inevitable at temperatures above  $0^{\circ}\text{K}$ , and indeed must be present in Di-An. However, in this system, as in many geologically significant systems, mutual solubility is often not detected at ordinary levels of precision, and is therefore ignored.

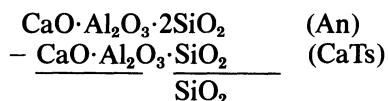
## Non-binary Solid Solution: The Role of Al in Pyroxene

If we consider the prospects for mutual solubility between Di and An from a crystal-chemical point of view, we can see why such solubility should be extremely limited. The small  $\text{Mg}^{++}$  ion would rattle around like a pea in a box in the larger  $\text{Ca}^{++}$  site in anorthite, and tend to decrease the stability of the structure. The other diopside-forming cations, Ca and Si, are already present to a sufficiency in An. Turning to the diopside structure, we again find no prospects in the Ca and Si from anorthite, but the Al ion is quite another matter. Al can enter diopside, although not necessarily in the form of the anorthite molecule.

There are several ways in which  $\text{Al}^{+++}$  may enter a pyroxene structure. That it does enter in nature is shown by the fact that most natural pyroxene analyses show  $\text{Al}_2\text{O}_3$  as a major constituent. The mineral augite is characterized in Dana's *Textbook of Mineralogy* as "aluminous pyroxene" (Ford, 1932). A number of hypothetical "pyroxene molecules" containing Al have been proposed as end members toward which diopside might show solid solution. Among these is CaTs, the *calcium Tschermak's molecule*,  $\text{CaAlAlSiO}_6$ . This compound is not found as a mineral, but it can be synthesized in the laboratory, and studies by the quenching method show that single crystals can be grown having compositions toward CaTs from Di. CaTs being, like An, a member of the system  $\text{CaO-Al}_2\text{O}_3\text{-SiO}_2$ , it is clear that An is capable of furnishing the constituents of CaTs for solid solution in Di. It is almost certain (Kushiro and Schairer, 1970) that the diopside crystals observed in the system Di-An incorporate significant amounts of CaTs "stolen" from anorthite.

## A Relevant Graphical Treatment

The effect of stealing CaTs from anorthite to make more pyroxene is to enrich liquids in silica.<sup>9</sup> This can be shown chemically from the following subtraction:



The exchange can be studied in a more general way chemographically, by examining part of the system  $\text{CaO-Al}_2\text{O}_3\text{-MgO-SiO}_2$  (CAMS). This quaternary system can be represented compositionally as a three-dimensional figure, a tetrahedron, shown in perspective in Fig. 5.6. This is an X-X plot, i.e. a strictly compositional plot to examine the purely geometrical relationships between components and phases. The front face of the tetrahedron is the ternary system  $\text{CaO-Al}_2\text{O}_3\text{-SiO}_2$  (CAS); the floor is the ternary system  $\text{CaO-Al}_2\text{O}_3\text{-MgO}$  (CAM); the left rear face is the ternary system  $\text{CaO-MgO-SiO}_2$  (CMS), and the right rear face is the ternary system  $\text{Al}_2\text{O}_3\text{-MgO-SiO}_2$  (AMS). A line (altitude) bisecting the front face from  $\text{SiO}_2$  to CA (i.e.  $\text{CaO} \cdot \text{Al}_2\text{O}_3$ ) contains the composition of both An and CaTs. The position of An can easily be plotted in the CAS triangle as follows. An is  $\text{CaO} \cdot \text{Al}_2\text{O}_3 \cdot 2\text{SiO}_2$ , hence the C:A ratio is 1:1, hence An must lie on the CA-S line. The CA:S ratio is 2:2, hence An plots halfway along the CA-S line. (Another trick is to plot, in turn, lines from each corner of the CAS triangle: from C to A:S = 1:2, and from A to C:S = 1:2, the line from S to C:A =

<sup>9</sup>CaTs need not come from crystalline An, but from the normative An in the liquid.

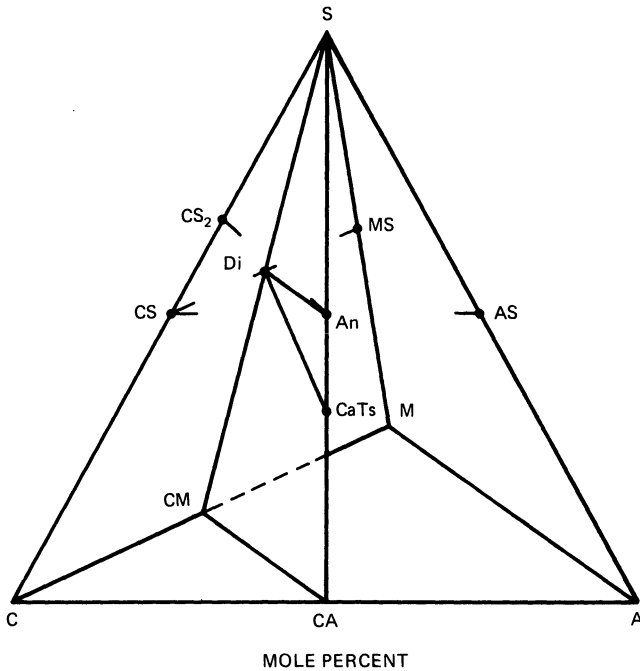


**Figure 5.6.** The tetrahedron CAMS, the system  $\text{CaO-Al}_2\text{O}_3\text{-MgO-SiO}_2$ . The CM-CA-S plane is shown in Fig. 5.7.

1:1 having already been plotted.) The position of CaTs is plotted in similar fashion: CaTs is  $\text{CaO} \cdot \text{Al}_2\text{O}_3 \cdot \text{SiO}_2$ , with C:A:S = 1:1:1, so the composition plots at the center of gravity of the triangle, i.e. at the junction of lines from each apex to the 1:1 point on each opposite side.

A further point of chemographic interest is that An lies midway on the line from CS ( $\text{CaSiO}_3$ ; wollastonite, Wo) to AS ( $\text{Al}_2\text{SiO}_5$ ; kyanite, sillimanite, andalusite).

The left rear face (CMS) of the tetrahedron contains a bisecting line S-CM on which lies the composition of Di. Di is  $\text{CaO} \cdot \text{MgO} \cdot 2\text{SiO}_2$ , or CMS 1:1:2; like An, it plots halfway along the altitude of the triangle. Of collateral interest, it also plots halfway between CS (= Wo) and MS ( $\text{MgSiO}_3$ ; enstatite).

It now appears that the system Di-An can be treated successfully in terms of the plane CM-CA-S, which contains all the solid phases in the tetrahedron of importance to our problem. This plane, a ternary system, is sketched in Fig. 5.7a. Fig. 5.7b is a distorted blow-up of the central portion of CM-CA-S, showing qualitatively the expected solid solution from Di toward CaTs. The join<sup>10</sup> Di-An lies across the CM-CA-S plane, and one

<sup>10</sup>When considered as part of a larger system (CAMS), a subsystem such as Di-An is commonly referred to as a join.

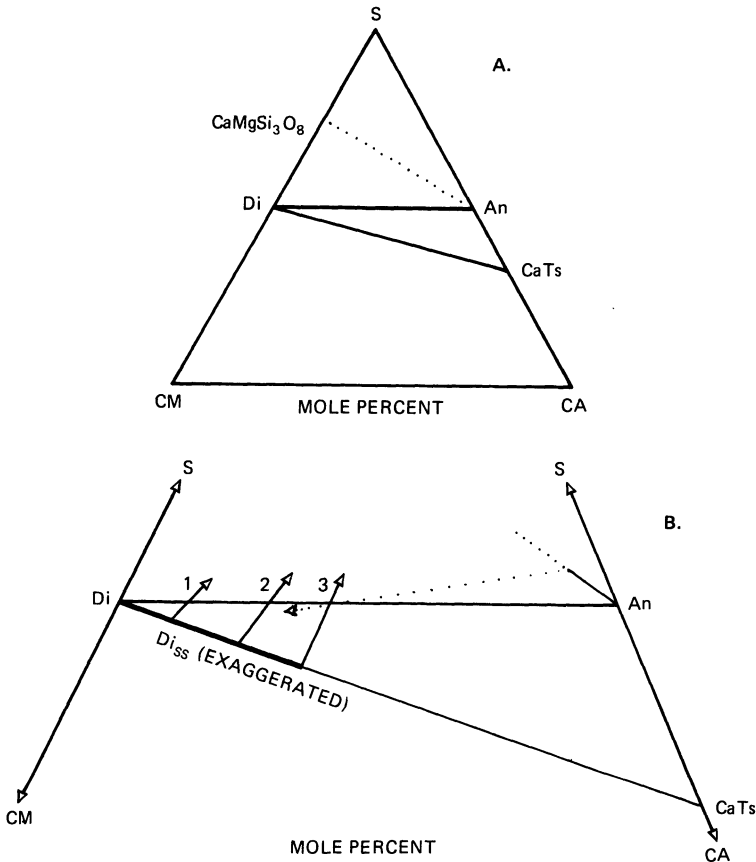


**Figure 5.7.** Solid solution of diopside toward CaTs (calcium Tschermak's molecule). A shows the entire CM-CA-S plane, and B shows the central portion of that plane. Dotted lines show effects of solid solution toward  $\text{CaMgSi}_3\text{O}_8$  from An.

may imagine the  $T$ - $X$  plot of Fig. 5.1 arising out of the page from this line. Temperature information is thereby lost, the  $T$ - $X$  plot being projected along its  $T$  axis onto the page. Compositional information is preserved. We see that bulk compositions truly in Di-An, such as 1, 2, and 3, will yield crystals, not of pure Di, but of solid solutions toward CaTs, or  $\text{Di}_{\text{ss}}$ . Since these crystals lie on the CM-CA side of the Di-An line, they must coexist with liquids, indicated by arrowheads, on the S side of the Di-An line. The tie line connecting two phases ( $\text{Di}_{\text{ss}}$  and  $L$ ) in such a ternary plot must pass through the bulk composition if no other phase is present. Conversely, any second phase must lie on a straight line connecting the first phase and the bulk composition from the first phase, by the same reasoning as shown in the subtraction on p. 54.

Diopside is not the only phase that shows solid solution in this system. As might be expected from the general case shown in Fig. 5.5, anorthite

shows some solid solution as well, in this case toward the join CMS and probably toward the component  $\text{CaMgSi}_3\text{O}_8$  (Murphy, 1977). Such a tendency is illustrated by the dotted lines in Fig. 5.7. If we assume that bulk composition (3) in Fig. 5.7b represents the cotectic composition, then the crystallization of anorthite will tend to counteract the effect of CaTs in the diopside, but as the arrows show, the anorthite effect is weak in its ability to counteract the silication of the cotectic liquid.

## Petrologic Consequences

It is clear from this graphical analysis that entry of Al into Di causes enrichment of the liquids in  $\text{SiO}_2$ ; upon cooling, they must become progressively more and more silica-oversaturated with respect to the join Di-An. This is true of all liquids from the eutectic E to, but not including, pure diopside. This is an interesting discovery, since we shall be much concerned with the over- or under-saturation of liquids with silica during fractional crystallization, and clearly the entry of CaTs into diopside must cause oversaturation in this case.

As to phase rule considerations, it is apparent that the system Di-An is at least ternary, perhaps rigorously confined to the plane  $\text{CaO} \cdot \text{Al}_2\text{O}_3 + \text{CaO} \cdot \text{MgO} + \text{SiO}_2$  in the system CAMS. The phase rule must then be written  $W_p = 4 - \phi$ , so that all the equilibria we have discussed are of a higher variance by one than we had assumed. The assemblage  $\text{Di}_{\text{ss}} + L$  is divariant ( $W_p = 2$ ); and the assemblage  $\text{Di} + \text{An} + L$  is univariant ( $W_p = 1$ ), and not a eutectic assemblage at all. A four-phase assemblage, probably  $\text{Di} + \text{An} + \text{SiO}_2 + L$ , is required for a ternary isobaric eutectic, and the three-phase assemblage  $\text{Di} + \text{An} + L$  merely lies on a line leading to the four-phase point. The non-binary nature of Di-An was noted and discussed by Osborn (1942), who found the solidus, shown as an isotherm in our Fig. 5.1, to curve downward slightly toward the Di side of the diagram.

## Summary of Basic Principles

Diopside and anorthite, two important components of basaltic magma, form an approximately binary system of the eutectic type whose lowest melting point,  $1274^\circ\text{C}$ , is more than  $100^\circ\text{C}$  below that of Di alone and more than  $250^\circ\text{C}$  below that of An alone. This temperature, where Di, An, and  $L$  all coexist, and where a unique composition ( $\text{Di}_{158}\text{An}_{42}$ ) is completely liquid, is not far above those measured in natural basaltic lavas ( $1200 \pm 30^\circ\text{C}$  for most basalts). Intermediate mixtures of Di and An appear to form a reasonable, though greatly oversimplified, model of basalt. From this model, one learns

that fractional crystallization does nothing to the ultimate composition of the liquid, although it can produce liquids approaching the “eutectic” composition which may be separated in space from their fractionated crystals. Fractional melting of diopside-anorthite mixtures is capable of producing substantial quantities of “eutectic” liquid while leaving behind a highly refractory anorthite residuum which will remain unmelted in a further temperature rise of well over 250°C.

Incorporation of Al into diopside, almost surely as  $\text{CaAlAlSiO}_6$ , may help to account for a silica-oversaturation trend in some basaltic liquids. It also lends itself to a straightforward example of chemographic analysis in a multicomponent system, a technique which is of great value in thinking about both rocks and the complex model systems which represent them.

## ***G-X* Diagrams**

The  $G$  stands for the Gibbs function or the Gibbs free energy, a function which is minimized at equilibrium. The partial molar free energy or chemical potential  $\mu$  can be used as well. The  $X$  stands for composition, as before. In  $G-X$  diagrams  $X$  is best plotted in mole units rather than weight units. The purpose of discussing  $G-X$  diagrams is multiple. In the first place, they give us an intuitive understanding of what phase diagrams are all about, an understanding which in fact can prevent us from drawing incorrect phase diagrams. In the second place, they emphasize the fact that phase diagrams are mere symbols of more profound thermodynamic truths, and they remind us that if the behavior of  $G$  with composition is known as a function of  $T$  and  $P$ , then phase diagrams can be calculated *a priori*. Many people have in fact assumed that the day would soon arrive when we could cease experimentation and calculate everything we want to know from first principles. Unfortunately this is not generally the case (although it is sometimes well worth doing), because very often the melting experiments are inherently more sensitive generators of information than the calorimeters used to find the Gibbs energy. Here we shall emphasize the use of  $G-X$  diagrams as intuitive guides to the nature of phase diagrams.

The bottom part of Fig. 5.8 is a schematic  $T-X$  diagram of Di-An. Above it are drawn five *isothermal*  $G-X$  diagrams for different temperatures marked on the  $T-X$  diagram ( $T_5$  is not marked, but lies below  $T_4$ ). In all five  $G-X$  diagrams, the liquid is described by a continuous, convex-downward curve. This curve changes position and shape with temperature, but is always convex down. It shows that the free energy of a melt of a pure compound is locally maximum, and is diminished by dilution with a second component, to a minimum at some special value of  $X$ . The free energy of a mechanical mixture of two pure solid compounds is directly additive, so

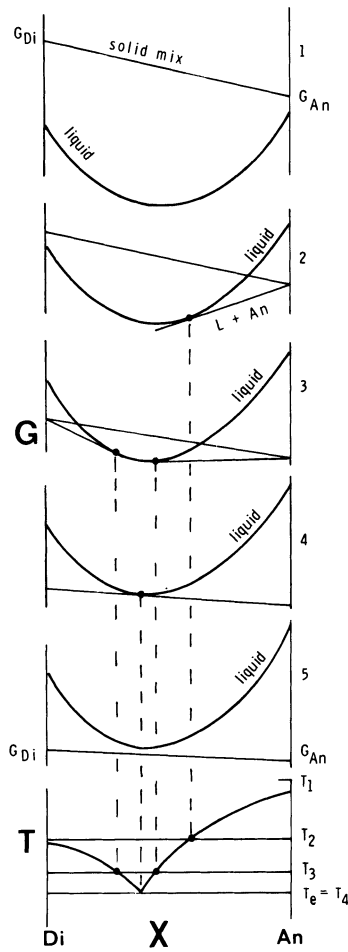


**Figure 5.8.** Superimposed Gibbs energy ( $G$ - $X$ ) and  $T$ - $X$  diagrams for the system diopside-anorthite, ignoring solid solution.

it varies linearly as a function of molar  $X$  (for discussion see Zavaritskii and Sobolev, 1964).

In part 1 of Fig. 5.8, the temperature ( $T_1$ ) is above the melting point of An and no crystals are present. The  $G$ - $X$  diagram proclaims this because, at equilibrium,  $G$  is minimized, and for all  $X$  the melt has lower  $G$  than any combination of crystals. Moreover, note that  $G$  of  $An_L$  falls below  $G$  of  $An_S$ , wherein  $L$  and  $S$  signify liquid and solid. This means that anorthite melt is stable relative to anorthite crystals. At the melting point of An, the  $G$  values of  $S$  and  $L$  would coincide. If anyone wonders why the liquid and solid curves are placed as they are, the answer is, in Eddington's immortal words, because I put them there. They are drawn so as to be compatible

with the known  $T$ - $X$  diagram. *In principle* they could be drawn from experiments involving heats of solution and entropies, but *in fact* they are drawn to explain the observed geometry of the melting diagram, and they are schematic.

In part 2 of Fig. 5.8, representing temperature  $T_2$ , a tangent to the liquid curve can be drawn from the  $G$  of pure An crystals; for any point on this tangent,  $G$  for the system is minimized relative to  $G$  for either liquid or crystalline mixture alone. This signifies the stability of anorthite crystals with liquid of a certain composition given by the point of tangency. To the left of this point, liquid has everywhere a lower  $G$  than any combination of crystals, and the system there is evidently still liquid. The isotherm  $T_2$  in the  $T$ - $X$  diagram portrays the conventional statement of these facts. At  $T_3$ , two tangents to liquid occur, one each from diopside crystals and anorthite crystals. There are now two  $S + L$  equilibria at this temperature, separated by a small region in  $X$  where liquid alone is stable. Finally, at  $T_4$ , the eutectic temperature, Di, An, and eutectic liquid all lie on a single line, signifying the invariant coexistence of these three phases. At  $T_5$ , somewhere not far below  $T_4$ , any mechanical mixture of solids is minimized relative to liquid, and no liquid occurs. Note that the free energy of the liquid is by no means undefined at  $T_5$ ; it is just not minimized anywhere with respect to solids, so liquid is not stable.

Further examples of  $G$ - $X$  diagrams are given in succeeding chapters.

## Chapter 6

# Plagioclase: The System An-Ab

### Introduction

The feldspar of basalts is by no means pure anorthite, but instead an intermediate plagioclase near  $An_{50}$ . This means that we could much improve the Di-An model of basalts if we could study a model of  $Di-An_{50}$ , or in other words part of the ternary system Di-An-Ab. It would be folly to do this, however, without first examining the nature of all the binary combinations, An-Ab and Di-Ab as well as Di-An, already discussed.

The system An-Ab, or the plagioclase system, turns out to be a binary system with continuous and complete solid solution between the end members.<sup>1</sup> As such, it is a famous example of such a system, and an excellent one for illustrating the properties of such systems as well as for revealing some important geological principles, most notably that of fractional crystallization. The plagioclase system was first successfully studied by Bowen (1913), although it was the subject of the first investigation at the Geophysical Laboratory (Day and Allen, 1905), a study remarkable for its pioneering efforts and frustrations before the advent of the quenching method.

<sup>1</sup>As far as we know this is strictly true at high temperatures and low to moderate pressures. It is not true at metamorphic temperatures, or at high pressures.

## Preparation and Melting of Albite

Anorthite having been discussed in Chapter 5, we need discuss only albite before turning to the binary system. Albite is not a straightforward composition to synthesize, and its melting point determination encounters severe problems.

Albite,  $\text{NaAlSi}_3\text{O}_8$  is related to anorthite,  $\text{CaAl}_2\text{Si}_2\text{O}_8$ , by the exchange  $\text{NaSi} \rightleftharpoons \text{CaAl}$ . It is thus more siliceous and less aluminous, and contains an alkali cation in place of an alkaline earth cation. Stated in terms of oxides, the composition is  $\text{Na}_2\text{O} \cdot \text{Al}_2\text{O}_3 \cdot 6\text{SiO}_2$ , or 1:1:6. The synthesis is in principle like that of anorthite; the sources of silica and alumina are identical, and the source of  $\text{Na}_2\text{O}$  is  $\text{Na}_2\text{CO}_3$  converted from the bicarbonate  $\text{NaHCO}_3$ . The first step is to make a sodium disilicate glass ( $\text{Na}_2\text{O} \cdot 2\text{SiO}_2$ ) from the carbonate and pure silica. This glass lies in the binary system  $\text{Na}_2\text{O} - \text{SiO}_2$ , and forms a compound whose melting point is agreeably low,  $874 \pm 3^\circ\text{C}$  (Schairer and Yoder, 1971). The mixture of carbonate and silica must be heated very slowly, over many days, to bring about the slow escape of  $\text{CO}_2$ ; if the heating rate is too fast, an appreciable amount of the volatile Na will escape as well, and even with extremely slow heating, a small deficiency in final weight is usually noted, which is made up by an appropriate small addition of sodium carbonate. The final disilicate glass is crystallized, to avoid weighing errors due to absorption of  $\text{H}_2\text{O}$ , since the glass is very hygroscopic.

Albite glass is made by weighing and mixing appropriate proportions of sodium disilicate, silica, and alumina, and heating these slowly to the beginning of melting of  $\text{Na}_2\text{O} \cdot 2\text{SiO}_2 - \text{SiO}_2$ ,  $788 \pm 2^\circ\text{C}$ , followed by heating to  $1200^\circ\text{C}$ , with many successive fusions at  $1500^\circ\text{C}$  to  $1600^\circ\text{C}$ , separated by crushings, till all alumina is dissolved and the glass is optically homogeneous. The procedure, and a discussion of alkali loss, is reported by Schairer and Bowen (1956).

The melting point of albite is difficult to determine because of the reluctance of albite glass to nucleate crystals of albite, and difficulty encountered in melting albite crystals. The difficulties can be partly overcome by ordering the viscous melt for several months at successively lower temperatures above the melting point. Melts treated in this way will form sparse albite crystals when held for a few days at  $1110^\circ\text{C}$ , whereas freshly prepared melts are so disordered that no crystals will form even in five years at  $1025^\circ\text{C}$  (Schairer and Bowen, 1956). The ordering process has been aptly described as "acclimatization" by Schairer (1951), and falls in the class of pre-freezing phenomena discussed by Ubbelohde (1965, Chapter 12).

The high viscosity of albite melt not only slows down the ordering process in the melt, but also hinders melting, so that albite crystals can be superheated over short time scales. The melting point must therefore be determined by observation, in quenched charges, of whether the sparse

albite crystals are growing (faceted) and therefore below the melting point at the temperature of the experiment, or dissolving (rounded) and therefore above the melting point during the experiment. By such criteria, the melting point can be shown to lie between 1115°C and 1120°C, and is taken to lie at 1118°C (Greig and Barth, 1938; Schairer and Bowen, 1956).

## Liquidus and Solidus

The phase diagram for melting in An-Ab, as determined by the quenching method, is shown as a  $T$ - $X$  plot in Figure 6.1. The upper curve is the liquidus curve, which connects the melting point of An at 1553°C to that of

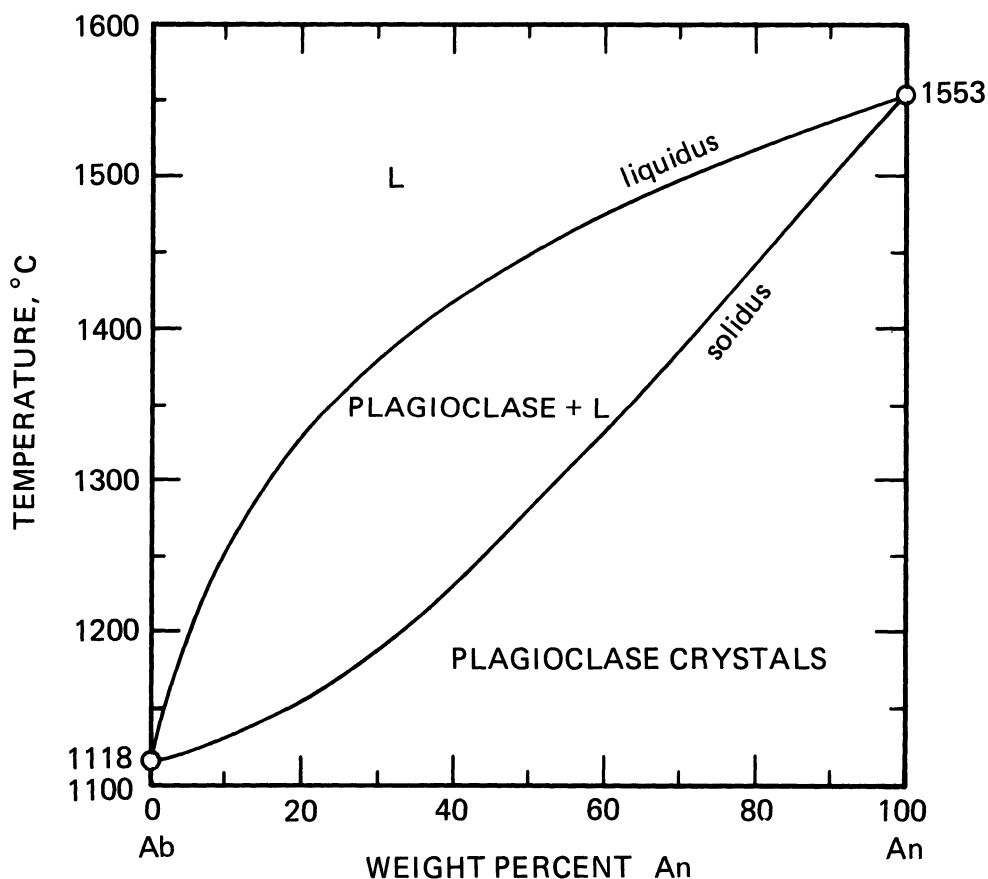


**Figure 6.1.** Plagioclase melting relations: the system anorthite (An)—albite (Ab) (after Bowen, 1913). The melting point of An is from Osborn (1942), and that of Ab from Greig and Barth (1938). Base of diagram measures 10 cm.

albite at 1118°C, and gives the composition of the liquid at any temperature. The lower curve is the solidus curve, likewise connecting the two melting points, which gives the composition of the crystalline solution of plagioclase feldspar at any temperature. Together, the two curves form what is often called a *melting loop*, or *S + L region*. The region above the liquidus is a one-phase region of liquid alone, and that below the solidus is a one-phase region of crystals alone.

## Variance

The number of components is two (An, Ab), so at constant (e.g. atmospheric) pressure  $W_p = 2 + 1 - \phi = 3 - \phi$ . Above the liquidus or below the solidus, the system is in one phase, *L* or *S*, and  $W_p = 2$ ; in these regions both temperature and composition must be specified to describe the system completely.

No single phase lies within the loop, but any point there represents a bulk composition at an isotherm, the intersection of the isotherm with the liquidus giving the liquid composition, and the intersection of the same isotherm with the solidus giving the composition of coexisting crystals. Both liquidus and solidus therefore denote two-phase equilibrium, and along these curves  $W_p = 1$ ; these are univariant curves. Stipulation of a single variable, temperature, is sufficient to describe the system completely as consisting of a liquid, say An<sub>36</sub>, coexisting with crystals, say An<sub>72</sub> for a temperature of 1400°C. The system is always univariant when both crystals and liquid are present; there is no invariant point between An and Ab. This means that fractional crystallization can exert a profound change on the composition of liquid, as we shall see.

## Lever Rule

A distorted sketch of part of the plagioclase loop is shown in Figure 6.2. The dashed vertical line labelled BC denotes the chosen bulk composition. At temperature  $T_1$ , the bulk composition lies at the liquidus, and the system is essentially all liquid.<sup>2</sup> The length of the lever *l* represents the amount of liquid. At the lower temperature  $T_2$ , the system is about half crystallized, as the equality of levers *s* and *l* indicates; the fraction of liquid remaining is given by  $l/(s + l) = 0.5$ . At temperature  $T_3$ , the liquid is virtually gone, and the system is virtually solid, as indicated by the existence of lever *s* only.

<sup>2</sup>(Although saturated with a trace of plagioclase crystals.)

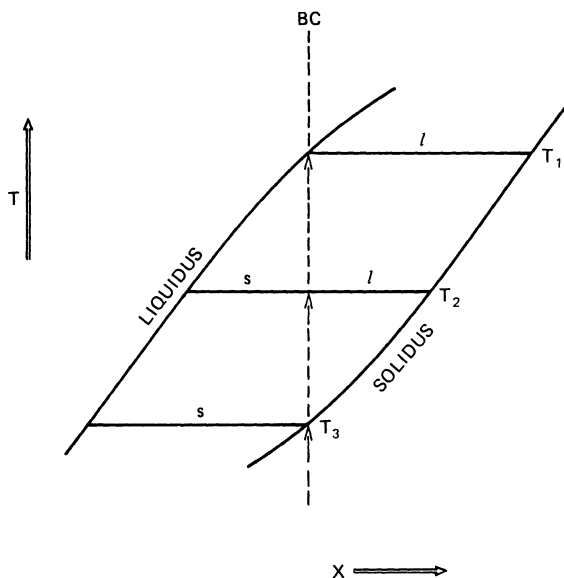


Figure 6.2. Illustration of the lever rule in a binary loop.

## Equilibrium Crystallization

The phase diagram is redrawn in Figure 6.3 with a few isothermal tie lines to illustrate the course of crystallization of a bulk composition  $An_{60}Ab_{40}$ . Upon cooling from above the liquidus, a melt of this composition begins to crystallize at  $1474^{\circ}\text{C}$ , where it first attains the liquidus. The first crystals to form, at this temperature, have the composition  $An_{86}$ ; clearly they are very calcic, and far different from the liquid in composition. As heat is removed and the temperature lowered, the liquid composition changes toward Ab along the liquidus curve and the total crystal composition changes toward Ab along the solidus curve. The change in liquid composition results from the removal from the liquid of crystals more calcic than the bulk composition. At the same time, as the diagram shows, an increase of Ab in the liquid necessitates an increase of Ab in the crystals. There is a partition ratio  $Ab_s/Ab_l$  which is always less than one, and which varies uniformly throughout the diagram. The variation of this partition ratio for the solidus is plotted in the upper part of Fig. 6.3. The change of total crystal composition to more and more Ab-rich values, so as to maintain equilibrium with liquid, demands that early-formed calcic crystals *react* with liquid to change, in the solid state, to more sodic crystals. This involves tetrahedral  $Al \rightleftharpoons Si$  exchange as well as octahedral  $Na \rightleftharpoons Ca$  exchange in the crystal structure, and if equilibrium is to be maintained, the temperature of the system must fall slowly enough to permit thorough intracrystalline diffusion

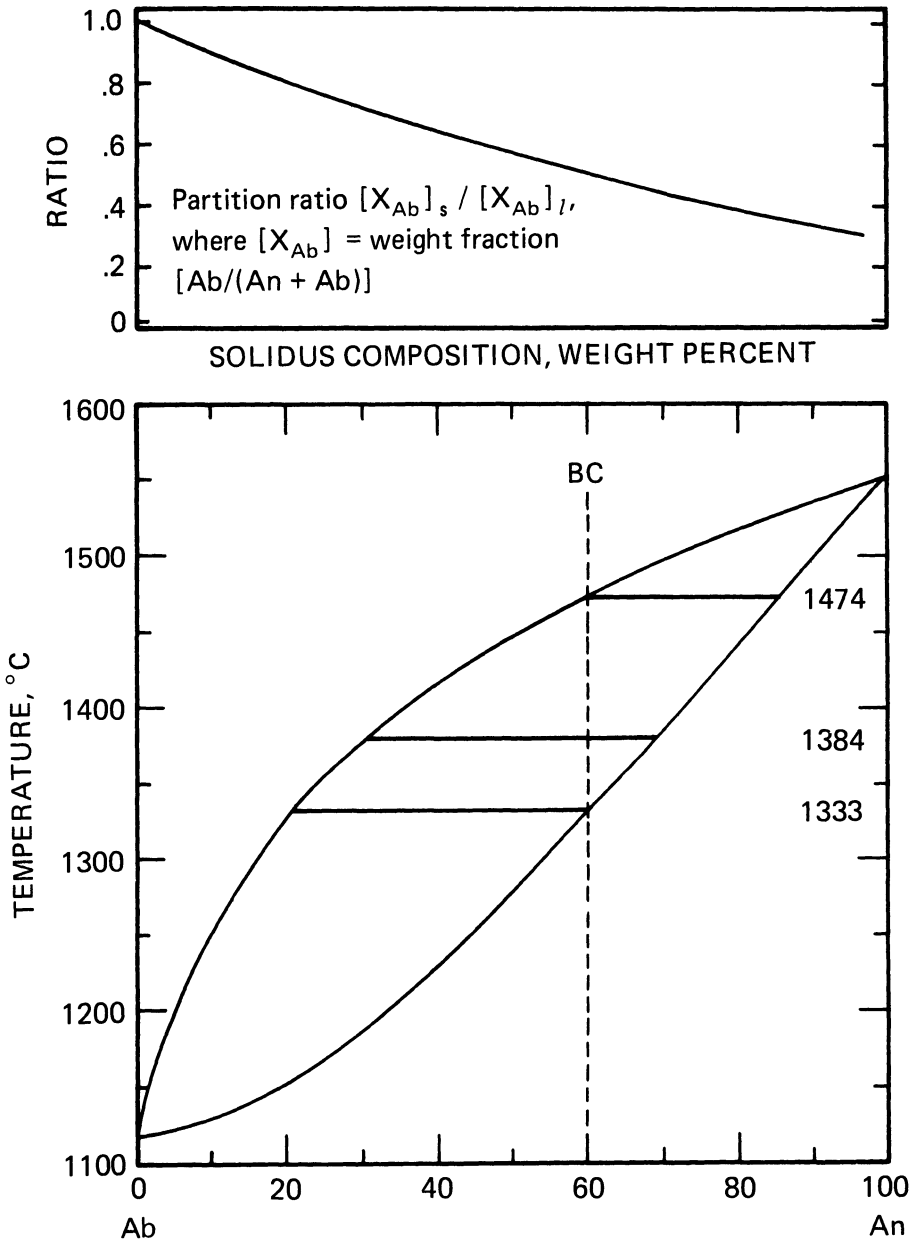


Figure 6.3. Crystallization in the system An-Ab.

and reaction. As the size of the crystals increases, these will become more and more of a problem.

The equilibrium course of crystallization is therefore a reaction course of crystallization, reaction of crystals with liquid proceeding in infinitesimally small steps as the temperature is lowered in infinitesimally small

steps. This is a nice example of what is called a thermodynamically reversible path.

The crystallization and reaction process continues, with falling temperature, until all the liquid is used up. As the final lever shows, this must happen the moment the total crystal composition has reached the initial bulk composition,  $An_{60}$  in our example, at a temperature of  $1333^{\circ}C$  and a liquid composition of  $An_{20}$ . Any further lowering of temperature results only in the cooling of a mass of crystals having composition  $An_{60}$ .

## Fractional Crystallization

As may be surmised from the comment above concerning diffusion and reaction within feldspar crystals, it would not be totally surprising if the temperature were to fall too fast for reactions to proceed to completion. Such a process would result in zoning of the feldspar crystals, a feature so common in igneous rocks that its absence is remarkable. The failure of reaction leads, in one degree or another, to *fractional crystallization* of a profoundly different nature from that in a binary eutectic system such as Di-An. Fractional crystallization, by zoning or physical removal of crystals (perhaps by floating or sinking) is probably never a perfect process in nature, but it may approach perfection, and an idealized perfect model is amenable to theoretical treatment and hence useful for a limiting model.

Starting again with a melt of bulk composition  $An_{60}$ , crystallization again begins at  $1474^{\circ}C$  with the separation of crystals of  $An_{86}$ . With perfect fractional crystallization these crystals never react in the least with the liquid, but are isolated, and with falling temperature the next batch of crystals is slightly more sodic than the first, but it also fails to react with the liquid. At any instant, the crystals just being formed have the equilibrium composition given by the solidus, so fractional crystallization is a process involving thermodynamic equilibrium on a microscopic scale, although not on a macroscopic scale. The fractionally removed crystals constitute the instantaneous solid composition (ISC), and the locus of the ISC with time and falling temperature is the solidus curve, which is an *ISC path*. The isolation of the ISC prevents the exchange reaction  $NaSi \rightleftharpoons CaAl$  from occurring. Failure of this reaction therefore conserves Na, Si (or normative Ab) in the liquid and causes the maximum possible depletion of Ca, Al (or normative An) in the liquid. The total solid composition (TSC) resulting from fractional crystallization is a numerical construct, whose value is given by the sum over all ISC's so far produced. The TSC may be determined graphically, and the lever rule applied, as shown later in the chapter. The important thing to note for present purposes is that the TSC always lags behind the ISC. By the time the liquid has reached such a temperature and composition as to produce crystals of  $An_{60}$ , the total solid composition is still far more calcic than this. Since the total solid composition is more calcic than the bulk composition, it is clear that a good deal

of liquid remains, having a composition of  $An_{20}$ , whereas in the equilibrium process the last of the liquid was just disappearing at this composition. Continued perfect fractional crystallization results in the production of more and more sodic crystals, in equilibrium with more and more sodic liquid, until both liquid and crystals reach the composition of albite, at which point the liquid is used up. The total solid composition produced by this process is  $An_{60}$ , the bulk composition, but the actual crystals produced range from  $An_{86}$  to  $An_0$  in such a distribution as to yield a mean composition of  $An_{60}$ . The liquid composition during the process has ranged from  $An_{60}$  to  $An_0$ . The liquid has continually decreased in quantity, and the very Ab-rich fractions amount to only a small part of the original. Likewise, the abundance of Ab-rich crystals or zones is small compared to that of intermediate and calcic crystals or zones. Nevertheless, if a sample of the liquid were drawn off and isolated late in the process, a finite amount of albite-rich rock would have resulted.

Fractional crystallization is thus capable of producing a range of liquids all the way from the initial composition of the melt to pure albite, a result distinctly different from that of equilibrium crystallization. The presence of very albite-rich plagioclase in interstitial patches in basaltic rocks shows that the fractional crystallization process operates with considerable efficiency in nature, and leads to the proposition that at least some acidic rocks (those high in silica and alkalis) may have been produced by fractional crystallization.

## Equilibrium Melting

Equilibrium melting follows the reverse of the path of equilibrium crystallization. For crystals of  $An_{60}$ , melting begins, on heating, at a temperature of  $1333^{\circ}\text{C}$  with the production of a liquid  $An_{20}$ . With further heating, both the melt and the crystals change composition toward An, along the liquidus and solidus curves respectively, and the process terminates at  $1474^{\circ}\text{C}$ , when the liquid attains the composition  $An_{60}$  and the last crystal to disappear has the composition  $An_{86}$ . If the system were examined at any instant of time during the process, it would be impossible to tell whether a melting or a crystallization process was taking place.

## Fractional Melting

If, at the instant of melting, each fraction of liquid could be removed from the crystalline assemblage, a fractional melting process would result, in which the remaining crystals would be continuously changed toward anorthite, which they would finally reach. In our example, the mean composition of all the liquid generated would be  $An_{60}$ , the bulk composition, but the

successive fractions would range from  $An_{20}$  at the start to  $An_{100}$  at the end. Continuous removal of liquid modifies the lever relationship. Each fraction of liquid is generated by enriching residual crystals in Ca, Al. The next fraction of liquid is generated at a higher temperature, and behaves as though the melting process were beginning all over again. The succession of crystal compositions, which are left as residua, changes along the solidus. There are no hiatuses in the melting process. Completion of melting is not achieved at  $1474^{\circ}\text{C}$ , as it was in equilibrium melting, but only at  $1553^{\circ}\text{C}$ , the melting point of anorthite.

The effect of fractional melting is to leave behind crystalline residua, and over a certain range ( $An_{60}$ – $An_{86}$ ) these would be indistinguishable from settled crystals produced on fractional crystallization. However, the residua produced on fractional melting attain more calcic compositions than could possibly be produced by crystallization of an  $An_{60}$  melt, although only at very high temperatures.

## Assimilation

The plagioclase system furnishes a fine opportunity for discussing the possibilities of changing the composition of liquids by the assimilation of crystals. As an exercise, imagine a half-crystalline mixture, say a bulk composition of  $An_{50}$  at a temperature of  $1384^{\circ}\text{C}$ , into which an extraneous crystal of albite is now introduced. The albite crystal, whose melting point is  $1118^{\circ}$ , will clearly melt, changing the liquid slightly toward albite in composition. The calories required for this process will, to a first approximation, be a large number corresponding to the heat of fusion of albite, and a smaller number corresponding to the specific heat of pure albite melt over the range—from  $1118^{\circ}$  to nearly  $1384^{\circ}$ . Presuming these calories to be furnished by the melt, the process will occur only by virtue of the crystallization of some calcic feldspar, nearly  $An_{69}$  in composition. The latent heat of crystallization of calcic plagioclase must furnish the latent heat of fusion of albite and an additional increment of heat for warming the newly-formed albite liquid. The temperature at the end of the process will be slightly lower than it was before the albite is added, as is implied by the formation of some calcic plagioclase crystals. Clearly, contamination of an intermediate melt by albite can change the composition of the residual liquid, but it cannot increase the quantity of liquid. The process is by nature self-defeating, requiring the crystallization of a greater mass of liquid than can be gained by the melting of the albite. One may infer that contamination of magma by less refractory material is a likely process near intrusive contacts, but one which accelerates the solidification of the magma. In our example, we have assumed the contaminant to be at its melting temperature, whereas in nature the contact rock would be a good deal colder, and much

heat would be lost by the magma in raising the albite to the melting temperature.

The assimilation of more calcic feldspar is a somewhat different proposition. Again assuming  $T = 1384^\circ$ ,  $BC = An_{50}$ ,  $L = An_{31}$ ,  $S = An_{69}$ , suppose a crystal of exactly  $An_{69}$  is introduced, having previously been raised to  $1384^\circ$ . Such a crystal is in equilibrium with the liquid and the other crystals at this temperature, so no reaction will take place. The sole result is that the bulk composition of the system is now changed slightly toward An, so the crystallization process will terminate at a slightly higher temperature than before, the liquid having to expend some excess energy on making over the new crystal of  $An_{69}$  as crystallization proceeds. Now suppose instead that a crystal of  $An_{80}$  is introduced. This crystal, if melted, would have been in equilibrium with a liquid of  $An_{48}$  at a temperature of  $1442^\circ$ ; it is clearly not in equilibrium with our liquid  $An_{31}$  at  $1384^\circ$ . The crystal will react with the liquid, giving up Ca, Al in exchange for Na, Si. This will enrich the liquid in Ca, Al, and the phase diagram tells us that this will require a total crystal composition slightly more calcic than  $An_{69}$ , and a temperature slightly above  $1384^\circ$ . Evidently the reaction of  $An_{80}$  to a less calcic composition takes place with the evolution of heat; it is an exothermic reaction. In adding a calcic crystal, we have moved the bulk composition toward An, but in remaking it, we have also used up some liquid. The resulting ratio of crystals to liquid is now somewhat greater than it was before, and this assimilation process is, again, a self-defeating one in that it uses up liquid.

The effect of the above process on the crystal-liquid lever is not evident without a quantitative example. The following example is adapted, with slight numerical changes, from Bowen (1928, p. 186), which should be consulted for a more complete discussion. 50 g of melt having the composition  $An_{50}$  is cooled till the bulk composition just intersects the liquidus, at  $1448^\circ$ , with formation of a few crystals of  $An_{81}$ . At this point, 50 g of crystals of  $An_{90}$ , also heated to  $1448^\circ$ , are added. If equilibrium were reached isothermally, the result would be crystals of  $An_{81}$ , almost all of which were made over from  $An_{90}$ , and a liquid of  $An_{50}$  composition. The bulk composition, however, is now  $An_{70}$ , and the lever rule gives  $F_L = 11/31 = .355$ ,  $F_S = 20/31 = .645$ . This loss of liquid ignores the heat effect. The present crystalline mass contains  $64.5 \times .81 = 52.25$  g An, and  $64.5 \times .19 = 12.25$  g Ab. The original crystals of  $An_{90}$  contained 45 g An and 5 g Ab. Taking the latent heats of fusion of An and Ab as 104.2 and 51.7 cal/g, respectively, we may calculate the heat effect of the isothermal process. We have gained from the liquid 14.5 g of solid, namely 7.25 g An and 7.25 g Ab, and we have therefore gained  $7.25 (104.2 + 51.7) = 1130$  cal, which would have to be removed to keep the system at  $1448^\circ$ . If instead this heat remains within the system, we may calculate the temperature rise, assuming a heat capacity for the system of .32 cal/g and using the latent heats of fusion stated above. This temperature rise comes out to about  $10^\circ$ , hence

the final temperature would be 1458°. At 1458° the crystals have a composition of  $An_{83}$  and they amount to 56 g, with liquid ( $An_{53.5}$ ) amounting to 44 g. We have thus used 6 g liquid to convert 50 g  $An_{90}$  to 56 g  $An_{83}$ . Clearly, the reaction of calcic crystals with liquid is such as to affect the crystalline material more strongly than the liquid. The liquid becomes only slightly more calcic while decreasing appreciably in quantity. Assimilation of foreign material affords little prospect of accounting for a widespread variety of magmas, although it nicely accounts for many effects observed near contacts.

## The Lever Rule with Fractional Crystallization and Melting

Use of the lever rule requires knowledge of the total solid composition (TSC), the bulk composition (BC), and the liquid composition ( $L$  in crystallization, TLC in fractional melting). In fractional crystallization, the TSC is not given directly by the phase diagram, and in fractional melting, the TLC is not given. The problem of using the lever rule with these fractional processes therefore reduces to the problem of finding the TSC or the TLC. This problem has an easy graphical solution (Morse, 1976). Fig. 6.4 illustrates several examples. We may begin by examining the case of fractional crystallization, starting with a bulk composition  $An_{60}$ .

The initial and final points on the TSC path are known; the first is the solidus composition,  $An_{85.5}$ , and the last is the bulk composition,  $An_{60}$ , because the total of all crystals produced must equal the bulk composition. The final TSC is achieved only at 1118°C, the temperature of final crystallization. The TSC path for fractional crystallization must, then, run between the initial solidus and the bulk composition at 1118°C. How does it run between these points? The answer is obtained by a graphical approximation.

For simplicity in the following discussion, let

$$Ab \equiv X_{Ab}, \text{ the weight fraction } Ab/(An + Ab).$$

Let the ratio of  $Ab$  in the total solid composition to  $Ab$  in the liquid be

$$R = Ab^{TSC}/Ab^L.$$

An independent solution for  $R$  will give the total solid composition associated with any liquid.

For the initial and final states, assuming a bulk composition of  $An_{60}$ , we have

	$Ab^{TSC}$	$Ab^L$	$R$
<i>Initial</i>	0.145	0.40	0.363
<i>Final</i>	0.40	1.00	0.400



Having the TSC path, it is a simple matter to obtain the fraction of liquid  $F_L$  by the lever rule or by the relation  $F_L = (Ab^{BC} - Ab^{TSC}) / (Ab^L - Ab^{TSC})$ .

The example shown in the figure gives  $F_L = 0.31$  at  $1380^\circ\text{C}$ .

A second example is shown in the figure for bulk composition  $An_{40}$ . In this case,  $R$  varies from 0.41 to 0.60, and the TSC path runs from  $An_{76}$  on the solidus to  $An_{40}$  at  $1118^\circ\text{C}$ , following very closely along the solidus at first.

In the case of fractional melting, it is the TLC path which is desired, the TSC path being the solidus. Again, the initial and final points are known, the first being on the liquidus and the last being the bulk composition at  $1153^\circ\text{C}$ , because the sum of all liquids produced must equal the bulk composition just as the last trace of liquid is formed at  $1553^\circ\text{C}$ . The TLC path between the initial and final points is found by forming the ratio  $R' = An^{TLC}/An^{TSC}$ , where  $An$  is the weight fraction  $X_{An}$ , and letting it vary as a linear function of the solidus composition, as shown by the right-hand line in the upper part of Fig. 6.4. Solutions for  $An^{TLC}$  are then found for arbitrarily chosen values of  $An^{TSC}$ , and plotted at the appropriate solidus temperatures. The TLC curve for the bulk composition  $An_{60}$  originates at  $An_{20.5}$  and rises to  $An_{60}$  as shown in Fig. 6.4. From this curve, the bulk composition, and the solidus,  $F_L$  can be obtained with the lever rule, or by the relation  $F_L = (An^{TSC} - An^{BC}) / (An^{TSC} - An^{TLC})$ .

## G-X Diagrams

In Fig. 5.8 of the last chapter, we saw a conventional explanation of the  $G$ - $X$  relations in a binary eutectic system. The development of such an analysis for binary solid solutions originated with H.W. Bakhuis Roozeboom around 1890, and was given its present graphical treatment by Van Rijn van Alkemade (1893). Among the earliest users of such diagrams in geology were Day and Allen, whose monograph with Iddings on "The isomorphism and thermal properties of the feldspars" (1905) was the first product of the young Geophysical Laboratory of the Carnegie Institution of Washington. This is a remarkable paper, because although the authors determined only the liquidus of the plagioclase system, they were able to conclude through the use of Roozeboom's principles that it was indeed a complete binary solid solution series. In the course of doing so, they gave a very fine exposition of  $G$ - $X$  diagrams. Let us now turn to the plagioclase system and Fig. 6.5. In this Roozeboom Type I system, we can no longer speak of a mechanical mixture of pure crystals, and so we have *two* solution curves in  $G$ - $X$  space, one for liquid and one for solid. Crystallization begins at  $T_1$  with the coincidence of  $S$  and  $L$  curves for pure  $An$ . For all other

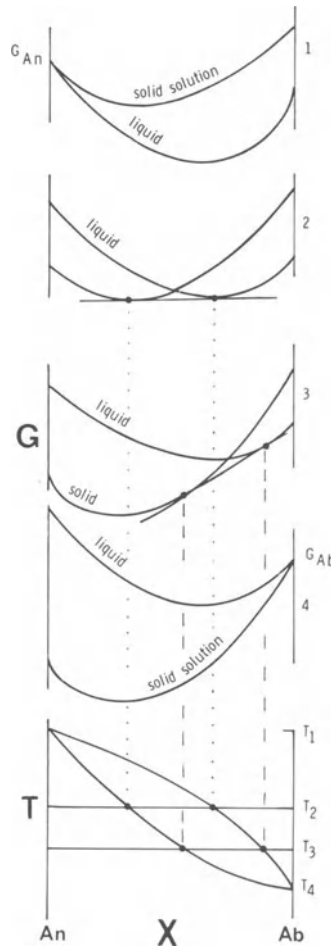


**Figure 6.5.** *G*- and *T*-*X* diagrams for the plagioclase system.

values of *X*, liquid is stable relative to solid; minimum *G* is achieved on the *L* curve relative to the *S* curve. At  $T_2$ , minimum *G* is obtained on a tangent to the two curves, and any point on this tangent signifies coexistence of crystalline solution and melt. The composition of the crystalline solution is given by the tangent on the solid curve; that of the melt by the tangent on the liquid curve. To the left of the crystal tangency, crystalline solution is everywhere minimized in *G* relative to liquid; this part of the system is solid. To the right of the liquid tangency, the liquid curve minimizes *G*; this part of the system is liquid.

At  $T_3$ , the picture is qualitatively the same, but the points of tangency have migrated further toward Ab. Finally, at  $T_4$ , the curves unite at the melting point of pure Ab and the rest of the system is solid. At lower

temperatures, the curves become farther apart. It should be noted both for this system and for the previous one that the absolute values of  $G$  change directly and continuously with temperature, but at different *rates* for solids and liquids. This is what causes the solid curve to “overtake” the liquid curve with falling temperature. It is also worth noting here that despite the experimental difficulties of locating the solidus accurately, see what a problem it would be (at  $T_3$  for example) to locate the tangent points accurately by correct placement of the  $G$ - $X$  curves. This is why phase diagrams are often more a source than a goal of thermodynamic data.

## Chapter 7

# Diopside-Albite: A Complex System

### Introduction

It would be folly to suppose that diopside-albite is a binary system. We have already found, in Di-An, that diopside shows incorporation of Al when that element is present. In this case, it is to be expected that diopside will steal Al from albite. The bad news does not end with this, for the albite will also steal Ca from diopside to make plagioclase, and the resulting effects on residual liquids are both important and difficult to analyze.

The principle that pure albite does not crystallize from liquids containing Ca is one enunciated by Bowen (1945, p. 88) and called the "plagioclase effect." The plagioclase effect continues to operate after the original endowment of normative anorthite is used up, and when this happens (presumably by theft of Ca from normative augite) the inevitable result is to produce an excess of alkali silicate in the liquid, as we shall see. Excess of alkali over the normative amount which is required to form feldspar is a situation dependent on the alkalies/alumina ratio, and when it occurs, liquids are said to be *peralkaline*. When an excess of silica also occurs, as in the case at hand, liquids are said to be *acid* as well as *peralkaline*; rhyolitic rocks of this nature include pantellerite and comendite. Analysis of the system diopside-albite furnishes, at least in a general way, insight into how such peralkaline acid trends may develop.

## Pseudobinary $T$ - $X$ Diagram

The phase relations of diopside-albite have been studied by Schairer and Yoder (1960), who plotted the results in a  $T$ - $X$  diagram (Figure 7.1) which may be termed pseudobinary. Several curious features of this diagram immediately reveal its non-binary nature. Although the liquidus curves intersect more or less sharply, their junction does not constitute an isobaric eutectic, for a substantial range of crystals + liquid remains below this point. In the albite-rich portion of the diagram, the plagioclase liquidus rises from that of pure albite (1118°C) to a maximum of 1148°, and then falls to 1133° at  $\text{Ab}_{91}\text{Di}_9$ , where it joins the diopside liquidus. The plagioclase liquidus then *continues* to fall in temperature, where covered by the diopside + liquid field. The phase diagram is to be read directly, without the usual implications of binary diagrams. At a composition of  $\text{Ab}_{75}\text{Di}_{25}$ , for example, the diagram simply announces the facts that, on cooling, Di crystals appear at 1226°, that these are joined at 1122° by plagioclase crystals, and that complete solidification does not occur until somewhere around 1050°. To the left of  $\text{Ab}_{91}\text{Di}_9$ , taking as an example  $\text{Ab}_{95}\text{Di}_5$ , plagioclase crystals appear, on cooling, at 1148°, and are joined at 1096° by diopside crystals; complete solidification (= beginning of melting) occurs only at 1028°.

Application of the phase rule to this situation quickly reveals the non-binary nature of the system. Supposing it were binary,  $c = 2$ , and  $W_p = 3 - \phi$ , so that a three-phase assemblage of diopside, plagioclase, and liquid should be invariant. Instead, the diagram shows a range as large as 90°C

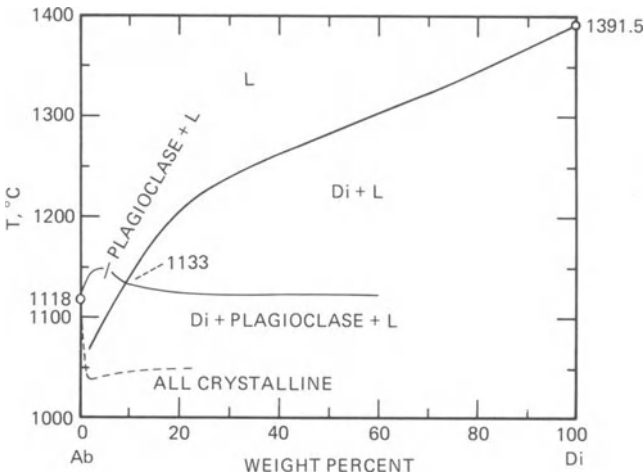


**Figure 7.1.** The system diopside-albite, after Schairer and Yoder (1960). This is not a binary system, but merely a  $T$ - $X$  “road map” of phase relations encountered along the Di-Ab composition line.

over which this three-phase assemblage occurs. Moreover, the assemblage shows a wide compositional range, so it must be at least divariant. The components therefore must number at least four. The reasoning below suggests in fact that five components are required for adequate representation of all phases in this system.

## Components and Liquid Trends

The system diopside-albite contains the elements Na, Ca, Mg, Al, Si, and O. We have no particular reason to believe that oxides would not serve as well, so we may choose as our first set of components the oxides  $\text{Na}_2\text{O}$ ,  $\text{CaO}$ ,  $\text{Al}_2\text{O}_3$ ,  $\text{MgO}$ ,  $\text{SiO}_2$ . This is like our old friend CAMS (Chapter 5) with N (i.e.  $\text{Na}_2\text{O}$ ) added. These oxides must surely suffice for describing the system, but they may not be the minimum valid set. To choose the most appropriate components, we should give some attention to the expected compounds and the effect on the liquid of removing them.

Let us assume that the feldspar produced in this system is rigorously binary, a member of the Ab-An series. Let us further assume, for the moment, that Al enters diopside in the form of CaTs,  $\text{CaAl}_2\text{SiO}_6$ . We shall then need Di, CaTs, Ab, and An to represent the compositions of the crystals. Removal of such crystals from bulk composition which lie rigorously in Di-Ab will result in liquids depleted in CaTs and An, and our object is to inquire how the compositions of such liquids may be represented. Without worrying about quantitative considerations, we want to know qualitatively in what sort of chemographic space these liquids will lie. To discover this, we can make a few arbitrary subtractions, just as done with the ternary analysis of Di-An.

Using the abbreviations C, A, M, S, N for the oxides, and choosing a bulk composition of 2 Di + 4 Ab, we get the initial oxide composition shown in the top row of Table 7.1. From this we subtract one mole of CaTs,  $\text{CaO} \cdot \text{Al}_2\text{O}_3 \cdot \text{SiO}_2$  (1:1:1), and then one mole of An,  $\text{CaO} \cdot \text{Al}_2\text{O}_3 \cdot 2\text{SiO}_2$  (1:1:2). The result can then be expressed in terms of enstatite, sodium disilicate, and quartz (or 2 enstatite,  $2\text{Na}_2\text{O}$  and 11  $\text{SiO}_2$ ). Evidently the entry of CaTs and An into crystals must lead to enrichment of the liquid in  $\text{MgO}$ ,  $\text{Na}_2\text{O}$ , and  $\text{SiO}_2$ .

The liberation of  $\text{MgO}$  and  $\text{SiO}_2$  suggests the further possibility, indeed likelihood, that the pyroxene is not merely a solid solution toward CaTs from Di, but also a solid solution toward En, as we know natural augites to be. With a view to supplying Ca for plagioclase, we could also treat the Al in pyroxene as Mg-Tschermak's molecule,  $\text{MgAl}_2\text{SiO}_6$ , instead of CaTs. Table 7.2 shows the result of this assumption, starting with an initial bulk composition of 1Di + 4Ab. The result is similar to that of Table 7.1 except for the absence of  $\text{MgO}$  in the residual liquid.

**Table 7.1** Effect of Removal of Ca-Tschermak's Molecule and Anorthite From a Bulk Composition in Di-Ab. CAMSN are the Oxides of Ca, Al, Mg, Si, and Na. CaTs is  $\text{CaAl}_2\text{SiO}_6$ , An is  $\text{CaAl}_2\text{Si}_2\text{O}_8$ , En is  $\text{MgSiO}_3$ , Disil. is  $\text{Na}_2\text{Si}_2\text{O}_5$ , and Q is Quartz. For Discussion, See Text.

	<i>C</i>	<i>A</i>	<i>M</i>	<i>S</i>	<i>N</i>
Initial, 2 Di + 4 Ab	2	2	2	16	2
less CaTs	-1	-1		-1	
	1	1	2	15	2
less An	-1	-1		-2	
Result	0	0	2	13	2
less 2 En			-2	-2	
	0	0	0	11	2
less 2 disil.				-4	-2
				7	
less 7 Q				-7	
				0	

Note: See also Kushiro (1973), p.505.

Natural diopsidic augites commonly show CaTs when their analyses are recalculated, but Mg is usually recalculated as En. The model of Table 7.1 is probably somewhat more realistic than Table 7.2, if the "released" MgO SiO<sub>2</sub> is considered as residing in the pyroxene rather than the liquid. Both models leave little doubt that the liquid will be enriched in Na<sub>2</sub>O and SiO<sub>2</sub>

**Table 7.2** Effect of Removal of Mg-Tschermak's Molecule and Anorthite From a Bulk Composition in Di-Ab. Abbreviations as in Table 7.1.

	<i>C</i>	<i>A</i>	<i>M</i>	<i>S</i>	<i>N</i>
Initial, Di + 4 Ab	1	2	1	14	2
less MgTs		-1	-1	-1	
	1	1	0	13	2
less An	-1	-1		-2	
Result	0	0	0	11	2
less 2 disil.				-4	-2
				7	0
less 7 Q				-7	
				0	

as a result of the incorporation of Al in pyroxene and Ca in plagioclase. A little consideration will show that this conclusion is valid for crystals composed dominantly of Di and Ab, instead of CaTs and An, since addition of diopside and albite to both sides of the equations represented by Tables 7.1 and 7.2 has no effect apart from dilution.

Returning to the choice of components, it seems clear that  $\text{Na}_2\text{O}$  and  $\text{SiO}_2$  will have to be included in order to represent the vector of the liquid. At the outset, we concluded that Di, CaTs, Ab, and An should be included.

Instead of working solely with the oxides, it is convenient to choose combinations of oxides where practicable, thereby restricting the composition space within CAMSN to the region of interest. We have no interest, for example, in compositions very near CaO or MgO. We may choose instead the join  $\text{CaSiO}_3 - \text{MgSiO}_3$  to represent diopside, the join  $\text{CaSiO}_3 - \text{Al}_2\text{O}_3$  to represent CaTs, and the join  $\text{CaSiO}_3 - \text{Al}_2\text{O}_3 - \text{SiO}_2$  to represent An. In this way,  $\text{CaSiO}_3$  serves triple duty. Our five components can then be



Four dimensions are required to represent five components in composition space ( $X - X$  space). In order to make a graphical display of chemographic relations, we are limited to three dimensions; a tetrahedron drawn in perspective would suffice. One corner of the tetrahedron will need to have two labels, representing two components separately or together, as occasion demands. The combination of  $\text{Na}_2\text{O}$  and  $\text{Al}_2\text{O}_3$  is convenient. The corner so labelled may be considered  $\text{Al}_2\text{O}_3$ , onto which  $\text{Na}_2\text{O}$  is projected from an unseen dimension. The resulting chemographic space, which may help in visualizing the behavior of the system Di-Ab, is shown in Figure 7.2. The phases Di, CaTs, Ab are plotted on edges of the tetrahedron, and An is plotted on the floor. The join Di-Ab is plotted as a heavy line across the interior of the tetrahedron. An arbitrary amount of solid solution from Ab toward An is shown by a heavy bar. A plausible arbitrary region of solid solution around Di is shown in the  $\text{CaSiO}_3 - \text{MgSiO}_3 - \text{Al}_2\text{O}_3$  face. A line connecting a composition of  $\text{Di}_{\text{ss}}$  to the plagioclase bar near Ab represents the join along which the total solid composition is expected to lie for some temperature and bulk composition. The assumed solid composition such as TSC, when connected to the bulk composition BC, implies that the liquid lies on the extension of line TSC-BC, as the arrow labelled *L* indicates. This arrow is presumably the vector into  $\text{Na}_2\text{O} - \text{SiO}_2$  space discussed above.

In order for a quantitative treatment to be given, the true compositions

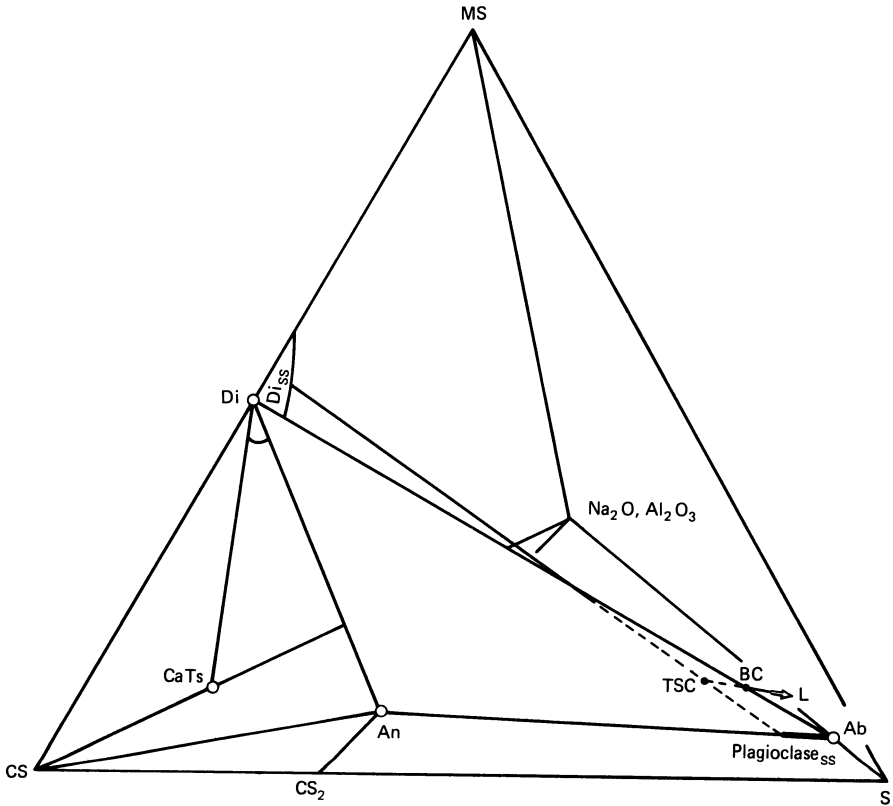


**Figure 7.2.** Graphical analysis of a liquid vector from diopside and plagioclase. For abbreviations, see text. The vector from BC to L is pointing toward your right from behind the plane Di-Ab-An.

of experimental pyroxene and plagioclase crystals would have to be known. To date, these have not been discovered; X-ray data are insensitive to the compositional ranges encountered, and the crystals are too small for optical work. Possibly larger crystals could be grown by superheating the melts to destroy potential nucleation sites, and cooling slowly through the liquidus. Larger crystals could be analyzed with the electron microprobe, and data for a variety of temperatures and bulk compositions would permit the liquid vector to be calculated for various stages of solidification. Without such data, it is difficult to do much more with this system.

Schairer and Yoder (1960) found no evidence for phases other than diopsidic pyroxene and plagioclase in runs thought to be completely crystallized. This could not be correct, according to our analysis, unless excess  $\text{Na}_2\text{O}$  and  $\text{SiO}_2$  were taken up in one of the crystals, presumably plagioclase. Instead, it may be that small amounts of sodium silicate and quartz are present in the runs, but undetected by optical methods. Alter-

natively, undetected glass is still present, or the pyroxene and plagioclase have returned to compositions of pure Di and pure Ab during cooling, an extremely unlikely event.

## Petrologic Considerations

The system diopside-albite forms an important part of our model for basalts, the basalt tetrahedron, being a part of the critical plane of silica undersaturation, which is the ternary system Di-Fo-Ab. The critical plane is so-called because it divides the two regions of undersaturated model rocks, and it is an important tenet of the classification of Yoder and Tilley (1962) that this plane has genetic as well as taxonomic significance. The critical plane (actually some nearby plane) may not be penetrated by liquids during fractionation at low pressures, and this notion is strongly implied by successions of natural lavas which seem to remain solely on one side or the other of a natural analog of the critical plane.

To show experimentally that the critical plane has this genetic function, it is thought sufficient to show that the plane is a *thermal barrier*, which means that liquidus temperatures should fall, away from the plane, either toward silica or toward nepheline. If this were so, fractional crystallization could only drive liquids away from the plane, not through it.

Schairer and Yoder (1960) have concluded that the system is in fact close to a thermal barrier, because when small amounts of either nepheline or silica components are added, liquidus temperatures are lowered, and fractional crystallization must drive liquids away from the plane. Moreover, complete crystallization of such mixtures show either nepheline or a silica mineral as crystalline phases, depending on whether the mixture was under- or over-saturated, respectively. Experimentally, therefore, Di-Ab is a thermal barrier, and Di-Ab-Fo may then also be one.

The experimental evidence is not completely in harmony with our theoretical analysis of the course of residual liquids in Di-Ab. The former suggests Di-Ab as a thermal barrier, but the latter suggests that bulk compositions in Di-Ab must yield liquids rich in soda and silica. If the theoretical analysis is correct, it implies that if a thermal barrier does exist, it must be one involving CaTs-bearing pyroxene and An-bearing plagioclase rather than pure Di and Ab. The appreciable three-phase melting intervals in Di-Ab show that the non-binary nature of the system is by no means trivial; there must be a significant liquid vector toward Na<sub>2</sub>O-SiO<sub>2</sub>-rich compositions, and the late stages of crystallization may be more important than liquidus relations in evaluating fractionation effects.

In summary, it has to be concluded that Di-Ab may to a first approximation be considered a thermal barrier, and that some natural analog of this join may indeed be a thermal barrier. Our basalt model is not perfect,

however, and complications appear to exist near the critical plane which should make us cautious in refining too much upon it. On the other hand, Di-Ab affords a reasonable basis for interpreting the origin of peralkaline acid liquids by fractional crystallization from basaltic compositions, and if the thermal barrier has philosophical weaknesses, they must be such as to cause an oversaturated trend of residual liquids rather than an undersaturated trend. Further discussion of the imperfection of diopside-plagioclase as a thermal barrier is given by Kushiro and Schairer (1970).

## Chapter 8

# Diopside-Anorthite-Albite

### Introduction

The system Di-An-Ab allows us to study a basaltic model consisting of diopside and an intermediate plagioclase, a model which is much closer to the real thing than we have studied before. The fact that the two joins Di-An and Di-Ab are not binary means of course that Di-An-Ab is not a three-component, or ternary, system. The reasoning of the last chapter suggests that it must be described as a quinary ( $c = 5$ ) system, CAMSN, and Figure 7.2 shows the location of the Di-An-Ab plane in this system. The non-ternary nature of the system means that liquids will always lie on the  $\text{SiO}_2$ -rich side of this plane, driven there by crystals somewhat richer in  $\text{Al}_2\text{O}_3$  than the plane. When the plagioclase composition is near An, it is expected that the  $\text{Di}_{\text{ss}}$  will have a composition approximately towards CaTs from Di, and as the plagioclase approaches Ab, the  $\text{Di}_{\text{ss}}$  will become somewhat more magnesian. These effects mean that, as a part of the *generalized* critical plane of the basalt tetrahedron, Di-An-Ab has the same properties as Di-Ab, so we should expect that liquids might become oversaturated with silica by fractional crystallization in this system, but not undersaturated.

Having said this, it is now convenient to ignore for a while the non-ternary nature of the system and treat it as ternary for purposes of analysis. For intermediate compositions in the system, this is not a serious oversimplification as far as geometry is concerned, although it should always be remembered that crystals and liquids do not lie rigorously in the plane Di-An-Ab.

### Properties of Triangles

Quantitative treatment of a ternary system requires that compositions be plotted in an  $X-X$  plot, conveniently a triangle. Temperature information will then have to be contoured on this triangle, so the result will have precisely the properties of a topographic map, with two dimensions serving to locate points geographically (compositionally) and a third, projected dimension serving to summarize height (temperature).

It is common to plot compositions in an equilateral triangle, although other triangles have the same properties and can be used equally well. An equilateral triangle representing components A, B, and C is shown in Figure 8.1a. The corner labelled A signifies 100% A, and so on. The side opposite A is the locus of all points devoid of A, or in other words it is a binary system B-C. To plot a given amount of A, a distance from B-C along the altitude toward apex A is measured; since the altitude represents 100% A, then half the altitude represents 50% A, and so on. A point ABC may then be plotted by finding the intersection of any two altitudes (“ladder rungs”),

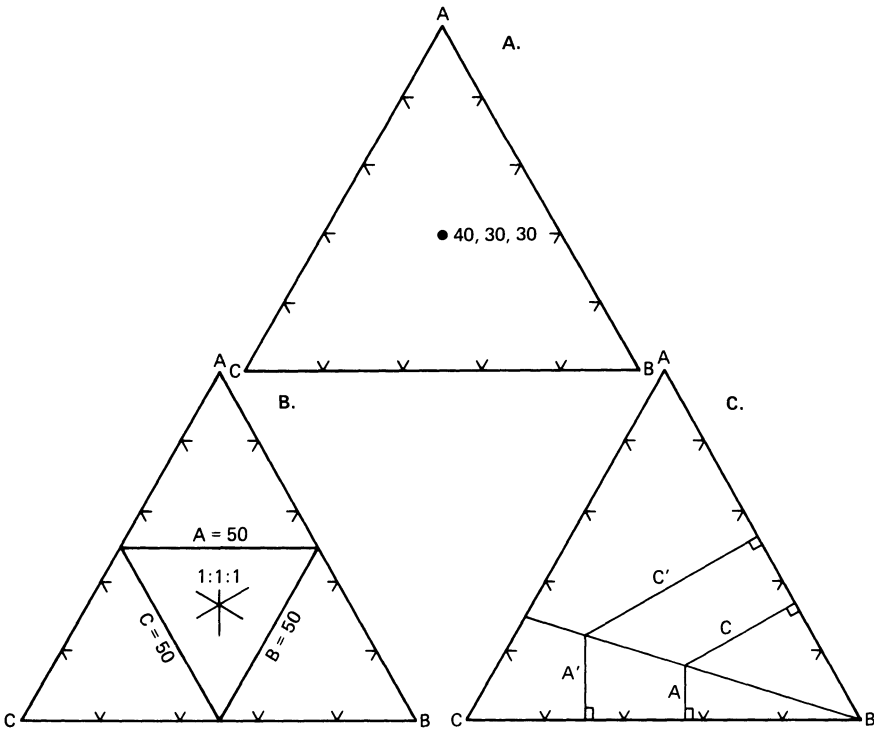


**Figure 8.1.** Plotting of points and ratios in a triangle. A. The plotted point has the composition 40% A, 30% B, 30% C. B. Location of 50% lines and the center of gravity. C. Proof that a line radial from B is a line of constant A:C.

such as an amount of A and an amount of B. The point  $A_{40} B_{30} C_{30}$  is plotted, for example, in Figure 8.1a. It is to be noted that ternary plots are concerned only with variables of constant sum (i.e. which can be recalculated to 1, or 100, or any convenient sum); a corner may not, for example, represent a ratio.

It is useful for "eyeball" plotting of points to note that the lines representing 50% A, 50% B, 50% C form an equilateral triangle whose apices lie at the midpoints of the legs of the parent triangle (Figure 8.1b). A point representing the 1:1:1 composition falls at the center of gravity for both triangles.

A very useful property of triangles, already mentioned in Chapter 5, is that a line from any apex such as B is a line of constant ratio of the other two components, such as A:C. The proof of this is shown in Figure 8.1c; the ratio of altitudes A:C is clearly the same as the ratio of altitudes A':C', by similar triangles. This property of constant ratio for apical lines means that the *removal* of some component such as B, say by crystallization of a phase B, drives the remaining material (liquid) directly away from B.

## Deduction of the Ternary $T$ - $X$ Projection

Having some knowledge of each of the three bounding binary systems, we are in a position to sketch the general relations in the ternary system, provided there are no interior compounds or other surprises. A convenient way to do this is to surround the ternary composition triangle with each of the three binary  $T$ - $X$  plots folded down into the plane of the paper, so that their  $T$  axes remain normal to the sides of the triangle. This is done in Figure 8.2. The reference temperature at the base of each  $T$ - $X$  diagram is arbitrarily taken as  $1100^\circ$ . Our goal is to map the *liquidus surfaces* in the ternary plot; we shall not be able to see through these to map the solidus surfaces, although a solidus map could be constructed instead of a liquidus map.

The obvious things to plot first are intersections of liquidus surfaces. The first of these is the eutectic in Di-An, at  $An_{42}Di_{58}$ . When projected along the  $T$  axis, this falls at the 42:58 point on the Di-An leg of the triangle. This point represents the 3-phase equilibrium  $Di+An+L$ . An analogous point occurs in Di-Ab, and although this point is by no means a eutectic, it does represent a 3-phase equilibrium,  $Di+Ab+L$ .<sup>1</sup> Both these points represent, in general,  $Di+Plag+L$ . In the binary systems (if they were binary), this assemblage would be invariant. In a ternary system,  $W_p = 4 - \phi$  and the assemblage should be univariant. The two supposedly invariant points

<sup>1</sup>Actually  $Di_{ss}+Ab_{ss}+L$ , but we ignore for the time being the non-ternary nature of the system.

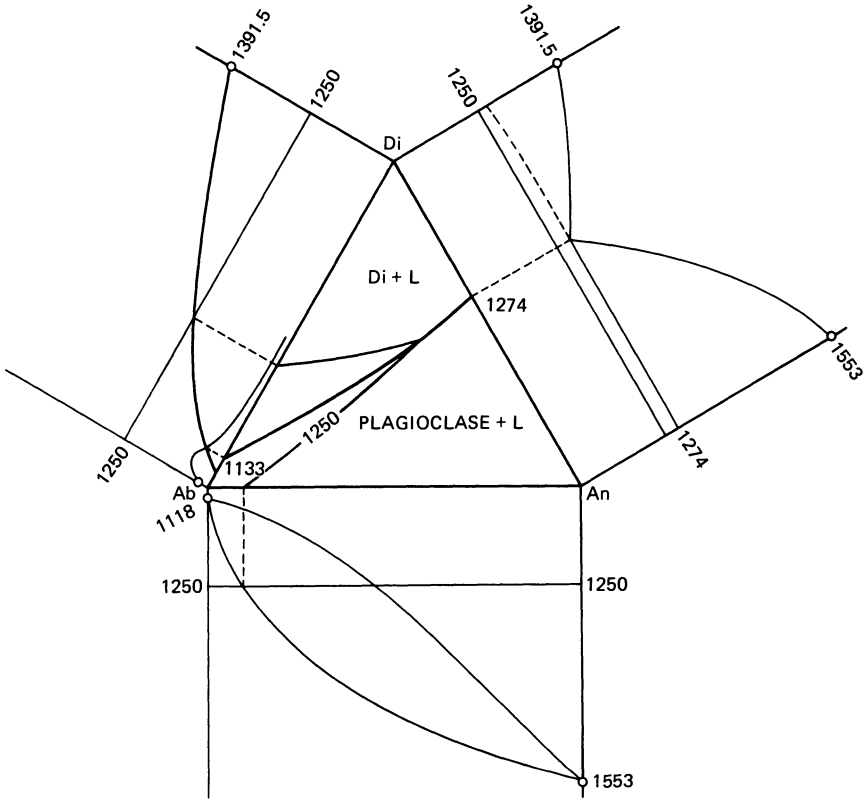


**Figure 8.2.** Deduction of the ternary  $X-X$  plot of Di-An-Ab from the three bounding  $T-X$  binaries. The central triangle is the  $X-X$  plot, and the  $T-X$  plots, joined to the triangle at the 1100°C isotherms, may be considered folded-down walls of a  $T-X$  prism of which the triangle is the base.

then must be connected by a univariant line running through the triangle. There is no reason for such a line to be straight, so we shall draw it curved; it is the heavy line in the triangular part of Fig. 8.2.

There is no liquidus intersection for An-Ab. The resulting ternary diagram is very simple. There appear to be two primary fields, one in which Di appears first on the liquidus, and another in which Plag. appears first on the liquidus. These primary phase fields are exactly analogous to their binary counterparts in Di-An and Di-Ab. The line separating the two fields is a field boundary (or cotectic), supposedly also a univariant line. This line slopes in temperature from 1274° at Di-An to 1133° at Di-Ab. It is like a stream on a topographic map. To summarize thermal information about the liquidus surfaces on the ternary diagram, we shall have to draw contours of temperature. One of these is drawn in Figure 8.2, for the temperature 1250°. The contour can be accurately located at two of the three edges of the triangle. At the third, Di-An, it does not intersect a liquidus surface.

The contour must, however, cut the field boundary somewhere between Di-An and Di-Ab. Recalling the “rule of V’s” from topographic maps, the contour must go through an inflection where it crosses the “stream” (field boundary), and the “V” must point “upstream” (toward higher temperature). A shape such as drawn in Figure 8.2 is therefore consistent with the information available to us. Other contour lines could be sketched in after the same fashion.

The likening of the field boundary to a stream is quite apt, since the field boundary represents the locus of all liquids in equilibrium with both diopside and plagioclase, and these liquids must clearly move down-temperature along the line with crystallization.

To summarize the geometry of our deduced system Di-An-Ab, a perspective drawing (Figure 8.3) is useful. The temperature axis is vertical, so the complete model is a triangular prism arising from the  $X$ - $X$  base. The field boundary and the  $1250^\circ$  isothermal plane are shown in the drawing,

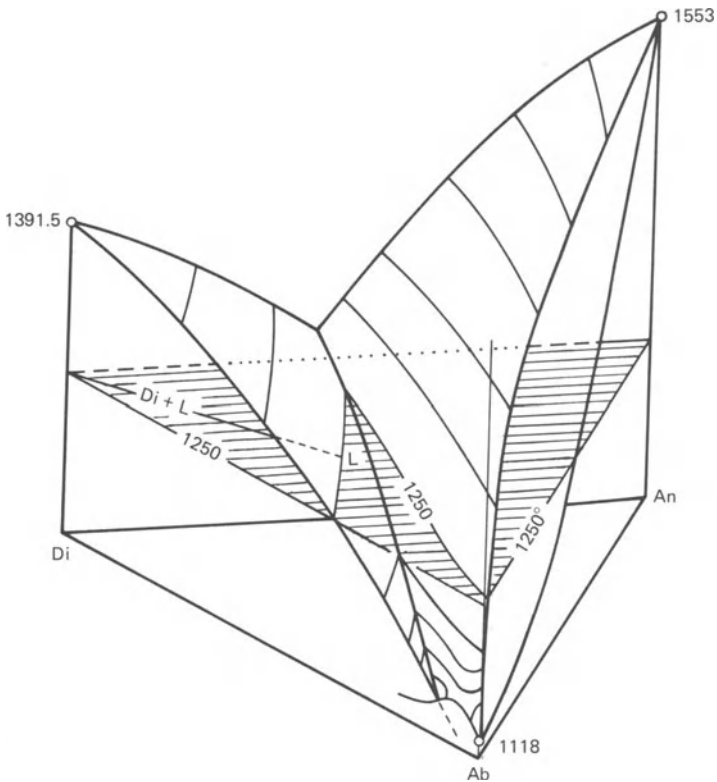


**Figure 8.3.** Perspective drawing of the ternary  $T$ - $X$  prism Di-An-Ab- $T$ . The two intersecting liquidus surfaces are shown ruled with temperature contours. An isothermal plane ( $1250^\circ\text{C}$ ) is shaded.

along with some other, schematic temperature contours. A single isothermal (1250°) *tie line* between a liquid *L* and Di crystals is also shown.

In normal use, the liquidus surfaces and temperature information are projected parallel to the *T* axis onto the *X-X* plane, and such ternary phase diagrams are therefore *T-X* projections. They are capable of rigorous and quantitative interpretation, as we shall see.

### The Experimental Ternary Diagram

The diagram which we have deduced may be correct in principle, but it is not very useful, since it surely has no quantitative reliability. The position of the field boundary must be located by experiment, and the compositions of plagioclase solid solutions in equilibrium with a given liquid must be determined experimentally. The experimentally determined phase diagram, modified slightly from that of Bowen (1915), is shown as Figure 8.4.

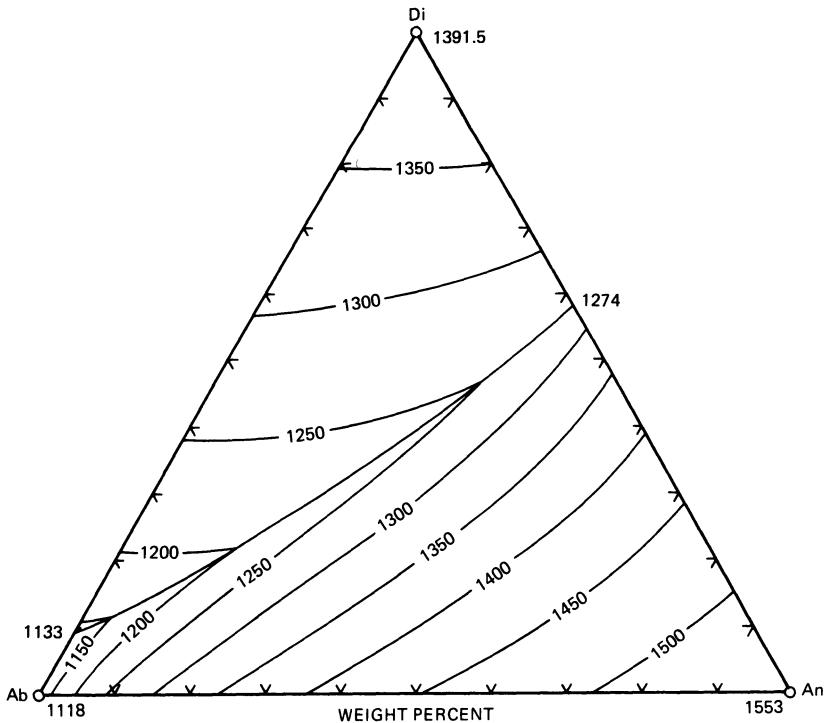


**Figure 8.4.** Phase diagram, after Bowen, of the system Di-An-Ab. The Di-Ab sideline is revised after Schairer and Yoder (1960) and the Di-An sideline after Osborn and Tait (1952). See also Kushiro (1973). Base of diagram measures 10 cm.

The maximum number of coexisting phases indicated by the phase diagram is 3, and the minimum variance at constant pressure is therefore 1. The univariant nature of the plagioclase diagram therefore exerts its influence in the ternary system, and since the addition of the component diopside is accompanied eventually by the phase diopside, the lower limit of variance is the same in the ternary system as in An-Ab. This implies that fractional crystallization, as in An-Ab, can have a profound effect on the course of the liquid.

## Equilibrium Crystallization

### THE DI + L FIELD

Considering equilibrium crystallization, and assuming a ternary system, let us start with a bulk composition of  $\text{Di}_{60}\text{An}_{20}\text{Ab}_{20}$ , in the Di + L field. This composition is labelled A in Figure 8.5a. When solid, it must consist of diopside and plagioclase of composition  $\text{An}_{50}$ . A melt of this composition is cooled, until it reaches the Di + L liquidus surface, at about  $1300^\circ$  (point A, Fig. 8.5), at which point crystals of Di begin to form. Removal of Di from the liquid causes the latter to move directly away from Di toward  $\text{An}_{50}\text{Ab}_{50}$ . This process continues until the liquid reaches the field boundary, at about  $1235^\circ$  (point B, Fig. 8.5), at which point a plagioclase also begins to crystallize.

Now it must be determined by experiment what composition this plagioclase has; the original work tells us that the feldspar in equilibrium with Di and liquid at this temperature is  $\text{An}_{80}$ . A new *tie line* is established between the liquid and plagioclase of this composition, and this tie line also generates a *three-phase triangle* Di-An-L, shown in Figure 8.5b. The long leg of this triangle, Di-An<sub>80</sub>, is the tie line connecting crystals, and the apex on the field boundary represents the composition of liquid. Further crystallization of both Di and calcic plagioclase must drive the liquid to the left, but the coexistence of three phases means that the system is univariant, and therefore that the liquid must move in univariance, i.e. along the field boundary. As the liquid moves thus toward  $\text{Di}_9\text{Ab}_{91}$  in response to crystallization, it demands equilibrium with more and more sodic plagioclase, so the latter continually reacts with liquid, as in An-Ab. As both liquid and plagioclase become more sodic, Di remains fixed in composition, and the three-phase triangle *pivots* to the left around Di as a pivot point (Fig. 8.5c). The rate at which this motion occurs is a function of the rate of heat loss and the reaction time required for the plagioclase crystals. During the

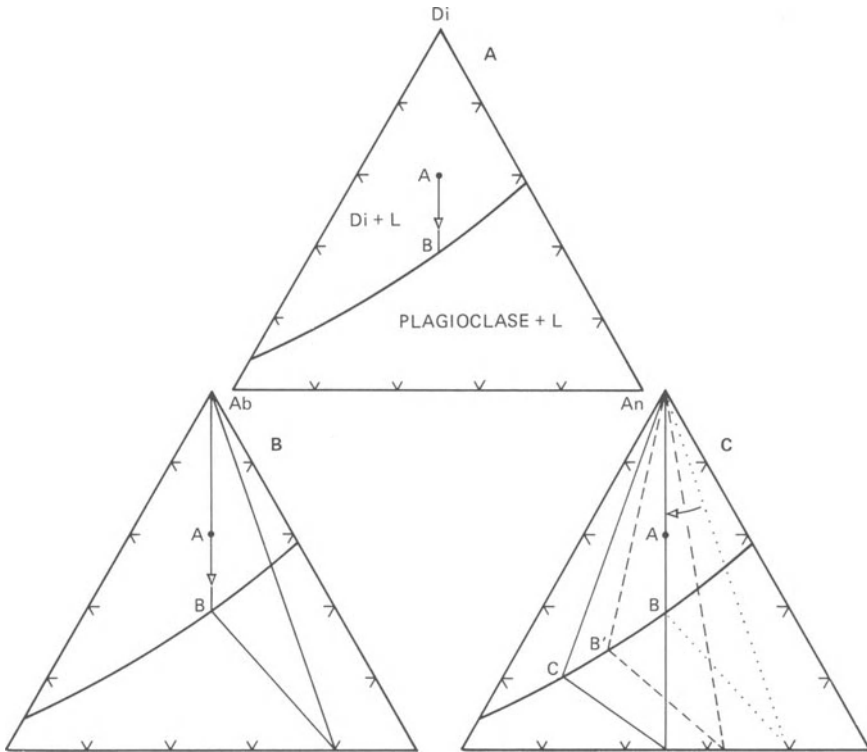


**Figure 8.5.** Three stages in the equilibrium crystallization of a mixture *A* in Di-An-Ab. A. Crystallization of Di has driven the liquid directly away from Di from *A* to *B*. B. Same temperature as A, showing first three-phase triangle, Di-B-plagioclase. C. Motion of the three-phase triangle from initial to final position. The motion is a rotation around Di as a pivot.

sweep of the three-phase triangle, both diopside and plagioclase increase in amount. Although we know nothing of the rate, we do know when the process terminates, for at the moment when the last iota of liquid disappears, the plagioclase must have the initial bulk composition of  $An_{50}$ , and experimental evidence shows that the last liquid has the composition shown by point C, Figure 8.5c, which is about  $An_{19}$  in terms of its potential plagioclase composition. At this juncture, it is to be noted that the long leg (the solid-solid leg) of the three-phase triangle cuts the bulk composition (*A*), and the total solid composition coincides with the bulk composition. The tie line C -  $An_{50}$  has a slightly flatter slope than the preceding plagioclase-liquid tie lines, and we learn from the experiments that this is a general rule in this system, except near the Ab corner. The temperature of final crystallization is given for liquid C from the contours of Fig. 8.4 as about  $1200^{\circ}$ .

## THE PROJECTED PLAGIOCLASE LOOP

It is to be remarked that the coexistence of  $An_{50}$  crystals with liquid at  $1200^\circ$  in this case is quite unlike the case of the binary system An-Ab; in the latter, a liquid at  $1200^\circ$  would coexist with crystals of about  $An_{32}$ . The presence of diopside clearly has a drastic effect on the temperature-composition relations of plagioclase and liquid. This effect can be appreciated readily by reference to Figure 8.6, in which the *projected* plagioclase loop for diopside-saturated liquids is compared with the binary An-Ab plagioclase loop. The Di-An-Ab loop is projected from Di onto the An-Ab- $T$  face of the  $T-X$  prism (Figure 8.3). The liquids lie on the field boundary in the ternary system, and the crystals lie in the plagioclase prism face. The projected loop is plotted by simply reading the An/(An+Ab) ratios of both ends of  $L$ -Plag. tie lines (as in Fig. 8.5c) at various temperatures. The

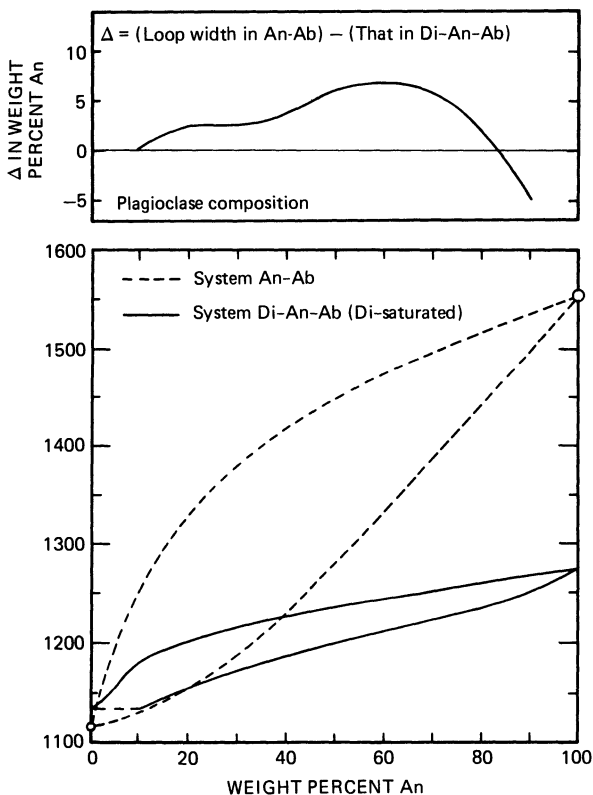


**Figure 8.6.** Projected plagioclase loop in Di-An-Ab compared with pure plagioclase. The lower diagram shows the two loops, and the upper one monitors the change in loop width as a function of the solidus compositions.

diopside-saturated loop is a great deal flatter, ranging from 1274°, the Di-An eutectic temperature, at the calcic end to 1133°, the Di + Ab + L liquidus, at the sodic end. The loop is also somewhat narrower in the intermediate region, compared to the pure plagioclase loop. For example, a plagioclase of composition An<sub>70</sub> coexists with a diopside-saturated liquid of An<sub>37</sub> potential plagioclase composition at 1223°, whereas in the pure system such a plagioclase coexists with a liquid of An<sub>31</sub> at about 1380°. Again, a solidus composition of An<sub>50</sub> coexists with Di-saturated liquid of An<sub>19</sub> at 1200°, but coexists with pure plagioclase liquid of An<sub>12</sub> at 1280°. The loop is thus narrower by some 7% An in the plagioclase composition range of most interest to basalts and gabbros. The difference in loop widths is plotted against the crystal composition at the top of Figure 8.6.

Both the flattening and narrowing of the loop in the presence of diopside are instructive in terms of basalt and gabbro genesis. The flattening indicates very clearly the marked temperature effect of adding only one component, diopside. The resulting crystallization temperatures are very close to those observed in natural basaltic lavas, such as 1150° for olivine + augite + plagioclase + L (Peck, Wright, & Moore, 1966). The narrowing of the loop suggests that natural magmas will produce plagioclase crystals considerably closer to their normative plagioclase compositions than the simple binary loop would predict, an important consideration in the interpretation of deep-seated gabbroic rocks, especially the plagioclase-rich anorthosites, whose parent magmas are the objects of much speculation because they may not be directly sampled.

The flattening of the plagioclase loop for liquids saturated with diopside has an important effect on the rate of change of plagioclase composition as a function of temperature (Wyllie, 1963), as compared to crystallization in the plagioclase field alone. Moreover, liquids in the plagioclase field move, as we shall see, approximately along lines of equal calcium content, whereas liquids on the field boundary move almost directly across contours of equal Ca. It therefore follows that Ca is depleted much more rapidly when diopside and plagioclase crystallize together than when plagioclase crystallizes alone (Morse, 1979a).

#### THE PLAGIOCLASE + L FIELD

Point D, Figure 8.7a, represents a bulk composition of (An<sub>65</sub>) 85%, Di 15% and the plagioclase must have the composition An<sub>65</sub> at the end of crystallization. This initial melt lies in the plagioclase + L field, and the path of the liquid is not as simple as that in the Di + L field. Upon cooling, the melt intersects the liquidus surface at about 1420°, with the production of some plagioclase crystals of about An<sub>87</sub> as the initial tie line indicates. Removal of this plagioclase composition from the liquid tends to drive the

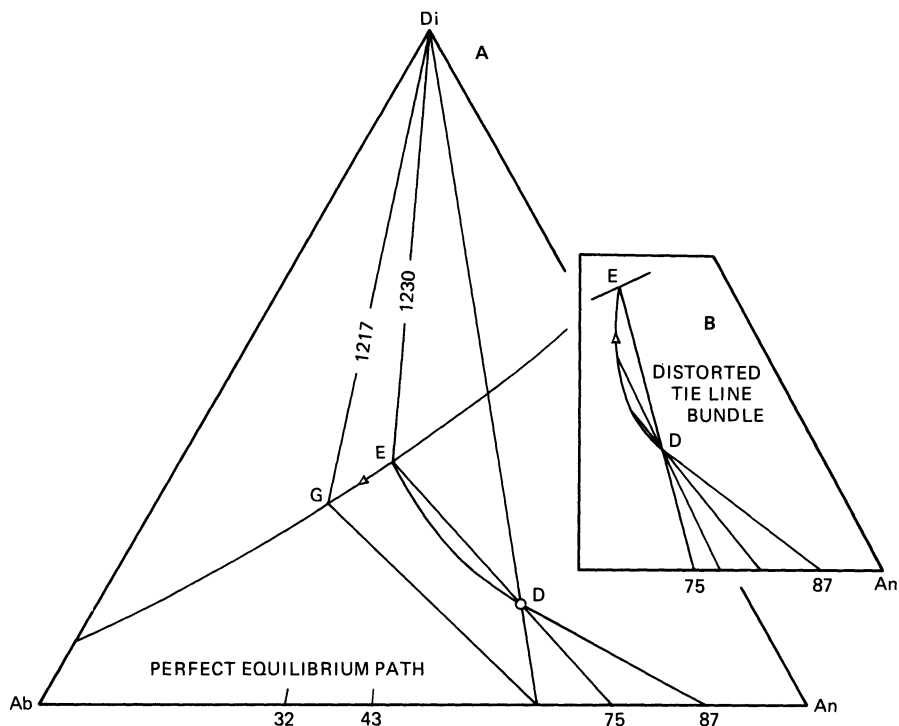


**Figure 8.7.** Perfect equilibrium crystallization of mixture *D* in Di-An-Ab. The liquid path is curved from *D* to *E*, and from *E* to *G*, where crystallization is complete. The inset (*B*) shows the constraint on the liquid path imposed by the plagioclase composition and the bulk composition *D*.

liquid directly away from  $An_{87}$ , but simultaneously, as this happens, crystals and liquid react to convert the plagioclase to a slightly more sodic composition. Therefore, the liquid may not move directly away from  $An_{87}$  for more than an instant of time, and the liquid must in fact follow a curved path. The restrictions on this path are shown in a distorted sketch, Figure 8.7b. The tie line connecting crystals and liquid must at all times pass through the bulk composition *D*. As the crystals become more sodic, the tie line rotates clockwise about the bulk composition as a pivot. Some sample tie lines at different stages of the process are shown in Figure 8.7b.<sup>2</sup> The curved path terminates at the field boundary at a point (*E*) shown by experiment to have a potential plagioclase composition of  $An_{43}$ , at a temperature of about  $1230^\circ$ , and the plagioclase coexisting with this liquid has the composition  $An_{75}$ . This plagioclase-liquid tie line is the last one to cut the bulk composition, for with the onset of diopside crystallization, a

<sup>2</sup>For construction purposes, it is important to know that these tie lines are tangents to fractionation paths. The position of *L* along a tie line is given by the point of tangency.

three-phase triangle is formed, and the rest of the crystallization process is identical in principle to the late stages of crystallization beginning in the  $Di + L$  field. The three-phase triangle pivots about  $Di$ , and the process is terminated when the solid leg cuts the bulk composition, at which point the plagioclase crystals have just reached  $An_{65}$ , the last drop of liquid has composition  $G$  (about  $An_{32}$  in potential plagioclase) and the total solid composition is  $Di$  15%, ( $An_{65}$ ) 85%.

The curved path  $D-E$  has a further interesting property. The tangent to this path at any point, extended to the plagioclase join, gives the fictive composition of what is being removed from the liquid to react with the plagioclase crystals and convert them to more sodic compositions. It is important to distinguish this "fictive plagioclase", being removed from the liquid at any instant, from the actual plagioclase crystal composition, which is the integrated composition of all crystals produced and reacted during the course of crystallization up to the moment of consideration.

It is also noteworthy that the curved liquid path  $D \rightarrow E$  is unique; no other bulk composition can yield the same liquid path, but each bulk composition follows its own unique course of crystallization. The path is dependent upon both the composition and the mass of crystals with which the liquid is in equilibrium.

A tangent to the liquid path  $E - G$ , when carried back to the solid-solid leg of a three-phase triangle, gives the fictive  $Di:Plag$  ratio of material being removed from the liquid at any instant. This ratio varies from about  $Di$  50%,  $Plag.$  50% at  $E$  to about  $Di$  45%,  $Plag.$  55% at  $G$ . At the moment when the liquid arrives at  $E$ , there is a discontinuous jump in this ratio from  $Plag.$  100% to  $Plag.$  50%, and the inheritance of this behavior from that in the parent binary system  $Di-An$  (Chapter 5) is clear.

## ISOTHERMAL SECTIONS

It is often useful to review the properties of ternary systems by means of complete isothermal sections which show the various two- and three-phase fields. Such sections become particularly important in the interpretation and application of experimental results. Isothermal sections can be constructed from any ternary liquidus diagram showing temperature contours, provided the slopes of tie lines between liquid and crystals are also known. Four isothermal sections for  $Di-An-Ab$  are shown in Figure 8.8, and these illustrate in another way the equilibrium crystallization processes just discussed. The liquid region, at any temperature, is simply the area enclosed by the pertinent temperature contour on the liquidus diagram. For temperatures greater than  $1274^{\circ}C$  (the  $Di-An$  eutectic), the  $L$  region is a band across the diagram, separating the region of  $Di + L$  from the region of  $Plag + L$  (Fig. 8.8a). At temperatures less than  $1274^{\circ}C$ , the liquid region

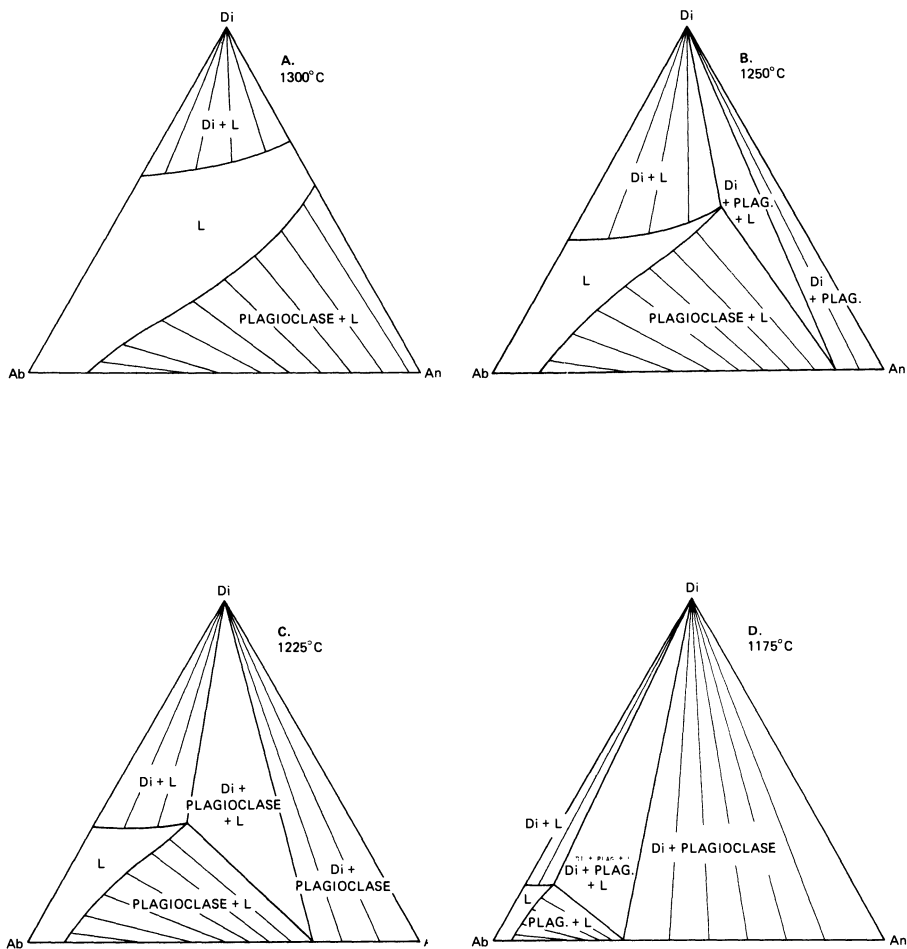


**Figure 8.8.** Closure of the liquid field illustrated in four isothermal sections of Di-An-Ab.

terminates at a point on the field boundary which is also an apex of the three-phase triangle  $Di + Plag + L$  (Fig. 8.8b–d). Another apex of this three-phase triangle lies at the  $Di$  corner, and the third lies on the plagioclase join. The liquid region is a one-phase region, the three-phase triangle is a three-phase region, and there are three two-phase regions denoting either solid-liquid equilibria ( $Di + L$ ,  $Plag + L$ ) or solid-solid equilibria ( $Di + Plag$ ). In two of the two-phase regions, tie lines radiate from the  $Di$  apex, and these can be drawn with no further information. In the  $Plag + L$  region, tie lines must be drawn according to the experimentally determined plagioclase and liquid compositions.

The three isothermal sections of Fig. 8.8b–d illustrate the sweep of the three-phase triangle across the diagram as it pivots about the  $Di$  apex with falling temperature. The  $L$  apex of the triangle follows the boundary curve shown on the liquidus diagram (Fig. 8.4).

The isothermal sections direct our attention away from the special bulk compositions discussed earlier and toward regions of coexisting phases instead. They show, with falling temperature, a progressively smaller field where bulk compositions are expressed as liquid only, progressively smaller  $Di + L$  and  $Plag + L$  fields, a progressively broader  $Di + Plag$  field. Within any one-, two-, or three-phase field, a variety of bulk compositions consist of the same phase or collection of phases at a given temperature. The experimental determination of isothermal sections aids in the construction of summary diagrams like the liquidus diagram.

## VARIANCE

The isothermal (isobaric) sections serve very well to illustrate the variance of the ternary system at various stages of crystallization and for various bulk compositions. Assuming a ternary system,  $W_p = c + 1 - \phi = 4 - \phi$  and the 1-, 2-, and 3-phase regions are therefore isobarically 3-, 2-, and 1-variant respectively when temperature is also a variable, as in the liquidus diagram (Fig. 8.4). In the isothermal, isobaric sections, however, we have  $W_{p,t} = c - \phi$ , or in other words a second arbitrary restriction on variance, and the 1-, 2-, and 3-phase regions are 2-, 1-, and 0-variant respectively. For example, in the 1-phase liquid region, which is isobarically, isothermally divariant, two composition variables must be specified to describe the system, (i.e. to identify the liquid composition) or two such variables (such as the  $Di/An$  or  $Ab/An$  ratios) may change without changing the state of the system, namely liquid. In a 2-phase region, only one compositional variable need be specified to describe the system, either a plagioclase composition (for  $Plag + L$  and  $Plag + Di$ ) or a liquid composition (for  $Di + L$ ). And in the 3-phase triangle, the mere coexistence of 3 phases means that the

compositions of all phases are completely defined; the phase compositions are invariant.

#### COMPLETION OF EQUILIBRIUM CRYSTALLIZATION

Any interior composition in Di-An-Ab can be expressed in terms of two solid phases, Di and a plagioclase feldspar of specific composition. When the system exists in these two specific phases, their tie line cuts the bulk composition and no liquid can be present. This is another way of saying that the last of the liquid (G, Fig. 8.7), on crystallization, will have been used up just as the last increment of rotation of the Di-Plag tie line takes place, to bring the tie line onto the bulk composition (D, Fig. 8.7). The last liquid present on crystallization will therefore, in general, lie in the supposedly ternary system on the univariant boundary curve, and the final stages of crystallization will be univariant, polythermal, as in the An-Ab system. The reaction  $L = \text{Di} + \text{Plag} + \text{cals}$  will continue with falling temperature until the liquid is used up. The composition of the final liquid is dictated solely by the initial bulk composition, except that it must lie on the boundary.

#### APPLICATION OF THE LEVER RULE

The lever rule may be simply applied in ternary systems to any assemblage of two phases. An isothermal tie line Di - L intersects the bulk composition A in Figure 8.9a. The bulk composition divides the tie line into two segments, denoted  $l$  and  $s$  in the diagram, representing respectively the proportions of *liquid* and *solid*. The weight fraction of the system which has crystallized as Di by the time the liquid has advanced to point L is given by  $s/(s + l)$ . As with the binary lever rule (Chapters 5 and 6), it is important to know which segment of the line represents liquid, and which represents solid. This is self-evident if it is recalled that the initial state, when the first crystal of diopside is just forming, is given by the tie line A-Di; the liquid lies at the bulk composition and the system consists almost solely of liquid. Therefore the  $l$  or liquid segment is always that segment lying between the bulk composition and the crystalline phase. The  $s$  or solid segment grows with falling temperature while the  $l$  segment remains unchanged in this case.

In the case of the two phases plagioclase and liquid, the  $s$  and  $l$  segments both change length, as shown in Figure 8.9b. In this case, two tie lines are shown for two temperatures,  $T_1 > T_2$ .  $P_1$  and  $L_1$  are the plagioclase and

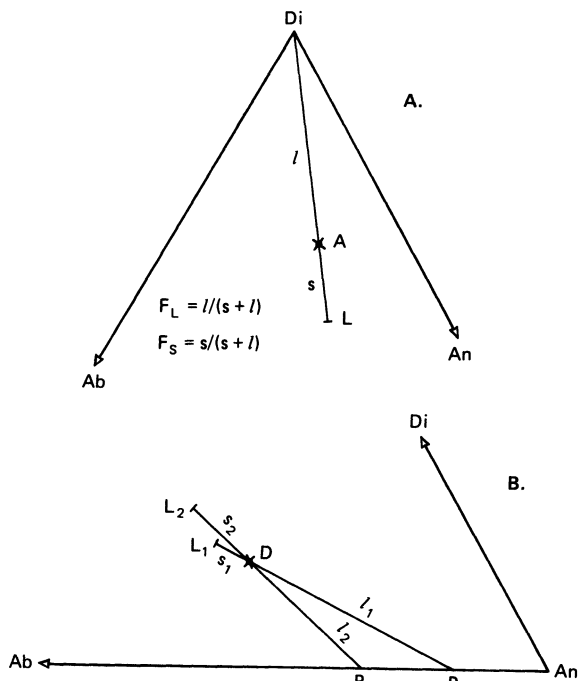


**Figure 8.9.** Lever rule in a ternary system (Di-An-Ab). A. Illustration from the diopside + liquid field. B. Illustrations from the plagioclase + liquid field at two different temperatures.

liquid, respectively, at temperature  $T_1$ , and the fraction of the system represented by crystals is given by  $s_1/(s_1 + l_1)$ . A larger fraction of crystals is shown by the tie line  $P_2 - L_2$  for temperature  $T_2$ ; not only has the length of the  $s$  segment increased over that at  $T_1$ , but the  $l$  segment has diminished by virtue of the reaction of plagioclase from  $P_1$  to  $P_2$  with falling temperature. Therefore the fraction of crystals,  $s_2/(s_2 + l_2)$ , is appreciably greater than at  $T_1$ .

When two phases are both solid, i.e. Di + Plag, the lever rule applies to give the fraction of each, in the same fashion as the  $l - s$  levers. The segment of the tie line between A and Di (Figure 8.10) represents the fraction of plagioclase, and the segment between A and  $P_2$  represents the fraction of diopside.

When three phases occur, all the ratios of interest can be determined by means of levers. The total solid composition (TSC) now lies within the ternary diagram on the Plag - Di leg of a three-phase triangle, and its position on this leg must be determined first, as follows. It is apparent that the tie line between the TSC and the liquid must always lie through the bulk composition, as in Figure 8.10. Therefore a line from  $L_1$  through the bulk composition A locates the TSC on the leg Di -  $P_1$ . The segment A-

TSC, by analogy with the segment A - Di in Figure 8.9a, must represent the liquid fraction, while the segment A -  $L_1$  represents the solid fraction. A convenient measure of the solid : liquid ratio is the fraction of liquid remaining, or  $F_L$ , which is given by  $l/(s + l)$ , and amounts to 0.31 in the illustration (Fig. 8.10). Among crystals, the fraction of plagioclase may be found by forming the fraction  $(Di-TSC)/(Di-P_1)$ , but since in this case the solid-solid leg of the three-phase triangle is radial from one corner of the phase diagram, the ratio can be read directly from the coordinates of the diagram. The fraction of plagioclase is 0.27 in Fig. 8.10. In a similar manner, the exact composition of liquid  $L_1$  can be determined from the coordinates of the diagram and the extension of the leg  $L_1 - Di$ .

In summary, we may extract the following information from Fig. 8.10. A liquid, formed by equilibrium crystallization from bulk composition A,

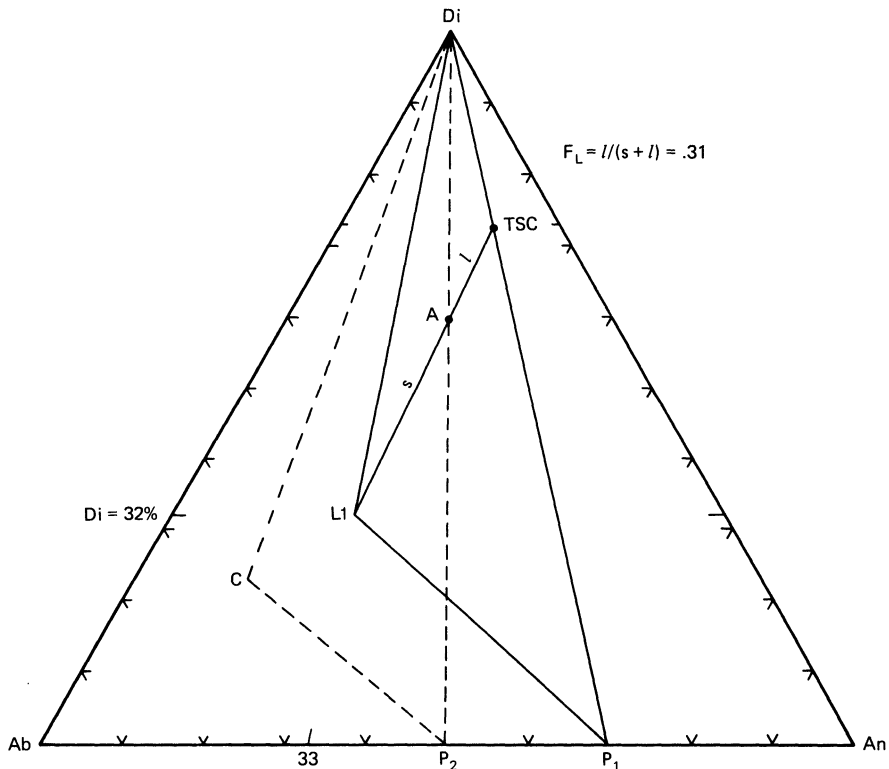


**Figure 8.10.** Lever rule for a three-phase assemblage in Di-An-Ab. The position of the total solid composition (TSC) is found by drawing a line from the liquid ( $L_1$ ) through the bulk composition (A) to the solid-solid leg ( $Di-P_1$ ) of the three-phase triangle. The lever rule is then applied in the usual way, with the bulk composition as fulcrum. The *dashed* three-phase triangle refers to a lower temperature, at which crystallization is completed.

coexists with plagioclase and diopside, has composition  $L_1$  (Di 32%, (An<sub>33</sub>) 68%), and amounts to 31% by weight of the original mixture. The remainder of the original mixture has crystalline composition TSC, or Di 73%, (An<sub>70</sub>) 27%.

The final three-phase triangle involving liquid C and plagioclase An<sub>50</sub> is shown with dashed lines in Fig. 8.10. It is apparent, from the fact that one leg of this triangle cuts the bulk composition A, that crystallization has been completed, and  $F_L = 0$ .

A series of such analyses can be made for various stages of equilibrium crystallization, and the path of the total solid composition can then be drawn for the entire history of crystallization. This is done in Fig. 8.11, where the TSC path is shown as a heavy curved line. All the three-phase triangles from which points on this path were constructed are shown, and beside the liquid apex of each of these triangles is shown  $F_L$ , or the fraction of liquid remaining. It should be noted that the initial portion of the TSC path is represented by the point Di; only when the liquid has reached point

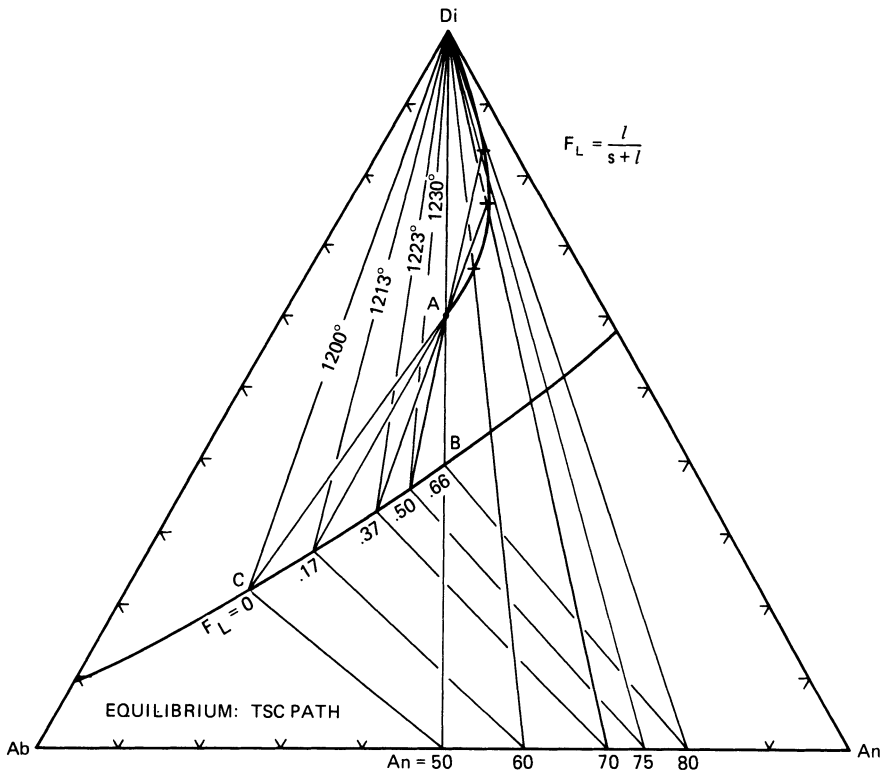


**Figure 8.11.** Path of the total solid composition (TSC path): diopside field of Di-An-Ab. The TSC leaves Di when  $F_L = .66$  and follows the curved path to A. The path is constructed from a series of TSC positions found as in Fig. 8.10.

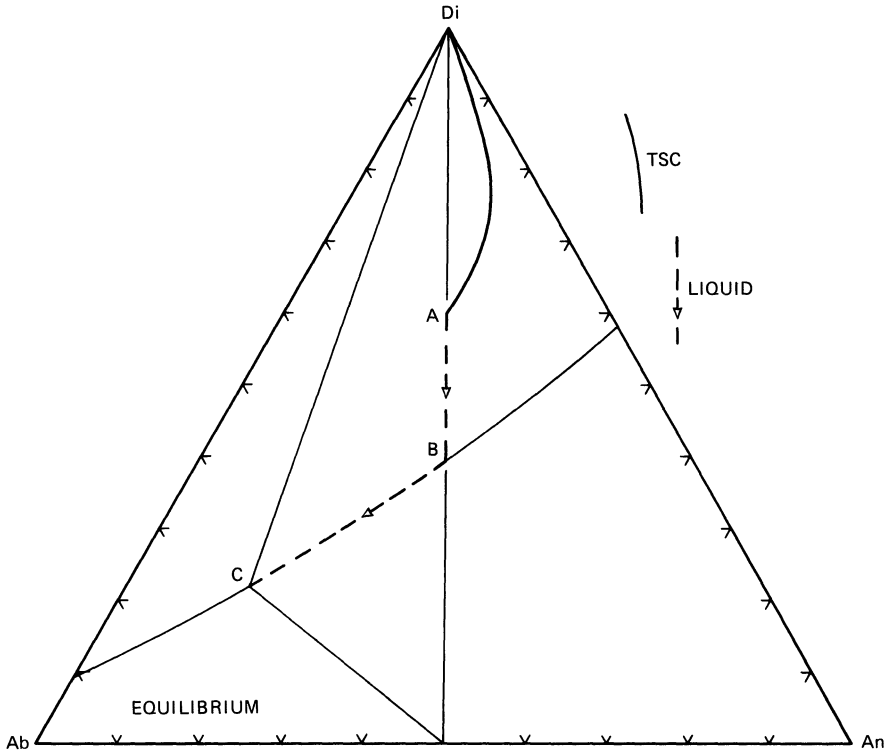


**Figure 8.12.** Summary of liquid and TSC paths for bulk composition A. Note that the TSC remains at Di until the liquid reaches B.

B ( $F_L = .66$ ) does the TSC move off the composition of pure diopside. In other words, 34% of the initial mass must have crystallized before the liquid reaches the field boundary. The remaining crystallization history can be read from the diagram in complete detail. For example, when  $F_L = .37$ , the liquid has composition Di 33%, ( $An_{37}$ ) 67%, and the solids consist of Di 76%, ( $An_{70}$ ) 24%, together constituting 63% of the initial mass. Such analyses may be useful in interpreting the crystallization history of both basaltic lavas consisting of crystals and glass, and gabbroic intrusive rocks whose textures suggest equilibrium crystallization.

Fig. 8.12 summarizes the liquid and TSC paths for bulk composition A. It should be noted that the TSC path lying away from Di applies only to the crystallization interval B-C in terms of liquid composition.

A TSC path for the crystallization of the plagioclase-rich bulk composition D is derived in Fig. 8.13. The first portion of this path, corresponding to the motion of liquid from D to E on the field boundary, is confined to the plagioclase series between  $An_{87}$  and  $An_{75}$ . Thereafter, the TSC rises along a curved path to D as the liquid continues to produce diopside and plagioclase. This TSC path and the liquid path which produced it (taken

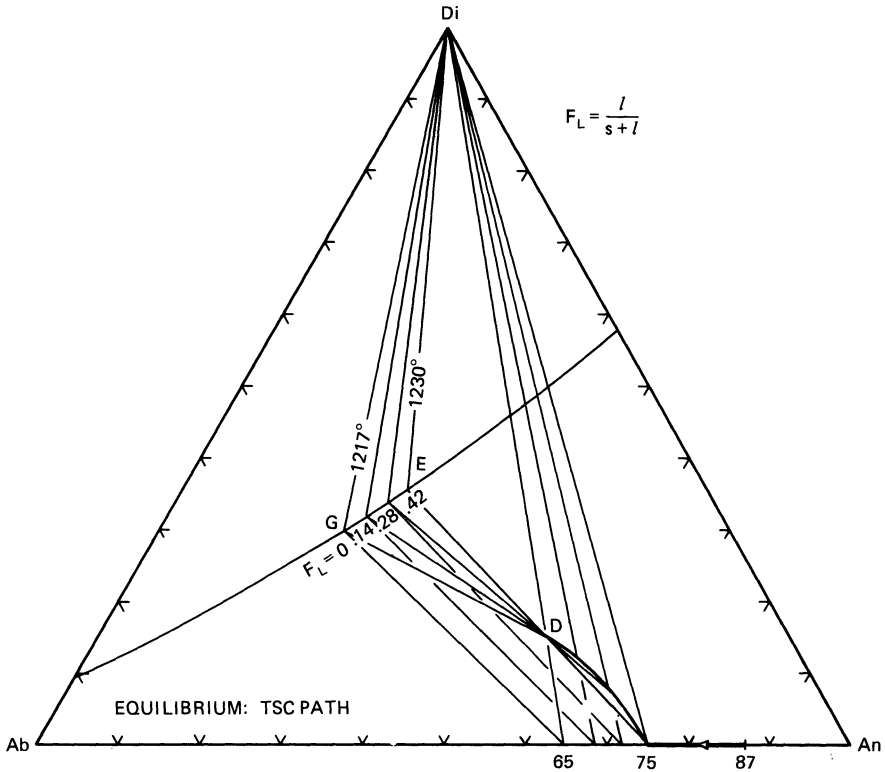


**Figure 8.13.** TSC path: plagioclase field. As the liquid moves from D to E (path not shown) the TSC moves from An<sub>87</sub> to An<sub>75</sub> along the plagioclase sideline. While the liquid moves from E to G, the TSC moves from An<sub>75</sub> to D along the curved path. The construction of the TSC path follows the same method as for composition A (Fig. 8.11).

from Fig. 8.7) are compared in Fig. 8.14. The segment E-G of the liquid path corresponds to the segment 75-D of the TSC path.

### Fractional Crystallization

The “ternary” system Di-An-Ab is strongly dominated by the plagioclase join in its crystallization behavior, and as noted earlier, fractional crystallization has a profound effect on the late stages of crystallization, as in the plagioclase system itself. Moreover, we shall see that fractional crystallization of liquids within the plagioclase field has an immediate effect on the course of liquid composition. It is convenient to begin with the Di + L field, which is simpler.

Fractional crystallization in the Di + L field begins as it does in Di-An:

crystals of Di are removed as soon as they form, and the liquid composition changes directly away from Di. At any instant, there is only an infinitesimal amount of crystalline Di in equilibrium with the liquid, and each new liquid composition therefore has all the properties of an initial liquid of new bulk composition. Accordingly, when the liquid reaches the field boundary, as at B in Fig. 8.5, it cannot be distinguished from an initial liquid formed in equilibrium with plagioclase and diopside. The textures of many basaltic and gabbroic rocks suggest simultaneous crystallization of pyroxene and plagioclase from an early stage of their history, and it is fair to suppose that these magmas may have been brought to the appropriate field boundary by fractional crystallization due to sinking of pyroxene while the magma was being emplaced.

Continued fractional crystallization, now of plagioclase and diopside, drives the liquid to lower temperatures along the field boundary. Even though crystals may be removed as soon as they are formed, the liquid experiences equilibrium with both kinds of crystals, and cannot therefore

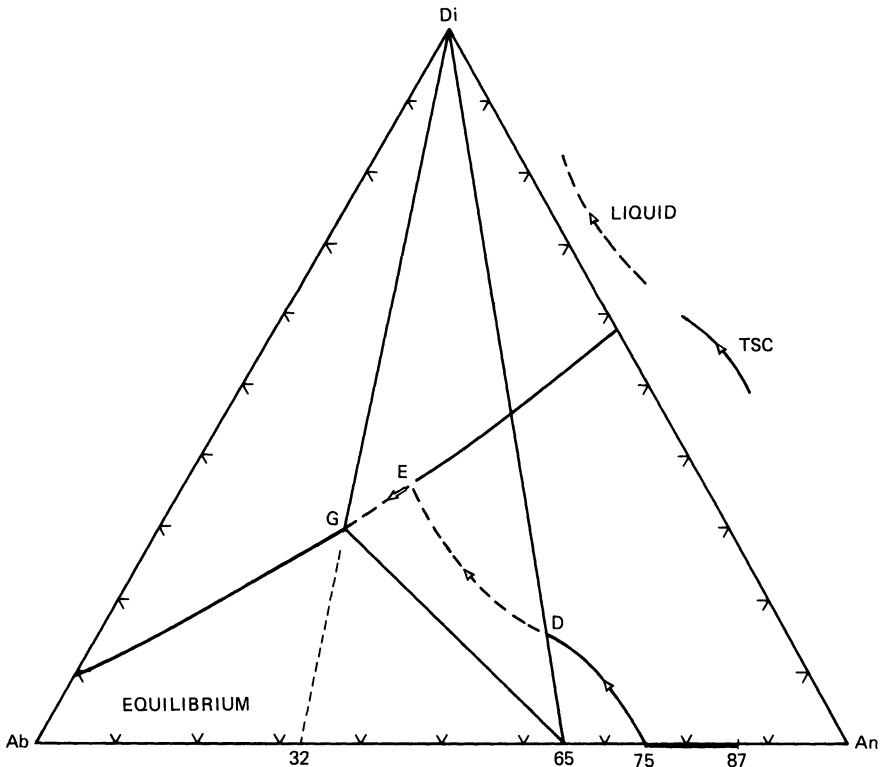


**Figure 8.14.** Summary of liquid and TSC paths for bulk composition D. The TSC path along the plagioclase sideline is found from tie lines through D from the liquids along path D-E.

leave the field boundary or its variance of one. The plagioclase crystals formed during this process have compositions given at any instant by the slope of experimentally-determined Plag - *L* lines for the given isotherm. The array of plagioclase crystals formed over a period of time has a continuous range of compositions, from calcic to sodic, expressed either as accumulated homogeneous crystals of differing composition, or as zoned crystals, depending on whether the fractionation mechanism involves physical separation of crystals or rapid cooling which prevents equilibrium of crystalline cores with liquid. The history of the fractionating liquid is now exactly similar to that of fractionating liquids in An-Ab, the only differences being related to the presence of Di crystals and the lower temperatures due to the presence of the Di component. As in the pure plagioclase system, theoretically perfect fractional crystallization drives the liquid all the way to the An-free sidelines Di-Ab; in truth, we are aware that the plagioclase effect will prevent crystallization of pure Ab in this Ca-bearing system, and cause Na-Si enrichment in the liquid, so the very late stages of fractional crystallization are scarcely worth discussing in terms of the ternary model. If the system were truly ternary, a eutectic in Di-Ab would be the ultimate destination of the liquid.

Fractional crystallization of liquids initially in the plagioclase field involves new principles of liquid paths. Recall that with equilibrium crystallization, liquids were at all times constrained to lie on a tie line (Fig. 8.7) which passed through the initial bulk composition to plagioclase crystals. In the case of perfect fractional crystallization, the liquid knows nothing of the initial bulk composition, and each new liquid composition behaves as a new initial liquid composition. The liquid need yield only enough Ab component at a given instant to furnish the current plagioclase composition; it need *not* yield Ab component to make over all the previously-formed crystals, as it was required to do in equilibrium crystallization. The liquid therefore becomes Ab-rich more rapidly than in equilibrium crystallization, that is, it follows a more Ab-rich path, such as the one illustrated in Fig. 8.15. This path is curved, inasmuch as the composition of current plagioclase crystals changes continuously with falling temperature. However, the curvature is slight compared to that of the equilibrium path (Fig. 8.7). The exact path must be determined experimentally, by finding the slopes of plagioclase-liquid tie lines at different temperatures and compositions and constructing a series of isothermal sections such as those in Fig. 8.8. The *fractionation path* is a curve whose tangent at any temperature gives the composition of plagioclase crystals separating from the liquid; such a path can be constructed from the temperatures, liquid compositions, and tie-line slopes read from the isothermal sections. In the plagioclase field, all fractionation paths emanate from the An corner.

In the example shown in Fig. 8.15, the initial plagioclase separating from liquid D is An<sub>87</sub>, just as in the case of equilibrium crystallization. The fractionating liquid moves away from this plagioclase composition for only

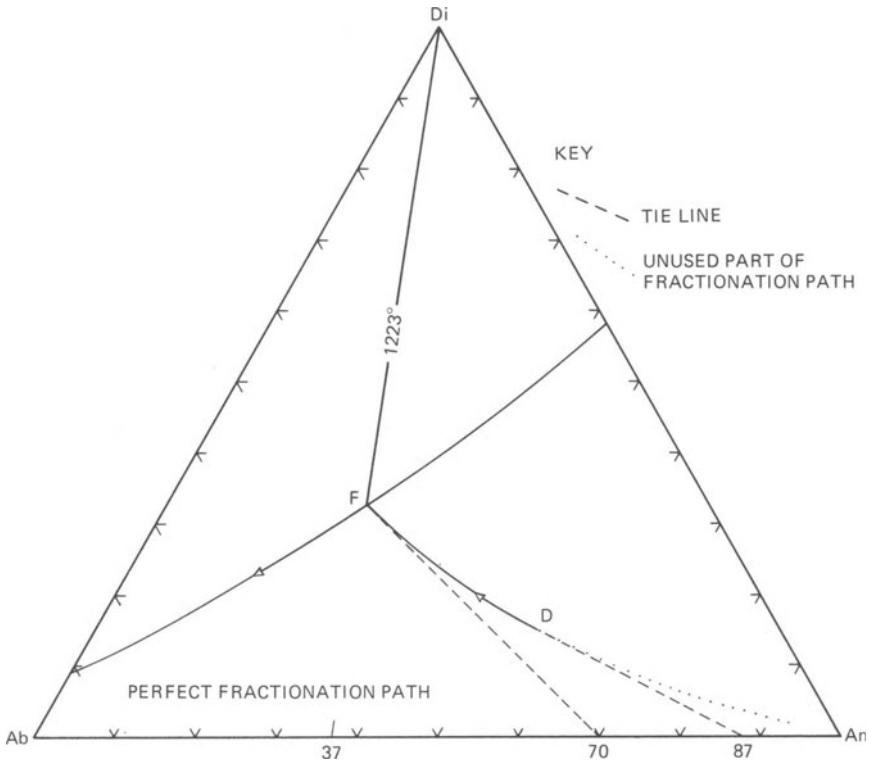


**Figure 8.15.** Liquid path with fractional crystallization, bulk composition D. The plagioclase composition at any moment lies on a tangent to the fractionation path D-F. The liquid path extends from D through F to the Di-Ab sideline.

an instant of time, but then moves, at an infinitesimally lower temperature, away from an infinitesimally more sodic plagioclase composition. When the liquid reaches F on the boundary curve, it has a composition of Di 33%, (An<sub>37</sub>) 67%, and is in equilibrium with traces of crystals of diopside, and plagioclase of composition An<sub>70</sub>, given by the tangent to the fractionation path at F.

Inasmuch as the fractionation path is a function of *current* plagioclase composition only, in contrast to the *integrated* plagioclase composition controlling equilibrium crystallization, it is apparent that any liquid lying along the path D-F will follow the same path. This is unlike the case of equilibrium crystallization, in which every bulk composition yields a different path. In Fig. 8.15, D is a point lying on a fractionation path which extends backward (dotted) toward An. This whole path is shown as one of a family of fractionation paths in Fig. 8.16. These curves show the courses of liquids produced by fractional crystallization from any of a wide range of bulk compositions in the Plag + L field. Similar fractionation paths (straight lines) are shown in the Di + L field. Equilibrium paths may be

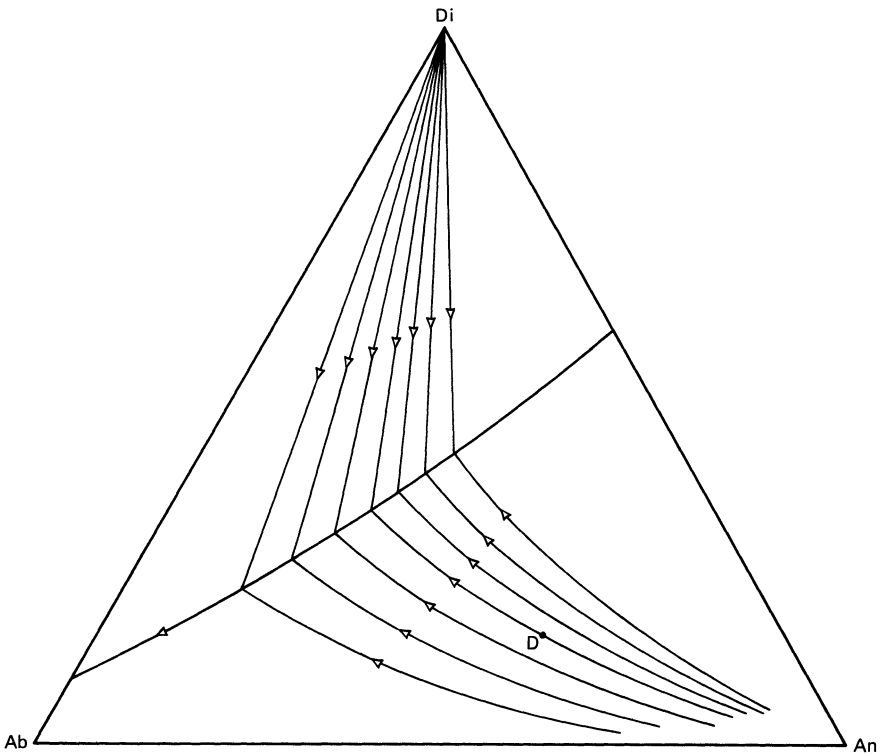


**Figure 8.16.** Sample fractionation paths in Di-An-Ab. All paths in the plagioclase field emanate from An.

found from a collection of fractionation paths, inasmuch as equilibrium liquids lie on a succession of fractionation paths, at points of tangency with tie lines through the bulk composition. An exceptionally clear discussion of these matters is given by Bowen (1941).

The completion of fractional crystallization, once the liquid has reached the field boundary, is the same as with bulk composition A, in the Di + L field (Fig. 8.12); removal of plagioclase and diopside crystals from the liquid causes the latter to move down the field boundary, ideally until a eutectic in Di-Ab is reached, but in fact, eventually out of the Di-An-Ab ternary into chemographically more complex space. The liquid composition may thus cover an extreme range over a large range of temperature, compared to the equilibrium case.

Some aspects of equilibrium and fractional crystallization may be compared by inspection of Figs. 8.7 and 8.15, in which the initial bulk composition D is the same. The equilibrium liquid path reaches the field boundary at E, where plagioclase crystals have the composition  $An_{75}$  and the liquid has a potential plagioclase composition of  $An_{43}$ . The fractionation liquid path reaches the field boundary at F, where the analogous compositions are  $An_{70}$  and  $An_{37}$ , respectively. The two paths D-E and D-F are

compared directly in Fig. 8.17. The most important difference between the two paths is that of the limiting final liquid composition, point G in the equilibrium case and point F' in the fractionation case (Fig. 8.17).

Use of the lever rule requires the total solid composition to be correctly known. There are three stages in any fractional crystallization process when the TSC is accurately known: at the start, at any time until the liquid has just reached the field boundary, and at the end. The starting TSC is given by the solidus, i.e. a tie line from the liquid to diopside or a plagioclase. When the liquid has just reached the field boundary, or at any time before it does so, the TSC is given by a lever from the liquid through the bulk composition to the solids. At the end of crystallization, the TSC is equal to the bulk composition. The only stage of crystallization for which the TSC is not immediately obtainable by construction is the stage during which the liquid lies on the cotectic  $L(\text{Di}, \text{Plag})^3$ . In this book, we shall use two methods of finding the TSC for cotectic liquids. The first is an approximate method, completely graphical, and the second is the more

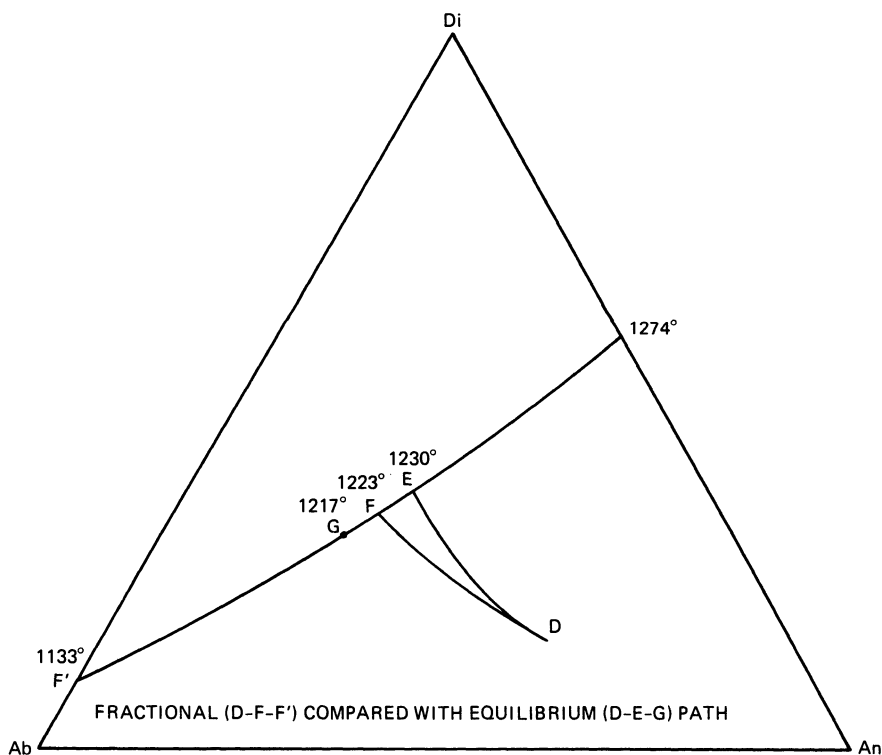


**Figure 8.17.** Comparison of fractional and equilibrium crystallization paths for bulk composition D.

<sup>3</sup> $L(\text{Di}, \text{Plag})$  signifies "liquid in equilibrium with crystals of diopside and plagioclase." It is a convenient shorthand for denoting an equilibrium without regard to the direction of reaction.

formal treatment in which the ratio  $R$  is calculated, as was done for the plagioclase system. The second method is described later in the chapter.

Fractional crystallization in the Plag. +  $L$  field yields liquid  $F$  from bulk composition  $D$ , Fig. 8.18, by crystallization of plagioclase crystals ranging from  $An_{87}$  to  $An_{70}$  in composition. Now liquid  $F$  and the *mean* crystalline plagioclase composition must, together, add up to bulk composition  $D$ ; therefore, a line (not a tie line) from  $F$  through  $D$  to the plagioclase sideline yields the mean plagioclase composition, in this case  $An_{80}$  (Fig. 8.18), slightly more calcic than the mid-range value between  $An_{70}$  and  $An_{87}$ . Measurement of the two segments of this line, with application of the lever rule, yields the value  $F_L = .46$  (54% solidified), which is to be compared with  $F_L = .42$  at  $E$  in the equilibrium case (Fig. 8.13). The fraction of liquid remaining can be similarly determined for any liquid along the fractionation path  $D-F$ .

As the liquid moves from  $F$  toward  $Ab$ , we have no direct way of measuring the integrated plagioclase composition. However, assuming ternary equilibria, resulting in termination of fractional crystallization at  $Ab_{91}Di_9$  on the "binary" sideline, we can draw (Fig. 8.19) a rigorous final construction line from this point to  $An_{65}$ , the required *mean* plagioclase composition for bulk composition  $D$ . This construction line may be viewed as a Plag -  $L$  leg of a construction triangle whose other two legs are  $Di-L$  and  $Di$ -mean Plag. We may *interpolate* additional construction lines between  $(Ab_{91}Di_9)$ - $(An_{65})$  and  $F-D$  by equally dividing the angle subtended by these known lines. These interpolated construction lines then yield a series of liquid compositions on the field boundary and a related series of mean plagioclase compositions. The  $Di$ -Plag legs arising from these derived, mean

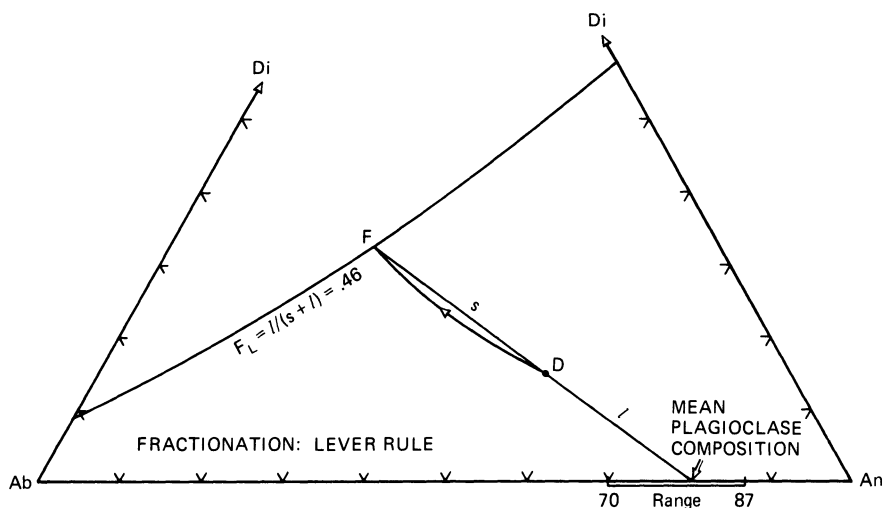


**Figure 8.18.** Lever rule with fractional crystallization. A line from liquid  $F$  through bulk composition  $D$  defines the mean plagioclase composition, which is a TSC.

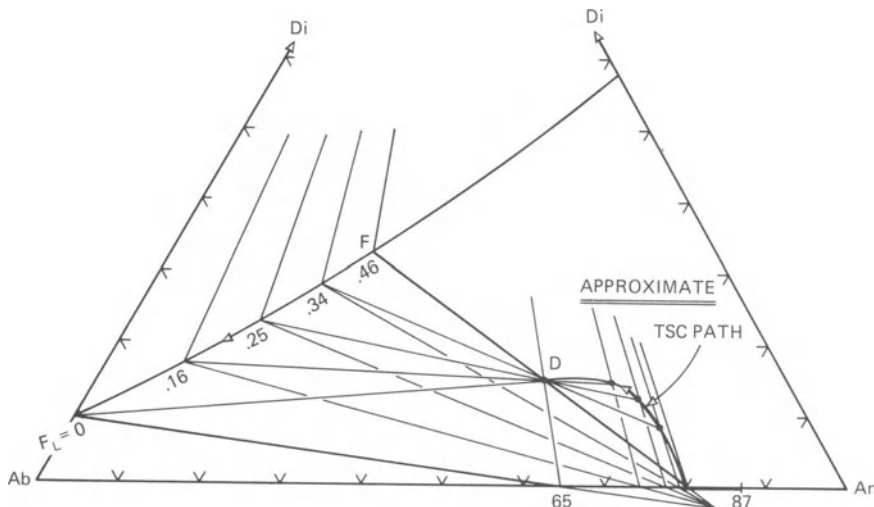


**Figure 8.19.** Approximate TSC path for fractional crystallization of bulk composition D. The path along the plagioclase sideline is exact. The curved path is generated from construction triangles Di-L-mean plagioclase, and the mean plagioclase composition is interpolated between An<sub>80</sub> and An<sub>85</sub> (see text). The main point of the exercise is to apply the lever rule and find the fraction of liquid remaining at any stage of the process.

plagioclase compositions then contain the loci of the total solid compositions, which in turn are found by means of construction lines running from the various liquid compositions through D, the bulk composition. Application of the lever rule to these lines through D yields the *approximate* fraction of liquid remaining,  $F_L$ , and the *approximate* TSC path is drawn through the terminations of these lines on the Di-Plag legs. The path as drawn in Fig. 8.19 runs from An<sub>87</sub> to An<sub>80</sub> on the plagioclase join, then climbs steeply in Di content, finally approaching D in a direction toward Ab<sub>91</sub> Di<sub>9</sub>. The related fractions of liquid remaining are posted in the figure next to the liquid composition.

This procedure rests on the assumption that the interpolated construction lines should be evenly prorated throughout the angle made by the two known construction lines.<sup>4</sup> Although the results are approximate, they are

<sup>4</sup>A formal calculation of the relation between mean plagioclase composition and  $F_L$  can also be made by means of the Rayleigh (1896) distillation equation, which may be written for our purposes:

$$\overline{Ab}^{xt} = Ab_0^i (1 - F_L^K) / (1 - F_L)$$

where  $\overline{Ab}^{xt}$  is the mean concentration of Ab in the (TSC) plagioclase,  $Ab_0^i$  is the initial concentration of Ab in the liquid, and the exponent  $K$  is the Nernst distribution coefficient ( $Ab^{xt}/Ab^l$ ); see for example Neuman, Mead, and Vitaliano (1954) and Gast (1968). The distribution coefficient  $K$ , however, is not constant but variable, and interpolation of this coefficient for various stages  $F_L$  is equivalent to the graphical interpolation used in Fig. 8.19. Greenland (1970) has discussed the Rayleigh equation for variable  $K$ , but analytic expressions for its variation have not been compiled for systems of geologic interest.

useful as illustrations of the amounts of residual liquids which have compositions corresponding to natural rocks or their idealized models. For example, if liquids with potential plagioclase composition more sodic than  $An_{10}$  be accepted as models for granitic or syenitic rocks in Di-An-Ab, Fig. 8.19 suggests that a bulk composition such as D can yield about 14% of its initial mass in the form of such residual liquid. Composition D, however, is not basaltic, having enough plagioclase to be classed as gabbroic anorthosite. A basaltic bulk composition of Di 40%, ( $An_{50}$ ) 60% lies almost precisely on the boundary curve, and by the same kind of analysis about 19% of its initial mass falls in the class of liquids with potential plagioclase less than  $An_{10}$  and Di less than 16%. This analysis therefore suggests that respectable volumes of "granitic" or "syenitic" magmas could be generated by fractional crystallization of basaltic magma, although other factors not considered here no doubt constrain this estimate further.

Perhaps one of the most interesting features of the Di-An-Ab phase diagram is the fact, mentioned above, that a reasonable model basalt of Di 40% ( $An_{50}$ ) 60% falls almost on the boundary curve. Natural basalts which show textural evidence of simultaneous crystallization of plagioclase and augite are so common as to suggest that they crystallized on a natural analog of the boundary curve. Whether they fortuitously arrived at such a magic composition when they were generated in the mantle, or achieved the boundary curve by removal of plagioclase or augite in transit from the mantle, is not clear; our model diagram suggests, however, that the second case, low-pressure fractional crystallization, would be adequate to explain the phenomenon.

### Rock Paths (ISC Paths)

The TSC path in equilibrium crystallization is an example of a crystal path (Presnall, 1969) or, to bring home the relevance to nature, a *rock path*. A rock path describes the changing assemblage of crystals produced during crystallization or melting. Although in the case of equilibrium crystallization the rock path is identical with the TSC path, it is not so in fractional crystallization, where the TSC path is merely a geometrical convenience. We have already pointed out that the tangent to the liquid path at any point contains the composition of material being instantaneously removed from the liquid. In the case of equilibrium crystallization, this material is fictive, and has no physical expression save as an incremental part of the TSC. In the fractional case, however, the material being removed is physically isolated and preserved. This material constitutes the instantaneous solid composition (ISC), and the fractional rock path is the ISC path. The ISC lies at all times on the tangent to the liquid path *and* on the tangent to the TSC path. Fig. 8.20 illustrates the fractional rock path for bulk composition

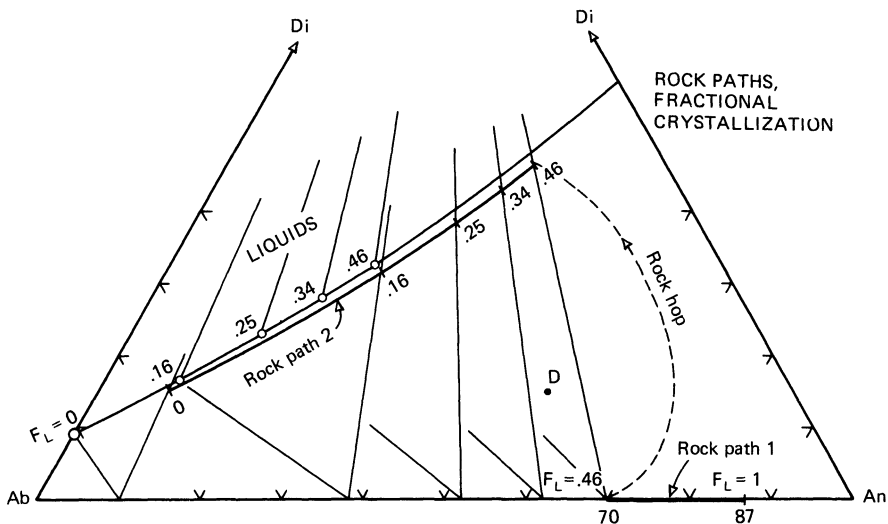


**Figure 8.20.** Rock paths in fractional crystallization of bulk composition D. The “rock hop” is a discontinuous change from pure plagioclase to gabbro. Rock path 2 terminates within the ternary diagram because of the “plagioclase effect”. In a truly ternary system it would terminate on the Di-Ab sideline.

D, and also illustrates the generality that fractional rock paths are discontinuous. The first part, labelled rock path 1 in the figure, results from the liquid path from D to F (Fig. 8.18) where the liquid produces plagioclase only from  $An_{87}$  to  $An_{70}$ . As soon as the liquid reaches F, diopside begins to crystallize, and the tangent to the liquid path is now the tangent to the field boundary. The material being instantaneously removed from the liquid is now gabbroic rather than anorthositic, and can be identified as the point where the tangent to the liquid path cuts the solid-solid leg connecting Di with  $An_{70}$ . A discontinuous “rock hop” thus occurs between the first and second parts of the rock path. The remainder of the rock path (Fig. 8.20) is smoothly continuous until the liquid is exhausted. The fractionation stages  $F_L$  are identified in the figure along the rock path as well as at the liquid apex of each 3-phase triangle. These numbers emphasize the familiar expectation that the plagioclase composition in rocks produced by fractional crystallization will be more calcic than are the liquids from which they crystallize.

The second part of the rock path in Fig. 8.20 lies very close to the field boundary, which may give the impression that rock paths in general tend to follow liquid paths. This is *not* necessarily the case, and is true here only because the field boundary is smooth and so nearly straight. A sharply curved field boundary would yield a quite divergent rock path. However, it is of geological interest to note that, because of the near-straightness of the field boundary, model basaltic magmas may be expected to yield fractional rock paths not unlike the liquid paths.

In terminating the rock path in Fig. 8.20, the non-ternary nature of the system has been recognized, and the final plagioclase formed by the liquid lying in the Di-Ab sideline is assumed to have a composition of  $An_{10}$ . In a truly ternary system, the rock path would terminate where the liquid path terminates, as it would, for example, in the system An-Ab.

## Equilibrium Melting

We consider two cases, in which the bulk rock composition is alternatively diopside-rich and plagioclase-rich. In the first case, we may take composition A, Fig. 8.5 as the rock composition. Fig. 8.5c shows that point C is the last liquid left on crystallization, so it must therefore represent the beginning-of-melting liquid composition for bulk composition A. Melting therefore begins, in this plagioclase-bearing diopside rock, at a temperature of 1200°, and as heating continues, the liquid changes toward B (Fig. 8.5) at the expense of plagioclase and diopside crystals. At B, plagioclase is used up, and the liquid changes composition toward A as heat is added. The path is therefore the reverse of equilibrium crystallization.

The second case is a duplicate of the first, in principle. The bulk composition D in Fig. 8.7 may be considered as the rock. Melting begins at 1217°, with production of liquid G. With continued melting, liquid achieves composition E, and finally D, after Di crystals have disappeared.

In both cases, equilibrium melting is the exact reverse of equilibrium crystallization: levers and TSC paths may be used at any stage of the process to determine the quantitative yield of liquid.

It is of particular note that melting of any homogeneous *bulk* composition is initiated at the *equilibrium* termination of crystallization temperature, which is the *solidus* for the rock in question. The solidus is not the lowest-temperature point on the liquidus surface, such as 1133° on Di-Ab, unless the rock itself is a heterogeneous mixture containing domains of that special, low-melting composition.

The lesson to be learned from equilibrium melting is that it would be impossible to distinguish a magma so formed from a magmatic residue of a crystallization process.

## Fractional Melting

The initiation of fractional melting is the same as in the equilibrium cases cited above. However, continuous removal of liquid occurs, and the melting path is unlike the reverse of the equilibrium crystallization path. The first

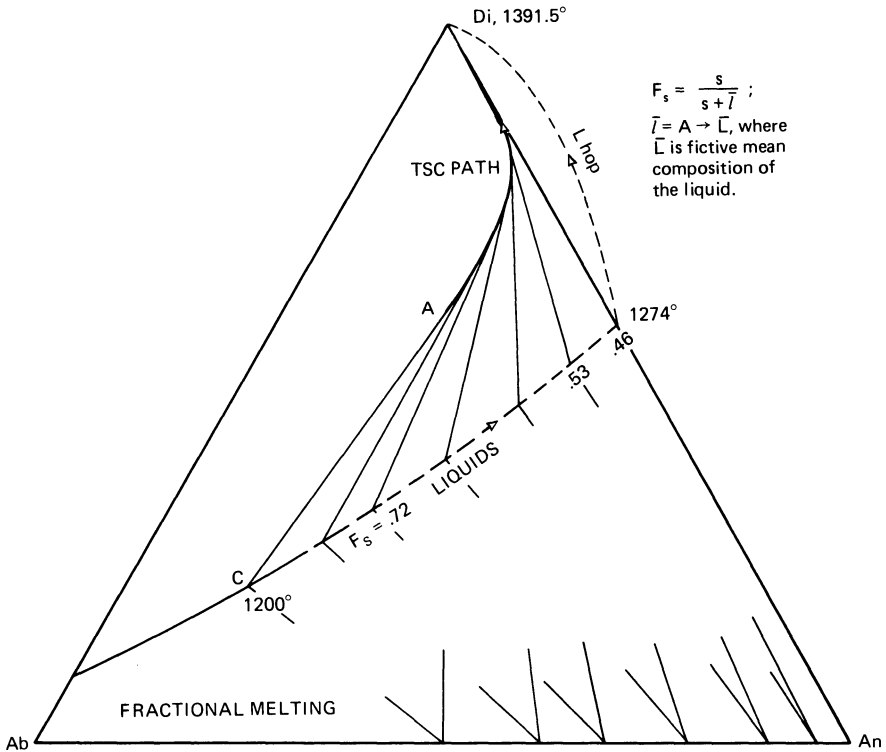


**Figure 8.21.** Fractional melting of bulk composition A in Di-An-Ab. The fictive mean composition of the liquid removed ( $\bar{L}$ ) always lies on the extension of a line from the TSC through A. This mean composition is not shown in the diagram, but its locus runs from C to a point directly beneath A, and then approaches A while Di is being melted.

increment of melting of bulk composition A in Fig. 8.11 or Fig. 8.21 yields liquid C, and drives the TSC away from AC. The liquid-TSC tie lines are not constrained to pass through A, however, and each new TSC acts as a new solid composition about to melt for the first time. The resulting *reverse* TSC path is unlike the crystallization TSC path, being a curve whose tangent at any point runs to the composition of liquid being fractionally removed. Plagioclase, as in the system An-Ab (Chapter 6), is not completely dissolved until it reaches the composition of pure anorthite, because fractional removal of liquid changes the crystalline composition continuously toward An. Fractional melting therefore yields a series of liquids all the way along the field boundary to Di-An, as shown in Fig. 8.21, and the path of solid residua leads sharply toward Di-An before curving toward tangency with it. The TSC lies at all times on a Di-Plag leg of a 3-phase triangle; a number of these are suggested at the bottom of Fig. 8.21. When all of the Ab component is finally exhausted by fractional melting, the TSC

lies at  $Di^5$  and the liquid lies at the Di-An eutectic, at  $1274^\circ$ . No further melting takes place until the melting point of Di itself,  $1391.5^\circ$ , is reached. The entire melting path is then characterized by a series of univariant liquid fractions on the field boundary from  $1200^\circ$  to  $1274^\circ$ , followed after a "liquid hop"<sup>5</sup> by a pure diopside liquid at  $1391.5^\circ$ . No liquid of composition A is generated, nor is any liquid lying off the field boundary, except the diopside liquid. Fractional melting therefore produces a result very different from equilibrium melting, including a large hiatus in melt production, which is probably a natural barrier to further melting.

Fractional melting of plagioclase-rich compositions may produce an even larger melting hiatus. This is illustrated for bulk composition D (Di 15%,  $An_{65}$ ) 85%) in Fig. 8.22. Initial liquids lie on the field boundary from G to H, and their fractional removal drives the TSC backward to  $An_{78}$  on the plagioclase join. In this initial melting interval, covering a small temperature span from  $1217^\circ$  to  $1235^\circ$ , diopside crystals are completely used up. Note that the last liquid of this series (H, Fig. 8.22) has the model composition of basalt. The solid residuum now consists solely of plagioclase,  $An_{78}$ , and no further melting can take place until the temperature of  $1430^\circ$  is reached, after which the remainder of fractional melting involves only the plagioclase series (Chapter 6). It is doubtful if such temperatures as  $1430^\circ$  are often achieved in the crust and upper mantle, and this large melting hiatus is likely to bring the melting process to an end. Such a production of gabbroic (strictly, leuconoritic) melt from gabbroic anorthosite, leaving an anorthosite residuum, has been invoked to explain certain field relations around the anorthosite massifs of Egersund, Norway (J. Michot, 1960). The interpretation is open to debate, but the phase diagram does indicate that the process is at least possible, and likely to be terminated upon the incorporation of all Di into the liquid.

It should be noted that equilibrium melting yields no hiatuses, because liquid is continuously available to act as a solvent for crystals. Perfect fractional melting requires continuous removal of liquid, hence a continuous change in the composition of any given reaction volume. It is unlikely, of course, that such a perfect process occurs in the crust or mantle of the earth; we presume instead that a finite volume of liquid, perhaps as much as 5 to 15 percent of the whole, is required before liquid can be extracted from its enclosing rock by flow. The nearest natural approach to fractional melting may then be a succession of small-batch processes, and the results will be in some way intermediate between those of equilibrium and fractional melting. The principle, embodied in fractional melting, of arresting the

<sup>5</sup>The TSC path terminates at pure Di. This may be proved by noting that the *L*-TSC tie line is tangent to the TSC path; consider several three-phase triangles successively closer to the Di-An sideline. For any infinitesimally small component of Ab in the liquid, the TSC must have a component of motion toward the Di-An sideline, and therefore cannot lie on that sideline at all.

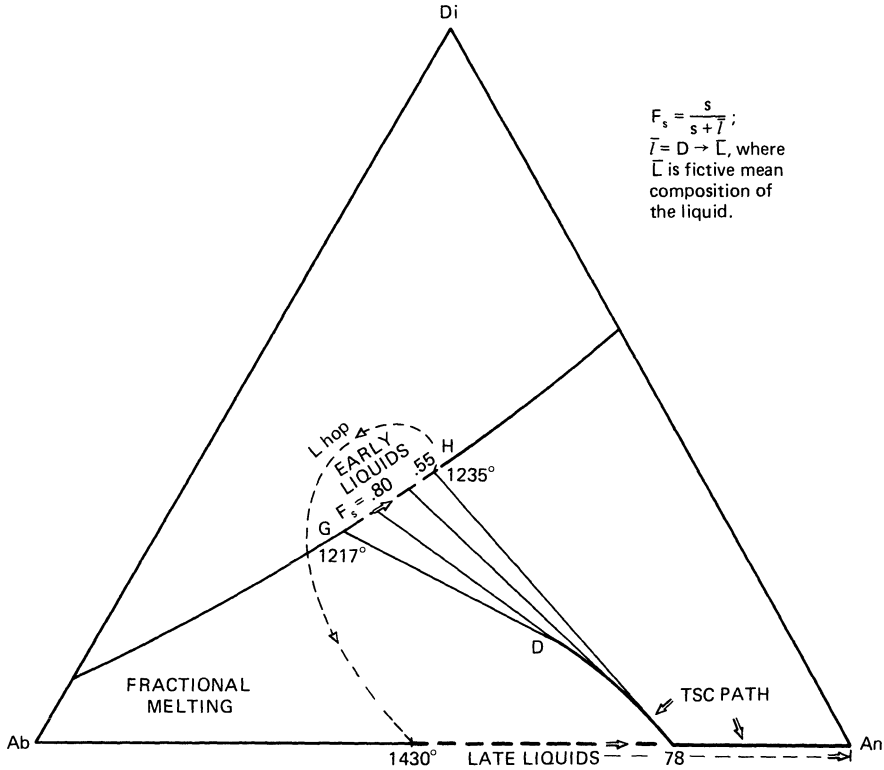


**Figure 8.22.** Fractional melting of bulk composition D in Di-An-Ab. See Figure 8.25 for further details.

melting process by consumption of the whole amount of one phase, may very well operate effectively in such batch processes.

### Complications Due to Non-ternary Nature

We have already seen in Chapters 5 and 7 that the systems Di-An and Di-Ab are not strictly binary, but must be analyzed in terms of four or five components for rigorous interpretation. It is therefore clear that the system Di-An-Ab, which incorporates and joins the two other systems, cannot be strictly ternary. A rigorous analysis of the system must at the very least incorporate the components needed for Di-An and Di-Ab individually, namely CaO, Al<sub>2</sub>O<sub>3</sub>, MgO, SiO<sub>2</sub>, and Na<sub>2</sub>O. In discussing Di-An and Di-Ab, we have deduced that the non-binary nature of these systems can be laid at the door of “impurities” contained in crystals of diopside and plagioclase, specifically Al and Mg in diopside and Al and Ca in sodic plagioclase. The

non-ternary nature of Di-An-Ab must clearly be due to the same effects. It is probably unnecessary to develop a rigorous geometrical analysis of this system in terms of five components, but the graphical treatment developed in connection with Di-Ab and embodied in Fig. 7.2 should serve for an adequate qualitative appreciation of the importance of non-ternary effects in Di-An-Ab. As deduced in Chapter 7, the net effect of "impurities" contained in crystalline phases is to enrich residual liquids in  $\text{Na}_2\text{O}$  and  $\text{SiO}_2$ . Enrichment of residual liquids in  $\text{SiO}_2$  holds for both Di-An alone and Di-Ab alone; enrichment in  $\text{Na}_2\text{O}$  holds for Di-Ab alone. Crystallization of Di in Di-An-Ab will therefore result in silica enrichment, and crystallization of plagioclase will tend to cause enrichment in  $\text{Na}_2\text{O}$  over and above that required by available  $\text{Al}_2\text{O}_3$  to make the Ab molecule in the liquid. This  $\text{Na}_2\text{O}$  enrichment results from the "plagioclase effect" of Bowen (1945) already mentioned as the principle that pure Ab cannot crystallize from a melt which contains Ca.<sup>6</sup> This effect is probably minor while intermediate plagioclase is crystallizing, but significant for Ab-rich liquid compositions. Although this effect may easily account for the peralkaline acid rocks, as suggested in Chapter 7, some opposing set of effects apparently cancels the plagioclase effect in all those rock series which are *not* peralkaline acid. These opposing effects are not clearly understood at present.

## Summary of Basic Principles

The model system Di-An-Ab illustrates many of the most important principles of liquidus phase diagrams, and the appreciation of these principles is demanding enough upon the reader that we ought to pause and take stock of where we stand, both with regard to phase diagrams and with regard to basalt genesis.

Any ternary diagram has certain geometrical properties which allow simple, quantitative interpretation of liquid paths and TSC paths. Perhaps the most powerful of these properties is that a straight line radiating from any apex is a line of constant ratio of the other two apices. Thus we observe that in equilibrium *or* fractional crystallization in the Di + L field, the liquid path is a straight line away from Di.

The continuous variability of plagioclase composition with temperature causes all liquid paths in the Plag. + L field to be curved; more strongly so

<sup>6</sup>Internal evidence for the plagioclase effect probably resides in the original work of Bowen on Di-An-Ab (1915), where no data on plagioclase-liquid tie lines suggest a tendency for a *clockwise* rotation of the tie lines lying near the Ab corner, which would be required if the plagioclase composition swept smoothly toward Ab. Instead, the tie line slopes suggest a plagioclase perhaps as calcic as  $\text{An}_{15}$  for the liquid lying on the Di-Ab sideline. Preliminary electron probe analysis of very small plagioclase crystals in experimental runs reveals a finite An content, probably smaller than  $\text{An}_{10}$  (H. S. Yoder, Jr., personal communication, 1968).

in the case of equilibrium crystallization, since the liquid must make over earlier-formed plagioclase, and less strongly in the case of fractional crystallization. No two equilibrium paths coincide; each different bulk composition has its own equilibrium path. Fractionation paths, on the other hand, are the same for a whole variety of bulk compositions which lie on the path.

When a liquid has reached the field boundary from either primary field, the equilibrium is univariant (at constant pressure), and the liquid is forever after constrained to the field boundary in both equilibrium and fractional crystallization. In equilibrium crystallization, the end of crystallization is reached when the solid-solid leg of a three-phase triangle cuts the bulk composition. A similar termination exists for fractional crystallization, but the mean rather than the momentary plagioclase composition must be used as one end of the solid-solid leg.

The lever rule may be used to determine the solid/liquid ratio at any stage of equilibrium crystallization, and also the ratio of plagioclase to diopside among the solids, always by using the bulk composition as the fulcrum, and the solid composition on an apex (Di), sideline (Plag.) or solid-solid leg of a three-phase triangle (Di + Plag.) as one terminus of the lever, the liquid being the other terminus. A modified lever rule may be used to approximate the course of fractional crystallization.

In fractional crystallization, rock paths are discontinuous, and their later stages tend to mimic the continuous liquid paths if the field boundary is nearly straight.

TSC paths within the ternary diagram are always curved, the curvature being more pronounced for the fractional case than for the equilibrium case. In equilibrium melting, the TSC path and the liquid path are both simply the reverse of the equilibrium crystallization paths. In fractional melting, the TSC path is unlike the reverse of either equilibrium or fractional crystallization, and the liquid path is discontinuous, from which we may infer that when one solid phase is used up, the melting process is effectively halted, at least for a long time.

The ternary model for Di-An-Ab is imperfect because the Di actually contains CaTs and no plagioclase of composition  $\text{NaAlSi}_3\text{O}_3$  may occur in the Ca-bearing system. The model can be made qualitatively adequate by stating that residual liquids tend to become enriched in  $\text{Na}_2\text{O}$  and  $\text{SiO}_2$  as a result of these complexities of crystal composition.

Model "basalts" composed of equal amounts of plagioclase and diopside fall almost on the boundary curve in Di-An-Ab, and a similar conjunction in nature would explain why many basaltic rocks carry phenocrysts of both a pyroxene and a plagioclase, or have textures which otherwise suggest simultaneous growth of both pyroxene and plagioclase. Fractionation of such model basalts yields solid rocks of gabbroic composition grading toward feldspar-rich, pyroxene-poor rocks analogous to some syenites, or else crystalline networks of zoned minerals among which may be found

“trachytic” (or at least Ab-rich) patches representing highly fractionated residual liquid. Fractionation leads toward late-stage liquids or rocks which in two important ways resemble those often formed in association with basalt: they are both feldspar-rich and alkali-rich. The ternary system therefore serves as a better model for the fractionation of basaltic magma than any of our previous models. Diagrams with plagioclase do not make very good models for genesis of basalt magma in the mantle, because plagioclase is probably unstable in the regions of interest. However, the melting paths may serve as good models for certain deep crustal melting processes, provided these occur and can be identified in the field.

### Lever Rule with Fractional Crystallization and Melting

The system Di-An-Ab is sketched in Fig. 8.23, with a bulk composition BC composed of (An<sub>60</sub>) 85 percent, Di 15 percent in the plagioclase + liquid field. It is assumed for convenience that the system is ternary. A segment of a liquidus fractionation line<sup>7</sup> BC-F is shown dotted. While the liquid moves from the bulk composition BC to F, the instantaneous solid composition spans the range An<sub>84</sub> to An<sub>65</sub>. As long as the total solid composition remains on the plagioclase sideline, there is no problem in rigorously determining  $F_L$ ; for example when the liquid has just reached F in the figure, a line from the liquid through the bulk composition to the plagioclase sideline defines the total solid composition, and the lever rule yields  $F_L = 0.49$ .

Now the trouble starts. As diopside (Di) crystallizes, the total solid composition must rise into the triangle along some such path as shown in Fig. 8.23. As in the plagioclase system, we have the initial and final states corresponding to  $F_L = 0.49$  and  $F_L = 0$  (we ignore all the non-ternary effects). The corresponding values<sup>8</sup> for  $R$  are 0.328 and 0.400, starting out smaller than in the plagioclase system, since the component Di narrows as well as flattens the projected plagioclase loop (Wyllie, 1963). An assumption of linear  $R$  between the initial and final states yields the values of  $Ab^{TSC}$  and  $F_L$  in Table 8.1. For each value of  $Ab^L$ , the calculated value of  $Ab^{TSC}$  is used to plot the Di-plag<sup>TSC</sup> leg of a construction triangle. A lever that defines the position of the total solid composition on this leg is then found by connecting the composition of the liquid with the bulk composition. The lever rule may be applied to each such lever, to yield  $F_L$ . These levers are not tie lines in the usual sense. The array of total solid composition points

<sup>7</sup>Fractionation curve of Bowen; the term “liquidus fractionation line” was suggested by Presnall (1969).

<sup>8</sup>The values of  $Ab^L$ ,  $Ab^{TSC}$ , and  $R$  are taken relative only to plagioclase component, that is, they are projected from diopside. The terms are defined on p. 71.

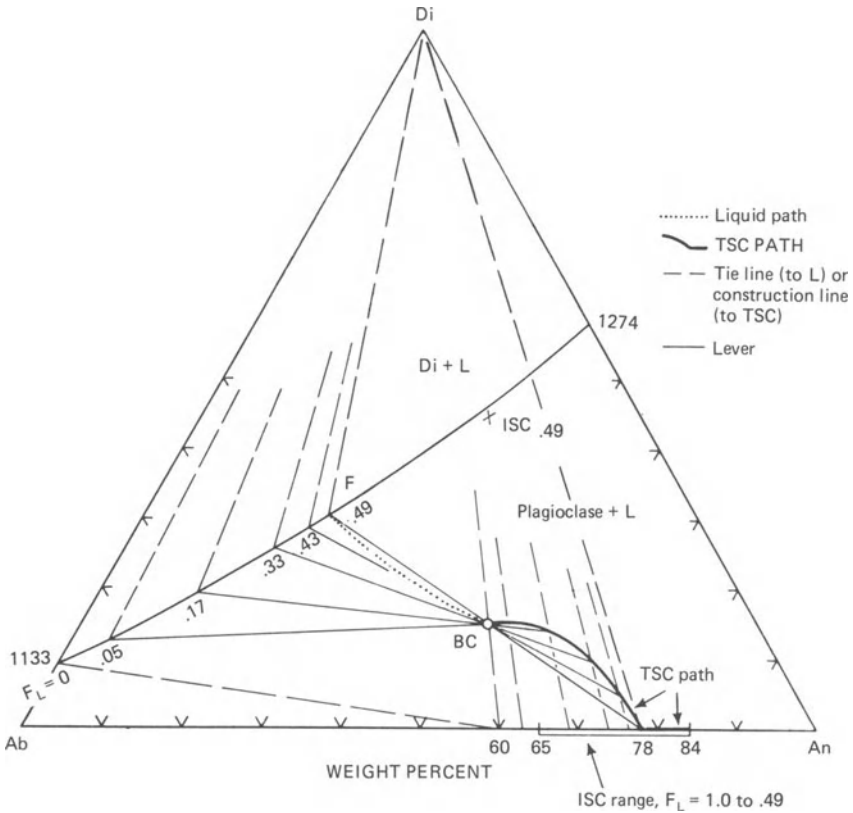


**Figure 8.23.** Portion of the phase diagram Di-An-Ab. The system is treated as ternary here, although it is not. The bulk composition BC is (An<sub>80</sub>) 85 percent, Di 15 percent. Truncated lines radial from the Di apex are like the legs of three-phase triangles, but the Di-Plag legs meet the total solid composition of the plagioclase, not the solidus composition. The *L* (Plag) fractionation path is shown dotted. The remaining *L* (Plag, Di) path follows the field boundary. The Ab<sup>TSC</sup> values for the Di-Plag legs are found from a graph (not shown) of *R* versus liquid composition. The positions of TSC's on these legs are found from levers passing through BC from the liquids. These levers yield the fractions of liquid (*F<sub>L</sub>*) indicated. The TSC path connects the derived TSC points. The point labelled ISC is the instantaneous solid composition for the liquid at *F<sub>L</sub>* = 0.49; it is located by the tangent to the liquid path and the (Di-An<sub>65</sub>) leg of a three-phase triangle. Reproduced, by permission, from Morse (1976).

found in this way may be connected to form the TSC path, as shown in Fig. 8.23. The Di + Plag instantaneous solid composition path is not shown in Fig. 8.23, but it lies just below the cotectic curve, being in turn produced by tangents to that curve. A single ISC, the instantaneous solid composition produced when *F<sub>L</sub>* = 0.49, is plotted in the figure.

Fractional fusion of the same bulk composition, illustrated in Fig. 8.24, begins with the generation of liquid at 1213°C on the field boundary.

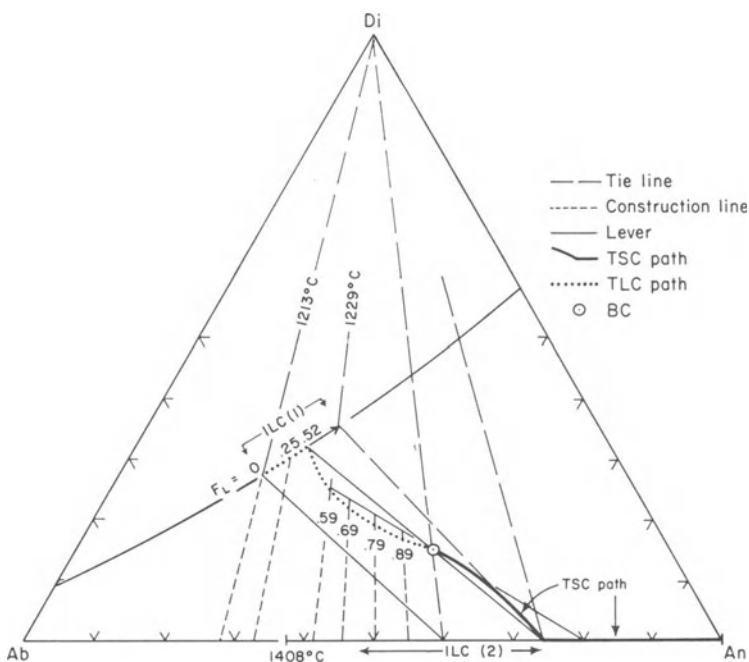


**Figure 8.24.** Fractional fusion in Di-An-Ab, using the same bulk composition as in Fig. 8.23. The dotted line is the total liquid composition (TLC) path. Two instantaneous liquid composition (ILC) paths are shown, one on the field boundary and one on the plagioclase sideline. The TSC is driven away from BC by tangents to ILC's. The TLC path is constructed from the ratio  $R'$ , which yields  $An^{TLC}$ , and from intersections with levers through the bulk composition from the total solid composition. Sample levers are shown at  $F_L = 0.52$  and  $0.59$ . Reproduced, by permission, from Morse (1976).

Extraction of this and succeeding liquids (instantaneous liquid compositions, ILC's) drives the total solid composition away from the bulk composition along the TSC path (crystal path of Presnall, 1969) shown in the figure. The first instantaneous liquid composition path is confined to the cotectic. The melting process is arrested at  $1229^\circ\text{C}$ , upon the loss of all Di from the total solids. Up to and including this moment, the total liquid composition is given simply by the intersection of the cotectic with a line through the bulk composition from any chosen point on the TSC path. Henceforward, after a large rise in temperature ( $179^\circ\text{C}$ ), the total liquid composition accrues plagioclase components only, following the dotted path in the figure. The value of  $R' = An^{TLC}/An^{TSC}$  varies from 0.493 to 0.600 during this melting of residual plagioclase, and linear variation of  $R'$  is assumed in order to estimate intermediate values of  $An^{TLC}$  for chosen values of  $An^{TSC}$ . The TLC path is then plotted, using  $An^{TLC}$  lines radial from diopside, intersected by TSC-BC lines which are also levers from

**Table 8.1** Values of  $R$ ,  $Ab^{TSC}$ , and  $F_L$  for selected values of  $Ab^L$ , bulk composition ( $An_{60}$ ) 85 percent, Di 15 percent

	$Ab^L$	$R$	$Ab^{TSC}$	$F_L$
<i>Initial</i>	0.4	0.400	0.160	1.0
	0.5	0.350	0.175	0.74
	0.67	0.328	0.220	0.49
	0.70	0.334	0.234	0.43
	0.75	0.346	0.260	0.33
	0.85	0.366	0.310	0.17
	0.95	0.389	0.370	0.05
	<i>Final</i>	1.0	0.400	0.400

which  $F_L$  may be determined. Two levers are shown in Fig. 8.24, at  $F_L = 0.52$  and  $0.59$ .

About half the mass of this bulk composition can be extracted, in the limit, as haplodioritic liquid before diopside is used up. The  $179^\circ\text{C}$  increase needed to produce further melting of plagioclase is probably adequate insurance against such an event in nature.

## Derivation of Fractionation and Equilibrium Paths

Fractionation paths (lines) are simply found by tangents to moving liquid or solid compositions, depending on whether the process is crystallization or melting. Equilibrium paths are, in turn, derived from fractionation paths. The plagioclase field of the system Di-An-Ab serves very well as a general case with which to illustrate the principles. It is convenient to follow here the terminology of Presnall (1969), whose work may be consulted for further examples.

We shall use an idealized version of the system Di-An-Ab as an example, and it is convenient to begin with the derivation of solidus fractionation lines in fractional fusion. Consider the system ABC, Fig. 8.25, which mimics the system Di-Ab-An. The inset shows an isothermal three-phase triangle  $ALB_{ss}$ , where  $L$  is the liquid apex and  $AB_{ss}$  is the solid-solid leg. This leg contains a continuum of possible TSC's which are in equilibrium with liquid  $L$ . Fractional fusion must drive each of these TSC's, initially, directly away from  $L$ . Accordingly, all lines radial from  $L$  in the vicinity of the solid-solid leg are trajectories of TSC's and tangents to TSC paths in fractional fusion.

A map of such tangents for the ternary system may be constructed by drawing a number of three-phase triangles (which must be known from

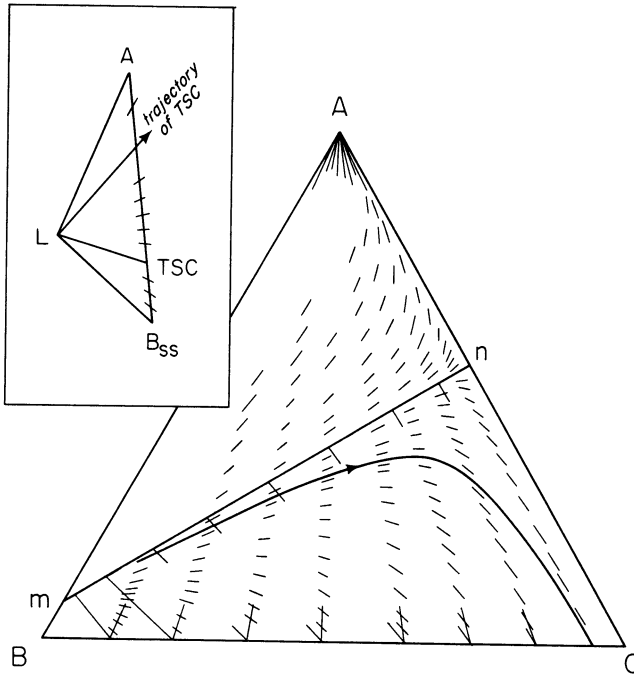


**Figure 8.25.** Derivation of solidus fractionation lines (Presnall, 1969). Insert shows a three-phase triangle whose liquid lies on the cotectic  $mn$ . Any point on the solid-solid leg is a possible TSC in equilibrium with that liquid, and with fractional melting all TSC's would move directly away from  $L$  at first. Short lines radial from  $L$  along the solid-solid leg are therefore tangents to continuous TSC paths. An array of such tangents and a sample solidus fractionation line are shown in the main figure.

experiment) and drawing, radial from the liquid apex, an array of short tangents to TSC paths on each solid-solid leg. Such an array is shown in the main portion of Fig. 8.25. Tick marks on the cotectic  $mn$  indicate the location of liquid apices and  $L$ - $B_{ss}$  legs of the three-phase triangles, and the collections of short tangents from each liquid are arranged along solid-solid legs whose ends are shown in the diagram. A solidus fractionation line is drawn through the array of short tangents so as to fall smoothly among them. Any number of other such lines (along which TSC paths must lie) could be drawn in a similar manner. Note that above the cotectic  $mn$ , all solidus fractionation lines lead directly to  $A$ , whereas below  $mn$  they all lead to the sideline  $BC$ . Line  $mn$  is itself a solidus fractionation line in this idealized case, but the curved cotectic in the system  $Di-An-Ab$  is not.

The case of fractional crystallization is not confined to the univariant equilibrium  $L(AB_{ss})$ , but involves divariant equilibria such as  $L(B_{ss})$ . Accordingly, much more experimental information on tie line slopes is needed for a satisfactory derivation of liquidus fractionation lines. Fig. 8.26 shows

an isotherm which is the locus of all liquids saturated with  $B_{ss}$  at that particular temperature. It is determined experimentally that the crystal-liquid tie lines have the slopes shown. A sample liquid  $L$  is in equilibrium with crystal ISC. Upon fractional crystallization,  $L$  must move, initially, directly away from ISC. An infinitesimally short line through  $L$  toward ISC is therefore part of a liquidus fractionation line, and the line  $L$ -ISC therefore gives the tangent to a fractionation path at  $L$ . Such a fractionation path is shown as a dotted line. The template of tie lines allows one to draw an array of such short tangents lying on the isotherm.

To complete the template of short tangents for purposes of drawing liquidus fractionation lines, the above exercise must be repeated for a variety of different isotherms. A map representing such a construction is shown in Fig. 8.27, where two sample fractionation paths are drawn in. Fractionation paths above  $mn$  are, of course, simply straight lines radial from A.

Further details on the construction of liquidus fractionation lines, and the derivation from them of equilibrium liquid paths, are to be found in Bowen (1941) and Roeder (1974).

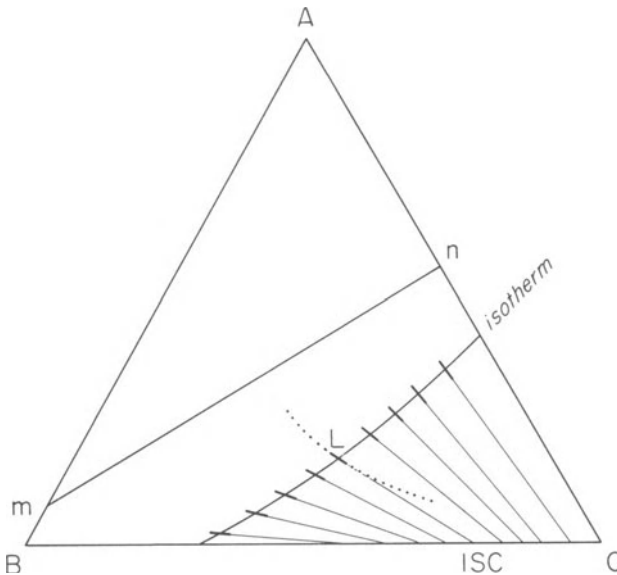


**Figure 8.26.** Derivation of liquidus fractionation lines (Presnall, 1969). Crystal-liquid tie lines are known from experiment to lie as shown from liquids along the isotherm. Each tie line, where it passes through the isotherm, is tangent to a liquid path in fractional crystallization (a segment of one being shown as a dotted line). An array of such tangents for different isotherms is shown in the next figure.

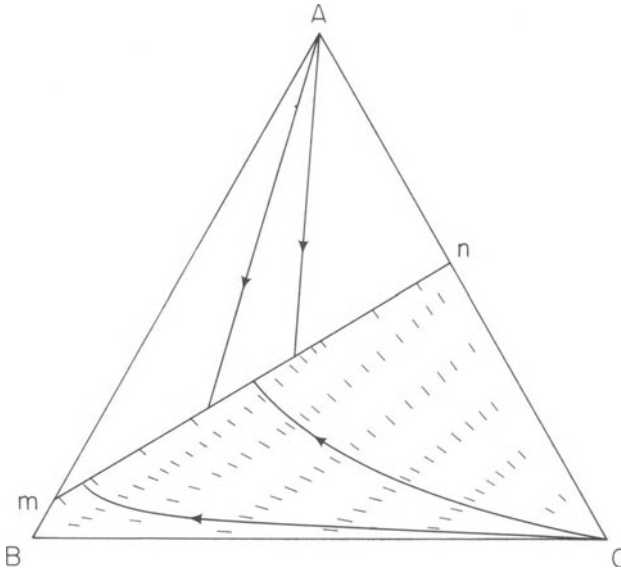


**Figure 8.27.** Array of short tangents on isotherms, which collectively define the trajectories of liquidus fractionation lines. Two such lines are shown in full.

## Equilibrium Paths

It is simple to derive an equilibrium path from an array of fractionation paths, and in practice, that is how it is done. Consider the point  $X$  in Fig. 8.28a; it is a bulk composition, and the exercise involves crystallization. The curve lying near  $X$  is a fractionation path (liquidus fractionation line). The straight line passing through  $X$  is a tie line tangent to the fractionation line at  $L$ , which is the liquid end of the tie line. The other end is the crystal composition, TSC. Since the bulk composition  $X$  may be expressed in terms of  $L$  and TSC, the tie line is a lever. The point  $L$  lies simultaneously on the fractionation line and (because the tie line passes through  $X$ ) on an equilibrium path. Evidently, the equilibrium path is the locus of all points such as  $L$  which lie on fractionation lines at points where tie lines through  $X$  are tangent to those fractionation lines. To illustrate this, two such points are located in Fig. 8.28b. The tie lines  $L_1B_1$  and  $L_2B_2$  are tangent to fractionation lines at  $L_1$  and  $L_2$ . The equilibrium path is then drawn so as to run from  $X$  through  $L_1$  and  $L_2$ .  $B_0$  is the initial TSC, and  $B_1$  and  $B_2$  are successive TSC's at lower temperatures. For further details, see Bowen (1941).

An assembly of solidus fractionation lines may be used to derive the equilibrium TSC path followed during either melting or crystallization. In Fig. 8.29, curves  $f_1$ ,  $f_2$ , and  $f_3$  are solidus fractionation lines similar to that on Fig. 8.25.  $X$  is the bulk composition. Tangents to the fractionation lines which pass through  $X$  lead backward to liquids  $L_1$ ,  $L_2$ , and  $L_3$  on the

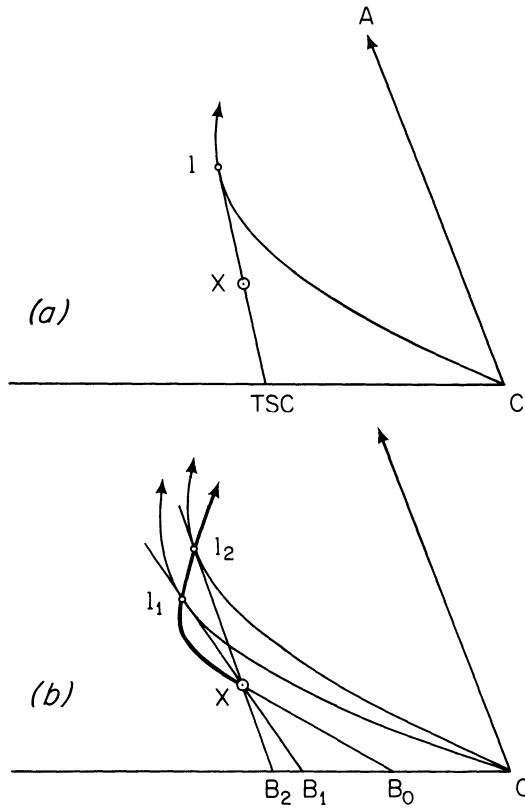


**Figure 8.28.** Derivation of equilibrium liquid paths from liquidus fractionation lines (curvatures exaggerated for clarity). A: Tie line through bulk composition X is tangent to fractionation path at  $l$ , which is a point on the equilibrium path. B: An array of points  $l$  derived as in (A) define the equilibrium liquid path.

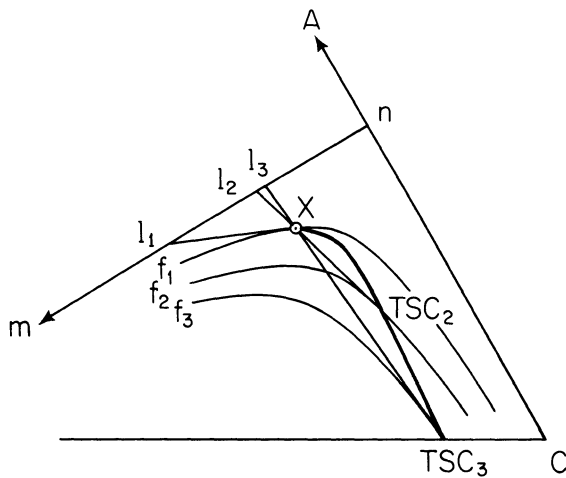


**Figure 8.29.** Derivation of equilibrium TSC path from solidus fractionation lines (after Presnall, 1969). X is a bulk composition, the first TSC on melting and the last TSC on crystallization. Tie lines from liquids are tangent to solidus fractionation lines at X, TSC 2, and TSC 3.

cotectic  $mn$ . The points of tangency are labelled X (which is TSC 1), TSC 2 and TSC 3. Since these points of tangency lie simultaneously on tie lines through X and on the fractionation lines, they lie on the equilibrium TSC path (heavy line). Note that this is the same whether the process is melting ( $X \rightarrow \text{TSC}_3$ ) or crystallization ( $\text{TSC}_3 \rightarrow X$ ), involving liquids  $L_1$ ,  $L_2$ , and  $L_3$ . It may be noted further that in Fig. 8.13 we found the crystallization TSC path directly by running tie lines from cotectic liquids through the bulk composition to the solid-solid legs of three-phase triangles. If you go back to the start of this section you will see that the construction of solidus fractionation lines also involves three-phase triangles, and hence the present construction (Fig. 8.29) is directly related to the earlier one.

## Chapter 9

# Forsterite-Diopside-Anorthite: A Basaltic Analog

### Introduction

Our models for basalt have so far dealt only with plagioclase and pyroxene, the two dominant minerals in most basalts. We have ignored olivine and calcium-poor pyroxene, but these are fundamentally important minerals in any classification scheme of basalt, and are furthermore centrally involved in our study model, the basalt tetrahedron (Chapter 2). The present chapter explores a phase diagram containing iron-free olivine, namely forsterite, thereby illuminating some important principles of rock genesis as well as some simple but useful new principles of phase diagrams.

It may be noted that we are avoiding iron-bearing systems in our initial models; there are two reasons for this. One is that most basaltic rocks contain more moles of Mg than of Fe, and the Mg end-members of ferromagnesian solid solution series are therefore more suitable as first-approximation models. The second reason is that Fe, having two important oxidation states, requires special experimental and theoretical treatment which we shall consider in due time, but can cheerfully avoid for the moment. The most important result of adding Fe to our model systems will be to lower temperatures of crystallization toward and very close to those actually observed in natural laws.

In now considering magnesian olivine, we are taking a big step away from fantasy and toward realism, for the following reason. The source region of basalt magma in the mantle is thought to consist largely of an olivine-rich rock resembling peridotite. If so, then every basalt has at some stage been in contact with olivine, and must owe many of its characteristics to this contact.

## Preparation and Melting of Forsterite

It should be a simple matter to prepare forsterite, (Fo,  $\text{Mg}_2\text{SiO}_4$ ) by combining appropriate weights of pure MgO and pure  $\text{SiO}_2$  to yield the molar ratio  $2\text{MgO} \cdot \text{SiO}_2$ . Like most everything apparently simple, however, this little scheme has a catch: the melting point of forsterite turns out to be more than one hundred degrees higher than that of the platinum crucibles, furnace windings, and thermocouples usually employed in the laboratory. A glass, therefore, is not readily made. Bowen and Andersen (1914), and later Grieg (1927), used furnaces and crucibles made of iridium, and optical pyrometers to overcome these difficulties. Crystalline forsterite can be made reasonably well by sintering the  $2\text{MgO} \cdot \text{SiO}_2$  mixture at high temperatures for a long time. The product is likely to contain some unreacted MgO and  $\text{SiO}_2$  even after several months, but with patience it can be made homogeneous enough to use as a component of other mixtures. Liquid can be made in an iridium apparatus, but it cannot be quenched to a glass; quench-crystals form instead.

The melting point of forsterite, determined by the above authors, is accepted as  $1890^\circ\text{C}$ , but an uncertainty of perhaps  $\pm 25^\circ$  should be attached to this value because of the experimental difficulties.<sup>1</sup>

## Two Sidelines: Forsterite-Diopside and Forsterite-Anorthite

The interior of the ternary system Fo-Di-An can be predicted from the nature of the three sidelines, as was done in Chapter 8 for Di-An-Ab, but the prediction is somewhat crude owing to complexities in the sidelines. We shall skip the predictive exercise this time in order to get on with the matter at hand, but a brief presentation of the sidelines is in order.

Forsterite-diopside was found by Bowen in 1914 to be a binary eutectic system with a eutectic at  $\text{Fo}_{12}\text{Di}_{88}$ ,  $1387^\circ\text{C}$ , just slightly below the melting point of Di itself. As shown in Fig. 9.1, the system is actually non-binary with a peritectic at  $1388.5^\circ\text{C}$  (Kushiro and Schairer, 1963).

Forsterite-anorthite is non-binary over some of the composition range, because spinel ( $\text{MgAl}_2\text{O}_4$ ) appears at the liquidus. The equilibrium diagram of Fig. 9.2, modified from Andersen (1915) by Osborn and Tait (1952), shows the phase relations encountered along the Fo-An join. Point C represents equilibria among Fo, An, Sp, and L; it looks like a eutectic, but application of the phase rule leads to the following result:

<sup>1</sup>The value of  $1890^\circ\text{C}$  is compatible with more recent high-pressure experiments by Davis and England (1964).

$$W_p = c + 1 - \phi$$

$$= 3 - \phi, \phi = 4, W_p = -1 \text{ (imaginary)}$$

and in order for the variance to be zero or greater,  $c$  must be increased to at least 3. Letting spinel be an added component,  $W_p = 4 - \phi = 0$ , and the point C is an isobaric invariant point. It is not a eutectic, because the composition of the liquid cannot be represented as a positive combination of the solid phases, but instead lies outside the diagram, toward  $\text{SiO}_2$  (because spinel is a non-silicate). Point C, for this reason, is called a *peritectic point*. The points A and B in Fig. 9.2, and the liquidus between them, also represent equilibria with spinel, and here, too, the liquid does not lie in the composition plane Fo-An.

To see where the liquid does lie in the  $\text{Sp} + L$  field, we would need to draw the quaternary CAMS system and some of its interior surfaces. However, we can easily find the sense of motion of this liquid by means of a subtraction diagram (Table 9.1). The table shows that removal of spinel from a bulk composition consisting of Fo + An yields a liquid enriched in Di and  $\text{SiO}_2$ . The reaction can be written formally as

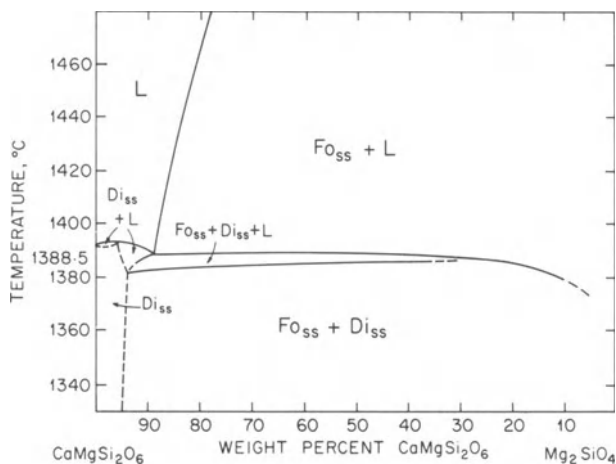
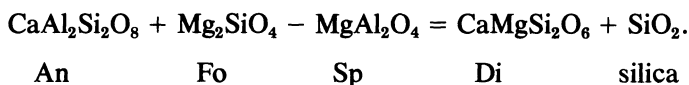


**Figure 9.1.** Revised equilibrium diagram of the system diopside ( $\text{CaMgSi}_2\text{O}_6$ )-forsterite ( $\text{Mg}_2\text{SiO}_4$ ), from Kushiro and Schairer (1963). The system is not binary because of solid solution in both forsterite (Ca as  $\text{CaMgSiO}_4$ ) and diopside (Mg as  $\text{MgSiO}_3$  and perhaps  $\text{Mg}_2\text{SiO}_4$ ). A further description of solid and liquid compositions along this join may be found in Kushiro (1972), discussed in Ch. 12 of this text. For the purposes of this chapter, the join will be treated as binary, with a eutectic (which is really a peritectic) at  $1388^\circ\text{C}$ .

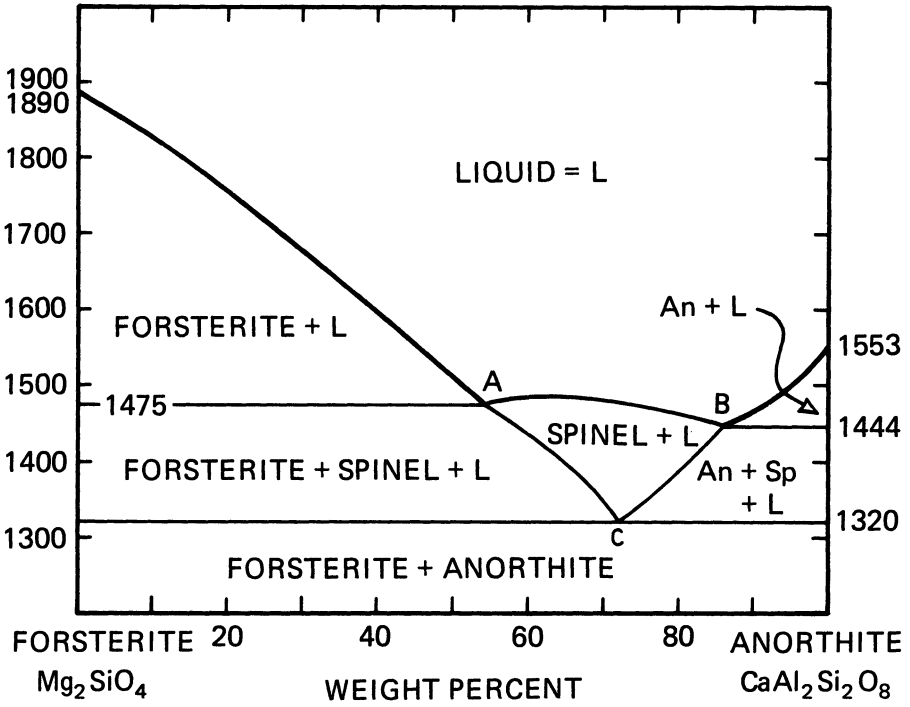


Figure 9.2. Equilibrium diagram of the system forsterite-anorthite. The system is non-binary between and below points A and B, and in this region should be read like a road map rather than a conventional T-X plot (see text).

Table 9.1. Effect of Removing Spinel From a 1:1 Bulk Composition of Anorthite and Forsterite.

	C	A	M	S	
	1	1		2	= An
+			2	1	= Fo
	1	1	2	3	= BC
-		1	1		- Sp
	1	0	1	3	
-	1		1	2	- Di
				1	= SiO <sub>2</sub>

Reaction: An + Fo = Sp + Di + SiO<sub>2</sub>

Or An + Fo - Sp = Di + SiO<sub>2</sub>

Now it is a matter of experience that spinel is unstable in the presence of much excess silica, and therefore it can be expected that when  $\text{SiO}_2$  is sufficiently concentrated in the liquid by the removal of spinel, a reversal of the above reaction will ensue, converting spinel back into other crystalline phases. This is precisely the secret of point C, below which  $\text{Fo} + \text{An}$  coexist without any spinel. The history of crystallization in the spinel +  $L$  region of Fig. 9.2 can therefore be characterized as follows: crystallization of spinel causes  $L$  to leave the diagram into a more silica-rich space. With cooling toward  $1320^\circ$ , however, spinel begins to react with liquid, drawing the latter back toward the plane of the diagram, which it finally reenters at point C, becoming exhausted just as the last bit of spinel is used up. Analogous events occur in parts of Fo-Di-An. In equilibrium crystallization, spinel is only a transient phase, eventually becoming used up by reaction with liquid. Removal of spinel by fractional crystallization can, however, exert a permanent influence on the course of liquids. We shall postpone further discussion of spinel equilibria to the end of the chapter.

### Treatment of Fo-Di-An as a Ternary System

The diagram of Osborn and Tait (1952) is shown in Fig. 9.3. It is not difficult to recognize the relations near the sidelines, which themselves consist of the three systems Di-An (Chapter 5), Fo-Di, and Fo-An, just discussed. The first two are eutectic systems, and their invariant points must therefore be the termini of univariant lines in the ternary system. These two univariant lines, from the eutectics in Di-An and Fo-Di, meet at point E ( $1270^\circ$ ) in the ternary diagram, where they are joined by a third univariant line, thus forming what appears to be a *ternary eutectic point* (point E). It is a property of isobaric ternary eutectic points that they are isobarically invariant, consist of four phases, and mark the junction of three isobarically univariant curves. In this case, the phases are Fo, Di, An, and  $L$ , and by the phase rule

$$C = 3, W_p = c + 1 - \phi = 4 - \phi, \phi = 4$$

$$W_p = 0$$

The three univariant curves each represent equilibria among three phases:  $\text{Fo} + \text{Di} + L$ ,  $\text{Di} + \text{An} + L$ , and  $\text{Fo} + \text{An} + L$ . The latter is a curve which we have not seen before, but which we might have deduced from the existence of point C in Fig. 9.2, which represents coexisting  $\text{Fo} + \text{An} + L + \text{Sp}$ . This prediction would have been justified because, as we have already seen, the removal of spinel causes the liquid to move toward Di and  $\text{SiO}_2$ , so as it moves toward Di in the ternary plot of Fig. 9.3, it must eventually achieve a silica richness sufficient to destroy spinel by reaction, hence yielding the  $\text{Fo} + \text{An} + L$  equilibrium.

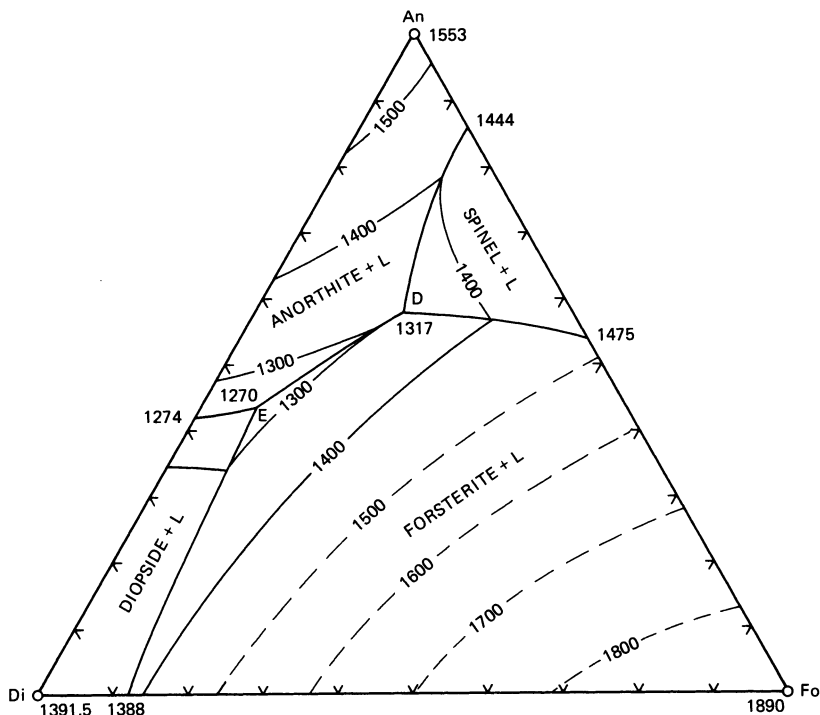


**Figure 9.3.** Equilibrium diagram of the system forsterite-diopside-anorthite. The system is non-ternary for reasons discussed in the text. Point E resembles (and very nearly is) a ternary eutectic. Base of diagram measures 10 cm.

The ternary point E fails of being a true eutectic because of the CaTs content of the diopside, which we have previously encountered. The composition of the Di cannot be exactly represented in the Fo-Di-An plane, and therefore the liquid at E cannot lie exactly in that plane. Point E is called a *piercing point* rather than a eutectic, because the liquid lies outside the plane of the diagram. The non-ternary effect is, as before, an enrichment of the liquid in  $\text{SiO}_2$ . To a first approximation, however, the system behaves as a ternary eutectic system in this region, and we shall treat it as one for the present.

A ternary eutectic is thermally like a catch-basin into which streams (univariant lines) run. All liquids must move down-temperature in primary phase fields and along univariant lines to the eutectic, where they complete their crystallization isothermally. Conversely, all solid assemblages begin to melt with production of liquid of eutectic composition, recalling to us the original definition of a eutectic (Guthrie): the lowest melting point of a system.

The thermal properties of a ternary eutectic, ternary univariant lines, and a ternary divariant surface may be appreciated by examination of Fig. 9.4, which shows the temperature at E, Fig. 9.3, compared to temperatures

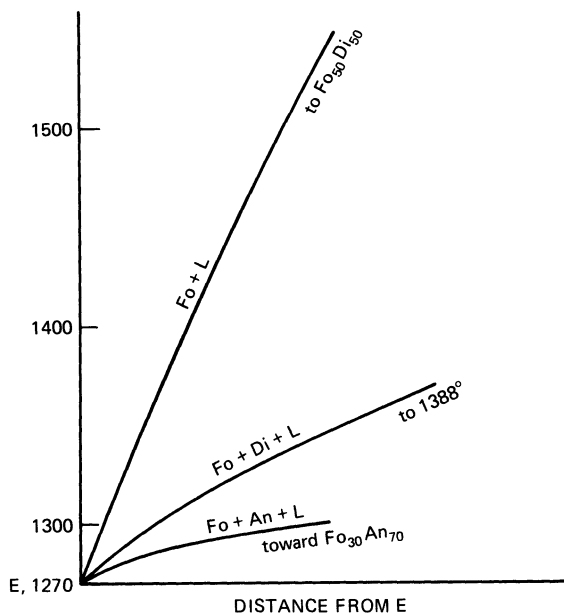


**Figure 9.4.** Temperatures along various paths approaching point E, Fig. 9.3, to illustrate the effects of the number and kinds of solid phases on melting or crystallization temperatures.

along the field boundaries  $\text{Fo} + \text{An} + L$  and  $\text{Fo} + \text{Di} + L$ , and to temperatures along the surface  $\text{Fo} + L$  toward the  $\text{Fo}_{50}\text{Di}_{50}$  composition. By analogy to topography, the “valley walls” ( $\text{Fo} + L$ ) are very steep compared to the “stream gradients” represented by the univariant field boundaries. Accordingly, unless we are to expect enormous rates of heat production in the earth, we will not expect liquids to lie very far from a field boundary—we will not expect them in general, to climb far up “valley walls.”

There are four primary fields in Fig. 9.3;  $\text{Fo} + L$ ,  $\text{Di} + L$ ,  $\text{An} + L$ , and  $\text{Sp} + L$ . We reserve the  $\text{Sp} + L$  field for later discussion, along with liquids which encounter spinel equilibria, as shown in Fig. 9.5. This figure shows that the phase diagram may be divided into spinel and non-spinel parts: any initial liquid in the area enclosed by the dashed lines  $\text{An-D-Fo}$  will encounter spinel; any initial liquid outside that area will not. We will call the non-spinel part the “basaltic region.”

#### EQUILIBRIUM CRYSTALLIZATION

Crystallization in any of the three primary fields in the basaltic region is a simple affair, obeying the same rules as that in the  $\text{Di} + L$  region of  $\text{Di-An-Ab}$  (Chapter 8). We may illustrate the process by considering a bulk

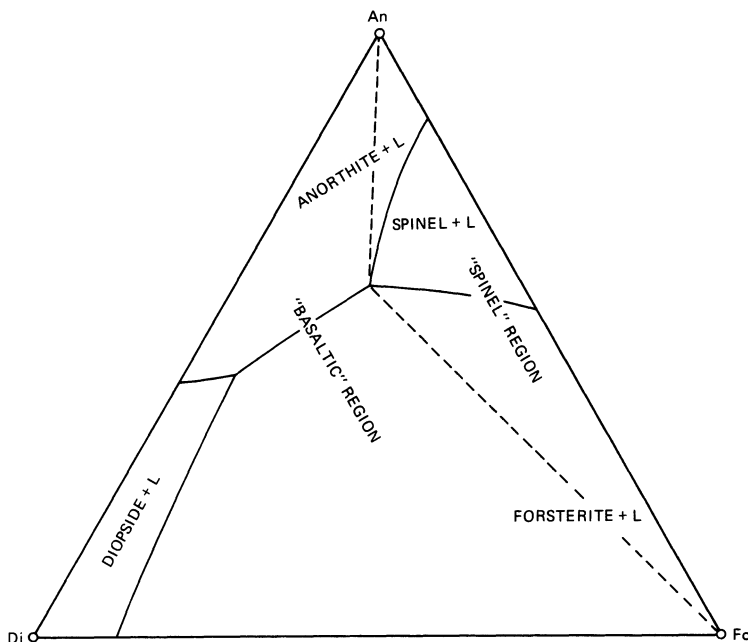


**Figure 9.5.** “Basaltic region” and “spinel region” of the system Fo-Di-An. Bulk compositions to the right of the dashed line will encounter spinel equilibria on crystallization; other bulk compositions will not.

composition in the  $Fo + L$  field,  $Fo_{30}Di_{30}An_{40}$ , point G, Fig. 9.6. Crystallization of Fo begins, on cooling, at a temperature of  $1450^\circ$ , and drives the liquid directly away from the Fo corner, thus preserving a constant ratio of Di to An. The liquid eventually reaches the field boundary with An at  $1290^\circ$ , where the liquid has a composition of  $Fo_{13}Di_{37}An_{50}$ . At this point An begins to crystallize, generating the three-phase triangle An-Fo-L. Two legs of this triangle are shown within the diagram of Fig. 9.6; the other leg is the sideline An-Fo. The liquid now moves in univariance ( $W_p = 4 - \phi$ ,  $\phi = 3$ ,  $W_p = 1$ ) along the field boundary toward E, driven by the crystallization of An + Fo. As this happens, the three-phase triangle cannot pivot, because of the fixed composition of Fo and An, so instead the angles change as L moves toward E. The liquid finally reaches E,  $1270^\circ$  and at this moment Di begins to crystallize.

Now the phase rule tells us that the 4-phase equilibrium  $Di + Fo + An + L$  is isobarically invariant ( $W_p = 0$ ), and this means that neither the temperature nor composition of the liquid at E may change as further heat is removed. Evidently, then, crystals must form in the exact ratio of Fo:Di:An of the liquid composition E, until the completion of crystallization. This is exactly the same behavior as we saw in Di-An, treated as a binary eutectic system. The completion of crystallization is an isothermal process.



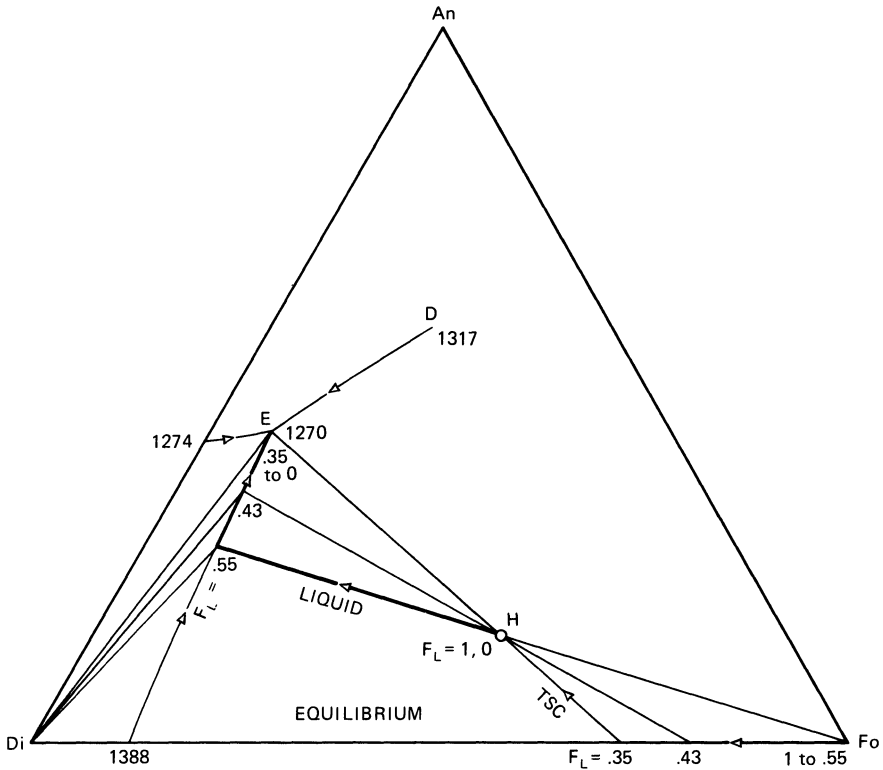


**Figure 9.7.** Equilibrium crystallization of bulk composition H ( $FDA = 50, 15, 35$ ). The liquid lies at H when  $F_L = 1$ , and the TSC lies at H when  $F_L = 0$ . The heavy line is the liquid path.

Identical principles govern the equilibrium crystallization of a more mafic bulk composition H, Fig. 9.7,  $Fo_{50}An_{15}Di_{35}$ . In this case, removal of Fo from the liquid drives the latter to the  $Fo + Di + L$  field boundary, and An is the last crystalline phase to appear, when the liquid reaches E. The liquid and TSC paths are shown in the figure, and should be compared with those in Fig. 9.6.

## Fractional Crystallization

Once the equilibrium crystallization paths and processes are understood, then fractional analogs are easily deduced. Fig. 9.8 illustrates the fractional process for a liquid of initial bulk composition G (see Fig. 9.6 for comparison). The liquid path is identical with the equilibrium case, inasmuch as no solid solution occurs. The rock path is discontinuous, and is given at all

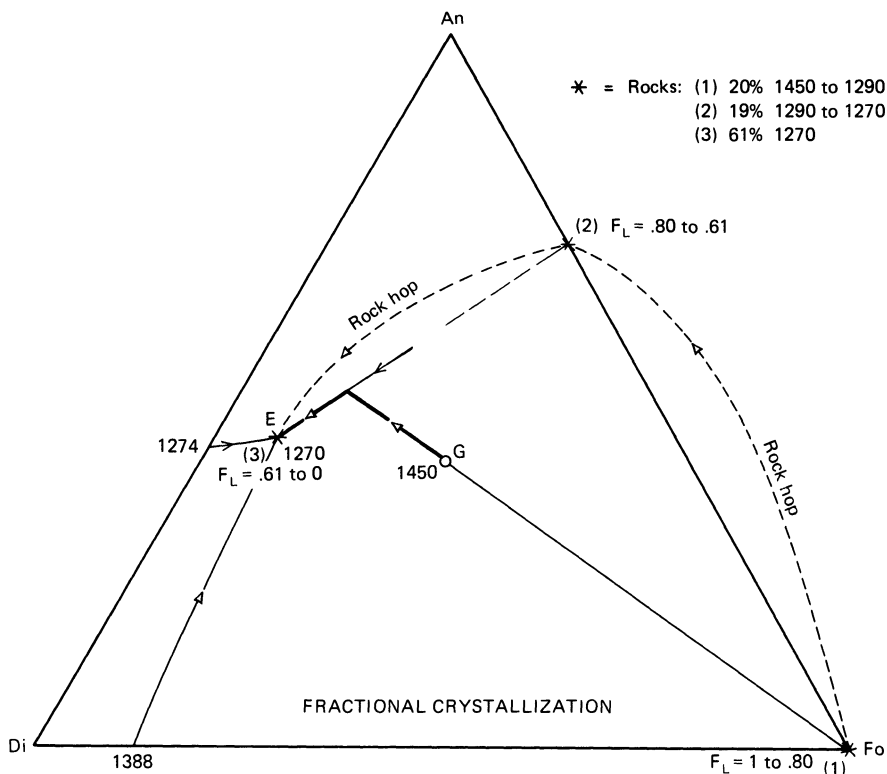


**Figure 9.8.** Fractional crystallization of bulk composition G. Note that the liquid path (heavy line) is identical with that in the equilibrium case (Fig. 9.6), whereas the ISC follows no continuous path, but resides at three points in sequence, the points being separated by instantaneous, discontinuous “rock hops.”

times by the tangent to the liquid path. The TSC path is the same as in the equilibrium case, and yields the same fractions of liquid remaining,  $F_L$ . Thus from  $F_L = 1$  to  $.80$ , the rock composition is solely Fo; a dunite is produced. From  $F_L = .80$  to  $.61$ , the rock composition is that of an allivalite (point 2, Fig. 9.8), having around 70% An and 30% Fo; the change from dunite to allivalite at  $F_L = .80$  is an instantaneous “rock hop.” At  $F_L = .61$ , another rock hop occurs, as the liquid reaches E. The rock composition now jumps to E, and olivine gabbro is produced. The first and third stages of the rock path are indistinguishable from the equilibrium case, but the second stage of plagioclase-rich allivalite represents a product unlike that found at any stage of equilibrium crystallization.

Natural rocks like those at (2) in Fig. 9.8 occur; more commonly they carry intermediate (Na-bearing or  $Fe^{+2}$ -bearing) plagioclase and olivine and are called *troctolites*. The Kiglapait layered intrusion in Labrador consists of early troctolites overlain by olivine gabbros (which then grade into ferrosyenites); the transition from troctolite to olivine gabbro is sudden,

and it is a discontinuous rock hop precisely like that between (2) and (3) in Fig. 9.8.

Fractional crystallization of a liquid such as H, Fig. 9.7, embodies the same principles. The reader may wish to verify by his own analysis that the rock compositions produced are dunite (Fo), olivine pyroxenite (Di + Fo) and gabbro of composition E.

## Equilibrium Melting

Still ignoring the  $Sp + L$  field, we may say that the equilibrium melting process for a crystalline assemblage in Fo-Di-An is just the reverse of the equilibrium crystallization process (Figs. 9.6 and 9.7). For any such composition, melting begins at 1270°, with production of liquid having the composition of E. At the end of this isothermal stage, one of the crystal species Fo, Di, or An is exhausted in the mixture, and the liquid moves off E along one of the three univariant field boundaries. Upon exhaustion of a second crystal species, the liquid moves in divariance across a primary phase field, dissolving the last crystal species until the bulk composition is reached. The liquid path and the TSC path are both continuous. It is good practice to analyze for oneself the equilibrium melting process for bulk compositions such as G and H, Figs. 9.6 and 9.7.

## Fractional Melting

With continuous removal of liquid, the melting behavior is significantly different in only one important respect: at the termination of isothermal production of liquid having composition E, there ensues a hiatus wherein no further melting takes place with rising temperature until the solidus of one of the sidelines (Fo-An, Fo-Di, or Di-An) is reached. Examples are shown for bulk crystal compositions G and H in Figs. 9.9 and 9.10. In both of these, it may be observed that the TSC path on fractional melting is the same as that on equilibrium melting, or the reverse of that for crystallization. Again, it should be stressed that this holds true only when there is no solid solution, for we recall that in Di-An-Ab the TSC paths are somewhat different for fractional and equilibrium melting.

In Fig. 9.9, liquid E is produced isothermally until the TSC reaches the Fo-An sideline. The amount of liquid E produced on melting is 61% of the mass of the system (bulk composition G), and this liquid is indistinguishable in composition and amount from that produced on fractional crystallization. Any further melting involves only the sideline Fo-An. At this point it is well to recall the existence of a spinel field, Fig. 9.2. Melting in this pseudobinary

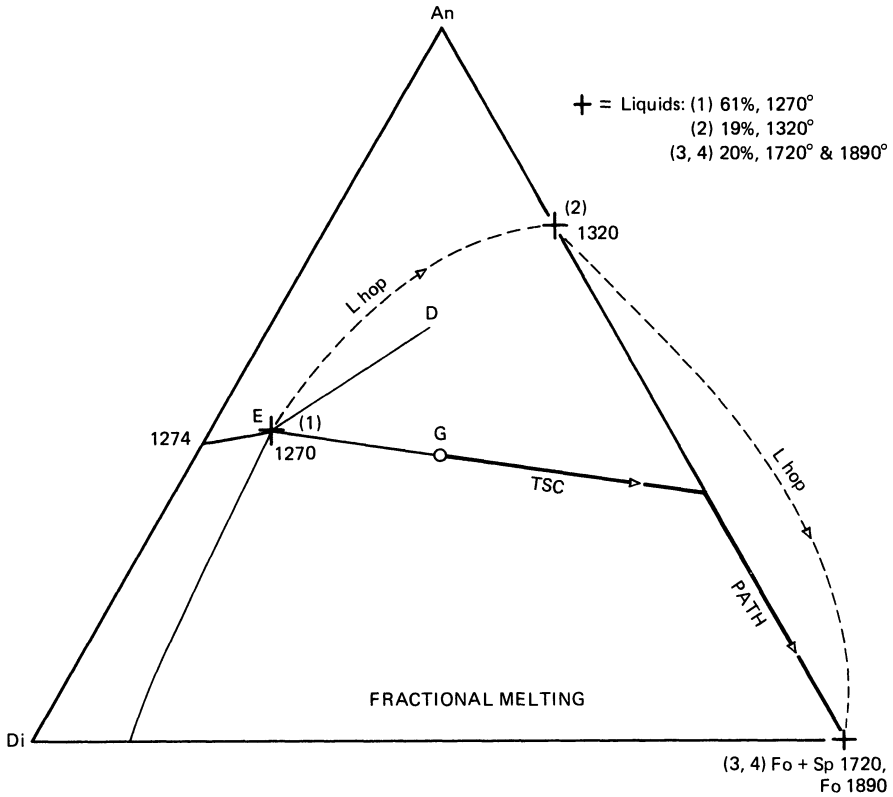


**Figure 9.9.** Fractional melting of bulk composition G. Note that the TSC path (heavy line) is continuous and is the reverse of the equilibrium crystallization TSC path (Fig. 9.6), whereas the liquid resides at three points in sequence, separated by instantaneous “liquid hops.”

sideline begins at 1320° (after a 50° rise in temperature from E in the “ternary” system), with production of liquid C, at  $Fo_{28}An_{72}$ . The reaction is  $Fo + An = Sp + L$ . Now the composition of the liquid is fixed at C, and the TSC changes toward Fo, away from An and C, with a small component of motion toward Sp. In other words, some spinel is being built up in the crystalline residue. The reaction continues until An is exhausted, when the TSC consists of Fo and Sp crystals. No further melting takes place until the Fo-Sp eutectic is reached (at about 1720°C). Here a new invariant liquid is produced until spinel crystals have disappeared, and at this point no further melting takes place until Fo itself melts at 1890°C. These facts are summarized by two “liquid hops” in Fig. 9.9, where liquid No. 2 corresponds to point C in Fig. 9.2. It is a *coincidence* that liquid No. 2 lies very close to the fractionally-produced rock No. 2 in crystallization (Fig. 9.8), but it is instructive to note that a temperature of 1320° is required to make *liquid* of composition 2, Fig. 9.9, whereas the *rock* of composition 2, Fig.

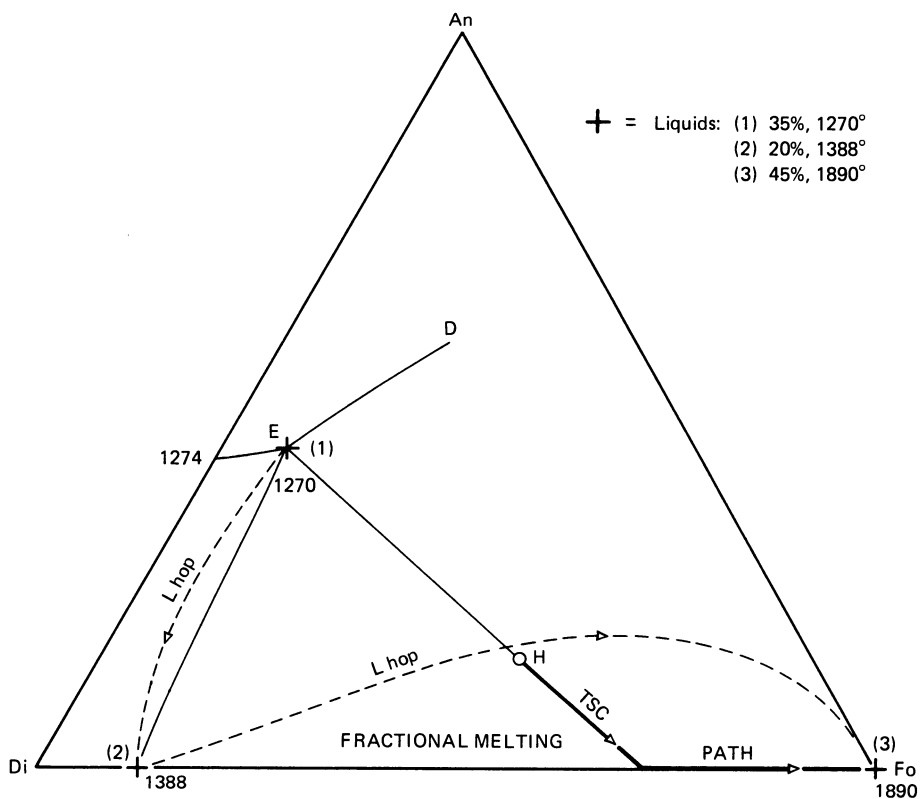


**Figure 9.10.** Fractional melting of bulk composition H. The principles of Fig. 9.9 are duplicated here.

9.8, is produced at temperatures from 1290° to 1270°. The moral of this story is that simplified rock compositions can be attained at lower temperatures by fractional crystallization than by fractional melting followed by equilibrium crystallization.

Fractional melting of composition H is illustrated in Fig. 9.10, which the reader should attempt to analyze for himself. Notice again the coincidence between a fractional liquid composition at 1388°,  $\text{Di}_{88}\text{Fo}_{12}$ , and the rock composition  $\text{Di}_{89}\text{Fo}_{11}$  produced at lower temperatures (1320° to 1270°) by fractional crystallization. It is now apparent that this coincidence is not entirely fortuitous, but is caused by the near-straightness of the field boundary  $\text{Fo} + \text{Di} + \text{L}$ , so that the tangent to the liquid path (field boundary) on crystallization nearly coincides with the origin of the field boundary at the sideline eutectic.

The lever-rule liquid mass fractions on fractional melting are nearly identical to the *solid* mass fractions on crystallization, because of the near-straightness of the field boundaries. It must not be assumed that they *are* identical. They may be rigorously determined as shown by the following example, using Fig. 9.10. When the TSC has reached Fo-Di, the lever rule

shows that 35% of the initial mass H has been liquified. Sixty-five percent is therefore still solid, and composed of Di + Fo crystals. Application of the lever rule from point 2, 1388°, along the Di-Fo sideline, gives about 31.5% liquid of composition (2), 1388°, when the TSC has reached Fo. This is 31.5% of the Di-Fo mass, but  $31.5 \times .65$  of the *initial* mass H, or about 20% of the initial mass obtained as a second liquid at 1388°.

## Discussion of Melting

One very interesting feature of ternary eutectic melting, whether of the fractional or equilibrium type, is the large volume of eutectic liquid produced isothermally, as at E in Figs. 9.9 and 9.10. We have seen in Fig. 9.10 that a bulk composition having only 15% of its initial mass as An yields 35% of its mass as liquid E, which is basaltic in nature. It can easily be shown by means of similar triangles that the liquid yield is 35% whenever the initial An content is 15%, and whatever the initial Fo:Di ratio. The basaltic region of the Fo-Di-An ternary diagram may, then, be contoured as to the mass yield of liquid E for varying bulk compositions, as in Fig. 9.11. This figure suggests that an ultramafic rock composed of olivine and diopside with only a trace—4%—of plagioclase would yield 10% of its mass as isothermal basaltic liquid, which is probably sufficient to become mobilized and emplaced elsewhere as magma or lava. It is, then, an important general property of eutectic systems that a meaningful amount of eutectic liquid is likely to result from melting (or crystallization, for that matter) even for bulk compositions very near one of the sidelines.

The geological importance of this result deserves brief examination. It might be argued that the production of liquid isothermally is of little importance, since the latent heat of fusion is bound to require many more calories than the mere heating of the rock, whose heat capacity is far lower than the latent heat of fusion. On the other hand, it must be said that the latent heat represented by the fusion of only 10% of the mass is likely to be less than or equivalent to that required to raise the temperature of the whole system by 1°C. Therefore melting may well be terminated in nature at or near the point where isothermal production of liquid ceases, because one solid phase is used up.

On the other hand, it is very unlikely that a truly eutectic relation will be encountered in dry natural rocks, whose minerals are, without any important exception, solid solutions. Recalling the plagioclase diagram (Ch. 6) and Di-An-Ab (Ch. 8), we have learned the eutectics are not expected to occur in the presence of solid solution. There will be, therefore, a restricted likelihood of truly isothermal liquid production in nature. We cannot say there is *no* likelihood of isothermal melting in nature, because the presence of H<sub>2</sub>O in the system will generate another type of eutectic behavior, as we

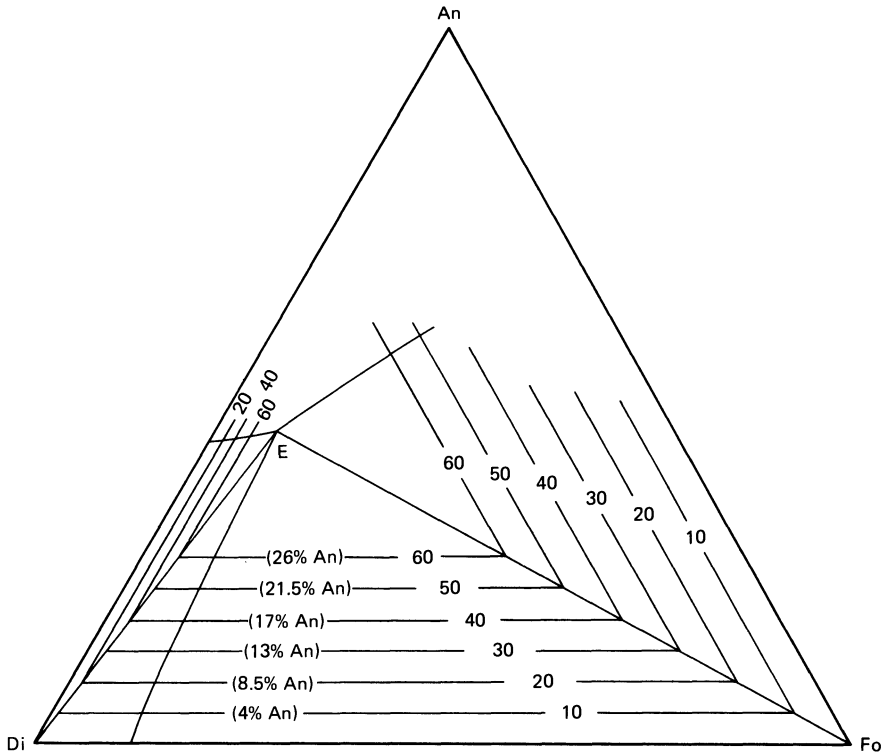


**Figure 9.11.** Percentage of eutectic liquid produced on melting in Fo-Di-An. The contours show that the percentage of liquid E is sensitive only to the content of the component beyond E in the bulk composition. The contours also show the amount of liquid left ( $F_L$ ) when the liquid first arrives at E on crystallization. Non-ternary effects are ignored.

shall ultimately see. Even in the absence of a truly isothermal melting process, however, it is correct to say that when a four-phase point such as E becomes a piercing point because of solid solution, it retains certain eutectic-like properties. Melting in the presence of three solid phases may involve the input of fewer calories than continued melting after one of these solid phases has disappeared.

The principles of eutectic melts are, then, important to bear in mind for concepts of magma generation, but difficult to evaluate in completely general terms.

### Effects of Non-ternary Nature

We have learned that Di-An is not strictly binary, due to incorporation of Al in Di (as CaTs), and therefore it is clear that point E in Fig. 9.3 cannot truly be a ternary isobaric eutectic, because the compositions of Di and L do not lie strictly in the Fo-Di-An plane. Note, however, that liquids

approaching E along Fo + An + L are truly ternary until Di actually begins to crystallize at E. Note further that crystallization of diopside will not materially change the Fo-Di-An ratio of the liquid from that of E, a fact which is borne out by the experimental difficulty of showing *any* range of temperature at E. In truth, we are aware that the liquid must move off the Fo-Di-An plane toward SiO<sub>2</sub><sup>2</sup>, but evidently it does not move very far. Accordingly, we can expect some tendency toward silica-saturation in natural analogs of the Fo-Di-An model, although this tendency may be cancelled by other effects. The non-ternary nature of the system when the liquid projects to E is far less important than the effect of adding Ab to the plagioclase, for example.

A more drastically non-ternary behavior is seen when the Sp + L field is encountered. In terms of basalt genesis, this field is a somewhat specialized problem, first because of the relative scarcity of (olivine + plagioclase)-rich liquid, and second, because addition of Fe<sup>+2</sup> to the olivine or SiO<sub>2</sub> to the system tends to eliminate the Sp + L field. For these reasons, a detailed treatment of the Sp + L field is somewhat of a digression from our central purpose, and so it is included as an addendum to this chapter for future reference, or for those who are curious about it.

## Summary

The system Fo-Di-An is an interesting model of basalt because it contains a four-phase point E (Fo + Di + An + L) which comes very close to the olivine:augite:plagioclase ratio of many natural olivine basalts. By inference, the natural examples may achieve this ratio by a modest amount of fractional crystallization if their composition lies anywhere near the model four-phase point. Moreover, while plagioclase is not an expected phase in the upper mantle site of basalt magma generation, its presence in small quantity in a high-level ultramafic rock could cause the generation of appreciable quantities of basaltic liquid if melting were to occur in the deep crust or uppermost mantle.

The system treated here is of further interest as an example of a nearly ternary, nearly eutectic system. It serves as a model for discussion of crystallization and melting paths in ternary eutectic systems without solid solution, and it can be seen that these paths are simpler than those in systems where solid solutions play a role.

Addition of the single component Ab to the system generates the quaternary system Fo-Di-An-Ab, which is the critical plane of the basalt tetrahedron expanded to include An. This quaternary system is discussed by Yoder and Tilley (1962, p. 395).

<sup>2</sup>Away from SiO<sub>2</sub>, according to Presnall *et al* (1978), as discussed in Chapter 18. If their interpretation is correct, the effect of Mg in anorthite must outweigh the effect of CaTs in diopside, contrary to expectations.

### Addendum: The Spinel + Liquid Field

The spinel + liquid field in Fo-Di-An requires special geometrical treatment, since the phases spinel and liquid do not lie in the Fo-Di-An plane.

An elementary comprehension of what goes on in the Sp + L field can be gained by means of three-dimensional sketches of a quaternary system which contains all the phase compositions of interest. What system should this be? Choosing all the oxide components of Fo, Di, and An, we find CaO, Al<sub>2</sub>O<sub>3</sub>, MgO, and SiO<sub>2</sub> (CAMS), which will surely suffice, as spinel (MgAl<sub>2</sub>O<sub>4</sub>, or MgO · Al<sub>2</sub>O<sub>3</sub>) can be expressed as a member of the group. Fig. 9.12 is a perspective view of the tetrahedral volume CAMS, within which is drawn the system Fo-Di-An. This system is part of the plane CaO·2SiO<sub>2</sub> - 2MgO·SiO<sub>2</sub> - 2Al<sub>2</sub>O<sub>3</sub>·SiO<sub>2</sub> (CS<sub>2</sub> - Fo - A<sub>2</sub>S). The idealized spinel composition lies on the MA edge, well out of the plane of the Fo-Di-An system. *Removal* of Sp from a liquid *in* that plane will, therefore, drive the liquid away from the Fo-Di-An plane and into the volume Fo-Di-An-SiO<sub>2</sub>, which is shown as a distorted tetrahedron in the figure. A line in the figure from Sp through the Sp + L field of Fo-Di-An illustrates the fact that the liquid must lie in this distorted tetrahedral volume, and not in any other volume of the CAMS parent tetrahedron.

To examine the geometrical relations further, we may remove the tetrahedral volume Fo-Di-An-SiO<sub>2</sub> and redraw the part near the Fo-Di-An base, as in Fig. 9.13, in which the SiO<sub>2</sub> apex lies upward, out of the picture. Fig. 9.13 is a perspective view, and Sp is plotted in an arbitrary position below the Fo-Di-An plane and toward the observer. Now it can be seen that the lines which bound the Sp + L region in the Fo-Di-An plane are simply the traces of intersection of that plane with the surfaces An + Sp + L and Fo + Sp + L. These two surfaces, in turn, intersect in the line Fo + An + Sp + L, and it is this line which generates the piercing point D in the Fo-Di-An plane. The surfaces do not terminate in Fo-Di-An, but extend below it, and in fact are part of a multi-faceted boundary surface of the Sp + L field which occupies a large volume around Sp in the CAMS tetrahedron.

Two arbitrary bulk compositions in Fo-Di-An are labelled 1 and 2 in Fig. 9.13. Both lie in the Sp + L field, which means that when a liquid of composition 1 or 2 begins to crystallize, Sp is the first crystalline phase to form. Removal of Sp from the liquid drives the latter out of the plane Fo-Di-An, toward a more SiO<sub>2</sub>-rich composition, until it hits one of the surfaces Fo + Sp + L or An + Sp + L. The liquid then continues along this surface in divariant equilibrium as it crystallizes either Fo or An in conjunction with spinel, as shown by arrows in the figure. Crystallization continues until the liquid reaches the four-phase, isobarically univariant ( $W_p = 1$ ) curve Fo + An + Sp + L. Now at this point, the liquid finds itself in an awkward position. It is told that it must maintain equilibrium with Fo + An + Sp, yet no tangent to the univariant curve cuts the Fo-An-Sp plane in the

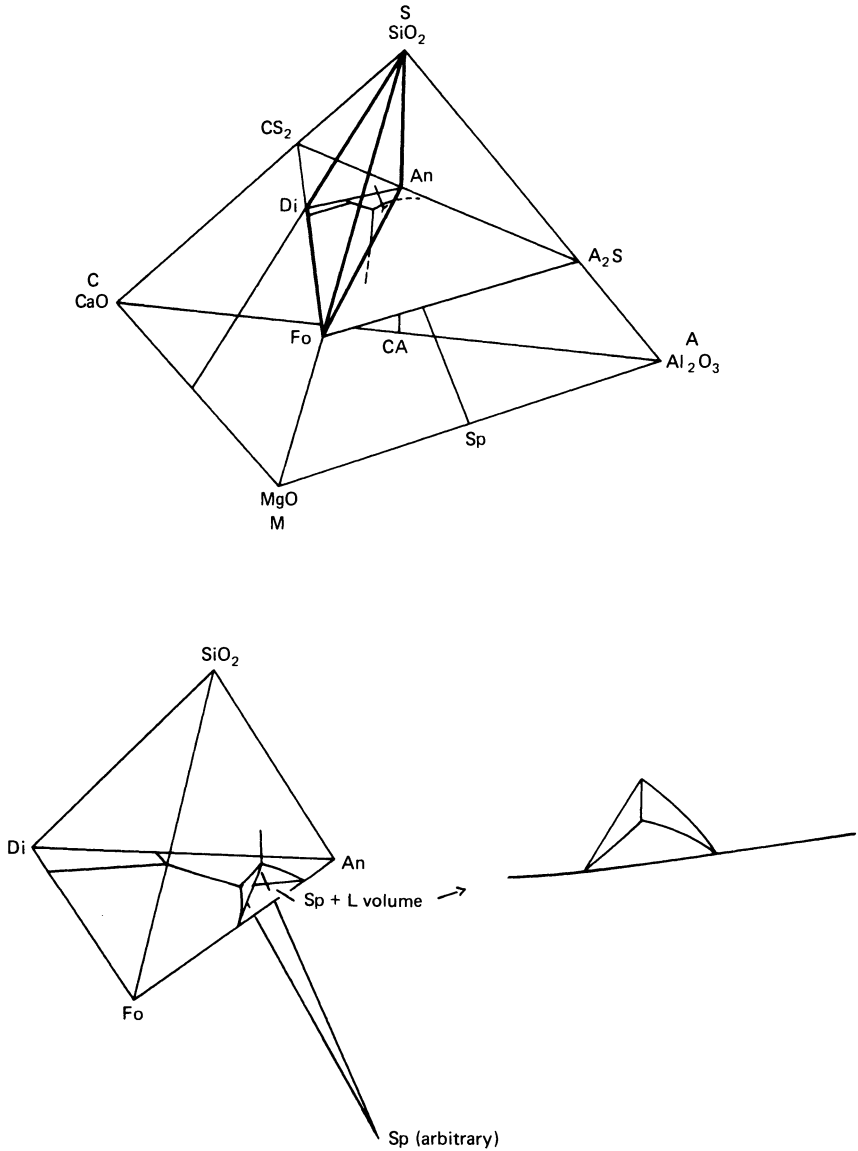


**Figure 9.12.** Position of the Fo-Di-An plane in the C-A-M-S tetrahedron. The lower sketches show progressively closer views of the spinel + L volume shown in Fig. 9.13.

CAMS tetrahedron. This univariant equilibrium cannot, therefore, represent mere crystallization by the reaction  $L = Fo + An + Sp + \text{cals}$ . There is only one way in which the liquid can remain on the univariant curve, and that is by eating Sp, not producing it, and the reaction then becomes  $L + Sp = Fo + An + \text{cals}$ . (Another way of saying this is to say that the tangent

DISTORTED SKETCH

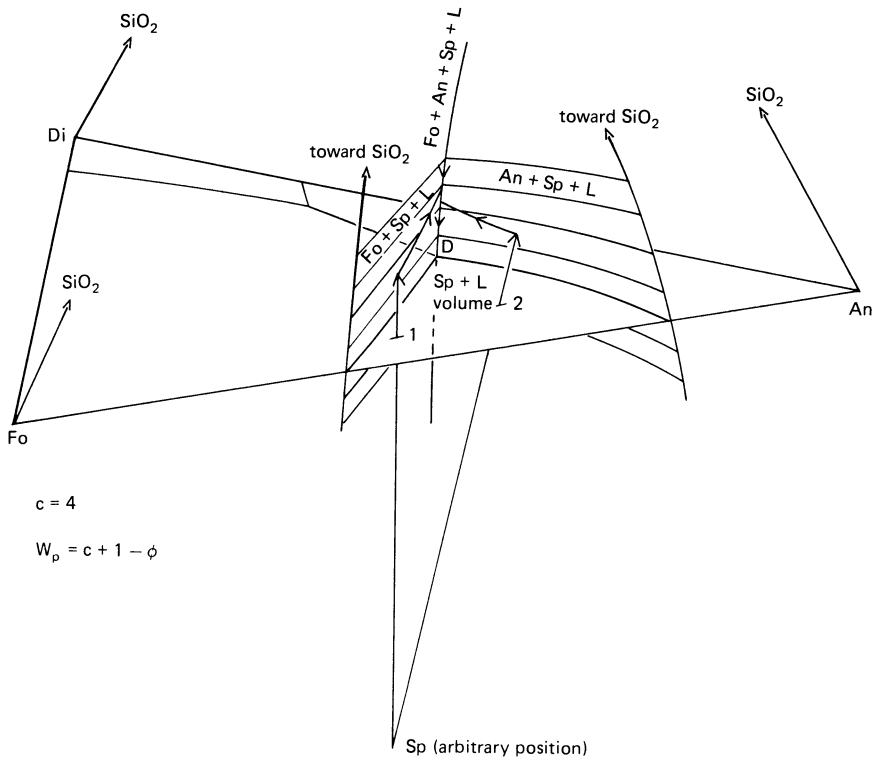


**Figure 9.13.** Courses of liquids in the spinel +  $L$  field of Fo-Di-An-SiO<sub>2</sub>.

to the liquid path does cut Fo-An-(minus Sp), in which (minus Sp) is an imaginary point produced by an inversion of the Sp position through the  $L$  position.)

The result of the reaction  $L + Sp = Fo + An + cal$ s is that  $L$  now moves *toward* Sp rather than away from it, by the simple expedient of *resorbing* or dissolving the previously-formed spinel crystals. In other words, the liquid is too silica-rich to permit spinel to persist, and instead, spinel reacts with the liquid to permit formation of more Fo + An. The spinel reaction terminates just as the liquid reaches D, for at this point all of the previously-formed spinel is used up, and the system now consists only in Fo + An +  $L$ , where  $L$  lies at D. Since Fo, An, and D are all coplanar in Fo-Di-An, it is evident that the system is now truly ternary, and crystallization proceeds as previously described.

In the equilibrium crystallization process just described, it is seen that an exact balance exists between the amount of Sp formed and the amount dissolved, so that the liquid returns precisely to the Fo-Di-An plane. Any fractional crystallization of Sp would, then, destroy this balance by locking

up Sp crystals in the rocks and leaving excess  $\text{SiO}_2$  in the liquid, which would ultimately be expressed as the mineral enstatite (= Fo +  $\text{SiO}_2$ ) or the minerals enstatite and quartz. Removal of Sp would thus cause silica saturation or oversaturation of the liquid.

Equilibrium melting of compositions rich in Fo and An begins with production of eutectic liquid at E at 1270°C (see Fig. 9.6), until Di crystals are used up. The liquid then dissolves Fo and An while moving toward the peritectic D, which it attains at 1317°C. Spinel crystals now form on melting, by the reaction  $\text{Fo} + \text{An} = \text{Sp} + L$ , and the liquid leaves the Fo-Di-An plane toward  $\text{SiO}_2$  (Fig. 9.13). When either Fo or An crystals are completely dissolved, the liquid leaves the univariant line in Fig. 9.13 and continues along one of the divariant surfaces  $\text{An} + \text{Sp} + L$  or  $\text{Fo} + \text{Sp} + L$ . When the last of Fo or An crystals is dissolved, the liquid dissolves spinel until it returns to the Fo-Di-An plane, at which point all spinel is used up and the system consists of liquid only. This is exactly the reverse of equilibrium crystallization.

Fractional melting is quite different. As long as any Di crystals remain, liquid E is produced at 1270°C, and the TSC moves directly away from E to the Fo-An sideline. No liquid of peritectic composition D is produced. The next liquid is liquid C of Fig. 9.2, at 1320°C. Continuous extraction of this liquid takes place, so that crystals of Fo + An continue to generate liquid C on melting. However, small amounts of crystalline spinel are generated continuously by the reaction  $\text{Fo} + \text{An} = \text{Sp} + L$ . Therefore when, for example, An is used up, the next liquid is that of the Fo + Sp eutectic at about 1720°C. If the final crystalline residue is Fo, the final liquid is formed at 1890°C; if the final crystalline residue is Sp, the final liquid is formed at 2135°C, the melting point of pure spinel. Of course these are temperatures vastly higher than expected in the upper mantle.

Fractional melting therefore ignores the  $\text{Sp} + L$  field in Fo-Di-An and produces liquids E and C, of which E is the only one of high petrological interest. A crystalline residue of Fo + An would probably be immune to further melting in the crust and upper mantle.

The above principles of equilibrium and fractional crystallization and melting apply equally well to compositions initially outside the  $\text{Sp} + L$  field in the plane Fo-Di-An, i.e. any composition in the triangular area An-D-Fo of Fig. 9.5. Liquids in the Fo + L field, for example, crystallize Fo on cooling until they hit the  $\text{Fo} + \text{Sp} + L$  surface where it intersects the Fo-Di-An plane. Further cooling yields crystals of Sp as well as Fo, driving the liquid toward  $\text{SiO}_2$ -rich compositions along the  $\text{Fo} + \text{Sp} + L$  surface, till they reach the  $\text{Fo} + \text{Sp} + \text{An} + L$  univariant line, where the spinel reaction begins as before, bringing the liquid back into the Fo-Di-An plane at D.

## Chapter 10

# Incongruent Melting: The System Forsterite-Silica

### Introduction

Up to now we have concentrated on developing the phase relations in and around the critical plane in the basalt tetrahedron, described in Chapter 2. This critical plane is the plane which separates nepheline-normative bulk compositions from hypersthene-normative ones. Hypersthene is modelled, in the fundamental basalt tetrahedron, by its magnesian end member, enstatite,  $\text{MgSiO}_3$  (or  $\text{MgO} \cdot \text{SiO}_2$ ). Enstatite appears at the apex of another triangular plane in the tetrahedron, the plane Di-Ab-En, called the plane of silica saturation by Yoder and Tilley (196we. This plane marks the transition from (enstatite + forsterite) - normative bulk compositions to (enstatite + quartz) - normative bulk compositions. It also truly marks the division between solid, equilibrium assemblages of enstatite + forsterite, to the left, and enstatite + quartz, to the right. However, it does *not* precisely divide the crystal + liquid equilibria  $\text{En} + \text{Fo} + L$  and  $\text{En} + \text{Q} + L$ . Instead, an important phenomenon exists near the plane, wherein the assemblage forsterite +  $L$  extends to more silica-rich compositions than the plane itself, with or without enstatite, thus providing a possibility for liquids to become silica-oversaturated by fractional crystallization of forsterite. To see why this is so, we must now examine the so-called *incongruent* melting behavior of enstatite in the system Fo-SiO<sub>2</sub>.

Incongruent melting occurs when a compound, in this case enstatite, does not melt directly to a liquid of its own composition, but instead undergoes a dissociation reaction to another solid phase plus liquid.

The nomenclature of materials having the composition  $\text{MgSiO}_3$  is com-

plicated by the existence of several crystalline polymorphs of different symmetry. We shall call the composition itself enstatite (En), as a molecular or normative name. The actual crystalline phase which appears in experiments at high temperatures is an orthorhombic polymorph called protoenstatite (Pr); at lower temperatures, this inverts either to a second orthorhombic polymorph, enstatite, or a monoclinic polymorph called clinoenstatite. Protoenstatite is not found in nature, indicating that one or both of the polymorphic transitions is rapid and proceeds with ease.

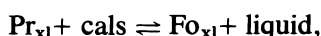
The enstatite composition may be made by sintering MgO and SiO<sub>2</sub>, as with forsterite, or by thoroughly melting such a mixture and crystallizing it below 1500°C.

### Incongruent Melting of Enstatite

When crystalline enstatite is heated, it melts at 1557°C, but as the experiments of Bowen and Andersen (1914) clearly show, the result is not simply liquid, but liquid plus crystals of forsterite. Specifically, Bowen and Andersen observed at 1556° only crystalline MgSiO<sub>3</sub>, and at 1558° only glass and forsterite in their experimental charges. The melting reaction therefore cannot be



but is instead of the type



in which the liquid must be more SiO<sub>2</sub>-rich than MgSiO<sub>3</sub>, because Fo is SiO<sub>2</sub>-poor relative to MgSiO<sub>3</sub>. This type of melting is termed incongruent, because the liquid is not coincident in composition with the phase which undergoes melting.

Having observed this incongruent melting behavior, Bowen and Andersen were able to locate the liquid composition in the usual manner, by the quenching method. They located the completion-of-melting reactions, Fo + L = L, for several compositions near MgSiO<sub>3</sub>, and traced this liquidus curve downward to its intersection with the 1557° isotherm which represents the melting reaction of MgSiO<sub>3</sub>. The result is shown in the binary diagram of Fig. 10.1, which is a portion of the full diagram MgO-SiO<sub>2</sub>. The liquid generated at 1557° contains about 61% SiO<sub>2</sub> by weight, compared to slightly less than 60% by weight of SiO<sub>2</sub> in MgSiO<sub>3</sub> (the molecular weights of MgO and SiO<sub>2</sub> are very near 40 and 60, respectively). The lever rule, applied to Fig. 10.1, shows that only slightly more than 5% Fo is generated by the melting reaction, along with 95% liquid.

The relations near the enstatite composition are shown more clearly in the slightly distorted sketch of Fig. 10.2. The composition of the liquid in

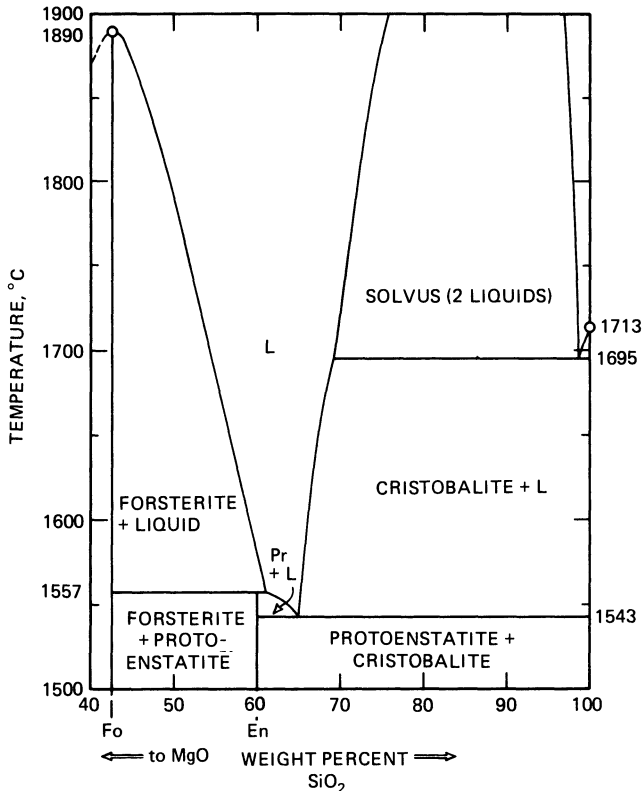


**Figure 10.1.** Phase diagram of the system forsterite-silica, after Bowen and Andersen. Note that the abscissa is scaled in terms of the components MgO, SiO<sub>2</sub>.

equilibrium with Pr and Fo at 1557° lies at R, a 3-phase, isobarically invariant reaction point. Point R is a special type of reaction point called a *peritectic point*. A peritectic point identifies the composition of a liquid which cannot be expressed as a positive combination of the solid phases with which it is in equilibrium. Instead, in this case, the liquid composition can only be expressed as Pr *minus* Fo. Graphically, this means that the peritectic point lies on the extension of a line connecting the two solid phases, unlike a eutectic point, which lies between the two solid phases. Reactions which take place at a peritectic point are often termed *odd*, which can be remembered by associating it with the positive-negative combination of solid phases needed to express the liquid composition. Eutectic reactions, conversely, are said to be *even*.

To the right of point R, the phase diagram is of the simple binary eutectic type (see Di-An, Chapter 5), involving the phases protoenstatite, cristobalite and liquid. The liquidus curve  $Pr + L = L$  passes through point R, and its metastable extension (dashed) shows schematically that the unrealizable, metastable, congruent melting point of MgSiO<sub>3</sub> lies on a maximum at a temperature slightly above 1557°. By an accident of nature, this congruent melting point happens to be overlapped by the Fo + L field at 1 atm

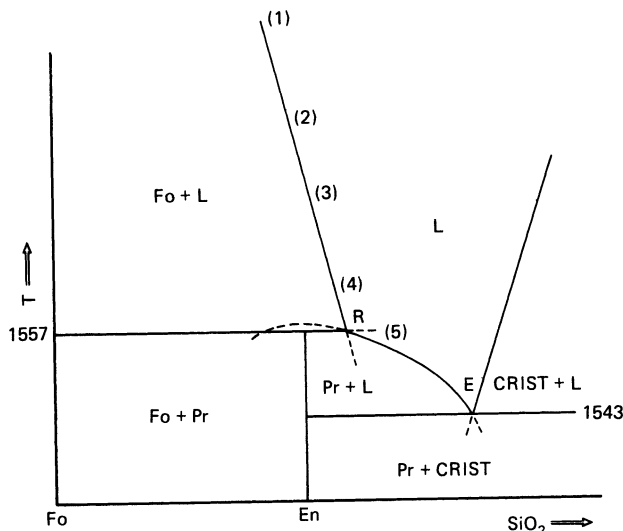
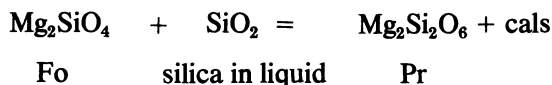


**Figure 10.2.** Enlarged sketch of the protoenstatite region in Fo-SiO<sub>2</sub>.

pressure, although at high pressures, as we shall eventually see, the Fo + L field recedes “behind” the En composition and the melting of MgSiO<sub>3</sub> becomes congruent.

### Equilibrium Crystallization Paths

We begin with a liquid of bulk composition 1, Fig. 10.2, perceiving that this liquid lies to the Fo side of the En composition. Such a liquid, on cooling, first crystallizes Fo; the phases are now two, Fo + L, and the variance  $W_p$  is 1, constraining the further course of the liquid to the isobarically univariant Fo liquidus curve. Crystallization of Fo continues until the liquid reaches R, when the temperature is 1557°C. At this moment, a reaction sets in, as the liquid has become too rich in silica for Fo to be unambiguously stable. The reaction converts crystals of Fo to Pr, and may be expressed as



At this point the phases are three, and  $W_p = 0$ ; the temperature and compositions of the three phases are invariant. The total solid composition (TSC), which was at Fo, now moves along the 1557° isotherm toward the composition 1, by addition of Pr crystals. When the TSC reaches composition 1, the original bulk composition is now expressed as crystalline Fo +

Pr, and no liquid therefore remains. Crystallization is therefore completed through reaction of the liquid at point R until it is exhausted.

Beginning at point 2, of composition  $\text{MgSiO}_3$ , a liquid cools until Fo begins to crystallize, and the events are exactly the same as in case 1, the liquid remaining finally at R as the TSC moves from Fo toward En along the  $1557^\circ$  isotherm. In this case, however, the destruction of Fo by reaction with liquid is complete; the last drop of liquid converts the last crystal of Fo into Pr, and a monomineralic mass of pyroxene results.

A liquid of composition 3, containing more silica than the composition  $\text{MgSiO}_3$ , has a somewhat longer biography. This liquid also produces Fo crystals as it starts to crystallize, but when these have fully reacted with the invariant liquid at R, the TSC lies at the composition En, still short of composition 3. The liquid now coexists with only one crystalline phase, Pr, and is therefore free to move in univariance down the  $\text{Pr} + L$  curve toward E. The remaining crystallization history is just that of any binary eutectic diagram: the TSC remains at En as crystals of Pr are produced, until the liquid reaches the eutectic E,  $1543^\circ$ . At this point, crystals of cristobalite begin to form, and the TSC moves toward E until it achieves the composition 3, when the liquid is finally exhausted. It is most important to note that the final result of equilibrium crystallization of composition 3 is an assemblage of protoenstatite and cristobalite. Of forsterite, which was the first crystal to form, there is no trace. All the forsterite has disappeared during the reaction when the liquid was at R. Under equilibrium conditions, no rock would preserve magnesian olivine crystals in the presence of a later silica mineral, because of the reaction relation between olivine and liquid. The completion of reaction insures that the disappearance of olivine will be followed by the appearance of a silica mineral.

A liquid of composition 4, coinciding with R, would produce, on cooling, only an infinitesimal trace of Fo at R, which would immediately react to Pr. Thereafter the course of the liquid would be the same as in the case of composition 3, the system behaving as a binary eutectic system.

Finally, a liquid of composition 5 behaves solely as a liquid in a binary eutectic system, crystallizing only Pr along the initial liquidus, then Pr and Cr at E.

The silica-rich portion of the system beyond E is a binary eutectic region offering no complications. Bulk compositions in this region are probably rare, and irrelevant to basalts in any event.

In summary, equilibrium crystallization of bulk compositions in the neighborhood of En will be likely to produce Fo as an initial crystalline phase (unless the liquid lies to the right of R), and some or all of the Fo crystals will inevitably be destroyed by reaction with liquid R. Such a reaction is seen in many rocks as a reaction rim of orthopyroxene around grains of olivine, testifying to the silica-saturated nature of the residual liquid, analogous to liquid R. This textural evidence of the olivine reaction

relation in basalts is fundamental evidence for silica saturation, and forms a sufficient basis for applying the epithet *tholeiite* or *subalkaline basalt*. Persistence of olivine, in spite of reaction, can be caused by several circumstances. Under model conditions of equilibrium it can only mean that the bulk composition lies to the left of En in Fig. 10.2. Partial rims of orthopyroxene on olivine can be accepted as evidence for this condition. Complete rims, however, may indicate failure of complete equilibrium, wherein olivine persists only because it was shielded by the orthopyroxene rim from further reaction with liquid R. In such a case, the bulk composition *may* have been oversaturated, i.e. lying to the right of En, and the texture would represent a crystallization history intermediate between equilibrium and fractional crystallization.

## Fractional Crystallization

Examination of the foregoing section and Fig. 10.2 will suggest that fractional crystallization may occur either through removal of olivine by sinking or flowage transport, or through the isolation of olivine grains from the liquid by shells of orthopyroxene. For all bulk compositions discussed above, perfect fractional crystallization will always result in the attainment of the eutectic E by the liquid. The residence of the liquid at R will be instantaneous, as the ISC undergoes a discontinuous hop from Fo to En. A final ISC hop to E occurs when the liquid reaches E. Fractional crystallization can only lead to silica-oversaturation of compositions like liquid 1, originally silica saturated. The incongruent melting of enstatite guarantees this result.

## Melting

Melting of any mixture of protoenstatite and cristobalite crystals begins when the temperature reaches 1543°, with the production of eutectic liquid E. When equilibrium is maintained, the liquid moves off along the curve E-R (assuming the bulk composition lies to the left of E) as soon as the cristobalite is used up. Liquids along this liquidus curve continue to dissolve Pr until it is used up, if the initial bulk composition lies between R and E. If the initial bulk composition lies to the left of R, then the liquid must halt at R, while the reverse of the crystallization reaction occurs, i.e.,  $Pr + cals = Fo + L$ ; this is the odd, or incongruent melting reaction. This reaction ceases when Pr is used up, and then the liquid must follow the forsterite liquidus until Fo is used up, at which point the system consists only of

liquid; melting is completed. We see, in this process, the manufacture of crystals of forsterite, a silica-undersaturated mineral, during the melting of a silica-oversaturated mixture. If equilibrium melting is arrested during this process residual crystals of Fo will remain set in the glass or matrix which represents liquid.

Melting of any mixture of forsterite and protoenstatite begins at 1557° with the incongruent melting reaction, producing liquid R and more Fo at the expense of Pr. This reaction continues as the TSC moves toward Fo, and ceases only when Pr is used up and the TSC equals Fo. After this, melting continues, as before, as liquid along the forsterite liquidus dissolves Fo crystals until they are gone.

It is interesting to note that the melting of the silica-saturated assemblage Fo + Pr yields, by odd reaction, a silica-oversaturated initial liquid, which continues to form, isothermally, as long as any Pr remains. Thus in an equal mixture of Fo and Pr, somewhat more than half of the mass would melt isothermally to a silica-oversaturated liquid which, if removed and then observed, would show no clue of having come from a rock saturated with olivine. When you think of it, this is really a rather startling result, a bold stroke calculated to keep the student of nature on his toes.

The possibilities of fractional melting should be considered in light of the principles just discussed. Fractional melting of Pr + Cr mixtures yields liquid E which, fractionally removed, causes the TSC to move toward Pr at 1543°. Melting ceases when Cr is used up, resuming again only at 1557°, with a discontinuous liquid hop from E to R. Fractional removal of liquid R occurs during the melting of Pr, during which time Fo must accrue in the TSC, due to the incongruent melting of Pr. About 95% of the mass of Pr will have been removed as liquid when all the Pr is used up; the remaining 5% is now crystalline forsterite, which will not melt until a temperature of 1890° is reached, an event not likely to occur in the earth's upper mantle. Fractional melting produces liquid hops and continuous rock paths, as we have seen before. However, in this particular system the results of fractional melting are qualitatively and compositionally similar to the results of equilibrium melting, the chief difference being the absence of any liquids of composition other than E or R.

## Summary

The melting of enstatite must be treated in the system Fo-SiO<sub>2</sub> because of the phenomenon of incongruent melting, which yields liquid more silica-rich than En, and crystals of forsterite. Fractional crystallization of liquids initially containing normative olivine as well as orthopyroxene will yield liquids containing normative quartz; hence the incongruent melting behavior

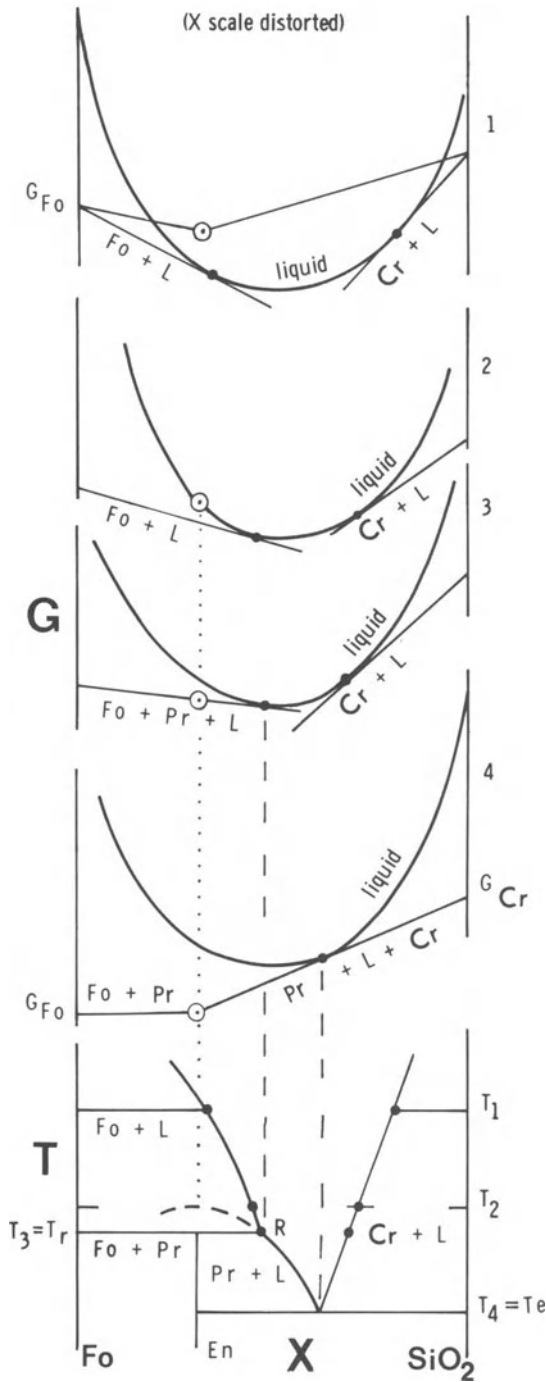


Figure 10.3. G- and T-X diagrams for the system forsterite-silica.

of enstatite furnishes an easy transit *toward* silica across the plane of silica saturation for liquids in the basalt tetrahedron. Perfect fractional removal of olivine must, indeed, produce silica-oversaturated residual liquids, and even imperfect fractional removal will be likely to do so. The rimming or corrosion of olivine crystals by orthopyroxene in many basaltic rocks testifies to the common occurrence of such fractionation, as does the frequent appearance of quartz in the mesostasis of such rocks. The melting of olivine-orthopyroxene rocks likewise yields a silica-oversaturated liquid which, if crystallized, will produce a silica mineral. The crystalline residuum of such a melting process will be enriched in olivine.

## G-X Diagrams

Having got this far, it would be best to attempt a *G-X* diagram for Fo-SiO<sub>2</sub> before looking too hard at Fig. 10.3. Such an exercise teaches some profound truths about incongruent melting, and these are best learned by struggling along on one's own.

For those who have done this or are too impatient, Fig. 10.3 tells the story. The right half of the diagram simply describes a eutectic type subsystem and needs no further comment: see Fig. 5.8 for comparison. The  $T_1$  section shows the equilibrium Fo + L as being minimized in *G* relative to protoenstatite (Pr, circle in *G-X* space) alone or combined with either Fo or SiO<sub>2</sub>.  $T_2$  is the *metastable* congruent melting point of Pr, which now lies *on* the liquid *G-X* curve but is still undercut by the stable pair Fo + L. Observe that nothing special is required in the shape of the liquid curve to account for incongruent melting. It is only the relative Gibbs energy of the participating solids which determines the incongruency, and by applying as little as 2 kbar pressure, we can bring the melting of enstatite clear of the Fo + L equilibrium by sufficiently raising  $G_{\text{Fo}}$  relative to  $G_{\text{En}}$  to bring the tangent point on the liquid curve around to the left of the En composition. Section  $T_3$ , at the temperature of the reaction point R, shows that Fo, Pr, and liquid are collinear in *G-X* space. This condition implies their stable coexistence. A sketch between  $T_3$  and  $T_4$  would show a new Pr + L tangent isolating Fo from L. Section  $T_4$  shows the eutectic condition.

## Chapter 11

# Forsterite-Anorthite-Silica: Incongruent Melting in a Ternary System

### Introduction

In the ternary system Di-An-Ab, we saw that the complete solid solution of plagioclase had a dominant influence on the course of liquids in the ternary system. We shall now see that the incongruent melting of orthopyroxene in the system Fo-SiO<sub>2</sub> is carried over into a ternary system when a component such as anorthite is added. This ternary system is one of the most useful in illustrating the importance of the reaction relationship of olivine in igneous petrology. The system is the An-analogue of the right half floor of the basalt tetrahedron (Fig. 2.1), and as such is fundamental in establishing the role of the plane of silica saturation, modelled in this system by the line An-En.<sup>1</sup> This role is like that of a check valve: liquids which pierce the plane toward SiO<sub>2</sub> cannot return, at atmospheric pressure, because of the incongruent melting of En to Fo + L.

The system Fo-An-SiO<sub>2</sub> has often been used as a basis for discussing the origin of tholeiitic layered basic igneous complexes (e.g. Irvine, 1970; Jackson, 1970). It has a useful role to play in such discussions, and no doubt its higher-pressure and Fe, Na-bearing equivalents will have an even more important role to play when they have been studied.

<sup>1</sup>This line was called a conjugation line in the original work by Andersen (1915), and by many others since. It is also an Alkemade line or a join. The term conjugation line has, over a period of time, become confused in the literature, and it is perhaps best to drop the name.

## Binary Joins

The joins Fo-An and Fo-SiO<sub>2</sub> have already been discussed in Chapters 9 and 10. An-SiO<sub>2</sub> was initially studied by Rankin and Wright (1915), and by Andersen (1915); it was redetermined by Schairer and Bowen (1947) to be a binary eutectic system with a eutectic at SiO<sub>2</sub> 49.5% by weight, at 1368°C.

## Primary Phase Regions

The ternary system determined by Andersen (1915) and shown in Fig. 11.1 could be rather accurately predicted from the bounding binary joins. It contains features reminiscent of Di-Fo-An and Fo-SiO<sub>2</sub>, particularly the non-ternary Sp + L field, the two-liquid field between En and SiO<sub>2</sub>, and the cristobalite-tridymite inversion. It is no surprise to find large fields of Fo,

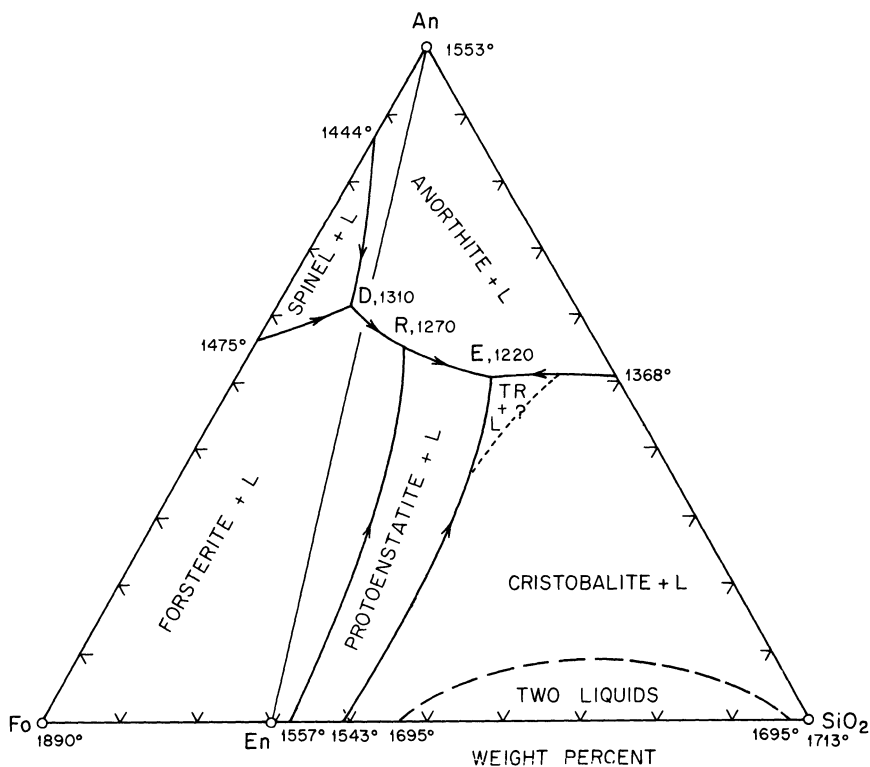


**Figure 11.1.** Phase diagram of the system Fo-An-SiO<sub>2</sub>, after Andersen (1915) and Irvine (1975). Tridymite–cristobalite boundary is highly speculative, based on Andersen’s judgment that tridymite occurs below 1300° C. The inversion temperature is below the solidus on the An–SiO<sub>2</sub> sideline (Longhi and Hays, 1979). Base of diagram measures 10 cm.

An, and  $\text{SiO}_2$  polymorph adjacent to their respective corners. Two pairs of these fields meet in the cotectic field boundary curves DR and 1368E; using conventional notation these curves could be designated  $L$  (Fo, An) and  $L$  (An, Tr), respectively. The third pair, Fo +  $\text{SiO}_2$ , is prevented from occurring by the intervention of the intermediate compound En, probably crystallizing as protoenstatite (Pr) everywhere in its primary phase field. This phase occurs together with An on the cotectic  $L$  (An, Pr) and with  $\text{SiO}_2$  on the cotectic  $L$  (Pr,  $\text{SiO}_2$  polymorph). All the curves so far mentioned are cotectics, in which the reaction is *even*, as discussed in Chapter 10; for example,  $L = \text{An} + \text{Pr}$ , where all quantities are positive. The curve  $L$  (Fo, Pr), on the other hand, is odd or peritectic, the reaction being  $L = \text{Pr} - \text{Fo}$ , just as it is in the bounding system Fo- $\text{SiO}_2$ . Geometrical reasons for knowing that this reaction remains peritectic all along the curve will be given shortly.

The spinel +  $L$  field plays the same role in this system as in Fo-Di-An. Spinel occurs far outside the composition plane of the system, so liquids in equilibrium with Sp lie off the plane in the opposite direction. Point D is a reaction point at which, if continuous equilibrium is maintained, the liquid returns to the plane Fo-An- $\text{SiO}_2$  just as all the Sp is consumed in reaction. By examination of Fig. 9.12, one may be able to discern that upon crystallization of spinel, the liquid moves into the volume Fo-An- $\text{CS}_2$ - $\text{SiO}_2$  in the system CMAS, and returns to the plane Fo-An- $\text{SiO}_2$  when the solids consist only of Fo + An. Further discussion of the Sp +  $L$  field, although of some importance to certain picritic rocks, need not be attempted here. Our discussion will be confined to the "basaltic region" of the diagram in which spinel is not involved.

## Cotectic Crystallization

Point E, Fig. 11.1, is an isobaric ternary eutectic which is the goal of all liquids in the system. Its temperature, 1220°C, is appreciably lower than that of the piercing point in Fo-Di-An, 1270°C, and comes within the range of natural lava temperatures, which are usually lower by virtue of having other components such as Fe and alkalis. The variance of point E is zero under the isobaric restriction, that is,  $c = 3$  (F,A,S),  $\phi = 4$  ( $L$ , An, Tr, Pr), and  $W_p - c + 1 - \phi = 4 - 4 = 0$ . Converging at this point are three isobaric univariant curves, all cotectic, and crystallization of any bulk composition in the right half of the diagram (strictly anywhere to the right of a line from An to En) will drive liquids to one of these curves and thence to E, as in any ternary eutectic system. Application of the principles set forth in Chapter 9 will lead to a correct analysis of any such crystallization path, and both the continuous equilibrium and fractional cases of crystallization and melting are straightforward. Except for two examples to follow later, it is left to the reader to work out such examples for himself, preferably on

paper, to keep rigorous track of TSC and other paths and to apply the lever rule. The cristobalite-tridymite transition is an internal phase transformation of silica, and proceeds with a relatively minor heat effect. When divariant liquids cross this isothermal boundary, they are briefly arrested at isobaric univariance while cristobalite inverts to tridymite (or vice versa on heating).

## Equilibrium Crystallization

We shall consider all cases of crystallization and fusion involving the eight bulk compositions indicated in Fig. 11.2. All but two of these (V and W) involve peritectic crystallization. It is appropriate to follow Andersen, Bowen and many others in looking first at the sequence of compositions P,Q,S,T which span the range from silica undersaturation (P) through saturation (Q) to oversaturation (S,T).

In all exercises such as these, it is important to pause and consider, right at the start, how the bulk composition will be realized in the solid state after crystallization is complete. This requires an ability to look through the liquidus map, ignoring it completely, and identify the solid phases surrounding any bulk composition. Ignoring spinel, there are only four such

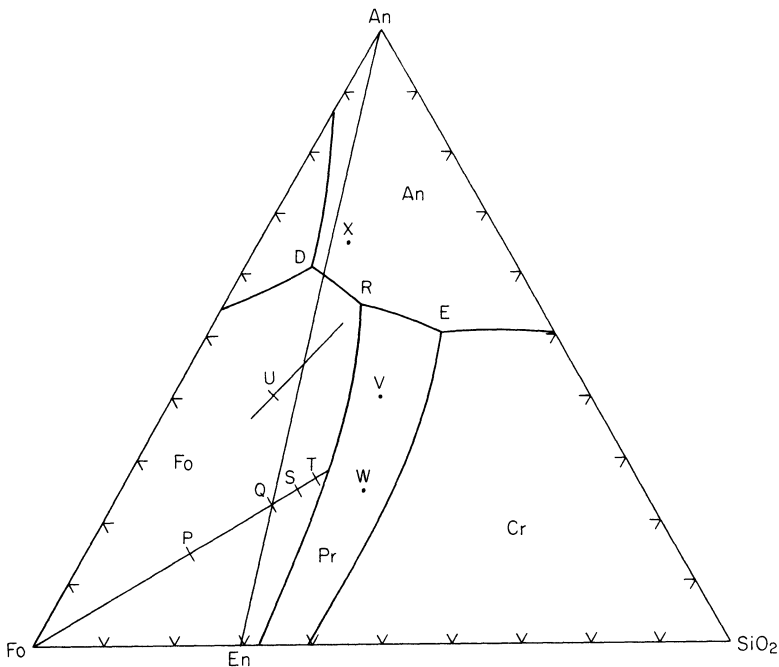


**Figure 11.2.** Location of bulk compositions discussed in the text.

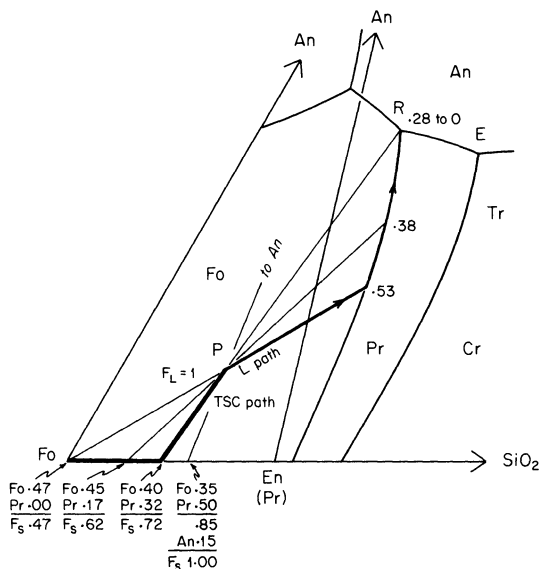


**Figure 11.3.** Equilibrium crystallization of bulk composition P. The figures at the ends of levers show the compositions of the solids at various stages of crystallization.

solid phases to consider: Fo, An, Pr, and Tr (Cr never occurs in the final assemblage, because it inverts to Tr). Assuming equilibrium, bulk composition P will end up as a mixture of Fo, An, and Pr; Q as An + Pr, and both S and T as An + Pr + Tr. Now, looking at the invariant points R and E, it is evident from the field labels that liquid R coexists with Fo, An, Pr, while liquid E coexists with An, Pr, Tr. Accordingly, we may correctly surmise that when olivine remains in the TSC, the final liquid will be R, and when Tr occurs in the TSC, the final liquid will be E. Such a preview is always a helpful reminder of how things will proceed in a crystallization exercise.

The equilibrium crystallization of bulk composition P is illustrated in Fig. 11.3. Since P lies in the primary phase field labelled Fo, the liquid will at first move directly away from Fo, until it reaches the peritectic field boundary L (Fo, Pr). At this moment,  $F_L = .53$ ,  $F_S = .47$ , the TSC being expressed as crystals of Fo. Pr now crystallizes, according to the field label, and the liquid is constrained by univariance to the field boundary. This field boundary is an exact analogue of point R in Fig. 10.2, Fo-SiO<sub>2</sub>, where we saw that, because En lies *between* L and Fo, the reaction was odd, i.e.  $L = Pr - Fo$ , or  $Fo + L = Pr$ . This is an incongruent reaction. In the ternary case, the geometry appears at first confusing, since En (Pr) lies off the line L - Fo and cannot immediately be seen to lie “between” those phases. This confusion is easily rectified by looking at the *tangent* to the field boundary L (Pr, Fo), shown in Fig. 11.4b. As mentioned on an earlier page, the fictive material being removed from the liquid, here called the

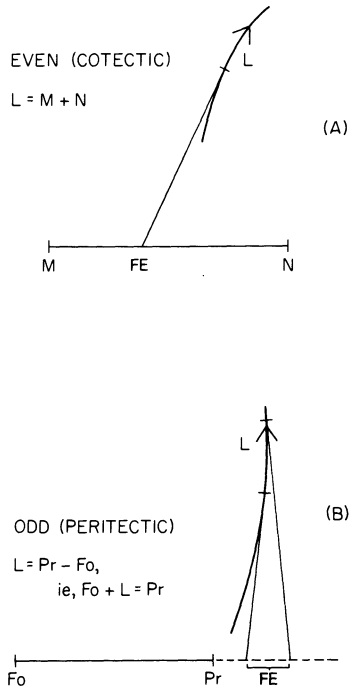


**Figure 11.4.** Criteria for odd and even reactions. A. Even reaction; the tangent to the liquid path falls between the two crystalline phases M and N. B. Odd reaction; the tangent to the liquid path falls outside the line segment connecting the two crystalline phases.

*fictive extract*, FE, must at all times lie on the tangent to the liquid path (here the field boundary). This tangent cuts the line Fo-Pr *beyond* Pr, and Pr can now be seen to lie between Fo and the FE; hence the reaction is odd, as in the binary system Fo - SiO<sub>2</sub>. It will be observed that *all* tangents to the peritectic curve L (Pr, Fo) lie outside the line segment Fo - Pr, and therefore that the curve is indeed peritectic or odd throughout its length. The ternary geometry for an even (cotectic) reaction is shown for comparison in Fig. 11.4a. In this case, the tangent to the liquid path cuts the line segment joining the phases A and B, and the FE is a positive linear combination of the two phases.

Back to Fig. 11.3. As the liquid moves toward R, crystals of Pr form at the expense of Fo + L, and the TSC moves toward Pr from Fo. Levers to the TSC path are shown at  $F_L = .38$  and  $.28$ , and the ratio of the two solid phases is given at the TSC end of these levers. This ratio is determined by applying a lever between Fo and Pr with a fulcrum at the TSC. At  $F_L = .28$ , the liquid has reached R, an isobaric invariant point. As long as the system is invariant, the liquid cannot move; the TSC now approaches R and P simultaneously, as An and Pr crystallize and Fo is consumed. Crystallization



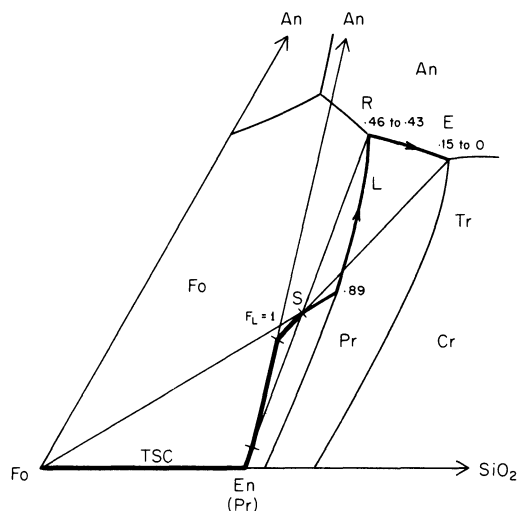


**Figure 11.6.** Equilibrium crystallization of bulk composition S.

Bulk composition T, Fig. 11.7, runs out of Fo before the liquid can get to R, i.e. at  $F_L = .68$  when the TSC equals Pr alone. No longer constrained to the peritectic curve by Fo, the liquid now moves directly away from Pr across the divariant field Pr + L, and the TSC remains at Pr from  $F_L = .68$  to  $.51$ . Now An joins the assemblage, and the TSC moves along En - An just as it did with bulk composition S. The liquid reaches E at  $F_L = .28$ , and remains there until TSC = T.

Note that failure of the olivine reaction at any stage of the process starting at P would result in fractional crystallization, giving rise to liquids Q, S, T in turn. This case is treated in detail somewhat further on.

Figure 11.8 calls attention to the limiting fields of bulk compositions whose daughter liquids do or do not reach R. All those lying to the left of the line En - R must produce liquid R; those to the right of this line (such as T) never do. Moreover, bulk compositions to the left of the line En - E must yield liquids which approach E via L (An, Pr), while those to the right of that line must approach E via L (Pr, Tr). The angles marked  $\alpha$  in the figure are the minimum angles at which isotherms in the field Pr + L may intersect the peritectic curve. These angles are defined, at any point, by the peritectic curve and the L path directly away from En, and if an isotherm were to intersect the field boundary at any smaller angle than  $\alpha$ , the temperature would have to rise with the crystallization of Pr. This is impossible, for although there are examples of so-called "retrograde melting" in the laboratory, they all involve the input of energy in some other form than thermal energy, and we have here no such case. Liquid paths such as these, constrained away from a field boundary, are occasionally useful as guides in constructing isotherms on liquidus surfaces.

For those bulk compositions whose liquids never reach R in Fig. 11.8, it

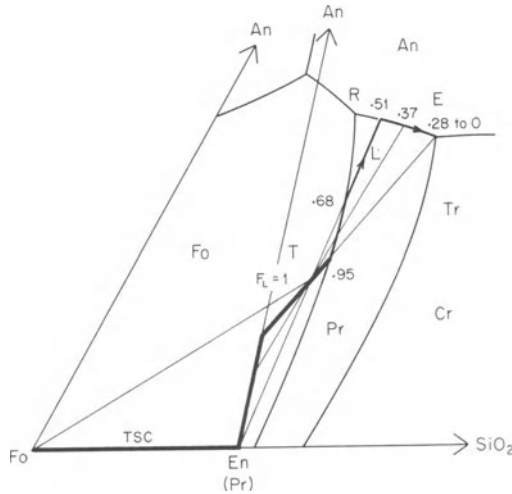


**Figure 11.7.** Equilibrium crystallization of bulk composition T.

is interesting to note the unusual fact that these liquids eventually leave the *L* (Pr, Fo) field boundary and cross the divariant field. This is, of course, due to the peritectic nature of the curve and the loss of Fo (by reaction) from the equilibrium. Only peritectic curves can allow a liquid to leave in this manner; cotectic curves have no such property, and no liquid paths can cross the Pr field except directly away from Pr itself.

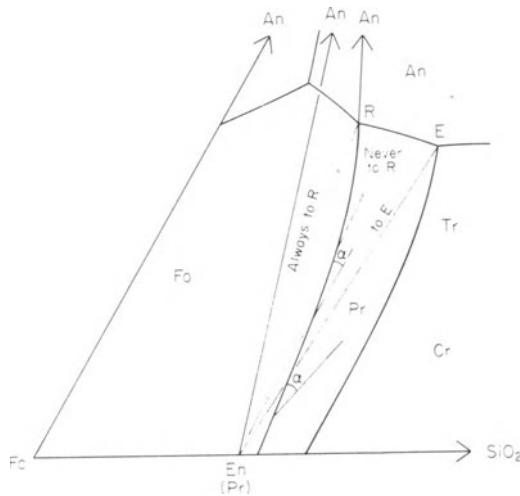


**Figure 11.8.** Delineation of regions of bulk composition whose equilibrium liquids always reach R or never reach R. The angle  $\alpha$  is the minimum angle at which an isotherm may intersect the peritectic curve.

Several other bulk compositions yield crystallization paths which are straightforward yet instructive. Two are shown in Fig. 11.9. Composition U is so located that the liquid goes directly to R, whereupon reaction occurs and the TSC moves from Fo to U by addition of An and Pr simultaneously in the proper ratio. To verify that the reaction is odd when the liquid is at R, the reader can calculate for himself that Fo is consumed during the reaction, knowing that  $F_{Fo} = .26$  when the liquid just reaches R, and calculating the final proportions of Fo, An, and Pr as done in Fig. 11.3. (Note from Fig. 11.2 that the An content of U is 40%.)

All liquids having bulk compositions to the left of UR will crystallize An before reaching the reaction point R. Those to the right of UR will behave like the P, Q, S, T group previously discussed.

Liquid W, Fig. 11.9, crystallizes Pr only until  $F_L = .68$ , when Tr joins the solids and the liquid is constrained to the cotectic. The FE, always tangent to the liquid path, forms its own path on En-SiO<sub>2</sub> as the tangent sweeps along that line. This is an even reaction, as the FE lies between the solid phases Pr and SiO<sub>2</sub>. The TSC moves toward the FE, at all times, and its path toward Tr from Pr is shown. At  $F_L = .50$ , the liquid has reached E, and is henceforth constrained there; the FE now also lies at E, and the TSC moves toward E to W.

Bulk composition X, Fig. 11.10, illustrates the case of a liquid which reaches the L (An, Fo) cotectic before it reaches point R. At  $F_L = .82$ , Fo begins to crystallize along with An, and the TSC begins to move along the line An - Fo. The liquid reaches R at  $F_L = .65$  and remains there until  $F_L = .39$ , while the TSC moves directly toward R. Now all Fo is exhausted by reaction, and the liquid moves toward E with production of An + Pr. The

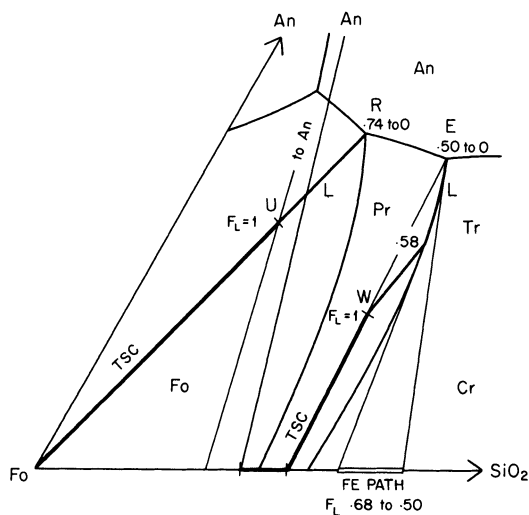


**Figure 11.9.** Equilibrium crystallization of bulk compositions U and W.

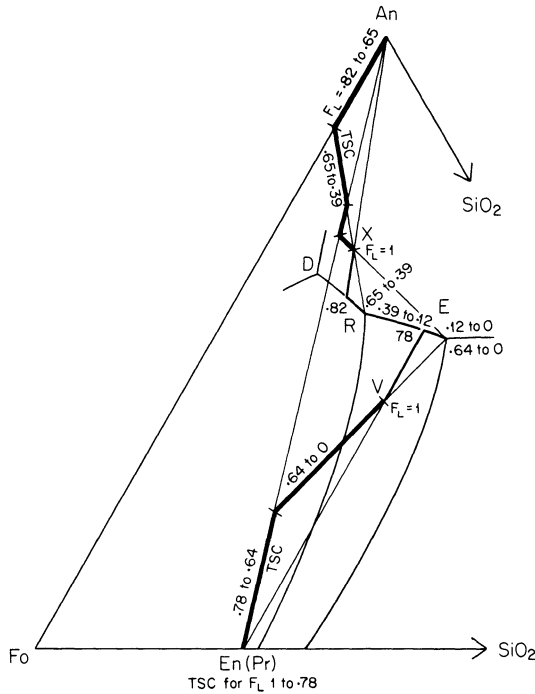


**Figure 11.10.** Equilibrium crystallization of bulk compositions V and X.

liquid reaches E at  $F_L = .12$ , and completes its crystallization there. The rock produced is a slightly oversaturated anorthositic norite, all vestiges of olivine having disappeared by reaction. A very different series of rocks results from fractional crystallization, to be described shortly.

The equilibrium crystallization of liquid V is also illustrated in Fig. 11.10, and the reader may verify for himself the liquid and TSC paths for this composition.

### Fractional Crystallization

There are important differences, both qualitative and quantitative, between fractional and equilibrium crystallization of any bulk composition whose daughter liquids involve a reaction relation. In the fractional process, no reaction is possible; all the olivine produced remains in the accumulated solids, and the liquid always reaches E. We may first examine in detail the fractional crystallization history of several familiar bulk compositions, and then comment on the differences between the cases of fractional and continuous equilibrium crystallization.

For bulk composition P, Fig. 11.11, the liquid follows the dotted path

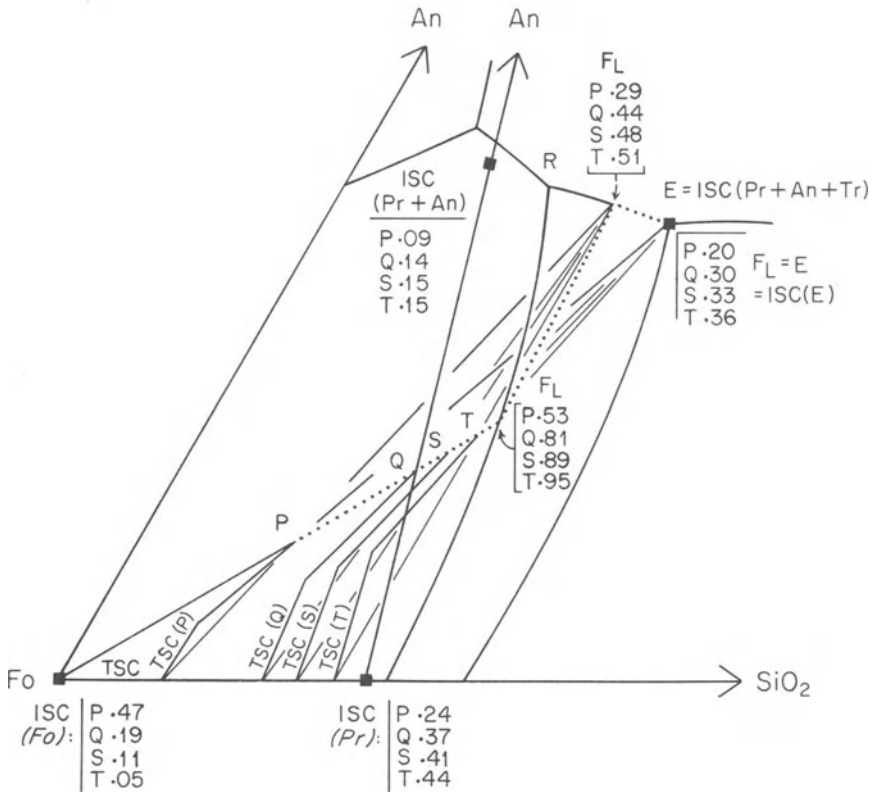


**Figure 11.11.** Fractional crystallization of bulk compositions P, Q, S, and T. The figures posted near the ISC's are the fractions of each ISC produced for each of the bulk compositions. The liquid path is dotted.

with fractional crystallization. At  $F_L = .53$ ,  $L$  reaches the field boundary with Pr, but is not constrained to the boundary because Fo is isolated from reaction. The liquid therefore moves directly away from Pr until it reaches the cotectic  $L$  (Pr, An), which it follows to E, which it reaches at  $F_L = .20$ . The four ISC's (i.e. model rocks) produced in this process are Fo, Pr, a mixture of Pr and An near the ratio 43:57, and a mixture of Pr, An, and Tr in the ratio of E. Analogous natural rocks would be dunite, bronzitite, norite, and, assuming some Na and K, quartz monzonite. The fraction produced of each of these model rocks may be calculated with the aid of the TSC path. This always runs toward the ISC, in this case from Fo toward Pr, then toward Pr and An, and then toward E. Levers applied to the TSC through P from any liquid along the fractionation path yield  $F_L$  or  $F_S$ , and the fraction represented by any given ISC is found from differences in successive values of  $F_L$  or  $F_S$ . Thus the initial ISC, Fo, amounts to 47% of the total mass, this being found directly. The next ISC, Pr, amounts to 24%, being 100 times the increment in  $F_S$  as the TSC moves directly toward

Pr. The third ISC, Pr + An, amounts to 9%, again found from the difference in  $F_S$  during the time in which the TSC moves toward this ISC. The fourth ISC, E, amounts to 20%. The fraction of each ISC formed may *not* be found by applying a lever from the ISC, but must be calculated from the differences in  $F_L$  or  $F_S$ . Values of the fraction of each ISC for each of the bulk compositions P, Q, S, and T are posted in Fig. 11.11. The same liquid path is followed for all these bulk compositions, each of which in turn quite naturally yields less Fo and more Pr, Pr + An, and E compositions. By comparison with Figs. 11.3 to 11.7, it can be seen that the amount of residual liquid E is much greater in the case of fractional crystallization, the increase being proportional to the amount used in the peritectic reaction under equilibrium conditions. It may also be seen that the model rocks (ISC's) produced in the later stages of fractional crystallization are very different from any rocks (TSC's) produced in the equilibrium process. Most noteworthy among these are the ISC's which correspond to norite and quartz monzonite in nature.

The fractional crystallization of bulk compositions U, V, W, and X is illustrated in Fig. 11.12. Again, the weight fraction of each ISC produced is posted for each bulk composition. For bulk composition U, the ISC's are

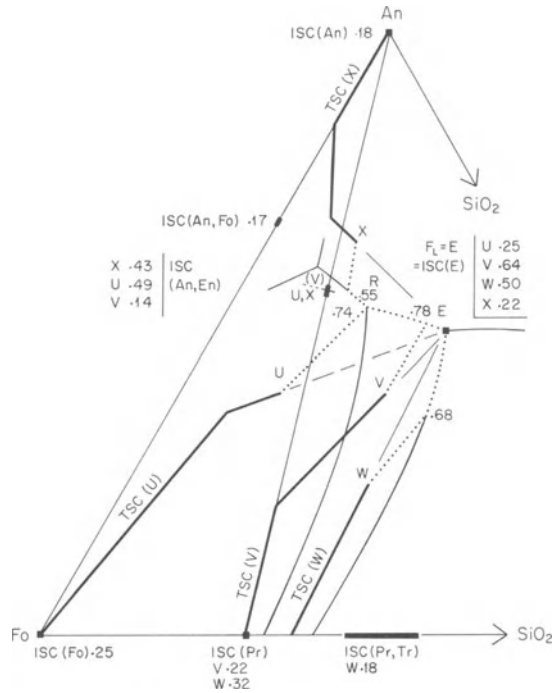


**Figure 11.12.** Fractional crystallization of bulk compositions U, V, W, and X. The liquid path is dotted.

Fo, An + Pr in the maximum range of ratios allowed by tangents to the curved path RE, and E. For V, the ISC's are Pr, Pr + An, and E. For W, the ISC's are Pr, Pr + Tr [(note the relatively large range of Pr:Tr ratios resulting from the sharper curvature of the  $L$  (Pr, Tr) cotectic), and E. For X, the ISC's are An, An + Fo (corresponding in nature to allivalite or troctolite), An + Pr, and E. All TSC paths converge toward E in their final stages, but it should be recalled that the TSC is composed of an ensemble of ISC's; no small homogeneous volume of rock has the composition of the total solids. The same TSC paths will be found in fractional fusion, discussed below, but in that case they do represent locally homogeneous compositions. Fractional crystallization of compositions U and X produces enhanced volumes of liquid E compared to the equilibrium process, as may be verified by comparison of the values of  $F_L$  posted in Fig. 11.12 with those in Figs. 11.9 and 11.10. On the other hand, no increase in the amount of liquid E results from the fractional crystallization of bulk compositions V and W, because no olivine is involved in the crystallization of these silica oversaturated bulk compositions. This emphasizes once again that it is the reaction relation of olivine which so profoundly affects the fate of liquids with fractional crystallization in this system with an incongruent-melting compound. This relation pertains only to those liquids which would reach R on equilibrium crystallization, as classified in Fig. 11.8.

The further details of fractional crystallization of bulk compositions U, V, W, and X are straightforward, and should need no elaboration beyond that to be found in Fig. 11.12.

## Equilibrium Melting

No special diagrams are needed for analysis of equilibrium melting, which proceeds as always in precise reversal of the equilibrium crystallization process. Several of the previously discussed bulk compositions should be examined to appreciate that this is so. Both the crystalline and liquid products of equilibrium fusion are identical in composition and amount to those of equilibrium crystallization, and in deep-seated environments the two processes might well yield indistinguishable products.

## Fractional Melting

When liquid is continuously removed as it is generated, the TSC always moves directly away from the liquid (ILC), either in a straight line or in a curved path, depending on whether the ILC is fixed (as it is in Fo-An-SiO<sub>2</sub>) or continuously changing (as in systems with crystalline solutions). The

paths which aid in analyzing fractional melting are those of the TSC and total liquid composition (TLC), both of which are continuous, just as they both are in fractional crystallization. The ILC, like the ISC in fractional crystallization, jumps discontinuously from one discrete composition to another (in “L hops”). Unlike the crystallization ISC, however, the ILC has no continuous motion, even locally, like that produced in the ISC of crystallization by a sweeping tangent to a curved liquid path. In the basaltic part of the system Fo-An-SiO<sub>2</sub>, there are only two ILC’s, and these are the invariant points R and E. A single detailed example of fractional melting should suffice to establish the general principles for the entire system.

Bulk composition T, Fig. 11.13, lies within the solid-phase triangle En-An-SiO<sub>2</sub>. It is composed, in the subsolidus condition, of En + An + Tr. Upon heating to 1220°C, liquid E forms at the triple junction where all three solid phases coexist. With the addition of more heat, this liquid continues to form isothermally, driving the TSC directly away from E until it reaches the An - En tie line, or in other words, until tridymite is exhausted. This occurs at  $F_L = .28$ , and we may note that so far the process is the exact reverse of equilibrium crystallization (Fig. 11.7) or for that matter, fractional crystallization (Fig. 11.11). This underscores a geologically important point, namely that so long as melting produces an invariant liquid the batch removal of a large volume of liquid is indistinguishable from the fractional or ideally continuous removal of that liquid. This is important because very small quantities of liquid, present as thin films or isolated pockets, are not likely to collect together and move out of the rock; continuous removal is unlikely in nature, but batch removal of as much as 28% melt is highly probable.

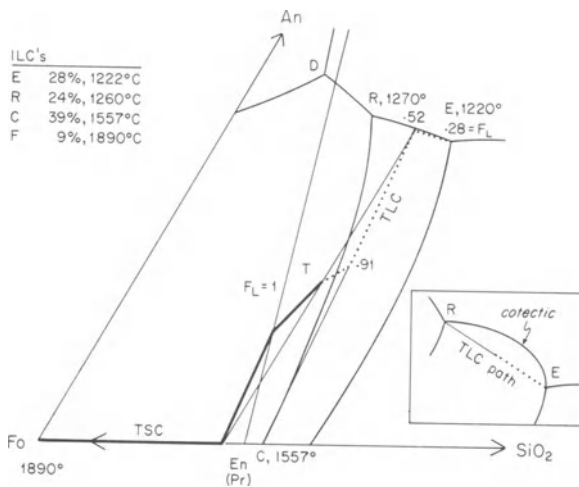


**Figure 11.13.** Fractional melting of bulk composition T. The TLC path is dotted. *Inset:* The TLC path lies on the mixing line RE, not the cotectic curve from R to E.

The TSC in our example, now being devoid of Tr and isolated from the solvent melt, will not melt further until the solidus temperature of An + En is reached, when liquid R (the second ILC) will form at 1270°C. The melting reaction is now  $An + Pr = Fo + L$ , and Fo now accrues in the TSC as melt R is formed. The reaction is completely analogous to the reverse of crystallization of bulk composition Q, Fig. 11.5, and it will continue, whether or not continuous removal is effected, until An is exhausted in the solids. By construction of a TLC path and a lever to the TSC, this event is found to occur at  $F_L = .52$ . *Note especially* (see inset to Fig. 11.13) that the TLC path is a straight mixing line between E and R, and has nothing to do with the cotectic L (Pr, An). The amount of liquid R formed is evidently  $.52 - .28 = .24$ . Again, it is to be observed that batch removal of this liquid at 1270°C would be equivalent to its continuous removal. Upon its removal, no further melting can take place until the solidus of En - Fo is reached at 1557°C, point C in Fig. 11.13. This is the peritectic point in the system Fo - SiO<sub>2</sub>, and further fractional melting is confined to this binary system. The entire family of ILC's and their amounts is summarized in Fig. 11.13; the TLC moves next on the mixing line toward point C and finally toward pure Fo, and it is used solely for applying the lever rule.

Generalizing from the analysis of bulk composition T, it is possible to construct the summary diagram of Fig. 11.14, which shows the TSC paths of representative bulk compositions throughout the basaltic region of the phase diagram. All bulk compositions to the right of the lines An - E and E - En yield liquid E alone as the ternary liquid, while all others yield some quantity of liquid R, either in addition to liquid E or alone. TSC paths and tabular comparisons of the liquid fractions E and R of fractional crystallization and fractional melting are given for selected bulk compositions in the figure. Of particular note among the tabulated values of  $F_L$  is that certain bulk compositions produce none of a given liquid by one fractional process but an appreciable quantity by the other process. Specifically, silica undersaturated solid mixtures such as P and U yield no liquid E upon melting, but liquids of such bulk compositions yield plenty of liquid E upon fractional crystallization. No liquids below a line Fo - R yield any of liquid R on fractional crystallization, but the corresponding solid mixtures (down to the limiting line En - E) do produce liquid R upon melting.

## Application to Basalts and Related Rocks

The system Fo-An-SiO<sub>2</sub> contains representatives of all three of the major minerals of basalt: plagioclase, pyroxene, and olivine. It also contains a silica mineral which would be found as quartz in nature, and demonstrates the incompatibility of magnesian olivine and quartz in the presence of liquid. The Fo-An sideline is an analogue of the critical plane of undersat-

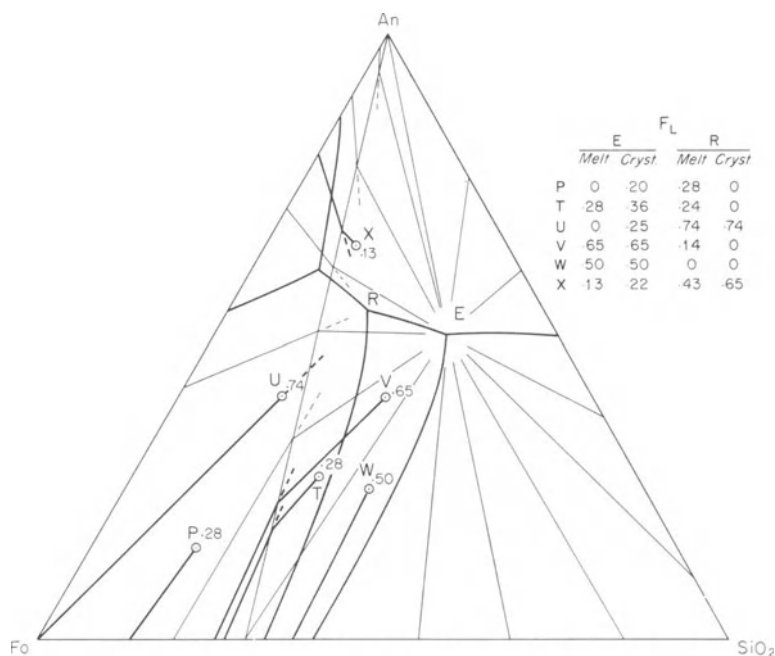


**Figure 11.14.** Fractional melting summary diagram, showing TSC paths for the entire system Fo-An-SiO<sub>2</sub>. All TSC paths are radial from E or R. The figures posted by each lettered bulk composition are the fractions of initial liquid, either E or R. The table compares fractions of liquids produced on fractional melting and fractional crystallization.

turation in the basalt tetrahedron (Fig. 2.1), and the En-An tie line is an analogue of the plane of silica saturation. By no process can liquids represented by the one atmosphere phase diagram fractionate *toward* the critical plane when Fo or Pr are crystallizing; in contrast, all liquids producing olivine will fractionate through the plane of silica saturation and reach E, a silica-rich eutectic. The principles exemplified by the phase diagram are directly pertinent to the crystallization of olivine tholeiites, norites (especially lunar norites which consist of nearly end-member An and En), hypersthene basalts, tholeiites, and quartz basalts or quartz gabbros. In particular, the reaction relation of olivine with liquids on *L* (Pr, Fo) or at R is comparable to that observed in natural olivine tholeiites, which frequently show early olivine crystals with orthopyroxene reaction rims wherever olivine occurred in close proximity to a sufficiently silica-oversaturated liquid. Preservation of olivine in such rocks, by armoring with plagioclase or reaction rims of pyroxene, is generally accompanied by a mesostasis or intersertal network of late granophyre or micropegmatite containing quartz. Thus in a single thin section, one may commonly observe the results of imperfect fractional crystallization beginning with the early removal of olivine from reaction and ending with a silica-rich residual liquid

closely modelled by the point E. On the other hand, slowly cooled rocks of suitable chemistry may be found in which all traces of early olivine have been removed by reaction under conditions approaching continuous equilibrium crystallization.

The sequence of ISC's produced on fractional crystallization is closely modelled by the successive layered cumulate zones of many strongly differentiated layered intrusions. The experimental sequence, for tholeiitic liquids plotting anywhere in the primary phase field of olivine, is Fo, Pr, Pr + An, and E, corresponding to the following zones in an idealized natural layered complex: dunite, bronzitite, norite, and granophyre. Among famous examples of tholeiitic intrusions which exhibit all or some of these zones are the Stillwater complex of Montana, the vast Bushveld igneous complex of South Africa, the Muskox intrusion of the Northwest Territories, Canada, the Great Dyke of Rhodesia, and numerous more weakly differentiated sills such as the Triassic Palisades and Dillsburg sills of New Jersey and Pennsylvania. All of these can be found described in the single convenient volume on layered intrusive igneous rocks by Wager and Brown (1968). The system Fo-An-SiO<sub>2</sub> has been used extensively by Jackson (1970) and Irvine (1970), among others, as a model for the detailed crystallization history of such complexes. (It should be noted that a drafting error apparently originating with Morey (1964) has persisted in some of these later works, with the result that an arrow incorrectly points toward R on the cotectic RE.)

The system Fo-An-SiO<sub>2</sub> is particularly appropriate to the study of anorthosite and related plutonic igneous rocks, which are composed principally of plagioclase and hypersthene, locally with lesser amounts of olivine or quartz. In the Nain complex of Labrador, for example, are several bodies showing upward gradation from olivine bearing rocks such as troctolite or leucotroctolite, through norite or leuconorite, to noritic rocks with interstitial quartz or micropegmatite. Apart from the plagioclase richness of these bodies, which may perhaps be accounted for by high pressure and the mechanical concentration of plagioclase, the major rock sequences may be readily explained in terms of the model system Fo-An-SiO<sub>2</sub>. Point Y, Fig. 11.15, represents a liquid of noritic composition consisting of about 40% En, 60% An. The fractional crystallization of such a liquid yields ISC's analogous to the following rocks: troctolite 38%, norite 50%, and quartz monzonite 12%. If a slightly quartz-normative initial composition is chosen instead, such as Y', the respective ISC percentages are 20% troctolite, 57% norite, and 23% quartz-bearing rock. Liquid R itself yields about 74% norite, 26% quartz-bearing rock, and liquid Z yields 50% each of norite and quartz-bearing rock. Now large quantities of granitic rocks ranging from diorite through granodiorite to quartz monzonite (adamellite) occur in close association with anorthosites, in the Nain complex as elsewhere in the world. If we assume that liquid E is an approximate model for quartz monzonite or granite (it contains 26% quartz, 24%

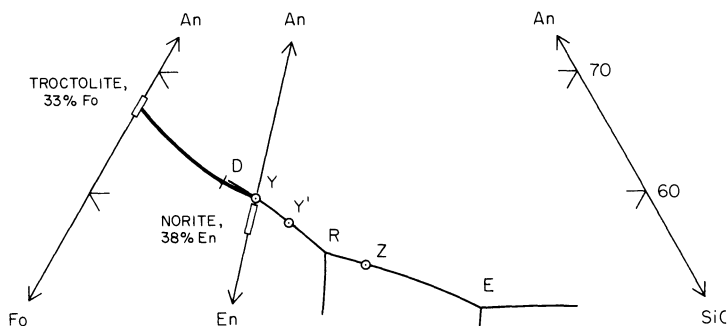


**Figure 11.15.** Portion of the system Fo-An-SiO<sub>2</sub>: location of several bulk compositions relevant to the anorthosite problem. The heavy TSC path is shown for the fractional crystallization of bulk composition Y.

orthopyroxene, and 50% plagioclase), we can see from the above exercise that only one of the bulk compositions, Z, yields a subequal volume of norite and model quartz monzonite. Therefore, if the volumes of anorthositic (noritic) and granitic rocks are subequal, as they appear to be in terms of outcrop area at Nain, and if the two rock types are to be considered cognate, a parent liquid similar to Z is required, and this is quartz dioritic in nature, with 13% normative quartz. On the other hand, liquid Z never produces any olivine, so it cannot be the parent of anorthositic rocks which are underlain by troctolites. The two bulk compositions Y and Y', saturated and slightly oversaturated respectively, both produce troctolites and smaller amounts of liquid E (12% and 23%). Each of these therefore makes a more appropriate parent magma for anorthosite, and each allows a small or moderate amount of granitic rock to be cognate, but not a subequal amount. From such a simple model one is likely to prove little or nothing about the parent magma of anorthosite, but one can gain much insight into the constraints which more elaborate experimental models might provide, and the implications of even the simple model are probably worth taking seriously.

As a final application of the system, consider the proposal of Michot (1960) that a crustal melting event produced a noritic liquid and an anorthositic residuum. The phase diagram tells us that for any quartz-normative bulk composition, the first liquid on melting will be E, with 26% quartz, hence granitic. The only other liquid produced on fractional melting will be R, perhaps a quartz norite, and the residuum will become olivine bearing as orthopyroxene is destroyed. It therefore appears that the presence of quartz in the proposed product of the partial melt, combined with the presence of olivine in the crystalline residuum, would strengthen the argument for the proposed melting event, whereas the absence of either key mineral would weaken the argument.

It is especially noteworthy that no liquid of strictly noritic (An + En only) or troctolitic (An + Fo) composition is generated by fractional melting

in this system, despite the fact that both rock types are abundantly produced by fractional crystallization of a considerable range of bulk compositions. Equilibrium melting can produce such liquids only at appreciably higher temperatures, unlikely to be reached in nature. It therefore follows that if liquids having the composition of norite occur in nature, they are most likely the products of melting in more complex systems or at higher pressures, or both. The abundance of noritic rocks both on the Earth and on the highlands of the Moon suggests that they are not so likely to be the products of a unique noritic liquid as they are to be the fractional crystallization products of a wider range of liquids having noritic affinity.

## Chapter 12

# Forsterite-Diopside-Silica: Pyroxenes and Their Reactions

### Introduction

The system Forsterite-Diopside-Silica (Fo-Di-SiO<sub>2</sub> or “FDS”) is one of the most illuminating systems in basalt petrology; it is also one of the most complex, and indeed, it is only because of the very diligent reinvestigation of the system by Kushiro (especially 1972) and his colleagues that we can now begin to appreciate the subtleties of crystallization, melting, and reaction in this system. Like Fo-An-SiO<sub>2</sub>, this system illustrates the reaction relationships of olivine and pyroxene, but in this case there are three varieties of pyroxene, all involved in reactions with olivine and to some extent with each other. These synthetic pyroxenes represent all the varieties of pyroxene occurring in silica saturated basaltic rocks (augite, pigeonite, and hypersthene), and the system now under discussion forms a foundation for understanding many of the complex relations among these pyroxenes in nature. The system at atmospheric pressure can be applied to a large variety of natural basaltic rocks, including layered intrusions as well as volcanic rocks, and at high pressures, it furnishes several interesting and relatively simple models for generating the classical spectrum of basalt magma types in the mantle.

Aside from its central importance as a model for basaltic rocks and liquids, the system Fo-Di-SiO<sub>2</sub> furnishes a very large variety of principles relating to the deduction of liquid and crystal paths and reactions in ternary phase diagrams. It will be appropriate to pursue these principles in some detail, especially toward the end of the chapter, even though some of the deductions must be tentative because of a few lingering experimental uncertainties.

## Bounding Joins

Fo-Di and Fo-SiO<sub>2</sub> were discussed in Chapters 9 and 10, respectively. The join Di-SiO<sub>2</sub> was determined by Bowen (1914) to be binary, with a eutectic between diopside and tridymite near 15 wt. % SiO<sub>2</sub>. The system was restudied by Schairer and Kushiro (1964), who found that the equilibrium among diopside, tridymite, and liquid at this point is not eutectic but univariant, because diopside crystals do not have the composition of pure CaMgSi<sub>2</sub>O<sub>6</sub>, instead containing small amounts of both Mg<sub>2</sub>SiO<sub>4</sub> and MgSiO<sub>3</sub> in solid solution. The liquid therefore lies in the general direction of CaSiO<sub>3</sub>, and the univariant curve terminates in the system CaO-MgO-SiO<sub>2</sub> at 1320°C at a eutectic involving the added phase wollastonite (CaSiO<sub>3</sub>). The same variability of diopside (i.e., Di<sub>ss</sub> as we shall henceforth call it) causes the equilibrium among liquid, Di, and Fo to be univariant; the liquid is enriched in CaO, and terminates in a ternary eutectic with the phase åkermanite (Ca<sub>2</sub>MgSi<sub>2</sub>O<sub>7</sub>) at 1357°C in the system CaO-MgO-SiO<sub>2</sub>. Neither of these excursions of liquids from the system Di-Fo-SiO<sub>2</sub> affects the relations within the system, and they can be ignored for present purposes.

## Ternary Compounds: Olivine and Pyroxenes

The only invariant, stoichiometric compounds in the system are the polymorphs of silica : tridymite and cristobalite.

Forsterite shows a small range of solid solution toward Ca<sub>2</sub>SiO<sub>4</sub> (monticellite), amounting to 1.6 wt. % of that component at its maximum, when Fo<sub>ss</sub> coexists with Di<sub>ss</sub>.

Diopside shows some solid solution toward Fo<sub>ss</sub>, as well as a large range of solid solution toward MgSiO<sub>3</sub>, analogous in nature to the augite composition range. The composition of Di<sub>ss</sub> is variable with temperature and with the nature of the coexisting phases. The composition range of Di<sub>ss</sub> found by Kushiro (1972) at 1390±2°C is shown in Fig. 12.1. This temperature is very near the liquidus point of pure diopside. The Di<sub>ss</sub> phase occupies a lens-shaped field on the Fo side of the En-Di join, and at lower temperatures this lensoid field is enlarged lengthwise toward MgSiO<sub>3</sub> and sideways so as to include the En-Di join. Although the details of Di<sub>ss</sub> composition variation are important to the interpretation of crystallization in the Di-rich part of the system, the variation toward En is the main feature to be noted for most of the discussions of this chapter.

Pyroxenes encountered along and near the join Di-En are of three types: diopside solid solution (Di<sub>ss</sub>), crystallizing in the monoclinic space group *C2/c* "iron free pigeonite" (hereafter Pig), crystallizing in the monoclinic space group *P2<sub>1</sub>/c* and the orthorhombic protoenstatite solid solution (Pr<sub>ss</sub>), which inverts on cooling to enstatite with space group *Pbca*. The *T-X* phase

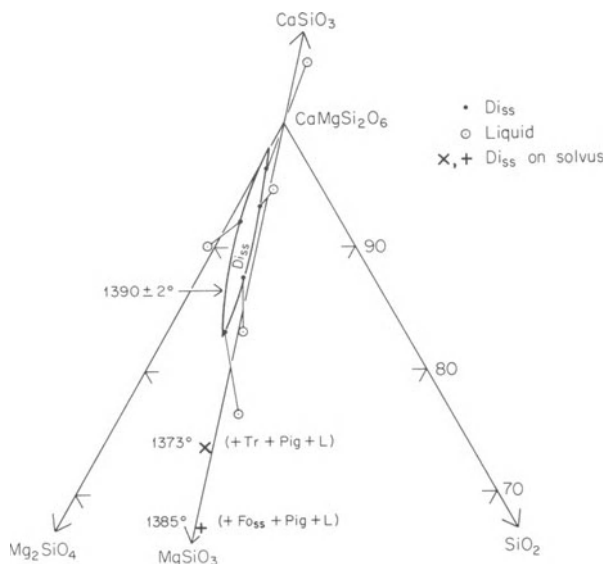


**Figure 12.1.** Composition range of diopside solid solution ( $Di_{ss}$ ) at  $1390 \pm 2^\circ\text{C}$ , after Kushiro (1972). Abbreviations:  $Fo_{ss}$ , fosterite solid solution;  $L$ , liquid;  $Pig$ , pigeonite;  $Tr$ , tridymite.

relations along the pyroxene join are shown in Fig. 12.2. This is a *pseudobinary* section, because while most of the pyroxenes lie in or near the section (on or near the join), the liquids in equilibrium with pyroxenes do not. The liquidus relations may be ignored for present purposes; they will become apparent when the full ternary system is discussed, and suffice to say for now that the liquid curves in Fig. 12.2 are merely sections through the liquidus and peritectic surfaces in the ternary system. The main point of Fig. 12.2 is to show the relations among the pyroxenes. The three shaded regions show the compositional range of homogeneous pyroxene in each of the three structural groups. The limits of mutual solubility are solid-saturation curves, or *solvi*, which were briefly mentioned in Chapter 5. A narrow solvus bounds the region of coexisting  $Pr_{ss} + Pig$ , and a much wider solvus bounds the region of coexisting  $Pig + Di_{ss}$ . For any temperature, and any bulk composition within the solvus, the compositions of the two coexisting phases are invariant. Each single-phase (shaded) region is bounded upward by a *solidus* of the usual type; that for  $Di_{ss}$  cannot be shown at this scale, so it is merged with the liquidus in the drawing. The solidus for  $Pr_{ss}$  is very steep, and indicates the very small range of  $Di$  substitution allowed by this phase. The solidus for pigeonite, combined with the liquid curve  $L$  ( $Fo, Pig$ ), amounts to a truncated melting loop analogous to a portion of the plagioclase loop. The solidus for  $Di_{ss}$  will be discussed toward the end of the chapter. Note from the diagram, Fig. 12.2, that only two pairs of pyroxenes may coexist with liquid:  $Pr_{ss} + Pig$ , or  $Pig + Di$ . The

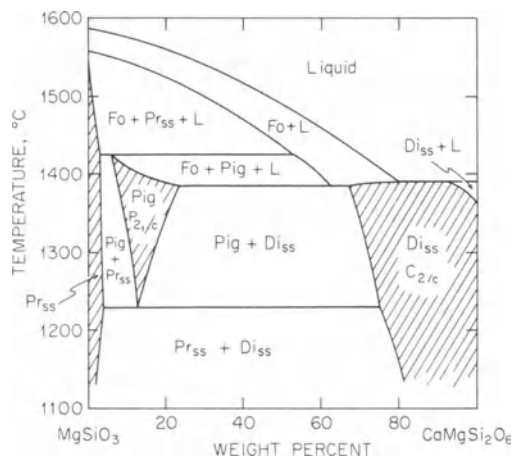


**Figure 12.2.** *T-X* diagram of the join enstatite-diopside. Shaded areas are fields of homogeneous single pyroxene; they are separated by three solvi. Liquid curves are sections through surfaces, and in general they do not represent liquids in equilibrium with these pyroxenes. The solidus and liquidus of  $Di_{ss}$  are locally merged in the diagram because of the narrow temperature interval between them. Abbreviations as in Fig. 12.1. After Kushiro (1972).

pair  $Pr_{ss} + Di$ , found in nature as enstatite (or bronzite or hypersthene) plus augite, does not occur with liquid, and here the phase diagram appears to fail us. However, it is to be noted that the pigeonite field terminates downward in temperature, and it can readily be imagined that the additional components of natural magmas could depress the temperatures of liquid-crystal equilibria below the stability of pigeonite, thus permitting equilibria among  $Pr_{ss}$ ,  $Di_{ss}$ , and  $L$ .

## The Ternary System

The system  $Fo-Di-SiO_2$  was studied by Bowen (1914), and discussed extensively in his book (1928). The two-liquid field in the silica-rich part of the system was studied by Greig (1927). Bowen correctly determined the field boundary between pyroxene and silica minerals, shown in Fig. 12.3, but did not have access to the X-ray and other methods needed to distinguish the various species of pyroxene or their solvi. He assumed from the evidence at hand a continuous series between enstatite and diopside. Modern reinvestigation of the system has extended over a period of more than ten years, beginning with the recognition of a Ca-poor pyroxene -  $Di_{ss}$  boundary by Schairer and Yoder (1962), continuing through a revision of that boundary by Kushiro and Schairer (1963), the discovery of iron free pigeonite by Kushiro and Yoder (1970), and the current revision by Kushiro

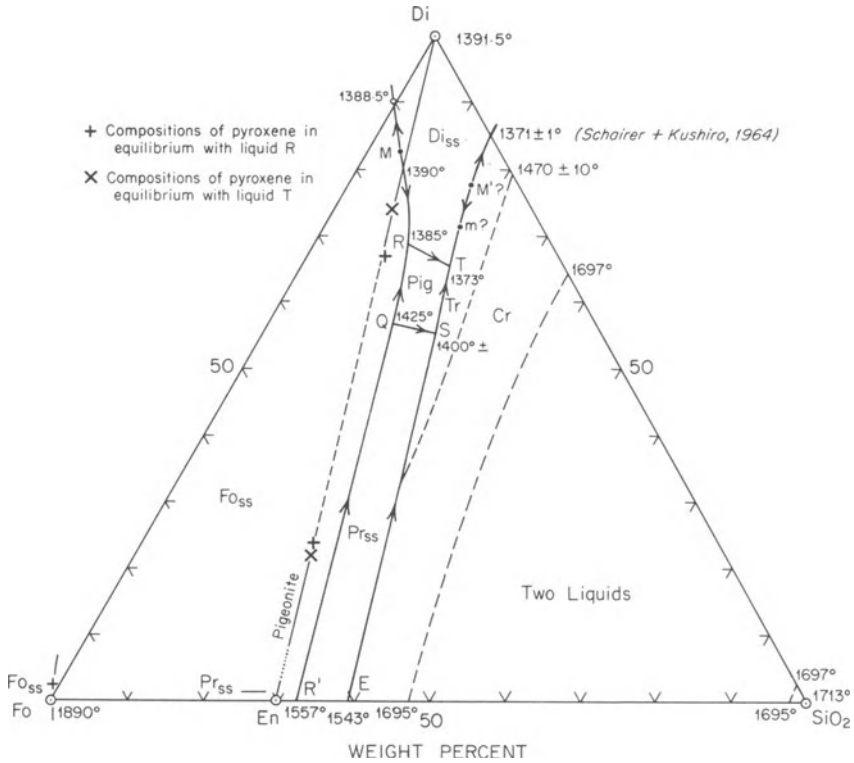


**Figure 12.3.** Phase equilibrium diagram of the system Fo-Di-SiO<sub>2</sub>, revised by Kushiro (1972) after Bowen (1914). Field of two liquids from Greig 1927). Points m and M' are added for reasons discussed toward the end of the chapter.

(1972). The latter study represents a very great advance in technique, as it is based on electron probe analysis of glass and crystal compositions, using relatively few starting mixtures and runs. This technique allows the very precise location of univariant curves and invariant points by direct analysis of the glass (“liquid”) coexisting with the solid phases observed in the run products. It also permits precise delineation of solid phase composition limits, as in Fig. 12.1, which is based on this method.

The phase diagram shown in Fig. 12.3 is adapted closely from that of Kushiro (1972). The dominant features of this simple-looking diagram are the large field of Fo<sub>ss</sub>, overlapping most of the length of the En-Di join, the univariant curves<sup>1</sup> R'QRM of liquids in equilibrium with olivine and a pyroxene, and the univariant curves ESTmM' of liquids in equilibrium with

<sup>1</sup>The plural “curves” is correct, despite the fact that the boundaries of olivine, pyroxenes, and silica mineral look continuous at the scale of the diagram. Each of these boundaries is actually composed of three segments, one for each pyroxene species, and the intersections at Q, R, S, and T must all be junctions of non-collinear curves.

pyroxene and a silica mineral. Ignoring the geologically uninteresting fields of two liquids and cristobalite, there are five primary phase fields:  $Di_{ss}$ ,  $Fo_{ss}$ , Tr, Pig, and  $Pr_{ss}$ . The pigeonite field is small, but all liquids must reach it unless the bulk composition is so restricted as to yield only  $Pr_{ss}$  or  $Di_{ss}$  with olivine or silica. All other liquids reach and then depart the Pig field on fractional crystallization.

The curve QS is a peritectic reaction curve, as we shall see, and points Q, R, S, and T are invariant reaction points, as we shall also see.

The Di-En join, constituting one edge of the plane of silica saturation in the basalt tetrahedron, separates the solid assemblages into two main groups, those with olivine and those with tridymite. A bulk composition may be expressed in the solid state in terms of one or the other of these antithetic minerals, plus one of the following five pyroxenes or pyroxene pairs:  $Di_{ss}$  alone,  $Di_{ss} + Pig$ , Pig alone, Pig +  $Pr_{ss}$ , or  $Pr_{ss}$  alone. There are thus ten possible multiphase solid assemblages, plus three coincidental single phase assemblages,  $Di_{ss}$  or Pig or  $Pr_{ss}$ .

The points labelled M and M' in the diagram are liquidus *maxima*, and the point labelled m is a liquidus *minimum*. These will be discussed toward the end of the chapter.<sup>2</sup>

## Equilibrium Crystallization

We shall consider only those bulk compositions in the primary phase field of  $Fo_{ss}$ . The analysis will in every case require knowledge of the tie lines between pyroxene solid solutions and liquids, just as in the case of plagioclase plus liquid in Di-An-Ab. In the present case, the solid solutions fall within the ternary system, rather than along one edge, but the principles are the same. The solid solutions are of limited range, however, and certain special compositions are known to occur with certain invariant liquids, so it is a simple matter to find a set of pyroxene-liquid tie lines which must be sufficiently close to the actual ones, even though these have not been determined in detail experimentally.

It is convenient to work with a distorted cartoon of the actual system, so that graphical relations can be displayed and analyzed with clarity. Such a "toy" system is shown in Fig. 12.4; although the distortion is gross, the essential relationships of the actual system have been preserved. The labels

<sup>2</sup>Points m and M' were deduced by Prof. Peter Robinson, to whom I am grateful, from the work of Kushiro (1972). The arguments used later in the chapter in support of these points are based on Kushiro's data and on geological occurrences, which suggest that residual liquids do not leave the system as they would if M' were absent. The analysis is disputed (in private, at the risk of a case of beer) by one noted authority, but direct evidence for the existence of m and M' is provided by the work of Schairer and Yoder (1962, Fig. 19). The treatment in this chapter is probably overcautious.

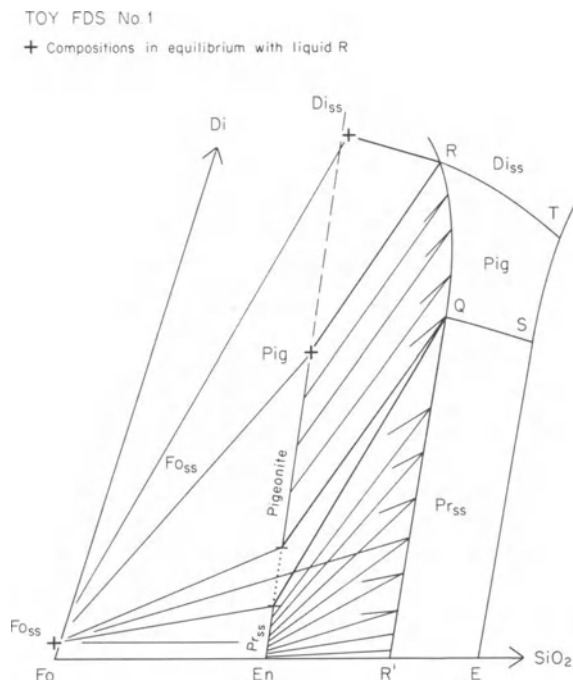


**Figure 12.4.** Tie line template; slopes of pyroxene-liquid tie lines in a distorted (toy) sketch of the FDS system. Heavy tie lines are experimentally established, lighter ones are interpolated.

of primary phase fields tell us that liquid Q coexists with crystals of  $Fo_{ss}$ ,  $Pr_{ss}$ , and Pig. At the same time, the dotted gap signifies the miscibility gap (see Fig. 12.2) of pigeonite and protoenstatite solid solution, and we know that when these two crystalline phases coexist, they are mutually saturated. Liquid Q therefore lies at the corner of a three-phase triangle Q-Pig- $Pr_{ss}$ , and two legs of this triangle establish the tie line slopes Q-Pig and Q- $Pr_{ss}$ . At the other limit of  $Pr_{ss}$  compositions, the tie line must be En-R', on the binary join Fo-SiO<sub>2</sub>. It is sufficient for any purpose to assume that all the other  $Pr_{ss}$ -liquid tie lines are evenly distributed between the limiting ones En-R' and  $Pr_{ss}$  (Pig) - Q. (As usual, the phase in parentheses denotes saturation of the preceding phase with the component bracketed.)

By a similar analysis, the tie lines between pigeonite solid solutions and L (Pig,  $Fo_{ss}$ ) may be established within reasonable limits. Kushiro (1972) has located the compositions of Pig and  $Di_{ss}$  in equilibrium with liquid R and with each other, by direct electron probe analysis. These solvus compositions are indicated by plus signs on Fig. 12.4. We therefore have two known pigeonite-liquid tie lines, i.e., R-Pig( $Di_{ss}$ ) and Q-Pig( $Pr_{ss}$ ). These happen to be nearly parallel in the actual system (Fig. 12.3), and are drawn so in Fig. 12.4. The intermediate L-Pig tie lines are interpolated.

The entire suite of tie lines shown in Fig. 12.4 is valid only for liquids

saturated with  $\text{Fo}_{\text{ss}}$ . For liquids saturated with  $\text{SiO}_2$ , a similar analysis can be performed using, instead, points S and T, and the curve EST. Figure 12.5 shows the results of such an analysis, assuming little change in the width of the  $\text{Pr}_{\text{ss}}$ -Pig solvus but a known and significant widening of the Pig- $\text{Di}_{\text{ss}}$  solvus with falling temperature; again, Fig. 12.2 will aid in visualizing the solvus relationships. All liquids along QS lie at the apex of three-phase triangles  $L$ - $\text{Pr}_{\text{ss}}$ -Pig, so the liquid-pyroxene tie lines must flatten as liquids move from saturation with  $\text{Fo}_{\text{ss}}$  to saturation with  $\text{SiO}_2$ . By use of Figs. 12.4 and 12.5, any desired tie line between pyroxenes and liquid can be deduced, and we shall have frequent recourse to these figures as templates for tie line slopes.

We may begin the analysis of crystallization with bulk composition 1, Fig. 12.6, plotted on a second toy system, somewhat less distorted than the first. The liquid occurs in the primary phase field of  $\text{Fo}_{\text{ss}}$ , and initially moves directly away from  $\text{Fo}_{\text{ss}}$  while olivine crystallizes.<sup>3</sup> The liquid reaches the Pig field boundary at  $F_L = ".64"$  (quotation marks because the diagram is

<sup>3</sup>In fact, the composition of  $\text{Fo}_{\text{ss}}$  plotted is that in equilibrium with liquid R. Slightly "purer" (less-Ca-rich) compositions occur with liquids unsaturated with  $\text{Di}_{\text{ss}}$ , and the crystal composition reaches pure Fo for liquid R'. For graphical convenience, we shall assume the plotted composition of  $\text{Fo}_{\text{ss}}$  to be invariant, although in fact there must be a small composition change with falling temperature, and the actual liquid path across the  $\text{Fo}_{\text{ss}}$  field would be concave downward.

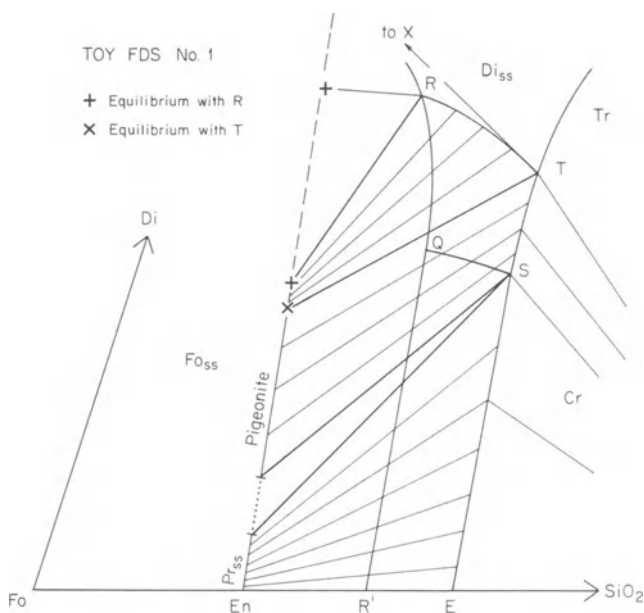


**Figure 12.5.** Another tie line template; slopes of tie lines from pyroxene to silica-saturated liquids. Conventions as in Fig. 12.4.

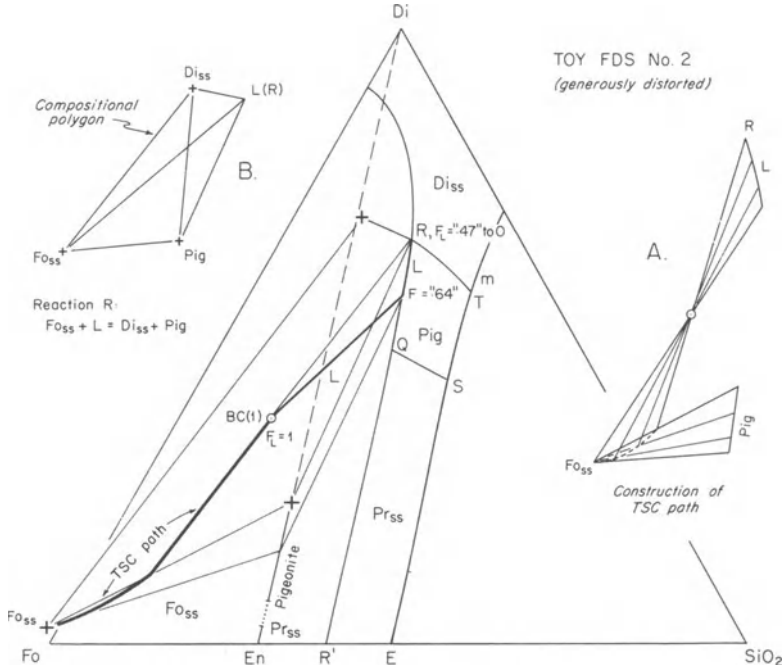


**Figure 12.6.** Toy FDS diagram No. 2, with equilibrium liquid and TSC paths for bulk composition 1. Insets: A, construction of TSC path (dashed) from  $Fo$ - $Pig$  tie lines and solid-liquid levers; B, analysis of reaction of liquid  $R$ . Quotation marks appear around values of  $F_L$  because the diagram is distorted.

distorted), and now  $Pig$ , of composition to be determined by reference to a tie-line template like that of Fig. 12.4, begins to crystallize. The TSC now moves from  $Fo_{ss}$  toward  $Pig$ , as shown in inset A, as the liquid moves toward  $R$ . The reaction is evidently odd,  $L = Pig - Fo_{ss}$ , because the tangent to the liquid path lies on the extension of the tie line  $Fo_{ss}$ - $Pig$ ; the liquid path is therefore peritectic. The isobaric variance,  $W_p$ , is 1. When  $L$  reaches  $R$ , the phases are four ( $Di_{ss}$ ,  $Fo_{ss}$ ,  $Pig$ ,  $L$ ), and  $W_p = 0$ ; the fictive extract therefore lies at  $R$ , and the TSC moves directly toward  $R$  until it reaches the bulk composition. We are left with crystals of olivine (partly resorbed and reacted to pigeonite), pigeonite, and diopside solid solution, the latter tending to fill spaces between aggregates of olivine and pigeonite. The reaction at  $R$  must be odd, as shown in inset B. This “chemographic” diagram shows the relative positions of four phases participating in an equilibrium reaction. There is no way for the liquid to produce positive quantities of all three solid phases simultaneously, because it lies outside the composition triangle formed by those three phases, and cannot move away from them. The liquid must therefore produce a negative quantity of one phase, i.e., it must react with one of them, and the phase with which it reacts must lie across the tie line joining the other two phases, i.e., it

must be  $Fo_{ss}$ . The analysis boils down to finding which two tie lines cross, and writing the reaction in terms of the crossing tie lines:  $Fo_{ss} + L = Di_{ss} + Pig$ . If a bulk composition lay exactly on the  $Di_{ss} + Pig$  tie line, the end result would be  $Di_{ss} + Pig$ , with no excess of either  $L$  or  $Fo_{ss}$ . If the bulk composition lies to either side of that tie line, there will be a final excess of the phase toward which it lies, in this case  $Fo_{ss}$ . This type of chemographic analysis of reactions finds extensive use in the development of phase diagrams with variable pressure, where the location and identity of reactions in  $P-T-X$  space can be deduced purely from a knowledge of the compositions of all the phases. We shall not dwell upon the matter here, but it is appropriate to introduce such chemographic principles at this point, with a view to their further use later on.

For further analysis, it is convenient to choose a group of bulk compositions, labelled 2 through 6 in Fig. 12.7. These are plotted on toy FDS No. 1, which will be used, along with the tie line templates (Figs. 12.4 and 12.5) in the succeeding analyses. The solid phase assemblage of each bulk composition is listed in Fig. 12.7. It will be seen that only one, No. 2, contains olivine, and that the rest contain tridymite, which means that liquids must reach the  $SiO_2$  field boundary EST. The final TSC's for these latter compositions must lie on pyroxene-silica tie lines, as shown.

The crystallization of BC 2 is shown in Fig. 12.8. It is similar to the case of BC 1, except that  $Pr_{ss}$  is produced before  $Pig$ . The liquid moves away

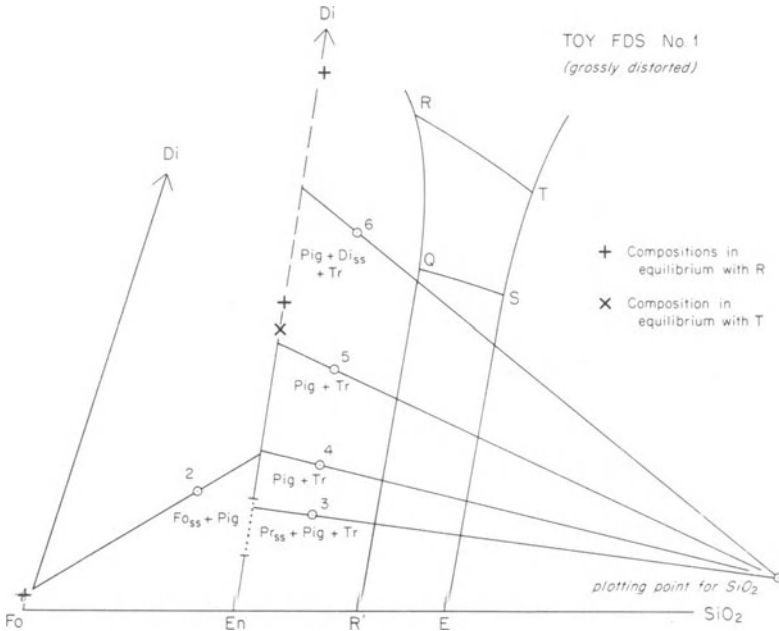
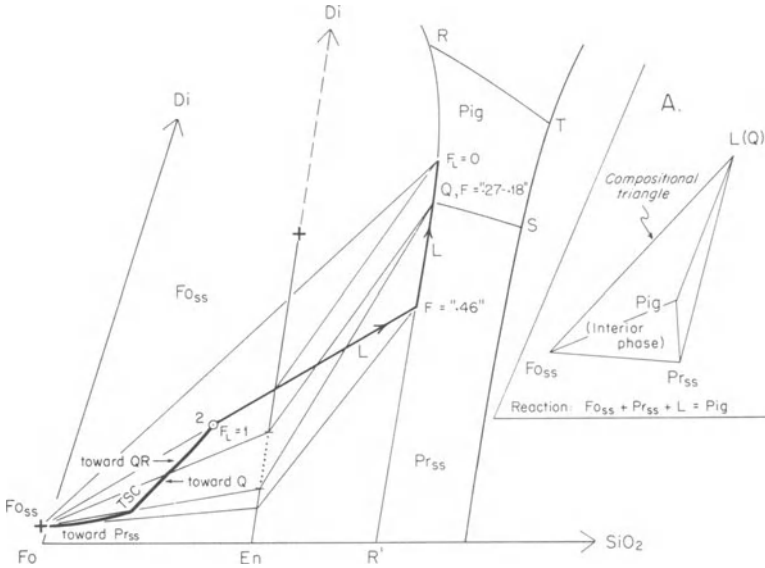


Figure 12.7. Location of bulk compositions 2–6 in toy FDS No. 1.



**Figure 12.8.** Equilibrium crystallization, BC (2). Inset A: analysis of reaction of liquid Q.

from  $Fo_{ss}$ , and when it reaches the field boundary with  $Pr_{ss}$ , the TSC begins to move toward  $Pr_{ss}$  from  $Fo_{ss}$ . The composition of  $Pr_{ss}$  is taken from the tie line template of Fig. 12.4. The tangent to the  $L$  path lies on the extension of the tie lines  $Fo_{ss} - Pr_{ss}$ , so the reaction is odd, i.e.  $L = Pr_{ss} - Fo_{ss}$ , as in the binary system  $Fo - SiO_2$ . Evidently, recalling BC 1, the entire boundary  $R'QR$  is peritectic. When the liquid reaches  $Q$ ,  $Pr_{ss}$  contains a maximum of  $Di$  component (it lies on the solvus with  $Pig$ ), and no further enrichment of  $L$  in  $Di$  can take place as long as  $Pr_{ss}$  remains in the TSC. The liquid therefore pauses at  $Q$  ( $W_p = 0$ ), while a reaction takes place among the four phases  $Fo_{ss}$ ,  $Pr_{ss}$ ,  $Pig$ , and  $L$ . The chemographic relations of this reaction are shown in inset A. Pigeonite is an interior phase within the compositional triangle  $L - Fo_{ss} - Pr_{ss}$ . There are no crossing tie lines in this case. The only chemical reaction which can be written is one in which  $Pig$  is created or destroyed from the three corner phases, in this case created with falling temperature. The chemographic relations indicate that  $L$ ,  $Fo_{ss}$ , and  $Pr_{ss}$  are *all three* consumed in the production of  $Pig$ . The reaction is odd, and may be written  $L = Pig - Fo_{ss} - Pr_{ss}$ , or rearranged as in inset A of the figure. During the time of this reaction, the FE lies with the liquid at  $Q$ , and the TSC must move directly toward  $Q$ , by accruing  $Pig$  at the expense of  $Pr_{ss}$ . When all  $Pr_{ss}$  is used up, the system returns to an isobaric variance of one, and the liquid now continues along the boundary  $QR$ , producing pigeonite at the expense of  $Fo_{ss} + L$ . During this time, the tie lines  $Pig - L$  may be inferred from Fig. 12.4, and the TSC path is slightly curved (concave upward) as the composition of  $Pig$  changes slightly. The position of the final

liquid along QR is found from the tie line template, knowing that the final composition of Pig must lie on a line from  $F_{O_{ss}}$  through the BC. This course of crystallization illustrates that both  $Pr_{ss}$  and Pig have a reaction relation to olivine, and that an invariant condition occurs temporarily at the reaction point Q, while  $Pr_{ss}$  is in effect converted to Pig.

Bulk composition 3, Fig. 12.9, is the first of our silica-oversaturated examples. In the solid state, it consists of  $Pr_{ss} + Pig + Tr$ , and these products must be kept in mind during the analysis. We may note right away that only the invariant liquid S is in equilibrium with all three of these solid phases, so evidently the final liquid will be of composition S. The final pyroxenes will consist largely of Pig, with a small amount of  $Pr_{ss}$ , as indicated by the pyroxene end of the solid-solid leg of the final three-phase triangle.

The liquid first crystallizes  $F_{O_{ss}}$ , and then reaches the  $Pr_{ss}$  boundary. The tie line template, Fig. 12.4, is used to determine the initial composition of  $Pr_{ss}$ . The liquid moves in univariance along the boundary toward Q, but does not reach Q because the TSC reaches  $Pr_{ss}$  at  $F_L = ".49,"$  when a tie line to  $Pr_{ss}$  from L passes through the BC. At this moment, all  $F_{O_{ss}}$  has been used up by reaction. The liquid now moves in divariance across the  $Pr_{ss}$  field, continually tied to varying  $Pr_{ss}$  through the BC. The path of the liquid across the field is determined by first finding its goal on ES. This is found by seeking a tie line on the template, Fig. 12.5, which passes through BC (3) to  $Pr_{ss}$  from liquids on the silica-saturated boundary ES. This is the initial tie line of liquid in equilibrium with a silica mineral, L ( $Pr_{ss}$ , Tr), and the final one of the equilibrium L ( $Pr_{ss}$ ). The liquid compositions at  $F_L =$

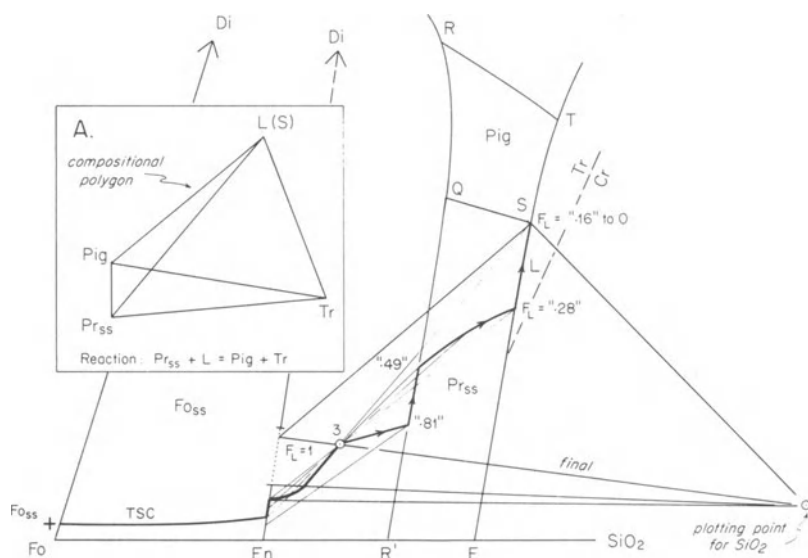


**Figure 12.9.** Equilibrium crystallization, BC (3). Inset A: analysis of reaction of liquid S.

“.49” and  $F_L = “.28”$  may thus be found rigorously, and a slightly curved path connecting them represents the equilibrium liquid path. (Rigorous construction of this path would first require construction of the fractionation paths from  $Pr_{ss}$ , but both these and the equilibrium paths are so nearly straight that a rigorous treatment would be a waste of effort.) As the liquid follows this path, the TSC moves along the  $Pr_{ss}$  composition line. At  $F_L = “.28”$ , Tr begins to crystallize, and the liquid is confined in univariance to the boundary  $L$  ( $Pr_{ss}$ , Tr). The TSC moves in a curved path along the solid-solid legs of a series of three-phase triangles, the initial and final legs of which are shown in the figure. The tangent to the liquid path cuts the  $Pr_{ss}$  - Tr tie lines, and the reaction is even, i.e.,  $L = Pr_{ss} + Tr$ . At S, the liquid begins to produce Pig, the composition of  $Pr_{ss}$  having reached saturation in diopside component, and the liquid remains at S and at invariance until crystallization is completed. The final TSC path approaches S directly until it reaches the bulk composition. The reaction of liquid S is odd, as may be determined in inset A: S lies exterior to the triangle  $Pr_{ss}$  - Pig - Tr; the tie lines  $L - Pr_{ss}$  and Pig - Tr cross, and the reaction requires subtraction of  $Pr_{ss}$  to yield Pig + Tr. From the analysis, it is clear that the boundary curve ES is cotectic, but that the point S is peritectic.

Bulk composition 4, Fig. 12.10, consists of Pig + Tr in the solid state. The initial stages of crystallization are like those of BC 3, just discussed; the TSC moves from  $Fo_{ss}$  to  $Pr_{ss}$  while the liquid follows the peritectic boundary from  $F_L = “.81”$  to “.48.” At  $F_L = “.48”$ ,  $Fo_{ss}$  is exhausted,

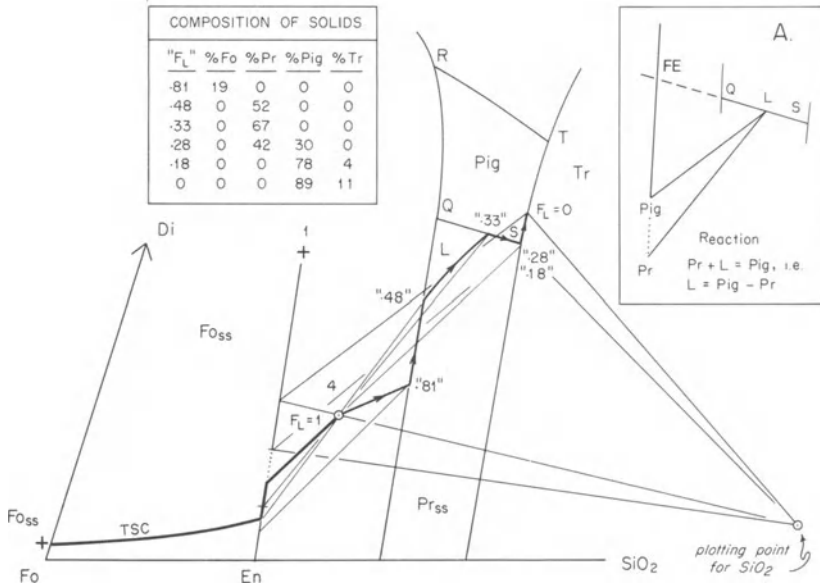


**Figure 12.10.** Equilibrium crystallization, BC (4). Inset A: analysis of reaction of liquid on QS.

and the liquid moves across the  $Pr_{ss}$  field to a point on QS to be determined with the aid of Figs. 12.4 and 12.5 together. This point is the apex of a three-phase triangle  $Pr_{ss}$  - Pig - L. The liquid now follows QS in univariance, while the TSC moves across the gap toward Pig by virtue of accruing Pig crystals at the expense of Pr crystals. Inset A shows that the reaction is odd along this curve, as the tangent to QS cuts the extension of Pr - Pig. The ratio of Pig to  $Pr_{ss}$  increases as the liquid approaches and reaches S; the liquid now sits at S while the remaining crystals of  $Pr_{ss}$  are consumed, and the TSC moves straight toward S. The reaction is the same as illustrated in inset A, Fig. 12.9, namely  $Pr_{ss} + L = Pig + Tr$ . When the TSC reaches the limiting, En-saturated Pig - Tr tie line, all  $Pr_{ss}$  has been exhausted by reaction, and the liquid is free to move in univariance along ST, producing only Pig + Tr in an even reaction. The TSC moves on a succession of Pig - Tr legs, always tied to L through BC, along a slightly curved path until it reaches BC. The final L - Pig tie line is found from the template, Fig. 12.5, using the final Tr - Pig leg to find the intercept on Pig. The table posted on Fig. 12.10 shows the evolution of the TSC from pure  $Fo_{ss}$  to Pig + Tr. Of special note is the massive destruction of  $Pr_{ss}$  while the liquid sits at S, from 42% Pr at  $F_L = ".28"$  to 0% Pr at  $F_L = ".18."$  During this process, Pig rises from 30% to 78%, as the fraction of solids rises from .72 to .82. Very little Tr (4%) is formed during this reaction.

Bulk composition No. 5, Fig. 12.11, also consists of Pig + Tr in the solid state, but the liquid path avoids QS altogether. (After some consideration of Figs. 12.4 and 12.11, it may be seen that this is so because BC 5 lies

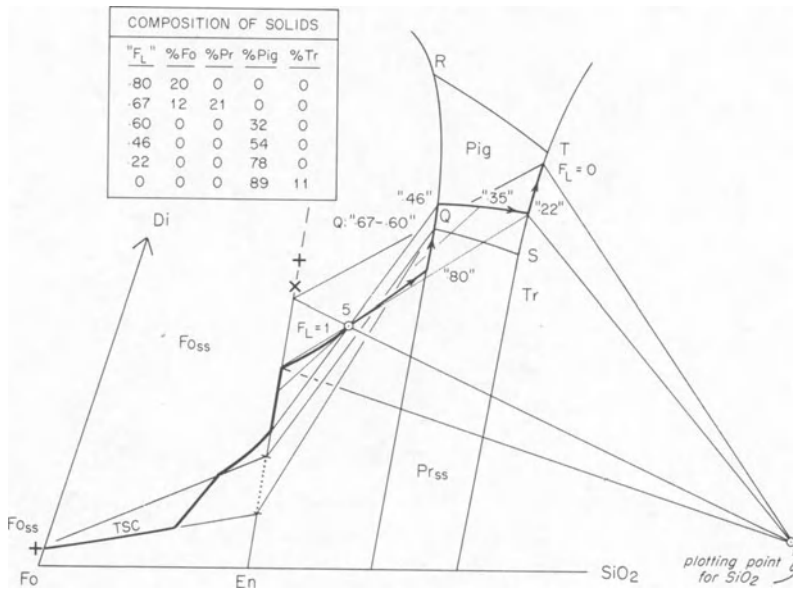
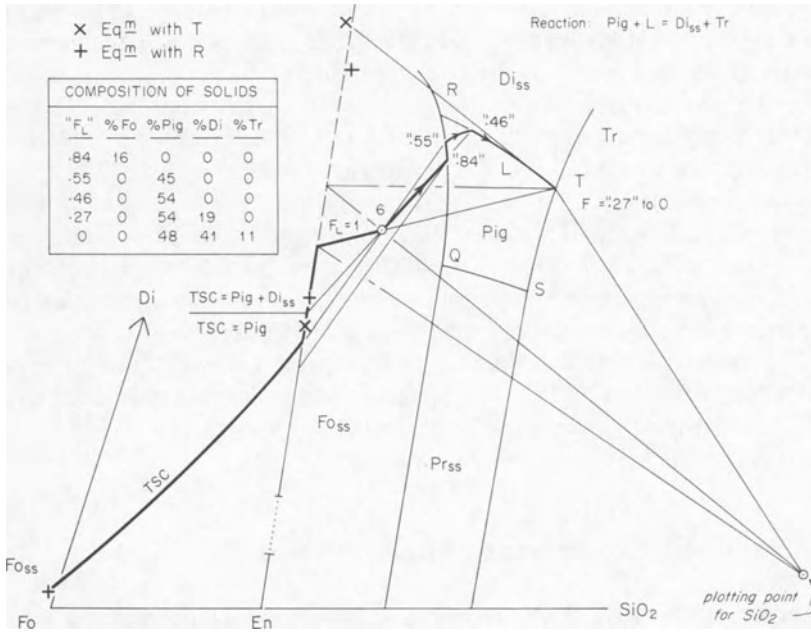


Figure 12.11. Equilibrium crystallization, BC (5).



**Figure 12.12.** Equilibrium crystallization, BC (6).

above the tie line Q - Pig (Pr), whereas BC 4 lies below that tie line. Liquids in the small triangle Q - Pr<sub>ss</sub> - Pig (Fig. 12.4) always reach Q; those below Q - Pr (Pig) reach QS between Q and S, and those above Q - Pig (Pr) reach some point along QR, avoiding QS). The liquid produces Fo<sub>ss</sub> and then Pr<sub>ss</sub> until it reaches Q. The TSC now moves directly toward Q, until all Pr<sub>ss</sub> is exhausted by reaction. Fo<sub>ss</sub> still remains, as shown by the lever Q - BC, so the liquid now moves along QR, in the reaction  $L + Fo_{ss} = Pig$ . At  $F_L = ".46,"$  Fo<sub>ss</sub> is exhausted and the L - Pig tie line cuts BC. The liquid now moves in isobaric divariance across the Pig field, to a point on ST determined by use of Fig. 12.5. Now Tr joins Pig in the solids, and the TSC moves off the Pig composition line, in a curved path along successive Pig - Tr legs to the BC. The final L - Pig tie line is found from Fig. 12.5. The table posted on Fig. 12.11 summarizes the history of the TSC.

Bulk composition 6, Fig. 12.12, lies in the solid field of Di<sub>ss</sub> + Pig + Tr. The liquid crystallizes Fo<sub>ss</sub> until  $F_L = ".84,"$  at which time pigeonite begins to form. The TSC now moves toward Pig, which it reaches at  $F_L = ".55"$  upon the destruction of all Fo<sub>ss</sub>. The liquid now leaves the peritectic L (Fo<sub>ss</sub>, Pig) and moves across the Pig field. The composition of Pig is still variable, and it reaches a point between the + and the X on the diagram just as the liquid reaches the Di<sub>ss</sub> boundary. The two special pigeonite compositions indicated by these marks are the Di-saturated compositions on the solvus for liquids at R and T, respectively. Liquids along RT are in equilibrium with Pig and Di<sub>ss</sub> compositions between these pairs of marks in their

respective composition regions. The liquid moves along RT, crystallizing mutually saturated Pig and  $Di_{ss}$ , while the TSC moves toward Di across the solvus. Note that the TSC is a two-phase mixture, and that no single pyroxene phase occurs within the solvus. The reaction along RT is even, but we reserve the proof of this until later, when it can be shown more clearly with another drawing. The liquid reaches T at  $F_L = “.27”$ ; here, the reaction is clearly odd,  $Pig + L = Di_{ss} + Tr$ , because T lies exterior to the triangle  $Di_{ss} - Tr - Pig$ . This invariant, four-phase equilibrium continues, as the TSC approaches T directly, until the latter reaches the BC. The table of TSC's shows complete destruction of  $Fo_{ss}$  and partial destruction of Pig by peritectic reactions. (Note that the gain of Pig between  $F_L = “.46”$  and “.27” is almost zero.) The final crystalline products will be larger crystals of Pig, partly rimmed by  $Di_{ss}$ , and somewhat finer-grained interstitial masses of  $Di_{ss} + Tr$  (quartz at room temperature).

## Summary of Equilibrium Crystallization

The liquid paths of BC's 1 to 6 have from two to five legs, and it is evident that equilibrium crystallization may be a highly complex process in this system. Olivine is partly or wholly destroyed by reaction along the peritectic curve R'QR, and  $Pr_{ss}$  may also be destroyed by reaction along QS. The determination of whether reactions are odd or even may be made with the aid of compositional polygons or triangles—so-called chemographic diagrams—which simplify the writing of chemical reactions. The TSC paths in equilibrium crystallization are straight toward any invariant liquid, curved when they represent a mixture of two or more solid phases, and straight along the pyroxene join when the TSC consists of pyroxenes.

## Fractional Crystallization

A few detailed examples will suffice to illustrate the principles of fractional crystallization in Fo-Di-SiO<sub>2</sub>. Bulk composition 1 is illustrated in Fig. 12.13. The liquid moves away from  $Fo_{ss}$ , then away from Pig across the Pig field along a very slightly curved path until it reaches the  $Di_{ss}$  boundary RT. The liquid is constrained to this cotectic curve by crystallization of  $Di_{ss} + Pig$ , the latter in insignificant amounts. When the liquid reaches T, reaction is prevented by fractionation, and the liquid continues along the cotectic Tm, on which, with the crystallization of  $Di_{ss}$  and Tr, it moves to the *minimum* m, where crystallization is completed. More will be said later about the crystallization of  $Di_{ss}$ , and the properties of the postulated minimum m, but suffice it to say for now that if such a minimum does indeed exist, it must

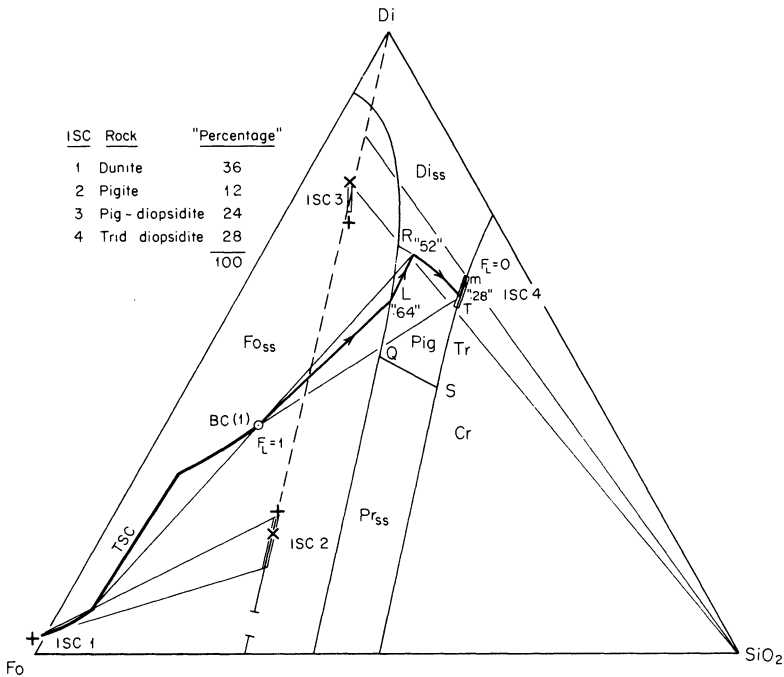


**Figure 12.13.** Fractional crystallization, BC (1). Abbreviation: ISC, instantaneous solid composition.

be the goal of all liquids in the basaltic part of the system with fractional crystallization. Note that the liquid, in this example, is constrained to only two field boundaries ( $Di_{ss}$  - Pig and  $Di_{ss}$  - Tr), and passes quickly through invariant point T, finally reaching m, which is said to be *invariant by restriction* because it lies on a line between a special composition of  $Di_{ss}$  and  $SiO_2$ . For this equilibrium, the system can be described in terms of these two components alone, and  $W_p = 0$  when  $\phi = 2 + 1 = 3$ . The ISC's produced during the fractional crystallization process are of special interest, as these are models of the rocks which would be produced by such a process in nature. The ISC's and their approximate amounts are posted in Fig. 12.13 (the distortion of the diagram accounts for the approximate nature of the figures). ISC 1 is  $Fo_{ss}$ ; ISC 2 is Pig, of a composition range which can be determined from the tie line boundaries, Figs. 12.4 and 12.5; ISC 3 is  $Di_{ss}$  with a minor amount of Pig, and ISC 4 is a mixture of  $Di_{ss}$  and Tr which lies on the tangent to the liquid path Tm. Of course all other ISC's also lie on tangents to their respective L paths. The amount of each ISC produced is found by applying the lever rule to the TSC at each major stage of crystallization. The TSC path, in turn, follows successive tangents to ISC's, and is terminated at any stage by a lever through BC from L. Such a termination is shown for  $F_L = .52$ , where the TSC has just stopped moving toward Pig from  $Fo_{ss}$ . Another such termination is shown

at  $F_L = “.28,”$  where the TSC has just stopped moving toward  $Di_{ss}$  and has begun to move toward ISC 4. The model rocks produced during fractional crystallization are tabulated in the figure; the natural version of “pigite” would probably be orthopyroxenite of the so-called “Stillwater type”, i.e. inverted pigeonite with fat exsolution lamellae of augite in the former basal planes of pigeonite. The natural version of diopsidite might be described as clinopyroxenite. One would not expect to find a quartz-augite rock corresponding to “tridymite diopsidite”, for by this stage of a fractional crystallization process, other components of natural magmas would become major, and one would expect to find abundant feldspars, and iron-enriched mafic minerals. Such a final-stage rock might well be a hedenbergite (or ferroaugite) quartz monzonite, and we can assume that rocks and liquids along Tm are oversimplified models of rocks having the general character of granitic rocks.

A very different suite of ISC's results from the fractional crystallization of BC 2, Fig. 12.14, a reasonably close model of an ultramafic magma rich in olivine and undersaturated with respect to silica. The liquid moves, as always, away from the ISC's, which are, in turn,  $Fo_{ss}$ ,  $Pr_{ss}$ , Pig, Pig + Tr, and  $Di_{ss} + Tr$ . Natural varieties of the first three ISC's would be the monomineralic rocks dunite, orthopyroxenite of the Bushveld type (with thin (100) exsolution lamellae of augite), and orthopyroxenite of the Stillwater type (with thick exsolution lamellae of augite in the former (001) planes of pigeonite, now “inverted” to hypersthene). ISC's 4 and 5 are more remote from typical natural rocks, but might be realized in nature as quartz diorite and quartz monzonite.

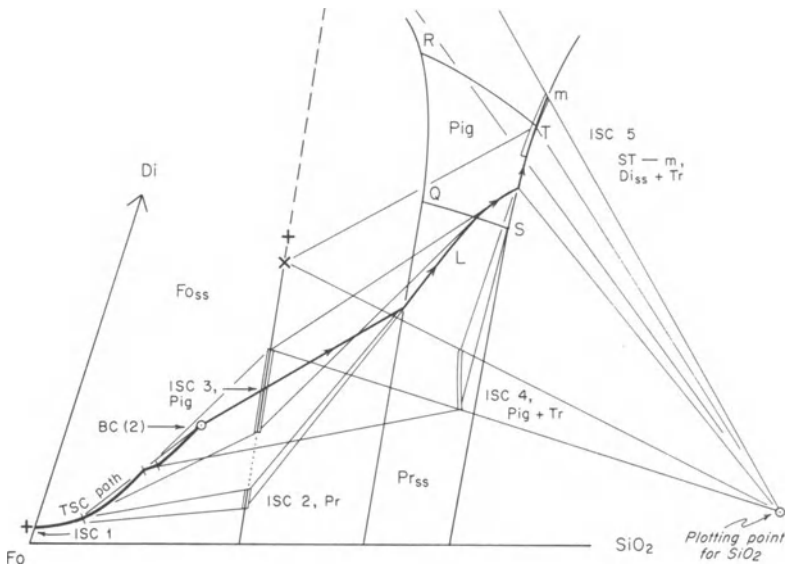


Figure 12.14. Fractional crystallization, BC (2).

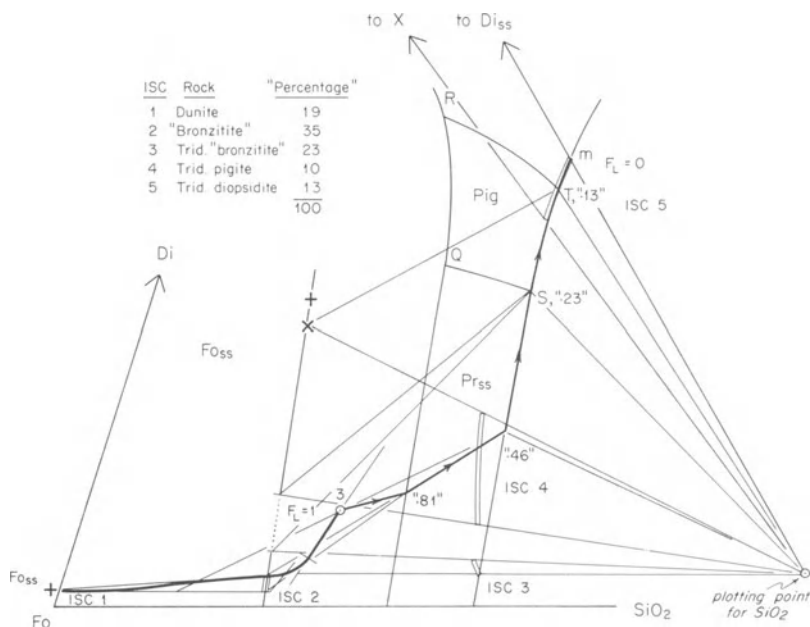


Figure 12.15. Fractional crystallization, BC (3).

BC 3, Fig. 12.15, produces larger amounts of silica-saturated ISC's, consistent with its silica oversaturated location in the diagram. The ISC's and their amounts are tabulated in the figure, and it is left to the reader to verify these for himself, recalling that the TSC always moves toward the ISC, and is "stopped" at any stage by a lever through BC from *L*.

Fractional crystallization paths are summarized for five other bulk compositions in Fig. 12.16, drawn approximately to correct scale. The bulk compositions are denoted by their Fo-Di-SiO<sub>2</sub> ratios. ISC 1 is common to all bulk compositions, and in this case the initial Ca content of Fo<sub>ss</sub> is correctly shown as varying with the Ca content of the BC. ISC's 2, 3, and 4 are shown only for BC 65-15-20; ISC 5 is common to all bulk compositions. Values of *F<sub>L</sub>* are shown only for BC 65-15-20. TSC paths are shown for three of the five bulk compositions. The two silica-saturated bulk compositions are collinear from Fo<sub>ss</sub> with their undersaturated counterparts; they share the same liquid paths. Liquid and TSC paths should be verified by inspection, or worked out where incompletely shown.

### Summary of Fractional Crystallization

Liquids produced in fractional crystallization from the Fo<sub>ss</sub> field all arrive at *m*. The only special path common to all bulk compositions occurs along the cotectic curve EST*m*. Each initial Di:SiO<sub>2</sub> ratio yields a different liquid

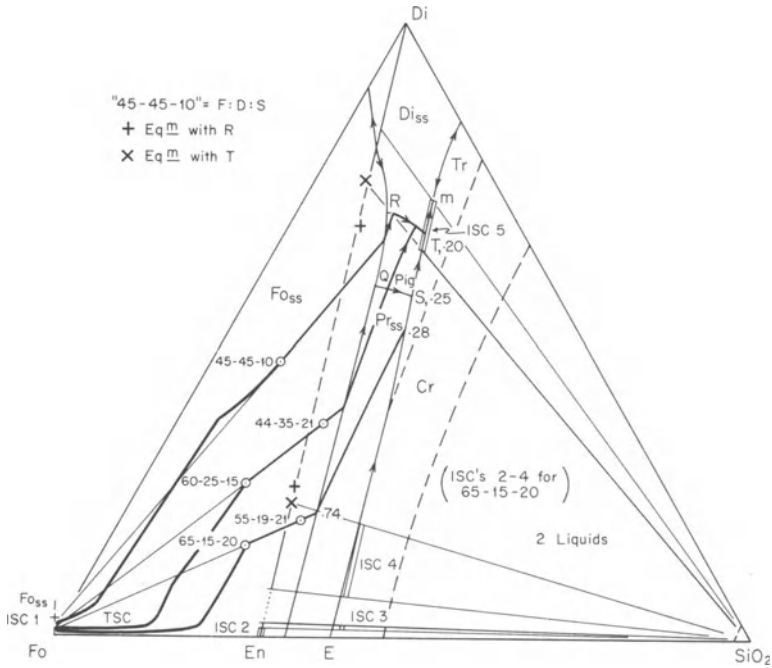


**Figure 12.16.** Fractional crystallization of five bulk compositions, represented on a nearly scale-true diagram.  $F_L$  is shown only for the bulk composition Fo-Di-SiO<sub>2</sub> 65-15-20. TSC paths are omitted for the two silica-oversaturated bulk compositions.

path to m. Di-poor liquids reach m via the cotectic and T, while more Di-rich liquids reach Tm via the pigeonite field and cotectic RT. Failure of olivine and pyroxenes to react with liquid permits preservation of these phases as cumulate layers or isolated segregations, and increases the final amounts of SiO<sub>2</sub>-producing liquids. Common natural rocks for which fractional crystallization in this system serves as a model are dunite, bronzitite (or orthopyroxenite of the Bushveld type), orthopyroxenite of the Stillwater type, and websterite. All residual liquids and ISC's are oversaturated in SiO<sub>2</sub>, and serve as crude models for granitic liquids and rocks produced by fractional crystallization of ultramafic, basaltic, and intermediate liquids. It is interesting that even so mafic a liquid as 65-15-20 yields as much as 20% "granitic" residual liquid lying on the curve Tm.

### Fractional Melting

Both equilibrium and fractional melting require knowledge of Pig - L and Pr<sub>ss</sub> - L tie lines (Figs. 12.4, 12.5) if the initial TSC contains one of these pyroxenes as the single pyroxene phase. The liquid composition at the

beginning of melting is obtained from these tie lines. Equilibrium melting is the exact reverse of equilibrium crystallization, and need not concern us further. Fractional melting requires construction of the TSC path, and can easily be summarized after running through one example. This is shown in Fig. 12.17 for a bulk composition in the solid field of Pig + Tr. The figure is distorted, and the values of  $F_L$  are pertinent only to the distorted drawing, not to reality.

The tie line from  $\text{SiO}_2$  through BC gives the initial composition of pigeonite in the TSC. By use of the tie line template, Fig. 12.5, the composition of liquid on ST in equilibrium with this pigeonite and Tr is found to be that labelled  $F_L = 0$  in Fig. 12.17. Removal of this liquid causes the TSC to change directly away from it, but the successive liquids also move continually toward S, so that the initial TSC path away from BC is slightly curved. Eventually the TSC reaches the limiting Pig - Tr tie line, and further melting involves the production of  $\text{Pr}_{ss}$  in the TSC, by reaction. The liquid is now at S, in isothermal equilibrium with three solid phases, and the TSC moves directly away from S. After a short time, Tr is exhausted in the solids, and at  $F_L = .29$  the melting now involves  $\text{Pr}_{ss} + \text{Pig}$ , with production of  $\text{Fo}_{ss}$  in the solids. The liquid now lies at Q; the TSC moves directly away from Q, and the TLC moves directly toward Q. This melting process ceases when Pig is exhausted in the solids, at  $F_L = .40$ , and the liquid now moves along  $\text{QR}'$  with increasing production of  $\text{Fo}_{ss}$ .

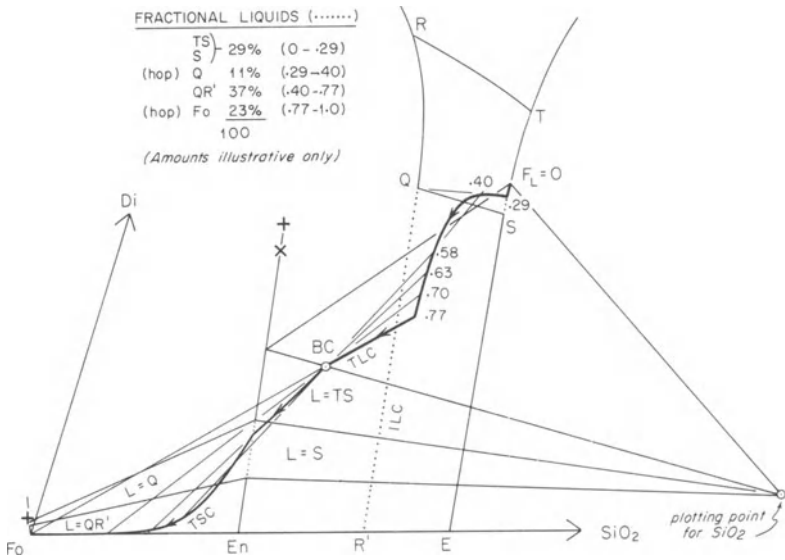


**Figure 12.17.** Fractional melting, using toy FDS No. 1. The ILC path is dotted, and the TLC path is heavy. The identity of liquid being removed is labelled for each solid composition region. The TLC path is straight toward S while the solids lie in Pig +  $\text{Pr}_{ss}$  +  $\text{SiO}_2$ , and is straight toward Q between  $F_L = .29$  and .40.

The TSC path toward Fo is now essentially like the TSC path in the Di field of Di-An-Ab, Fig. 8.21, converging to pure Fo as the liquid reaches R' and as the composition of  $Pr_{ss}$  reaches pure En. The final instantaneous liquid has the composition of Fo, at 1890°C. The complete list of liquids (ILC's) is: TS from  $F_L = 0$  to S, S alone, Q alone, QR', and Fo. The model quantities of these liquids are posted in Fig. 12.17; they are obtained with the aid of the TLC path, which always runs toward the ILC, and which is terminated at any stage by a lever through BC from the TSC. Sample levers are shown at five different values of  $F_L$  TLC. The TLC path has straight segments toward S, toward Q, and toward Fo, and is elsewhere curved. The TLC may or may not be realized in nature as a homogeneous entity; in principle, it is possible to draw off the liquid continuously and mix it in an "inert" reservoir (such as a dunite). Alternatively, successive liquid fractions could be drawn off into separate conduits and preserved separately. The TLC is a graphical convenience, but at times may also represent a valid model for earth processes. Certain batches of liquid, especially the invariant liquids at S and Q, need not be drawn off continuously to achieve fractional melting. Batch removal of these liquids is equivalent to fractional removal. It is of interest to note that fractional *crystallization* tends to produce liquids which avoid the invariant points Q, R, and S (Fig. 12.16), while fractional *melting* may yield fair amounts of such liquids. Accordingly, a natural liquid which could be determined to be just saturated with olivine, orthopyroxene, and pigeonite could reasonably be a product of equilibrium crystallization or fractional melting, but less reasonably a product of fractional crystallization.

TSC paths in fractional melting are summarized in Fig. 12.18, where Di-rich compositions are ignored. Following the principles illustrated in Fig. 12.17, it can be seen that the major portion of the silica-oversaturated region is dominated by a bundle of TSC paths emanating from invariant point T. The silica undersaturated region is dominated by a bundle emanating from R. The liquid or range of liquids from which each TSC flees is labelled in each of the solid-phase regions. These TSC paths are the solidus fractionation lines of Presnall (1969).

## Diopside-Rich Compositions

We have heretofore avoided detailed discussion of Di-rich compositions, because most of the geologically interesting parts of the system Fo-Di-SiO<sub>2</sub> can be provisionally treated without getting involved in the complex nature of  $Di_{ss}$ . It is important, however, to come to grips with these complexities eventually, both for geologic reasons and for experience in the principles of interpreting phase diagrams. Not all of the measurements necessary for a completely confident interpretation have yet been made, partly because a

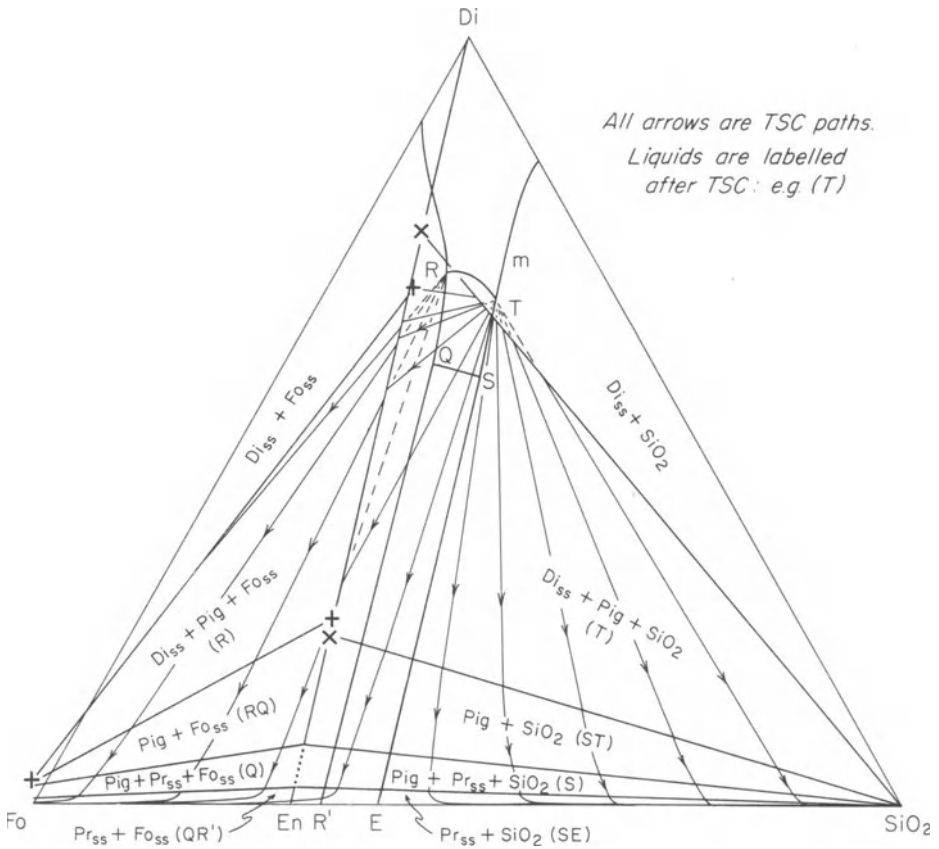


**Figure 12.18.** Summary of fractional melting in Fo-Di-SiO<sub>2</sub>.

great deal happens in this part of the system over a very small temperature range. The interpretation to be offered here is speculative with respect to the existence of the minimum *m* and the maximum *M'* on the *Di<sub>ss</sub>* - Tr boundary, but there are sound reasons for accepting this interpretation as the most probable, given the data and the geologic knowledge which we have at hand.

It will be recalled from Fig. 12.1 that *Di<sub>ss</sub>* shows a relatively large range of composition at 1390°C. It is also known that pure CaMgSi<sub>2</sub>O<sub>6</sub> melts incongruently, 1391.5°C being the liquidus point (Kushiro, 1972). This phenomenon is indicated in Fig. 12.1, where it will be seen that a tie line from *Di<sub>ss</sub>* to a CaSiO<sub>3</sub>-rich liquid passes through pure CaMgSi<sub>2</sub>O<sub>6</sub> at 1390°C. The lozenge-shaped field of *Di<sub>ss</sub>* at 1930°C may be conceived as the map of an elongate island at a “water level” (temperature) of 1390°C. Assuming that the island has a smooth shape, as suggested by the map outline, then raising the temperature should have the effect of shrinking the lozenge proportionately in all directions. The last bit of the island to become

submerged should be a point about in the center of the lozenge. Such a point would be defined as the composition of  $Di_{ss}$  of *maximum thermal stability*. Its stable temperature limit is probably appreciably above the liquidus of pure  $CaMgSi_2O_6$  itself—perhaps around  $1395^\circ C$ .

Now if  $Di_{ss}$  by itself has a special composition of maximum thermal stability, it follows that there must exist special  $Fo_{ss} - Di_{ss}$  and  $Di_{ss} - SiO_2$  tie lines of maximum thermal stability. These will not terminate at the  $Di_{ss}$  maximum, but on shoulders of that maximum in line with the saturating phase ( $Fo_{ss}$  or  $SiO_2$ ). The arrangement of crystal-liquid tie lines found by Kushiro (1972), including many not shown in Fig. 12.1, tends to confirm these deductions. An interpretation of these relations is shown in Fig. 12.19. In this figure, the line labelled “model  $Di_{ss}$ ” is meant to represent the axis of the lozenge in Fig. 12.1; it lies off the join  $Di - En$ . A most stable

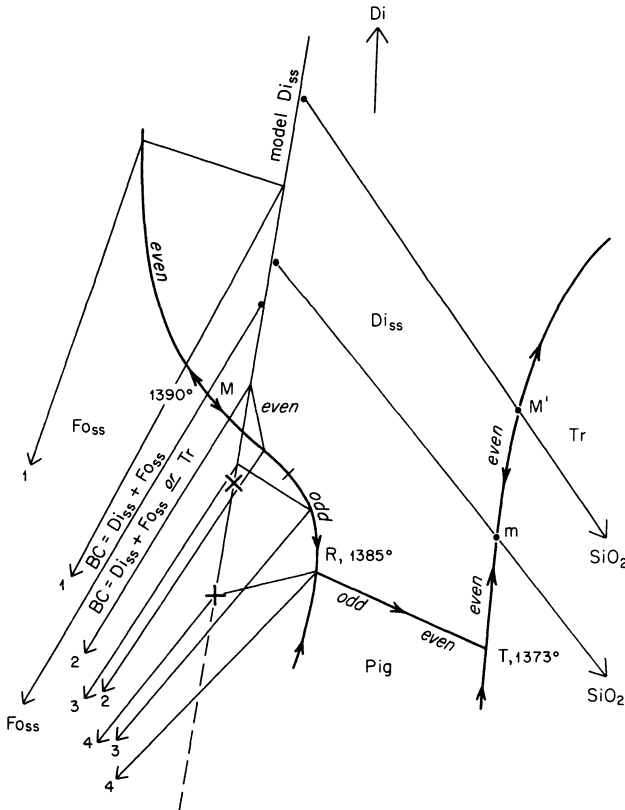


**Figure 12.19.** Cartoon of liquid curves and tie lines in the Di-rich portion of the system. M and M' are maxima; m is a minimum. The symbols X and + have their conventional significance, as labelled in Fig. 12.3 et. seq. Four 3-phase triangles with  $Fo_{ss}$  are depicted. The labels “odd” and “even” refer to the type of reaction along segments of curves.

$Di_{ss}$  ( $Fo_{ss}$ ) occurs near this model line, very near or even at the tip of the lozenge in Fig. 12.1; at 1390°C. The tie line joining this composition of  $Di_{ss}$  to  $Fo_{ss}$  is a unique tie line of maximum thermal stability. If precisely these two compositions of  $Fo_{ss}$  and  $Di_{ss}$  are heated together, they will melt at 1390° to a liquid which lies exactly on the tie line joining them. This is known as a *degenerate equilibrium*, when three ternary phases are collinear so that in discussing them the ternary system has degenerated to a special binary system composed of the two phases at the ends of the tie line. In the present case, no other tie lines between  $Fo_{ss}$  and  $Di_{ss}$  can occur at this high a temperature. The composition of the unique liquid produced on melting this special assemblage of maximum thermal stability is itself a *maximum* (M in Fig. 12.19) on the  $L$  ( $Fo_{ss}$ ,  $Di_{ss}$ ) curve. All other liquids on this curve move away from M on crystallization. The temperature of M is taken as 1390°C; the composition lies off the join Di-En, as shown in the figure.

Compositions in the vicinity of M crystallize with even reaction, the liquids moving away from both  $Di_{ss}$  and  $Fo_{ss}$  together. Kushiro's data, however, show that  $Di_{ss}$  compositions move rapidly toward En with falling temperature, reaching the + symbol at 1385°C, in equilibrium with liquid R. Because of the chemographic arrangement of +, R, Pig, and  $Fo_{ss}$ , it is clear that the reaction of liquid R is  $L + Fo_{ss} = Di_{ss} + Pig$ ; the reaction is odd, since  $Fo_{ss}$  has a negative sign when considered as a product of liquid on cooling. This equilibrium is denoted by the three-phase triangle labelled 4 in the figure. Triangle 3 also shows an equilibrium in which the reaction is odd, i.e.,  $L = Di_{ss} - Fo_{ss}$ , because the tangent to the liquid path cuts the extension of the tie line  $Di_{ss} - Fo_{ss}$ . As the temperature rises toward 1390°, the composition of  $Di_{ss}$  moves so rapidly toward Di that the reaction becomes even, the tangent to the liquid path now cutting the  $Di_{ss} - Fo_{ss}$  tie line itself. A small tick mark on the liquid path indicates the transition between odd and even reactions; at this point the tangent to the liquid path falls exactly on the  $Di_{ss}$  end of the  $Di_{ss} - Fo_{ss}$  tie line. Liquids moving from M to R first produce and then consume  $Fo_{ss}$ , as the reaction changes from even to odd. This reaction sequence may occur for both silica saturated and oversaturated bulk compositions.

Liquid R is in equilibrium with both  $Di_{ss}$  and Pig, the former having the most En-rich limit permitted by the solvus, at the composition denoted by the + sign. At temperatures below R, the En-saturated composition of  $Di_{ss}$  moves *away* from En, down the limb of the solvus (recall Fig. 12.2), thus reaching X in the figure when the liquid is at T, 1373°C. The tangents to the curve RT do not all fall to the En side of this set of  $Di_{ss}$  solvus compositions for reasons to be explored shortly; hence the reaction is partly odd and partly even along the curve RT. The reaction at T is odd, namely  $L + Pig = Di_{ss} + Tr$ . This is because the tie line  $Di_{ss} - SiO_2$  from composition X falls below point T. Once pigeonite is used up in reaction, the liquid is free to proceed along Tm in an even reaction,  $L = Di_{ss} + Tr$ .

Analytical data indicate that the  $Di_{ss}$  of maximum thermal stability in

equilibrium with  $\text{SiO}_2$  lies well toward Di from that in equilibrium with  $\text{Fo}_{\text{ss}}$ . The tie line from this unique maximum  $\text{Di}_{\text{ss}}$  ( $\text{SiO}_2$ ) must generate a maximum ( $M'$  in Fig. 12.19) on the curve  $L$  ( $\text{Di}_{\text{ss}}$ , Tr). If such a maximum exists, as seems probable, then the minimum  $m$  must also exist, because as we have just seen, liquids move northward from T along the  $\text{Di}_{\text{ss}}$  - Tr curve, and must move southward as well as northward from  $M'$ . The properties of a ternary minimum are like those of a maximum in that liquid  $m$  lies collinear with a special composition of  $\text{Di}_{\text{ss}}$  and Tr; the system is degenerate, and  $m$  is invariant by restriction ( $c = 2$ ,  $\phi = 3$ , and  $W_p = 0$ ). Further discussion of crystallization at a minimum is given below.

### Nature of the Diopside-Pigeonite Boundary

The experimental evidence indicates that the boundary curve RT is nearly straight, or at least not strongly curved. Because of this and the locations of  $\text{Di}_{\text{ss}}$  in equilibrium with liquids on RT, crystallization processes involving this curve are special. The tie lines from diopside solid solution to R, T, and two points on RT are shown schematically in Fig. 12.20. For simplicity it is assumed here that RT is rigorously straight. Each of the tie lines is part of a three-phase triangle Di-Pig-L. Forsterite and silica occur as additional saturating phases for liquids at R and T, respectively.

Consider the bulk composition B which, when fully crystallized, will

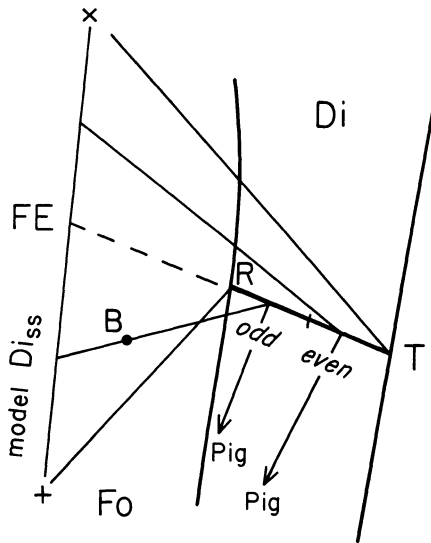


**Figure 12.20.** Later stages of equilibrium crystallization of bulk composition B. The liquid lies on RT and is connected by a lever through B to the TSC, which consists of diopside solid solution. The liquid has just reached RT via paths described in the text. It now proceeds down RT toward T while pigeonite (Pig) is added. The composition of  $\text{Di}_{\text{ss}}$  will move toward X in the figure. Point FE is the fictive extract, on the tangent to RT.

consist of  $Di_{ss}$ , Pig, and Tr. In order to achieve this TSC, the liquid will need to reach T and then produce Tr by reaction. At present, bulk composition B consists only of  $Di_{ss} + L$ . The reader may verify for himself that the liquid got from B to its present location via the reactions  $L = Fo$ ,  $L = Di - Fo$ , and  $L = Di$ . The scene depicted in Fig. 12.20 occurs just as the liquid has reached RT. In order for crystallization to proceed any further, the liquid must move toward T. In doing so, it will encounter tie lines to diopside that fall progressively above B, and therefore pigeonite must be continually added to the TSC. The *reaction* along this part of curve RT is therefore undeniably  $L = Di_{ss} + Pig$ , an *even reaction*. Nevertheless, the curve itself here is *odd*, because its tangent lies on Di minus Pig.

How can there be an even reaction on an odd curve? First, note that this can happen only during equilibrium crystallization; in fractional crystallization the liquid would leave the curve RT. Secondly, we note that the curve is odd because its tangent falls to the negative side of one of the equilibrium crystal compositions. The part of the curve nearer T is an even curve, because its tangent now falls *between* Di and Pig, the composition of  $Di_{ss}$  having moved upward.

Liquids must always move away from the material being extracted from them. In fractional crystallization, this material is the tangible ISC. However, in equilibrium crystallization, with solid solutions, the material being extracted from the liquid is not identical with the equilibrium crystal composition, but is instead the material *needed to convert the crystals to their new compositions*. In this book, this material is called the *fictive extract*; it always lies on the tangent to the liquid path. For the case being considered, the fictive extract lies at the point labelled FE in Fig. 12.20. Point FE must contain a positive quantity of Pig, since pigeonite is crystallizing. It must also contain a positive quantity of the fictive  $Di_{ss}$  component being removed from the liquid to convert  $Di_{ss}$  toward the top of the diagram. This fictive  $Di_{ss}$  component, therefore, must simply lie above FE on the  $Di_{ss}$  line. A retrospective analysis of the equilibrium liquid path  $L = Di$  across the corner of the diopside field will show that this fictive material, always on the tangent to the  $L$  path, has lain above FE all the time while diopside crystallized alone. It is thus possible to map the location of the fictive extract and to show that when the liquid first touches the  $L$  (di, Pig) boundary curve, the fictive extract jumps discontinuously from some location near X to the point FE.

Another example of the fictive extract is shown in Chapter 15, in connection with Fig. 15.21.

## The Diopside Field

Bulk composition 8, Fig. 12.21, lies in the solid field of  $Di_{ss} + Tr$ . Crystallization begins with the production of  $Di_{ss}$ , which moves toward Di with falling temperature, causing the liquid to follow a concave-down path.

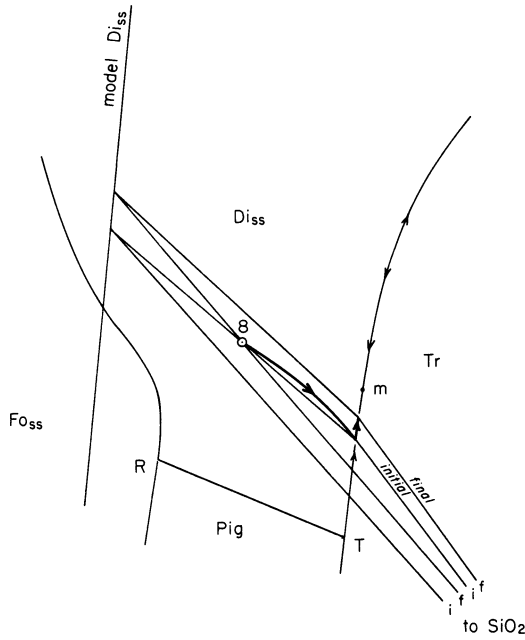


**Figure 12.21.** Equilibrium crystallization of bulk composition 8. Initial tie lines to  $Di_{ss}$  are not shown.

The liquid path is shown in the figure; it reaches a point on  $T_m$  such that the  $Di_{ss} - L$  tie line passes through the bulk composition. This arrival initiates the first three-phase triangle  $Di_{ss} - L - Tr$ . The liquid now moves along the curve  $T_m$  until the  $Di_{ss} - Tr$  leg of the three-phase triangle cuts  $BC$ , when crystallization ceases. The principles are exactly the same as those in  $Di - An - Ab$ , where a solid solution (plagioclase) occurs with a phase of fixed composition ( $Di$ ). If Fig. 12.21 is turned on its left side, a resemblance to the liquid path in  $Di - An - Ab$  will be discerned. The behavior of  $Di_{ss}$  is that of an ordinary solid solution loop, although the liquid in this case does not lie on the  $Di_{ss} - En$  join. The minimum  $m$  has nothing to do with this particular crystallization path.

The general properties of minima may as well be introduced here, in any event. Fig. 12.22 shows the hypothetical system  $A - B$ , with a minimum melting relationship. The diagram is to a first approximation equivalent to two binary loops butted together at  $m$ , and equilibrium crystallization in either loop follows the same principles as for plagioclase. The point  $m$  occurs at the point of *tangency* of solidus and liquidus; here, a special composition of solid  $AB$  and a special composition of liquid are identical, and lie at the same temperature. The tangent to  $m$  must be isothermal, i.e., horizontal. A liquid of composition  $m$  would crystallize isothermally at  $T_m$  to a homogeneous crystal of composition  $m$ . If such a minimum-melting system is embedded in a solvus, a eutectic system such as that shown in Fig. 5.5 results, in which the crest of the solvus and the bottom of the

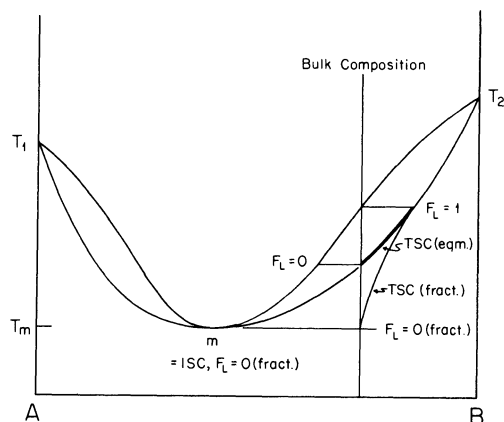


**Figure 12.22.** Hypothetical binary system with a minimum melting composition (m).

minimum loops are metastable and not shown. With this general and sketchy introduction to melting minima, we may now turn to a depiction of  $Di_{ss}$  relations in  $Fo$ - $Di$ - $SiO_2$ , by means of two *projections*.

Projections of pictures may be achieved in various ways; for example with the light behind the observer, or shining toward the observer from behind the screen. We are already familiar with projections along a temperature axis onto a composition plane, as seen in all our polythermal ternary diagrams. What we now propose to do is to project liquid and solid compositions related to  $Di_{ss}$  from one or another saturating phase,  $Fo_{ss}$  or  $SiO_2$ . Fig. 12.23 illustrates how such a projection from  $Fo_{ss}$  is derived. The aim is to visualize the  $T - X$  relationships of liquid and  $Di_{ss}$  when these two phases do not lie in the same  $T - X$  plane. The right hand side of Fig. 12.23 is the desired  $T - X$  projection, separated from the parent  $X - X$  plot by a *fold line*. The parent  $X - X$  plot will be recognized, it is hoped, from Fig. 12.19. The line  $Di_{ss} - En$  is chosen as the base of the projection plane  $T - Di_{ss} - En$ . We wish to map onto this  $T - X$  plane all compositions of  $Di_{ss}$  and  $L$  which are saturated with  $Fo_{ss}$  and with each other. This is done by means of rays from  $Fo_{ss}$ , which either pass through the point to be projected and then on to the reference plane, or pass through the reference plane to the point. In either case, the intersection of the ray with the reference plane is the desired projection point. Those of the second type are indicated with arrows backward along the ray, whereas those of the first type are indicated with arrows forward along the ray. The fold line is set off an arbitrary distance from the reference plane, and the projection points are carried from the reference plane to the fold line by normals to both. The fold line marks the transition from  $X - X$  to  $T - X$  plot.

In the  $X - X$  plot, tie lines are shown between  $Di_{ss}$  and liquid. One of these tie lines is the unique line  $Fo_{ss} - M - Di_{ss}$ , and this plots in projection as a point, a maximum, in the  $T - X$  diagram. Three other tie lines are projected, one of them being  $+ - R$  at the bottom of the  $X - X$  diagram.

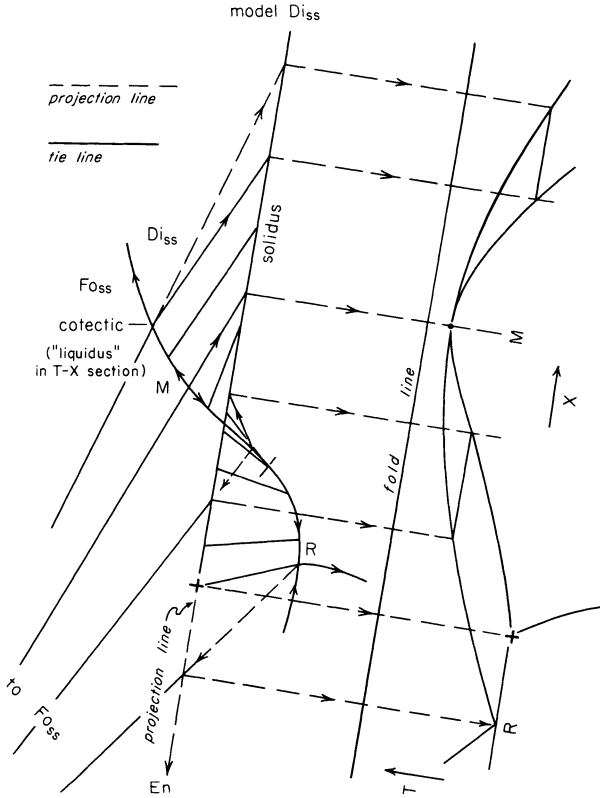


**Figure 12.23.** Scheme of projecting liquid and crystal compositions saturated with  $Fo_{ss}$  onto a  $T-X$  plane. All crystal compositions are assumed to lie on the model  $Di_{ss}$ -En line, which is also taken as the base of the  $T-X$  plane. A number of crystal-liquid tie lines are shown, four of which are chosen for projection.

Such tie lines are isothermal lines in the  $T - X$  diagram. From the disposition of such tie lines, properly assigned to their respective temperatures, the full  $T - X$  projection from  $Fo_{ss}$  can be constructed. It consists of a maximum  $M$  joining a pair of loops, one of which terminates in the  $Pig - Di_{ss}$  solvus at an apparent eutectic,  $R$ . This point is, in fact, of the eutectic type with respect to  $Di_{ss} + Pig$ , but as we know, it is a peritectic with respect to  $L + Fo_{ss}$  (this peritectic relationship cannot be shown in the projection, but it would be apparent in a projection from  $Di$  onto the  $Fo-SiO_2$  sideline). The significant property of the maximum is that the projected solidus and “liquidus” become tangent there. The term “liquidus” is put in quotation marks because this curve is in fact the cotectic (elsewhere peritectic) equilibrium  $L (Fo_{ss}, Di_{ss})$ .

The projection of Fig. 12.23 is repeated at another scale in Fig. 12.24, along with a projection from  $SiO_2$  of the compositions of phases saturated with  $SiO_2$ . This projection is also made onto the  $Di$ -En- $T$  plane. In the  $Fo_{ss}$

projection, Fig. 12.24a,  $Fo_{ss}$  is to be understood as an added phase in all regions, since this is a projection from  $Fo_{ss}$ . Similarly, Cr or Tr is to be understood in all labels on Fig. 12.24b. In the upper figure, Q is seen to be a reaction point where  $Pr_{ss}$  is converted to Pig; compare Fig. 12.2, which shows the  $T - X$  section along Di-En rather than the *projection*. Point R shows even reaction relative to  $Di_{ss} + Pig$ , as mentioned above. The change from odd to even reaction along the curve RM cannot be discerned in the  $T - X$  diagram, as it is a property of ternary relations involving  $Fo_{ss}$ , the projecting phase. In Fig. 12.24b, the  $Di_{ss}$  composition labelled X is the same as in previous diagrams, e.g., Fig. 12.19, and the projection from  $SiO_2$  emphasizes that this composition has a peritectic relationship to liquid T when tied to  $SiO_2$ . The isothermal tie line Pig - X - T truncates the  $Di_{ss} - L$  loop to the left of the minimum m. It is on this segment of the loop that the final stages of crystallization of bulk composition 8, Fig. 12.21, take place. The remainder of the right hand side of the diagram illustrates the supposed maximum on the  $L (Di_{ss}, Tr)$  curve. In both figures, the behavior of  $Di_{ss}$

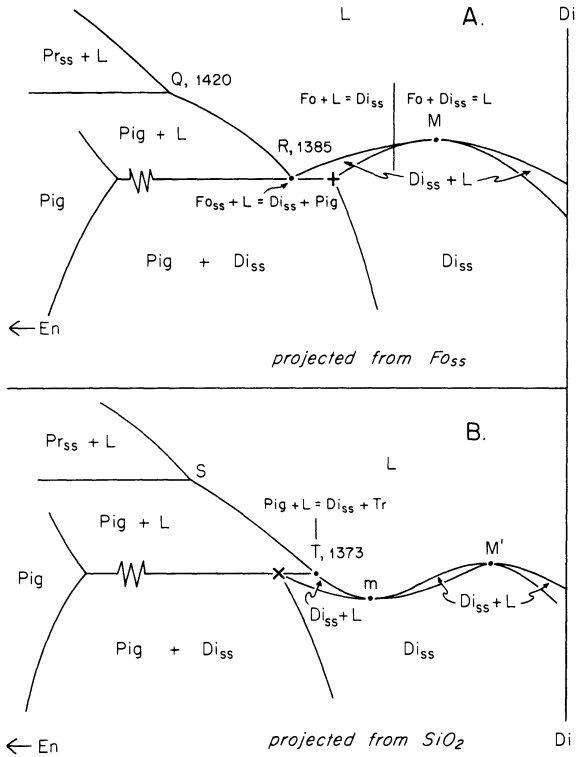


**Figure 12.24.** Schematic  $T-X$  relations of  $Di_{ss}$ -liquid equilibria. A, projected from  $Fo_{ss}$ ; liquids are those along R' Q R M in Fig. 12.3. B, projected from  $SiO_2$ ; liquids are those along E S T m M' in Fig. 12.3.

near pure  $\text{CaMgSi}_2\text{O}_6$  is left unspecified; further discussion of these relationships is given by Kushiro (1972).

### Application to Basalts and “Granites”

The minimum  $m$  prevents liquids from leaving the Fo-Di- $\text{SiO}_2$  system by fractionation, and is consistent with natural fractionation sequences which lead to pyroxene-quartz-feldspar rocks rather than to wollastonite-bearing siliceous rocks which would result from fractionation out of the system, beyond the maximum  $M'$ . Although the natural systems are usually iron-rich, thus making comparison with the system FDS rather tenuous, the analogy is probably valid as a provisional consideration.

The main features of the system FDS as a model of natural rocks occur in the basaltic region. As already discussed, the reaction of olivine to both  $\text{Pr}_{\text{ss}}$  and  $\text{Pig}$  is a phenomenon for which much evidence exists in natural rocks. The reaction relationship between  $\text{Pr}_{\text{ss}}$  and  $\text{Pig}$ , as modelled by the equilibria along QS, is a matter which has been hotly debated among field workers. Again, the natural sequence is the same, but involves iron enrichment leading to the stabilization of  $\text{Pig}$  instead of  $\text{Pr}_{\text{ss}}$ . However, iron enrichment occurs with falling temperature, and may simply be a parallel effect rather than a causal one. In any event, it is a common experience to find, in tholeiitic layered intrusions, sills, and lava flows the sequence olivine-hypersthene-pigeonite, and the present system serves as a good starting model for this sequence. An added feature of the natural rocks is that this sequence commonly occurs in the *constant* presence of augite, rather than leading to late crystallization of a clinopyroxene, as would be implied by the system FDS. Reasons for this will not be rigorously explored here, but it can at least be said that the lowering of crystallization temperatures by  $\text{Fe}^{2+}$  and other components of natural magmas serves to embed the liquid-crystal equilibria more deeply into the diopside—Ca-poor pyroxene solvus, and to stabilize diopside in equilibrium with liquid and the other mafic phases. In this way, it is possible to imagine a cotectic relation among Ca-poor phases (including olivine), liquid, and diopside, in company with peritectic relations between the Ca-poor phases.

The reaction relation of olivine plus liquid to orthopyroxene is the hallmark of tholeiitic basalts. This reaction occurs for all liquids along  $R'Q$  (Fig. 12.3 et. seq.), hence for all bulk compositions within the triangle  $\text{Fo}_{\text{ss}} - Q - R'$ , whether they are olivine tholeiites in Fo-Di-En or oversaturated tholeiites in Di-En- $\text{SiO}_2$ . The reaction of olivine plus liquid to pigeonite is an entirely equivalent reaction on QR. The long reach from  $R'$  on Fo- $\text{SiO}_2$  to R in the ternary system practically guarantees that the reaction will occur in any situation remotely approaching equilibrium crystallization, for almost any liquid of tholeiitic affinity. In pure fractional crystallization, the sequence olivine—Ca-poor pyroxene would be encountered instead, but in

natural processes the theoretical limit of fractional crystallization can never be pervasively maintained, so natural rocks are bound to show, somewhere, evidence of the reaction, commonly as a reaction rim along the corroded edge of an olivine crystal.

The system Fo-Di-SiO<sub>2</sub> has been used extensively in the interpretation of tholeiitic layered intrusions formed by large-scale fractional crystallization and crystal settling, particularly by Irvine and Smith (1967) and Irvine (1970). Although there have been important modifications in the system since that time, the general conclusions are interesting and valid. In brief, these are that in the Muskox layered intrusion, Canadian Northwest Territories, fractional crystallization of a magma analogous to bulk composition 60-25-15 in Fig. 12.16 produced a series of ISC's very closely modelled by the experimental system, namely peridotite, orthopyroxenite, and websterite (Cpx - Opx rock). Modal analyses of the actual rocks, when plotted in the FDS system, fall in distinct concentrations almost exactly where they would be predicted from the experimental ISC. The experimental diagram is therefore shown to be a quantitatively rather accurate model of natural processes, and with the benefit of such hindsight, it might be possible to use modern analytical methods to construct slightly modified versions of the experimental system, accurate in subtle details of pyroxene compositions and reactions, for each natural body of rock.

The system Fo-Di-SiO<sub>2</sub> also serves as an excellent starting model for the generation of basaltic magma in the mantle. We shall eventually examine the high-pressure relationships of this system, but the low-pressure version serves to illustrate several important principles. One is that no matter how Ca-poor or silica-poor the model mantle composition is in the triangle Fo-R-R', the initial liquid produced on heating is moderately to very Ca-rich, and silica oversaturated at low pressures. For example, if the bulk composition falls in the field of Fo<sub>ss</sub> + Pig + Pr<sub>ss</sub>, the initial liquid is Q, with more than 50% diopside component relative to orthopyroxene. This fact no doubt explains why tholeiitic basalt is almost invariably saturated or nearly saturated with augite, of which it produces large quantities during crystallization. Moreover, it is clear, as already mentioned, that liquids saturated with several phases, such as Q, S, and liquids along QR', are much more likely to be generated by either fractional or equilibrium melting than by fractional crystallization from ultramafic liquids. This principle follows from the extensive presence of odd reaction curves in the system, which shed liquids on fractional crystallization but hold them on melting.

## G-X Diagrams for Systems with Maxima or Minima

Melting at a maximum or minimum has been introduced in this chapter because such behavior occurs in the system Fo - Di - SiO<sub>2</sub>. Here we have used projected liquid and solid compositions, because the system is ternary.

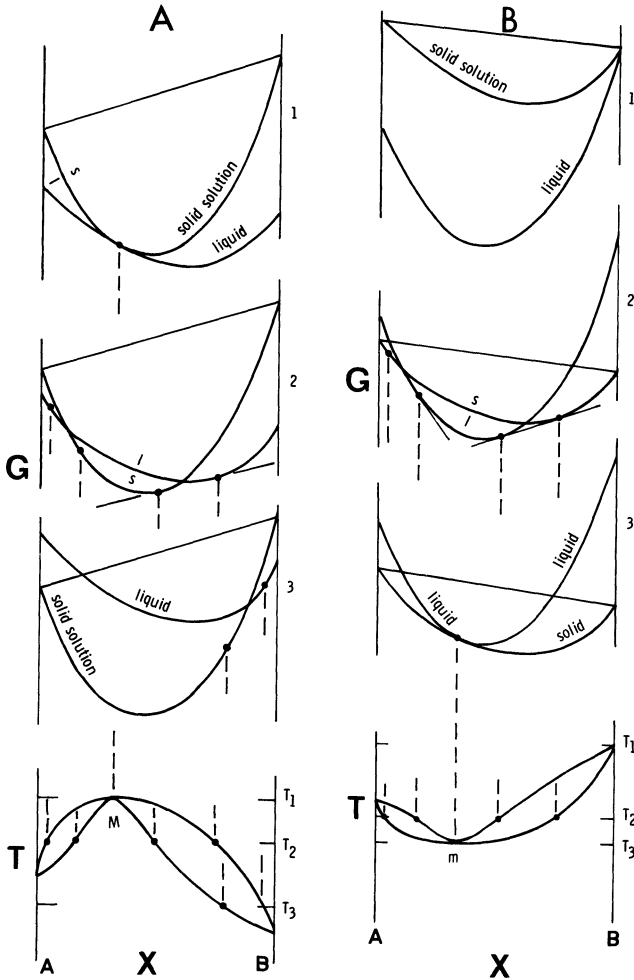


**Figure 12.25.** G- and T-X diagrams for systems showing melting at a maximum (A) and at a minimum (B).

However, the principles apply to simple binary systems, and, in turn, the G-X diagrams for a binary system can be used to illustrate the principles operating in a ternary system.

Figures 12.25a and b show two related types of system displaying, respectively, melting at a maximum and melting at a minimum. They can be analyzed essentially as for the plagioclase system, but with the observation that at either a maximum or a minimum, both solidus and liquidus *must* coincide on an *isothermal* tangent in T-X space, and in G-X space the solid and liquid G-X curves simply have a common tangent point. The common tangent has zero slope in T-X but not in G-X. It is common to see diagrams which violate this principle, especially in having liquidus curves

entering a minimum at a high angle. This is incorrect. It may happen that the liquidus curves approach closely before swinging in a tight arc to isothermal tangency, but that would imply a very large difference in the radius of curvature of the liquid and solid  $G-X$  curves (see section 3 of Fig. 12.25*b*), and this is unlikely, to say the least, in silicate systems in which the melts are highly polymerized and structurally analogous to the crystalline solutions from which they form. Such are the insights one may gain from an appreciation of  $G-X$  diagrams, which constantly rescue the practicing petrologist from error (if he remembers to use them).

## Chapter 13

# Layered Intrusions: A First Glance

### Introduction

When we seek to find out whether phase diagrams are good models of natural systems, it is helpful to turn to layered intrusions. These bodies represent natural experiments in fractional crystallization on a grand scale, and in them, a stratigraphic record is preserved of the rocks (ideally the ISC's) produced on fractional crystallization of magma, in most cases basaltic, but in some cases ultramafic or granitic or intermediate.

In examining briefly the relevance of phase diagrams and layered intrusions to each other, the comparisons made here will in most cases be qualitative or semiquantitative. This is partly because precise measurement of rock volumes, ratios, and compositions is extremely difficult and as yet unsatisfactory for most layered intrusions. Furthermore, the most pertinent experimental models would be at least quaternary systems, for example Fo-Di-SiO<sub>2</sub>-An, for which the internal geometries are as yet poorly known. Despite these apparently gloomy circumstances, it is possible to make some very successful tests of simple phase diagrams as models for natural processes, and of proposed natural processes in terms of phase diagrams.

### Layered Intrusions

If a large volume of basaltic magma is emplaced in the earth's crust and allowed to cool, the following things will most likely happen.

1. The initial shape of the magma body will tend not to be spherical, but flat and tabular or else lopolithic or funnel-shaped, depending on the level and manner of emplacement and the structural fabric and stress environment of the enclosing rocks.
2. Cooling will be very slow, perhaps taking 1 million years for the crystallization of a body  $2000 \text{ km}^3$  in volume. The rate of cooling will be governed by the initial temperatures of magma and wall rock, the specific heat of the magma and its products, the latent heat of crystallization, the thermal conductivity and specific heat of the wall rocks, distance beneath the earth's surface, and the heat absorbed in melting or metamorphic reactions, among other things. Since complete crystallization may involve a range of  $300^\circ\text{C}$  or less (e.g.,  $1200^\circ\text{C}$  to  $900^\circ\text{C}$ ), an average cooling rate of  $3 \times 10^{-4}$  deg/year is implied, and another 3 million years (or very likely more) may be required to bring the body to ambient temperature.
3. Because of slow cooling, nucleation and crystallization will proceed very slowly, leading perhaps to average population densities like one to ten crystals per cubic meter of magma (about 1 to 10 parts per million), although probably more than this at the main cooling surfaces such as walls and roof. There is a good chance that crystals and liquid will closely approach equilibrium with respect to diffusion.
4. Crystals will tend to sink, being denser than their parent liquids, and they will therefore accumulate on the floor of the intrusion, which may be a relatively flat initial wall-rock surface, or a feeder which eventually becomes choked with crystals. This statement ignores the problem of plagioclase, which may be less dense than some liquids (Morse, 1979b).
5. The magma will convect, because it cools more rapidly at the top. The simplest convection pattern would be a single toroidal cell, with an upward bore at the center, outward dispersion along the roof, downward motion along the walls, and inward convergence along the floor. Convection current velocities like 1 cm/yr have been postulated as average.
6. The convection currents, particularly upward ones near the roof center, may effectively elutriate minerals of different density (actually of different Stokes settling velocity, which depends on mass, hence size as well as density). Separate generations of, say, plagioclase and mafics, will follow one another down along the walls and eventually accumulate on the floor, but in a given layer there will exist different generations of light and dense minerals. A steady-state flow regime will continually produce an "average rock" accumulating on the floor.

7. Any change in convection current velocity will change the elutriation rate between two minerals of contrasting inherent settling velocity. Such a change will be remembered at the floor, where variation in mineral ratios will be seen as layering. Other types of layering may occur, but this may be an effective working model for the origin of so-called rhythmic layering. The following types of factors may affect the production of layers: accelerations caused by the previous proto-layer in transit; accelerations due to slumping, for example induced by earthquakes; changes in cooling rate; varying crystal growth regime at the floor. A discussion of the plagioclase problem and the role of kinetic effects near the floor is given by Morse (1979b).
8. As the successive layers of crystals build up on the floor, they will cover and isolate underlying layers, thus sealing them off from reaction with the main body of magma. By this sealing-off process, fractional crystallization of the main body of magma is achieved. Removal of layer after layer of crystals from interaction with the main magma drives the magma composition away from the bulk composition.
9. In response to changing magma composition, succeeding generations of crystals will have more and more advanced compositions in terms of solid solutions, and new phases may appear from time to time as new field boundaries are reached by the fractionating liquid. The change of mineral compositions with stratigraphic height has been called "cryptic layering" or "cryptic variation" or "mineral variation".
10. The end product will be a tabular or basin-shaped or funnel-shaped pile of *cumulate rocks* in which the upward stratigraphic variation preserves a record of the temporal changes in the magma throughout crystallization. Such stratified rocks show many of the familiar features of exogenic clastic sedimentary rocks, including size and shape sorting, laminar fabric, graded bedding, scour-and-fill features, and slump breccias. The cumulate rocks are in every sense sedimentary rocks preserving conventional stratigraphic records, except that they are deposited from magma rather than from water or air.

This pretty tale of prediction is told with the benefit of hindsight. The first clear exposition of most of these principles was made in a revolutionary and fascinating monograph by Wager and Deer (1939) on the Skaergaard intrusion of East Greenland. This spectacular body of Eocene rocks, exposed in a mountainous and still deglaciating coastline, is complete enough to have provided the key to interpreting layered igneous rocks, and it was rightly hailed as the definitive proof of fractionation principles long

before suspected in extrusive rocks and predicted in the laboratory. The task of measuring the volumes and chemistry of the various parts of this intrusion continues today, chiefly by A.R. McBirney and associates. A detailed modern summary of the intrusion is given by Wager and Brown (1968). We shall return to a discussion of this body in due time.

## Kiglapait Intrusion

It is convenient to use this intrusion as a first example. With this and other bodies, a brief and greatly simplified description of field relations will be followed by a simple treatment in one or more phase diagrams.

The Kiglapait intrusion on the coast of Labrador was found in 1957, at the inception of a long study of the Nain anorthosite and related rocks (Morse, 1969). The intrusion underlies an area of about 560 km<sup>2</sup>, being about 11 times larger in area than the Skaergaard, and is remarkable for several reasons: its stratigraphy is apparently complete from base to roof; it was emplaced, without serious pervasive contamination, into refractory anorthosite and other dry country rocks; and it falls mineralogically and probably chemically on the natural analog of the critical plane of silica undersaturation. A simplified stratigraphic column is shown in Fig. 13.1. The vertical dimension is the geometrically determined "percent solidified" scale, or in other words, it gives the relative position of the upward-growing magma/crystal interface at any stage of solidification. The complementary values of  $F_L$  are also listed. Attention is directed to the 94% of the intrusion called the Layered Group<sup>1</sup>, composed of all material exclusive of border zones. The Layered Group consists of a Lower Zone of troctolite and an Upper Zone of olivine gabbro to syenite (more correctly, ferrosyenite). All are cumulate rocks, composed of the *cumulus* minerals which sank and the varying amounts of material crystallized from a pore liquid (*intercumulus liquid*) which was trapped among the settled crystals. The Lower Zone consists almost solely of cumulus plagioclase and olivine in the approximate ratio 75:25. The base of the Upper Zone is marked by the first accumulation of augite, and at higher levels in the Upper Zone, magnetite, apatite, and calcic sanidine (mesoperthite) appear as cumulus minerals. The uppermost rocks are varieties of syenite. Figures 13.2 and 13.3 illustrate typical layered rocks of the Lower and Upper Zones.

The transition from Lower to Upper Zone can be modelled in the system Fo-Di-An, although it is to be kept in mind that the actual minerals are intermediate rather than end members of the species olivine, clinopyroxene, and plagioclase. Part of the phase diagram is shown in Fig. 13.4a. The spinel

<sup>1</sup>Originally called Layered Series, but changed to Group in order to conform with standard stratigraphic nomenclature.

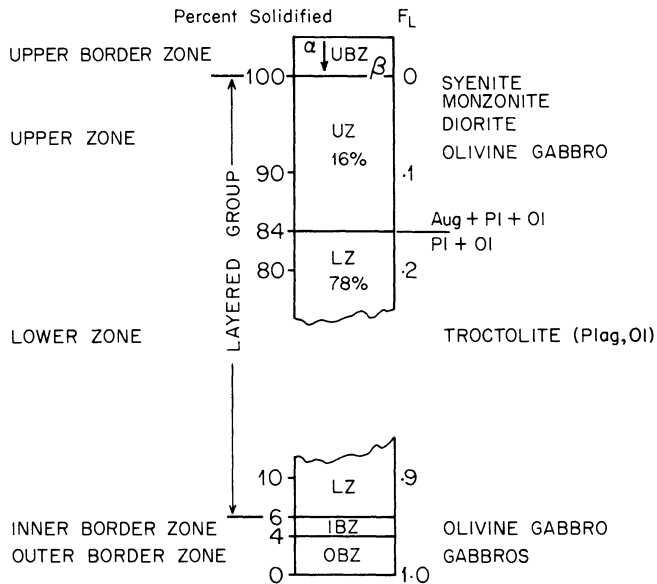


**Figure 13.1** Stratigraphic column of the Kiglapait intrusion, Labrador, after Morse (1969).

field is omitted, because spinel is not encountered in these rocks, and it can be shown that the spinel field disappears with addition of sufficient FeO and Na<sub>2</sub>O. The cotectic *L* (Plag, OI) is assumed to extend toward the composition OI<sub>30</sub> Plag<sub>70</sub> beyond point D. A parent magma plotting on the extended cotectic at the point labelled BC would produce troctolite as an ISC on fractional crystallization, from  $F_L = 1$  to  $F_L = .22$ . When the liquid reached the piercing point, clinopyroxene would join the crystalline assemblage, and the new ISC would be an olivine gabbro. This final ISC would amount to 22% of the original mass.

The first ISC corresponds very closely to the actual Kiglapait Lower Zone, the chief difference being that the model contains more olivine (30%) than the real rocks (about 20%). The second ISC also corresponds quite closely to actual Kiglapait Upper Zone rocks, which have a color index near 50, and much less olivine than the troctolites (generally less than 10%). Augite is not as plentiful in average rocks as is Di in ISC (2) of the diagram, however.

In a qualitative sense, the system Fo-Di-An nicely accounts for the upward transition from troctolite to olivine gabbro in the Kiglapait. In a semiquantitative way, it suggests the approximately correct ratio of Lower to Upper Zone. There is no reason, however, to believe that Fo-Di-An should be a quantitatively correct model for such magmas as the Kiglapait. One would expect both pressure and the complexities of magma chemistry to have some effect on the locations of boundaries and "invariant" points.

Existing experimental data are inadequate to show these effects reliably



**Figure 13.2** Layered troctolite of the Kiglapait Lower Zone. The dark layers are olivine-rich, and the light layers are locally average rock. The thin section (inset) of an average rock shows only cumulus olivine and plagioclase, with two grains of oxide minerals.

in the ternary system. However, it is possible to estimate the effects at the Fo-An sideline. The effect of adding Fe can be estimated from the work of Lipin (1978; see also Ch. 17), and the effects of adding Ab and pressure can be estimated from the work of Emslie (1971). These effects on the position of the plagioclase-olivine cotectic are indicated in Fig. 13.4b, taken from Morse (1979*d*). Note that Fig. 13.4b is plotted in oxygen units, discussed in Appendix 1B. The modal (volume) composition of Lower Zone liquids has been calculated in detail by Morse (1979*d*) and the path of these compositions, representing the cotectic olivine-plagioclase trace for the natural liquids in terms of the three components augite, plagioclase, and olivine, has been plotted as a heavy line in Fig. 13.4b. This line is entirely consistent with the 1 bar estimate at the sideline, and its slope is similar to that in the experimental system Fo-Di-An. The cotectic trace is less consistent with the 4 kbar estimate, which could indicate that the pressure was somewhat less than 4 kbar, but probably indicates to a greater degree the effects of adding other components such as Fe-Ti oxides, not considered in the estimates.

In summary, the modal trace determined for the Kiglapait intrusion may serve as an interim field boundary for natural magmas similar in overall composition to the Kiglapait magma, until such a boundary can be located

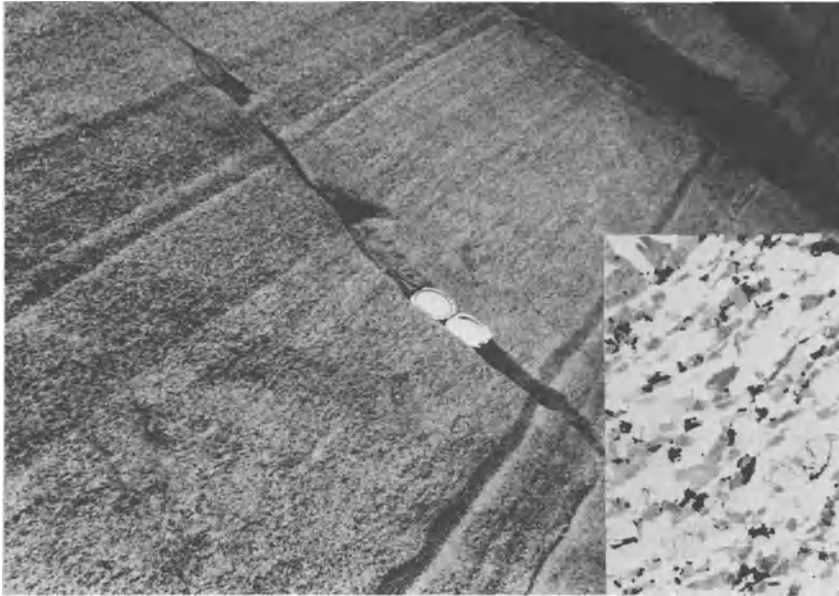


**Figure 13.3** Layered olivine gabbro of the Kiglapait Upper Zone. The thin section (inset) contains cumulus plagioclase, olivine, and augite (with dark rods and plates of exsolved Fe-Ti oxide), and some independent Fe-Ti oxide minerals.

experimentally. The importance of locating the cotectic trace for troctolitic liquids lies in the fact that, using such an estimate, one can in principle distinguish rocks of rigorously cotectic origin from those enriched in either plagioclase or olivine by one or more mechanical processes.

## Skaergaard Intrusion

Some things come in neat little packages, like the Skaergaard intrusion and pocket editions of the complete Shakespeare. The analogy is not made without purpose, for a first turn through either package reveals unsuspected wonders, but so does the *n*th turn. This intrusion in East Greenland has formed the standard of geochemical data and petrologic information on the fractionation of basaltic magma; at least 60% of the elements of the periodic table have been analyzed in Skaergaard rocks in the past four decades. The depositional and erosional features of current-laid crystal layers are so well displayed here as to have given rise to important principles of cumulate rocks as records of magmatic fractionation (Wager, Brown, and Wadsworth, 1960). These are discussed toward the end of the chapter.

The lowermost exposed rocks of the Skaergaard intrusion consist of

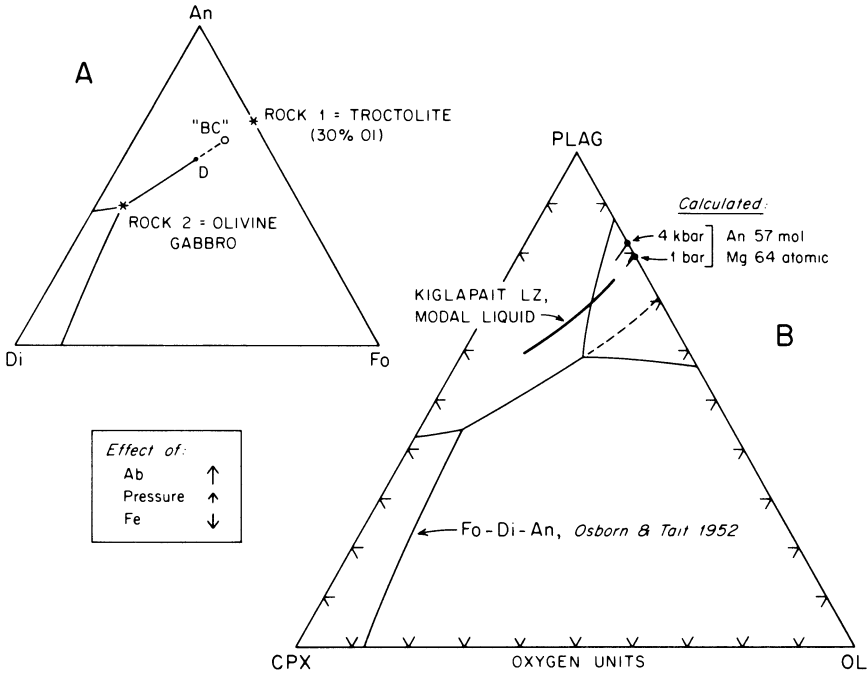


**Figure 13.4** (A) The system Fo-Di-An, showing the ideally expected Kiglapait rocks corresponding to (1) Lower Zone and (2) Upper Zone from the fractional crystallization of a hypothetical parent magma BC. (B) Lower Zone liquid path determined from modal analyses of the intrusion (Morse, 1979d).

cumulus plagioclase and olivine. These are joined, upward, by cumulus augite, pigeonite, magnetite, and apatite. Olivine disappears some distance after the arrival of pigeonite, and reappears shortly before apatite becomes a cumulus mineral. The reason for this famous “olivine hiatus” has to do with the reaction principle, which we have already discussed, and with the stability of iron-rich olivine in the presence of silica minerals, which is yet to be discussed in a later chapter. Upper levels of the intrusion, from the end of the olivine hiatus upward, also contain quartz and micropegmatite. The olivine hiatus and the quartz-micropegmatite intergrowths are abundant testimony to the silica-oversaturated, tholeiitic trend of magmatic differentiation.

The cumulus mineral sequence olivine + plagioclase; augite; pigeonite (each one added to the last) may easily be explained in principle with the phase diagrams Fo-Di-An and Fo-Di-SiO<sub>2</sub>. These are shown in Fig. 13.5, with a bulk composition arbitrarily chosen to lie on the extended L (An, Fo) cotectic and to have a Di/Fo ratio of 1. The base of the Skaergaard Lower Zone is modelled in Fo-Di-An by ISC (1), a troctolite. The arrival of cumulus augite is modelled by ISC (2), olivine gabbro, and it will be appreciated that the Skaergaard sequence is in principle identical with the

Kiglapait sequence (Fig. 13.4) until now. The Kiglapait contains no cumulus Ca-poor pyroxene, however, whereas the Skaergaard contains pigeonite. In the system Fo-Di-SiO<sub>2</sub> (Fig. 13.5b), ISC (2) consists of Di<sub>ss</sub> + Fo<sub>ss</sub> in a ratio dictated by the tangent to the *L* (Di<sub>ss</sub>, Fo<sub>ss</sub>) curve; this is analogous to ISC (2) in Fo-Di-An. We have seen that in the pure system Fo-Di-SiO<sub>2</sub>, an odd reaction would ensue along the curve *L* (Di<sub>ss</sub>, Fo<sub>ss</sub>), and of course under the conditions of fractional crystallization this would cause the liquid to leave the peritectic curve and cross the Di<sub>ss</sub> field. A clinopyroxenite would result. In the Skaergaard case, however, a cotectic relation between pigeonite and augite occurs instead, and it is reasonable to assume that the geometry of the complex natural system is such that no odd reaction occurs among olivine, augite, and liquid. ISC (3), Fig. 13.5b, represents the addition of pigeonite to the natural crystal assemblage. In the model diagram, the assemblage is Di<sub>ss</sub> + Pig, and olivine is now absent. In the actual intrusion stratigraphy, olivine persists to a slightly higher level than this, but then disappears at the start of the olivine hiatus. The two diagrams therefore give satisfactory qualitative explanations for the sequential appearance of augite and pigeonite, and the disappearance of olivine.

In the actual intrusion, this sequence is accompanied by strong iron enrichment, for reasons yet to be discussed (Chapter 16), and eventually pigeonite becomes unstable with respect to iron-rich olivine plus liquid.

To illustrate both the difficulties and benefits of trying to make a quantitative match between phase diagrams and natural rocks, attention is called to Fig. 13.6, a partial representation of Fo-Di-An. On this diagram are plotted the normative F:D:A ratios of three analyzed Skaergaard rocks

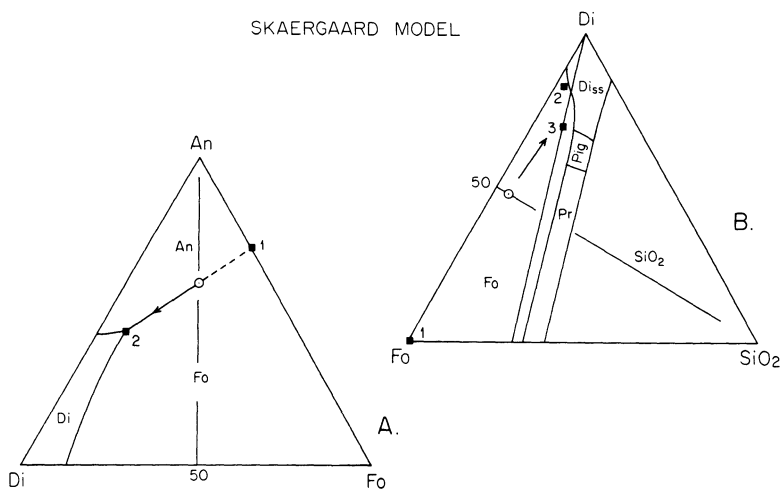


**Figure 13.5** The systems Fo-Di-An (a) and Fo-Di-SiO<sub>2</sub> (b), showing the model ISC's corresponding to an idealized Skaergaard sequence.

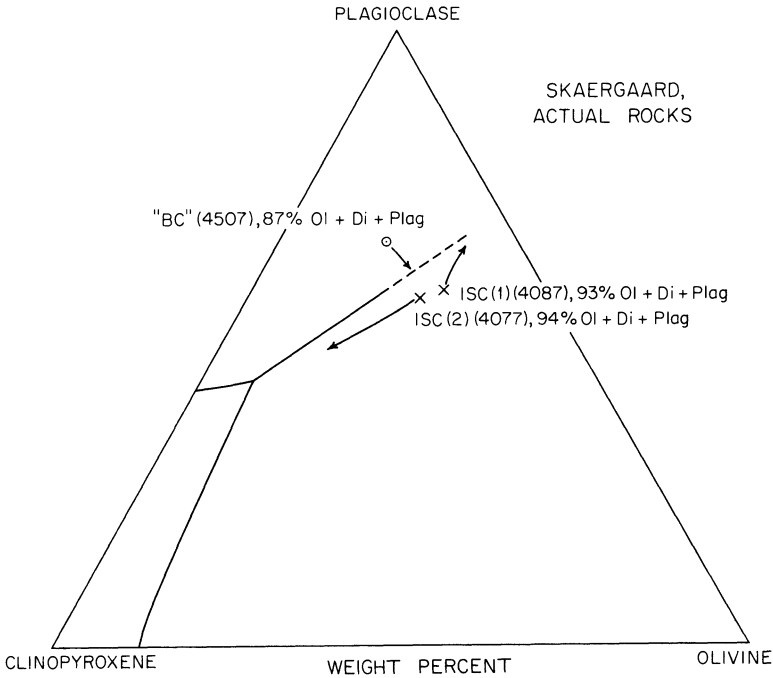


**Figure 13.6** The system Fo-Di-An with normative plots of three analyzed Skaergaard intrusion rocks. The analyses are taken from Wager and Brown (1968), Tables 4 and 5. Arrows indicate relocations needed for consistency; see text.

(Wager & Brown, 1968, Tables 4 and 5). One of these, sample E.G. 4507, is from the fine-grained marginal rocks, and it was considered by the authors to represent, as closely as any rock, the original magma composition. Of the other two samples, E.G. 4087 represents the base of the exposed layered group, an “average rock” plagioclase-olivine cumulate, and E.G. 4077 represents the first olivine gabbros after the arrival of cumulus augite. It is also described as an average rock in the sense that it is neither a dark nor a light layer as near as can be determined in the field. If the model and plotted points were correct in every way, the three plotted rocks should all be collinear, corresponding to the three points plotted in Fig. 13.5a. There are always dangers in plotting normative compositions directly onto phase diagrams, but in this case the projection is made over a short distance, because all three compositions consist of around 90% normative olivine, diopside, and plagioclase. Because of this, the severe failure of the points to form a collinear plot cannot be ascribed solely or even largely to the plotting procedure. The alleged bulk composition is much too plagioclase-rich to be consistent with the two cumulate rocks. Similar conclusions emerge from the experimental work of Tilley, Yoder, and Schairer (1963) on this rock, in which the crystallization sequence is plagioclase, olivine, clinopyroxene. Arrows are drawn in Fig. 13.6 to show

how the points would have to move in order to have the correct relationship to each other.

Another feature of interest in Fig. 13.6 is the closeness together of the two cumulate rocks. The first, ISC (1), clearly contains a large amount of augite, and it may reasonably be deduced that an appreciable quantity of intercumulus liquid was trapped in this rock among the cumulus plagioclase and olivine crystals. According to the diagram, the amount of trapped liquid was close to 30% if the liquid had the composition of the piercing point. Similarly, ISC (2) is almost surely too augite-poor to represent adequately a cumulate olivine gabbro. This must be a plagioclase-olivine-(augite) cumulate in which relatively little of the crystallizing augite came to rest; in other words, the mineral ratios were no doubt disturbed by mechanical crystal sorting effects.

The phase diagram is useful in showing that these particular rocks are not internally self-consistent as representatives of bulk composition and crystallization products, despite the fact that the overall Skaergaard crystallization sequence is readily explained in terms of simple systems.

## Stillwater Complex

A number of large layered intrusions are characterized by a basal ultramafic zone, overlain by gabbro, norite, or anorthosite. Among these are the gigantic Bushveld Igneous Complex of South Africa, the Great Dyke of Zimbabwe, the Muskox intrusion of Canada, and the Stillwater Complex of Montana. All are Precambrian in age. The latter is exposed over a length exceeding 40 km, and apparently represents the basal and middle portions of a thick sheet, the upper parts of which are now lost to view. The petrology of the complex is the subject of a memoir by Hess (1960), and more recent studies by Jackson (1961, 1970) have contributed greatly to the understanding of stratigraphic complexities in this and other layered intrusions. We shall focus here only on the discovery and analysis by Jackson of *cyclic units*.

In the Stillwater, as in certain other layered complexes, the basal Ultramafic Zone is characterized by stratigraphic cycles superimposed on the smaller-scale features of rhythmic layering. Jackson (1961) has recognized at least 15 such cycles in the Peridotite Member, each one typically consisting essentially of the sequence: olivine cumulate; orthopyroxene-olivine cumulate; orthopyroxene cumulate. (The economically important mineral chromite also occurs in certain olivine cumulates, but this will be ignored for present purposes.) The idealized rock sequence in each cycle is therefore: dunite; harzburgite; bronzitite. Actual rocks of these precise compositions occur only where the retention of intercumulus liquid has been minor. The orthopyroxene cumulate (upper) part of each cycle is

sharply succeeded by the olivine cumulate basal part of the next higher cycle. The Peridotite Member is succeeded upward by a thick Bronzite Member, followed by an even thicker sequence of plagioclase-bearing rocks. Of special importance is the fact that within the Peridotite Member there is a gradual up-stratigraphic progression of chemical composition from *cycle to cycle*, which means that whatever process caused the repetition of cycles also caused a long-term irreversible fractionation trend in the bulk magma.

Such cyclic stratigraphy could be ascribed to repeated injections of parent magma, each batch fractionating from the olivine field to the orthopyroxene field of such a model system as Fo-An-SiO<sub>2</sub>. Jackson, however, considers the long-term fractionation trend overlaid on all cycles to mitigate against this interpretation, unless one accepts that the repeated injections arrived from another reservoir of magma which was itself undergoing fractional crystallization. Instead, Jackson argues for a periodic convective overturn of the entire magma in a closed system to account for the start of each new cycle. Such an overturn is considered to have thoroughly mixed the main magma with the locally fractionating batch, and to have caused resumption of olivine crystallization.

The effects of such a mixing process may be analyzed graphically with the aid of an enlarged view of part of the system Fo-An-SiO<sub>2</sub>, Fig. 13.7. Eight mixing events are depicted in the diagram. The first three occur entirely within the olivine field. The liquid moves away from BC by crystallizing olivine, and when it reaches the barb labelled (1), convective overturn and complete mixing take place. The main magma is now depleted in olivine enough to bring its composition to crossbar (1) on the liquid path. (The position of this crossbar is arbitrarily chosen, and of course its actual position would depend upon the ratio of locally fractionated liquid to the main magma.) During the second period of crystallization, the liquid advances to barb (2), and is then mixed back to crossbar (2). The rock cycles representing the first three crystallization events would of course consist wholly of olivine, being "beheaded" in the sense of Jackson (e.g., 1970). The fourth crystallization event, however, yields orthopyroxene (Opx) as the liquid reaches and passes the Pr field boundary. After an excursion away from En, the liquid is mixed with the previous main magma (crossbar 3), and from now on the mixing events take the main magma further and further from the old olivine-liquid mixing line. When the main magma reaches crossbar (6), conveniently chosen to lie on the peritectic field boundary, olivine can no longer crystallize, and succeeding crystallization events produce only Opx until the *L* (Plag, Opx) cotectic is reached.

Ideally, such a series of crystallization-mixing events would produce three olivine cumulate-orthopyroxene cumulate cycles, and two orthopyroxene cumulate cycles before producing norites. No cycle would contain the olivine-orthopyroxene cumulate assemblage which occurs persistently as the middle part of each cyclic unit, because the peritectic field boundary

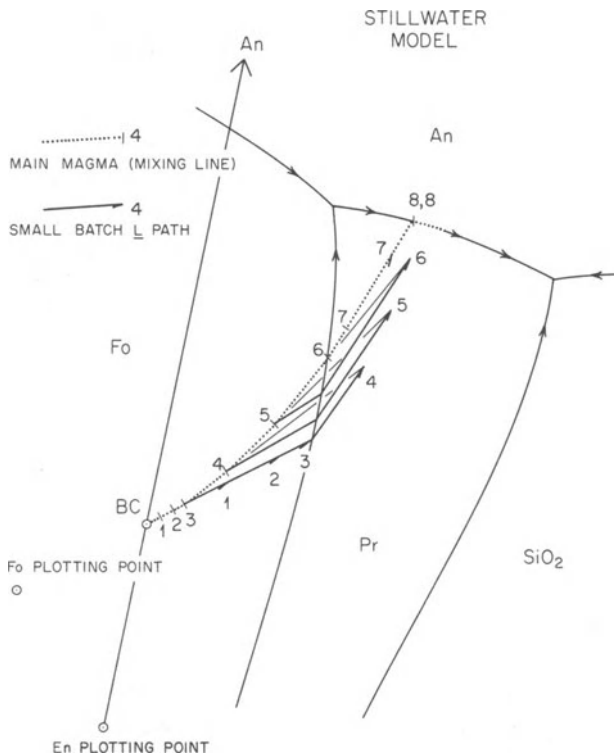


**Figure 13.7.** A modification of Jackson's (1967) mixing model for cyclic units in the Stillwater Complex. Each numbered barb represents the advance of a small batch of magma before convective mixing with the main magma. The periodically mixed main magma follows the dotted path.

does not permit simultaneous crystallization of both olivine and orthopyroxene. However, the middle parts of units described by Jackson contain relatively minor olivine and invariably show an upward increase in the Opx:Ol ratio, and it is quite possible that they represent physically mixed gradations between pure olivine and orthopyroxene cumulates. It could also be argued that differing levels of nucleation caused olivine crystallization to persist longer in one part of the crystallizing liquid than another, or that olivine crystallization persisted for a time "by mistake" (i.e., metastably) after the initial nucleation of orthopyroxene. Therefore, the crystallization-mixing mechanism proposed by Jackson appears reasonable in principle, and can be approximated by the graphical analysis shown in Fig. 13.7.

The graphical analysis also suggests that a test of the proposed mechanism may possibly be available. The main magma mixing line shows ever-increasing plagioclase content after the Opx field boundary has once been reached. If it were possible to determine, in certain rocks, the composition

of trapped intercumulus liquid (postcumulus material of Jackson), the amount of plagioclase in this material should increase with stratigraphic height within the Ultramafic Zone, if the model is correct. Such a trend would not rule out fractionation in a subjacent chamber, but it would at least rule out repeated injections of fresh parent magma. The test may be too difficult to apply with sufficient accuracy, but it is probably worth trying.

An alternative scheme for producing olivine-orthopyroxene cumulates was proposed by Irvine (1970), who suggested rather persuasively that pressure conditions may have permitted *cotectic* crystallization of olivine and orthopyroxene followed, with further fractionation, by a peritectic relationship. This is a thermodynamic equilibrium solution as opposed to my inherently kinetic solutions, suggested above. Further experimental work at elevated pressure may well decide the matter.

It should be explained that the graphical analysis of Fig. 13.7 follows the ideas expressed in Jackson's (1970) text, but differs from his drawings.

## Muskox Intrusion

This remarkable body occurs in the Canadian Northwest Territories, and consists in its exposed area of a funnel-shaped mass tapering southward into a feeder dike. Sharp gravity anomalies suggest that the exposed body is only a small part of a very substantial intrusion to the north, overlain by the Proterozoic and Paleozoic sedimentary rocks of the Coronation Gulf geosyncline. The intrusion has a gabbroic (tholeiitic) chilled margin, but the exposed layered rocks are overwhelmingly dominated by ultramafics, with characteristic cyclic units. It is among the most recently discovered of the great layered intrusions, and has received intensive study by members of the Canadian Geological Survey (e.g., Smith, 1962; Smith and Kapp, 1963, Smith, Irvine, and Findlay, 1966; Irvine and Smith, 1967). A petrologic assessment of this and other layered intrusions by Irvine (1970) is perhaps the first thorough attempt to apply phase diagrams to layered intrusions. What follows is drawn largely from this latter work.

The repetition of cyclic units in the Muskox ultramafic and mafic rocks led Irvine and Smith (1967) to conclude that repeated influxes of relatively undifferentiated magma occurred, and moreover that these influxes probably came from the large, hidden reservoir to the north, using the presently exposed outcrop area as a thoroughfare to volcanic vents located southward. Such behavior would also account for the ultramafic nature of the layered rocks, assuming a tholeiitic magma which crystallized large amounts of mafic minerals before plagioclase.

The diagrams of Fig. 13.8 indicate the general crystallization sequences of Muskox rocks. Fig. 13.8a is Irvine's deduced Ol-Cpx-Plag diagram

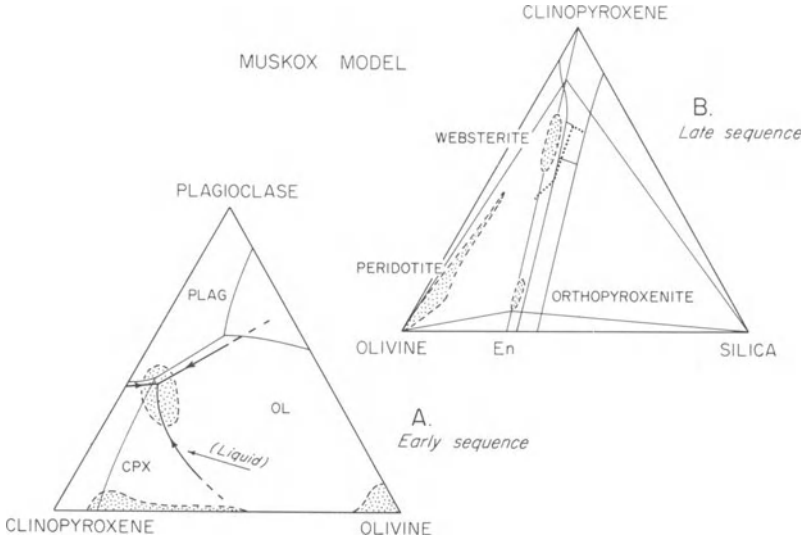


**Figure 13.8.** (A) The projected system Ol-Cpx-Plag compared with Fo-Di-An, and showing the fields (stippled) occupied by Muskox rocks of the early sequence. (B) The system Fo-Di-SiO<sub>2</sub>, showing the superimposed Ol:Cpx:Plag fields (stippled) of Muskox rocks of the late sequence. Both diagrams adapted from Irvine (1970).

superimposed on the experimental Fo-Di-An system. The strong curvature in the *L* (Cpx, Ol) boundary is suggested by the experimental work of Hytönen and Schairer (1961) on the system En-Di-An. Actual modal analyses of the lower ultramafic group of Muskox rocks plot with strong concentrations in the stippled areas, and are thus dunites, olivine clinopyroxenites, and olivine gabbros, as would be expected from fractionation of such a liquid as indicated in the figure. Although the diagram and the rock sequence closely resemble the pure system discussed in Chapter 9, Irvine explains the wide variation in Ol:Cpx ratios of olivine clinopyroxenite as due to the strong curvature of the Ol+Cpx cotectic. It is readily seen that a liquid moving along such a curved boundary with fractional crystallization would yield a wide range of ISC's on tangents to the liquid path. The inward extents of the fields of modal dunites and olivine clinopyroxenites are reasonably explained by the incorporation, in the accumulated rocks, of about 10% intercumulus liquid.

Although the curvature of the *L* (Cpx, Ol) boundary is credible in terms of experimental evidence, it does not seem to be the only reasonable explanation for a wide range of Cpx:Ol ratios. This range could perhaps also be ascribed to varying perfection in the relative sorting of olivine and pyroxene in the presence or absence of currents, or to different stages of fractionation in different levels of the crystallizing magma. The latter idea amounts to a secular motion of the Ol + Cpx cotectic interface away from the principal cooling surface. Having mentioned this idea once before in

connection with the Stillwater cyclic units, I should perhaps illustrate the notion with Fig. 13.9. This figure purports to show nuclei only in a column of magma at two different times, assuming cooling at a lower interface and progressive upward migration of isotherms with time. It is assumed that all crystals settle to the floor, and do so rapidly with respect to the upward motion of the cotectic interface. At time 1, the part of the column yielding olivine is large relative to the part yielding both nuclei, and the steady-state ratio of olivine to pyroxene arriving at the floor is large. At time 2, the steady-state yield of olivine to the floor is relatively smaller, and the modal percentage of pyroxene is larger. At an even later time, not shown, the cotectic interface would reach the uppermost limit of nucleation, and only at that time would the maximum, cotectic yield of pyroxene at the floor be realized. Such a mechanism must operate often in nature, when a new cumulus phase appears, for seldom if ever does a cumulate sequence show the arrival of a second phase in full modal abundance in the first layers; instead, it is common to see a gradual buildup of the second phase to some standard abundance level.

Figure 13.8b shows a recent version of the system Fo-Di-SiO<sub>2</sub> with stippled areas representing modal concentrations of the upper ultramafic group of Muskox rocks. The sequence peridotite-orthopyroxenite-websterite is evident in the diagram, and the effects of some 20–30% trapped intercumulus liquid are seen especially in the peridotite and orthopyroxenite

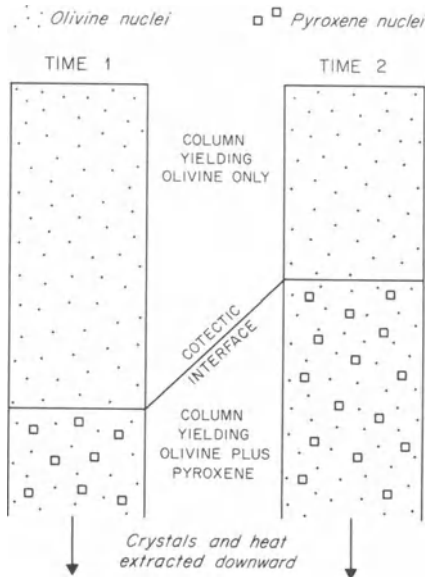
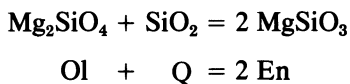


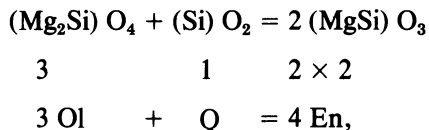
**Figure 13.9.** A kinetic model for explaining the systematic increase of Cpx/Ol ratios in cyclic units of the Muskox intrusion (see Fig. 13.8a). For discussion, see text.

modal concentrations. A liquid path such as shown in the dotted line would yield such a sequence of rocks, except that the experimental system as now understood would predict pigeonite after orthopyroxene, and would predict a more clinopyroxene-rich range of websterite. Possible reasons for these apparent discrepancies will be entertained below.

Irvine (1970) has developed two useful projections of the quaternary system Fo-Di-An-SiO<sub>2</sub> in order to analyze the sequences of crystallization observed in the Muskox and other layered intrusions. The principal facts to be accounted for in the Muskox are the upward change from the lower repeated sequence: olivine; clinopyroxene + olivine; plagioclase + olivine, Fig. 13.8a to the upper repeated sequence: olivine, orthopyroxene, clinopyroxene + orthopyroxene; plagioclase + clinopyroxene + olivine (Fig. 13.8b in part). In order to make quantitative comparisons, Irvine has recalculated the chemical analyses of layered rocks and chilled margins as Barth-Niggli katanorms (Chayes and Métais, 1964), which are cation norms, similar to the CIPW norm but omitting the last step of converting molar amounts back to weight amounts. Phase diagrams are also plotted in *cation equivalents*<sup>2</sup> rather than weight percent so that they can be compared directly to the plotted chemical analyses. This procedure eliminates the ambiguities which arise when plotting, in weight percent, mineral compositions which are not pure end-member compositions. For example, the iron end member pyroxene FeSiO<sub>3</sub> (ferrosilite, Fs), plotted on the join Fe<sub>2</sub>SiO<sub>4</sub> (fayalite) - SiO<sub>2</sub> does not fall at the same place as MgSiO<sub>3</sub>, plotted on a superimposed join Mg<sub>2</sub>SiO<sub>4</sub> - SiO<sub>2</sub>, in weight percent. When plotting molar amounts or cation equivalents, one may plot olivine in general at one corner, SiO<sub>2</sub> at another corner, and orthopyroxene in general (En + Fs) at a single point between the two corners. The cation equivalent formulation, as the name implies, is based on the number of cations in a formula, not the number of moles. Thus the molar equation



becomes, in cations,



and Opx plots at the point 3 Ol, 1Q in a cation equivalent diagram.

The model system Fo-Di-An-SiO<sub>2</sub> used by Irvine in 1970 lacked a pigeonite field. The behavior of this field as An is added to the face Fo-Di-SiO<sub>2</sub> is as yet experimentally undetermined. However, one may speculate on geological grounds that the inner geometry of the quaternary system

<sup>2</sup>See Appendix 1B.

should permit the assemblages  $Cpx + Opx + Ol + Plag$  and  $Cpx + Pig + Plag \pm SiO_2$ . A preliminary and quite speculative step toward such a solution is shown in Fig. 13.10 for the pure endmember system  $Fo-Di-An-SiO_2$ . The figure is introduced at this time primarily to illustrate the projections of Irvine, and we may postpone for a while the matter of how the pigeonite field closes off with increasing plagioclase content in the generalized system  $Ol-Cpx-Plag-Q$ .

The two projections which Irvine found useful are 1) the  $Ol$  projection from  $Ol$  into the plane  $Cpx-Plag-Opx$ , and 2) the  $Cpx$  projection from  $Cpx$  onto the  $Ol-Plag-Q$  plane. In terms of Fig. 13.10, these amount to 1) a map of the  $Fo$ -saturated surfaces projected onto the  $Di-En-An$  plane, and 2) a map of the  $Di$ -saturated surfaces projected onto the base. The second of these will have the general appearance of  $Fo-An-SiO_2$ , and the first will have the general appearance of a ternary eutectic system where the fields of  $An$ ,  $Pr$ , and  $Di$  meet in a point. The view chosen by Irvine for the latter projection is with the eye at  $Fo$ , looking toward the  $Di-En-An$  plane, with

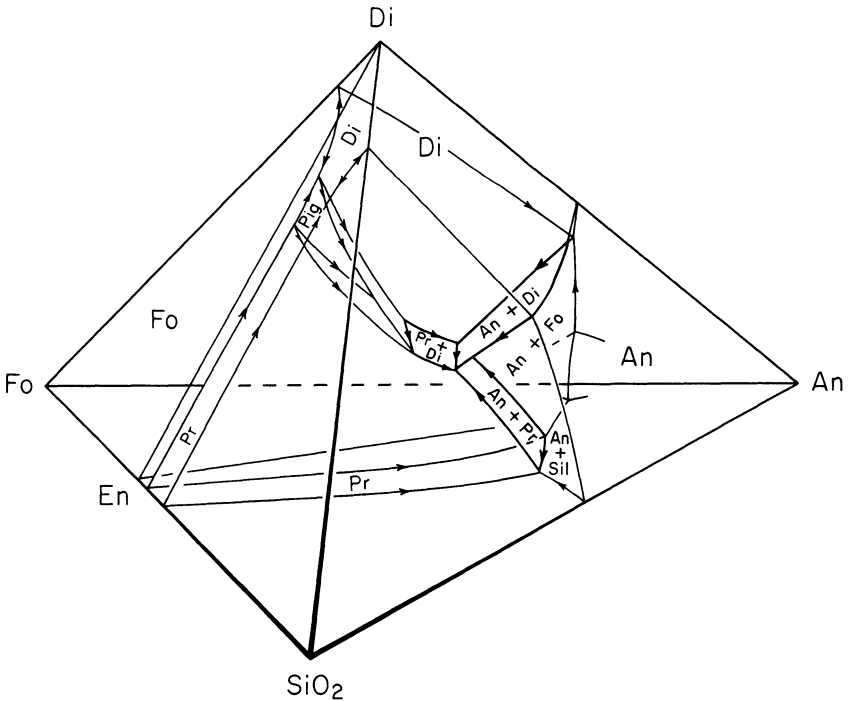


**Figure 13.10.** Speculative arrangement of internal relations in the system  $Fo-Di-An-SiO_2$ . The projections of the following two figures ignore the  $Pig-Di_{ss}$  surface altogether. The termination of this surface is discussed later in the chapter. The ternary face  $Di-An-SiO_2$  is taken from Clark, Schairer, and de Neufville (1962).

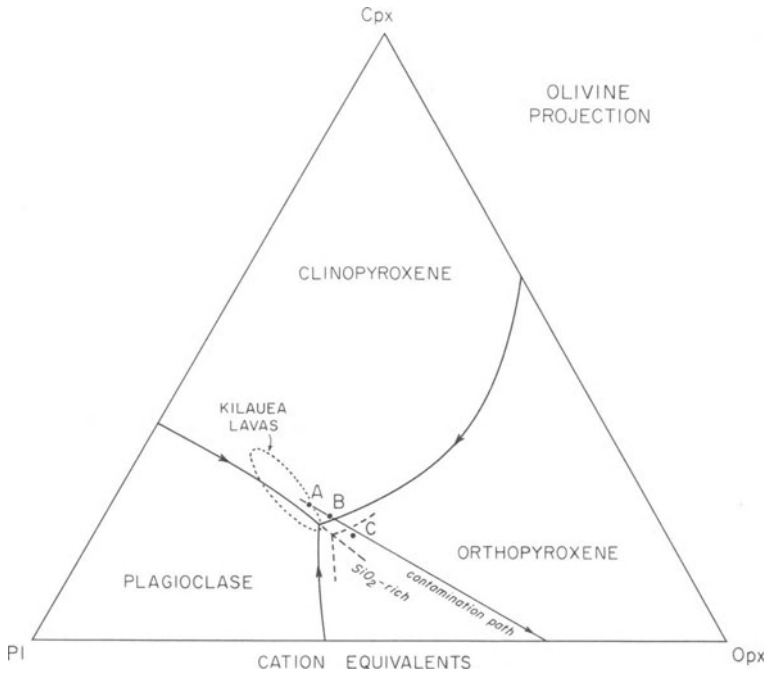


**Figure 13.11.** Projection from olivine of the olivine-saturated liquid surface in the system Ol-Cpx-Plag-SiO<sub>2</sub>, approximately equivalent to the same surface in Fig. 13.10, mapped onto the Opx-Pl-Cpx plane. After Irvine (1970). The plotted compositions represent the Muskox chilled margin (A), and hypothetical liquids formed by contamination with granophyre (B and C). The dashed field boundaries represent equilibria in the absence of olivine.

En at the right. It is to be remembered that in all projections the labelled assemblages are always saturated with the projecting phase.

The projections used by Irvine (1970) are not those of the pure end member quaternary system, but of Ol-Cpx-Plag-Q in general. The projections, redrawn in Figs. 13.11 and 13.12, were cannily drawn with the aid of all available experimental data and selected data on natural rocks. The success of the projections is attested by the fact that Kilauea lavas plot in regions which are consistent with their general crystallization history. For example, in Fig. 13.11, these lavas plot with concentrations in the dotted ellipse, and as the projection would predict, they tend to contain phenocrysts of augite and plagioclase in company with olivine, and to show later crystallization of orthopyroxene. Similarly, the lava compositions are concentrated in Fig. 13.12 in an elongate pattern reaching back toward olivine (picritic basalts) and then following very closely along the *L* (Plag, Ol) boundary.

Fig. 13.11 represents equilibrium with olivine except along the short

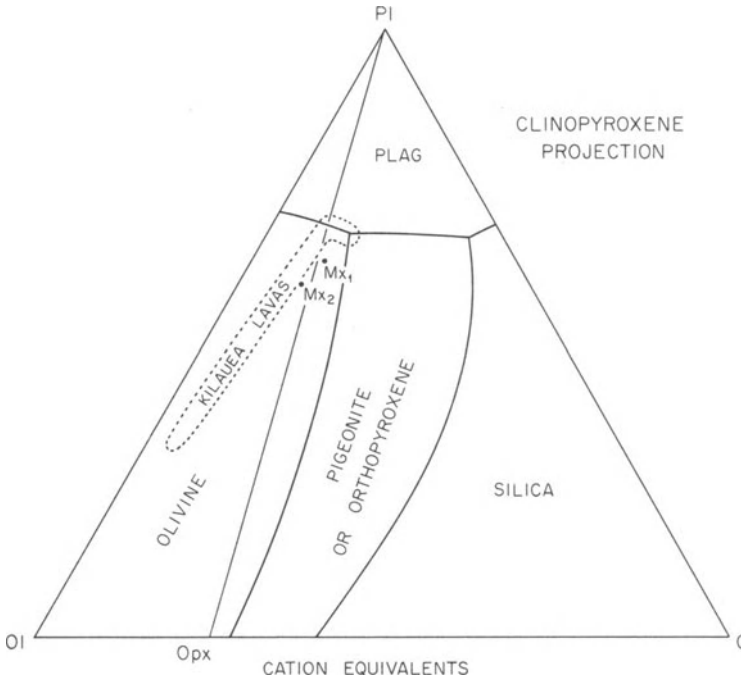
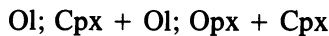


**Figure 13.12.** Projection from clinopyroxene of the Cpx-saturated liquid surface in the system Ol-Cpx-Plag-SiO<sub>2</sub>, approximately equivalent to the same surface in Fig. 13.10, mapped onto the Ol-Plag-Q plane. The plotted compositions represent individual analyses of Muskox chilled marginal rocks.

dashed lines which represent the migration of field boundaries with silica in excess of that required for orthopyroxene. Bulk composition A is calculated directly from the Muskox chilled margin composition. Upon fractional crystallization, it gives the main sequence



found in the repeated cyclic units of the lower ultramafic group. Bulk composition B, on the other hand, yields the intermediate sequence



which is found between the lower and upper sequences. Bulk composition C yields the upper sequence



to which the dashed boundaries apply, since fractionation involving the Ol-Opx boundary leads quickly to silica oversaturation. The line through A and B leads toward a model granophyre composition, and it is Irvine's contention, backed by persuasive independent evidence, that the upward

changes in crystallization sequence result from gradual contamination of succeeding magma batches by partially melted roof rocks. (The intrusion is capped with a granophyre sheet and contact breccia which provide direct evidence for melting of the overlying country rocks.) Such a long-term contamination scheme, dependent in part on the time available for melting significant amounts of country rock, can satisfactorily account for all the principal crystallization sequences in the Muskox, including some extended examples treated by Irvine but omitted here. It is considered that the repeated and almost quantitative flushing-out of the magma chamber by new magma batches ceased at a time corresponding to upper parts of the exposed intrusion; these upper parts show strong evidence of iron and albite enrichment consistent with a late-stage closed system history for the final magma batch.

Figure 13.12 shows the locations of two analyzed Muskox chilled marginal samples, both of which are consistent with the lower sequence of the ultramafic group: olivine; clinopyroxene + olivine; plagioclase + olivine. Evidently these chilled marginal samples are internally consistent with the observed crystallization order.

The projections developed by Irvine (1970) have been used by him to illuminate and discuss the crystallization of many other layered intrusions, all tholeiitic. The projections are remarkably successful in their consistency with either the natural or experimentally determined crystallization sequences.

## The Pigeonite Field in Fo-Di-An-SiO<sub>2</sub>

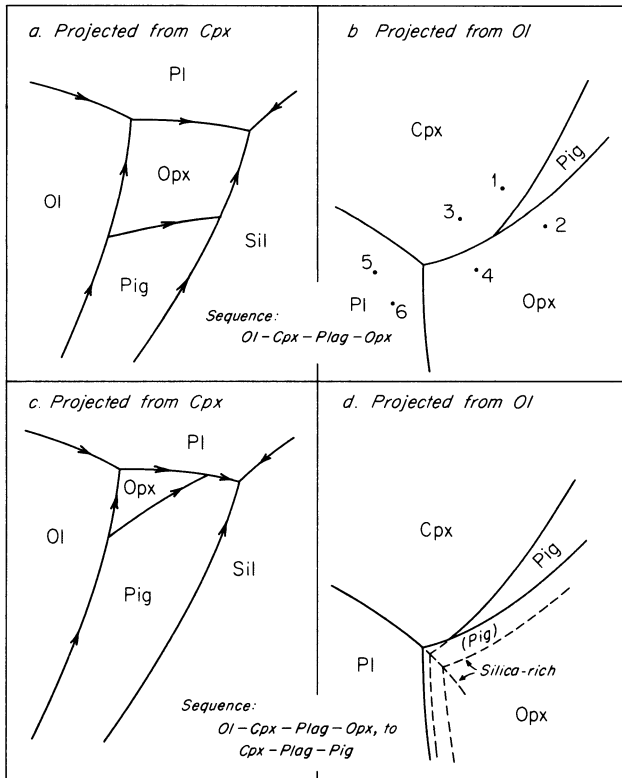
The sequence [olivine + plagioclase + augite] + orthopyroxene → pigeonite is commonly observed in tholeiitic basalt fractionation products. The succession Opx → Pig always takes place with increasing iron enrichment, so that pigeonite is characteristically a lower-temperature product with higher Fe/Mg ratio compared to orthopyroxene. Both Ca-poor pyroxenes commonly occur with augite and plagioclase. It is therefore prudent to explore the innards of the Fo-Di-An-SiO<sub>2</sub> tetrahedron to see if an appropriate termination of the pigeonite field can be found which will yield the commonly observed sequence.

Fig. 13.10, as mentioned previously, has a provisional solution which, in the present absence of internal data, may suit as well as any. If the Pig-Di boundary surface led straight to the An + Di surface, there would be no possibility of Di-Opx equilibrium, which the natural rocks appear to record. It is therefore assumed that the Pig-Di boundary surface must lead to the Pr + Di boundary surface. The configuration shown in Fig. 13.10 permits the sequences

- 1. Fo + Di; Pig; Pr; An (unlikely)
- 2. Fo; Pr; Pig; Pr + Di; An (unlikely)
- 3. Fo + Di; Pr; An (common)
- 4. Fo; Pr; Di; An (reasonable)
- 5. Fo + An; Pr; Di (reasonable)
- 6. Fo + An; Di; Pr (reasonable)

Points corresponding to each of these sequences are plotted in the Ol-projection, in the upper part of Fig. 13.13

The upper part of Fig. 13.13 represents projections similar to Irvine's from Cpx and from Ol, assuming that the pigeonite field closes as in Fig. 13.10. An interesting feature of the Cpx projection is that the fields of Opx and Pig appear to be reversed from their locations in Fo-Di-SiO<sub>2</sub>; this is a result of the projection from Cpx, and of course the appearance of reversal is illusory, as can be determined by examining the Di-saturated relations in Fo-Di-SiO<sub>2</sub>. The upper part of Fig. 13.13 does, however, make no provision



**Figure 13.13.** Cpx and Ol projections of the termination of the pigeonite field. Upper diagrams: as drawn in Fig. 13.10. Lower diagrams: as inferred to occur with complex magma compositions, notably including FeO.

for the desired sequence  $\text{Opx (Di)} \rightarrow \text{Pig (Di)}$ . The lower part of Fig. 13.13 suggests a modified way of terminating the pigeonite field at an oblique angle to the curve  $L$  (Cpx, Plag, Ca-poor Px). This amounts to lifting the quaternary part of the  $L$  (Pig, Di) surface in Fig. 13.10, leaving it attached at the ternary hinge in  $\text{Fo-Di-SiO}_2$ , and letting it sweep across the quaternary univariant curve just mentioned. Such an enlargement of the interior pigeonite field would probably occur with addition of  $\text{FeO}$  to the system, because we find in nature that the transition  $\text{Opx} \rightarrow \text{Pig}$  is favored by iron enrichment. The relations in the lower part of Fig. 13.13 *do* permit the sequence  $\text{Opx (Di)} \rightarrow \text{Pig (Di)}$  with increasing silica content, although the transition occurs (for plagioclase equilibria) only after olivine ceases to crystallize. This is not a severe restriction; for one thing, we know that in some tholeiitic bodies (e.g., Skaergaard) the disappearance of olivine and the appearance of pigeonite are closely related in time, and for another thing, the progressive "sweeping out" of the Opx field by iron enrichment could generate the  $\text{Opx} \rightarrow \text{Pig}$  transition in the continued presence of olivine.

This is a necessarily brief and incomplete exploration of the various possibilities for the internal arrangements of the system  $\text{Ol-Cpx-Plag-SiO}_2$ . It is offered partly in an attempt to resolve the problem, but more particularly as an exercise in deducing phase relations, starting from known experimental, geological, and theoretical constraints. The analysis is best pursued further with the aid of more information from the field and laboratory.

## Adcumulate Theory

Among the important matters so far avoided in this discussion of phase diagrams and layered intrusions is the matter of adcumulate growth in crystal layers deposited from magma. A brief review of this important principle is warranted here.

Hess (1939) was perhaps the first to point out the seeming incongruity of any layer of rock which apparently consists only of settled minerals of constant composition. No sediment can accumulate with a porosity of zero, and many recent studies in both field and laboratory have suggested that a porosity of up to 40% is very likely to occur in natural crystal cumulates. If the pore liquid is trapped and sealed off by further sedimentation, it must crystallize in place over a substantial temperature range, and the results should be zoned crystals and new phases. How then can a layer consist of pure olivine, or pure bronzite, or pure plagioclase, without interstitial pockets of gabbro and zoned crystals? The answer suggested by Hess, and thoroughly elaborated by Wager, Brown, and Wadsworth (1960), was called adcumulus growth by the latter authors.

Adcumulus growth requires the diffusion of chemical components from the intercumulus liquid (occupying pore space) to the overlying magma reservoir. Presumably, the main magma must be continuously flowing past the interface, and must act as an infinite reservoir for chemical exchange. As the concentrations of low-temperature components such as Fe and Na tend to build up in the intercumulus liquid, these components must diffuse down concentration gradients into the passing stream of main magma. Similarly, as components such as Mg and Ca are depleted by continued overgrowth of material on cumulus crystals, they must be replenished by diffusion into the intercumulus liquid from the main reservoir. The main requirement for such a process is that the rate of sedimentation be sufficiently low relative to the rate of diffusion. In order to make a perfect adcumulate rock, the diffusion channels must remain open down to the stage of thin films. The existence of near-perfect adcumulates shows that these requirements are met with near perfection in some intrusions at certain times.

If the conditions are not met, and specifically if the sedimentation rate becomes so rapid as to prohibit effective diffusive exchange altogether, the resulting cumulate rock will consist of cumulus crystals and interstitial postcumulus material of variable composition. Rocks approaching such a state are frequently observed, and they are called *orthocumulates*. Rocks intermediate between the two limiting kinds are called *mesocumulates*. There are no generally accepted quantitative cutoff criteria to separate the three classes of cumulates, which is probably just as well.

A little reflection will show that adcumulates, having constant mineral composition, must be the products of isothermal growth. They become completely solidified at the same temperature as that at which the cumulus crystals formed. Orthocumulates become completely solidified only after cooling through perhaps several hundred degrees, as the liquid fractionates in place. An alternating succession of adcumulate layers and orthocumulate layers will consist for a very long time of solid layers among layers of crystal mush. Any earthquake or other physical disturbance, including loading or flow along a slope, will tend to disturb the crystal mush layers, causing such features as small-amplitude folds, auto-intrusion, and brecciation. Such features can be seen in layered intrusions, providing convincing evidence for the proposed solidification mechanisms.

In terms of phase diagrams, perfect adcumulates represent the limiting condition of perfect fractional crystallization, and they have compositions analogous to the ISC's of fractional crystallization exercises. Orthocumulates represent imperfect fractional crystallization, and have compositions analogous to ISC's contaminated with, say, 40% liquid. Mesocumulates, in which perhaps half the intercumulus liquid succeeds in exchanging with the reservoir, are equivalent to ISC's with, say, 20% admixed liquid. The Skaergaard layered rocks plotted in Fig. 13.6 probably approach orthocumulates, and the Muskox rocks plotted in Fig. 13.8 are reasonably called

mesocumulates. The Lower Zone of the Kiglapait intrusion consists largely of rocks very closely approaching adcumulates (Morse, 1979c).

The assessment of the characteristic amount of trapped intercumulus liquid in a given layered group or part thereof is very important to the establishment of quantitative chemical models of fractionation, and especially partition ratios of elements between crystals and liquids. Wager (1960) first pointed out that a single chemical element, namely phosphorus, could be used as a measure of percent intercumulus liquid in rocks where apatite was not yet a cumulus phase. A perfect adcumulate (having no cumulus apatite) should contain no phosphorus. Each increment of trapped liquid should contain a predictable amount of P, which may now occur in apatite crystals so small as to be overlooked. By measuring the actual P content of the rock, and knowing the general trend of P with time in the parent magma, one may deduce the amount of intercumulus liquid relative to cumulus crystals. Such a method has been extended to a least-squares fit of many trace elements by Paster, Shauwecker, and Haskin (1974).

Perhaps the most spectacular kind of evidence for adcumulate growth occurs in the Fe-Ti oxide layers of such intrusions as the Kiglapait. In this intrusion, a layer up to 2/3 m thick commonly consists of more than 99% Fe-Ti oxide, the adcumulus growth process having almost quantitatively removed all silicate components.

Adcumulate growth theory is a modern triumph of observational petrography. As with the best of powerful theories, its consequences are so obvious and so potent in the further interpretation of layered rocks that it achieved almost immediate acceptance. Its advent, coupled with the advent of the electron probe, may be said to mark the rebirth of microscope petrography as a respected and essential tool of petrology.

## Chapter 14

# Nepheline-Silica and the Rest of the Basalt Tetrahedron

### Introduction

In this chapter we return to the basalt tetrahedron as a model for the crystallization of basalt magma, and conclude the discussion of phase diagrams related to this system at one bar pressure. A brief discussion of the system Nepheline - Silica ( $\text{NaAlSi}_3\text{O}_8$  -  $\text{SiO}_2$ ) serves to introduce the important principle of the *thermal barrier* (or thermal divide) which tends to prevent silica-undersaturated liquids from producing *critically* undersaturated residua and vice versa. A review of the rest of the tetrahedron serves as a summary of earlier chapters and as a conclusion regarding the lessons of the fundamental basalt tetrahedron. This review will serve as the background for examination, in succeeding chapters, of the effects of other components and of pressure on the phase relations of basaltic systems.

It is to be emphasized that in this chapter no attempt is made to provide a thorough discussion of basalt genesis, but instead to focus on some of the theoretical constraints and principles provided by phase diagrams.

### Nepheline-Silica

Nepheline,  $\text{NaAlSi}_3\text{O}_8$  or  $1/2 (\text{Na}_2\text{O} \cdot \text{Al}_2\text{O}_3 \cdot 2\text{SiO}_2)$ , is the most important of the feldspathoid group of minerals from the standpoint of rock genesis. As we have seen, the standard CIPW norm calculation reflects the central importance of this mineral among the critically undersaturated natural

rocks. By the convention of this calculation, silica deficiency is first remedied by converting albite to nepheline, and the appearance of *ne* in the norm is always sufficient evidence of a critically undersaturated rock warranting such names as alkali basalt, basanite, olivine nephelinite, etc. Nepheline may occur in such rocks as part of a late mesostasis, intergrown with alkali feldspar, or more rarely as independent crystals. The natural mineral always contains “excess” silica (deficient alkali and aluminum) when it is soda rich, the amount of this “excess” decreasing as the composition of  $Ne_{ss}$  varies toward  $KAlSiO_4$ .

Nepheline is synthesized, as is albite, from sodium disilicate ( $Na_2O \cdot 2SiO_2$ ) which serves to fix the volatile alkali metal, and  $Al_2O_3$ . The procedure is described in detail by Schairer and Bowen (1956). In the laboratory, a high temperature polymorph is encountered above  $1254^\circ C$ , persisting to the melting point at  $1526^\circ C$ ; this polymorph was named carnegieite in honor of Andrew Carnegie, the founder of the Carnegie Institution of Washington, but the name is not a legitimate mineral name because no naturally occurring example is yet known.

The system  $Ne-SiO_2$  (Greig and Barth, 1938; Schairer and Bowen, 1956) is an excellent example of a binary system with an intermediate compound, albite, which melts at a maximum and generates two eutectics, one with each of the end-member phases (Fig. 14.1). The Ne-rich portion of the diagram presents certain complexities which may be disposed of in a brief analysis.

As Fig. 14.1 shows, solid solution toward  $SiO_2$  is a feature common to both polymorphs of  $NaAlSiO_4$ , the sole exception being at the melting point of the substance, where the highest thermal stability is shown by the pure compound. The Ne-rich side of the diagram therefore shows large regions of solid  $Ne_{ss}$  and  $Cg_{ss}$  where no liquid is involved. Each of these regions is isobarically divariant ( $c = 2$ ,  $\phi = 1$ ,  $W_p = 3-1 = 2$ );  $T$  and  $X$  can be varied without changing the state of the system within each region. A small univariant *phase transition loop* originates at the inversion point,  $1254^\circ C$ , on the Ne sideline, and is truncated by the melting loop  $Cg_{ss} + L$  at  $1280^\circ C$ . This small two-phase field represents the mutual saturation limits of relatively silica poor  $Cg_{ss}$  and relatively silica-rich  $Ne_{ss}$  at any given temperature in the range  $1254-1280^\circ C$ . At any given temperature in this range, any bulk composition within the loop is represented by compositions of  $Cg_{ss}$  and  $Ne_{ss}$  lying on the solid saturation curves at the ends of an isothermal tie line. The lever rule may be applied to find the ratio of the solids to one another. As the temperature rises toward  $1280^\circ C$ , both solids become richer in  $SiO_2$ , but  $Ne_{ss}$  is always the more silica-rich of the two. When bulk compositions near the  $NaAlSiO_4$  composition are heated, a complete conversion to  $Cg_{ss}$  occurs over a temperature interval (as the  $Ne_{ss}$  lever becomes shorter and finally reaches length zero), and  $Cg_{ss}$  then begins to melt at the solidus somewhere between  $1280$  and  $1526^\circ C$ . The  $Cg_{ss} + L$  loop is (except for its lower truncation) like any simple binary melting loop

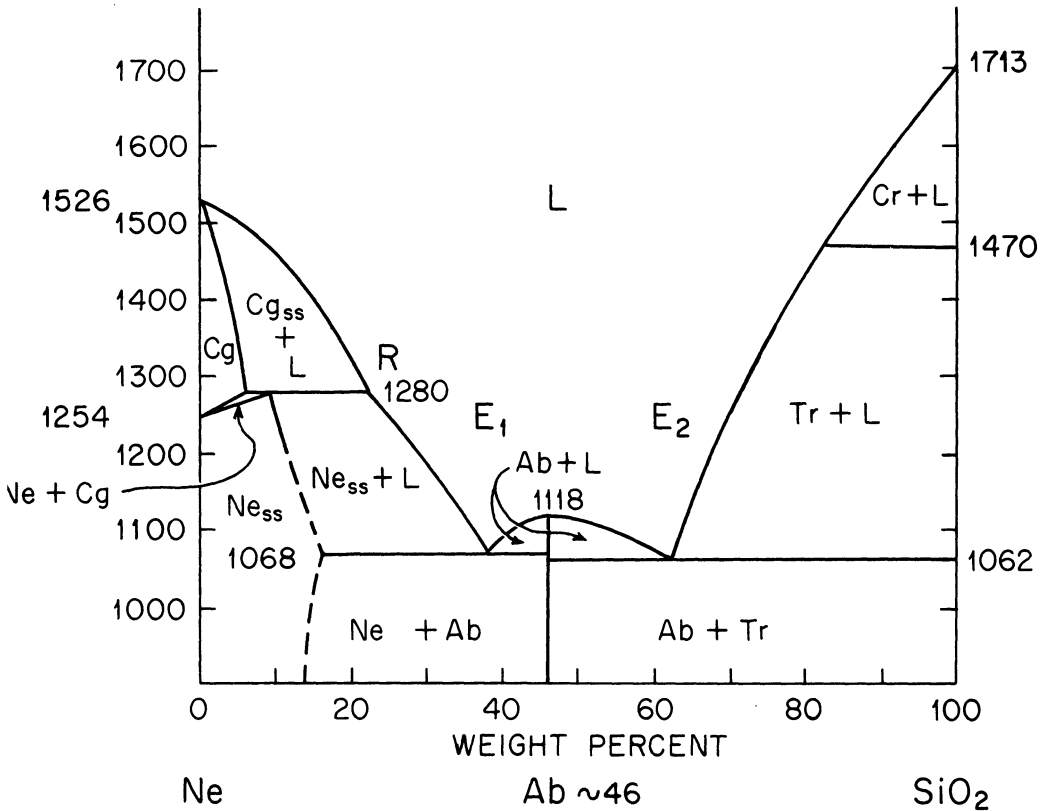


**Figure 14.1.** The system Ne-SiO<sub>2</sub>, after Schairer and Bowen (1956). See text for abbreviations. Base of diagram measures 10 cm.

(the plagioclase loop may serve as an example) and melting takes place with continuous conversion of the solids toward more silica-poor compositions.

If a bulk composition corresponding to Ne<sub>ss</sub>, say at 12% SiO<sub>s</sub>, is heated, a similar melting loop is encountered, and Ne<sub>ss</sub> also changes composition continuously away from SiO<sub>2</sub> as liquid is formed. The Ne<sub>ss</sub> + L loop is a close counterpart of the Cg<sub>ss</sub> + L loop, the two being joined at a discontinuity where, upon addition of heat, Ne<sub>ss</sub> is converted to Cg<sub>ss</sub> in the presence of liquid R. The coexistence of three phases marks this assemblage as an isobarically invariant one; the three phases are collinear, and R is evidently a peritectic (reaction) point for which the heat-removing reaction can be written  $L = \text{Ne}_{ss} - \text{Cg}_{ss}$ . The reaction, which is odd, can also be written  $L + \text{Cg}_{ss} = \text{Ne}_{ss}$ .

The field of Ne<sub>ss</sub> reaches its maximum SiO<sub>2</sub> content at 1068°C, the eutectic temperature of Ne<sub>ss</sub>-Ab mixtures. The limits of the Ne<sub>ss</sub> field in equilibrium with L or Ab are dashed because of experimental uncertainties, but follow the form expected for such a system, as discussed on an earlier

page (Fig. 5.5) where the properties of an idealized binary system are displayed in connection with the system Diopside-Anorthite. The dashed curve of  $Ne_{ss} (Ab)$  (read “ $Ne_{ss}$  saturated with albite”) is in fact the *solvus* of these two phases, and it is intersected by the *solidus*  $Ne_{ss} (L)$  at 1068°C.

The isobaric eutectic  $E_1$  involving  $Ne_{ss}$ , Ab, and  $L$ , can most easily be analyzed by ignoring all of the system to the  $SiO_2$ -rich side of Ab, whereby it becomes evident that  $Ne_{ss}$ -Ab is a simple binary eutectic sub-system of the larger system. The crystallization of any liquid lying between the albite composition and about 20%  $SiO_2$ , 80% Ne is a straightforward process typical of that in any binary eutectic system, ending with the isothermal crystallization of eutectic liquid  $E_1$  at 1068°C. Fractional crystallization has no effect on the composition of the final liquid, and only a minor effect on the amount of the final liquid if  $Ne_{ss}$  is the fractionally removed phase. Fractional crystallization of pure Ab has no effect on the amount of eutectic liquid. Equilibrium and fractional fusion are both straight-forward processes, the main result being the isothermal production of liquid  $E_1$  until one of the solid phases is exhausted.

The  $SiO_2$ -rich side of Ne- $SiO_2$  (Fig. 14.1) is also by itself a simple binary eutectic  $E_2$  between Ab and tridymite at about 62%  $SiO_2$ , 1062°C.

Figure 14.2 shows an alternative possibility for the phase diagram in the region of albite. In this figure, albite shows limited solid solution toward both Ne and  $SiO_2$ , and attains the pure composition  $NaAlSi_3O_8$  with liquid only at its melting point, 1118°C. A moderate degree of solid solution toward Ne was thought by Greig and Barth (1938) to occur, but was not verified by Schairer and Bowen (1956). Since that time, numerous authors have claimed evidence for such an  $Ab_{ss}$  field as shown in Fig. 14.2, based on classical wet chemical analyses of natural feldspars and on experimental studies. Most or all of these claims have been inconclusive because of well-known sources of error inherent in analytical procedures, or because of suspected kinetic difficulties (metastability) in experimental runs. A con-

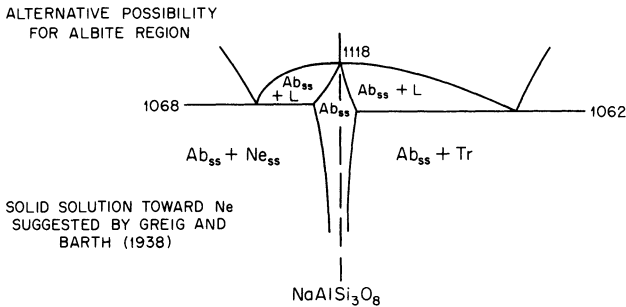


**Figure 14.2.** An alternative interpretation of the albite composition region in Ne- $SiO_2$ , assuming some solid solution of albite toward both Ne and  $SiO_2$ . For discussion, see text.

vincing resolution of the question awaits further work. There can be no doubt that such an  $Ab_{ss}$  region exists, but whether it is wide enough to have geologic significance is the question at hand. The nature of what might constitute "geologic significance" will be discussed shortly.

Assuming either configuration near  $Ab$ , it can be seen that albite melts at a local maximum; all liquids in the primary phase field of feldspar will move away from feldspar on crystallization, toward either  $E_1$  or  $E_2$ . The compound albite thus generates a thermal barrier or divide; no liquid can cross the divide, although two liquids lying infinitesimally near to each other (and to  $Ab$ ) may move in opposite directions, to  $E_1$  and  $E_2$ , thus appearing to yield either residual product from the "same" parent. Moreover, fractional or equilibrium fusion on either side of the divide will yield  $Ab$  as the final solid, and there is no way to drive the residual solid composition across the barrier. The eutectic  $E_1$  is an approximate model of the natural rock phonolite, which is the residual end member of the commonly observed natural alkali basalt fractionation series. Similarly, eutectic  $E_2$  is a synthetic analog of rhyolite, the common acid end member of tholeiitic suites. The composition of albite itself is a model of the natural rock trachyte, and one of the mysteries of petrology is why some fractionation trends terminate in trachyte (or the intrusive equivalent syenite), at an apparent maximum, instead of sliding off toward natural versions of  $E_1$  or  $E_2$ . Explorations of this so-called syenite problem to date have shown that the relative geometric relations are not changed by the addition of  $K_2O$ ,  $H_2O$ , and pressure (Morse, 1969). It is possible that an intricate interplay among Fe oxides and silicates, feldspar, and oxidation controls the fate of such liquids, at least in part. Another contributing factor may be the ability of feldspar to tolerate some deviation from the stoichiometric composition, as in Fig. 14.2, so that with complex magma compositions the thermal "barrier" has finite width, like a plateau rather than a sharp peak. A plateau would be more likely to hold residual trachytic liquids than a peak. This is the main reason for being interested in the extent to which Fig. 14.2 is correct.

## The Thermal Barrier in More Complex Systems

We have already seen, in Chapter 7, that the join Diopside-Albite is non-binary, and cannot itself be a thermal barrier, because liquids leave the system toward  $Na_2O$ - and  $SiO_2$ -rich compositions. Moreover, since  $Di-Ab$  is one edge of the critical plane  $Di-Ab-Fo$ , it is obvious that the critical plane itself is not a thermal barrier. Nevertheless, natural liquids *do* appear to fractionate away from augite, feldspar, and olivine toward either tholeiitic or alkali basaltic residua, and there are good grounds to suppose that a

thermal barrier exists, even though it is not exactly the critical plane in composition. It is appropriate to examine the extent to which the concept does hold up in experimental studies.

Yoder and Tilley (1962) discussed this question extensively, and the ternary diagrams of Fig. 14.3 are taken directly from their Fig. 11. These diagrams show the effect of adding, in turn, leucite (Lc), anorthite, forsterite, fayalite (Fa), diopside, and spinel to the system Ne-SiO<sub>2</sub>. Diagrams (c) and (e) are, respectively, the base and the rear face of the basalt tetrahedron (Fig. 2.1). For present purposes, we are concerned mainly with the arrows on boundaries crossing the join connecting albite to each of the other principal phases. Nevertheless, it is possible to recognize familiar relations, particularly in Fig. 14.3(c), where the incongruent melting of En (labelled Pr) is observed on the sideline Fo-SiO<sub>2</sub> and inside the ternary system as well. The field of Fo overwhelms this diagram, and covers most of the join Pr-Ab as well as most of the join Fo-Ab. The cotectic boundary *L* (Fo-Ab) crosses the Fo-Ab join very close to the Ab composition. Note that arrows point away from the line Fo-Ab on either side, showing that liquids tend either to the isobaric ternary eutectic *L* (Fo,Ab,Ne) or to its silica-saturated counterpart, *L* (Pr,Ab,Tr). The join Fo-Ab is a thermal barrier. Fractional removal of Fo from bulk compositions on either side of Fo-Ab can only magnify the effect of the barrier. The iron end member olivine, fayalite, shows a similar relationship in Fig. 14.3(d). Evidently all members of the olivine series should maintain the thermal barrier relationship with albite.

Diagram (e) shows that liquids move away from the join Di-Ab toward eutectics *L* (Di,Pl,Ne) and *L* (Di,Pl,Tr). As we have seen, the plagioclase effect causes liquids initially on the join to become enriched in Na<sub>2</sub>O and SiO<sub>2</sub>; therefore the join itself is not a thermal barrier, but despite this, compositions sufficiently rich in Ne will yield critically undersaturated residua. Evidently there is a thermal barrier in this system, although it does not precisely coincide with Di-Ab. In the absence of other components, the plagioclase effect will lead to silica-saturated sodic rocks (pantellerites) with molar Al<sub>2</sub>O<sub>3</sub> < (Na<sub>2</sub>O+K<sub>2</sub>O).

In diagram (f), it may be seen that equilibria among spinel, cordierite (Co), albite, and liquid will lead to a transit of the thermal barrier toward Ne. However, such equilibria cannot be of general importance for basaltic magmas, although spinel and cordierite might conceivably be produced in gabbros by assimilation of pelitic sedimentary rocks. The plagioclase join, diagram 14.3(b), acts as a thermal barrier in the system Ne-An-SiO<sub>2</sub>, driving liquids constantly toward either the Ne-Ab or Ab-Tr eutectic, possibly via either of the univariant equilibria *L* (Ne,Pl) or *L* (Tr,Pl). Whether a liquid first reaches one of these univariant curves, or the sideline Ne-SiO<sub>2</sub>, depends on how far the bulk composition lies from the join An-Ab, and whether crystallization is of the fractional or equilibrium type. However, when another calcic mineral such as diopside is present, the plagioclase

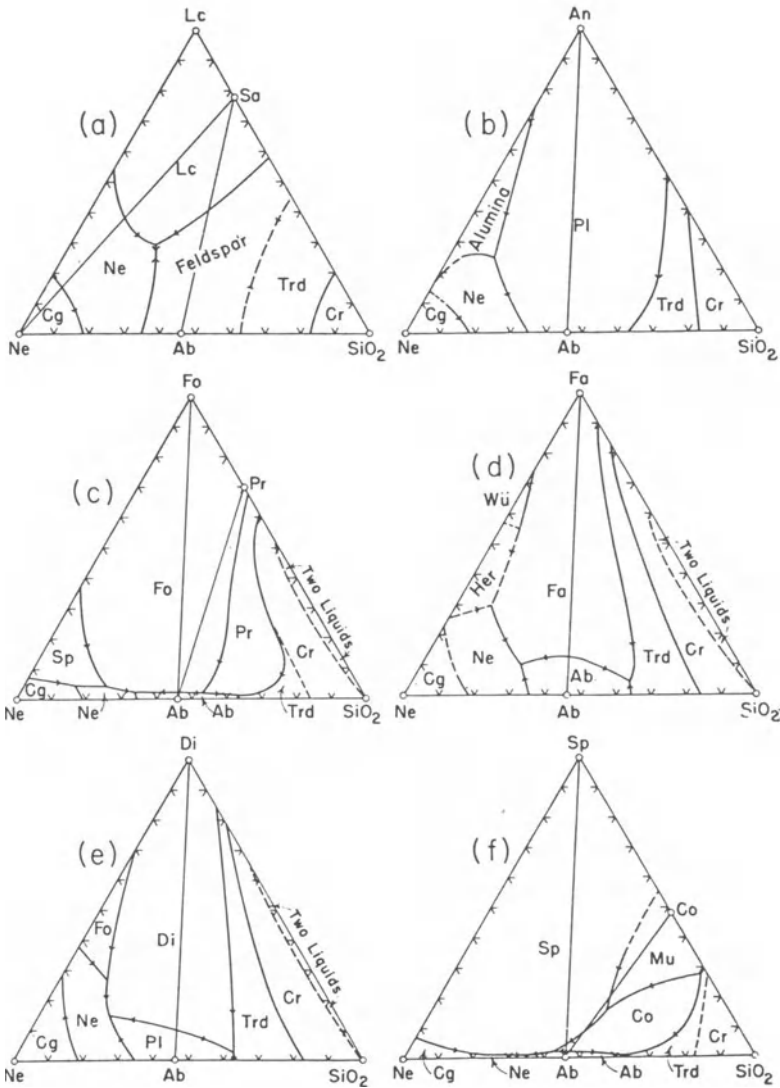


**Figure 14.3.** Phase diagrams illustrating the nature of the equilibrium thermal divides in relationship to the principal join Ne-SiO<sub>2</sub>. (a) Lc-Ne-SiO<sub>2</sub>: Schairer & Bowen (1935), Schairer (1950). (b) An-Ne-SiO<sub>2</sub>: Schairer (1954). (c) Fo-Ne-SiO<sub>2</sub>: Schairer & Yoder (1961). (d) Fa-Ne-SiO<sub>2</sub>: Bowen & Schairer (1938). (e) Di-Ne-SiO<sub>2</sub>: Schairer & Yoder (1960). (f) Sp-Ne-SiO<sub>2</sub>: Schairer & Yoder (1958). From Yoder and Tilley (1962), by permission.

effect will probably insure that the liquid reaches either the Ne or the Tr field, because the plagioclase will not reach the composition of pure Ab. By comparing diagrams (b) and (e) of Fig. 14.3, one may reach the conclusion that diagram (b) closely resembles the diopside-saturated surface in the

quaternary system Di-An-Ne-SiO<sub>2</sub>. It may be an instructive exercise for the reader to sketch for himself the tetrahedron representing this system, starting with the base Ne-An-SiO<sub>2</sub>, and placing Di at the upper apex so that the front face is diagram (e), Ne-Di-SiO<sub>2</sub>. The plane Di-An-Ab approximately bisects the tetrahedral volume, and the cotectic in this system serves as a guide for locating the *L* (Di,Pl) saturation surface. The Di-Pl cotectic is the thermal barrier in the quaternary system. It is the *L* (Di,Pl) saturation surface, projected onto the Ne-An-SiO<sub>2</sub> base, which shows approximately the same geometry as the Pl field in diagram (b), and therefore saturation with diopside will not appreciably alter the thermal barrier nature of the plagioclase join in that diagram.

Although we have not yet discussed potassium-bearing systems, it is possible to conclude from diagram (a) that introduction of a potassium feldspar component in small quantities will not alter the thermal barrier relationship. Diagram (a) is the system Ne-Lc (KAlSi<sub>2</sub>O<sub>6</sub>)-SiO<sub>2</sub>. The orthoclase composition (Sa, KAlSi<sub>3</sub>O<sub>8</sub>) lies on the sideline Lc-SiO<sub>2</sub>, and at high temperatures a continuous alkali feldspar series exists between sanidine and albite. Sanidine itself, and sanidine-rich feldspar generally, melt incongruently to Lc+*L*, and the liquids in equilibrium with these two phases may cross the barrier toward critically undersaturated compositions under conditions of equilibrium crystallization (they may not do so, however, under conditions of fractional crystallization, although by fractional removal of leucite, K-rich liquids may make the *reverse* transit from critically undersaturated to oversaturated compositions). The important feature of diagram (a), for all but the very special potassic basalts which need not concern us here, is that the Ab-rich part of the alkali feldspar join is in fact a thermal divide, and therefore the entire ternary feldspar join acts as a thermal barrier when the feldspars involved are plagioclases showing moderate enrichment in K as they reach lower contents of An.

We may therefore conclude from the diagrams of Fig. 14.3 that the plagioclase feldspars (including varieties as K-rich as anorthoclase, or calcic sanidine) constitute a thermal divide between merely undersaturated and critically undersaturated liquids, that this divide lies very near the critical plane in the basalt tetrahedron, and that the properties of the divide persist in the presence of iron-bearing silicates such as fayalite.

In a thorough discussion of this thermal barrier and the various mechanisms alleged to breach it, Yoder and Tilley (1962, p. 401–403) cite only one, other than those cited above in connection with Fig. 14.3, which may reasonably be considered to cause liquids to cross the critical plane at low pressure. This mechanism is oxidation or reduction of iron in the magma, a subject so important that it deserves treatment in a separate chapter. The effect of oxidation on silica saturation may be simply stated, however, by noting that if the ferrous iron normally incorporated in silicates (e.g., fayalite) is oxidized enough to cause formation of magnetite (FeO·Fe<sub>2</sub>O<sub>3</sub>), the crystallization of this non-silicate mineral will “release” silica to the

residual liquid which otherwise would have been bound up in ferrous silicates. The same result can be seen in the norm calculation; if enough FeO is converted to  $\text{Fe}_2\text{O}_3$  in an alkali basalt analysis, so much magnetite may be formed in the norm calculation that the analysis becomes hypersthene- or quartz-normative. This points up the great importance of accurate FeO/ $\text{Fe}_2\text{O}_3$  determinations when a correct classification of a basaltic rock is desired.

Apart from the effects of pressure and oxidation-reduction reactions, the concept of the thermal barrier appears to be a durable one. We may therefore state that at low pressures and within certain ranges of oxygen partial pressures, no normal basaltic liquid can make a transit of the natural critical plane of silica undersaturation; alkali basalts cannot be parental to olivine tholeiites, and vice versa. It is true that two parents on either side of the critical plane may be indistinguishably close together and yield very different residua, which might appear to have a common parentage. However, in principle, no single parent can yield both trends.

## The Critical Plane as a Model System

The critical plane in the basalt tetrahedron is the ternary system Fo-Di-Ab. Although pure Ab generates the thermal barrier discussed above, it is an unrealistic component by itself for basalt discussions; intermediate plagioclase would be far better. The discussion of critically undersaturated basalts can be improved by adding the component An to form the *critically undersaturated basalt system* (Yoder and Tilley, 1962, p. 394). This is the system Fo-Di-An-Ab, containing the principal silicate phases of basalt: plagioclase, clinopyroxene, and olivine. It can be sketched as a tetrahedron (an instructive exercise for energetic students) from the systems Di-An-Ab and Fo-Di-An, which we have previously examined, and some straightforward assumptions about Fo-Di-Ab. The liquidus surfaces in the tetrahedron are shown in Fig. 14.4, after Yoder and Tilley, who note several important features of the system and of the natural basalts which it represents. One of these is that the four-phase curve  $L$  (Pl,Fo,Di) extends across the system with a temperature range from 1270° to 1135°C; both the curve itself and the temperatures are very close to those in the olivine-free system Di-An-Ab, upon which we have already remarked (Chapter 8) as to the compositions and temperatures of liquids (like basalts). Saturation with olivine hardly changes the results. In fact, the quaternary system bears out what we have said all along about the success of Di-An-Ab and Fo-Di-An as models of basalt crystallization.

Yoder and Tilley used this system as a basis for discussing experimental studies on natural basalts. They had hoped to deduce parent-daughter relationships from the relative temperatures at which the natural rocks,

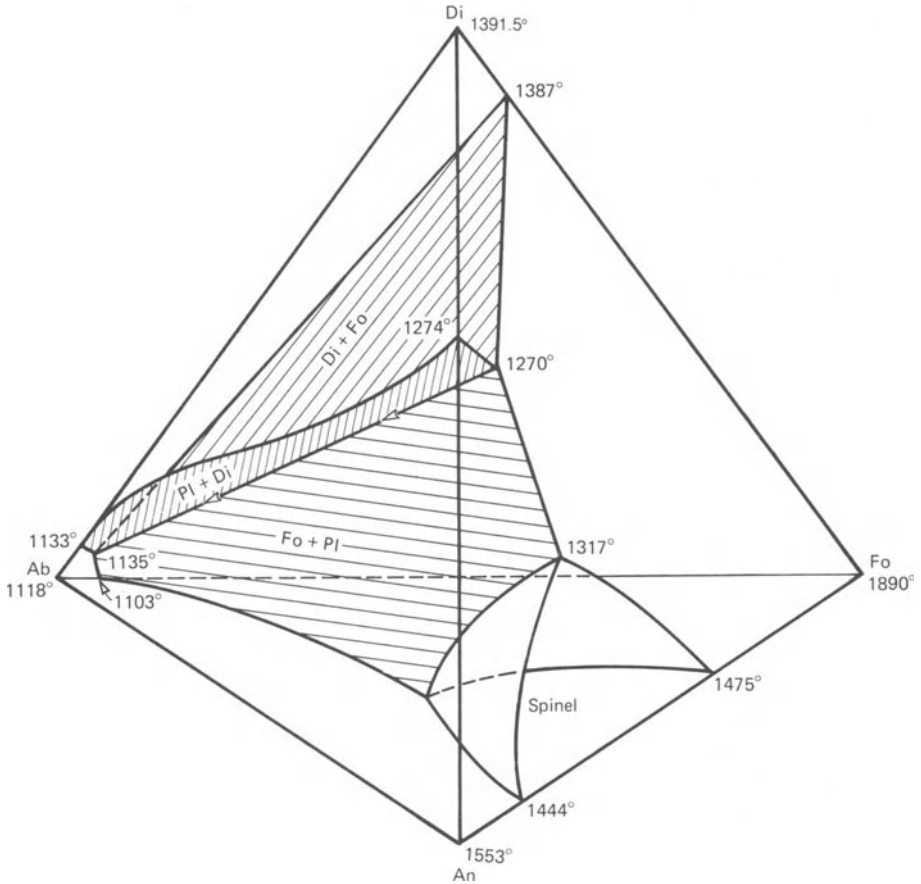


**Figure 14.4.** The system Fo-Di-An-Ab, the expanded critical plane of the basalt tetrahedron, from Yoder and Tilley (1962). Reproduced with permission.

when melted and then crystallized, reached the four-phase  $L$  (Pl,Fo,Di) saturation condition. However, they found that all the basalts studied reached this condition in a very small range of temperature ( $1155^{\circ}$  to  $1170^{\circ}\text{C}$ ), implying that they all lie very near the same fractionation path, or a set of equivalent fractionation paths in the several primary phase regions. This coincidence of thermal behavior and of composition suggested to Yoder and Tilley that “most basalts are themselves a product of fractional melting or crystallization” (1962, p. 397). This is somewhat understated, for it is almost obvious that, given an essentially peridotitic mantle, basalts must be the product of *partial* melting (not necessarily fractional in our current usage, i.e., that of Presnall, 1969), but more than that, they must be products of similar *controls* on partial melting in terms of the phases melted and left as solid residue, and of temperature-pressure regimes during ascent to the surface of the earth. It may happen that nearly all basalt magmas

undergo fractional crystallization of the primary (i.e., liquidus) phase during ascent; commonly this phase will be olivine, and when magmas arise so rapidly as to fail of fractional crystallization enroute, they may then be termed picritic or indeed, peridotitic. The aphyric basalts carry no phenocrysts of the primary phase, and if their parent magmas have reached saturation during ascent, they have passed through or resided in a region of  $T$ - $P$  such that saturation in a primary phase no longer occurs.

The critically undersaturated basalt system (Fig. 14.4) may provisionally explain why some basaltic magmas having compositions in or very near the critical plane produce trachytic (syenitic) residua instead of their Ne- or  $\text{SiO}_2$ -bearing counterparts, phonolite or rhyolite. A bulk composition in or sufficiently close to the critical plane should yield residua which remain within this system upon fractional crystallization, and should not become enriched in either Ne or  $\text{SiO}_2$ . If this is the only reason why trachytes occur, then it merely transfers the trachyte-syenite problem to the problem of why critically undersaturated basalts occur, because trachytes would then be the products only of critically undersaturated basalts (i.e., those *on* the critical plane). The abundance of trachytes in the oceanic association, and of syenites in the continental association, is high enough to engender the suspicion that controls during fractionation of basaltic magma are also important, although closeness of the parent magma to the critically undersaturated condition undoubtedly also plays a part.

## The Rest of the Basalt Tetrahedron

All the principal elements of the basalt tetrahedron have now been covered in our discussion; and can be summarized very briefly as follows.

- The critical plane divides the tetrahedron into three fundamentally different regions, the undersaturated basalts which fractionate away from the plane and toward Ne, the critically undersaturated basalts which always remain critically undersaturated in the trachyte trend, and the tholeiitic basalts which fractionate away from the plane and toward hypersthene or silica saturation.
- No common parent of both alkali basalt and tholeiite appears to exist at low pressures.
- Alkali basalt cannot, at low pressures, fractionate to produce tholeiitic basalt (unless oxidation is involved), nor can tholeiitic basalt fractionate to produce alkali basalt.
- Within the tholeiitic volume to the silica-rich side of the critical plane, olivine tholeiites may fractionate to produce hypersthene basalt or quartz basalt; the reverse process cannot occur. Olivine tholeiites can

be and no doubt often are parental to any of the suite of rocks having higher degrees of silica saturation, up to and including rhyolite (in small amounts controlled by the amount of alkalis,  $\text{Na}_2\text{O}$  and  $\text{K}_2\text{O}$ , in the initial magma).

- The system Fo-Di- $\text{SiO}_2$  is a satisfactory model for that part of the basalt tetrahedron to the right of the critical plane. Addition of An or plagioclase to this system (see, for example, Fig. 13.10) may improve our detailed knowledge of crystallization processes, but does not alter the fundamental parent-daughter relations among tholeiitic liquids as deduced from Fo-Di- $\text{SiO}_2$ .
- All major basalt types can be explained by the production in the mantle source region of three major primary magma types: undersaturated, critically undersaturated, and olivine tholeiitic. This is not to say that some magmas which could be daughters by fractionation may not also originate directly by partial melting in the mantle, but it does imply that genetic knowledge of the three primary magmas is necessary and perhaps sufficient for an understanding of the origin of most basalts.

## Chapter 15

# Potassium: Petrogeny's Residua System and Ternary Feldspars

### Introduction

The main effect of potassium when present in the small amounts typical of most basalts is to lower temperatures slightly and enter into the feldspar as small amounts of the orthoclase molecule,  $\text{KAlSi}_3\text{O}_8$ . Potassium is a large alkali ion (1.46 Å radius if we use the compilation of radii by Whittaker and Muntus, 1970), considerably larger than sodium (1.10 Å). Because of its large size, it is almost entirely excluded from the common mafic minerals of basalt, and it occurs in only limited amounts in calcic plagioclase. For this reason, K is conserved in residual liquids upon fractional crystallization of most basaltic compositions, because it finds a happier home in the liquid structure than in the structure of the average crystals. This effect is called *partitioning*. The result of the fractionation process can often be seen in the micropegmatite mesostasis (commonly sanidine + quartz) of some tholeiitic basalts. Although we may rightly say the effect of potassium is minor in such a role, we must nevertheless strive to consider its behavior in phase diagrams if we wish to follow the question of what basaltic liquids may *become* as they crystallize. Moreover, despite its small, seemingly trivial abundance in basalts, it would be a grave mistake indeed to treat potassium lightly in any discussion of basalt genesis, for even rather small variations in potassium content appear to be very important indicators of basalt type, source, or even mode of origin. And finally, there is a whole class of strange potassic igneous rocks, whose basic members may include leucite basalt. Although we shall not attempt here to explain *why* some suites of rocks are potassic, we shall at least explore some of the consequences. We begin

with the melting behavior of  $\text{KAlSi}_3\text{O}_8$ , potassium feldspar. This chemical formula is the *orthoclase component* (or CIPW molecule), but it is usually represented by the monoclinic, disordered polymorph *sanidine* at magmatic temperatures.

### Sanidine: The System Kalsilite-Silica

Sanidine is a bit tricky to prepare from scratch. Synthesis usually involves addition of potassium as the carbonate, and when the  $\text{CO}_2$  is sintered off, it commonly carries away some of the volatile K, which must be restored by adding a little extra potassium carbonate. The first component made is  $\text{K}_2\text{O} \cdot 6\text{SiO}_2$ , to which is then added  $\text{Al}_2\text{O}_3$ . The preparation of such starting materials is elegantly described by Schairer and Bowen (1955). A much more satisfactory way of making a starting material is to take natural microcline, readily available as large single crystals, and subject it to alkali chloride exchange, Waldbaum (1969). The ground feldspar is held for perhaps a day in a KCl melt, into which impurities such as Ba, Rb, and Na will diffuse out of the feldspar, being replaced there by K from the chloride melt. A second exchange may be made if desired. The KCl with impurities is simply dissolved in water after each exchange, leaving the feldspar intact. This will still be microcline in structure, but it may be converted to sanidine, if desired, by heat treatment near  $1000^\circ\text{C}$ . Such a procedure cannot guarantee a stoichiometric feldspar composition in terms of Al and Si, unless the starting material is stoichiometric.

If one now attempts to melt pure sanidine, one finds in the run, instead of glass alone, crystals of *leucite* ( $\text{KAlSi}_2\text{O}_6$ , Lc) plus glass. The crystals persist to very high temperatures. Obviously, the melting is incongruent. It must be described in terms of the binary system leucite- $\text{SiO}_2$ , just as the incongruent melting of enstatite must be described in terms of the system Fo- $\text{SiO}_2$  (see Ch. 10). And as with the case of enstatite, there is nothing really special about the incongruent melting of sanidine; interested readers may construct *G-X* diagrams to illustrate this in the manner done for Fo- $\text{SiO}_2$ .

The phase diagram, after Schairer and Bowen (1955), is shown in Fig. 15.1. This is actually the system  $\text{KAlSi}_2\text{O}_6$  (kalsilite, Ks) –  $\text{SiO}_2$ , for reasons which will later become apparent. The melting of sanidine involves only the portion Lc- $\text{SiO}_2$ . Leucite itself melts congruently at  $1686^\circ\text{C}$ , and cristobalite at  $1713^\circ\text{C}$ . The system is strongly reminiscent of Fo- $\text{SiO}_2$ . Sanidine melts incongruently at  $1150^\circ\text{C}$  to Lc and silica-rich liquid R. Sanidine and tridymite melt together at a eutectic at about  $990^\circ\text{C}$ . Crystallization and melting paths may be analyzed as for Fo- $\text{SiO}_2$ . R is a peritectic reaction point of isobarically zero variance:  $c = 2$ ,  $\phi = 3$ ,



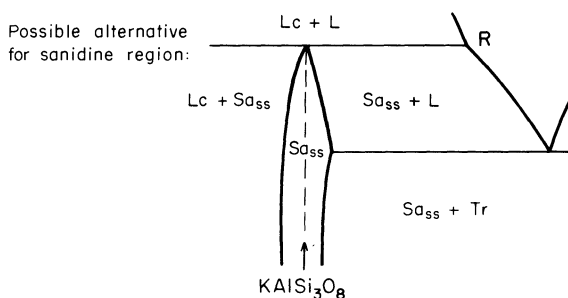


Figure 15.2. Possible solid solution of sanidine toward silica and leucite.

SiO<sub>2</sub>. Figure 15.2 indicates how the phase diagram might look in the latter case; it is presented mainly in order that we not lose sight of this possibility, for which there is some tenuous experimental evidence.

In contrast to albite, sanidine provides no thermal barrier. Clearly, removal of leucite from early liquids can cause a transit from silica undersaturated to silica oversaturated liquids. Just as clearly, this can happen only for potassic rocks. But where does the thermal barrier represented by albite give way to the incongruent relation shown by sanidine? Since we know of extensive solid solution in nature between albite and sanidine, it would appear to be a critical matter to know where the incongruent melting behavior takes over as the crystals become richer in orthoclase component. This means we should look at the system Ab-Or, which turns out to be novel to us in two ways: it is in part an example of a binary system with a *minimum melting relationship*, and in part a *non-binary section* showing incongruent melting. In order to understand completely the so-called *join* Ab-Or, we shall eventually need to look at the ternary system Nepheline-Kalsilite-Silica, called by Bowen "Petrogeny's Residua System." We turn first to the alkali feldspar join Ab-Or.

## Albite-Orthoclase

This join was studied by Schairer (1950), who found the crystallization behavior of the feldspars so sluggish that he was unable to determine a feldspar solidus. By 1969, James B. Thompson Jr. and David R. Waldbaum had completed a series of studies on the thermodynamic properties of sanidine-high albite crystalline solutions, and were able to calculate a phase diagram entirely consistent with Schairer's liquidus data (Waldbaum and Thompson, 1969). Although they suggested a method of testing their calculated solidus experimentally, this has not yet been done. But clearly, the calculated diagram is a great improvement over earlier ones in which the solidus was entirely conjectural. The series of papers by Thompson and

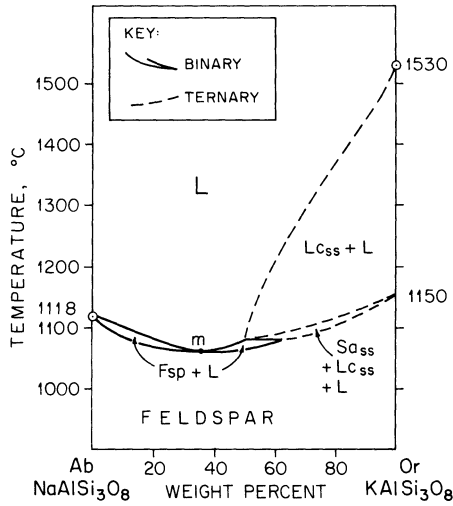


**Figure 15.3.** The system albite (Ab)-orthoclase (Or), after Schairer (1950). Fsp, feldspar solid solution; Lc, leucite. All equilibria involving leucite, i.e., from 1080°C, are ternary, not binary.

Waldbaum is a landmark in the theoretical and experimental treatment of crystalline solutions, and its principles find frequent use in advanced studies.

The join is shown in Fig. 15.3. On the Or sideline, the temperature 1150°C marks the incongruent melting of pure sanidine, and the temperature 1530°C marks the limit of the Lc + L field; these temperatures occur in Fig. 15.1 along the Or composition line. The rest of the diagram is too compressed to comprehend easily, so we turn instead to an expanded temperature scale in Fig. 15.4. In this figure we see right away the answer to our main question: the incongruent melting leaves off about half-way across the diagram toward albite. (This is no “magic number”, it is merely fortuitous that the melting behavior changes at about Or<sub>50</sub>Ab<sub>50</sub>.) There is a reaction point at 1080°C, below which the alkali feldspar join is binary, and above which are found equilibria involving leucite. Leucite does not lie in the join Ab-Or (see Fig. 15.1 for a reminder), so all liquids in equilibrium with leucite must also lie off the join, toward SiO<sub>2</sub>. It is for this reason that we call this part of the diagram “nonbinary”, which means ternary or higher order. In this case, as we shall find, ternary will do. It is a bit hard to understand such “pseudobinary” representations of higher order equilibria, but we have encountered these before, as in the spinel field of Fo-An, and one can learn to read them as road maps without worrying too much about the missing dimensions. One region that is still binary in the right half of the diagram is the region below the solidus, labelled “sanidine solid solution”. We see that this field is continuous to albite solid solution, and that the whole region represents an arbitrarily variable solid solution



this liquid begins to crystallize Lc, and the liquid becomes more sodic along the liquidus as the temperature falls. Nothing new happens until the system cools to about 1084°C, when Sa<sub>ss</sub> crystals now appear. We know that this equilibrium in the system Lc-SiO<sub>2</sub> is an odd reaction, in which Lc is converted to Sa. This conversion occurs here, too, although proof will have to await the ternary analysis. So Sa<sub>ss</sub> continues to form by reaction; its composition is given by the solidus. Finally, at 1080°C, all the leucite has been converted to Sa<sub>ss</sub>; the liquid lies once more in the join Ab-Or, and the system is now binary. The liquid composition at 1080°C is a type of *piercing point*, where a ternary boundary curve pierces a join. Note that with *any* amount of fractional crystallization (removal of leucite), the liquid will not return to this join at all, so the process cannot be adequately analyzed in this type of diagram.

Turning now to the less bizarre part of the system, we find a binary minimum subsystem of alkali feldspars. This looks a little bit like two plagioclase loops joined at their lower ends, and indeed ignorant people sometimes draw minimum diagrams that way. But we shall learn better, namely that *at* the minimum, the solidus and liquidus curves *must coincide*, and their common tangent *must be isothermal*, i.e., parallel to the composition axis. This means that the minimum composition is very special indeed—it might at first seem to be a “univariant point” (!), but of course there can be no such thing. The point is *invariant by restriction* because for that particular composition the system can be described as a one component system (the single component being a feldspar or liquid of the minimum composition), so for  $c = 1$ ,  $\phi = 2$

$$\begin{aligned} W_p &= c + 1 - \phi \\ &= 2 - 2 \\ &= 0 \end{aligned}$$

Such points, *invariant by restriction*, are also a type of *singular point*; here, singularity means the identity of feldspar and liquid compositions.

Otherwise, we treat crystallization in such a system just as we would in a plagioclase loop. To continue with our example, Or<sub>60</sub>Ab<sub>40</sub>, the liquid may now cool below 1080°C, maintaining equilibrium with Sa<sub>ss</sub> whose composition lies on the solidus. At a temperature near 1078°C, this solidus cuts the bulk composition, and the system is now entirely crystalline. The last liquid has a composition near Or<sub>48</sub>Ab<sub>52</sub>. Note that the liquid will not reach the minimum in equilibrium crystallization unless the bulk composition *is* the minimum.

Crystallization of Ab-rich liquids proceeds in a straightforward way, as may safely be left to the reader to ascertain.

Fractional crystallization in the truly binary part of the system will always yield liquid and a few crystals of the minimum composition. Only an infinitesimally small amount of minimum liquid will result, however.

TSC paths will terminate at 1063°C and the bulk composition, having originated at the solidus. Melting paths can be deduced from the principles of the plagioclase system, except that one should not attempt fractional melting into the incongruent region, but should instead wait to see the ternary system. Note!!! that on melting, *no* liquid of minimum composition will be produced except for a bulk composition at the minimum itself.

### Residua System, Ne-Ks-SiO<sub>2</sub>

#### LIQUIDUS DIAGRAM

The ternary system Ne-Ks-SiO<sub>2</sub> is shown in Figs. 15.5 and 15.6. The diagrams are based on extensive work by Schairer (1950), who was able only with difficulty to determine liquidus temperatures and the approximate

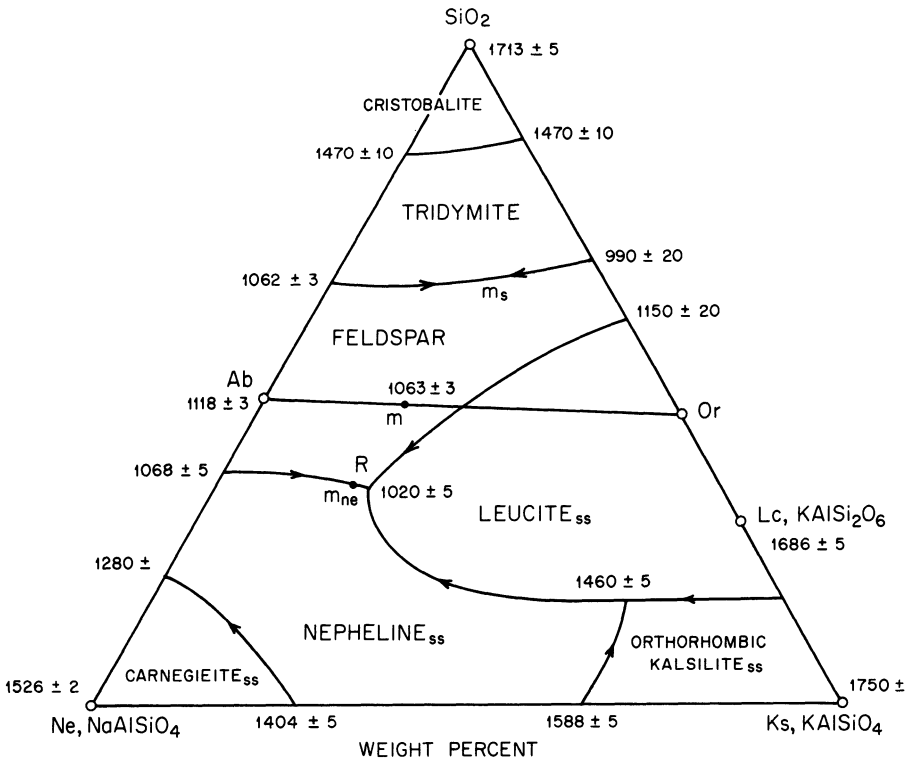


**Figure 15.5.** The system Ne-Ks-SiO<sub>2</sub>, after Schairer (1950). Letter m signifies a minimum: m<sub>s</sub>, silica-saturated; m<sub>ne</sub>, nepheline-saturated. Location of m<sub>s</sub> is conjectural; no experimental determination has been made. Base measures 10 cm.

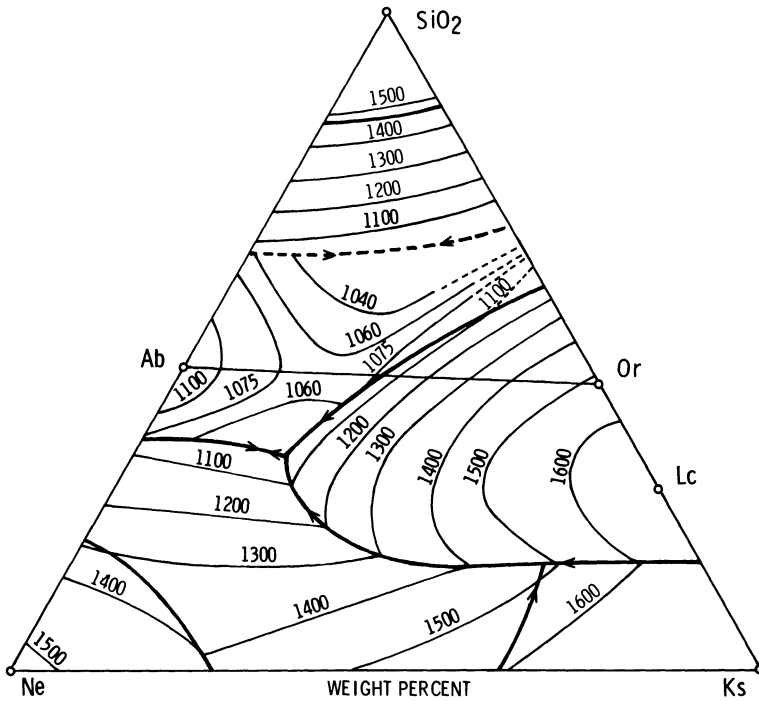


Figure 15.6. Isotherms in Ne-Ks-SiO<sub>2</sub>, after Schairer (1950). Base measures 10 cm.

locations of minima. Work on this system at one atmosphere pressure was to some degree supplanted by the revolutionary studies of Tuttle and Bowen (e.g., 1950, 1958) and others using elevated steam pressures to facilitate reaction and to correspond more closely to conditions at some depth in the crust of the earth. As a result, there are many details of the 1-bar system which we do not know, but can more or less adequately infer from studies at higher pressure. We do not, for example, know any tie lines in the dry system. It will suffice to analyze the diagram with inferred tie lines, and this has the added benefit that we can illustrate the principles without worrying excessively about the details.

Of the bounding binary systems, we have studied Ne-SiO<sub>2</sub> and Ks-SiO<sub>2</sub> already. Ne-Ks has been studied (Tuttle and Smith, 1958), although not with complete success; its main feature of importance to us is that it is dominated by a large range of solid solutions from kalsilite toward nepheline, and a smaller range of solid solutions from carnegieite toward kalsilite. The junction of these fields is not satisfactorily resolved with respect to the liquidus diagram of Fig. 15.5, so we shall be forced to make some arbitrary assumptions about relations near the base of the ternary diagram.

The features of chief interest in Fig. 15.5 are the large primary field of leucite solid solution, which overlaps the alkali feldspar join; the large fields of nepheline and feldspar solid solution; and the three *ternary minima*

which lie in what Bowen called a "thermal valley" and approximate the compositions of rhyolite ( $m_s$ ), trachyte ( $m$ ) and phonolite ( $m_{ne}$ ). (The point  $m$  is actually a binary minimum in Ab-Or.) These minima closely represent the natural residua from fractionation of, respectively, tholeiites, critical plane basalts, and alkali basalts, and it is for this reason that Bowen aptly called the system Ne-Ke-SiO<sub>2</sub> "petrogeny's residua system." The minimum  $m$  on the alkali feldspar join is known with fair accuracy, but compositions 5% to each side of Or<sub>35</sub> gave the same liquidus temperature, being bracketed by 1060°C (some crystals in glass) and 1065°C (all glass) in 3-week experiments. The minimum therefore could lie anywhere from Or<sub>30</sub> to Or<sub>40</sub>, but Or<sub>35</sub> is the central and best estimate based on the rise of liquidus temperatures beyond these compositions. The silica-saturated ternary minimum, here denoted  $m_s$ , has not been located experimentally. The location given in Fig. 15.5 is assumed, and we shall assume a temperature of about 980°C for purposes of discussion. The position and temperature are compatible with experiments at higher pressure. Similarly, the nepheline-saturated minimum, here denoted  $m_{ne}$ , has not been precisely located, but its position and temperature are much more tightly constrained by the liquidus data. It must lie to the left of the triple junction R labelled 1020°C, which is a reaction (peritectic) point, and yet close to that point, from liquidus data.

Another reaction point occurs at 1460°C, involving orthorhombic kalsilite, nepheline, leucite, and liquid. As with the several peritectics in Fo-Di-SiO<sub>2</sub> (Chapter 12), one can deduce that this point and R are peritectics because arrows flow away from them as well as toward them. This could not happen with an even (eutectic) reaction.

Of the *five* solid solutions feldspar, nepheline, leucite, carnegieite, and kalsilite in this system, only feldspar and leucite are known with any accuracy. We know the feldspar series to be complete at these high temperatures. Fudali (1963) showed that leucite contains up to about 40% by weight of the component NaAlSi<sub>2</sub>O<sub>6</sub> ("soda leucite," not jadeite!), and we shall interpolate compositions up to that limit in succeeding diagrams. Nepheline is known to contain vacancies, which amount to solid solution toward albite, and we will depict it essentially as determined at 5 kbar by Morse (1969a), although the solid solution limits must be somewhat different at the higher temperatures of the 1-bar diagram. Carnegieite solid solution is limited by the presence of nepheline and can be adequately deduced from the liquidus diagram and from the work of Tuttle and Smith. Kalsilite solid solution is poorly known, and complicated by the possible presence on the liquidus of a hexagonal polymorph. We shall be able to find suitable constraints on kalsilite composition and on leucite-nepheline tie lines near the 1460°C reaction point. Given these generalities, we now turn to a series of isobaric, isothermal sections to illustrate what can be inferred about this ternary system from the liquidus diagram and a few basic principles.

## ISOTHERMAL SECTIONS

The isotherms as determined by Schairer are shown in Fig. 15.6. These are based on a great density of points, and contain much detail not apparent at first glance.

Ten isothermal sections are shown in Fig. 15.7. These depict, in a down-temperature series, the instantaneous equilibria which aid in constructing crystallization or melting paths. Brief comments on each are given below.

**1600.** Small field of cristobalite + liquid near SiO<sub>2</sub> corner. An extensive field of Ks<sub>ss</sub> + L is already established, and this was joined at 1686°C by the beginnings of Lc<sub>ss</sub> crystallization. Since Ks crystallized first, we know that its solid solution toward Na-bearing compositions must be more advanced than that of Lc<sub>ss</sub>. The invariant ( $W_{p,t} = 0$ ) three phase triangle Lc-Ks-L reflects this condition; it is bounded by fields of Lc<sub>ss</sub> + L, + Lc<sub>ss</sub> + Ks<sub>ss</sub>, and Ks<sub>ss</sub> + L.

**1500.** Cr + L field has grown. Cg + L field is new. Ks + L field has shrunk drastically at the expense of Ne<sub>ss</sub> + L, newly arrived. The limits on Ne<sub>ss</sub> must be about as shown because the curve L (Ne, Ks) represents an odd reaction ( $L = \text{Ne} - \text{Ks}$ ). The topology around the three-phase triangle Lc-Ks-L remains unchanged.

**1400.** The inset shows the isothermal destruction of Ks at 1460°C by the reaction  $\text{Ks} + \text{L} = \text{Lc} + \text{Ne}$ . Note that in this reaction four phases coexist at equilibrium, and the system is isobarically invariant without an external imposition of fixed temperature ( $W_p = 0$ ,  $W_{p,t} = -1$ , which is irrelevant). At 1400°C, the silica polymorph is now tridymite. A larger field of Cg<sub>ss</sub> + L now occurs, as well as a 3-phase equilibrium Cg + Ne + L. The equilibrium Lc<sub>ss</sub> + Ne<sub>ss</sub> is well established, isolating Ks from further interaction with liquid. Both Lc<sub>ss</sub> and Ne<sub>ss</sub> have become much more sodic. The 3-phase solid triangle Lc-Ks-Ne is arbitrarily located; its limits are unknown except for certain logical geometric constraints.

**1300.** Much the same picture as before. The field of Cg<sub>ss</sub> + L is now nearly gone. Ne<sub>ss</sub> + L is approaching a configuration which will remain essentially unchanged to lower temperatures. Note the increased solution of Ne toward albite, and the enlarged field of Cg + Ne.

**1200.** Cg is now gone altogether. The liquid pool continues to shrink at the expense of Lc<sub>ss</sub>, Ne<sub>ss</sub>, and tridymite, each in equilibrium with liquid.

**1130.** Sanidine makes its appearance for the first time at 1150°C. We see it breaking into the Lc + L field as a 3-phase triangle with apex on Sa<sub>ss</sub>.

The tangent to the liquid boundary falls drastically outside the  $Lc + Sa$  line, hence on the negative extension ( $Sa-Lc$ ), and the reaction is odd,  $L = Sa-Lc$ .  $Lc_{ss}$  has advanced further toward soda leucite.

**1090.** Albite has entered from the left at  $1118^{\circ}\text{C}$ , and now forms an arc of  $Ab_{ss} + L$ . Note that, as with  $Lc_{ss}$  before, the maximum enrichment of the opposite component occurs on the join, whereas liquids to either side of the join are tied to less advanced solutions. The 3-phase triangle  $Sa + Lc + L$  has swept rapidly toward more sodic compositions, as dictated by the location of liquid on the field boundary where intersected by the isotherm. The liquid pool is now being constricted mainly from the sides, since the tridymite and nepheline liquidus surfaces are very steep.

**1070.** Recall that at  $1080^{\circ}\text{C}$  in the  $Ab-Or$  join, the leucite field disappeared. This event corresponds in the ternary system to the coincidence of the  $Sa_{ss} + L$  edge of the 3-phase triangle with the  $Ab-Or$  join. By  $1070^{\circ}\text{C}$ , this edge has fallen below the join, and the triangle has radically changed

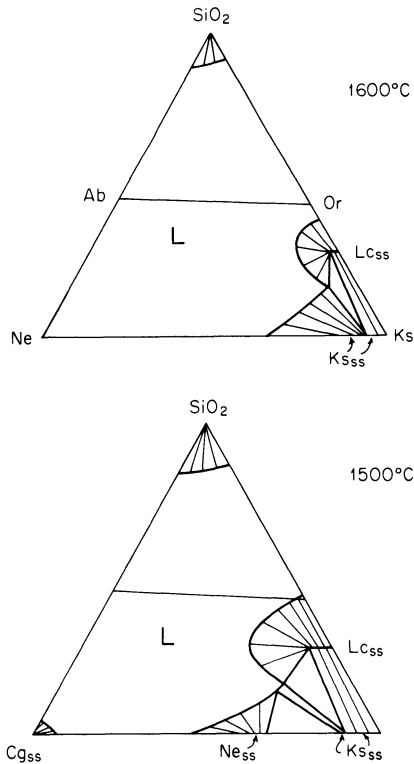


**Figure 15.7.** Isobaric, isothermal sections in Ne-Ks-SiO<sub>2</sub> at ten different temperatures, continued on following pages.

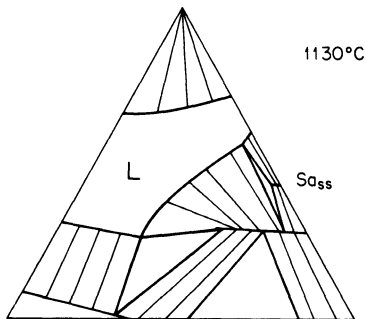
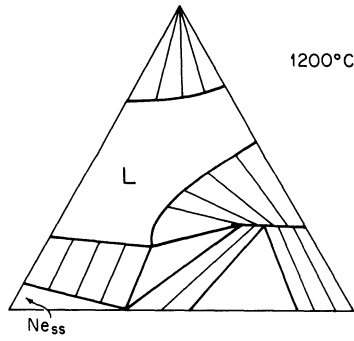
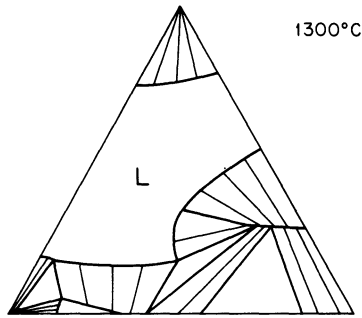
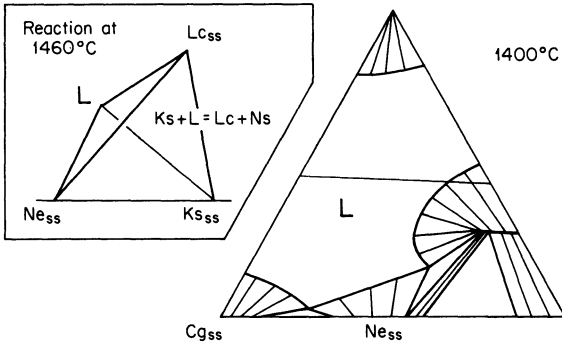


**Fig. 15.7 (Continued).**  
See opposite page.

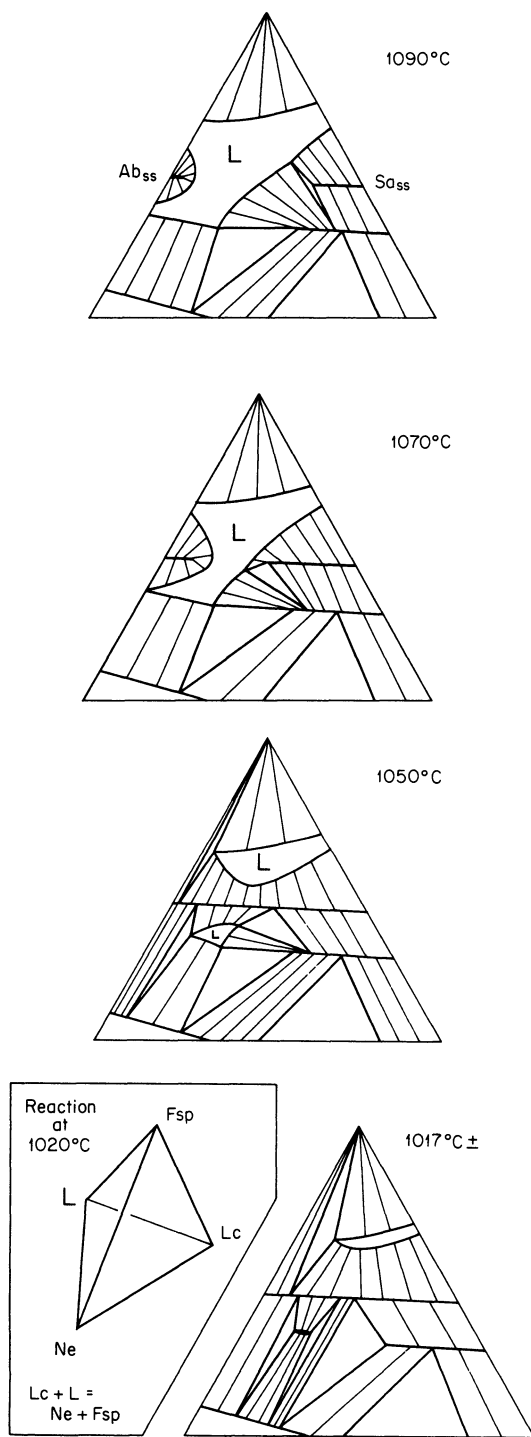


**Fig. 15.7** (Continued). See page 266.

shape from the initial one at 1130°C. Despite this, there has been no change in the nature of the reaction, which is still odd. The extent of sanidine solid solution is probably somewhat exaggerated in the 1070 section. Note that the  $Ab_{ss} + L$  field has grown considerably, and that  $Lc_{ss} + L$  has shrunk considerably. Clearly, this field will soon be wiped out.

**1050.** The alkali feldspar join has closed off at 1063°C, leaving a continuum of solid solutions in equilibrium with various other phases. From the left, we see the encroachment of a 3-phase triangle with  $Tr + Ab_{ss} + L$ ; this will sweep to the right leaving a solid triangle with  $Tr + Ab_{ss}$ , which has swept in from the left also. Two liquid pools (rhyolitic and phonolitic) are separated by the feldspar join. An almost complete range of Ab-Or solution coexists with rhyolitic liquid. A more limited range coexists with phonolitic liquid, bounded to the right by the 3-phase triangle  $Fsp + Lc_{ss} + L$ . (We can no longer distinguish the feldspar *compositionally* as sanidine, because of its intermediate composition, but it is undoubtedly of the sanidine structure.) The  $Lc_{ss} + L$  field is smaller than ever.

**1017±.** The peritectic reaction at 1020°C was  $L + Lc = Fsp + Ne$ , as shown in the inset. Now the  $Fsp + Ne$  field has grown to isolate  $Lc_{ss}$  from liquid. The extremal  $Lc_{ss}$  composition has now begun to withdraw, generating  $Ne + Fsp$ . Only a tiny pool of undersaturated liquid remains (presuming the minimum temperature to be 1015°C), bounded on each side by opposed 3-phase triangles each having the identity  $Ne + Fsp + L$ . These will, at 1015°C, meet and simultaneously become a single *line*  $Fsp + L + Ne_{ss}$  just as the last trace of liquid disappears. The feldspar and nepheline coexisting with this last liquid will have singular compositions, dictated by the collinearity, but *note* that the feldspar composition will not lie (except by chance) at the feldspar minimum on the join Ab-Or. It is important to understand the independence of the singular feldspar composition tied to  $Ne + L$ , and the minimum feldspar composition in equilibrium with its own liquid. This principle will be stressed again below.

Below 1015°C, not shown, the undersaturated portion of the residua system will consist of the following fields of solids:  $Ne_{ss}$  alone,  $Ne_{ss} + Ab$ -rich feldspar, with tie lines as in the 1017 section, a 3-phase field  $Ne_{ss} + Fsp + Lc_{ss}$ , two 2-phase fields  $Fsp + Lc_{ss}$  and  $Ne_{ss} + Lc_{ss}$ , the 3-phase field  $Ne_{ss} + Lc_{ss} + Ks_{ss}$ , and the field  $Lc_{ss} + Ks_{ss}$ .

The siliceous part of the system is still dominated by liquid equilibria at 1017°C. We presume that at 990°C, a new 3-phase triangle  $Sa_{ss} + Tr + L$  will enter from the right, and that the two triangles will meet at 980°C in a singular line through the ternary rhyolite minimum.

EQUILIBRIUM CRYSTALLIZATION

Two examples, both originating in the leucite field, will serve for now to illustrate equilibrium crystallization. The first bulk composition, BC-1 in Fig. 15.8, yields only sanidine and leucite. The liquid first moves in equilibrium through the leucite field, tied through the bulk composition to the TSC on the leucite join. It eventually reaches the field boundary, whereupon reaction ensues, using up leucite to make sanidine. The TSC advances toward the bulk composition along successive solid-solid legs of 3-phase triangles, as shown by the TSC path in the figure. Crystallization ceases when the Sa + Lc tie line cuts the bulk composition.

The crystallization of BC-2 is shown in Fig. 15.9. This composition lies within the terminal, invariant 3-phase triangle Ne + Lc + Fsp at 1020°C, and hence consists of these three phases when solid. The liquid initially moves along a path with small curvature while Lc<sub>ss</sub> crystallizes. It then moves along the field boundary, first dissolving a small amount of Lc<sub>ss</sub> as feldspar forms, and then, for reasons discussed later in this chapter, producing leucite again. The TSC rises along a curved path of relative enrichment in feldspar. The liquid then reaches the reaction point R at 1020°C, and remains there while the TSC moves directly toward R and to the bulk composition. This is accomplished by the crystallization of invariant Fsp + Ne at the expense of Lc and liquid.

Other equilibrium crystallization exercises, particularly with bulk compositions in the silica oversaturated region of the leucite field and on the feldspar join itself, can be undertaken by the reader for himself. Certain bulk compositions just below the feldspar join yield complex paths, and the nature of reaction along the leucite-feldspar boundary changes from odd to even for certain bulk compositions. These complexities are discussed in a section near the end of this chapter, to which the reader should refer for a rigorously accurate understanding of equilibrium crystallization. The present examples will suffice for an elementary understanding.

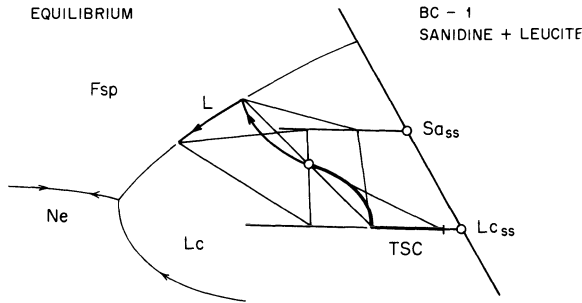
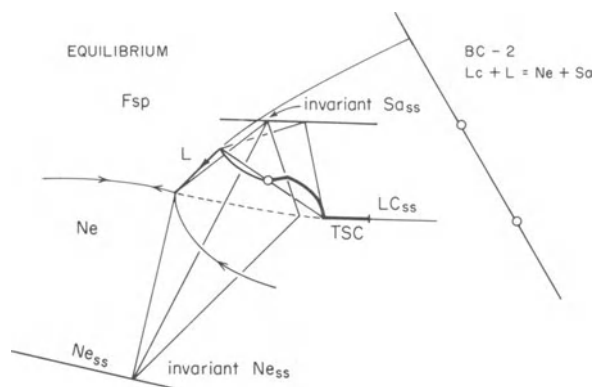


Figure 15.8. Equilibrium crystallization of BC-1.



**Figure 15.9.** Equilibrium crystallization of BC-2.

### PSEUDOLEUCITE

In some natural rocks, there occur patchy or stringy intergrowths of alkali feldspar and nepheline, often having the external outline of euhedral leucite phenocrysts. Such objects are called “pseudoleucite.” Figure 15.9 leaves little doubt that these may originate by reaction of liquid R with leucite phenocrysts, much in the manner of BC-2. Conceivably the reaction may run rapidly enough to convert all the leucite to Ne + Fsp in some rocks. The reaction need not be confined to such bulk compositions as BC-2, within the invariant quadrangle, for with some degree of fractional crystallization, a large range of Lc<sub>ss</sub> crystals could come into contact with peritectic liquid. Ideally, at equilibrium, these crystals would first be converted to the maximum soda leucite content before breaking down to Ne + Fsp, but in nature it is possible that the nepheline and feldspar will nucleate and grow rapidly from metastable Lc<sub>ss</sub> which is not at the limiting composition. Any liquid remaining after the conversion will then fractionate toward the minimum, enriching both Ne and Fsp in soda components.

While the peritectic reaction may theoretically account for pseudoleucite, Fudali (1963) has argued persuasively that most natural examples have originated by a simpler mechanism, namely the *subsolidus* breakdown of soda-rich leucite itself to nepheline + feldspar. At subsolidus conditions, soda leucite becomes unstable and spontaneously reacts to Ne + Fsp. In other words, the 3-phase triangle Ne + Fsp + Lc shifts toward potassic compositions with falling temperature. Given such behavior, there is no need to call upon crystal-liquid reaction to account for pseudoleucite, which can form in the solid state. Correct interpretation of natural occurrences must therefore depend to large degree on the chemical and textural evidence bearing on the reaction.

FRACTIONAL CRYSTALLIZATION

Using the same bulk compositions as treated above for the equilibrium case, we may examine two contrasting examples of fractional crystallization. These are shown in Fig. 15.10. In the case of BC-1, the liquid follows a shallow curve away from ISC-1, which lies on the leucite join. Upon reaching the field boundary, the liquid immediately ceases to produce leucite and instead begins to produce sanidine along a wide range of compositions. The liquid follows a fractionation path which must be determined by experiment, but which no doubt has the general form shown in the figure. The  $Sa_{ss}$  formed during this time constitutes ISC-2 (not labelled), and the TSC migrates toward ISC-2 as shown by the dotted path in the figure. When the liquid reaches the silica field boundary, tridymite crystallizes along with feldspar until the liquid is used up just as it reaches the ternary minimum. The minimum may lie either to the right or left of where the liquid hits the field boundary, not *at* that point except by chance. In Fig. 15.10, it is assumed that the ternary minimum lies to the right of the liquid path, and it should be noted that this will produce *reverse zoning* in the feldspar: successive layers will now be more Or-rich, whereas before they were more Ab-rich.

Bulk composition 2 (Fig. 15.10), yields undersaturated residual liquids. Again, the liquid leaves the Lc + Fsp field boundary the instant it arrives, when the ISC changes from  $Lc_{ss}$  to Fsp. The feldspar presumably lies on or very near the join, but is offset for clarity in the figure. The liquid now

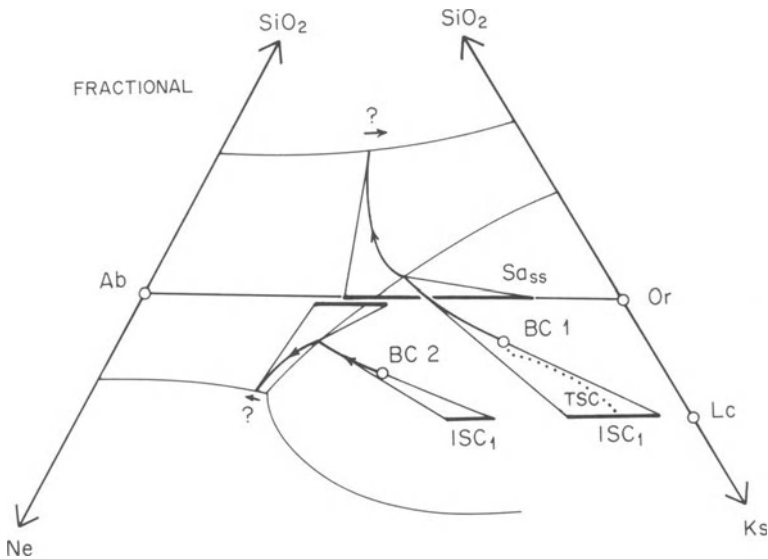


Figure 15.10. Fractional crystallization of BC's 1 and 2.

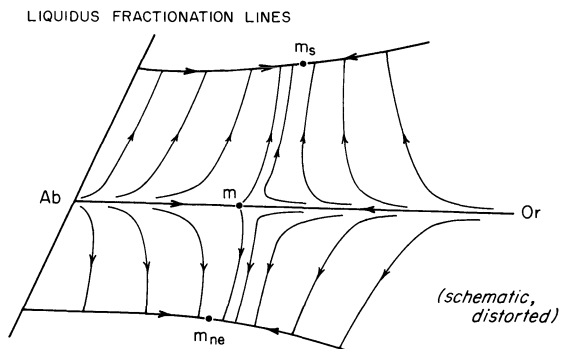


Figure 15.11. Liquidus fractionation lines in the feldspar field of Ne-Ks-SiO<sub>2</sub>.

follows a curved fractionation path across the feldspar field until it reaches the cotectic field boundary with nepheline. It then follows the cotectic to the undersaturated ternary minimum, which may lie to either side of the incoming liquid path. If the minimum lies to the left, normal feldspar zoning will continue to be produced; if to the right, reverse zoning will be produced. The final ISC (number 3) will lie on the Ne + Fsp leg of a three phase triangle, on the tangent to the cotectic, and will end up at the ternary minimum. The TSC path is not shown, but can readily be deduced by passing levers from liquid through the BC.

The two illustrated bulk compositions typify the contrasting trends of fractionation from the leucite field. In particular, they show that it is easy to breach the critical plane (strictly, the feldspar join) toward silica saturation by fractionation of leucite, but only for potassic compositions. Intermediate undersaturated compositions will fractionate toward the undersaturated minimum. Observe that between BC-1 and BC-2 there must exist a unique fractionation curve which arrives at the feldspar join just at its crossing with the field boundary. Liquids lying on this unique curve will theoretically stay on the feldspar join and go to the trachyte minimum at 1063°C. Given a slight amount of reaction with previously-formed leucite, however, they will again become undersaturated and move toward the undersaturated cotectic. On the other hand, given the slightest delay in feldspar nucleation, they will become oversaturated and move toward the silica oversaturated cotectic. Thus with slight imperfections in fractionation processes, an undersaturated parent liquid may produce either type of residuum, or conceivably both, in closely related areas.

Fig. 15.11 summarizes the *feldspar fractionation paths* or more precisely, the *liquid fractionation lines from feldspar* in the residua system. The diagram is distorted, to show relations away from the leucite field, but it corresponds qualitatively to relations observed at moderate pressure, where such fractionation is more likely to occur than at the low pressures of lava extrusion. There are several features of importance in this stylized diagram. First, fractionation paths originating rigorously on the feldspar join remain

on that join and terminate at  $m$ . All others terminate eventually at either  $m_s$  or  $m_{ne}$ , respectively the oversaturated and undersaturated ternary minima. All but two paths originate (either directly or in extension) at either pure Ab or pure Or. Two paths originate at  $m$ , the feldspar minimum. These are *unique* liquidus fractionation lines, and they have the interesting property of curvature, so they do *not* lead straight away from  $m$ . That this must be so was discussed in an elegant exposition by Bowen in 1941 and again by Tuttle and Bowen (1958). While this may at first seem surprising, it follows logically from the fact that the feldspar composition in equilibrium with liquid at either ternary minimum is not the composition  $m$ , and this in turn arises from the fact that a silica-rich liquid, for example, has different thermodynamic mixing properties from those of a pure feldspar liquid. Accordingly, the  $G$ - $X$  surfaces for liquid solutions off the feldspar join have points of tangency with feldspar solid solutions which are different from the points of tangency to liquids lying on the feldspar join itself. The curvature of the unique fractionation lines has the interesting consequence that liquid paths close to the join and close to the unique fractionation lines may undergo a reversal of curvature, and at the inflection point the feldspar zoning will become reversed. According to Fig. 15.11 (which may be incorrect in detail), silica oversaturated liquids approaching  $m_s$  from near the unique fractionation curve may produce still more strongly reversed zoning as they move along the cotectic toward  $m_s$ , and undersaturated liquids may cause feldspars to change from reverse to normal zoning as they move along the cotectic toward  $m_{ne}$ .

Note that the unique fractionation lines do *not* lead directly to either  $m_s$  or  $m_{ne}$ , but only to the cotectic somewhere near these points. This is because the addition of a saturating phase, tridymite or nepheline, generates a new criterion for equilibrium, namely a singularity wherein the saturating phase, ternary minimum liquid, and feldspar must all be collinear in the composition diagram. This can only be realized if the  $G$ - $X$  surfaces for liquid and feldspar, projected from the saturating phase, have a single common tangent at some special value of  $G$  and  $X$ . There are, of course, special fractionation lines which do lead directly to each of the ternary minima, but these do not originate at  $m$ . They originate at Or or Ab.

## FRACTIONAL MELTING

We may safely dispense with exercises in equilibrium melting, which as usual simply reverses the process of equilibrium crystallization. Turning to fractional melting and Fig. 15.12, we are reminded by the 3-phase triangle  $L$ -Fsp-SiO<sub>2</sub> that solidus fractionation lines are found by constructing a family of short tangents away from liquid on the solid-solid legs of several such triangles. One triangle is shown, with a dashed construction line

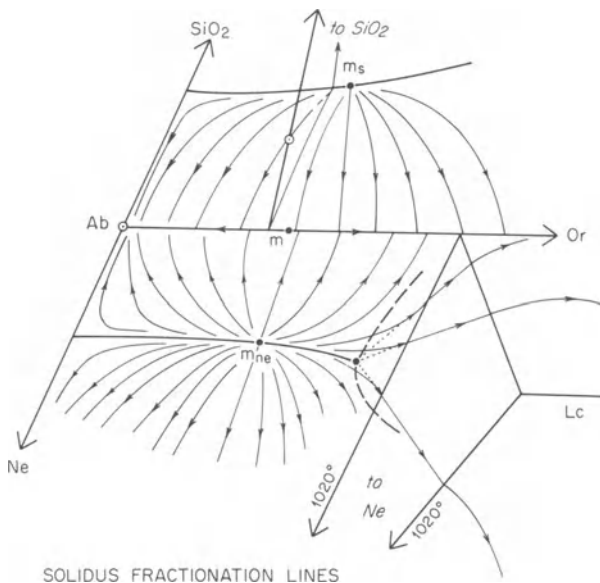


Figure 15.12. Solidus fractionation lines in the region of the three minima.

leading from the liquid apex to a circled solid composition, at which the construction line is tangent to a solidus fractionation line. The figure emphasizes those fractionation lines leading to the feldspar join and to the undersaturated regions. In the oversaturated regions, the repeated construction soon shows that all solidus fractionation lines must radiate from  $m_s$ . One of these is straight, because it is radial from SiO<sub>2</sub> through  $m_s$ . The fractional removal of liquid  $m_s$  merely chases the solid composition toward feldspar, which must have the same composition irrespective of the tridymite content along this singular line joining tridymite, invariant liquid, and invariant feldspar. Such unique fractionation lines are characteristic of systems with a ternary minimum. Note the fundamental contrast between such straight, unique *solidus* fractionation lines and the curved, unique *liquidus* fractionation lines in Fig. 15.11; it may require a little reflection on the differences between fractional melting and crystallization to come to terms with the difference in unique paths.

In the undersaturated portion of Fig. 15.12, the construction leads to the further conclusion that all solidus fractionation lines toward nepheline, as well as toward feldspar, also originate at the minimum, here  $m_{ne}$ . Again, the unique fractionation lines are straight away from  $m_{ne}$  in both directions.

Note that in no case does the unique solidus fractionation line lead to the feldspar minimum  $m$ , which has no control over solidus fractionation toward the feldspar join. For the special, singular compositions which lie on the unique lines, fractional melting resembles that in eutectic systems. The initial liquid has the composition of a ternary minimum, and it is extracted

isothermally until the saturating solid phase is exhausted. No further melting occurs until the temperature of the feldspar solidus is reached. Liquid is thereafter fractionally extracted over a continuous range of temperature.

For all other bulk compositions, not lying on singular lines, the initial melting temperature is a function of the particular bulk composition, rising with distance from the unique solidus fractionation line. Note that for a given 3-phase triangle, the initial melting temperature is indifferent to distance from the cotectic.

The distorted form of Fig. 15.12 serves to illustrate the interesting behavior of solidus fractionation lines involving the peritectic point R. Lines originating at  $m_{ne}$ , for bulk compositions sufficiently undersaturated, eventually encounter the invariant solid triangle Ne-Fsp-Lc. When they do so, the temperature has increased to 1020°C, and the liquid has moved continuously along the cotectic from the *direction of*  $m_{ne}$  to the reaction point R. It then remains at R, with isothermal removal of liquid, while the TSC moves in a straight line across the invariant solid triangle. When the TSC reaches the limiting side of the triangle where either nepheline or feldspar is exhausted, the temperature must now rise continuously from 1020°C along one of the leucite field boundaries, and the solidus fractionation line now curves continuously away from the straight segment. Note the sharp contrast with systems lacking solid solution (e.g., Fo-SiO<sub>2</sub>), in which extraction of peritectic liquid is followed by a large hiatus without melting.

Solidus fractionation lines are summarized at proper scale in Fig. 15.13, which permits some further comment. First, note that silica oversaturated bulk compositions follow fractionation paths originating at  $m_s$  and terminating at SiO<sub>2</sub>. Second, note that one line leads, by chance, directly to the feldspar minimum  $m$ . Third, note that all lines in the feldspar field originating at  $m_s$  terminate on the feldspar join; the liquidus field boundary with leucite plays no role here, since all liquids lie on the silica-saturated cotectic. If we assume that Or<sub>62</sub> is the solidus composition where feldspar begins to melt incongruently at 1080°C to leucite plus liquid, then all feldspars to the right of  $m$  (up to Or<sub>62</sub>) yield a series of continuous liquids on the join, eventually followed by a continuous series of liquids along the leucite field boundary as the total solid composition follows the heavy solidus fractionation line toward Lc<sub>ss</sub>. This heavy line is common to all compositions lying between  $m$  and Or<sub>62</sub>. Feldspars farther toward Or follow their own fractionation lines to the Lc<sub>ss</sub> join, and eventually to soda-free leucite along that join.

One peculiarity remains to be resolved, and that is the behavior of compositions close to the feldspar join but in the Lc + Fsp solid field. Observe that these are driven toward the feldspar join by extraction of liquids along the field boundary  $L$  (Lc, Fsp) near R. But then the liquid moves toward the feldspar join and eventually across it. No TSC can, therefore, remain on the feldspar join for more than an instant, at Or<sub>62</sub>. Fractionation lines approach infinitesimally close to the join, but touch it

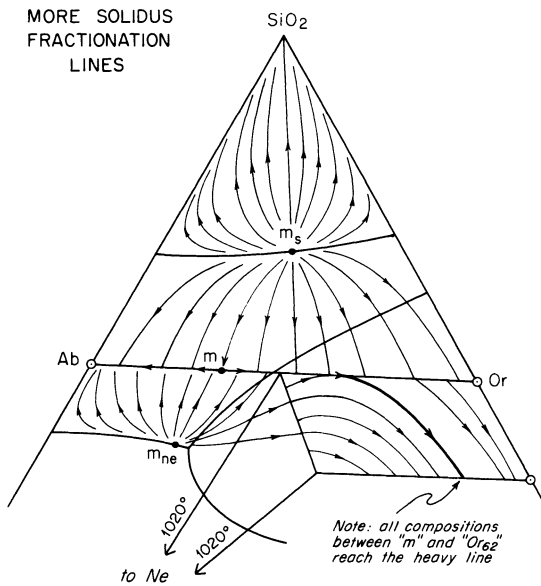


**Figure 15.13.** Solidus fractionation lines extended to the regions of leucite and silica mineral.

only at Or<sub>62</sub>, whereupon they immediately leave it along the heavy line. Clearly, fractional melting of a leucite-bearing composition will not yield an exactly saturated solid residuum, although it may eventually yield an oversaturated liquid. By contrast, many nepheline-bearing original compositions will yield solid residua strictly on the feldspar join.

Using Fig. 15.13, we may draw certain conclusions about fractional melting in this system at 1 bar. Melts of strictly minimum composition will be rare, restricted to singular bulk compositions lying on special lines. All other melts will be of variable initial temperature and composition on a cotectic or peritectic boundary. They will be extracted only over a continually rising temperature range except for those which reach R and stay there for a while. No melting process can yield undersaturated liquids from initially oversaturated compositions. A very restricted range of bulk compositions may yield undersaturated solid residua from initially saturated solid compositions.

#### PETROLOGIC SUMMARY

Once again, we return to the theme of what basaltic liquids may become on fractionation. In general, as Bowen long ago pointed out, they yield residua closely modelled by the system Ne-Ks-SiO<sub>2</sub>, and more specifically, these residua tend to lie in a relatively limited region, which Bowen called a

“thermal valley”, encompassing the three minima,  $m_{ne}$ ,  $m$ , and  $m_s$  (Fig. 15.14). Natural rocks closely corresponding to these three compositions occur in abundance, and their extrusive equivalents are called, respectively, *phonolite*, *trachyte*, and *rhyolite*. We may therefore speak informally, and quite appropriately, of the *phonolite minimum*, *trachyte minimum*, and *rhyolite minimum*. These are the logical and quite often defensible residua from fractionation of alkali basalt, critical plane basalt, and tholeiite, respectively.

In terms of actual liquidus temperatures, Bowen's thermal “valley” is not a valley at all, but a saddle, or negatively curved surface, with a culmination at the trachyte (syenite) minimum at 1063°C. If this is a saddle, the Ab-Or join is the horse, and cantle and pommel slope toward  $m$  along the feldspar join itself. The culmination, or seat, then slopes off away from the join toward the stirrups at  $m_s$  and  $m_{ne}$ . A cross section through the liquidus surface along the general line (transverse to the horse) through or near the three minima is shown in Fig. 15.15. This section is drawn to scale, and it leaves no doubt that  $m$  is a pronounced *maximum* relative to  $m_{ne}$  and  $m_s$ . It shows, furthermore, the very steep liquidus slopes leading to the two “stirrup minima”, especially from the directions of nepheline and silica. The feldspar minimum  $m$  is simultaneously a minimum in Ab-Or and a maximum relative to  $m_{ne}$  and  $m_s$ .

The general configuration of Fig. 15.15 is maintained at high pressure (to at least 10 kbar) in the presence of steam (Morse, 1969a). It is therefore somewhat surprising that trachytes exist at all, for one would suppose that the slightest deviation of a bulk composition from the critical plane (or feldspar plane) would lead to phonolitic or rhyolitic residual liquids. The common existence of trachytes and syenites requires, then, some mechanism for keeping liquids in the critical condition during fractionation, as well as a non-unique source mechanism for generating critical-plane liquids in the mantle. The fractionation control need only be minor if initial liquids

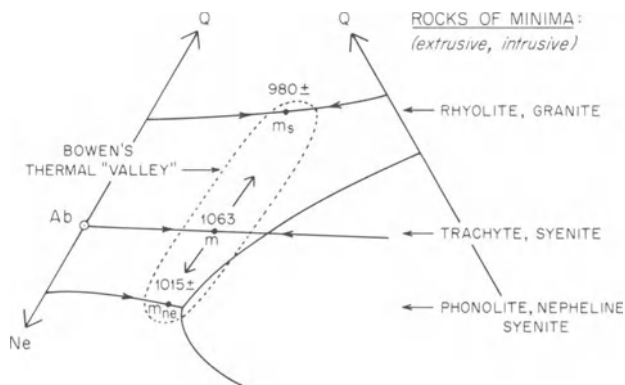
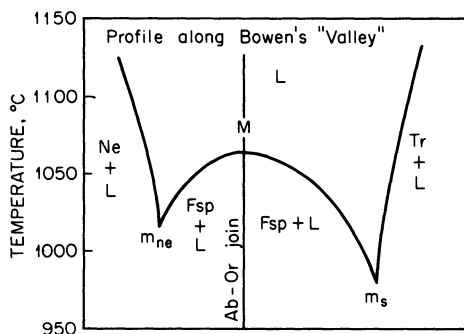


Figure 15.14. Bowen's thermal “valley” in the residua system.



**Figure 15.15.** Scale drawing of liquidus temperatures along Bowen's thermal "valley". The line of section connects the three minima, but may not be straight through M.

are *strictly* of the critical-plane type, for then they will have no inherent tendency to fall away from the feldspar join. But the source controls for generating such liquids repeatedly in the mantle are essentially unknown, and the "syenite problem" remains a thorn in the side of igneous petrology.

## Introduction to Ternary Feldspars

We shall take a very simplistic view of ternary feldspars, which can be quite complex in the plutonic environment. Our purpose here is simply to see how feldspars behave with fractionation in basaltic systems, and how well the join Ab-Or proxies for feldspars in general.

We begin unconventionally by introducing a ternary plot of feldspar analyses from *one thin section* of a basalt from Picture Gorge, Oregon, studied by D. H. Lindsley and Douglas Smith (1971). This is shown in Fig. 15.16. The feldspar composition ranges all the way from  $An_{84}, Or_{0.5}$  to  $An_{0.3}, Or_{59.8}$ . The Or content increases moderately from  $An_{80}$  to  $An_{40}$ , after which it begins to increase strongly, following a smooth curve which is convex toward Ab and nearly symmetrical about the bisector of the Ab corner angle. This extreme range of compositions can only be due to fractional crystallization, and from studies of many other basaltic rocks it is apparent that the trend found by Lindsley and Smith is the normal one.

The trend shown in Fig. 15.16, is, in effect, an ISC path of fractional crystallization plotted in the ternary feldspar diagram. We do not know what role was played by equilibrium reaction of crystals and liquid, but from the extreme range of compositions we may safely assume that it was very small. We must recall that the *liquids* from which these feldspars crystallized were *not* in the ternary feldspar plane, but basaltic to rhyolitic. Nevertheless, we may view Fig. 15.16 effectively as a phase diagram if we imagine liquids to be projected onto the feldspar plane from all other

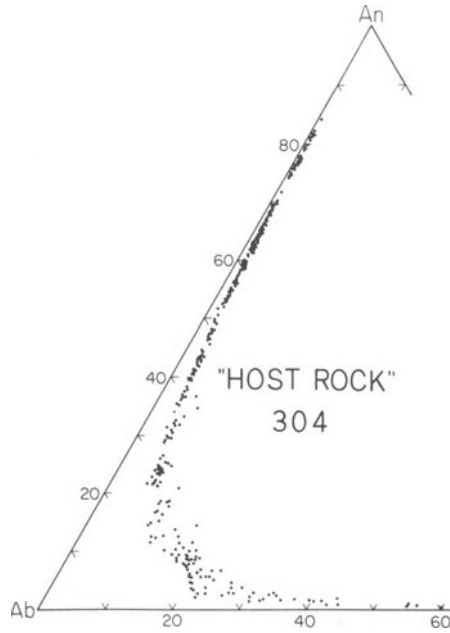


**Figure 15.16.** Plot of 304 feldspar analyses from a single thin section of Picture Gorge basalt, Oregon, by Lindsley and Smith (1971). Reproduced with permission of the authors and the Director of the Geophysical Laboratory. *Or* lies at the missing corner of the triangle.

components, and imagine the feldspars themselves to lie in the plane. Suppose we assume that the bulk feldspar composition lies somewhere near  $An_{60}$ . (We have no straightforward way of retrieving this from the plot, but a reasonably calcic composition is required by the calcic nature of the initial ISC.) Then the initial liquid must have contained slightly more *Or* than the ISC at  $An_{60}$ , for otherwise the ISC would equal the TSC at  $An_{60}$  and crystallization would be complete there. The *liquid path*, when plotted on Fig. 15.16, will need to lie very close to the ISC path, with tie lines reaching backwards to more *An*-rich ISC's. It appears as though the liquid must contain more *Or* than the normal coexisting feldspar, because otherwise it could never become *Or*-enriched. On the other hand, the difference in *Or* must be very small at first, because otherwise *Or*-enrichment in the liquid would proceed very rapidly and lead, as other experience shows, to crystallization of two feldspars. The diagram shows that we are concerned essentially with a single-feldspar trend which sweeps through the plagioclase series and into the sanidine structural series (which reaches over to the  $Ab_{60}Or_{40}$  region). We can therefore postulate the *qualitative* liquid path shown in Fig. 15.17, as a generalized example of basaltic feldspar fractionation. In this summary diagram, crystallization begins with the establishment of a tie line from liquid "BC" to the first feldspar, and continues with

feldspars tied by tangents to the liquid path. The feldspars fall along the ISC path. The end of the process is assumed to occur when the liquid and feldspar both reach a minimum on or near the Ab-Or join.

A very different result would arise from equilibrium crystallization, which is qualitatively displayed in Fig. 15.18. The initial BC-feldspar tie line must be the same as in the fractional case, but all others are different, since they must pass through the bulk composition. The liquid and TSC paths are much more strongly curved than in the fractional case.

It is helpful to consider the geometry of each type of crystallization in a *T-X* diagram as projected from An onto Ab-Or, shown in Fig. 15.19. It should be stressed that both liquids and crystals are projected; none lie in the section except possibly those at *m*. The initial difference in Or content between crystal and liquid has been greatly exaggerated for clarity. This initial isothermal tie line supposedly connects a liquid bulk composition near An<sub>60</sub> with a feldspar near An<sub>80</sub>. As fractional crystallization proceeds, both crystal and liquid become enriched greatly in Or with a large drop in temperature. Liquid and ISC paths are in principle the same as those in Fig. 15.17. Crystallization is assumed to terminate at a minimum. The fractional TSC path begins at the solidus and reaches the bulk composition

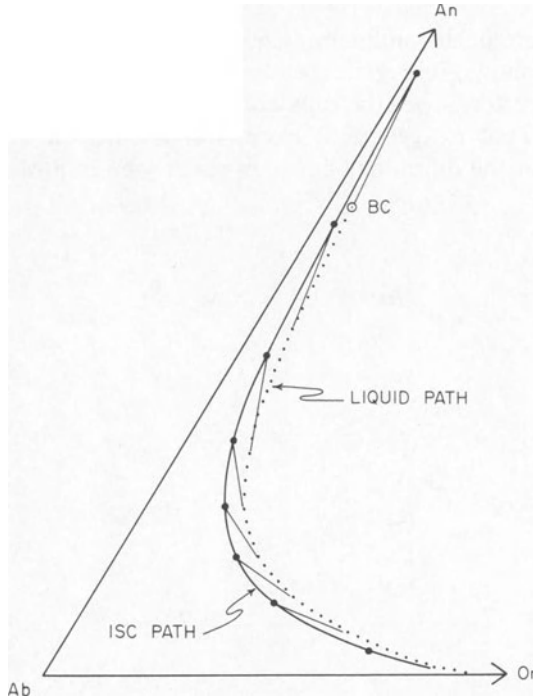


**Figure 15.17.** ISC path for fractional crystallization corresponding to the feldspar trend in Fig. 15.16, with inferred liquid path projected from all other components onto the feldspar plane.

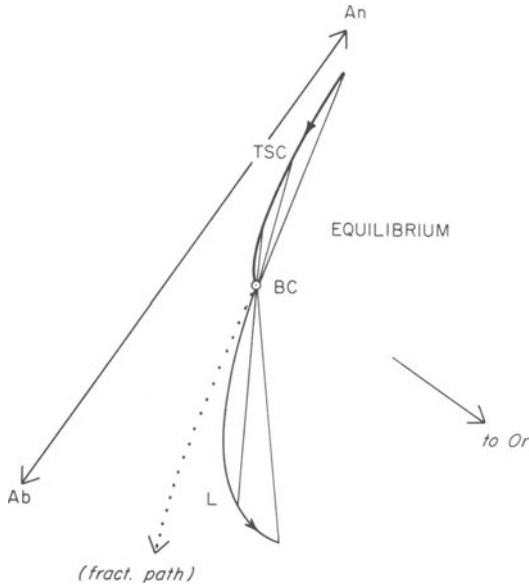


**Figure 15.18.** Scheme of equilibrium crystallization for Or-poor ternary plagioclase.

at the temperature of the minimum. Equilibrium crystallization, assumed to have the paths shown in Fig. 15.18, terminates at a much higher temperature. The TSC path reaches the bulk composition when the liquid has made a considerable (but exaggerated) excursion toward Or enrichment. Fig. 15.19 emphasizes the difference between paths seen in projection and those

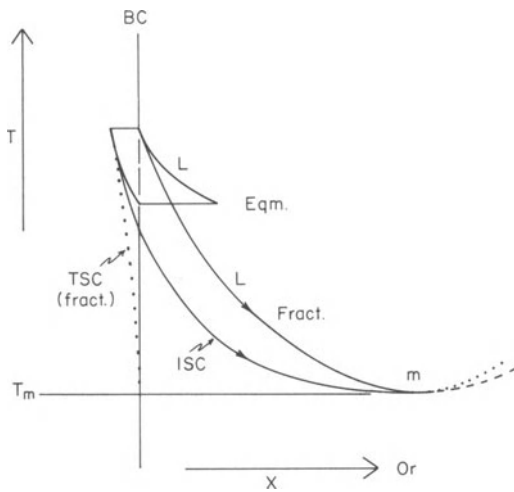


**Figure 15.19.** Comparison of equilibrium and fractional crystallization paths, in a  $T$ - $X$  section projected from An onto the Ab-Or join.

lying in a  $T$ - $X$  plane. In the latter case (i.e., in a binary system), there is only one liquidus and one solidus, whatever the process. In projection, and of course in the parent ternary diagram of Fig. 15.18, the liquid paths differ depending on the process, and so do the crystal paths. Each bulk composition falls on a unique equilibrium path. Families of bulk compositions lie along unique liquidus fractionation lines like the liquid path in Fig. 15.17.

The principles governing crystallization and melting paths in systems with ternary solid solution, like the feldspar system, are described by Roeder (1974).

#### CONCLUDING REMARKS ON FELDSPAR

The discussion above is intended to illustrate the familiar fact that in basaltic systems, the liquid is slightly enriched in potassium relative to feldspar. Fractionation of feldspar *and associated mafics* causes the feldspar fractionation trend which is typified by Fig. 15.16. We must now draw a very careful distinction between the foregoing illustrations and the pure ternary feldspar system itself. The assumed ISC paths result from the total fractionation of all phases, including, but not limited to, feldspar. In general, the feldspar contains almost all the K, and the mafic phases almost none. The crystallization of these K-poor mafic phases therefore must contribute greatly to the liquid fractionation trend: in particular, to its enrichment in Or. Fractional crystallization of a pure ternary feldspar liquid would certainly yield a trend falling much closer to the Ab corner of the diagram. It is conceivable, though unlikely, that the ratio of K in feldspar to K in liquid could be greater than 1.0 and still yield the trend shown in Fig. 15.16 by virtue of the subtraction of K-poor mafic minerals. Studies on natural systems such as the Kiglapait intrusion suggest that the ratio is indeed less than 1.0, but not much less, for intermediate plagioclases.

In view of these considerations, experimental study of the pure ternary feldspar system may be less fruitful than observational studies of natural rocks like that of Lindsley and Smith. It is also true that compositional equilibrium is very difficult to attain in the ternary feldspar system, and in fact no satisfactory experimental basis for the present discussion yet exists. A liquidus diagram was published by Franco and Schairer (1951), but that is of indirect pertinence to the present discussion. Experimental work at higher pressures in the presence of steam has been carried out by several workers, most notably Yoder, Stewart, and Smith (1957), and that work is highly pertinent to granitic rocks containing two feldspars (a plagioclase and an alkali feldspar). The existence of a ternary feldspar solvus which is intersected by low-temperature liquids in the system An-Ab-Or-H<sub>2</sub>O generates complications which are beyond the scope of the present discussion. A magnificent theoretical treatment of such problems was given by Stewart

and Roseboom (1962), and much can be and has been done by coupling their theoretical approach with observations of natural rocks. The difficulty of experimental study is underscored by the scarcity of new work on ternary feldspars, among which that of Seck (1971) is especially valuable. This work outlines the shape of the ternary feldspar solvus as a function of temperature, but does not compare closely with the single point determined by Morse (1969b). The change of the ternary solvus with pressure is essentially unknown.

Finally, it must be noted that the fractionation path observed by Lindlsey and Smith (Fig. 15.16) arose from relatively rapid cooling of a thick flow, and therefore quite surely represents a large degree of supercooling. This phenomenon produces crystals which do not lie on the equilibrium solidus, but instead lie nearer to the liquid. (Some of the scatter around the bend of the trend may result from varied degrees of supercooling.) The illustrated trend need not, therefore, pertain in detail to deep-seated fractionation processes which involve much less supercooling.

## Complex Crystallization of Solid Solutions

Curious things may happen during equilibrium crystallization when two solid solutions are present in a ternary system, for example leucite and feldspar in the system Ne-Ks-SiO<sub>2</sub>. Furthermore, curious things may happen whenever a liquidus field boundary crosses a solid solution join (such as the feldspar join) in such a system. Some analysis is required to know when the reaction on such a boundary is odd or even. The system Ne-Ks-SiO<sub>2</sub> offers a good opportunity to comment on such complex paths. The analysis offered here derives from that of Fudali (1963) and ultimately from the remarkable pioneering study of another system by Bowen and Schairer (1935).

### ODD AND EVEN REACTIONS

Consider Fig. 15.20, which shows part of the crystallization of a bulk composition BC located in the leucite primary phase field. Leucite has crystallized while the liquid has moved from BC to 1, at which time feldspar appears. Now leucite dissolves as feldspar forms, and the liquid moves along the field boundary in odd reaction. Eventually the liquid reaches R, where the invariant reaction will set in, but we are not concerned with that. By means of the lever rule, we may calculate the fraction of leucite present in the system, first by finding  $F_s$  from the levers through BC to the TSC, and then multiplying by  $F_{lc}$  (fraction of leucite in the solids) obtained from

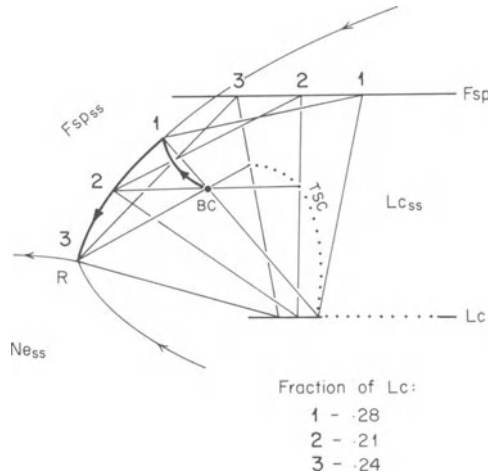


**Figure 15.20.** Partial equilibrium crystallization path from a bulk composition in the leucite field, showing first the loss and then gain of leucite. After Fudali (1963).

the solid-solid leg of triangles 2 and 3. We find the sequence 0.28, 0.21, 0.24. Clearly, leucite has been destroyed between 1 and 2, but *added* between 2 and 3. This can only mean that the reaction has changed from odd to even somewhere in the vicinity of 2.

This may at first seem an amazing result, apparently in contradiction with the positions of equilibrium feldspars and the tangent to the field boundary. But in equilibrium crystallization, the *material being removed from the liquid* at any instant is far in advance of the equilibrium crystal composition, and it is *this* material from which the liquid must always flee. We shall find that our tangent rule for odd and even reactions still holds true when we consider the material being removed from the liquid rather than the equilibrium compositions of solid solutions.

In Fig. 15.21, we see equilibrium compositions F and L tied to each other and to liquid. For the solid solution let us suppose that fictive feldspar material of composition  $f_1$  is being removed from liquid 1 to convert  $F_1$  toward  $F_2$ . Similarly, let us suppose that fictive leucite material of composition  $l_1$  is being removed from liquid 1 to convert  $L_1$  toward  $L_2$ . The liquid must always move away from what we may call the *fictive extract*, a summation of f and l. This fictive extract must therefore lie on the tangent to the field boundary, and its position on  $f_1l_1$  is defined by the intersection of this tangent with  $f_1l_1$ . In the case of liquid 1, it is clear that the tangent lies on the *extension* of  $f_1l_1$ , hence the fictive extract consists of  $f_1 - l_1$  and the reaction is odd: liquid equals fictive feldspar minus fictive leucite. In the case of liquid 2, the fictive compositions are so far advanced that the fictive extract is now a *positive* combination of feldspar and leucite, i.e.,  $f_2 + l_2$ . Now the reaction is even. The rule is that the liquid must always move away from the fictive extract, not from the equilibrium compositions.

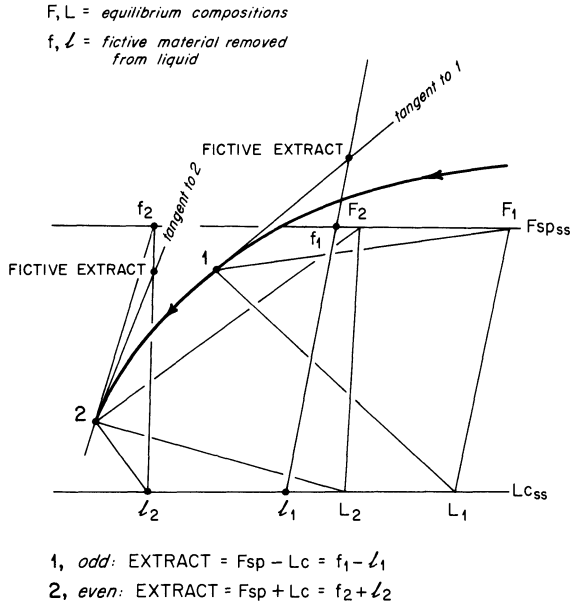


**Figure 15.21.** Illustration of the fictive extract and how it determines whether equilibrium crystallization is odd (case 1) or even (case 2).

It is sometimes erroneously said or implied that the reaction changes from odd to even when the fictive feldspar composition crosses the field boundary, but this is not the case (unless the boundary is straight). The change in sign occurs only when the *fictive extract* reaches the feldspar join from a negative position. One may construct on Fig. 15.21 a fictive tie line halfway between  $f_1/l_1$  and  $f_2/l_2$  and observe that the tangent to the liquid path halfway between 1 and 2 still cuts the fictive tie line at negative leucite. The correct location of the sign change is to be found by constructing the entire *path* of fictive extracts by such means and finding where this path cuts the feldspar join.

It should be noted that a fictive composition such as  $l_2$  may lie far beyond any actually attainable leucite crystal composition. Moreover, the fictive extract must be farther advanced for a large fraction of solids than for a small fraction, so it depends on the bulk composition.

What becomes of the fictive extract as the liquid approaches R? By now we know very well that when a liquid is invariant (as at R), the material being extracted from it must be invariant and coincident, hence at R. The path of the fictive extract therefore must terminate at R. As it does so, the partly fictive “three-phase triangles” of type 2- $f_2$ - $l_2$  in Fig. 15.21 shrink to a line passing through R. But *at* R, the reaction changes discontinuously to a totally different one in which all four phases are fixed in composition and now the fictive compositions and the equilibrium compositions are coincident.



FRACTIONAL CRYSTALLIZATION AND MELTING

In fractional crystallization, the fictive extract is always identical to the instantaneous *equilibrium* composition (the ISC) of the separating solids, and none of the above complexities arise. The liquid always moves away from the real ISC. Likewise in fractional melting, the TSC always moves away from the real ILC, and questions involving the geometry of fictive material do not arise. The complexities discussed in this section arise from the *equilibrium* reaction of crystals and liquid. The leucite-feldspar field boundary is peritectic along its entire length for fractional crystallization, but cotectic in places for equilibrium crystallization.

G-X Diagrams for the Albite-Orthoclase Join

The studies of Waldbaum and Thompson have led (1969) to an elegant presentation of *G-X* diagrams and calculated phase diagrams. Although these topics are a side issue to the matter of basalts, they are so fundamental to the advanced treatment of phase diagrams that we shall digress briefly to review them here. Four isothermal *G-X* diagrams illustrating the melting of sanidine-high albite are shown in Fig. 15.23. In contrast to the *G-X* diagrams shown earlier in this volume, which were drawn *a posteriori* from the phase diagrams, these more nearly represent *a priori* calculations from which the

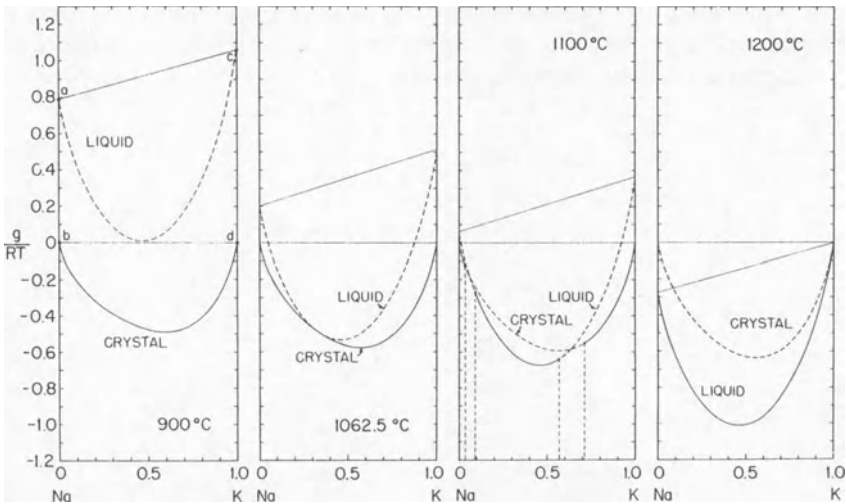


**Figure 15.23.** Calculated *G-X* diagrams for the melting of sanidines at 1 atm., from Waldbaum and Thompson (1969), reproduced by permission. Ordinate scale is described in the text. Abscissa is in mole units.

phase diagram was derived. This is not quite the case, because Schairer's (1950) determination of the minimum composition and temperature was used as input, along with the melting point of albite and the metastable congruent melting point of sanidine. For the rest, the calculation makes use of the *mixing properties* of the crystalline solution series, which is to say the non-ideal ways in which the entropy, internal energy, molar volume, and Gibbs energy are additive over the series from pure Ab to pure Or. These properties were calculated from a variety of thermodynamic data by Thompson and Waldbaum. Then the mixing properties of the melts themselves were calculated from Schairer's minimum determination alone, and finally the assumption was made, for lack of any relevant data, that the so-called excess entropy of mixing along the liquid solution series is zero. This is an assumption of ideal mixing, very likely not true in detail but not seriously in error for the purpose at hand. The procedure of calculation is beyond the scope of this book, and in fact it required a large amount of computer time because it involves an iterative solution to some complicated equations. The procedure is thoroughly described in the set of papers cited in Waldbaum and Thompson (1969).

Samples of the results are shown in Fig. 15.23. The figure is a particularly convenient representation of  $G$ - $X$  relations in that the motion (with temperature) of the  $G$ - $X$  curve for the solid solution is held fixed, while the curve for the liquid moves past it. This is done by the clever artifice of reducing the Gibbs energy to a difference, such that the quantity on the ordinate for either pure Ab crystal or pure Or crystal or any mechanical mixture of them is zero. The quantity plotted (divided by the product of the gas constant and the Kelvin temperature) is given by the relation

$$g \equiv \overline{G}(\text{crystal or liquid}) - N_1\mu_1^\circ, \text{ crystal} - N_2\mu_2^\circ, \text{ crystal},$$

where:

$\overline{G}$  = molar Gibbs energy

$N$  = mole fraction

$\mu^\circ$  = the chemical potential  $\partial G/\partial n$  at standard state ( $n$  = No. of moles)

1,2 = subscripts denoting components Ab and Or, respectively.

For pure substance 1,  $N_1 = 1.0$ ,  $N_2 = 0$ , and  $\mu_1^\circ = \overline{G}$ . Similarly for pure substance 2. This is why the value of  $g$  is zero for the mechanical mixture of pure solids. The quantity  $\overline{G}$ , however, includes the mixing effect for crystalline and liquid solutions, and is always less than a linear combination of end points. Without the reduction, the Gibbs energy of Ab would plot higher than that of Or, and without the further reduction of dividing by  $RT$ , these points and the crystal  $G$ - $X$  curve would move up along the ordinate with temperature.

Fig. 15.23 may be compared with the  $T$ - $X$  diagram, Fig. 15.26 (or Figs. 15.3 and 15.4). In the figure, the 1100° diagram illustrates the determination of solidus and liquidus compositions by double tangents to the curves. Numerical solutions for these double tangents at many closely spaced

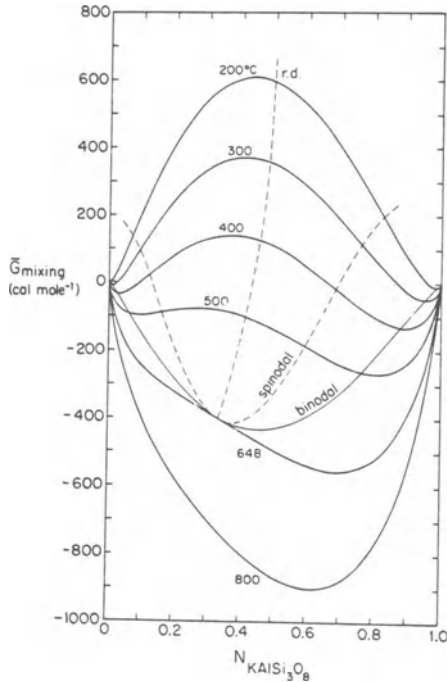


**Figure 15.24.** Calculated  $G$ - $X$  diagram for the sanidine solvus at 1 atm. The curves are isothermal sections through the Gibbs energy of mixing surface. From Waldbaum and Thompson (1969), by permission.

temperatures are given in the original reference, and it is these values from which the  $T$ - $X$  diagrams have been constructed. Note that in Figs. 15.23-15.26 the abscissa is in mole fraction rather than weight units, since mole units must be used in, and emerge from, all calculations.

Fig. 15.24 treats the alkali feldspar solvus, which is the curve bounding the miscibility gap in crystalline solutions at temperatures below the 1-atm solidus. The  $T$ - $X$  diagram of this solvus is shown in Fig. 15.26. Both diagrams illustrate features of solvi which we have not yet discussed, so we shall do so briefly here.

Figure 15.24 is a composite diagram showing isobaric (1 atm) slices through the  $G$ - $X$  surface at six different temperatures. The ordinate is the *molar excess Gibbs energy of mixing*, in calories per mole. The reference state is a mechanical mixture of the pure end-member phases at 1 atm and the temperature of interest, hence it is zero. The excess (positive or negative) molar Gibbs energy of mixing is a summation of the mixing properties of the molar internal energy, the molar volume, and the molar entropy. These quantities all change systematically with composition: the internal energy and volume deviate positively from a mechanical mixture of end members, while the entropy shows a negative deviation. The fundamental thermodynamic relationship is

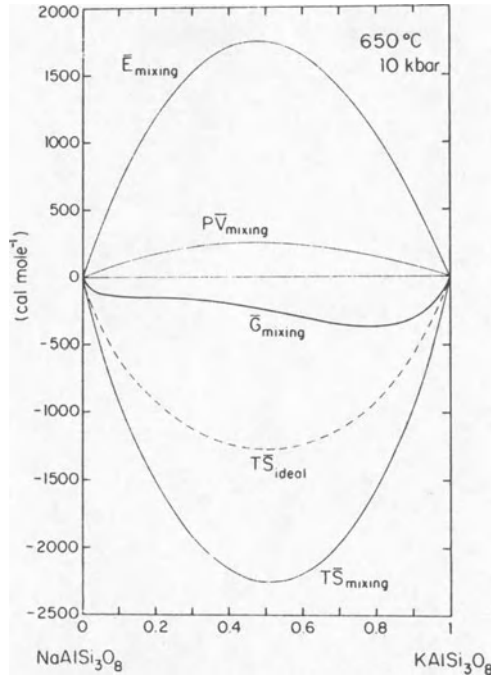


**Figure 15.25.** Mixing properties of sanidine solutions at 650°C and 10 kbar. From Thompson and Waldbaum (1969), by permission.

$$\begin{aligned}
 G &= H - TS, \\
 H &= E + PV \\
 G &= E + PV - TS,
 \end{aligned}$$

where  $G$  is the Gibbs energy,  $E$  is the internal energy,  $P$  is pressure,  $V$  is volume,  $T$  is Kelvin temperature, and  $S$  is entropy. These symbols represent the absolute quantities for a chemical system. By writing the mass-dependent (extensive) quantities  $G$ ,  $E$ ,  $V$ , and  $S$  with a bar over them, we denote the reduced or molar quantities, i.e.,  $\bar{G} = G/n$ , and the reduced quantities are inter-related mathematically in the same way as the absolute quantities. Fig. 15.25 shows the additivity of the reduced mixing quantities in the alkali feldspar system (sanidine structure) at 650°C and 10 kbar, relative to a reference state of a mechanical mixture of pure end members. Note here that while  $\overline{EPV}$ , and  $\overline{TS}$  appear almost perfectly symmetrical with composition, their summation in the heavy  $\bar{G}$  curve is highly asymmetrical, and the alkali feldspars belong to the class of *asymmetrical solutions*. This is further shown by the trace of the rectilinear diameter (r.d.) in Figs. 15.24 and 15.26. The rectilinear diameter is the mean composition of the coexisting phases on the binodal solvus, which is now to be discussed.

Two of the  $G$ - $X$  curves in Fig. 15.24 are characterized by a single curvature; these are for solutions at temperatures above (800°) or equal to

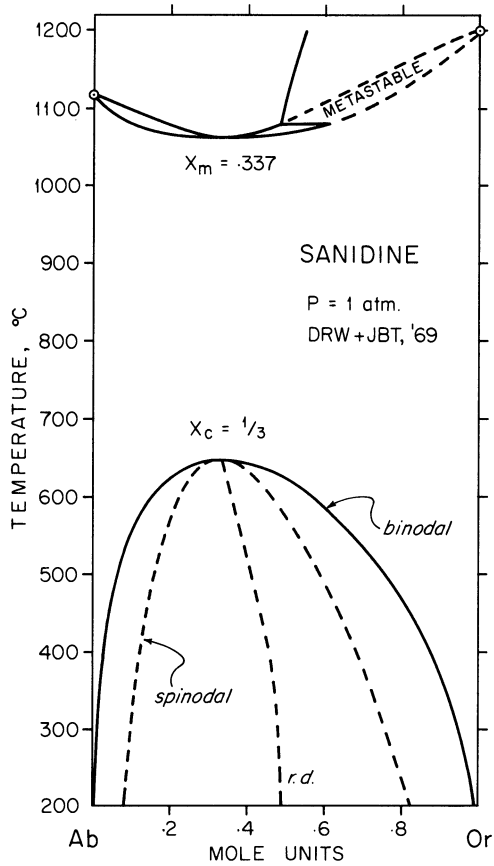


**Figure 15.26.** One-atmosphere phase diagram for Ab-Or, sanidine solutions, after Waldbaum and Thompson (1969).  $X_m$  is melting minimum and  $X_c$  is critical composition of solvus. Binodal and spinodal are explained in text; r.d. = rectilinear diameter.

(648°) the critical temperature of the solvus. The other four curves show both upward and downward curvature, characteristic of  $G-X$  curves for temperatures below the critical temperature of a solvus. The *stable* equilibrium compositions of the solvus limbs are given, for any selected temperature, by the common tangent points to the two *nodes* of the  $G-X$  curve. The solvus curve in  $T-X$  space which describes the locus of such double tangent points is called the *binodal* curve or binodal solvus. This curve defines the stable equilibrium composition of the coexisting feldspars. A mechanical mixture of two feldspars external to the binodal will lie at higher  $G$  than the common tangent and will therefore be metastable relative to the binodal pair; such a mechanical mixture will tend to come to the equilibrium compositions by diffusive exchange of alkalis. The crystals will do this along portions of the  $G-X$  curve having the second derivative

$>0$  (concave up), and this means that the rate of approach to minimum  $G$  will become less and less as the crystals approach the binodal compositions. In fact, kinetics being involved, such crystal pairs may closely approach but not attain the binodal compositions, and this causes problems for the experimentalist.

The same upward curvature extends inward past the binodal points; here also the feldspars are metastable with respect to diffusion. But along the  $G$ - $X$  curve there are two *inflection points* where the second derivative  $\partial^2 G / \partial N^2$  changes from positive to negative. These are the so-called *spinodal points*, and the curve describing their locus with temperature is called the spinodal curve or spinodal solvus. A homogeneous phase lying within the region bounded by this curve is inherently unstable with respect to internal diffusion. One way of appreciating this is to note that the isothermal  $G$ - $X$  slope increases toward the spinodal points in this region, and hence the change in  $G$  increases with composition. The spinodal curve may thus be regarded as the *limit of metastability* on going away from the binodal compositions. At the spinodal, metastability gives way to true instability as long as diffusion processes can act fast enough. A feldspar in this region of instability will tend to unmix (exsolve) spontaneously. Only if internal diffusion is too slow (as in quenching) will this fail to occur.

Fig. 15.24 shows the origin of the spinodal curve as the locus of inflections in the  $G$ - $X$  curves at various temperatures. Fig. 15.26 shows the  $T$ - $X$  trace of the spinodal. Note that it unites with the binodal at the critical point.

There is yet another type of solvus, called the *coherent solvus*, that takes account of the strain energy developed at the physical interface between two intergrown phases (phases which cohere). The coherent solvus does not unite with the other two at the critical point, but lies everywhere inside the spinodal. A valuable discussion of this phenomenon is given by Yund (1975). There is some question as to how far the concept of coherency applies to intergrowths of feldspars, pyroxenes, and amphiboles, because the exsolution directions in these minerals tend to be non-rational crystal planes (optimal phase boundaries) along which the lattice strain is minimized, possibly even to zero or a value very close to it, at the temperature of formation of the intergrowth (Bollmann and Nissen, 1968; Robinson et al., 1971).

Several properties of the alkali feldspar solvus shown in Fig. 15.26 deserve further comment. The figure pertains *only* to sanidine structures. For other feldspars with more ordered distributions of tetrahedral Al and Si, the solvus rises, perhaps as much as 230°C for microcline-low albite (Bachinski and Müller, 1971). The solvus also rises with pressure, at a rate of at least 14°C/kbar. Both these factors must be considered when thinking about melting of crustal rocks.

## Chapter 16

# Iron and Oxygen

### Introduction

In the systems heretofore discussed, we have dealt mainly with the six components  $\text{SiO}_2$ ,  $\text{Al}_2\text{O}_3$ ,  $\text{MgO}$ ,  $\text{CaO}$ ,  $\text{Na}_2\text{O}$ , and  $\text{K}_2\text{O}$ , among which may be found the principal phases or mineral components of the basalt tetrahedron and of basalts themselves: nepheline, albite, orthoclase, quartz, anorthite, plagioclase in general, forsterite, diopside, enstatite, and Fe-free pigeonite. Missing from this list are the Fe-Ti oxides, which require consideration of  $\text{FeO}$ ,  $\text{Fe}_2\text{O}_3$ , and  $\text{TiO}_2$  as components.  $\text{FeO}$  is required also for discussion of the ferrous silicate components of olivine and pyroxene. Phosphorus is also a constituent of importance in basalts, reporting either in groundmass glass or in apatite, which crystallizes during late fractionation stages when phosphorus becomes high enough to saturate the melt in apatite component. Present generally in minor quantities, phosphorus can be ignored for present purposes, always bearing in mind that its abundance level in basaltic magmas may contain important information which we may or may not be able to analyze correctly.

The above list of neglected components—oxides of Fe, Ti, and P—all have one very important property in common. They all tend to be conserved in residual liquids upon fractionation of basaltic magma, or conversely, to be incorporated into relatively low temperature melts on partial fusion of basalt. P commonly has the status of a minor element except after severalfold concentration by a fractionation or fusion process. Fe is a major element of basaltic rocks, commonly reaching levels of 10% (expressed as  $\text{FeO}$ ), and Ti commonly lies between 1 and 2%, expressed as  $\text{TiO}_2$ . We

shall ignore Ti for the present. It is both necessary and convenient to discuss Fe in some detail.

## Iron in Silicates

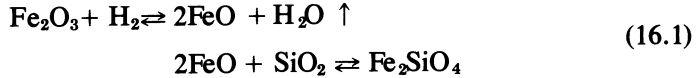
In common basaltic rocks, most of the iron in silicate minerals is ferrous iron,  $\text{Fe}^{2+}$ . We shall treat these minerals throughout as ferrous silicates, ignoring small amounts of  $\text{Fe}^{3+}$  which may be present but which do not, in large degree, affect the fractionation or genesis of basaltic magmas. The minor iron in leucocratic minerals such as plagioclase feldspar will also be ignored. Most of the ferrous iron in basaltic silicates can be accounted for in olivine and pyroxene, and for all practical purposes we may assert that ferrous iron occurs in these mafic minerals as a proxy for Mg, in three major solid solution series. The first of these is easily and satisfactorily modelled as the olivine series forsterite (Fo)-fayalite (Fa),  $\text{Mg}_2\text{SiO}_4$ - $\text{Fe}_2\text{SiO}_4$ . The pyroxenes are less clear-cut, but are composed of a Ca-rich (clinopyroxene) series and two Ca-poor (orthopyroxene, pigeonite) series in the pyroxene quadrilateral, diopside (Di)-hedenbergite (Hd)-enstatite (En)-ferrosilite (Fs), in which



The Ca-rich clinopyroxene series commonly contains up to 1/5 En-Fs in solid solution, and is known as the augite-ferroaugite-ferrohedenbergite series. The Ca-poor series commonly carries less than 1/10 Di-Hd in solution except when occurring as pigeonite. All three series, unsurprisingly, share the property that Fe lowers the melting temperatures.

## Fayalite

Fayalite (Fa) is a well-known product of blast furnace slags, and the common method of laboratory synthesis involves an analogous reaction of hematite plus quartz in a reducing atmosphere. Pure  $\text{Fe}_2\text{O}_3$  and  $\text{SiO}_2$  in appropriate proportions to yield the compound  $2\text{FeO} \cdot \text{SiO}_2$  are ground in agate under acetone to make an intimately mixed slurry. When dried, the fine-grained powder is sintered at an appropriately high temperature ( $>1000^\circ\text{C}$ ) in a stream of  $\text{H}_2$ - $\text{CO}_2$  gas which is mixed in suitable proportions to stabilize fayalite without leaving excess  $\text{Fe}_2\text{O}_3$  or making metallic iron. Techniques of gas mixing to control oxidation are described in the volume by Ulmer (1971). Fayalite is synthesized in such a procedure by a chemical reaction which may be characterized as



All experimental work involving a compound of FeO presents difficulties, for it is difficult or impractical to control the partial pressure of oxygen to just that value (or small range of values) which maintains Fe<sup>2+</sup> without excess Fe or Fe<sup>3+</sup>. Experimental techniques with ferrous minerals have commonly involved a compromise between what may be theoretically desirable and what may be expeditiously achieved. From the early work of Bowen and Schairer (1932), it has been a common practice to maintain most of the iron in the ferrous state during melting experiments by establishing equilibrium with an iron crucible in a nitrogen or other gas atmosphere, sometimes with iron wool within the charge as well. Experiments performed in nitrogen under these conditions will contain all three oxidation states of iron, but FeO predominates. Bowen and Schairer reported the melting point of fayalite as 1205°C, but this actually represents the incongruent melting of Fa to iron plus liquid in the system Fe-Si-O. Figure 16.1 illustrates the nature of this reaction in a strategically-chosen *T - X* section through the ternary subsystem Fe-SiO<sub>2</sub>-O. There are actually two sections, Fe-Fa and Fa-O, joined together at Fa. Each of these sections is binary by restriction, being compositionally degenerate so that Fe-Fa, extended slightly beyond the Fa composition, would rigorously express the reaction Fe + L = Fa, and Fa-O expresses the binary reactions Fa + O = L in the presence of iron, and Fa + O = L in the presence of magnetite. The derivation of these sections will become apparent on a later page,

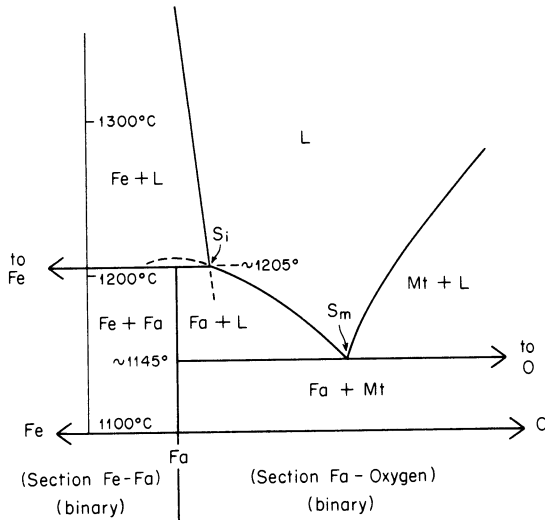


**Figure 16.1.** Two binary *T-X* sections joined at fayalite (Fa) to illustrate its melting relations. The sections are Fe-Fa and Fa-Oxygen, and are taken from Fig. 16.4.

where the full ternary system is discussed. Figure 16.1 is used here to show the general similarity of the melting behavior of fayalite to that of enstatite in the system  $\text{MgO-SiO}_2$ . Note, however, that the incongruity involves separation of a metal phase and an oxygen-rich liquid, rather than a silica-poor solid and a silica-rich liquid.

## The Fo-Fa Series

The system Fo-Fa as determined by Bowen and Schairer (1932) is shown in Fig. 16.2(a). This is not a binary system because the olivines and liquids are in equilibrium with metallic iron, and the liquids are enriched in oxygen relative to the stoichiometric olivine composition. This incongruity disappears, of course, at the melting point of pure Fo, and is probably of minor importance except at Fa-rich compositions. The diagram shown is actually a projection in the quaternary system  $\text{Mg-Fe-Si-O}$ , as will be explained shortly. It should be noted that because of the high temperatures involved, the liquidus was determined only to  $\text{Fo}_{25}$  and the solidus to  $\text{Fo}_{60}$ . The rest of the diagram is extrapolated to the melting point of Fo ( $1890 \pm 25^\circ\text{C}$ ). The main geological impact of the system is that the olivines constitute a binary loop in which Fa is enriched in liquids relative to solids, and in which temperatures are drastically lowered as the Fo content falls. The diagram accounts for the enrichment in iron relative to magnesium commonly observed in olivines of basalts and their daughters, including the appearance of fayalite in rhyolites and trachytes and their plutonic counterparts, granite and syenite. Pyroxenes undergo similar iron enrichment with falling temperature, and the olivine system furnishes an adequate preliminary example for the generalization that the main effect of FeO in magmas is to reduce temperatures of crystallization and promote enrichment of FeO in residual liquids, in parallel with enrichment of Ab as a result of plagioclase crystallization.<sup>1</sup> The story is not quite that simple, however, and we should now turn to a more detailed analysis of olivine melting as an introduction to the subject of oxidation and reduction in magmas. Figure 16.2(b) will be discussed shortly.

<sup>1</sup>It has been noted with an air of surprise (Roeder and Emslie, 1970) that olivine actually contains more FeO than the basaltic liquids from which it crystallizes. The phase diagram tells us that olivine crystals are enriched in the Mg component relative to the Fe component, and we find that this is still true in basaltic systems. Basaltic systems also fractionate Mg-olivine, enriching the liquid in components of Fe-olivine, as the phase diagram predicts. Of course basalt consists of much more than olivine, and it should occasion no surprise that a metal-rich silicate such as olivine should contain more FeO than the liquid, which also carries potential plagioclase and other components. Magnesian olivine also contains more MgO than the liquid. It is also true that plagioclase contains more  $\text{Na}_2\text{O}$  than basaltic liquid. The *relative* crystal/liquid partitions illustrated by phase diagrams of simple systems should never be misconstrued to imply anything about *total abundances* of a single end member or component in a complex magma.

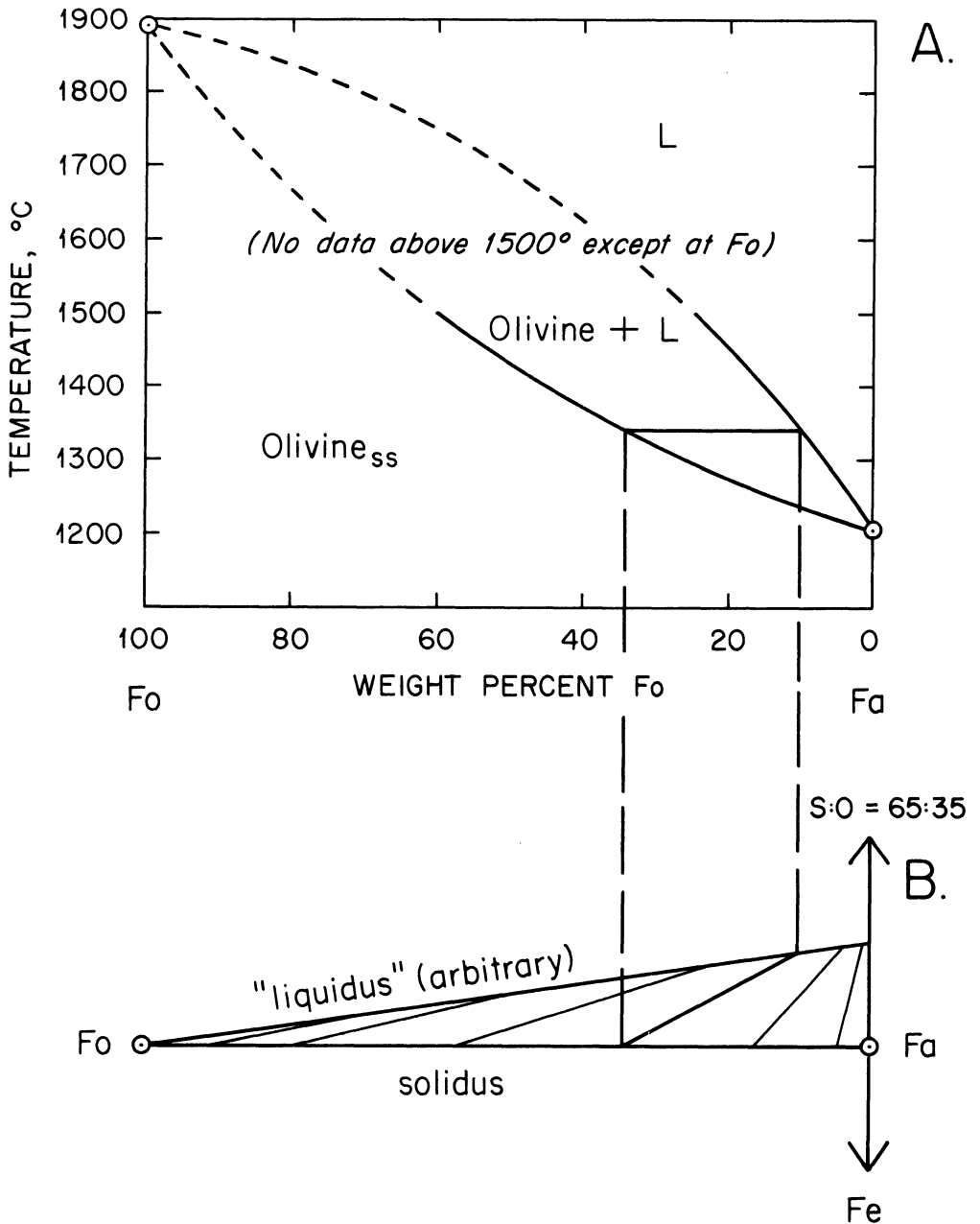


**Figure 16.2.** Melting of olivine in the presence of iron, after Bowen and Schairer (1932). A is the melting diagram, and B relates to Fig. 16.5, which see for discussion. Base of diagram measures 10 cm.

### Olivine Melting, Revisited

Both Figures 16.1 and 16.2 contain elements as yet unexplained, and we now undertake some explanations. Figure 16.3 depicts the system Fe-SiO<sub>2</sub>-O, showing the location of several phases important to basaltic rocks. Attention is called to the join FeO-SiO<sub>2</sub>, which contains fayalite, Fe<sub>2</sub>SiO<sub>4</sub>, and the end member orthopyroxene ferrosilite (Fs), FeSiO<sub>3</sub>. Ferrosilite is not stable at low pressures, a fact which makes the iron-rich orthopyroxenes of great importance as “natural barometers”—indicators of pressure during crystallization. Owing to this fact, we shall reserve discussion of ferrosilite to a later chapter where the effects of high pressure are considered. At 1 bar, the ferrosilite composition is represented by fayalite plus quartz or tridymite. Also shown in Fig. 16.3 are the compositions of magnetite (Mt, Fe<sub>3</sub>O<sub>4</sub>, or better, FeO·Fe<sub>2</sub>O<sub>3</sub>) and hematite (Fe<sub>2</sub>O<sub>3</sub>), on the join Fe-O. Not shown (for lack of room and geologic interest) is the mineral wüstite (German *Wüste* = desert), Fe<sub>1-x</sub>O, a variable solid solution occupying part of the range between FeO and Fe<sub>3</sub>O<sub>4</sub>.

Two tie lines of importance are shown in Fig. 16.3: that from Fe to Fa, and that from O to Fa. These are actually the section lines of Fig. 16.1, but we shall see them to better advantage in the next figure. On Fig. 16.3 are

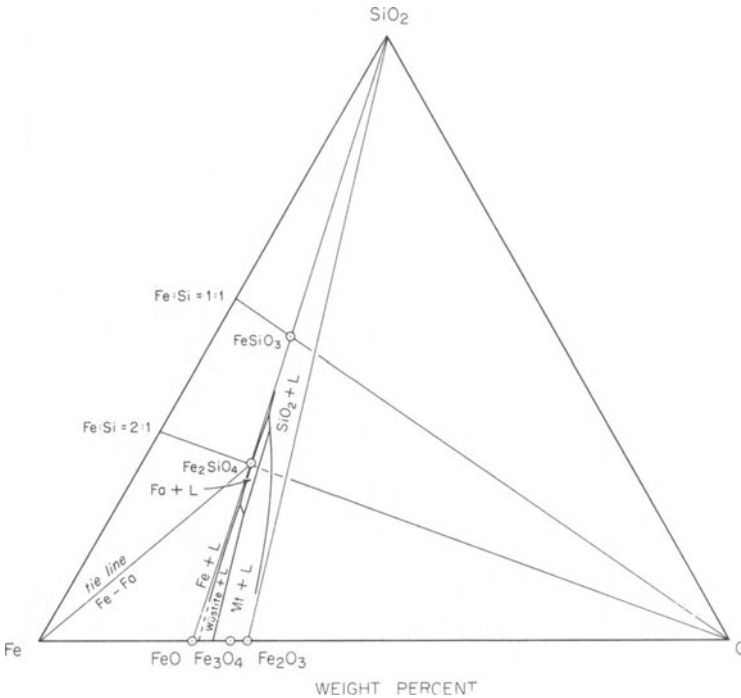


**Figure 16.3.** The system Fe-O-SiO<sub>2</sub>, after Muan and Osborn (1956).

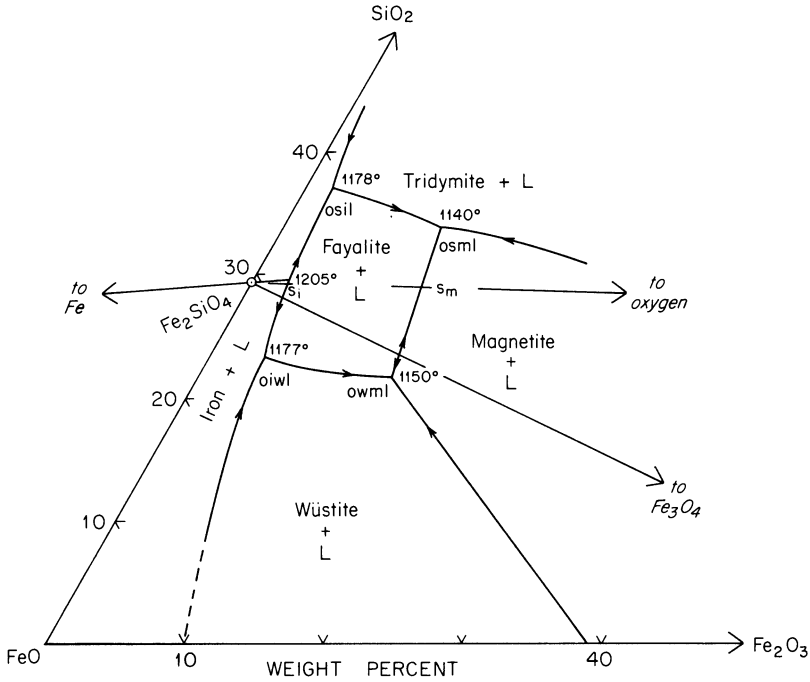
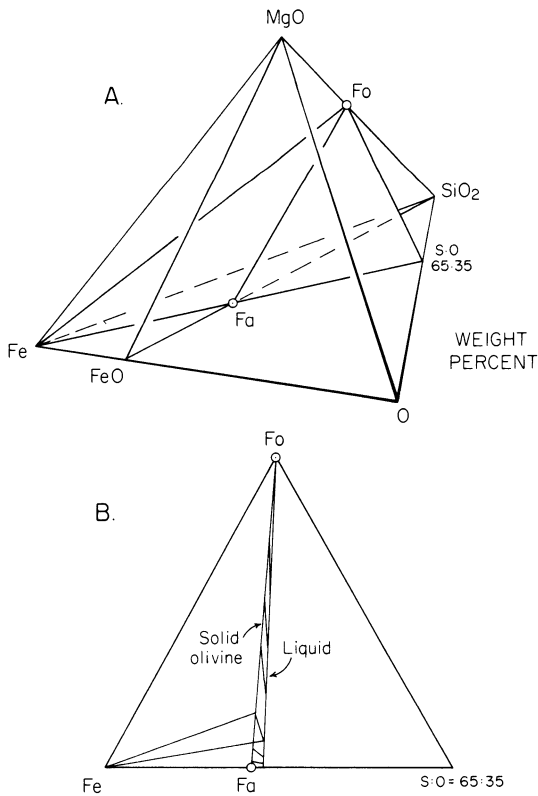


Figure 16.4. The system FeO-Fe<sub>2</sub>O<sub>3</sub>-SiO<sub>2</sub>, after Muan and Osborn (1956).

sketched the liquidus boundaries, highly compressed and difficult to appreciate, of SiO<sub>2</sub>, magnetite, wüstite, and iron, which collectively enclose the field of Fa + L. These boundaries are more readily seen in the system FeO-Fe<sub>2</sub>O<sub>3</sub>-SiO<sub>2</sub>, part of which is shown in Fig. 16.4. This figure is the lower left quarter of the full system FeO-Fe<sub>2</sub>O<sub>3</sub>-SiO<sub>2</sub>, and in it are depicted the same two tie lines Fe-Fa and Fa-O, now with much flatter slopes, as were shown in Fig. 16.3. Of special note is the squarish field of Fa + L, bounded by fields of Tr, Mt, Wü, and Fe. Ignore for now the lower case abbreviations *osil*, etc. The boundary L (Fa,Fe) contains the incongruent melting liquid at 1205°C which results when fayalite melts to iron plus liquid. This liquid composition must lie on the extended tie line from Fe to Fa (not the tick labelled S<sub>1</sub>), and it lies at a maximum on the curve L (Fa,Fe), which runs to 1178°C at a eutectic with SiO<sub>2</sub> and 1177° at a eutectic with wüstite. The field of iron + L covers the fayalite composition. The position of the 1205° liquid is a ternary expression of the familiar incongruent melting relationship. Fig. 16.1 is a section along the Fe-Fa line, abutted to a section along Fa-O. The 1205° maximum does not quite lie in the plane of the Fa-O section in Fig. 16.1 (hence the approximation ~1205° in the figure); the points S<sub>1</sub> and S<sub>m</sub> do lie in that section, and they represent the melting reaction Fa + O = L in the presence of iron and magnetite, respectively. These are so-called *singular points* arising from the collinearity of Fa, L, and O which causes the *degeneracy* of the ternary system into the binary

system Fa-O. These terms and points will be discussed at greater length in a subsequent analysis.

Having now seen the ternary geometry of the incongruent melting of fayalite, we may add MgO to the system to represent the melting of all olivines in the Fo-Fa series. The quaternary system MgO-Fe-O-SiO<sub>2</sub> is sketched in Fig. 16.5(a), the base of which is the ternary system just discussed (Figs. 16.3, 16.4). Fo occurs on the MgO-SiO<sub>2</sub> edge of the tetrahedron, and the triangular plane Fe-Fo-(SO=65:35) contains the series Fo-Fa. This plane is extracted in Fig. 16.5(b) as an equilateral triangle. Since the olivine series lies in the plane, and the crystals and liquids all coexist with metallic iron (the crucible), which lies at one apex, it is evident that the plane may be treated as a degenerate ternary system for the purposes of discussing the melting of olivine; that is, iron, olivine, and liquid all lie in the plane. The liquid is shown an exaggerated distance away from Ol and Fe (for clarity), and a few sample tie lines from liquid to crystal are shown across the liquid-crystal field. One sample three-phase triangle



**Figure 16.5.** A, the system MgO-Fe-O-SiO<sub>2</sub>. B, the Fe-Fo-(65:35) plane taken out of the above tetrahedron.

Fe-Ol-L is also shown. This gusset-shaped field of Fa-Fo-liquid is shown (distorted) in Fig. 16.2(b), where the  $X-X$  relationships of Fig. 16.5(b) are shown in relation to the  $T-X$  diagram, Fig. 16.2(a). One sample tie line is shown in both the  $T-X$  and the  $X-X$  sections. Together, the diagrams of Fig. 16.2 illustrate that the apparently binary loop is really a *projection* along the ternary plane of Fig. 16.5(b) onto a  $T-X$  section arising from the Fo-Fa join. The *liquids* are projected into the  $T-X$  section, whereas the crystals already lie in the section. The projection is made from (or to, depending on the arrangements of lamp, viewer, and screen) the corner Fe. It should be noted that the actual shape of the “liquidus” in the  $X-X$  plot is not known to me, and is arbitrarily represented as a straight line. Furthermore, it is not a liquidus in the strict sense, but a peritectic curve denoting an odd equilibrium with two solid phases. Here endeth Part I of the olivine story. Now we go on to consider fayalite and its relations to magnetite, silica, and oxygen, among other things.

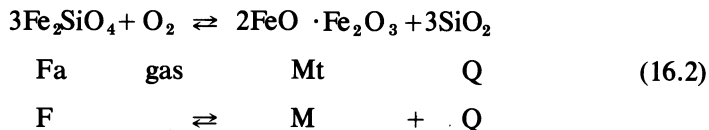
## Fayalite and Its Oxidation

Fifty years ago one would hardly have dreamed that one might discuss, let alone measure, the partial pressure of oxygen in a crystallizing (or long crystallized) magma. Even now one might ask, why bother? One answer has already been hinted on an earlier page, but it bears a brief amplification. Perhaps a historic context will help.

Bowen and Fenner long argued about whether the normal course of fractional crystallization led to iron-rich or alkali, silica-rich end products. Bowen (e.g. 1928, p. 110) favored the alkali, silica enrichment typical of the calc-alkali series: basalt-andesite-dacite-rhyolite, claiming no enrichment of iron. Fenner (e.g. 1929, p. 238) held that iron enrichment was the normal case. That these two able men were unconsciously comparing separate sets of conditions began to be evident with the work of G. C. Kennedy (1955), who showed that a higher state of oxidation favored the Bowen trend and more reducing conditions favored the Fenner trend. [The report in 1939 of strong iron enrichment in the Skaergaard intrusion (Wager and Deer, 1939) must surely have suggested such a dichotomy of process almost at once.] Osborn (1959), in a landmark study which for the first time put the matter of oxidation in magmas on a rigorous experimental basis, amply confirmed the Kennedy conclusions and discussed in detail the various mechanisms by which oxygen might influence the course of magmatic fractionation. It is now clear that an appreciation of oxidation-reduction reactions is essential for an enlightened approach to the problems of magmatic fractionation and perhaps even genesis. The recent progress on the matter owes much to Osborn and his colleagues at the Pennsylvania State University, using controlled gas atmospheres at 1 bar, and to H. P. Eugster and his colleagues

at the Johns Hopkins University; Eugster invented the oxygen buffer which has been essential to studies at high pressure.<sup>2</sup>

The resolution of the Bowen-Fenner uproar can be appreciated very quickly with the aid of a single and very important reaction:



This is the famous FMQ (QFM) oxygen buffer reaction; it is also a genuine magmatic reaction by means of which a high degree of silication may result in the residual liquid (right-hand arrow) or a high degree of iron (fayalite) enrichment may result in the residual liquid (left-hand arrow). In effect, the right hand arrow leads to the Bowen trend, and the left-hand arrow to the Fenner trend. The reactants may be considered normative components of the magma; the products are crystals produced by the magma. The reaction does not necessarily go to completion. Mechanistically, what happens is that if the initial partial pressure of oxygen is sufficiently high, magnetite will crystallize early in the fractionation history, thus locking up iron as oxide, and silicating the residual liquid. If the initial partial pressure of oxygen is low, magnetite may not crystallize at all, so that the iron will continue to crystallize as silicate, using maximum silica from the magma. Conditions intermediate to these two extremes may well be imagined.

It must be emphasized that it is the early—late—or never-crystallization of magnetite which has the effect on silica saturation in the residue, assuming a closed system. Of course it is also possible to imagine a contamination process in which respectably large quantities of oxygen are introduced to the magma (say as H<sub>2</sub>O vapor), causing massive precipitation of magnetite. A variety of such a mechanism was in fact invoked by Osborn as a model for the calc-alkali series. Although examples in which the partial pressure of oxygen rises with time are probably rare, such as case has been convincingly demonstrated for rocks of the Oslo Province by Czamanske and Wones (1973).

<sup>2</sup>The oxygen buffer consists of a fixed mineral assemblage surrounding the experimental charge, and ordinarily requires a semi-permeable membrane for diffusion of hydrogen between the buffer assemblage and the charge; the hydrogen acts as the messenger of oxygen fugacity from the buffer to the charge. The invention is a fine example of necessity being the mother. Eugster attempted to make the iron mica annite [KFe<sub>3</sub>AlSi<sub>3</sub>O<sub>10</sub>(OH)<sub>2</sub>] in a sealed platinum tube, using ferrous oxalate as the source of Fe<sup>2+</sup>. But he kept getting magnetite + sanidine instead, so he realized that hydrogen was escaping through the platinum and leaving excess oxygen behind which oxidized the iron. He first cured this by surrounding the platinum capsule with Zn + HCl, the classical Kipp generator, to create a back-pressure of hydrogen, and it worked. This led to Fe + HCl, then Fe + H<sub>2</sub>O (the iron-wüstite buffer), and finally a large variety of solid assemblages, with H<sub>2</sub>O as the source of messenger hydrogen. The oxygen buffer is not only a beautiful experimental discovery, but also a powerful concept when applied to geological systems. I am grateful to Hans Eugster for providing a brief account of the discovery. Descriptions of the technique may be found in Eugster (1959) and Eugster and Wones (1962).

## Oxygen in Melts

Before considering the buffering qualities of the FMQ reaction, we should perhaps consider the source and nature of oxygen in the natural magmatic environment. First it should be recalled that oxygen composes about 90% by volume of the earth's crust and most magmas. It must not be assumed that a gas phase, particularly one composed of oxygen, occurs with every magma. Gases which do occur with lavas are composed overwhelmingly of  $\text{H}_2\text{O}$  and  $\text{CO}_2$ , along with many other species in major or minor amount. Dissociation of  $\text{H}_2\text{O}$  to  $\text{H}^+ + \text{OH}^-$  occurs to some degree at all magmatic conditions, and selective leakage of the highly mobile  $\text{H}^+$  ion is a favorite means of increasing the partial pressure of oxygen in a magma. An influx of  $\text{H}^+$  leading to reduction is less likely, but conceivable. Many magmas do not possess a gas phase at all, particularly at high confining pressures which tend to force gaseous components into solution with the melt, to achieve reduction of volume. However, even with H and O in solution in a silicate melt, diffusion of H as momentary  $\text{H}^+$  is likely to occur, and an effective increase in the oxidation potential of the magma can thereby be achieved. Dissociation of  $\text{CO}_2$  into  $\text{CO} + 1/2 \text{O}_2$  is another possible mechanism of influencing oxidation. Once again, whether these species are present in a gas phase or merely as dissolved components is relatively immaterial. The initial ferrous : ferric ratio of a magma is an indication of its potential for oxidation and reduction. Even dry magmas contain ferric iron, except perhaps on the Moon, where equilibrium with metallic iron is the rule. Lunar magmas may then be characterized as having all their oxygens bonded to silicate structures (polymers in the liquid, crystals in the solid state), with none left over to make metal oxide, and indeed a deficiency to accommodate all the potential ferrous silicate component. Lunar equilibria are therefore dominated by the species  $\text{Fe} + \text{FeO}$ , or in other words, the iron-wüstite assemblage. Terrestrial basaltic magmas have enough oxygen to satisfy the silicate polymers and crystals, and still have some left over for metal oxides. Therefore Fe metal is absent (except in rare, perhaps freakish occurrences like Disko Island, Greenland), all iron is at least as oxidized as  $\text{FeO}$ , and some (or perhaps much) reports as  $\text{Fe}_2\text{O}_3$ . Melts and rocks may be considered as dominantly oxygen networks, and the amount and distribution of cations in polymers, crystals, and dissolved gases controls how much oxygen may be available for affecting the valence state of transition metals. To speak of oxidation and reduction in magmas is thus to imply something far more subtle and intricate than mere infiltration with oxidizing or reducing gases.

One might suppose (indeed one did, some years ago) that the potential interactions among cations and oxygen would be so numerous and interlocking as to defy conceptual analysis. Fortunately, while this may be true some of the time, there are important special cases where some kind of oxidation potential can be rigorously specified, and there are enough such

special cases in nature to yield, potentially, a rather detailed and specific picture of the influence of oxygen. There are even broadly limiting conditions which tell us something; for example, that the ferrous : ferric ratio is almost always greater than one already tells us that most magmas are far from being strongly oxidized. The most potent sort of information, however, arises from such reactions as the FMQ reaction, which uniquely specifies the oxidation state of a system as long as all reactants and products are present. It is now fitting to take a closer look at this oxygen buffer reaction, and to introduce a parameter to describe things related to oxygen without continually having to resort to such vague or inappropriate terms as oxidation potential, which really relates more appropriately to electrochemistry.

## Oxygen Fugacity and the Concept of the Oxygen Buffer

There are many ways to describe the behavior and amount of oxygen in a system, but for magmatic processes there are two functions which are most useful and conceptually helpful. These are the *partial pressure* and the *fugacity*. The partial pressure is a helpful concept because it is perhaps the most amenable to a mechanistic visualization. The air we breathe is a complex gas, at a pressure of about 1 bar (1 atmosphere), of which about 21% is oxygen. We therefore thrive under a partial pressure of oxygen of 0.21 bar. If we breathe into a paper bag, we gradually replace the oxygen with CO<sub>2</sub>, thus reducing the partial pressure of oxygen to values well below 0.21 bar until we become unhappy or unconscious. The partial pressure is easily evaluated, since the sum of the mole fractions times the partial pressures equals the total pressure, and one therefore needs only the analysis of the gas. The partial pressure of oxygen reflects the amount of oxygen present among other components of a gas phase, and is a convenient parameter as long as a gas phase exists, but it becomes undefined for the case where no gas phase exists, for example at high pressure in the presence of a splendid solvent such as a melt. *Fugacity* is a more general parameter which works well whether or not a gas phase is present. It is in fact an alternative expression of the chemical potential  $\mu$ , which is the partial molar Gibbs energy of a component,  $\partial G/\partial n$ . The relation between the chemical potential of oxygen and the fugacity ( $f$ ) is

$$\mu_{\text{O}_2} = \mu_{\text{O}_2}^\circ + RT \ln f_{\text{O}_2}, \quad (16.3)$$

where  $\mu_{\text{O}_2}^\circ$  refers to the chemical potential of oxygen in some standard state, and  $R$  and  $T$  are the gas constant and the Kelvin temperature, respectively. For an ideal gas  $f_{\text{O}_2} = p_{\text{O}_2}$ , and  $f/p \rightarrow 1$  as ideality is approached. Fugacity has the dimension of pressure, and is measured in bars or atmospheres. The  $f_{\text{O}_2}$  of a reaction is a continuous function of

temperature, and for solid : vapor equilibria, the  $\log f_{O_2}$  of a reaction has the happy property of being linear with respect to  $1/T$ , the reciprocal of the Kelvin temperature. This falls out of the Clausius-Clapeyron equation, which may be reduced to

$$\log P = -\frac{\Delta H}{2.303 RT} + C, \quad (16.4)$$

where  $P$  is pressure or partial pressure,  $H$  is the enthalpy,  $R$  and  $T$  have their usual meaning, and  $C$  is a constant. Figure 16.6 compares the  $f_{O_2}$  plot for the FMQ reaction with the  $f_{O_2}$ - $T$  plot.

The FMQ reaction is an oxygen buffer, which means that it is a regulator of  $f_{O_2}$ . As an analogy, a eutectic melting reaction is a temperature buffer in which the addition or subtraction of heat to or from the system has no effect on the temperature, as long as all reactants and products are present. The assemblage  $Di+An+L$ , for example, may be subjected to heat from a furnace without changing the temperature from 1274°C until such time as  $Di$  or  $An$  is consumed. Heat may also be extracted isothermally, until  $L$  disappears, at which time the assemblage loses its thermal buffering capacity. The calories in the thermal analogy may be likened to atoms of oxygen in the oxygen buffer reaction. How many calories need be added or

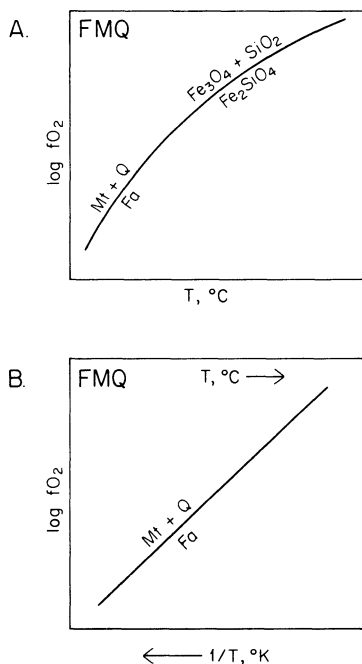


**Figure 16.6.** The FMQ buffer reaction plotted as a function of oxygen fugacity against (A)  $T^\circ\text{C}$ , and (B) reciprocal Kelvin temperature. In (B),  $T^\circ\text{C}$  is nonlinear but  $1/T^\circ\text{K}$  is linear.

subtracted, and how many oxygens, both depend on the initial state of the system and on its mass. As long as the specified buffer condition holds, the  $T$  or the  $f_{\text{O}_2}$  is constant and unrelated to numbers of heat or oxygen units involved in a flux.

We may place pure fayalite in a furnace and pass a stream of oxygen-rich gas over it, thereby beginning to oxidize it by reaction 16.2 to magnetite plus quartz. At constant temperature, a specific  $f_{\text{O}_2}$  will now be established and maintained as long as Fa, Mt, and Q remain in the assemblage. If the flow of gas continues, all fayalite will eventually be converted to Mt+Q, and the  $f_{\text{O}_2}$  will then rise without inhibition. If the gas is changed to a reducing mixture, Fa will be generated at the expense of Mt+Q, again at a specific  $f_{\text{O}_2}$ . The buffering capacity persists as long as there is one grain of each phase present—when the last crystal of any species goes, there goes the buffer.

The great beauty of the oxygen buffer principle is that the buffer is insensitive to other phases in the rock. If pure Fa, Mt, and Q coexist in a rock, the  $f_{\text{O}_2}$  of the rock system lies on the buffer curve in Fig. 16.6, no matter what liquid or other solid phases may also be present. Of course in the natural environment, the phases are not pure members of the Fe-Si-O system, but they do often closely approach such purity, and the principle holds, with appropriate changes in calibration, even for “dirty” phases, which usually contain Mg and Mn in some quantity, for example. The presence of Fa, Mt, or Q in a rock is *prima facie* evidence that the rock crystallized or equilibrated under  $f_{\text{O}_2}$ - $T$  conditions corresponding to the buffer curve or its “dirty” analog. Whether or not liquid partook of this equilibrium depends on the textural evidence for mutual crystallization *ex* liquid, or subsolidus reaction. As it turns out, plutonic rocks cool so slowly that the apparent temperatures recorded are rarely over 800°C, and commonly as low as 500°C, but many volcanic rocks record temperatures very close to their crystallization temperatures.

Here endeth Part II of the olivine story. We now undertake to describe the whole melting story at 1 bar pressure in terms of  $T$ - $f_{\text{O}_2}$  relations.

## Olivine Melting: A $T$ - $f_{\text{O}_2}$ Analysis

We have described the incongruent melting of olivine in the presence of iron metal at 1 bar, and we have described the solid state breakdown of fayalite to magnetite plus quartz as a function of  $T$  and  $f_{\text{O}_2}$ . In terrestrial rocks, we shall not generally expect to find metallic iron involved with olivine and liquid, whereas we do see evidence (in some granites) that fayalite, magnetite, and quartz have crystallized from a silicate melt. What are the melting relations of olivine along the FMQ buffer curve? How relevant is the iron-saturated olivine melting diagram to natural conditions?

Are there other oxygen buffer reactions relevant to olivine melting? One might perhaps suppose that a great deal of hit-or-miss experimentation with controlled  $f_{O_2}$  would be required to answer such questions. This is not the case. By means of a very powerful geometrical analysis due to the physical chemist F. A. H. Schreinemakers (published over the period 1915–1925) it is possible to organize information about coexisting phases in such a way as to write the set of all possible reactions among the phases and to deduce all the geometric relations among these reactions in  $P$ - $T$  space, or, for example,  $f_{O_2}$ - $T$  space. By means of such a Schreinemakers analysis, D. H. Lindsley was able to sit down and work out in a few hours all the relevant relationships among the phases fayalite, iron, silica, wüstite, magnetite, and liquid in the system Fe-Si-O, and plot them as a function of  $T$  and  $f_{O_2}$ . The only experimental data needed to fix the arrangement of 13 reaction curves were the previously-known  $f_{O_2}$ - $T$  slopes of four oxygen buffer curves, and the locations of two out of six invariant points. We shall now review the procedure followed by Lindsley, Speidel, and Nafziger (1968), because not only does the result answer the questions raised above, but also the system provides an elegant and satisfying introduction to the methods of Schreinemakers analysis, which is a powerful tool in petrology, both as a guide to laboratory experimentation and to the interpretation of field relations among minerals, particularly in metamorphic rocks.

We revert to the shorthand notation of the original paper, in which the phases considered are:

- $o$  = fayalite
- $s$  = tridymite or quartz
- $i$  = iron
- $w$  = wüstite
- $m$  = magnetite
- $l$  = liquid

The liquidus relationships of these phases at 1 bar are shown in Fig. 16.4. The boundaries of the fayalite field are reproduced in Fig. 16.7. These are labelled according to the phases in equilibrium along each curve; for example, the curve of the reaction olivine  $\rightarrow$  iron + liquid is labelled *oil*. This would be  $L(\text{Fe}, \text{Fa})$  in our usual notation. The system is ternary, Fe-SiO<sub>2</sub>-O. Along each of these three-phase curves, the isobaric variance  $W_p$  is equal to  $3 + 1 - \phi = 1$ . The four four-phase points *osil*, *osml*, *oiwl*, and *owml* are, by the same reasoning, isobarically invariant ( $W_p = 0$ ). Each of these invariant points is generated by the intersection of three univariant curves in the liquidus diagram. For example, the point *osml* involving fayalite, tridymite, magnetite, and liquid (i.e. essentially FMQ + L) is formed by the three curves *osl*, *sml*, and *oml*. In Fig. 16.8, these are given the labels (*m*), (*o*), and (*s*), respectively where *the label in parentheses*

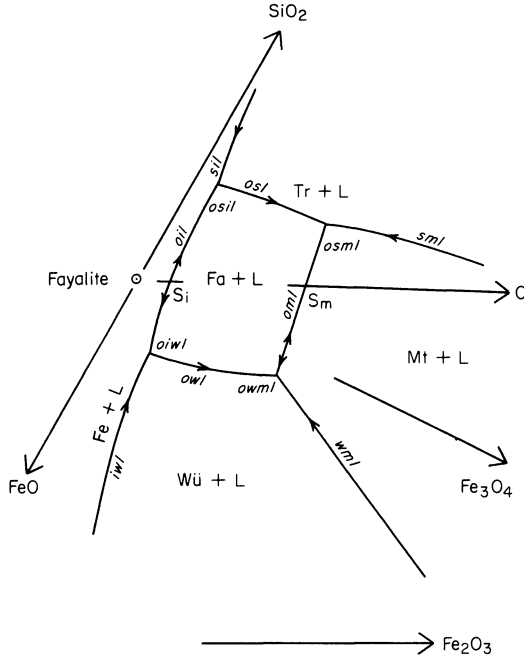


**Figure 16.7.** Part of the system Fe-SiO<sub>2</sub>-O, taken from Fig. 16.4. Labels are clarified in the text.

signifies the phase which is absent from the equilibrium along that curve.<sup>3</sup> This is a conventional and convenient shorthand for purposes of analyzing the arrangement of univariant curves around an invariant point. In this case, the label *osml* signifies the point itself, and (*m*) therefore designates a univariant curve involving equilibria among the other three phases, *o*, *s*, *l*, and so on. (After a little experience, this notation becomes second-nature.) One of the curves, (*l*), cannot be shown in the *T-X* projection of Fig. 16.8, because this is a liquidus diagram (map of the liquidus surface)

<sup>3</sup>The “missing” phase may be present in the system but it does not take part in the reaction.

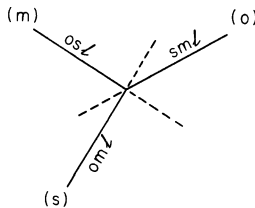


**Figure 16.8.** Liquidus curves in the vicinity of the point *osml*, showing labels used in the “missing phase” notation. Coordinates of the figure are the same as in the ternary diagram, Fig. 16.7.

and the curve ( $l$ ) involves the solids  $o$ ,  $s$ ,  $m$  in the *absence* of liquid. To study this curve, we shall need to plot an  $f_{O_2}$ - $T$  diagram. First, we need to examine the compositions of the phases relative to each other. We shall use for this purpose an oxygen projection onto the  $SiO_2$ -Fe join, and in so doing, we will never need to worry about whether oxygen is evolved or used in a reaction, since addition or subtraction of oxygen will occur normal to the page. The derivation of such a projection for the point  $osm\ell$  is shown in Fig. 16.9, along with a linear scale (*chemographic diagram*) showing the projected compositions. Only the relative compositions are needed; no matter if the distances are incorrect in Fig. 16.9(b).

In Fig. 16.9(b) we note that the projected composition of olivine lies to the right (Fe-rich side) of liquid; this is readily seen in Fig. 16.4 or 16.7, where it is clear that the composition of liquid at  $osm\ell$  lies toward  $SiO_2$  with respect to the projection line  $Fa$ - $O$ . By using the chemographic diagram, we may judge the nature of the reaction ( $o$ ) involving the phases  $s$ ,  $m$ , and  $l$ . The rule is that the reaction must represent the correct linear combination of phases. Among  $s$ ,  $m$ , and  $l$ , the following reactions are geometrically impossible:

$$s + l = m \quad (m \text{ lies outside the pair } s, l, \text{ and would have to be } -m)$$

$$m + l = s \quad (s \text{ lies outside } m - l).$$

The correct reaction is

$$s + m = l \quad (\text{or } s + l = -m),$$

because  $l$  lies between  $s$  and  $m$ . The reaction ( $o$ ) is therefore the congruent melting reaction  $Tr + Mt = L$ .

Our immediate goal is to plot the complete sequence of univariant

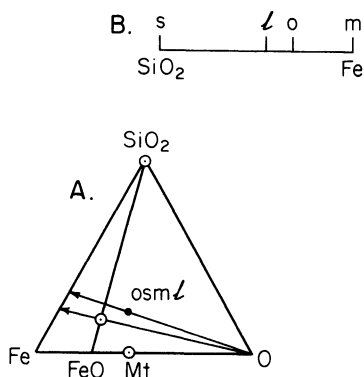


**Figure 16.9.** Chemographic diagram for the point  $osm\ell$ . A. Ternary diagram showing projections from oxygen through fayalite (circle on  $FeO$ - $SiO_2$  line) and liquid (at point  $osm\ell$ ) onto the join  $Fe$ - $SiO_2$ . B. Chemographic line  $Fe$ - $SiO_2$  showing projected positions of magnetite ( $m$ ), olivine ( $o$ ), liquid ( $\ell$ ), and the position of silica ( $s$ ) at the end of the line.

reaction curves around the invariant point  $osml$  in  $T-f_{O_2}$  space. For the moment, we are unconcerned with the calibration of  $T$  and  $f_{O_2}$ , and concerned only with the relative slopes and positions of curves. We shall use a plot similar to Fig. 16.6(b) of  $\log f_{O_2}$  versus  $1/T^\circ K$ , with the abscissa scale increasing to the left so that  $T$  increases to the right. In Fig. 16.10, the invariant point  $osml$  is arbitrarily located, and the reaction curve ( $o$ ) is plotted with a positive slope above the invariant point. There are two rules which govern the plotting of this univariant reaction curve. One is the *fundamental axiom* (our Rule 1) which says that the curve separates the region where the assemblage  $s + m$  is more stable from the region where  $l$  is more stable, each *relative to the other assemblage*. For “more stable” one can also substitute “less metastable”. (Note that nothing is implied about the stability of either of these assemblages relative to some other assemblage not directly involved in this reaction. Our analysis is concerned for now only with reactions in the *immediate vicinity* of the invariant point, and of the univariant curve.) The second rule (our Rule 2) is that the *metastable extension of ( $o$ )* must lie in a region where the phase  $o$  is stable (hence the usefulness of the missing-phase notation). Obedience to this rule insures that *no divariant assemblage can occupy an angular sector larger than  $180^\circ$*  about the invariant point. Both the use and the logic of these rules will become apparent after some experience is gained.

A third, informal rule (Rule 3) is that the slope and labelling of the reaction curve make sense from a physical, experimental, or geological standpoint. This is not essential for an eventually correct topological analysis but it is an efficient way to proceed.

In the current case, we have a melting reaction,  $s + m = l$ . It would be silly to plot  $l$  on the low temperature side of the curve. As to the slope, we have three basic choices, as suggested in Fig. 16.11: positive, negative, or infinite (slope zero is also a possibility, but one which we can usually ignore for a melting reaction. An infinite slope would imply that  $f_{O_2}$  has no effect on the temperature of melting. We would expect this to be the case for the reaction cristobalite  $\rightarrow$  liquid, for example, but not for the melting of an iron-bearing mineral, especially one like magnetite containing two oxidation

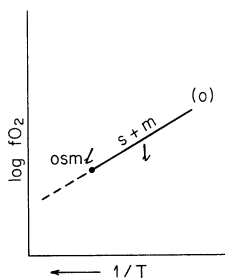


**Figure 16.10.** Arbitrary initial position of the univariant curve  $sm\ell$  in  $1/T - f_{O_2}$  coordinates.

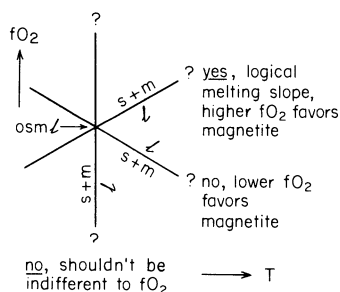


**Figure 16.11.** Choices of slope for the melting reaction  $s + m = l$ .

states of iron. A negative slope would imply that higher  $f_{O_2}$  favors liquid relative to magnetite, but this seems unreasonable, as liquid has no special need for  $Fe^{3+}$ , whereas magnetite certainly does. A positive slope is consistent with this need, and appears to represent a reasonable melting curve.

Which segment of the positive-slope curve in Fig. 16.11 should we choose as the stable segment, the one above the invariant point or the one below? The curve label is  $(o)$ , so if we choose the lower segment as stable, that implies that olivine is stable in the region above and to the right of the invariant point. We don't yet "know" that this is unreasonable, but since the invariant point involves  $osml$  it presumably will involve an olivine melting reaction, and to have olivine stable at higher  $T$  will mean that liquid will be stable at lower  $T$ , an unlikely event. It will be prudent to assume that the stable segment is the one above the  $W_p = 0$  point, as in Fig. 16.10.

It should be pointed out at this stage that we are using a short-cut analysis in trying to guess the most sensible configuration by the informal Rule 3. The procedure of Schreinemakers yields only the correct *sequence* of curves about an invariant point, and when the whole sequence is established, you know it is right because it is internally consistent. However, without additional information you don't know whether you have the physically correct configuration of the *whole set* of curves, or its *enantiomorph*. Reversing the stable and metastable segments of the  $(o)$  curve in Fig. 16.10 would in fact yield the enantiomorph, which would turn out to be geometrically correct but physically unlikely. A strictly formal analysis would require that an arbitrary choice be made for the first curve plotted, and that the test for enantiomorphism be applied after all the curves were plotted. Although potentially hazardous, our method of trying to make physically meaningful guesses early in the game is a worthwhile short-cut as long as we recognize the danger of becoming wedded to an incorrect notion.

We now wish to build onto Fig. 16.10 by adding the curves  $(s)$ ,  $(m)$ , and  $(l)$ . Starting with  $(s)$ , the assemblage is  $oml$ , and the reaction can be deduced by means of the bar graph in Fig. 16.9(b). The compositional relations do not permit a congruent melting reaction  $o + m = l$ , because  $l$  is not a

positive linear combination of  $o$  and  $m$ . The reaction is odd, i.e.  $o - l = m$  or  $o = m + l$ . Again we choose among the slopes represented in Fig. 16.11. We wish to have liquid on the high-temperature side, and magnetite on the high- $f_{O_2}$  side, so this requires  $m + l$  to lie on the right side of a curve with negative slope. If the metastable extension of the curve ( $s$ ) is allowed to fall on the low- $T$  side of the invariant point, it lies in a region where silica is, so far as we know, stable, because it occurs nearby with  $m$  on the curve ( $o$ ). Hence the configuration in Fig. 16.12 seems logical.

The reaction ( $m$ ) involves  $o$ ,  $s$ ,  $l$ , and the composition diagram, Fig. 16.9(b) indicates the congruent melting reaction  $o + s = l$ . A curve of negative or nearly infinite slope, with  $l$  on the high temperature side, would be satisfactory. A curve of positive slope would put the ferrous mineral olivine on the high- $f_{O_2}$  side, which is unreasonable. We cannot put the curve to the right of the curve ( $s$ ) (try it), because then we have olivine partaking of a reaction ( $o + s = l$ ) in a region beyond the breakdown of olivine itself ( $o = m + l$ ). This is impossible. An obvious rule is that in a correct sequence of reactions, the breakdown of a pure single phase comes last of all the reactions involving that phase. We therefore get the configuration of Fig. 16.13.

The reaction remaining to be plotted is ( $l$ ), involving  $o$ ,  $s$ ,  $m$ . The reaction is clearly  $o = s + m$ , the FMQ oxygen buffer reaction. Obviously the  $s + m$  side should lie toward higher  $f_{O_2}$ . Applying our second rule, this reaction ( $l$ ) must lie with its metastable extension in the region where liquid (the absent phase) is *stable*. This means that the stable part of ( $l$ ) must lie above the metastable extension of ( $o$ ). That the curve should have a positive slope, as we have already learned in Fig. 16.6(b), is perhaps less obvious. If it had a negative slope, that would mean that it is easier to oxidize olivine to silica plus magnetite at higher temperatures than at lower temperatures. Olivine would then be stable at relatively high  $f_{O_2}$  at low temperatures. We should commonly expect to see silica plus magnetite as crystallization products of magma, and we should expect to see evidence for subsolidus reaction of  $s + m$  to olivine (olivine reaction rims between magnetite and quartz). Instead, we commonly see olivine as a crystallization product and

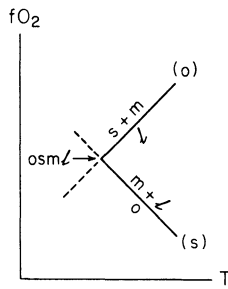


Figure 16.12. Addition of curve ( $s$ ).

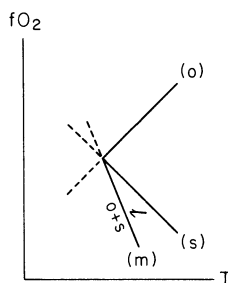


Figure 16.13. Addition of curve ( $m$ ).

magnetite + quartz as subsolidus reaction products. Actually, Fe tends to gain an electron more easily at higher temperature, and it is always true that at a given  $f_{O_2}$ , the ferrous  $Fe^{2+}$  state is favored at high  $T$  and the ferric  $Fe^{3+}$  state is favored at low  $T$ . In consequence, *all* oxygen buffer curves involving the element iron have positive slopes in  $f_{O_2}$ - $T$  space. The curve ( $l$ ) is therefore constrained to lie in a small region between slope = zero and the metastable extension of ( $o$ ), as in Fig. 16.14, which is the complete set of curves about the invariant point  $osml$ .

We now verify that Fig. 16.14 is correct insofar as the rules and logic are concerned. Three “assemblages”,  $s + m$ ,  $l$ , and  $o$ , occupy angular sectors no greater than  $180^\circ$ , which is correct according to Rule 2. We may also go around the sequence and follow the reactions in turn, to see if they make sense. Start with the  $s + m$  field. Crossing the ( $o$ ) curve, we see liquid coming in between  $s$  and  $m$ . Crossing the ( $s$ ) curve, olivine now intervenes between  $l$  and  $m$ . Crossing the ( $m$ ) curve,  $l$  becomes unstable and  $o + s$  can now coexist. Crossing the ( $l$ ) curve,  $o$  becomes unstable relative to  $s + m$  which is the assemblage begun at. The reactions appear to be in proper sequence. To see what an improper sequence would be like, try reversing the positions of ( $s$ ) and ( $m$ ), and you will see that the assemblage demanded by the lower side of the ( $m$ ) curve is not the same as that required by the higher side of the ( $s$ ) curve. *The entire region between any two curves must*

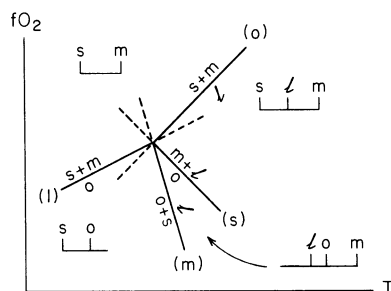
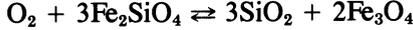


Figure 16.14. Addition of curve ( $l$ ) and final array of curves about invariant point  $osml$ . Chemographic diagrams show compatibilities of phases in each of the divariant regions between the curves.

be occupied by the same assemblage, whether or not that assemblage partakes of a reaction at one of the curves.

The advantages of using a chemographic diagram projected from oxygen should now be apparent. The reaction  $o = s + m$  can be deduced from the bar graph without concern for the reaction coefficients or the consumption of oxygen. From the reaction  $o = s + m$ , the full FMQ reaction



can readily be written when desired, but need not be for purposes of graphical analysis.

We have derived a valid sequence of univariant reaction curves about the invariant point  $osml$ , and it now remains to do the same for each of the other three invariant points in Fig. 16.7, independently, and then finally to put all the points and curves together in  $f_{\text{O}_2}$ - $T$  space, by using identical reactions which emanate different invariant points. We may now turn our attention to the invariant point  $osil$ .

The phases  $o$ ,  $s$ ,  $i$  and  $l$  are shown in the bar graph of Fig. 16.15(a), which is to be compared with the ternary diagram, Figs. 16.4 and 16.7. The composition relations are much the same as for  $osml$ , except that the liquid lies slightly closer to  $s$ . The curve ( $l$ ) involves  $o$ ,  $s$ , and  $i$ , and must represent the reaction  $o = s + i$  in the absence of liquid. The stable part of this curve must therefore lie below the invariant point, as in Fig. 16.15(a) so that its metastable extension lies in the field where liquid is stable. The reaction is

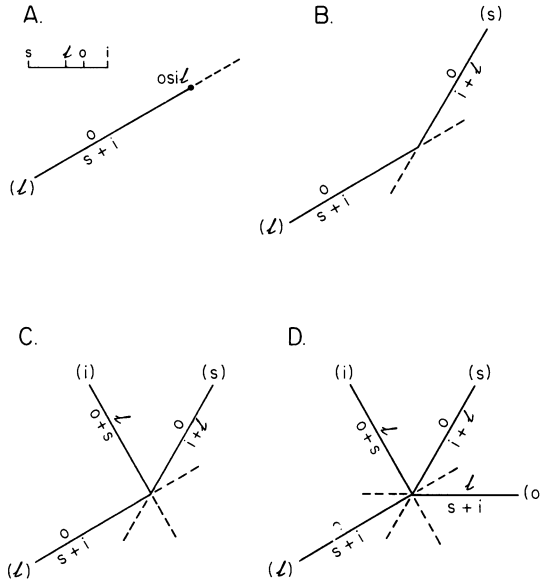
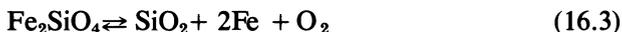


**Figure 16.15.** Development of the array of univariant curves about invariant point  $osil$ . Coordinates are  $f_{\text{O}_2}$  and  $1/T$ .

akin to the FMQ reaction  $o = s + m$ , except that in this case it represents a *reduction* of  $\text{Fe}^{2+}$  to  $\text{Fe}^0$ ; it is an oxygen buffer reaction



and clearly  $o$  must lie on the high- $f_{\text{O}_2}$  side. The curve is plotted with a positive slope in Fig. 16.15(a).

The reaction ( $s$ ) represents equilibrium among  $o$ ,  $i$ , and  $l$ , and represents the familiar incongruent melting of olivine,  $o = i + l$ . Raising the  $f_{\text{O}_2}$  should favor olivine over iron, and liquid should lie to the high  $T$  side of the curve, so a positive slope is indicated (try a negative slope to see if you agree). The stable part of the curve must lie above ( $l$ ), because reaction ( $s$ ) also limits the stability of olivine by itself. The stable segment then must lie above the temperature of *osil*, and it must lie  $180^\circ$  or less from curve ( $l$ ) so that the angular sector occupied by olivine is no greater than  $180^\circ$  (Rule 2). A solution meeting these conditions is shown as Fig. 16.15(b).

Reaction ( $i$ ), involving  $o$ ,  $s$ , and  $l$ , must be the melting reaction  $o + s = l$ ; the curve ( $i$ ) cannot lie above ( $s$ ) in temperature, since the disappearance of the pure phase  $o$  on curve ( $s$ ) prevents its subsequent appearance in a reaction at higher  $T$ . The curve should be fairly insensitive to  $f_{\text{O}_2}$ , neither  $o$  nor  $l$  requiring any large change in oxidation state. On the other hand, it is clear from Fig. 16.7 that  $l$  has the higher oxygen content, and should be slightly favored by  $f_{\text{O}_2}$  as well as  $T$ . Note that the metastable extension lies where  $i$  is stable, which would not be the case if the curve were plotted below the invariant point in  $f_{\text{O}_2}$ .

The reaction curve ( $o$ ) must now be plotted with its stable segment to the high- $T$  side of the invariant point, so that its metastable extension lies where  $o$  is stable. It must also lie so that the angular sector occupied by  $l$  alone is  $\leq 180^\circ$ . The assemblage  $s + i$  must lie on the low- $f_{\text{O}_2}$  side of the curve, to be contiguous with the same  $s + i$  assemblage on curve ( $l$ ), and also to leave metallic iron in the low- $f_{\text{O}_2}$  region. A flat or low positive slope is possible; a negative slope would imply that it is easier to oxidize iron at high  $T$  than at lower  $T$ , which is contrary to our experience. Therefore the curve ( $o$ ) is plotted with a nearly flat slope in Fig. 16.15(d). This is evidently a retrograde melting curve, in which the solid  $\rightarrow$  liquid reaction can occur with falling temperature *but with addition of energy in the form of oxygen*. (There is still no such thing as a free lunch, and retrograde melting reactions always involve pumping something else in instead of heat.)

Figure 16.15(d) may now be verified as to the correct sequence of reactions, as was done with invariant point *osml*. It is left to the reader to do this. Attention is called, however, to Fig. 16.14, curve ( $m$ ), which is the identical reaction to curve ( $i$ ) in Fig. 16.15(d), namely  $o + s = l$ . This common reaction will later be used to tie these two invariant points together in  $f_{\text{O}_2}$ - $T$  space.

Invariant point *omwl* offers a special treat, a *degeneracy* caused by the collinearity of  $w$  and  $m$  with oxygen. The composition diagram, Fig.

16.16(a), shows this as a superposition of  $m$  and  $w$  at the Fe terminus. Note also that  $l$  now plots slightly to the right of  $o$ , as may be verified with Fig. 16.4 or 16.7. The reaction ( $o$ ) involves equilibrium among the phases  $m$ ,  $w$ , and  $l$ , but there is no way to write a reaction involving  $l$  as a reactant or a product. The phase  $l$  is here an *indifferent* phase, and the reaction must be  $m = w$ , which is the magnetite–wüstite buffer reaction (MW):



Since this is a buffer reaction, the curve should have a positive slope similar to the other buffers, and since liquid is present, the stable part of the curve must lie above the invariant point. Obviously magnetite must lie on the high- $f_{\text{O}_2}$  side. The curve may be plotted as in Fig. 16.16(a).

Consider now the reaction ( $l$ ), involving equilibrium among  $o$ ,  $m$ , and  $w$ . Again we have an indifferent phase,  $o$ , and again the reaction must be  $m = w$ . In this case, the metastable extension must lie where liquid is stable, and the stable part below the invariant point. We now note that if the curve ( $l$ ) makes some angle with the curve ( $o$ ), Rule 2 will be violated, because either  $m$  or  $w$  will occupy an angular sector  $>180^\circ$ . The only solution is for these two curves to lie collinear, so that their stable segments and metastable extensions coincide, and their sector angles are equal to  $180^\circ$ . The same

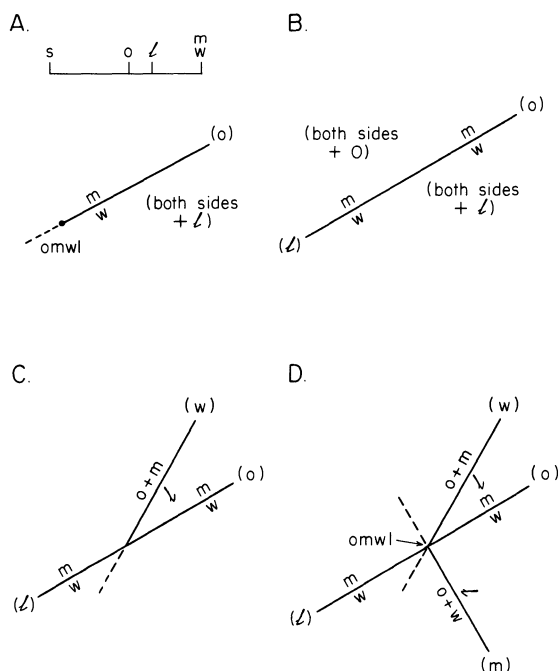


**Figure 16.16.** Development of invariant point  $omwl$  in  $f_{\text{O}_2}$  -  $1/T$  coordinates.

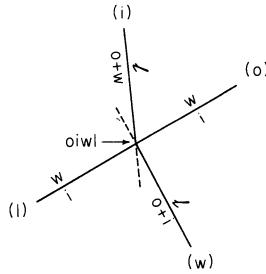


**Figure 16.17.** Invariant point  $oiwl$  in  $f_{O_2} - 1/T$  coordinates.

buffer reaction,  $m = w$ , occurs on both sides of the invariant point, but in the presence of olivine on one side and of liquid on the other side. The phases  $o$  and  $l$  do not participate in the reaction, but coexist stably with the equilibrium assemblage. The curve  $m = w$  is *univariant by restriction* because the system required to express these phases has degenerated to the binary system Fe–O, so  $c = 2$ ,  $\phi = 2$ , and  $W_p = 1$ . The curves  $(l)$  and  $(o)$  are plotted in Fig. 16.16b.

The reaction  $(w)$  is evidently  $o + m = l$ . Liquid should be favored by high temperature, and magnetite should be rather strongly favored by oxygen, so the curve should have a positive slope as shown in Fig. 16.16c, where it will be noted that the metastable extension lies in the field where  $w$  is stable.

The reaction  $(m)$  is also evidently a melting reaction,  $o + w = l$ . Its metastable extension must lie above the  $m = w$  curve and to the left of the stable part of curve  $(w)$ . Liquid should be favored by high  $T$ . A negative slope, while not obviously required by the relative oxygen contents of  $l$  and  $w$ , is reasonable, and the curve is plotted in Fig. 16.16d. If the negative slope is wrong, we shall be able to correct it later.

The sequence of reactions about the point  $omwl$  may now be verified in the usual way. No assemblage occupies a sector  $>180^\circ$ , and the sequence of reactions is orderly in that no curve falls outside the stability field of the reactants.

The invariant point  $oiwl$  will be seen to mimic  $omwl$  very closely, with a degeneracy of iron and wüstite, an  $i = w$  buffer reaction ( $Fe + O = \text{“FeO”}$ ) with indifferent phases  $o$  and  $l$ , and two melting reactions:  $(i)$ ,  $o + w = l$  and  $(w)$ ,  $o + i = l$ . The complete array of curves about  $oiwl$  is shown in Fig. 16.17, and can be verified in the usual way. The slope of  $(i)$  must be compatible with the slope of  $(m)$  leading to the invariant point  $omwl$  (Fig. 16.16d), since the reactions are the same,  $o + w = l$ . It now becomes apparent that these last two invariant points will be linked together by this reaction in  $f_{O_2}$ - $T$  space.

We now turn briefly to two special *singular points*,  $S_m$  and  $S_l$ , which are labelled in Figs. 16.4 and 16.7. These are points collinear with fayalite and oxygen, and they each represent the singular event which occurs when a

moving phase composition (in this case liquid) by coincidence reaches collinearity with two other phases. As mentioned on an earlier page, when  $o$ ,  $l$ , and the projecting component oxygen are all collinear, the system is degenerate, no other phases need enter the reaction, and the melting reaction is the *congruent* reaction  $o = l$ . The variance of the singular point is zero, because the third phase ( $m$  or  $i$ ) is not indifferent at each side of the singular point. We shall examine first the point  $S_m$  to see why this is so.

$S_m$  lies on the curve  $oml$  (Fig. 16.7), and this assemblage has appeared in two of our diagrams, as the curve ( $s$ ) at  $osml$  (Fig. 16.14) and the curve ( $w$ ) at  $owml$  (Fig. 16.16(d)). These two curves are shown in Fig. 16.18, along with the composition graphs illustrating the nature of the reaction. The curve  $oml$  emanating from  $osml$  is the odd melting reaction  $o = m + l$ ; the one emanating from  $owml$  is the even reaction  $o + m = l$ . Magnetite is necessary for the reaction on both sides of  $S_m$ , and so while the reaction at  $S_m$  is simply  $o = l$ , magnetite is a necessary third phase;  $c = 2$ ,  $\phi = 3$ , and  $W_p = 0$ .

As Fig. 16.7 indicates, the reaction  $o = l$  is not confined to  $S_m$  and  $S_1$ , but occurs all the way across the olivine field along the line  $Fa-0$ . Thus in Fig. 16.18,  $S_m$  is the terminus of a reaction curve  $o = l$  which runs across  $T-f_{O_2}$  space to  $S_1$ , the other terminus. The singular point  $S_1$  occurs on the curve  $oil$ , which is the standard fayalite-melting reaction for iron crucibles. This curve connects the invariant points  $osil$  and  $oiwl$  (Figs. 16.7, 16.15(d), 16.17), and is reproduced in Fig. 16.19, which may be analyzed in the same way as Fig. 16.18.

We now have all the information needed to plot the complete 1-bar  $T - f_{O_2}$  section for olivine equilibria in  $Fe-SiO_2-O$ , namely the curves about the four invariant points  $osml$ ,  $omwl$ ,  $oiwl$ , and  $osil$ , and the singular points  $S_m$  and  $S_1$ . The four buffer curves  $osm$ ,  $mw$ ,  $wi$ , and  $osi$  are experimentally known, but their relative positions are dictated in any event by the univariant curves emanating from invariant points, and the arrangement shown in Fig. 16.20 can be deduced without reference to experiment. It is easiest to start by plotting the curve  $o + s = l$  between  $osml$  and  $osil$ , and

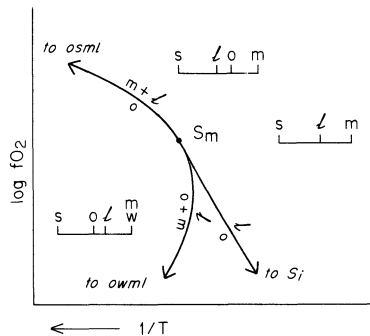
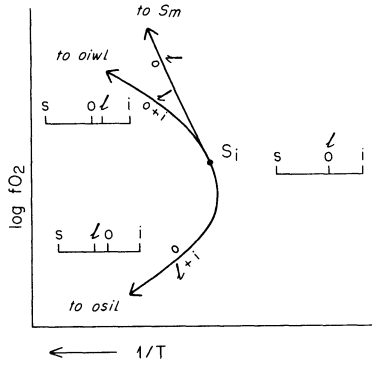
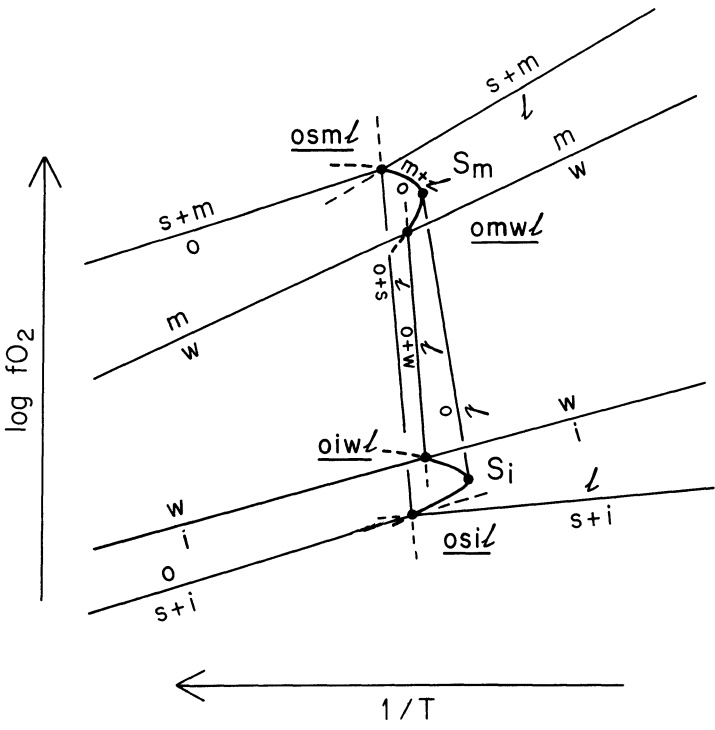


Figure 16.18. Relations about singular point  $S_m$ .



**Figure 16.19.** Relations about singular point  $S_1$ .

then the curve  $o + w = l$  between  $omwl$  and  $oiwl$ . Note that the temperatures of the invariant points are given in Fig. 16.4. The singular point curves of Figs. 16.18 and 16.19 are then plotted, and the singular points connected by a single line,  $o = l$ . This curve marks the absolute limit of fayalite stability as a function of  $f_{O_2}$  and  $T$ , but note that it is not likely to be achieved in nature.



**Figure 16.20.**  $T - f_{O_2}$  section through the system  $Fe-SiO_2-O$  at 1 atm pressure, after Lindsley, Speidel, and Nafziger (1968).

We can now answer the question, how relevant is the early determination of fayalite melting in iron crucibles? The melting occurs along the line between  $oiwl$  and  $S_1$  in Figure 16.20. The answer is, not very relevant in terms of  $f_{O_2}$ , because equilibrium with metallic iron is rare in terrestrial magmas, but not bad from the standpoint of temperature, since all the olivine melting curves have steep slopes. It may be seen that the not uncommon rhyolite-granite equilibrium  $osml$  and its relatives  $sml$ ,  $oml$ , and  $osm$  are quite restricted in  $f_{O_2}$ ; a relatively small drop in  $f_{O_2}$  will lead to wüstite equilibria. On the other hand, the reaction  $o + s = l$  may occur over the whole range of  $f_{O_2}$  from the stability field of magnetite to that of iron. The reaction  $o + w = l$  also occupies a large range of  $f_{O_2}$ . The FMQ oxygen buffer is destroyed by the melting of olivine, although the liquid on  $s + m = l$  is constrained to a somewhat similar  $T - f_{O_2}$  path. The MW buffer, on the other hand, is indifferent to olivine melting, and any liquids which should happen to be saturated in  $m = w$  would be controlled by that buffer, no matter what other phases should appear or disappear. From direct measurements in lavas and inferences from natural plutonic rocks, it appears probable that the MW buffer curve represents the lower  $f_{O_2}$  range of common terrestrial magmatic  $T - f_{O_2}$  paths, and that equilibria in the  $f_{O_2}$  range between MW and FMQ are very common. Equilibria outside the range of olivine, above the  $osm$  and  $sml$  curves, also occur in nature at least up to the hematite-magnetite (HM) buffer.

Figure 16.20 delineates the entire  $f_{O_2} - T$  stability field of pure fayalite, which is bounded by  $osm$ ,  $S_m$ ,  $o = l$ ,  $S_1$  and  $osi$ . The effect of adding MgO to the system will be to increase both the  $T$  and the  $f_{O_2}$  limits of the olivine field to the limit of pure  $Mg_2SiO_4$ , which is of course  $f_{O_2}$ -independent at 1890°C. Another effect of MgO is to stabilize orthopyroxene at 1 bar pressure, for pyroxene compositions with  $Mg/(Mg + Fe^{2+})$  greater than about 0.25. Orthopyroxene will be stabilized, in part, by the release of silica from olivine at the  $osm$  breakdown, so it will persist to higher  $f_{O_2}$  than the FMQ buffer curve. The effect of MgO on the system has been summarized in detail by Speidel and Nafziger (1968).

## Richardson's Rule

The treatment of Schreinemaker's Rules in this chapter is based on that of Lindsley *et al.* (1968) and on the thorough exposition by Zen (1966), which should be consulted for a rigorous and general understanding. The version of Rule 2 used here is a useful shortcut to the correct sequence of curves about an invariant point. An even more useful shortcut was suggested to me by Dr. S. W. Richardson in Oxford, October 1977. His version may be stated as follows, using the missing-phase notation:

The curve denoted by the missing phase lies with its metastable extension in the sector where the missing phase is generated by all other reactions, *stable or metastable*.

In using this rule, it is convenient to place small arrows on stable curves *and* their metastable extensions, pointing toward the sector where the missing phase is relatively more stable than its reaction products. The new curve is then placed so that its metastable extension lies between the arrows. This practice speeds up the correct placement of the curve.

As an example, consider the point *osil* (Fig. 16.15d). According to our version of Rule 2, the curve (*i*) could be placed between curves (*s*) and (*o*). Using Richardson's rule, the two closest arrows pointing into the desired sector stabilizing *i* would lie on the stable segment of curve (*o*) and on the *metastable* segment of curve (*s*). The correct placement of (*i*) would then immediately result from putting its metastable extension between the arrows. Further examples appear in the following chapter.

The value of Richardson's rule lies in the fact that correct placement of the new curve can be made immediately, before the reactants and products are written on the curve. In the case cited above, using the old rule, the incorrect position of (*i*) would have become clear only in attempting to write the full label. Richardson's rule prevents this type of unsuccessful trial. This seems to be the last word in the refinement of Schreinemakers' analysis to a straightforward and rewarding exercise.

## Chapter 17

# Iron-Bearing Olivines and Pyroxenes

### Introduction

In this chapter we continue to examine the effects of adding iron to simple magnesian systems. As expected, we shall find that Fe lowers the melting temperatures appreciably, but in addition we find that fundamental changes occur in the reaction relation of olivine to pyroxene. The chapter opens with a review of the system  $\text{MgO-FeO-SiO}_2$ , taken in part from the original research paper. It then continues with an iron bearing version of  $\text{Fo-An-SiO}_2$ , the effect of adding oxygen to  $\text{MgO-FeO-SiO}_2$ , and a brief discussion of quadrilateral pyroxenes.

### The System $\text{MgO-FeO-SiO}_2$

The olivines and Ca-poor pyroxenes of natural basaltic rocks are Mg-Fe solid solutions. We have seen the incongruent melting of enstatite in Chapters 10-12, and briefly discussed the olivine diagram in Chapter 16. But what happens to the incongruent melting of orthopyroxene as iron is added? The orthopyroxene series forms one corner of the plane of silica saturation, and we have concluded that liquids may penetrate this plane by the removal of olivine, because of the incongruent melting of pure En. If the melting becomes congruent as iron is added, however, liquids may or may not penetrate the plane depending on the iron content. These matters are illuminated by the relations among olivine, pyroxene, and silica minerals in the system  $\text{MgO-FeO-SiO}_2$  (Bowen and Schairer, 1935).

A simplified liquidus diagram of the system is shown in Fig. 17.1. There is a wedge-shaped field of pyroxene between the fields of olivine and silica minerals, but this wedge tapers to a line within the diagram, allowing the coexistence of iron-rich olivines and tridymite. We see immediately, therefore, that the olivine reaction relationship common to tholeiitic basalts gives way to olivine + silica compatibility, as we would expect from the existence of fayalite granites. Clearly, at some value of iron enrichment, the melting of pyroxene becomes congruent, but this does *not* occur at point O in Fig. 17.1 because liquid O is in equilibrium with a pyroxene between O and En. Fig. 17.1 represents a ternary liquidus map covering several binary solid solutions of the continuous type (like plagioclase), and a correct interpretation of the diagram requires careful analysis. It also explains many features found in real rocks, as we shall see.

The paper by Bowen and Schairer (1935) is a classical account of a powerful experimental attack and it is elegantly expressed in a style characteristic of the authors. Their descriptions of crystallization behavior in this system are thorough and lucid. The paper itself is frequently used as a direct source in teaching, and our purpose here is well served by reproducing, in facsimile, a portion of the original paper. This facsimile appears in Appendix 2, where a few marginal notes have been added to call attention to the meaning of the original as expressed in terms used in this book. The following discussion presumes some familiarity with the material in Appendix 2.

Perhaps the foremost petrologic result of the study by Bowen and Schairer was to illuminate the limits on the incongruent melting of Ca-free pyroxene. The systems Fo-An-SiO<sub>2</sub> (Ch. 11) and Fo-Di-SiO<sub>2</sub> (Ch. 12) predict that olivine is always in reaction relation to Ca-free pyroxene, and that the two species cannot be produced together for any significant time during fractional crystallization. On the other hand, many basic layered intrusions show extensive olivine-bronzite cumulates that appear to suggest cotectic crystallization. We now see that for liquids sufficiently rich in iron, that is the expected relationship. In part of the paper omitted here, Bowen and Schairer correctly predicted that high pressure would enlarge the field of pyroxene relative to olivine, and as we shall see, that effect eliminates the incongruent melting of pure En at low pressures corresponding to shallow depths in the crust. Hence, to summarize, the reaction relation holds for shallow, low pressure magmas (such as basalts) when they are relatively Mg-rich. It disappears at high pressure or for Fe-rich magmas.

Another classical problem illuminated by the experimental study is the *olivine hiatus* of fractionated tholeiitic layered intrusions, sills, and lava lakes. This is a hiatus wherein olivine ceases to crystallize at some magnesian composition and then reappears at a more iron-rich composition. As Bowen and Schairer emphasize (p. 210), such behavior is readily explained by the phase diagram, in which a liquid may leave the olivine-pyroxene field boundary but remain below the pyroxene join and eventually

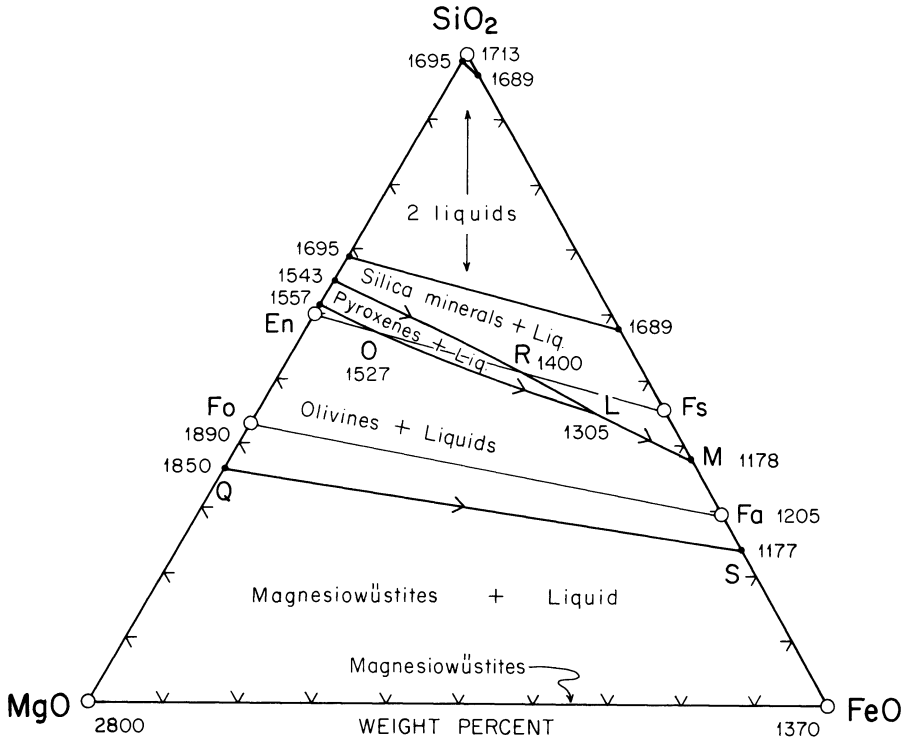


**Figure 17.1.** Liquidus diagram of the system  $\text{MgO-FeO-SiO}_2$ , after Bowen and Schairer (1935).

return to the field boundary, on fractional crystallization. This behavior owes much to the fact that the pyroxene join lies at a very low angle to the field boundary.

The olivine join represents the critical plane in the basalt tetrahedron, and the pyroxene join, the plane of silica saturation. Note that according to the phase diagram, liquids in equilibrium with olivine may *not* cross the metasilicate join toward silica unless they are very magnesian. Therefore it should be common experience to find liquids “trapped” between the two joins, and this is realized in the common occurrence of olivine tholeiites. Note further that late-stage, Fe-rich liquids will crystallize a silica mineral even though they lie to the silica-poor side of the pyroxene join. This result is ultimately due to the instability of ferrosilite at low pressure.

## Oxygen Content of Iron Silicate Liquids

One of the most startling results of the experimental study was the demonstration that appreciable amounts of  $\text{Fe}_2\text{O}_3$  (or dissolved oxygen) occur in liquids in contact with metallic iron. This implies that natural

terrestrial liquids crystallizing ferrous silicates contain even more dissolved oxygen than found by Bowen and Schairer in the presence of iron and under a nitrogen atmosphere. D. H. Lindsley (personal communication, January, 1979) has pointed out that this phenomenon may explain the very common late-stage oxidation of titanomagnetite to ilmenite plus magnetite found in basic plutonic rocks. If Fe-rich residual liquids contain excess oxygen relative to the crystals separating from them, as suggested also by the liquid compositions in the system Fe-SiO<sub>2</sub>-O, Ch. 16, then the inevitable result must be either a late-stage liquid + crystal oxidation reaction or the release of an oxygen-rich vapor phase at the end of crystallization. Such a vapor would be capable of "recharging" through the hot rock and oxidizing those minerals most susceptible to oxidation. These latter appear from petrographic evidence to be the Fe-Ti oxide minerals. A late, oxygen-rich liquid phase would explain the "oxysymplectites" of magnetite + hypersthene locally formed at the expense of olivine in some gabbroic rocks (e.g., Morse, 1969, Plate 34). These intergrowths represent in large part the oxidation of the fayalite component of olivine to magnetite and silica, which then combines with the remaining magnesian olivine to form hypersthene (Presnall, 1966, p. 785).

### The System Olivine-Anorthite-Silica

How does the effect of adding iron to pyroxene carry over into other systems? Is the incongruent melting of pyroxene influenced by adding plagioclase? Useful answers to these questions can be obtained by studying an iron-bearing version of the system Fo-An-SiO<sub>2</sub> (Ch. 11). Figure 17.2 shows the system Fo-An-SiO<sub>2</sub> itself, replotted in cation equivalents (see Appendix 1). The reason for using cation units is that pyroxenes of varying Mg/Fe ratio will then plot at a single point, rather than over a range as with weight units, and thus the iron bearing system can be compared directly with the Mg system and rigorously analyzed by itself. Fig. 17.2 is very similar to Fig. 11.1 because cation plots closely resemble plots in weight units.

The effect of adding iron is shown in Fig. 17.3, based on the work of Lipin (1978). This is a *liquidus map* of part of the plane: molar MgO<sub>59</sub>FeO<sub>41</sub> - An - SiO<sub>2</sub> in the quaternary system MgO-FeO-An-SiO<sub>2</sub>. The ratio of MgO to FeO is here expressed in *molar percent, not weight percent*. The Ol-SiO<sub>2</sub> sideline of Fig. 17.3 is taken directly from the work of Bowen and Schairer (1935), and corresponds to a line from the SiO<sub>2</sub> apex to MgO<sub>45</sub>FeO<sub>55</sub> (*weight units*) in Fig. 17.1. Lipin (1978) determined experimentally the locations of the piercing points D, R, and E, and reported their temperatures in the International Practical Temperature Scale of 1968. The reported values have been reduced to conform to the Geophysical Laboratory scale used through-

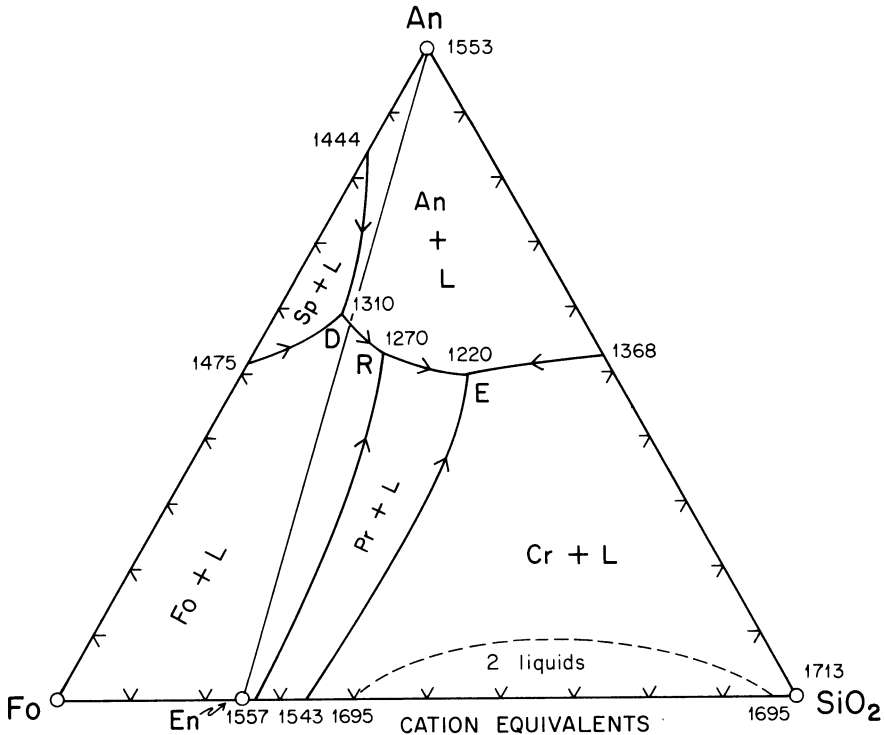


**Figure 17.2.** Liquidus diagram of the system Fo-An-SiO<sub>2</sub>, replotted in cation units. Based on data of Andersen (1915), Osborn and Tait (1952), and Irvine (1974).

out this book. The field boundaries near the piercing points are known from Lipin's work, but elsewhere they have not been precisely located, hence are shown dashed in Fig. 17.3.

On the whole, there is a striking similarity between Figs. 17.2 and 17.3. Clearly, the addition of Fe does not greatly alter the geometry of Fo-An-SiO<sub>2</sub>. The relative positions of D, R, and E are little changed. The primary phase field of anorthite is somewhat enlarged because the temperatures of the olivine and pyroxene fields are lowered with iron content. Note, however, that in nature the addition of iron would be accompanied by addition of albite, so the *plagioclase* field would be smaller than the An + L field in Fig. 17.3; it might instead look much like the An + L field in Fig. 17.2. It is important to note that no liquid to the left of E will remain in the plane of Fig. 17.3 with crystallization, because the separation of olivine or pyroxene crystals will drive the liquids toward lower Mg/Fe.

As before, R is a peritectic point representing the reaction  $O1 + L = An + Opx$ . It is of interest to examine the nature of the curve L (Opx, O1) between the O1-SiO<sub>2</sub> sideline and point R. On the sideline itself, the reaction is even (cotectic), because the MgO<sub>45</sub> (weight percent) line lies to the right of point *b* in Fig. 22 of Bowen and Schairer and hence the

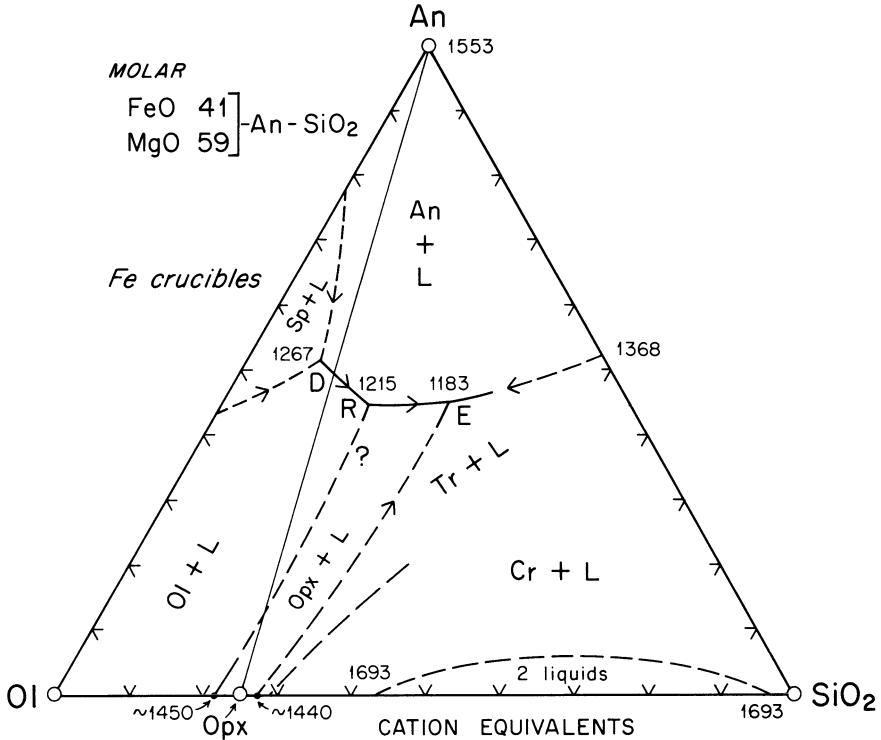


**Figure 17.3.** Liquidus relations in the system olivine-anorthite-silica for a molar ratio of MgO<sub>59</sub>FeO<sub>41</sub>, after Lipin (1978). Dashed lines represent inferred boundaries. Sideline Ol-SiO<sub>2</sub> is from Bowen and Schairer (1935). Query refers to curvature of boundary L (Ol, Opx).

pyroxene composition lies to the right of point O in that figure. In the quaternary system (pseudoternary plane of Fig. 17.3), the liquid moves sharply away from the sideline, hence away from olivine and pyroxene collectively, in such a way that the tangent to the liquid path clearly lies between Opx and Ol. The reaction along the curve is therefore also cotectic or even. Unfortunately, however, we have no knowledge of the curvature of the L (Opx, Ol) boundary as it approaches the piercing point R; this uncertainty is indicated by a query on Fig. 17.3. If the curvature is slight, as drawn, the boundary may be even all the way to R. If the curvature is stronger, as in the iron-free system (Fig. 17.2), then the boundary becomes odd on the way to R. In the latter case, equilibrium liquids will resorb olivine before reaching R and continue to do so at R; fractionating liquids will leave the boundary and cross the pyroxene field to the boundary RE, avoiding R altogether. If the boundary changes from even to odd, cotectic fractions of olivine + orthopyroxene will be succeeded by an interval of orthopyroxene alone before plagioclase joins the assemblage, and the sequence harzburgite-bronzitite-norite will result, with fractional crystalli-

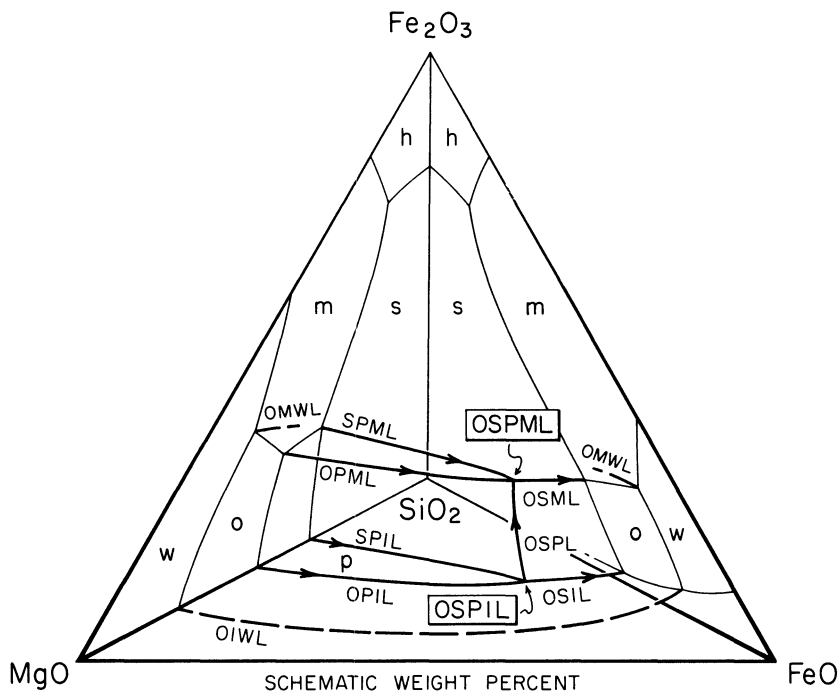
zation. If the boundary remains cotectic to R, no bronzitite event will occur between harzburgite and norite. In the Stillwater complex (see Ch. 13), olivine disappears before norite appears, suggesting that the  $L$  (Opx, Ol) boundary becomes odd near R. A complete evaluation would require not only data on the curvature in Fig. 17.3, but also data for other planes of different Mg/Fe ratio.

Figure 17.3 describes a plane of constant bulk composition, having atomic Mg 59 Fe 41, and ignores the minor amounts of  $Fe_2O_3$  present in the liquid. However, crystals coexisting with liquids in this plane are more magnesian than the plane itself, and in any process of crystallization, liquids will leave the plane toward more iron-rich compositions. This may not be a serious handicap to understanding if the geometry changes but little with increasing Fe, as seems likely. Lipin (1978) furnishes analyzed compositions of some liquids and crystals lying out of the plane.

In summary, the iron-bearing system olivine-anorthite-silica retains most of the features of Fo-An-SiO<sub>2</sub> except that the olivine-orthopyroxene boundary is cotectic at least in part. The boundary may be peritectic near the reaction point R. Future studies might well include planes of different Mg/Fe ratio, particularly those higher in Fe, and also plagioclase of intermediate composition. It is to be emphasized that Fig. 17.3 refers to equilibrium with metallic iron, and cannot be used rigorously for terrestrial magmas crystallizing at higher fugacities of oxygen. It should also be noted again, anticipating a later chapter, that increased pressure tends to move the pyroxene field toward olivine, thus strengthening the likelihood that the  $L$  (Opx, Ol) boundary will be even if the oxygen fugacity is sufficiently low.

## T- $f_{O_2}$ Relations in Mg-Fe-Si-O

The system MgO-FeO-SiO<sub>2</sub> discussed earlier in this chapter was, as we have said, studied in the presence of iron. For terrestrial rocks we are more interested in the phase relations at higher oxygen fugacities than dictated by equilibria with iron. Fig. 17.4 summarizes the effect of adding oxygen (as  $Fe_2O_3$ ) to the "ternary" system MgO-FeO-SiO<sub>2</sub>; the figure is similar to one compiled by Speidel and Nafziger (1968). Two triangular faces of the tetrahedron are familiar to us: the base, from Bowen and Schairer (1935), and the right face, from Muan and Osborn (1956). The interior of the diagram is also due to the latter authors. The figure is not to scale, and the equilibria with wüstite are incompletely shown. The main message of Fig. 17.4 is that there is a *magnetite saturation surface* (defined by labels OPML, SPML, OSPML, OSML) having the same essential geometry as the familiar curves of olivine, pyroxene, and tridymite with liquid on or near the base of the tetrahedron. The invariant point called "L" by Bowen and Schairer is now fully labelled OSPIL to show the presence of iron; it is a 5-phase point in a quaternary ( $c = 4$ ) system, and hence for the 1-atm



**Figure 17.4.** System  $\text{MgO-FeO-Fe}_2\text{O}_3\text{-SiO}_2$ , showing primary phase volumes. Abbreviations: *o*, olivine; *s*, silica mineral; *p*, pyroxene; *m*, magnetite; *L*, liquid; *h*, hematite; *w*, magnesiowüstite. After Speidel and Nafziger (1968).

isobaric restriction has  $W_p = 0$ ; it is an isobaric invariant point. A univariant curve, OSPL, runs from the iron-saturated invariant point to its magnetite-saturated analogue, OPSML. This curve OSPL and the four heavy lines leading to it from the left define the primary phase volume of pyroxene plus liquid, bounded by equilibria with iron, olivine, magnetite, or silica. The phase abbreviations follow the style of Chapter 16.

The liquidus relations of Fig. 17.4 and the associated reaction curves may be rearranged in  $T-f_{\text{O}_2}$  space with the aid of a Schreinemakers analysis, extending the analysis of Chapter 16 to the Mg-bearing system. Such an analysis can be done very simply with the aid of a correct compositional projection and the use of Richardson's rule. We begin with an analysis of the univariant curves in the *immediate vicinity* of the invariant point OSPIL, noting that our analysis will not necessarily describe correctly the univariant reactions farther away from the invariant point.

Where shall we plot the phase compositions? To do so within the tetrahedron would require a feat of three-dimensional visualization worthy of the most fanatical structural geologist; it would not be a rigorously quantitative exercise, and it would fail anyway because iron does not lie in the tetrahedron. We shall instead make use (as before in Chapter 16) of a very powerful method, a *projection* from oxygen of all the phases, this time

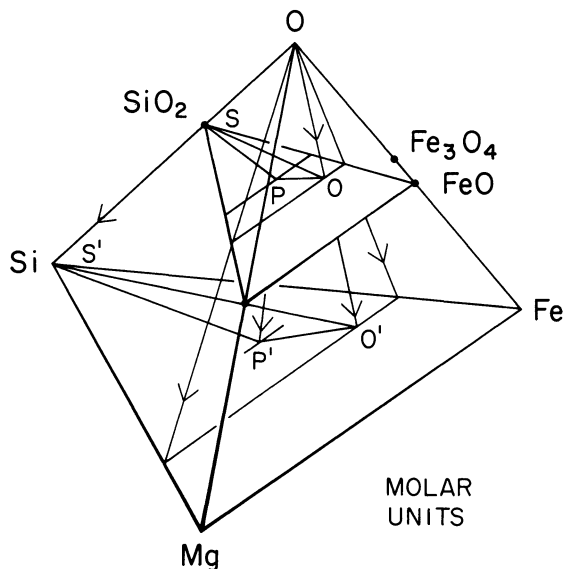


**Figure 17.5.** Projection from oxygen of a triangle  $ops$ , in the plane  $MgO-FeO-SiO_2$ , onto the base  $Mg-Fe-Si$  of the quaternary system  $Mg-Fe-Si-O$ . Letters  $o$ ,  $p$ ,  $s$  refer to olivine, pyroxene, and silica; the same letters primed refer to the projected compositions of these phases on the base. Pure magnetite plots at the point labelled  $Fe_3O_4$ , and projects to  $Fe$ .

onto the triangle  $Mg-Fe-Si$ . Such a projection is shown in Fig. 17.5; in the figure, the triangle  $osp$  is projected from  $MgO-FeO-SiO_2$  onto the base, where it is labeled  $o' s' p'$  in projection. Now the projected compositions all lie in the same plane as iron,  $Fe$ , and saturation with iron could be indicated by drawing lines from  $o'$ ,  $s'$ , and  $p'$  to  $Fe$ . Note for future reference the position of magnetite,  $Fe_3O_4$ , in Fig. 17.5; this will project to the  $Fe$  corner when we get around to it.

Fig. 17.6 summarizes the composition space as projected onto the base

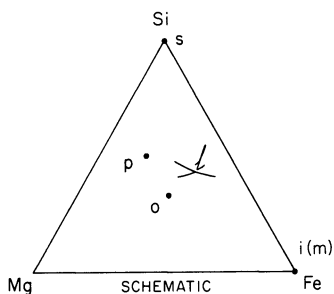
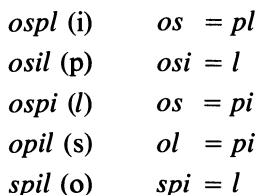


**Figure 17.6.** Chemographic triangle  $Mg-Fe-Si$ , showing the projected compositions of olivine ( $o$ ), pyroxene ( $p$ ), silica ( $s$ ), magnetite ( $m$ ), and liquid ( $l$ ). Iron ( $i$ ) lies on the base at the  $Fe$  corner, and is therefore not projected.

Mg-Fe-Si. The exact positions of *p* (pyroxene), *o* (olivine) and *l* (liquid) are of no concern as long as the *relative* positions are correct. Liquid is shown over a range of compositions merely as a reminder that it, as well as pyroxene and olivine, will have somewhat different compositions depending on the temperature and the nature of the reaction. We should recall that *l* lies toward oxygen, above the plane MgO-FeO-SiO<sub>2</sub> in Fig. 17.5; but this knowledge is not required for correct chemographic analysis in projection. It should be mentioned that the projected compositions of *o*, *p*, and *l* can be plotted exactly in their experimentally determined positions if desired; the projection is quantitatively rigorous.

The Schreinemakers analysis of invariant point OSPIL is illustrated in Figs. 17.7 and 17.8. If you start with the curve *ospl* and refer to Fig. 17.4, you will see at once that the curve must lie subparallel to the oxygen axis and terminate with iron at the lower end (and with magnetite at the upper end, as we shall see). We now write all the reactions about the invariant point, referring to Fig. 17.6 to see the chemographic relations that dictate the reactions. In shorthand form, the five reactions are as follows.



Curve (*p*) is known from Fig. 17.4 to lie at low temperature compared to the invariant point, and the same must obviously be true of curve *l*, a subsolidus reaction. The first three curves are therefore easily plotted. Curves (*s*) and (*o*) appear to offer problems at first, as their metastable extensions might lie anywhere between curves (*i*) and (*l*). But Richardson's rule solves the problem immediately, as shown in Fig. 17.8. For curve (*s*), merely draw arrows pointing toward the sector where *s* is generated by *all* the other reactions, stable *and* metastable (Fig. 17.8a). The result shows that the metastable extension of (*s*) must lie between curves (*p*) and (*l*). Note that the arrows are symmetrically disposed about the correct position of curve (*s*), and that two arrows point away from the stable segment of (*s*). The location of curve (*o*) is likewise determined with ease, as shown in Fig. 17.8b. We now have the complete geometry around invariant point *ospl*, and can verify from the chemographic diagrams that the sequence is correct because the tie lines are broken one at a time, or appear or disappear three at a time where liquid is involved in a triangular field (Fig. 17.7). The configuration of the tie lines in the sector between (*s*) and (*i*) is actually that of the invariant point itself; within the sector the composition of liquid changes with *T* and *f*<sub>O<sub>2</sub></sub>.

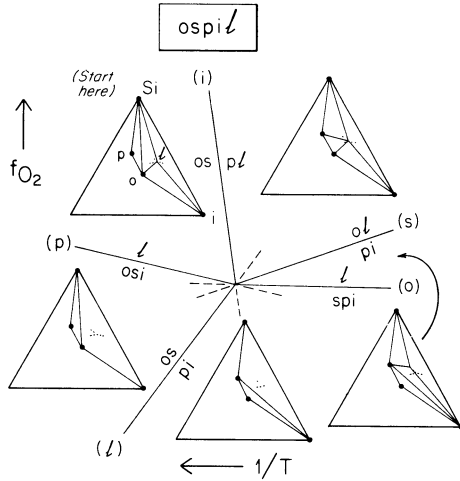


**Figure 17.7.** Invariant point OSPIL, with chemographic diagrams based on Figure 17.6.

With the benefit of Fig. 17.7, it is now child's play to construct the sequence of curves about invariant point OSPML. First, referring to Figs. 17.5 and 17.6, we note that  $m$  plots at the Fe corner where  $i$  plotted before. The list of reactions about OSPML is therefore identical to the list for OSPIL (see above) if  $m$  is everywhere substituted for  $i$  in the old list. This means, of course, that the sequence of curves must be the same about the two invariant points; however, the two bundles of curves are *enantiomorphous* to one another. This can easily be seen from the fact that OSPML is the upper terminus of the stable portion of curve  $ospl$ , hence it is a mirror

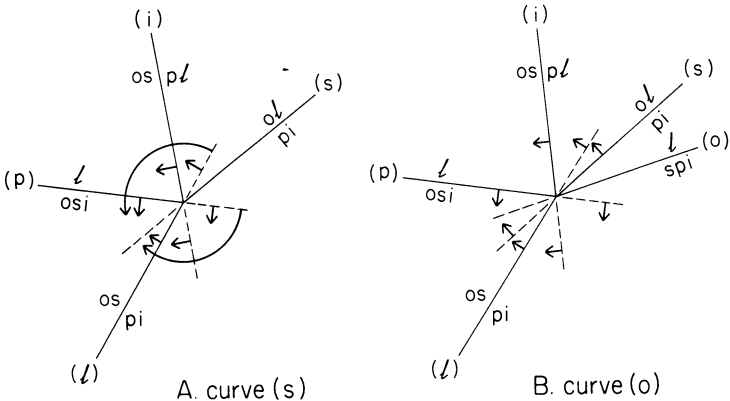


**Figure 17.8.** Use of Richardson's rule to locate the curves (s) and (o) about invariant point OPSIL.

image of OSPIL. The new bundle may therefore be obtained without further ado by reflecting across the normal to *ospl*; this has been done to obtain Fig. 17.9.

The two quaternary invariant points are united by curve *ospl*, as shown in Fig. 17.10. The figure is approximately scale-true, after Speidel and Nafziger (1968), who located curve *ospl* by experiment. Their version of this figure is quantitative and somewhat more complete than Fig. 17.10. The light lines near the left edge of the figure refer to the *ternary* equilibria in Fe-SiO<sub>2</sub>-O (Ch. 16), and involve several buffer reactions for the pure Fe system, such as *osm* (i.e., FMQ). In Fig. 17.10, quaternary equilibria are denoted by heavy lines and capital letters, ternary equilibria by light lines and small letters. The divariant regions between the univariant curves correspond to the ones shown (in composition space only) in Fig. 17.4; OPL and OSM are examples. OPL is the surface between OPIL and OPML; OSM is the surface between OSIL and OSML. It is worth some effort to compare Figs. 17.4 and 17.10 until the relation between them becomes clear. Fig. 17.10 can be characterized in two major ways: it shows the rise in *T* accompanying the addition of Mg to the Fe system, and it describes the incoming of a new phase, pyroxene. Note that the ternary *invariant points* (Fig. 17.10) generate quaternary *univariant lines* having the same label. It will be seen that the known coordinates of the curves about OSPML require a sharp curvature of OSML near the invariant point in order for the metastable extension to lie in the correct sector (see Fig. 17.9). Given the experimental data on the curves, without the Schreinemakers analyses, one would very likely draw an incorrect phase diagram at OSPML.

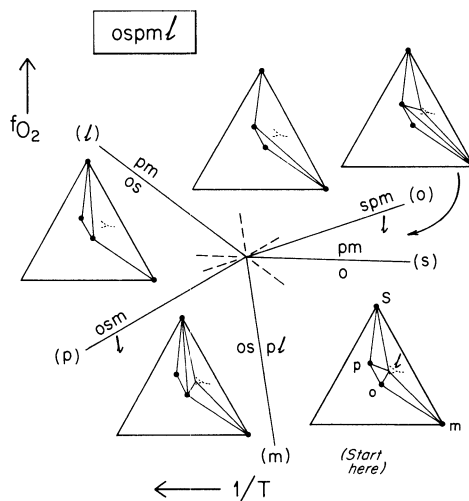
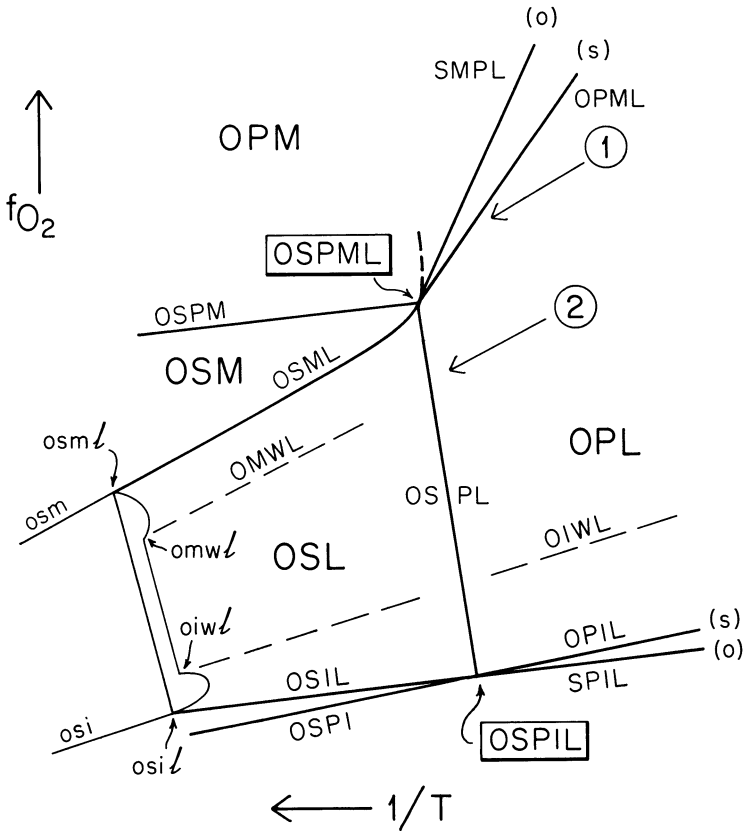


Figure 17.9. Invariant point OSPML with chemographic diagrams.



**Figure 17.10.** Arrangement of invariant points, univariant curves, and divariant regions in the system MgO-FeO-Fe<sub>2</sub>O<sub>3</sub>-SiO<sub>2</sub>. Heavy lines denote quaternary equilibria. Light lines denote ternary equilibria in the system Fe-SiO<sub>2</sub>-O, as discussed in Chapter 16. Points labelled (1) and (2) are bulk compositions discussed in the text. After Speidel and Nafziger (1968).

Crystallization paths can be followed qualitatively in both Figs. 17.4 and 17.10. Bulk composition (1) in the latter figure represents a liquid saturated with both olivine and pyroxene. It can be shown from external evidence (Morse, 1979; Morse, Lindsley, and Williams, 1980) that in a closed system such liquids follow a slope in  $T$ - $f_{O_2}$  space roughly like that of the FMQ buffer (OSM). Such a path would be concave upward in Fig. 17.4. The liquid will eventually encounter OPML, and then run along that curve as long as olivine and liquid survive. If olivine is lost on fractionation, the liquid will leave OPML but return to it as pyroxene and magnetite crystallize. The liquid may reach OSPML. At this peritectic point, pyroxene would be consumed by reaction, or with fractionation, the liquid would proceed along OSML. The sequence of rocks produced on fractionation would be harzburgite, magnetite-harzburgite, and then a rock consisting of fayalitic olivine, tridymite, and magnetite. Bulk composition (2), of lower oxygen

content, would encounter OSPL and there resorb pyroxene if equilibrium crystallization occurred, conceivably travelling along OSPL all the way to OSPML. With fractionation, such a liquid would blithely cross OSPL and continue along OSL to OSML or to the Mg-free system. In all such cases, the extraction of ferrous silicates must raise the oxygen content of the liquid and magnetite must crystallize in order to account for the oxygen in the liquid. It is very important to note that the oxygen *content* of the liquid *must rise* along paths (1) and (2) even though the oxygen *fugacity falls*. The two properties are not necessarily correlated directly.

If we saturate the entire system MFSO with an approximately inert phase like plagioclase, the MFSO equilibria will persist largely unchanged but the crystallization temperatures will all be lowered. Thus, the whole array of Fig. 17.10 will shift to the left, but *down* and to the left approximately along the paths of OSML and OSIL. The diagram is qualitatively applicable, therefore, to basalts, gabbros, diorites, and related rocks. Assuming feldspar saturation, the rocks fractionally produced by bulk composition (1) would then be olivine norite, magnetite-olivine norite, and perhaps quartz-magnetite-fayalite monzonite. In any case, at low pressures, Ca-poor pyroxene would disappear. The sequence wherein magnetite appears and Ca-poor pyroxene disappears is common in tholeiitic layered intrusions, but the disappearance of pyroxene is not, in general, related to a silica-saturated reaction point like OSPML, as we shall see.

## Role of Oxygen Fugacity in Complex Systems

Most of the principles of crystallization and fractionation pertaining to the system  $\text{MgO-FeO-Fe}_2\text{O}_3\text{-SiO}_2$  carry over into more complex systems, such as the diopside-bearing system obtained by adding CaO to the above list. Presnall (1966) has studied this system at various oxygen fugacities and given a useful review of its bearing on the crystallization of basaltic magmas; his review includes a summary and elaboration of earlier work by Osborn (1959) which first showed quantitatively the effect of oxygen fugacity on fractionation of basic magma. Osborn distinguished two limiting cases: crystallization at constant  $f_{\text{O}_2}$ , and crystallization at constant bulk composition. The former case requires membrane equilibrium with an external reservoir to supply oxygen, and can be regarded as a kind of open-system model. The second case requires isolation from the surroundings, as in the example we have considered (Fig. 17.10), and constitutes a closed-system model. One may readily see from Fig. 17.10 that imposing a constant oxygen fugacity on a crystallizing liquid would drastically alter the results, leading to strong silica enrichment caused by the abundant crystallization of magnetite; less extreme external regulation of oxygen fugacity would have a similar but less drastic effect. In either case, the Bowen trend of

alkali and silica enrichment would result. In the case of constant bulk composition, the Fenner trend of iron enrichment results.

Conditions approaching constant oxygen fugacity during fractionation would require substantial addition of free oxygen to the system, an event likely to be rare in nature. However, the Bowen trend does not require such an extreme condition as constant oxygen fugacity. The favorite mechanism for introducing oxygen has been the dissociation of  $H_2O$ , under the assumption that the differential escape of hydrogen (as a proton) from the magma system would occur with ease. Osborn (1959) suggested that the Bowen trend, calc-alkaline series of volcanic rocks could be accounted for by contamination of magmas with water as fractionation proceeded, a case strengthened by the common association of calc-alkaline magmas with orogenic zones where water would be readily available from the voluminous sedimentary pile. Further discussion of the contamination hypothesis is given by Presnall (1966) and Czamanske and Wones (1973).

## The Pyroxene Quadrilateral

In the system Fo-Di-SiO<sub>2</sub> (Chapter 12), we saw the coexistence of pigeonite with either diopside or protoenstatite. In Chapter 13 we deduced a relationship for plagioclase- and iron-bearing systems such that the assemblage Di + Pr<sub>ss</sub> would give way to Di + Pig with fractionation, to account for the sequence seen in tholeiitic layered intrusions. We have seen in this chapter the evidence for iron enrichment in Ca-poor pyroxenes, but of course pigeonite cannot be obtained in the Ca-free system. In order to understand the crystallization of *all three* pyroxenes: augites (or diopsides), Ca-poor orthopyroxenes, and pigeonites, we should have to consider the system CaO-MgO-FeO-SiO<sub>2</sub> (CMFS). However, pyroxene relations in this quaternary system are exceedingly complicated and difficult to study experimentally, for several reasons. Miscibility gaps (i.e., solvi) and polymorphic transitions occur in the pyroxene solid solutions, and these chain silicates may nucleate or persist metastably in experimental runs (and evidently in nature also). As in the case of the ternary feldspars, it will suit our purpose here to fall back on the data from natural rocks as a guide to the salient phase relations.

The plane CaSiO<sub>3</sub> (Wo) - MgSiO<sub>3</sub> (En) - FeSiO<sub>3</sub> (Fs) lies at 50 mole percent SiO<sub>2</sub> in the system CMFS, and it contains the pure CMFS analogues of the major rock-forming pyroxenes of basaltic rocks. None of these pyroxenes occur with compositions more calcic than 50 mole percent Wo, so it is common practice to pay attention only to the Wo-poor half of the ternary plane, namely the *pyroxene quadrilateral* defined by the truncated triangle: Di-Hd-En-Fs. Fig. 17.11 shows this composition region.

On Fig. 17.11 are plotted the pyroxene trends for two layered intrusions,

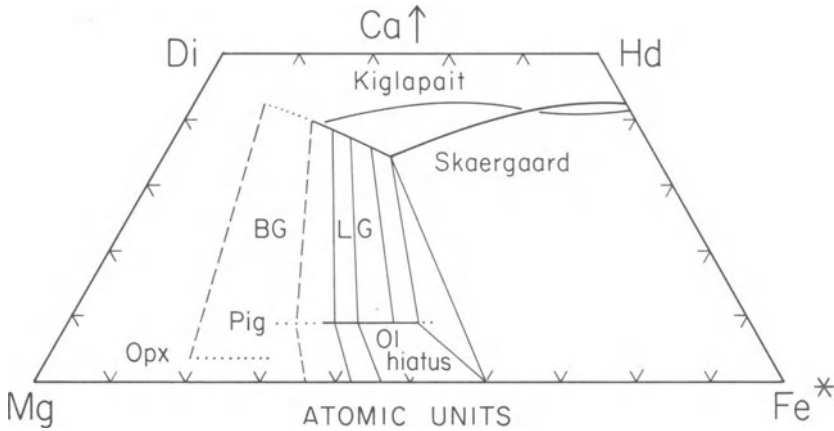


**Figure 17.11.** The pyroxene quadrilateral, showing olivine and pyroxene composition trends for the Skaergaard intrusion (Wager and Brown, 1968; augite trend after Chayes, 1969) and the augite composition trend for the Kiglapait intrusion (Morse, unpublished data). Di and Hd refer to diopside,  $\text{CaMgSi}_2\text{O}_6$ , and hedenbergite,  $\text{CaFeSi}_2\text{O}_6$ , respectively.  $\text{Fe}^*$  refers to  $\text{Fe}^{2+} + \text{Mn}$ . Other abbreviations: BG, Border Group; LG, Layered Group, Pig, pigeonite; Opx, orthopyroxene; Ol, olivine. Olivine compositions lie on the base of the quadrilateral.

the Skaergaard and the Kiglapait. Olivine occurs in both intrusions, except during the olivine hiatus in the Skaergaard intrusion, for which the compositional range in  $\text{Mg}/(\text{Mg} + \text{Fe})$  is marked on the diagram. Tie lines from olivine to Ca-poor pyroxene in the Skaergaard intrusion are shown for the limits of the olivine hiatus. Tie lines from olivine to augite are omitted for clarity, but can be interpolated as parts of three-phase triangles from the other two types of tie line shown.

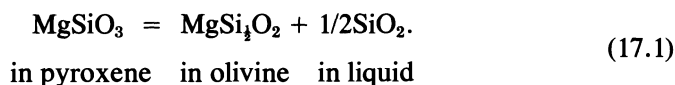
The Kiglapait intrusion is critically undersaturated in silica and contains no primary Ca-poor pyroxene. Its only pyroxene trend is the augite trend, which runs at approximately constant Ca across the diagram to the Hd-Fs sideline.

The Skaergaard trend is typical of olivine-tholeiitic layered intrusions, of which the Bushveld complex (Atkins, 1969) is another famous example. The trends for coexisting augite and Ca-poor pyroxene evidently describe the compositional traces of the pyroxene solvi in the quadrilateral. Since we know that temperature falls toward the Fe sideline and away from the Mg sideline in any such system, the decreasing Ca content of the augite limb of the solvus cannot be accounted for by falling temperature on a solvus with an isothermal crest line. It can be ascribed only to a solvus that is shaped like a plunging anticline, with axial trace running from about  $\text{Di}_{60}\text{En}_{40}$  on the Mg sideline to about  $\text{Hd}_{20}\text{Fs}_{80}$  on the Fe sideline. The augite trend follows a path of decreasing Ca until Ca-poor pyroxene disappears, after which it follows a path of rising Ca until it reaches the Fe sideline. The reason for this is clear: both augite and Ca-poor pyroxene must be

constrained to the solvus as long as they coexist; when the Ca-poor pyroxene disappears, augite is no longer constrained to the solvus but simply follows a path dictated by the liquid. This path eventually merges, for all practical purposes, with the Kiglapait path.

The question of why Ca-poor pyroxene disappears has been addressed at length by Lindsley and Munoz (1969), who studied the sideline Hd-Fs. These authors deduced from several lines of evidence that the polythermal traces of the two-pyroxene solvus for silica-saturated rocks would continue along extensions of the Skaergaard paths shown in Fig. 17.11. This deduction was amply reinforced by later discovery of lunar pyroxenes falling along or near such trends, although the case of lunar pyroxenes is complicated by metastable effects, among other things (see, for example, Bence and Papike, 1972). Among the evidence used by Lindsley and Munoz was the occurrence in Quebec and in Labrador of quartz monzonites with pyroxene pairs lying essentially on the extensions of the Ca-poor and Ca-rich solvus trends shown in Fig. 17.11. It is to be emphasized that these pyroxenes occur in company with abundant quartz, hence at silica saturation, whereas the Skaergaard and Bushveld intrusions have lost Ca-poor pyroxene long before their magmas become saturated in silica. Primary quartz is lacking in these intrusions except at very late stages of crystallization, where Mg is essentially absent. Lindsley and Munoz therefore reasoned that the disappearance of Ca-poor pyroxene could *not* be the result of a reaction relation among pyroxene, liquid, and a silica mineral (as on curve OSPL in MgO-FeO-Fe<sub>2</sub>O<sub>3</sub>-SiO<sub>2</sub>), because Ca-poor pyroxene disappeared before the field boundary with a silica mineral was reached.

The stability of Ca-poor pyroxene relative to olivine is dependent on the silica content of the magma. In the absence of sufficient silica, the pyroxene will tend to decompose to olivine and a more silica-rich liquid. Such a reaction cannot be seen in a liquidus phase diagram, which deals only with liquid saturation surfaces, but it can easily be represented by a chemical equation, namely:



By LeChatelier's principle, an increase in the concentration of silica would drive the above reaction to left; hence the maximum persistence of Ca-poor pyroxene will occur when the system is saturated with silica in the form of primary quartz, as in the Quebec and Labrador quartz monzonites. Conversely, a decrease in the concentration of silica would drive the reaction to the right, causing the disappearance of Ca-poor pyroxene in favor of olivine. It therefore appears that the limiting composition of Ca-poor pyroxene in tholeiitic intrusions is in some way related to the concentration of silica in the magma. Extending the argument further, if the concentration of silica remains sufficiently low throughout crystallization, no Ca-poor

pyroxene will occur, as in the case of the Kiglapait intrusion. We may therefore conclude that the pyroxene trends of layered intrusions are sensitive indicators of silica concentration.

It is preferable to deal in such cases with silica *activity* rather than concentration. For any component  $i$  the activity  $a_i$  is related to the mole fraction  $X_i$  by  $a_i = X_i \gamma_i$ , where  $\gamma_i$  is the *activity coefficient*, to be determined from experience. Ideal solutions are defined as those for which  $\gamma_i = 1.0$ , hence for which  $a_i = X_i$ . Activity coefficients for complex magmas are as yet essentially unknown, but can in principle be extracted through application of the law of mass action to cases where mineral compositions and liquid compositions are known. The *activity* is a thermodynamic property related to the chemical potential by

$$\mu_i = \mu_i^\circ + RT \ln a_i \quad (17.2)$$

where  $\mu_i$  is the chemical potential or partial molar Gibbs free energy of  $i$ ,  $\mu_i^\circ$  is the chemical potential at some standard state (such as the pure component  $i$  at the temperature and pressure of interest),  $R$  is the ideal gas constant, and  $T$  is temperature in Kelvins.

For reaction (17.1) we can write the equilibrium constant  $K$  for a given temperature and pressure as

$$K = \frac{a_{MgSi_4O_2} \cdot a_{SiO_2}^{1/2}}{a_{MgSiO_3}} \quad (17.3)$$

and taking the log of both sides, we get

$$\log K = \log a_{MgSi_4O_2} + \frac{1}{2} \log a_{SiO_2} - \log a_{MgSiO_3} \quad (17.4)$$

By rearranging and multiplying to eliminate the fraction, we get

$$\log a_{SiO_2} = 2 \log a_{MgSiO_3} - 2 \log a_{MgSi_4O_2} + 2 \log K \quad (17.5)$$

$\log K$  is equal to  $-\Delta G_r / RT$ , where  $\Delta G_r$  is the Gibbs free energy change for the reaction. This free energy change can in principle be calculated for any temperature of interest from tables of free energy such as those of Robie, Hemingway, and Fisher (1978). However, the results are very sensitive to small errors in the free energies of formation for forsterite and enstatite.

Equation (17.5) is a useful expression of the activity of silica for cases where the olivine and pyroxene have intermediate values of the Mg/Fe ratio. In such cases, the values of  $a_{MgSi_4O_2}$  and  $a_{MgSiO_3}$  can be estimated from the mole fractions of these components in the olivine and pyroxene, respectively, by use of experimentally determined activity coefficients as for example given by Williams (1972; 1971a). Measurement of the mineral compositions, combined with knowledge of the free energy of reaction and hence  $\log K$  for a given temperature, thus leads directly to an estimate of  $a_{SiO_2}$  in the liquid, provided that olivine and Ca-poor pyroxene co-existed

with liquid and that the temperature of crystallization can be estimated. An internally consistent set of constants is given in the paper by Morse (1979), where procedures of the calculation method are also described. Calculations of silica activity in the Skaergaard intrusion are given by Morse, Lindsley, and Williams (1980). The parallel relation between silica activity and oxygen fugacity (which is also an activity; note the identity of the definitions in equations 16.3 and 17.2) in basic magmas is also discussed in these papers.

In the latter regard, we have already seen some basic principles about the parallel relation of the oxygen and silica activities, starting with the FMQ reaction in Chapter 16 (equation 16.2) and the role of oxidation in magmas identified by Kennedy (1955), Osborn (1959) and others. It is clear from all these studies that oxidation and silication go hand in hand, for example in the oxidation of olivine to form magnetite and silica. It therefore appears that the pyroxene trends of Fig. 17.11 should say something about the relative oxidation states of the Skaergaard and Kiglapait intrusions, namely that the more silicated Skaergaard magma should have been more oxidized than the silica-undersaturated Kiglapait magma. Studies of the Fe-Ti oxide minerals in the two intrusions bear out this theoretical prediction.

Examples of the use of silica activities, and other calculations based on equilibrium constants, abound in the book by Carmichael, Turner, and Verhoogen (1972) and are also given in the papers of Lindsley, Brown, and Muir (1969) and Williams (1971*b*). Such calculations find increasing use in igneous petrology, and form an important extension of the experimental base provided by phase diagrams. An example based on Fig. 17.11 will serve to close this chapter.

We wish to find the activity of silica in the Skaergaard magma when Ca-poor pyroxene ceased to crystallize, liberating the augite composition from the pyroxene solvus. A magma saturated with a silica mineral (tridymite in this case) has  $a_{\text{SiO}_2} = 1.0$  by definition, and under such a condition an increase in the concentration of  $\text{SiO}_2$  would only serve to make more tridymite. Since we ascribe the loss of pigeonite to a low activity of silica, we will expect to find  $a_{\text{SiO}_2} < 1.0$ . For use of equation (17.5), we take as data the conditions at the 1580 meter level of the Skaergaard intrusion, corresponding approximately to the three-phase triangle shown in Fig. 17.11. Data are taken from Wager and Brown (1968), Lindsley, Brown and Muir (1969), and Morse, Lindsley, and Williams (1980). The temperature is taken as  $1364^\circ \text{K}$  ( $1091^\circ \text{C}$ ) and the pressure as 830 bars for this level of the intrusion. The term  $2 \log K$  for the pure end-member reaction  $\text{En} = \text{Fo} + \text{Silica}$  therefore works out to a value of  $-0.214$ , using the reaction constants given by Morse (1979) for the equation  $\log K = A/T + B + C(P - 1)/T$ . (The constants are  $A = -364$ ,  $B = +0.169$ ,  $C = -0.0193$ ).

The mineral compositions are olivine  $\text{Fo}_{40}$  and pigeonite  $\text{En}_{49}$ . To correct from pigeonite to hypersthene, we add 2 to obtain  $\text{En}_{51}$ , by reasoning explained in Morse (1979). The corresponding activities of components Fo and En in the crystalline solutions, taken from the activity-composition

relations given by Williams (1972 and 1971a), are 0.473 and 0.576, respectively. Equation (17.5) now reduces to

$$\begin{aligned}\log a_{\text{SiO}_2} &= 2(-0.240) - 2(-0.326) - 0.214 \\ &= -0.480 + 0.652 - 0.214 \\ &= -0.042\end{aligned}$$

and  $a_{\text{SiO}_2} = 0.9$ . We therefore have verified, from the mineral compositions and estimated crystallization conditions, that  $a_{\text{SiO}_2} < 1.0$ , and that the magma was not saturated with tridymite, a fact observed in the rocks. But more than this, we have obtained a specific value for the activity of silica when pigeonite disappeared from the Skaergaard magma, and we can say that  $a_{\text{SiO}_2}$  must have been less than 0.9 (assuming similar  $T$ ,  $P$  conditions) at a similar stage in the Kiglapait intrusion, in order for pigeonite not to have crystallized, and  $a_{\text{SiO}_2}$  must have been greater than 0.9 in the Quebec and Labrador examples where Ca-poor pyroxene continued to crystallize. By such exercises we gradually learn to attach meaningful numbers to the intensive parameters of state of crystallizing magmas.

## Chapter 18

# The Effects of High Pressure

### Introduction

Pressure increases with depth in the earth, to a maximum at the center. The rate of increase depends on the material present along the path followed; it is lower, for example, in sea water than in rocks. But a useful generalization, adequate for most petrologic purposes to moderate depth, is that the pressure increases by about 3 kbar for every 10 km. Inverting this, depth increases at a rate of about 3.3 km/kbar. A *bar* is defined as  $10^5$  pascals, and is about equal to an atmosphere of pressure. The bar and its multiples are therefore convenient units for earth science, ranging from millibars (mb) in the atmosphere through bars in the oceans, kilobars in the crust and upper mantle, and megabars (Mbar) in the deep mantle and core. The core-mantle boundary lies at a pressure of about 1.5 Mbar (1500 kbar).

As we have seen from the Clausius-Clapeyron equation (3.1), all materials that have a positive volume change on melting will have positive melting slopes,  $dT_m/dP$ . This is true of all the solid forms of  $H_2O$  except ice<sub>1</sub>, and of all known silicate materials at low to moderate pressures. The *rates* at which the melting temperatures increase with pressure vary from quite small, e.g. about 3°/kbar for anorthite, to rather large, e.g. about 15°/kbar for diopside. This means that phase diagrams will tend to change with pressure, with eutectics and cotectics shifting away from the phase with the higher  $dT_m/dP$ . Some familiar phase diagrams will change only a little, and others will change greatly, even so as to yield completely different relationships, as with the change to congruent melting for enstatite men-

tioned in the last chapter. New solid phases appear at high pressure in many systems, and these may affect the melting relations profoundly.

The source regions of basaltic magma quite surely lie in the range 5-30 kbar, and very commonly near 10 kbar (Presnall *et al.*, 1979). We shall therefore be concerned, in this book, with melting relations at moderate pressures, usually less than 30 kbar.

In this chapter, we review in sequence the high pressure melting relations of most of the systems previously discussed in this book. We shall be concerned chiefly with the geometrical relations of phase diagrams, both in  $P$ - $T$  space and in isobaric  $T$ - $X$  sections through  $P$ - $T$ - $X$  space. For ternary systems, we shall need to map thermal information onto the  $X$ - $X$  diagram at constant pressure, just as we did at 1 atmosphere pressure. The treatment in this chapter is introductory, and broader conclusions related to basalt genesis are reserved for Chapter 20. We first need a brief introduction to the methods of high pressure research.

## High Pressure Apparatus

The conduct of experiments at high pressure is now a routine matter in many laboratories, but it is a relatively young practice in geology, having reached high fruition only since about 1950. We shall undertake here only a very brief account of the main instruments in use today. The art of high pressure research owes much to the pioneering work of the physicist P.W. Bridgman at Harvard University in the early part of the century, and the two major instruments in use today for petrologic research were designed by geologists who were acquainted with his laboratory.

The most commonly used apparatus today for high pressures in the range 5-60 kbar is the so-called single stage or piston-cylinder or solid-media apparatus (Boyd and England, 1960); see also Ulmer, 1971, for a review of this and other types of apparatus.). If you take a short, thick-walled pipe, insert in it two tight-fitting opposed pistons that protrude beyond the ends of the pipe, and squeeze the pistons together with a hydraulic jack, you have a piston-cylinder apparatus. In practice, the lower piston is usually a static plug of tungsten carbide. The sample is placed between the pistons, and surrounded by a graphite cylinder which acts as a furnace when an electric current is applied through the piston, across the graphite, and out through the carbide plug. Temperature is measured by inserting a thermocouple next to the sample and guiding the leads through the piston, so they don't get sheared off. Pressure is measured by means of a gauge in the hydraulic line, and calculated for the sample chamber by calibration against known phase transitions.

The catch in this description is the misleading scale connoted by use of the words "pipe" and "cylinder". The pistons in common use are roughly

the size of your forefinger, but the cylinder may be about a foot in diameter and perhaps half a foot thick, with a piston-sized hole drilled along its cylindrical axis. To give the cylinder added strength, it is made up of several concentric rings, each with an interference taper, swaged into each other with great force. This scheme pre-stresses the piston chamber. Great efforts are made to reduce the friction between piston and cylinder and to reduce the shearing of the sample by directed stress. These ends are often accomplished by using pyrex glass or rock salt (which soften at high  $T$  and  $P$ ) in the sample chamber.

Samples to be used in the piston-cylinder apparatus are usually contained in noble metal tubing. A typical platinum sample tube might be two millimeters in diameter and 5 millimeters long, with crimped and welded ends. The amount of sample used is typically only a few milligrams. Water, if desired, is introduced to the tube before the sample by means of a hypodermic needle or fine syringe. Carbon dioxide may be introduced as well by adding crystals such as oxalic acid ( $C_2H_2O_4$ ). After the apparatus is assembled with the sample in position, the run may be brought to  $P$  and  $T$  in a matter of 2-3 minutes, and when the experiment has run the desired length of time, the charge is quenched in less than a minute by simply turning off the power to the furnace assembly.

The advantages of the piston-cylinder apparatus are that it is quick and easy to use, relatively inexpensive to maintain, capable of temperatures limited only by the materials used (around  $1650^\circ C$  for platinum capsules, but much higher,  $> 2100^\circ C$ , for graphite and other materials), and capable of routine pressures to 50 or 60 kbar. Its disadvantages are related mainly to the friction problem, which introduces errors particularly at low pressures, below 10 kbar, and some limitations on the precision of temperature control.

For pressures up to 5-10 kbar,  $800-700^\circ C$ , an externally heated cold-seal apparatus is often used, with water or argon as the pressure medium. This useful device was invented by O.F. Tuttle. The reaction vessel is a steel oblong cylinder, typically 3 cm in diameter and perhaps 30 cm long, along which a 6-mm hole is drilled to within several centimeters of one end. The sample, welded into a noble metal or silver tube, is pushed into the closed end with a filler rod, and the open end is sealed with a cone-in-cone seal held tight by a large nut threaded onto the open end of the reaction vessel. Water or gas is pumped under pressure into the vessel through an orifice in the cone-in-cone seal, and maintained at pressure by closing a valve in the pressure line. Pressure is monitored by a Bourdon-tube gauge in line with the delivery system. Heat is applied to the reaction vessel by putting a cylindrical furnace around it near the closed end, so that the seal area remains relatively cool. Temperature is measured by inserting a thermocouple into a well drilled off-center in the closed end of the vessel, so that the thermocouple junction lies beside the sample, separated from it by a few millimeters of steel. The run is brought part way to pressure by pumping

the pressure medium, then heated by applying the furnace and thus brought to  $P$  and  $T$  in a matter of some 10-15 minutes. It is quenched, at pressure, by removing the furnace and directing a jet of air against the vessel, followed eventually by a jet of water.

The advantages of the cold seal apparatus are its small expense, ease of operation, and suitability to accurate control of low pressures in the range 1-10 kbar. Its disadvantages are its limitation to low temperatures, beyond which the reaction vessel may fail by rupture, and some imprecision in temperature control and measurement, due in part to large thermal gradients.

The king of instruments for high pressure research with relatively large (>50 mg) samples is the internally heated gas medium apparatus or so-called gas apparatus. This was developed originally by Bridgman and modified for routine petrologic work by Yoder (1950). Its key feature is the Bridgman "unsupported area seal" which gets tighter the higher the pressure. The pressure vessel is a large steel alloy cylinder with a small axial hole into which is introduced the furnace assembly with its sample. The hole for the furnace assembly is of the order of 2 cm in diameter, and the enclosing cylinder is typically 20 cm in diameter by 50 cm long, wrapped with copper tubing through which water flows to cool the vessel. Each run typically contains four samples in welded platinum tubes, arranged around a thermocouple junction, embedded in granular alumina within a 30-gram, heavy-walled, platinum cylinder called a "block" (because it provides a high thermal inertia to the sample area). The block, typically 8 mm in outside diameter, rests inside a ceramic tube about 15 cm long, onto which is wound a platinum resistance wire to act as a furnace. This furnace array is cemented into a cylindrical nickel support housing, which in turn is connected at one end to a "head" about 4 cm in diameter, containing stacked washers of steel, copper, and leather. When the furnace assembly is put into the pressure vessel, one end of the head fetches up against a shoulder, and the other end is forced against the washers, and these in turn against the shoulder, by means of an enormous nut (really a hollow bolt) tightened with a 3-foot wrench. The longitudinal force against the flat sides of the washers makes them extrude radially into the walls of the sealing chambers of the pressure vessel, and when the pressure medium (argon) is pumped into the vessel through an orifice in the closed end, the washers are compressed even more, to tighten the seal. This is the unsupported area seal of Bridgman.

The gas apparatus is brought to pressure, after loading, by pumping argon into the pressure vessel and simultaneously into an intensifier consisting of a hydraulic ram with its chamber expanded. When the pumping limit (2-5 kbar) is reached, the ram is advanced past the pumping orifice and the pressure in the entire system is thus further intensified (to a conventional limit of 10 kbar) by the consequent reduction in volume. The

furnace is then turned on, being attached by welds to permanent pressure-tight leads through the head and thence through an axial hole in the nut. Pressure is monitored externally in the line to the intensifier by a manganin cell, whose emf is a nicely-known function of  $P$ . The run is rapidly quenched by turning off the power to the furnace.

The advantages of the gas apparatus lie in its precision of  $T$  and  $P$  measurement and control, to  $2^{\circ}\text{C}$  and a few tens of bars; in its hydrostatic application of pressure; and in its high temperature limit (near  $1700^{\circ}\text{C}$ ) at 10 kbar. Its disadvantages are in the somewhat lengthy preparation needed for each run, although on good days one can quench and reload in the space of an hour; in its practical limitation to 10 kbar; and in the shielding and precautions needed for safety. A gas apparatus at pressure is not unlike the chamber of a good artillery piece being fired, and any failure is likely to be explosive. Actually, only one real humdinger of a failure is known to me, and its cause was simply wear and tear, not altogether unanticipated. The nut stripped its threads and flew out, redesigning a substantial wall and overturning a tall glassed-in bookcase in the next room. But such events are rare and need not deter careful experimentalists. The gas apparatus is under-used today, and many jobs remain to be done with it in both igneous and metamorphic petrology.

The most spectacular instrument for high pressure research is unquestionably the opposed diamond anvil apparatus, recently developed at the National Bureau of Standards and taken to a level of high refinement by David Mao and Peter Bell at the Geophysical Laboratory, Carnegie Institution of Washington. The instrument is ridiculously simple in principle, consisting of two brilliant-cut diamonds with their points flattened off parallel to the tables and supported, point to point, in a small thumbscrew vise. The sample resides between the flattened points, surrounded by a gasket. The entire pressure cell is mounted in the optical path of a microscope so that experiments can be observed in progress with transmitted light, and it can be demounted for X-ray diffraction or spectroscopic studies. The catch is that the instrument must be beautifully designed and built to hold the alignment of the diamond, and the diamonds must be perfect, and masterfully dressed. Pressure is ingeniously measured by throwing a few grains of ruby in with the sample and observing the wavelength shift of a beam of laser light, which passes through a ruby crystal and is affected by the compression of the crystal. With this instrument, Mao and Bell have attained pressures near that of the core-mantle boundary, in a cell so perfect that the diamond failed by plastic flow rather than by cracking. Justly heralded as a window into the deep mantle, the diamond cell is an exciting vehicle for discovery about the earth and about the laws of physics.

We now return to the matter at hand, the results of experiments at high pressures.

### Representations of Melting Curves

Figure 18.1 shows three ways of representing the same melting curve  $S = L$ . All three are commonly used in geology. The third,  $-P$  versus  $T$ , is very sensible from the standpoint of viewing the earth in cross-section, but it can be confusing because the positive slope looks negative until one looks closely at the pressure axis. The first two types of diagrams are used most commonly, and we shall follow common practice by mixing them rather indiscriminately. This is annoying at first, but one gets used to it with practice.

The sources of melting curves will usually be referenced in the captions rather than in the text.

### Diopside

The melting curve for diopside to 30 kbar is shown in Fig. 18.2. Boyd and England (1963), assisted by S. P. Clark, Jr., followed a conventional practice in physics by fitting their experimental determinations to the Simon equation:

$$P - P_0 = A [(T/T_0)^c - 1] \tag{18.1}$$

This is a completely empirical relation, without any known physical significance.  $P_0$  is the intercept pressure for the phase of interest, 1 bar in the case of diopside, and  $T_0$  is the melting temperature (in Kelvins, i.e. deg. C + 273) at the intercept pressure. Procedures for fitting the curve are discussed by Clark (1959) and in the appendix to Boyd and England (1963). The constants for diopside are indicated in Fig. 18.2; note that  $T_0$  is 1392 + 273. The initial slope of the melting curve is given by  $T_0 / Ac$ , which here equals 15.4°/kbar. The curve shown is the liquidus trace; the solidus trace

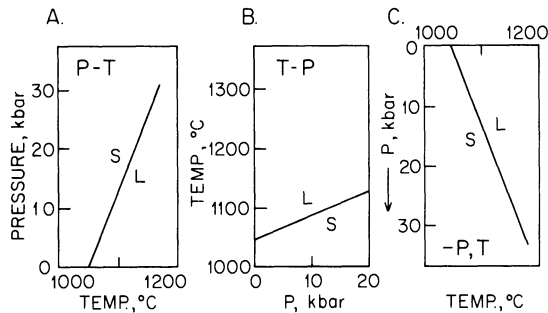


**Figure 18.1.** Three ways of showing the same melting curve as a function of pressure. The third diagram most closely resembles a vertical section into the earth, but the inversion of the pressure axis makes the positive slope look negative.

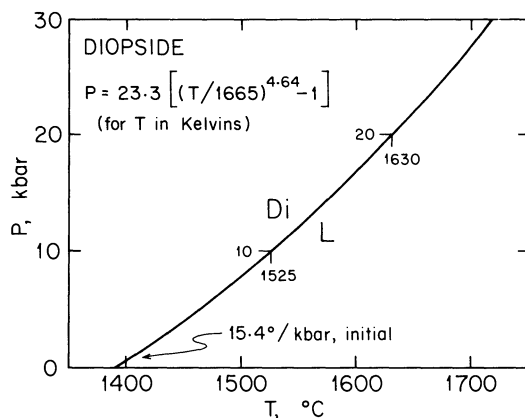


**Figure 18.2.** Melting curve for diopside at high pressure, after Boyd and England (1963).

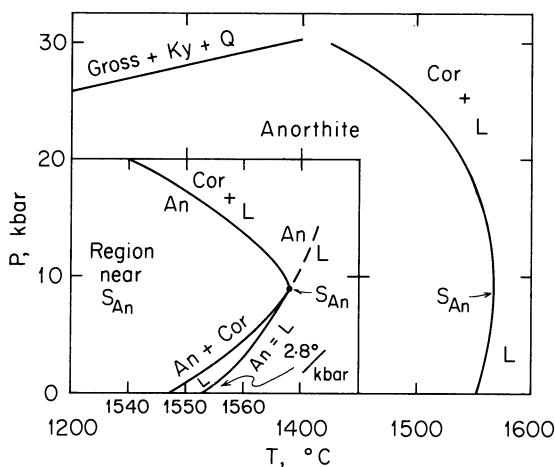
lies somewhat lower because of incongruent melting (see Fig. 12.2 and Kushiro, 1972).

## Anorthite

The melting of anorthite is much more complex than that of diopside at high pressure. The behavior followed, however, is a very common one among silicate minerals, and we shall see many further examples of it. The phenomena involve the generation of a singular point ( $S_{An}$ ) where the composition of the liquid exactly equals  $\text{CaAl}_2\text{Si}_2\text{O}_8$ . We have already seen singular points of this type in the system Fe -  $\text{SiO}_2$  - O, as for example  $S_m$  and  $S_i$  in Fig. 16.19.

In the anorthite system,  $S_{An}$  occurs at 1568°C and 9 kbar, where it is generated by the common tangency of two equilibria,  $An + L$  and  $An + Cor + L$  (see inset to Fig. 18.3). Corundum (Cor) occurs as an incongruent melting product of An above 9 kbar, and it forms a eutectic with An below 9 kbar. The curve  $An + Cor + L$  is a *continuous equilibrium* passing through the singular point with its metastable and stable extensions coincident; hence the curve is a continuous curve, and the only thing that happens as it passes through  $S_{An}$  is that the sign of the reaction changes from even (below  $S_{An}$ ) to odd (above  $S_{An}$ ). The curve  $An = L$  lies everywhere to the right of the equilibrium  $An + Cor + L$  except at the singular point, where the two curves unite. The *metastable* segment of  $An = L$  lies on the same side of  $An + Cor + L$  as the *stable* segment.

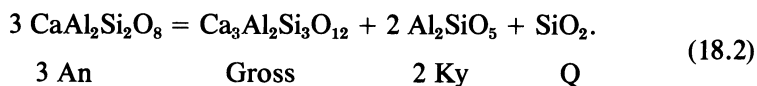
The explanation for all this complexity can be seen in Fig. 18.4. Part A of the figure shows the system CAS with the locations of An, the low-pressure liquid  $L_1$ , and the high-pressure liquid  $L_2$ . Part B of the figure



**Figure 18.3.** Melting and breakdown relations of anorthite at high pressure, after Goldsmith (1980).  $S_{An}$  is a singular point where the melting of anorthite becomes incongruent (see Fig. 18.4). Abbreviations: Gross, grossular; Ky, kyanite; Q, quartz; Cor, corundum; An, anorthite; L, liquid. For relations near the intersection of the subsolidus breakdown and the melting curve, see Lindsley (1968) and Wood (1978).

repeats the  $P$ - $T$  inset of Fig. 18.3, and shows the isobaric section lines  $C_1$  and  $C_3$  corresponding to the first and third sketches in part C of the figure. Part C represents the compositions as projected from CaO. At a pressure  $C_1$ , less than 9 kbar, we see in part C that the eutectic reaction  $Cor + An = L$  occurs at a lower temperature than the reaction  $An = L$ . As the pressure is raised, this eutectic migrates toward An. At 9 kbar, the pressure of the singular point, the liquid in equilibrium with corundum and anorthite has reached the composition of An. This generates the special  $T$ - $X$  configuration shown in the middle diagram of Fig. 18.4c. At pressure  $C_3$  the  $Cor + L$  field overlaps the composition of An and the melting relationship is incongruent, or odd. Note that in the last sketch of Fig. 18.4c, the metastable melting point of An at the top of the dashed curve lies higher than the incongruent melting point, as the arrangement of the curves in part B of the figure also shows. The  $T$ - $X$  diagram  $C_3$ , in fact, shows *why* the metastable extension of  $An = L$  must lie to the high temperature side of  $An + Cor + L$ .

As shown in Fig. 18.4b, the singular point  $S_{An}$  does not lie at the thermal maximum on  $An + Cor + L$  except by chance. By chance, in fact, it does lie indistinguishably close to the maximum, as shown in Fig. 18.3. This figure also shows that at high pressures, An breaks down to grossular plus kyanite plus quartz by the subsolidus reaction



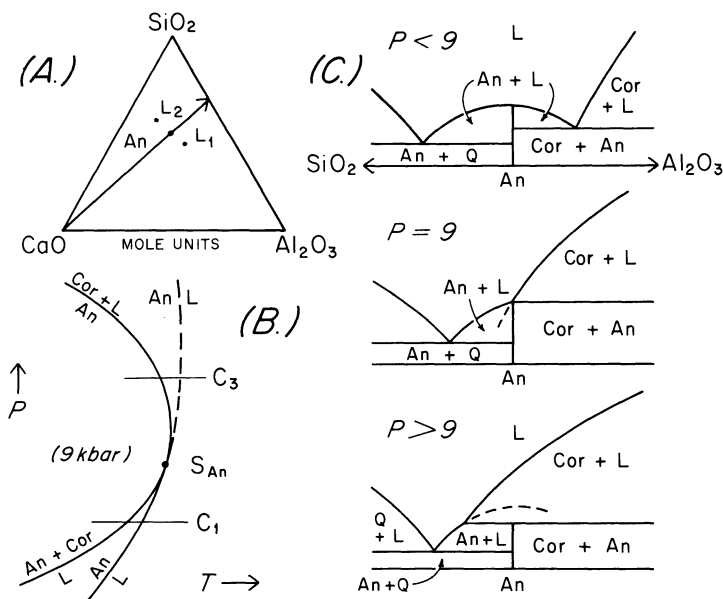


**Figure 18.4.** Explanation of the singular point  $S_{An}$ . A. Compositional space showing An projected from CaO onto sideline  $SiO_2-Al_2O_3$ . B.  $P$ - $T$  diagram showing the continuous equilibrium  $An + Cor + L$  and the stable and metastable parts of the equilibrium  $An + L$ .  $C_1$  and  $C_3$  refer to the first and third diagrams to the right. C.  $T$ - $X$  diagrams showing melting relations at a series of pressures, including the pressure of  $S_{An}$  (middle diagram).

The intersection of this reaction with the melting reaction is discussed by Wood (1978); it is complicated by the presence of CaTs,  $CaAl_2SiO_6$ .

## Diopside-Anorthite

Because the melting point of diopside rises much faster with pressure than that of anorthite, we shall expect to find that the diopside field is enlarged with pressure at the expense of the anorthite field. Fig. 18.5, an isobaric  $T$ - $X$  section at 10 kbar, confirms this expectation. At 10 kbar, the eutectic-like point  $Di + An + L$  has moved from 42% An to about 57% An, and the cotectic temperature has risen from 1274°C to 1382°C. The melting point for An, 1569°C, is the *metastable* melting point estimated from Fig. 18.3. The small field of  $Cor + L$  near An is omitted from the diagram.

An interesting feature of Fig. 18.5 is that the An liquidus moves hardly at all with pressure, and the shift of the cotectic is caused almost entirely by the diopside liquidus climbing up the anorthite liquidus.

The subsolidus relations of the system Di-An are even more complicated by entry of CaTs into the pyroxene than at 1 atm, and are ignored here.

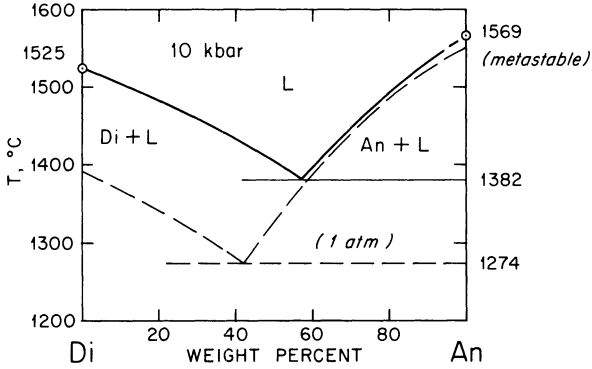


**Figure 18.5.** System Di-An at 1 atmosphere (dashed) and 10 kbar (solid lines). At 10 kbar, the melting of pure An is metastable relative to Cor + L. After Presnall *et al.* (1978).

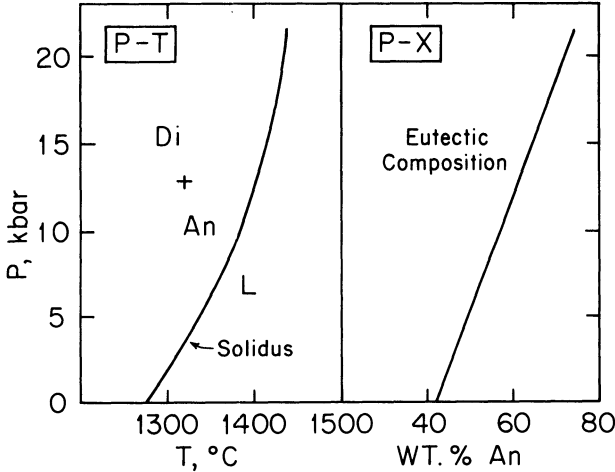


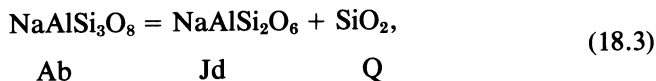
**Figure 18.6.** *P-T* diagram (left) and *P-X* diagram (right) showing changing temperature and composition of “eutectic” liquid in the join Di-An with pressure. Data from Fig. 4 of Presnall *et al.* (1978).

The change in the cotectic temperature for  $Di + An = L$  averages about  $11^\circ/\text{kbar}$  in the first 10 kbar, but the rate of change diminishes with pressure, as shown in Fig. 18.6. The *P-X* part of Fig. 18.6 shows the sensibly linear change in the “eutectic” liquid composition with pressure, to 20 kbar.

**Albite**

The initial melting slope for albite in *P-T* space is about  $14^\circ/\text{kbar}$ , and the melting curve is given by the Simon equation shown in Fig. 18.7. At

pressures near 30 kbar, albite breaks down to jadeite plus quartz according to the reaction



and complications arise in the melting relations. We shall return to these later.

Shown for comparison in Fig. 18.7 are the melting curve (metastable above 9 kbar) for An and the approximate *solidus* trace for intermediate plagioclase of composition An<sub>50</sub>. This solidus inherits most of its slope from albite, as is clear from the near parallelism of the two curves in contrast to their divergence from An = L.

## Plagioclase

The melting relations of plagioclase at 10 and 20 kbar are shown in Fig. 18.8. The 1-atm. diagram is sketched with the 10 kbar diagram for comparison. The essential features of the plagioclase melting loop are unchanged with pressure except for the higher temperatures of melting. However, equilibria with Cor + L begin to intrude at 9 kbar (see Fig. 18.3), and expand into the diagram as the pressure rises. At 20 kbar, only intermediate (to An<sub>64</sub>) and sodic plagioclase are stable with liquid of plagioclase composition, and calcic plagioclase coexists with corundum and a silica-rich liquid. The inset to the 20 kbar figure shows, schematically, the shape of the Plag + Cor + L loops, which unite at a maximum. The dashed part of the plagioclase melting loop at 20 kbar is metastable. Binary equilibria are

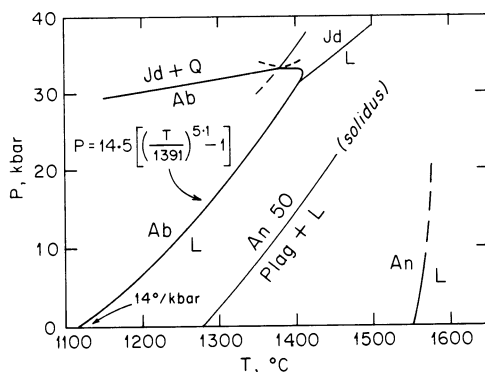


**Figure 18.7.** Melting curve for albite (Ab) with pressure, from Boyd and England (1963), with albite breakdown reaction and other jadeite (Jd) relations from Bell and Roseboom (1969). Shown also, for comparison, are the melting curve for An, from Fig. 18.3, and the *solidus* curve for An<sub>50</sub> plagioclase, from Fig. 18.8. The Ab = L curve may be seriously in error (Windom and Boettcher, 1977).

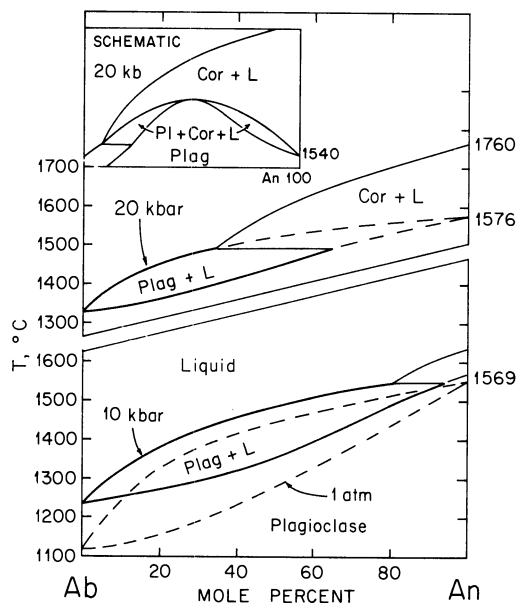


**Figure 18.8.** Melting relations of plagioclase at 10 and 20 kbar compared with 1 atm diagram (dashed). Compiled from data of Lindsley (1968) and Fig. 18.3 and 18.7. Where plagioclase loop is dashed, it is metastable relative to Plag + Cor + Liq. Inset shows schematically the stable relations at 20 kbar, from An<sub>30</sub> to An<sub>100</sub>. Further details are given by Lindsley (1968).

denoted by heavy lines, and ternary (incongruent) equilibria by light lines in the figure.

It is clear from Figs. 18.3, 18.7, and 18.8 that we cannot expect to find plagioclase at any great depth in the mantle. Intermediate plagioclase might be found at 20 kbar, given a suitable container, but by 30 kbar it would be represented instead by garnet, jadeitic pyroxene, kyanite, and quartz. Even more stringent restrictions occur, as we shall see, when plagioclase occurs with olivine.

### Diopside-Anorthite-Albite

The “diopside” present at high pressures in equilibrium with plagioclase will be a complex solution including some CaTs and Jd. The high-pressure phase relations are poorly known, but the most interesting feature of the ternary system is the location of the plagioclase-pyroxene cotectic. This is sketched in Fig. 18.9, with data for the Di-An sideline picked off Fig. 18.6. The positions of the ternary cotectic for 10 and 20 kbar are estimated from that determined by Lindsley and Emslie (1969) at 15 kbar.

The figure shows that high pressure shifts the cotectic towards plagioclase-

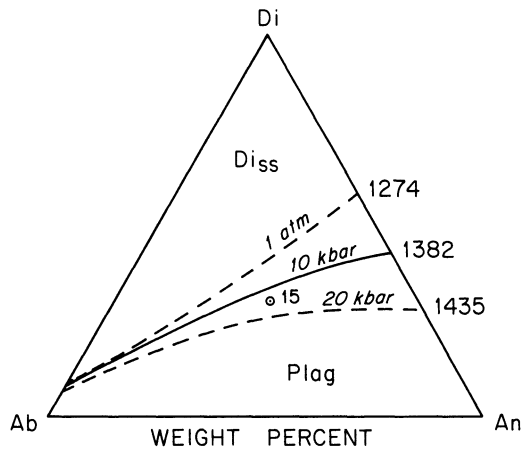


**Figure 18.9.** System diopside (Di) - anorthite (An) - albite (Ab) at 10 and 20 kbar compared to 1 atm. Di-An sideline after Presnall *et al.* (1978), and cotectic traces based on 15 kbar point determined by Lindsley and Emslie (1968).

clase, but not enough to account for very plagioclase-rich anorthosites. It should also be noted that entry of iron into the pyroxene would *reduce* the shift in the cotectic. An important principle emerges, nevertheless: a cotectic liquid generated at high pressure will, on rising into the crust and cooling at lower pressure, lie in the plagioclase field. It may crystallize plagioclase for a considerable time before it again reaches saturation with pyroxene. If the plagioclase should be separated mechanically, as by floating (Grout, 1928; Morse, 1968; Kushiro and Fujii, 1977), it could easily form a crystalline mass of anorthosite. Even after saturation is regained, plagioclase should tend to float while pyroxene sinks, and if cooling is slow enough to allow the crystals to move far enough, a bimodal rock suite should result, i.e. anorthosite overlying pyroxenite. Such a process is by no means the whole answer to the anorthosite problem, because there is evidence that very plagioclase-rich magmas existed (Wiebe, 1979), but some means of plagioclase concentration must be assumed for those anorthosites containing only a trace of mafic minerals.

## Forsterite

The melting curve of Fo is linear, within experimental error, to 30 kbar. As shown in Fig. 18.10, the slope is about 4.8°C/kbar. A similar value was deduced by Bowen and Schairer (1935), but is subject to some error, as discussed by Davis and England (1964).

The melting curve for enstatite composition is also shown in Fig. 18.10

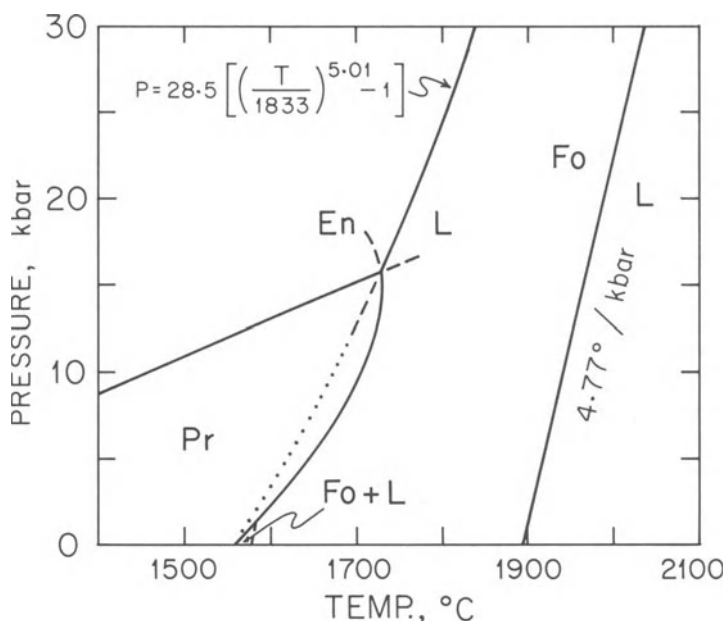


**Figure 18.10.** Melting curves of forsterite (Fo; Davis and England, 1964) and enstatite (Pr, En; Boyd, England, and Davis, 1964; Chen and Presnall, 1975). Fo curve is linear. Simon equation is given for En curve above 15 kbar.

for comparison; this will be discussed later in connection with the system Fo-SiO<sub>2</sub>.

### Forsterite-Diopside-Anorthite

Isobaric sections at 1 atm, 5, 10, and 20 kbar are shown in Fig. 18.11. A corundum + *L* field intrudes near the An corner at about 9 kbar. High pressure enlarges the fields of pyroxene and spinel at the expense of forsterite and anorthite. The 5 kbar section accidentally contains the singular point where all four phases coexist with liquid at 1292°C. The effects of high pressure preclude the coexistence of olivine + plagioclase + liquid if the system composition is rich in Mg and Ca, so allivalites (basic troctolites) must be products of relatively low pressure crystallization.

None of the intersections in Fig. 18.11 are truly isobaric invariant points, but rather piercing points, because of solid solution in pyroxene and consequent non-ternary behavior. Presnall *et al.* (1978) have determined the compositions of the important piercing-point liquids by electron probe analysis. They found that at 1 atm, the liquid at 1270°C (Geophysical Laboratory temperature scale) is *silica poor* relative to the ternary join, so the thermal maximum for the equilibrium *L*(Di, Fo, An) lies on the *silica-*

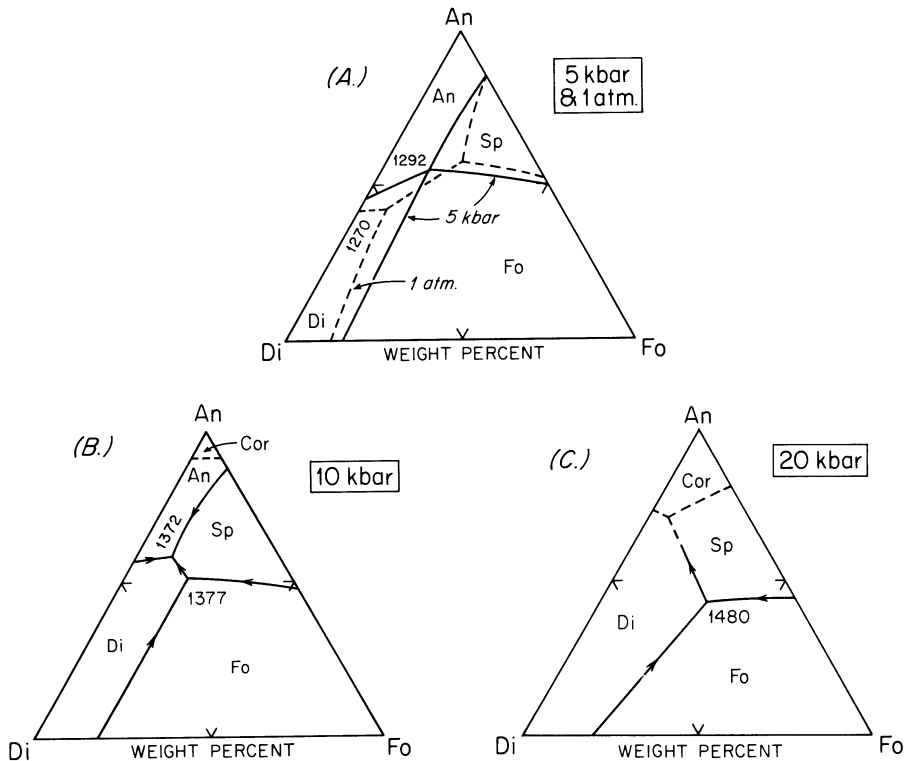


**Figure 18.11.** System Fo-Di-An at 1 atm and 5, 10, and 20 kbar, after Presnall *et al.* (1978). Temperatures are referred to the Geophysical Laboratory temperature scale. Sp = spinel, Cor = corundum.

rich side of the plane. Crystallization of pyroxene tends to drive liquids toward silica undersaturation, and the join Fo-Di-An is not a thermal barrier at 1 atm, although it closely approximates such a barrier. At about 5 kbar, the liquid lies in the ternary join, and at higher pressures it becomes *silica rich* as the fields of Fo and An move apart. Presnall *et al.* (1978), generalizing from the join Fo-Di-An, concluded that a thermal divide between alkali basalt and tholeiite exists to a pressure of about 4 kbar (except that crystallization of spinel would cause alkali basalt to fractionate to tholeiite). At higher pressure, to 12 kbar, they found that alkali basalt could fractionate to olivine tholeiite, but not *vice versa*.

From Fig. 18.11 it will be seen that initial melting reactions at high pressure will involve the production of spinel and a silica-rich liquid. In olivine-rich compositions, anorthite will be excluded from such events by a subsolidus reaction of olivine plus anorthite to pyroxene plus spinel. The beginning of melting for mantle compositions is therefore not usefully shown in the liquidus diagrams.

The point labelled 1377 in the 10 kbar diagram is a reaction point at

which  $Fo + L = Di + Sp$ . The point labelled 1372 is a piercing point where  $Di + Sp + An$  crystallize together from a silica-rich liquid that does not lie in the join.

### Silica

The subsolidus and melting relations of  $SiO_2$  at low pressures are shown in Fig. 18.12. Relations at negative pressures are extrapolated from higher pressures, and correspond to the phenomena that would occur in vacuum at varying degrees of evacuation. A region of gas is shown in the lower right-hand corner of the diagram, indicating that the vapor pressure of silica is very low. This is why we generally refer to silicate systems as condensed systems, because a gas phase of silicate composition never occurs at 1 bar pressure and at ordinary temperatures near the melting point. Every silicate, in principle, has a  $S-L-V$  triple point like that shown for  $Cr + L + Gas$  in the diagram, but at a pressure below that of interest for terrestrial geology.

All the intersections shown in Fig. 18.12 are derived with Schreinemakers' rules.

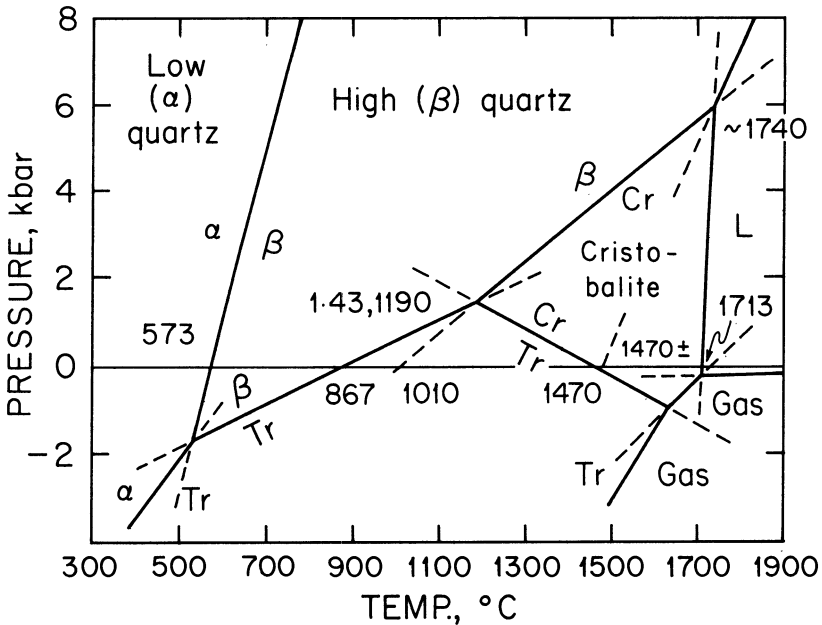


**Figure 18.12.**  $P$ - $T$  relations for the system  $SiO_2$  at low pressure. Relations below zero pressure are extrapolated. Abbreviations: Tr, tridymite; Cr, cristobalite; L, liquid. Data from Yoder (1950), Cohen and Klement (1967), Kracek (1953), Ostrovsky (1967), and Kracek and Clark (1966).

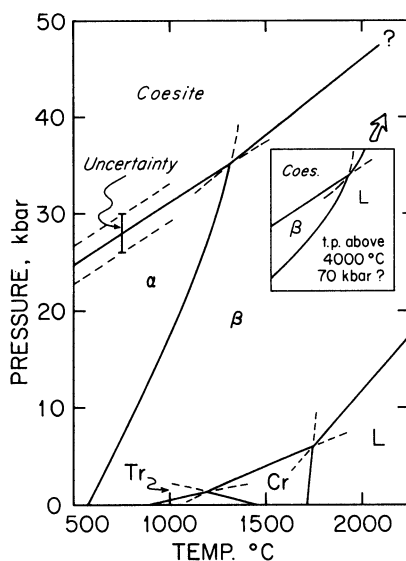


**Figure 18.13.** High pressure  $P$ - $T$  relations in the system  $\text{SiO}_2$ . Data from sources cited from Fig. 18.12;  $\alpha$  quartz-coesite curve from review by Weaver *et al.* (1979). Melting relations are inferred.

The diagram shows that tridymite is unstable above 1.4 kbar and cristobalite is unstable above 6 kbar. High quartz will be the polymorph appearing in most phase diagrams at high pressures.

Figure 18.13 shows the phase diagram over an expanded pressure range, to illustrate the sense of the melting curve and its intersection with the high-pressure polymorph coesite. The melting curve for quartz has not been experimentally determined, but is inferred from the metastable  $Q = L$  melting point obtainable at  $1480^\circ\text{C}$ , 1 atm (J.F. Hays, personal communication, 1979), or  $1470^\circ\text{C}$  as given by Kracek and Clark (1966).

## Forsterite-Silica

Figure 18.10 contained a sneak preview of the enstatite melting curve, and we now examine the relations in more detail with the aid of Figs. 18.14 and 18.15. We seek the pressure at which the melting becomes congruent. The  $T$ - $X$  part of Fig 18.14 shows the 1 atm melting relations of protoenstatite, Pr. The metastable melting point of Pr to  $L$  can be estimated to lie at about  $1560^\circ\text{C}$  at 1 atm. Chen and Presnall (1975) found an initial slope of about  $17^\circ/\text{kbar}$  for the melting reaction  $\text{Pr} = L$ . Assuming this slope to be constant, we can draw the curve  $\text{Pr} = L$  originating at  $1560^\circ\text{C}$  (metastably), as in the  $P$ - $T$  section of Fig. 18.14. The *liquidus* temperature for En composition at 1 atm is  $1577^\circ\text{C}$ , as shown in the left-hand diagram. If we assume that this

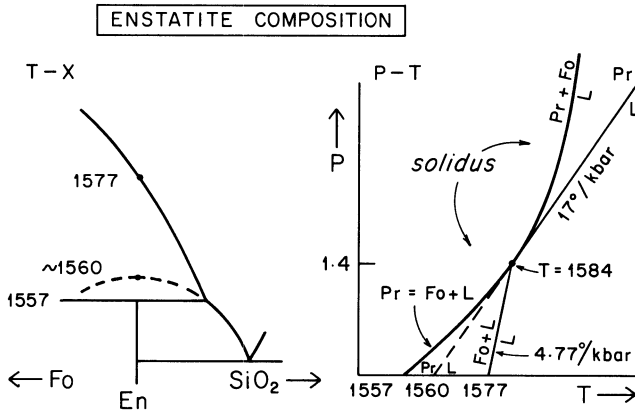


**Figure 18.14.** Melting relations of enstatite composition. Left,  $T-X$  diagram at 1 atm showing metastable melting point of Pr and the liquidus of En composition. Right,  $P-T$  diagram showing a singular point at 1.4 kbar where the continuous equilibrium  $Fo + Pr + L$  touches the curve  $Pr + L$ . See Fig. 18.4 for similar geometry about  $S_{An}$ .

temperature increases with pressure at the same rate as the melting point of Fo,  $4.77^\circ\text{C}/\text{kbar}$ , we obtain an intersection at 1.4 kbar,  $1584^\circ\text{C}$ , as shown in the  $P-T$  section. This intersection must denote the singularity where Pr for the first time melts to a liquid of its own composition. The geometry is essentially the same as previously encountered with anorthite, except that in this case the incongruent melting occurs at low pressure instead of high. The singular point in Fig. 18.14 lies where the continuous equilibrium changes sign from odd to even at the singular point.

Returning briefly to Fig. 18.10, it appears that Boyd, England, and Davis (1964) actually determined the equilibrium  $En = L$  in both its stable and metastable regions (see dotted part of the curve in the figure). The main difference between their work and the later work of Chen and Presnall (1975) was in the much longer run durations used by the latter authors, who confirmed the earlier work at pressures above 15 kbar, but determined the

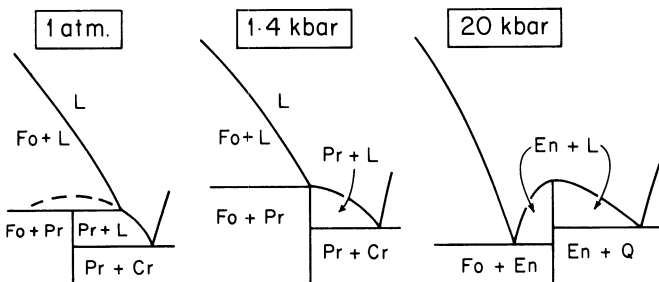


**Figure 18.15.** Isobaric (schematic)  $T-X$  sections showing the change from incongruent to congruent melting of protoenstatite. The  $Pr = En$  curve is shown in Fig. 18.10.

reaction  $Pr = L$  at lower pressures. Chen and Presnall also determined the melting reactions involving quartz and forsterite with  $MgSiO_3$ ; these curves are omitted here for clarity. An interesting feature of Fig. 18.10 is the rather strong curvature of the curve  $Pr = L$  as it approaches the invariant point  $L(Pr, En)$ . The subsolidus reaction  $Pr = En$  generates a *cusp* on the melting curve, a feature we shall encounter repeatedly in other systems. Such cusps are required, in principle, by Schreinemakers' rules. The curvature is a kind of premonitory phenomenon, probably reflecting the reorganization of the melt to a more enstatite-like structure as the pressure is increased. Protoenstatite and liquid must have very similar densities near 15 kbar, where the melting curve is nearly isothermal.

Figure 18.15 shows the  $T$ - $X$  geometry with increasing pressure. Although the En composition is rapidly uncovered with pressure, the shift of the eutectic  $L(Fo, En)$  toward Fo is very small, so that the liquid remains near the En composition even at 20 kbar.

The disappearance of the incongruent melting of enstatite composition at the low pressure of 1.4 kbar means that the reaction relation of olivine to orthopyroxene must be limited to low pressures. Similarly, the crystallization together of olivine and orthopyroxene in sills and layered intrusions can be accounted for by modest pressures (as well as iron content; Chapter 17) during crystallization. However, Presnall *et al.* (1979) show that for liquids approaching basaltic rather than ultramafic composition, the thermal barrier originating at En does not exist at any pressure up to 20 kbar.

The melting curves of enstatite composition with and without  $SiO_2$

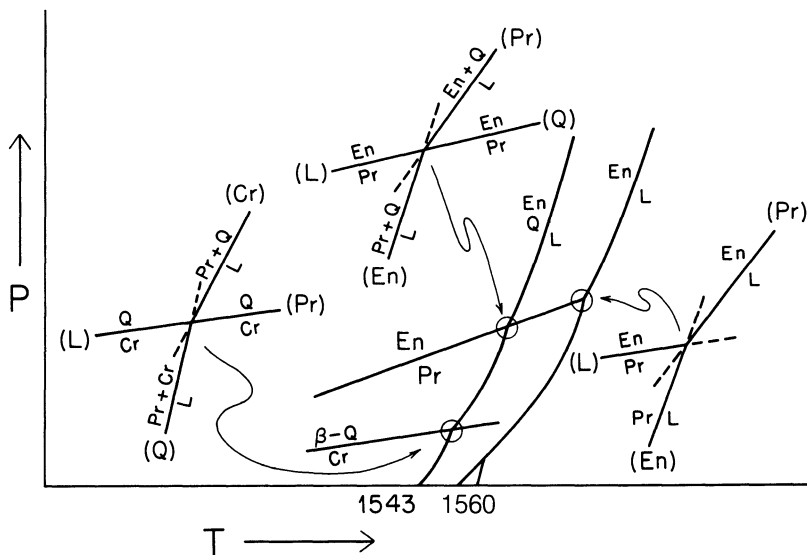


**Figure 18.16.**  $P$ - $T$  diagram showing the geometrical relations along the curves  $En + Q = L$  and  $En = L$  where they are intersected by the phase transformations  $Pr = En$  and  $Cr = \beta$  quartz.

encounter the polymorphic transitions  $Pr = En$  and  $Cr = \beta$  quartz at high pressures. The geometry of these intersections is shown schematically in Fig. 18.16, where it will be seen that cusps are generated on all the melting curves.

### Forsterite-Anorthite-Silica

The system at 10 kbar is shown in Fig. 18.17. As in the system Fo-Di-An, Fo and An are prohibited from coexisting, this time by the coexistence of  $En + Sp$ . This news increases our suspicion that troctolites must crystallize at relatively low pressure, and that plagioclase-bearing facies of the mantle must be restricted to modest pressures.

Forsterite and enstatite crystallize along a cotectic far into the diagram (Fig. 18.17), but their stable association with liquid terminates at the peritectic point T, where the reaction  $Fo + L = En + Sp$  sets in. Point R is a peritectic point involving  $Sp + L = En + An$ . Point E is a simple ternary eutectic in appearance, although the entry of Al into pyroxene at 10 kbar will cause liquid to lie out of the join.

The loss of olivine at point T illustrates the conclusion of Presnall *et al.* (1979) that enstatite cannot generate a thermal barrier for liquids rich enough in plagioclase component to be called basaltic. However, the addition of iron (see Chapter 17) may complicate the issue. It is significant that norites, rocks composed almost solely of plagioclase (about 75%) and orthopyroxene (25%), occur in abundance among anorthositic rocks, and tend to contain very little of either residual quartz or olivine. No phase diagram yet studied at moderate pressure adequately explains the existence

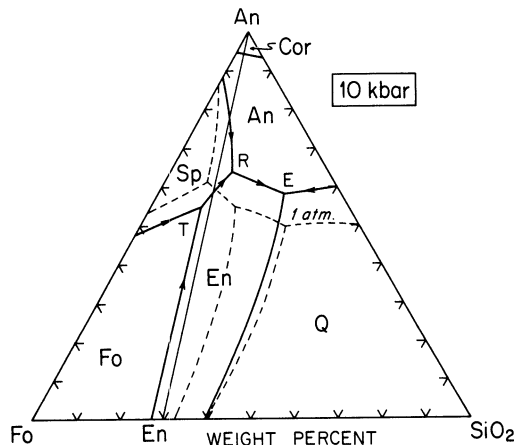


**Figure 18.17.** System Fo-An-SiO<sub>2</sub> at 1 atm and at 10 kbar, after Presnall *et al.* (1979).

of voluminous liquids of norite composition except by accidental restriction to the plagioclase-orthopyroxene join.

### Forsterite-Diopside-Silica

The system at 10 kbar is sketched in Fig. 18.18. The pigeonite field has (probably) disappeared, the pyroxenes are Di-rich and En-rich solid solutions, and Fo and En crystallize together. The pyroxene join forms a thermal barrier shedding liquids to either side. The olivine reaction relation is absent, since liquids in equilibrium with olivine are silica-poor. The first melt of a peridotite will be  $L(\text{Di}, \text{Fo}, \text{En})$ , and if the peridotite is diopside-poor, diopside will be used up first and the liquid will travel along  $L(\text{Fo}, \text{En})$  with further melting.

### Nepheline-Silica

The role of albite as a thermal barrier at 1 atm was stressed in Chapter 14. This barrier disappears at high pressure as albite melts incongruently to  $\text{Jd} + L$ , and eventually becomes metastable altogether relative to  $\text{Jd} + Q$ . The sequence in which this happens is illustrated schematically in Figs. 18.19 and 18.20. Here we find a continuous equilibrium  $\text{Ab} + \text{Jd} + L$  containing *two* singular points representing the degenerate reactions  $\text{Jd} = L$  and  $\text{Ab} = L$ . At relatively lower pressures, jadeite melts incongruently to  $\text{Ab} + L$  ( $P_1$  in Figs. 18.19 and 18.20), and the metastable melting point of  $\text{Jd}$  lies at a

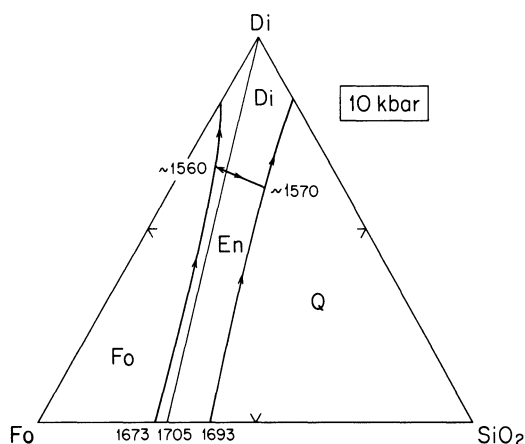


**Figure 18.18.** System  $\text{Fo-Di-SiO}_2$  at 10 kbar, after Kushiro (1969) and Presnall *et al.* (1979).

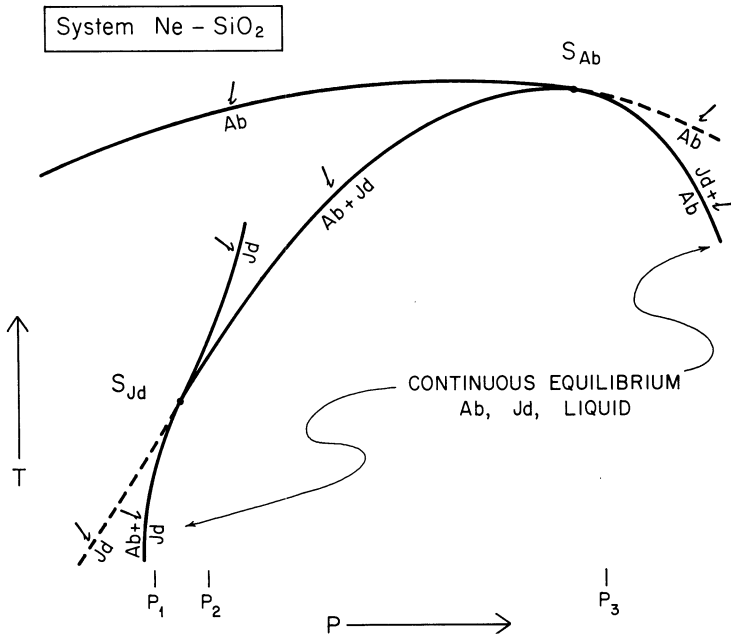


**Figure 18.19.**  $T$ - $P$  relations showing the melting behavior of jadeite (Jd) and albite (Ab) in the system Ne-SiO<sub>2</sub>, after Bell and Roseboom (1969).

higher temperature. As the singular point  $S_{Jd}$ , the liquid composition has backed off exactly to the jadeite composition, and melting can be described completely in terms of the one-component (degenerate) system NaAlSi<sub>2</sub>O<sub>6</sub>. At a slightly higher pressure  $P_2$ , jadeite forms a thermal barrier flanked by two eutectics  $L(Jd, Ne)$  and  $L(Jd, Ab)$ . With further increases in pressure, jadeite becomes stable to higher and higher temperatures, raising its liquidus eventually to reach and then cover the albite composition. At  $S_{Ab}$ , the system is again degenerate (to NaAlSi<sub>3</sub>O<sub>8</sub>) as the liquid reaches albite composition, and just above the pressure of  $S_{Ab}$ , at  $P_3$ , albite melts incongruently to  $Jd + L$ . The geometrical relations of the curves, and the changes of reaction signs from odd to even at the singular points, are in principle the same as with the anorthite diagram, Fig. 18.4, and require no further comment.

Melting and subsolidus relations in Ne-SiO<sub>2</sub> are shown to scale in the  $T$ - $P$  diagram of Fig. 18.21, where the solidus is emphasized for bulk compositions between and including Jd and Ab. The liquidus for Ab has previously been seen in Fig. 18.7. In Fig. 18.21, the two singular points  $S_{Jd}$  and  $S_{Ab}$  are flanked by two truly invariant points,  $I_{Jd}$  and  $I_{Ab}$ . The first of these marks the lowermost  $P$ - $T$  stability of Jd with liquid, and the second marks the upper limit of Ab with liquid.

Proceeding from the left along the solidus, we note that for all bulk compositions slightly less silica-rich than Ab, the melting begins with

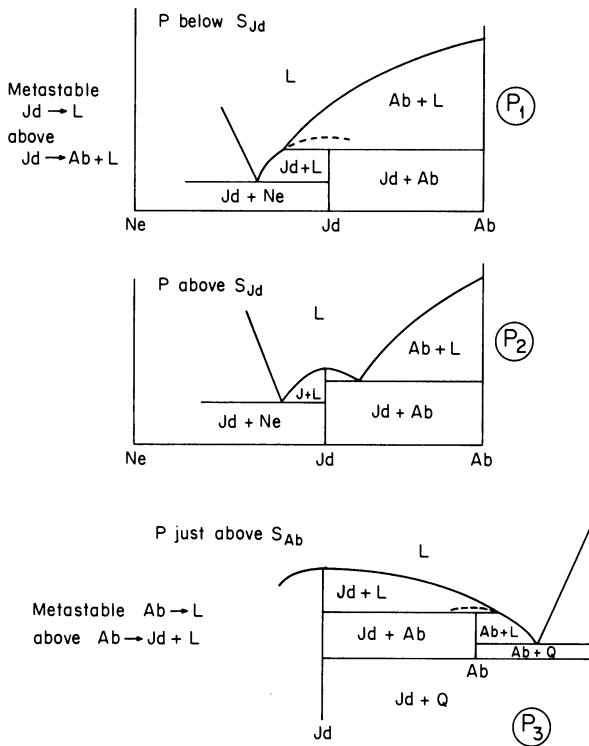
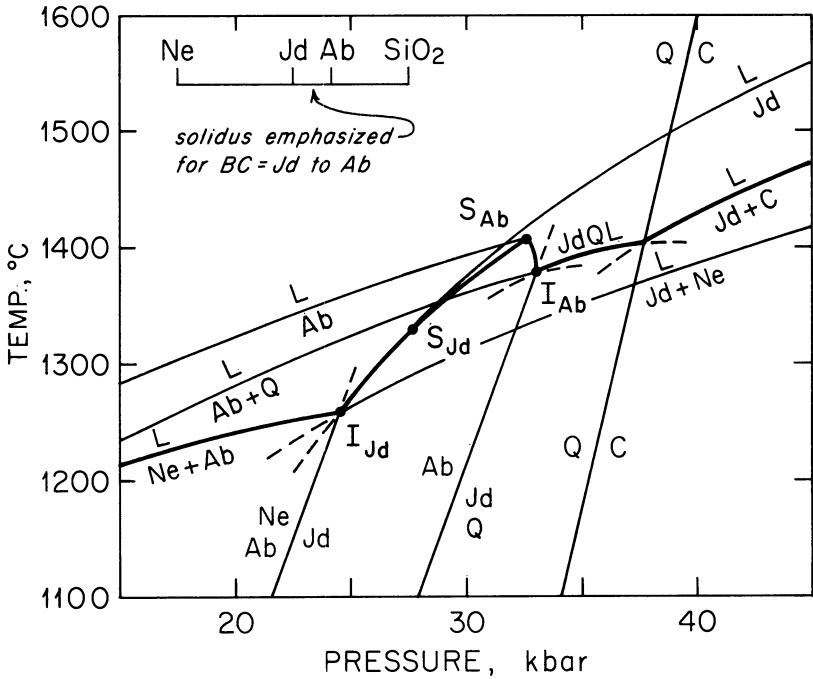


Figure 18.20.  $T$ - $X$  sections at three pressures shown as  $P_1$ - $P_3$  in Fig. 18.19.

production of liquid at the  $L(Ne,Ab)$  eutectic. This eutectic has a smaller slope  $dT_m/dP$  than the  $Ab = L$  curve, and the eutectic reaction terminates at about 24.5 kbar, at  $I_{Jd}$ , where it intersects the subsolidus reaction  $Ne + Ab = Jd$ . This invariant point is generated by the intersection of four univariant curves involving the phases  $Ne$ ,  $Ab$ ,  $Jd$ , and  $L$ . The labels of the curves, proceeding clockwise from the subsolidus reaction, are  $(L)$ ,  $(Jd)$ ,  $(Ne)$ ; see Fig. 18.19), and  $(Ab)$ . The solidus for the complete system  $Ne-SiO_2$  now runs along the  $(Ab)$  curve, the eutectic reaction  $Jd + Ne = L$ , but we are more interested in the restricted, mantle-like compositions between  $Jd$  and  $Ab$ . For these, the solidus is the reaction  $(Ne)$ , namely  $Jd = Ab + L$ ; see Figs. 18.19 and 18.20, section  $P_1$ . This curve has a greater slope than the curve  $Ab = L$ .

We now pause to note a very important feature of the melting curves around  $I_{Jd}$ . The  $T$ - $P$  slope of the solidus changes dramatically when a new phase appears, and the solidus forms a *cusp* at  $I_{Jd}$  (and at  $I_{Ab}$ , and at the point defined by the equilibrium  $Jd + Q + C + L$ ). If we imagine a mantle composed of  $Jd + Ab$ , and slowly raise a geotherm, having a slope like  $Ab = L$ , through the subsolidus region, it will first touch the solidus at  $I_{Jd}$ . The solid assemblage will now begin to melt to a liquid poorer in silica than the



**Figure 18.21.** Scale-true  $T$ - $P$  diagram showing high pressure reactions and melting relations in the system Ne-SiO<sub>2</sub>, after Bell and Roseboom (1969) Singular points  $S$  are shown in Fig. 18.19. Invariant points are labelled  $I$ .  $C$  = coesite. The solidus for composition from Jd to Ab is shown as a heavy line (after Presnall, *et al.*, 1979).

Jd composition, hence an alkalic liquid ( $P_1$  in Fig. 18.20). The melting process will absorb calories and may stabilize our rising geotherm to a fixed position. However, if the temperature continues to rise, the liquid composition will change *away* from Ne in either of two ways. First, suppose that jadeite is completely used up (see  $P_1$  in Fig. 18.20); then the liquid produced on further melting will move toward Ab by simple *dilution*. Second, suppose that Jd persists as a solid phase. Then, according to  $P_2$  in Fig. 18.20, the stable liquid composition will migrate through  $S_{Jd}$  to a eutectic composition between Jd and Ab, and this composition will continue to migrate toward (and beyond) Ab with rising  $T$  and  $P$ .

Although our assumed mantle composition is slightly ridiculous, the principles mentioned in the above paragraph are quite appropriate to the real earth, and are very important. The first principle, discussed in detail by Presnall *et al.* (1979), is that a cusp on a solidus should tend to lock or stabilize a geotherm, acting as a *thermal buffer*. We return to this principle in a more appropriate context in Chapter 20. The second principle is that *first melts* may tend to be *alkalic*, but as the proportion of melt increases, they become less alkalic and more silicic. Countless observations and

deductions support this principle. Among these are experimental determinations of liquid compositions produced at high pressure from natural and synthetic peridotites (e.g. Mysen and Kushiro, 1977), the abundant theoretical and empirical evidence that "large ion lithophile" (LIL) elements, including alkalis, are happier in silicate melts than in coexisting mantle-type minerals, and geochemical observations on natural lavas, combined with theory (e.g. Gast, 1968). We shall see other examples of this principle, again in a more appropriate context, in Chapter 20.

The remaining features of the heavy solidus in Fig. 18.21 can readily be followed by reference to the preceding figure for details. The negative melting slope of the reaction  $Ab = Jd + L$  is an interesting curiosity; it arises from the fact that the assemblage  $Jd + L$  is denser than  $Ab$ , because  $Jd$  is so very much denser than  $Ab$ .

## Kalsilite-Silica

The high-pressure melting behavior of sanidine composition,  $KAlSi_3O_8$ , is shown in Fig. 18.22. High pressure reduces the stability of the open framework silicate leucite ( $Lc$ ), and at a pressure of around 19 kbar, sanidine begins to melt congruently. The curve  $San = L$  is continuous through the singular point  $S_1$ , and its metastable (low pressure) segment runs to the metastable melting point at  $1200^\circ\text{C}$ , 1 atm, given by Waldbaum and Thompson (1969). The complete geometry of the melting relations is

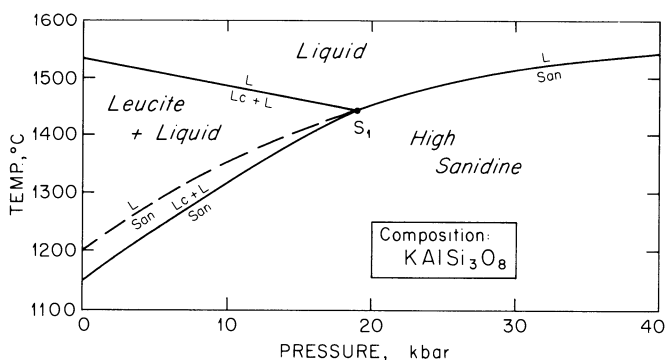


**Figure 18.22.** Melting relations of the composition  $KAlSi_3O_8$ , after Lindsley (1966a). Metastable 1-atm termination of  $San = L$  is from Waldbaum and Thompson (1969). Other 1-atm relations from Schairer and Bowen (1955). The curve  $Lc + L = L$  is univariant by restriction to composition  $KAlSi_3O_8$ . The other curves are univariant in the system  $Ks-SiO_2$ .  $S_1$  is a singular point shown also in the next figure.

shown schematically in Fig. 18.23. The figure is distorted for clarity; in reality,  $S_1$  lies at a higher temperature than  $S_2$ . The correct locations are  $S_1$ , 19.5 kbar, 1440°C;  $S_2$ , 28 kbar, 1415°C; and  $I$ , 30 kbar, 1400°C, as shown by Lindsley (1966a). The geometry of the singular points and the invariant point can be understood by reference to previous examples of the type, and to Fig. 18.23. It should be noted that the curve  $Lc + L = L$  in Fig. 18.22 is simply the liquidus for the restricted composition  $KAlSi_3O_8$ , and is not a true univariant curve in the binary system.

From the isobaric  $T-X$  sketches in Fig. 18.23, it may appear that the previously announced important principle about the alkalic nature of first melts is violated. Indeed it would be if the earth were rich in potassium relative to sodium, but it is not. The first liquid obtained on melting sanidine is silica rich, and only the higher pressure liquids are alkalic and silica undersaturated. But the opposite effect found in  $Ne-SiO_2$  dominates in nature because Na is more abundant than K in the earth. The case might be otherwise on another planet.

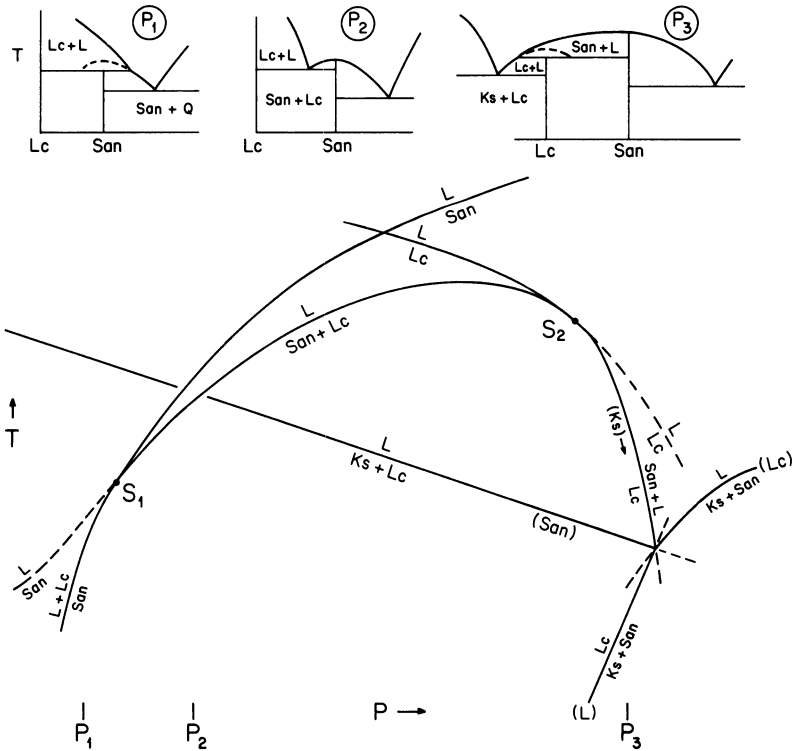


**Figure 18.23.** Distorted, schematic  $T-P$  diagram showing the continuous equilibrium  $San + Lc + L$  and the two singular points lying on it.  $T-X$  diagrams at top show isobaric relations at three selected pressures. After Lindsley (1966a).

## Alkali Feldspar

The initial melting slope for Ab is about  $14^\circ/\text{kbar}$  (Fig. 18.7) and the corresponding metastable slope for Or is about  $18^\circ/\text{kbar}$  (Fig. 18.22). The average slopes to 20 kbar are about  $10.4$  and  $12.8^\circ/\text{kbar}$ , respectively. Since  $\text{San} = L$  moves faster than  $\text{Ab} = L$ , the minimum composition in the alkali feldspar system should move somewhat toward Ab with pressure. The minimum lies near  $1/3$  Or,  $2/3$  Ab, so the rise in the minimum temperature should be something like  $1/3(12.8) + 2/3(10.4) = 11.2^\circ/\text{kbar}$ . The calculated minimum temperature at 20 kbar would thus be  $1063 + 224 = 1287^\circ\text{C}$ . At this pressure, no leucite field would be present, and the melting diagram would be of the simple minimum type terminating at  $\text{Ab} = L$ ,  $1325^\circ\text{C}$  and  $\text{San} = L$ ,  $1455^\circ\text{C}$ .

The alkali feldspar solvus also rises with pressure, at a rate variously estimated at  $13\text{--}20^\circ\text{C}/\text{kbar}$ . Assuming that the solvus crest (critical temperature,  $T_c$ ) lies at about  $650^\circ\text{C}$  at 1 atm., and assuming the largest value of  $dT_c/dP$ , the solvus and the solidus would intersect only somewhere near 60 kbar, where we know that Ab is grossly unstable relative to  $\text{Jd} + \text{Q}$ , so there is no prospect that two alkali feldspars will crystallize directly from the melt at any pressure in the system Ab-Or. There is therefore no need to draw the alkali feldspar diagram at 20 kbar: if we did, it would look essentially like Fig. 15-26 after removal of the leucite field and some adjustment of the temperatures and the minimum composition.

## Fayalite, and Olivine Solutions

The melting curve of fayalite has an initial slope of about  $8^\circ/\text{kbar}$ . The curve shown in Fig. 18.24 is a hand-calculated solution to the Simon equation using the combined data of Lindsley (1966b) and Akimoto, Komada, and Kushiro (1967). The position of the high pressure phase transformation to the spinel structure of  $\text{Fe}_2\text{SiO}_4$  is taken from the latter authors. Note the characteristic cusp in the melting curve where it is intersected by the polymorphic transition.

From the melting curves for forsterite and fayalite, and the assumption that little change occurs in the form of the melting loop at high pressures up to 50 kbar, the approximate form of the olivine diagram can be sketched as in Fig. 18.25. The melting points for the end members are indicated at 10 kbar intervals. Melting loops are sketched for 1 atm, 20 kbar, and 50 kbar. At 20 kbar, a liquid of composition  $\text{Fo}_{50}$  would be in equilibrium with crystals of composition  $\text{Fo}_{82}$  in weight percent. The equivalent mole percent values are  $\text{Fo}_{59}$  and  $\text{Fo}_{87}$ , and these are reasonably similar to typical values for basaltic liquids and peridotite, respectively.

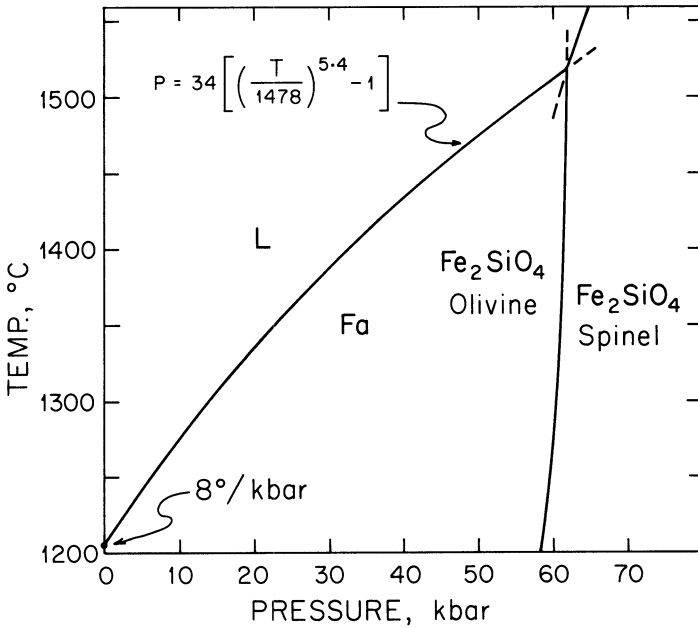


**Figure 18.24.** High pressure melting and breakdown relations of fayalite (Fa), after Lindsley (1966b) and Akimoto, Komada, and Kushiro (1967). The Simon equation represents an approximate fit to both sets of data, and differs slightly from that given by Akimoto *et al.*

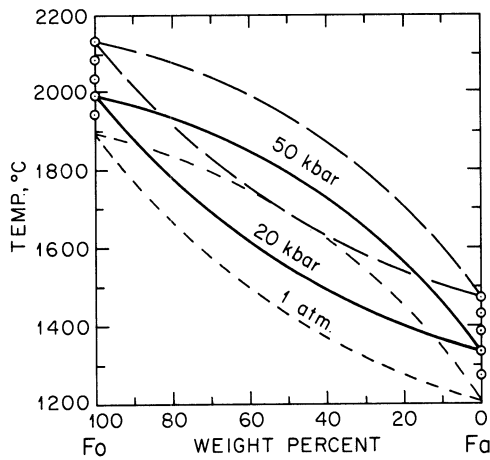


**Figure 18.25.** Approximate high pressure melting loops for olivine, compared with 1 atm diagram. Deduced from Figs. 18.10 for Fo and 18.25 for Fa. End member melting points are plotted for each 10 kbar to 50 kbar.

**Fe-SiO<sub>2</sub>-O**

Pressure stabilizes the pyroxene ferrosilite, FeSiO<sub>3</sub>, relative to Fa + Q, and the resulting  $P$ - $T$ - $f_{O_2}$  relations have been thoroughly expounded by Lindsley, Speidel, and Nafziger (1968). The present treatment takes up where we left off in Chapter 16. We omit all equilibria involving wüstite, and focus at first on equilibria among olivine, silica, liquid, magnetite, and iron. In Fig. 16.20, the 1-atm (isobaric) invariant point *osml* lies at higher  $f_{O_2}$  and lower  $T$  than the invariant point *osil*. These isobaric invariant points are univariant curves when the pressure restriction is removed, i.e. when  $W_p = 0$ ,  $W = 1$ . We can speak of a two-dimensional, 3-coordinate intensive variable space such as  $P$ - $T$ - $f_{O_2}$  space. The isobaric 1-atm diagram (Fig. 16.20) is a section through that space, normal to the pressure axis, at 1 atm. We now wish to turn around and look at the  $P$ - $T$  relationships, but it would not be useful to take a constant  $-f_{O_2}$  section through the  $P$ - $T$ - $f_{O_2}$  space, because arbitrary restriction to a constant  $f_{O_2}$  is neither experimentally convenient nor conceptually informative. Instead, we shall use a projection parallel to the  $f_{O_2}$  axis onto the  $T$ - $P$  plane. Such a projection preserves all of the geometrical properties of the curves and invariant points, and we only need to remember that any given equilibrium represents a variety of  $f_{O_2}$  values along its curve, i.e.  $f_{O_2}$  is variable and unspecified in the diagram. Fig. 18.26 is such a  $T$ - $P$  projection along the  $f_{O_2}$  axis.

In the figure, we see at the left two pyroxene-absent curves labelled (*p*). The high-temperature curve is the equilibrium *osil*, now univariant in  $T$ - $P$  projection. The low-temperature curve is the equilibrium *osml*. Both curves originate at the corresponding 1-atm points in Fig. 16.20 (but of course the equilibria pass continuously through the 1-atm points to conditions of vacuum, so they do not cease to exist at pressures below 1 atm). The pyroxene-absent equilibria encounter the pyroxene-forming reaction  $o + s = p$  shown in the figure by a straight line. The intersections so formed generate two truly invariant points, *ospil* and *ospml*. The sequence of curves around each of these points is obtainable from Schreinemakers' rules (or Richardson's rule) with the help of the chemographic diagrams. Samples of the compatibility diagrams are shown in the figure.

Because pyroxene lies on the line  $o$ - $s$ , the reaction  $o + s = p$  is degenerate and is truly univariant even though only three phases suffice to define the reaction. The assemblage *osp* itself does not begin to melt at 17 kbar, 1205°C (at *ospml*), but liquid is generated there in the presence of magnetite. Just above *ospml*, the equilibrium *osp* is the magnetite-absent reaction (*m*). The reaction then becomes both (*i*) and (*l*) near the invariant point *ospil*. The *osp* equilibrium is metastable above this invariant point, because now the tie line iron + liquid cuts the line olivine + pyroxene. The point *ospil* therefore represents the maximum stability of fayalite plus ferrosilite at any  $f_{O_2}$ . Curve *osp* represents the minimum stability of ferrosilite and the maximum stability of fayalite + quartz. The high pressures encountered

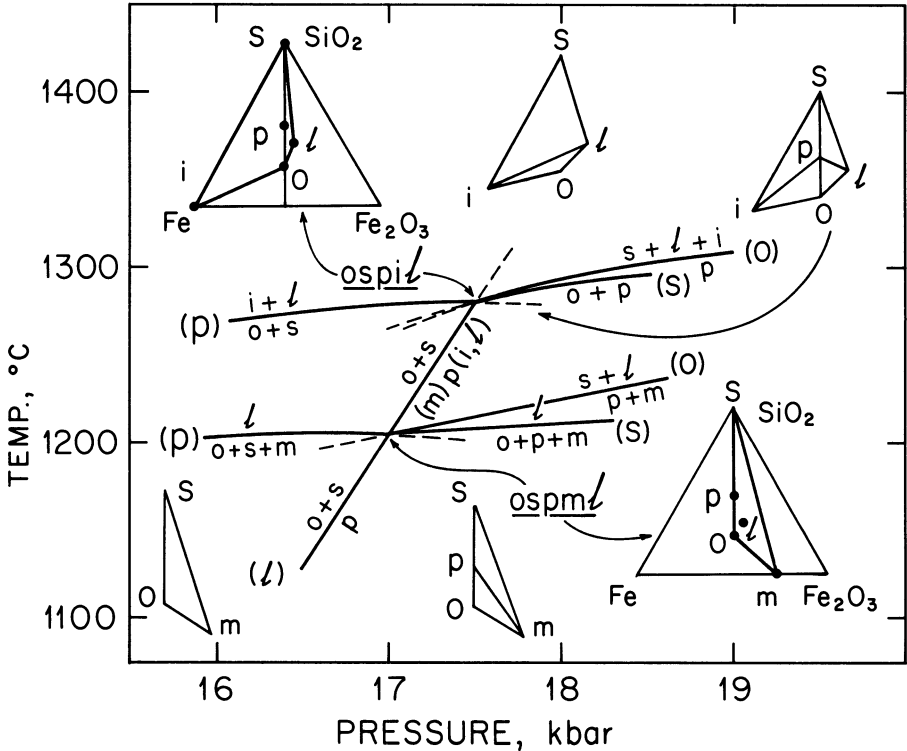


**Figure 18.26.** *T-P* projection for the system Fe-SiO<sub>2</sub>-O, after Lindsley, Speidel, and Nafziger (1968). Abbreviations as in Chapter 16 except for *p* = pyroxene, FeSiO<sub>3</sub>. Relations involving wüstite are omitted.

along this curve make it fairly obvious why fayalite + quartz are found in granites, but pure ferrosilite is not. As we shall see, however, addition of Mg changes the story.

We now return to *f*<sub>O<sub>2</sub></sub> - *T* space to recover a picture analogous to Fig. 16.20. But now we shall again *project* the equilibria, this time along the pressure axis onto the *f*<sub>O<sub>2</sub></sub> - *T* plane. In this way we shall be able to look at *f*<sub>O<sub>2</sub></sub> - *T* relations in complete detail, without concern for the pressure at which they occur. Fig. 18.27 is such a projection. The same two invariant points occur in this projection as in the *T - P* projection, and their arrangement is not unlike that of the points *osml* and *osil* in Fig. 16.20. Indeed, the equilibria (*p*) lead directly to the 1-atm invariant points and these are shown by dots in the figure. The curves are extended beyond the dots for convenience in labelling, and this means that parts of the curves (*p*) refer to pressures less than 1 atm.

The curves (*o*) and (*s*) in Fig. 18.27 have been corrected from those in the original paper, thanks to a timely communication (1979) from D.H. Lindsley.

The liquid-absent (*l*) curves in Fig. 18.27 separate the regions where  $p + m$  or  $s + i$  are stable relative to olivine. Connecting these two subsolidus curves is a ruled surface labelled *osp*. This surface is the locus of the reaction  $o + s = p$ , and it is everywhere rigorously parallel to the  $f_{O_2}$  axis. This means that the reaction  $o + s = p$  is independent of  $f_{O_2}$ . The surface is inclined to the pressure axis, and each ruling represents the trace of an isobaric plane intersecting the ruled surface. The trace of the ruled surface is shown in  $T$ - $P$  space by the curve *osp* in Fig. 18.26. Several isobars, including the 17 kbar isobar intersecting *ospml*, are labelled on the ruled surface in Fig. 18.27. We can make use of the labelled isobars to show examples of isobaric  $T$ - $f_{O_2}$  sections through  $P$ - $T$ - $f_{O_2}$  space, as shown in Fig. 18.28.

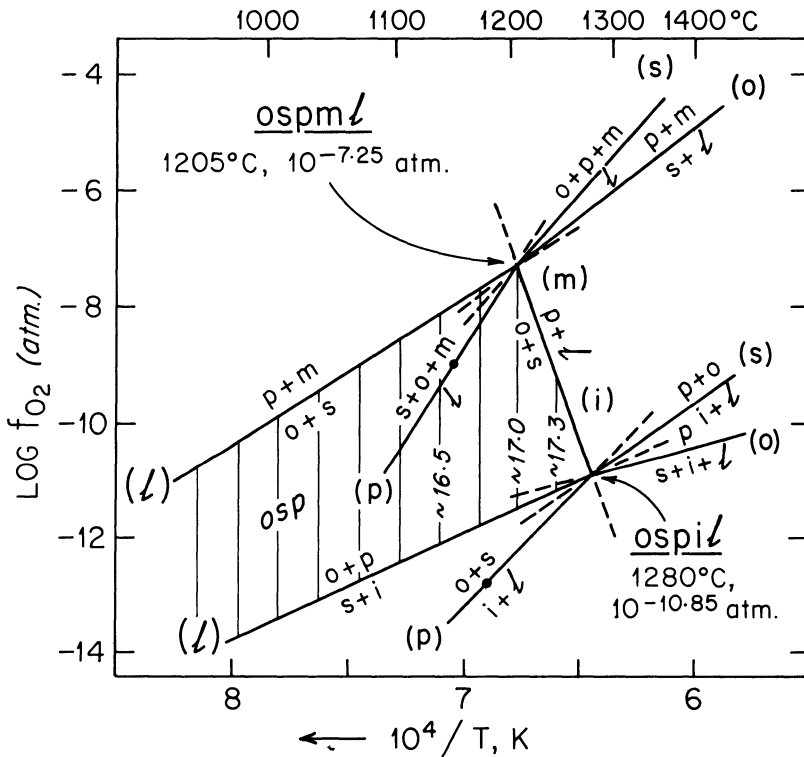


**Figure 18.27.** Projection of part of the system Fe-SiO<sub>2</sub>-O parallel to the pressure axis onto the  $T$ - $f_{O_2}$  plane, after Lindsley, Speidel, and Nafziger (1968). The ruled surface labelled *osp* is a divariant surface rigorously parallel to the  $f_{O_2}$  axis but varying in pressure; each ruling represents the intersection of an isobaric plane with the surface *osp* in  $P$ - $T$ - $f_{O_2}$  space. Several isobars are labelled with pressures corresponding to the isobaric sections shown in the next figure. Abbreviations as in the previous figure. Symbols in parentheses denote the missing phase of a truly univariant assemblage. Dots on curves *osml* and *osil* show the location of the 1-atm isobar on those curves.

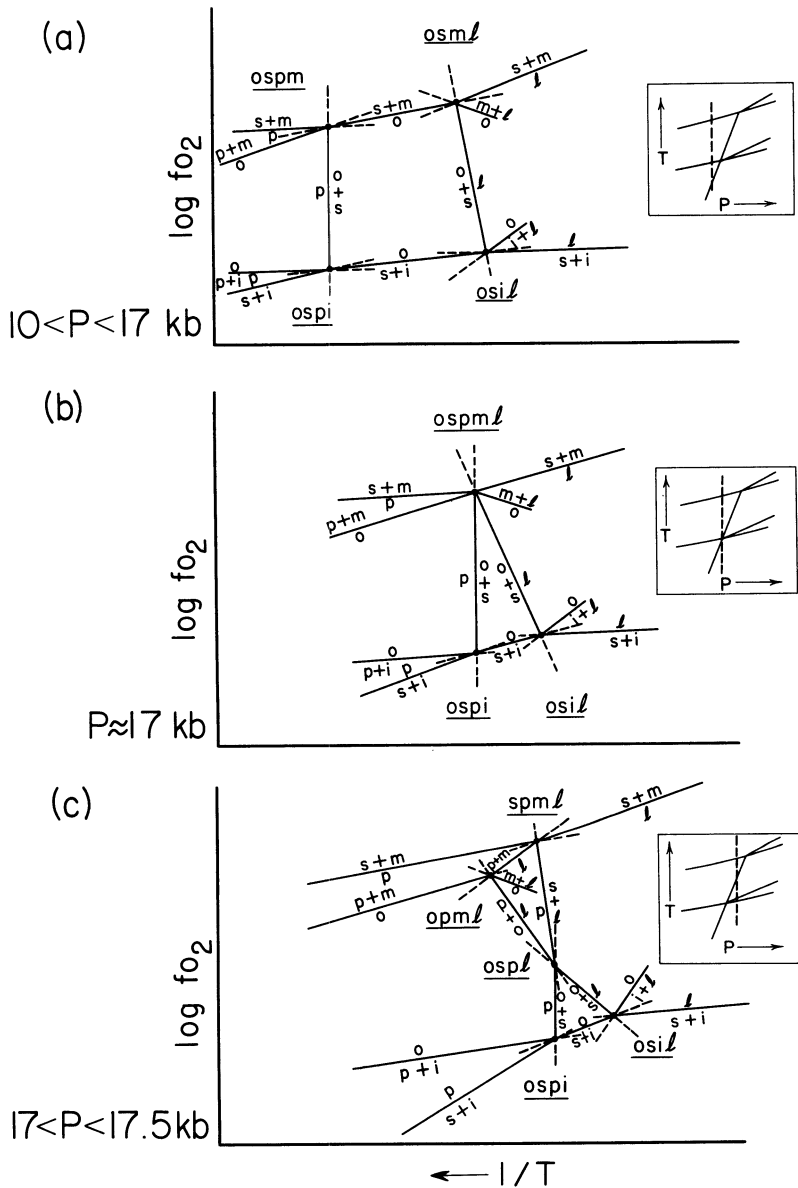


**Figure 18.28.** Schematic isobaric sections through  $P$ - $T$ - $f_{\text{O}_2}$  space for the system  $\text{Fe-SiO}_2\text{-O}$  at several high pressures. Insets show where each section is taken relative to the  $P$ - $T$  projection in Fig. 18.26. The singular points  $S_1$  and  $S_m$  are omitted; they would appear on the curves  $o\ i\ l$  and  $o\ m\ l$ , and would be connected by the curve  $o = l$  (see Fig. 16.20). **A.** Section at about 16.5 kbar. Points  $o\ s\ m\ l$  and  $o\ s\ i\ l$  are present at 1 atm. Points  $o\ s\ p\ m$  and  $o\ s\ p\ i$  reflect the stability of ferrosilite at high pressures. The curve  $o\ s\ p$  is rigorously parallel to the  $f_{\text{O}_2}$  axis and is equivalent to the 16.5 kbar isobaric ruling in Fig. 18.28. Points  $o\ s\ p\ m$  and  $o\ s\ p\ i$  reflect the intersections of curve  $o\ s\ p$  (Figure 18.27) at two different values of  $f_{\text{O}_2}$ . **B.** Section at about 17 kbar, the pressure of the invariant point  $o\ s\ p\ m\ l$ . **C.** Section at about 17.3 kbar.

From Lindsley, Speidel, and Nafziger (1968), reproduced by permission.

Diagram A of Fig. 18.28 illustrates the isobaric  $T$ - $f_{\text{O}_2}$  relations at 16.5 kbar, and is valid in principle for any pressure in the range 10-17 kbar. The  $osp$  curve, rigorously parallel to the  $f_{\text{O}_2}$  axis, is the 16.5 isobar in Fig. 18.27. Pyroxene is stable on the low-temperature side, and fayalite + quartz on the high-temperature side of the curve. The reaction is isobarically univariant because of degeneracy. It terminates at the isobaric invariant points  $ospm$  and  $ospi$ , (univariant lines in Fig. 18.27), where it intersects the curves  $o = s+m$  and  $o = s+i$  inherited from the 1-atm diagram, Fig. 16.20. New equilibria involving pyroxene are generated at the low  $-T$  sides of the invariant points. At the hi- $T$  sides, the curves  $osm$  and  $osi$  terminate in the familiar invariant points  $osml$  and  $osil$ , which have the same surrounding geometry as in Fig. 16.20. The singular points and the curve  $o = l$ , as well as all wüstite equilibria, are omitted from Fig. 18.28, but can be seen in Fig. 16.20.

As the pressure rises from 16.5 kbar, the reaction  $o+s = p$  moves to higher temperatures, rapidly compared to the melting reactions involving  $o+s$ ; see Fig. 18.26. Thus at 17 kbar, the curve  $osp$  has reduced the curve  $osm$  to a point, and intersected  $osml$  to form the truly invariant point  $ospml$  (Fig. 18.28b). This point, in the isobaric section, has "too many" (6) curves emanating from it, because these curves are really isobaric sections through divariant surfaces in  $P$ - $T$ - $f_{\text{O}_2}$  space. There could conceivably be as many as 10 such curves representing the 10 divariant surfaces  $pml$ ,  $sml$ ,  $spl$ ,  $spm$ ,  $oml$ ,  $opl$ ,  $opm$ ,  $osl$ ,  $osm$ , and  $osp$ . However, if both the limiting curves of a divariant surface lie at lower or higher pressure than the isobaric section, that surface will not cut the section and will not appear as a line. In the present case, six divariant surfaces have limiting curves that straddle the pressure 17 kbar, so six curves appear. Curves  $osm$  (at lower  $P$ ) and  $spl$ ,  $opl$ ,  $pml$  (at higher  $P$ ) do not appear in the section. The sequence of curves about the truly invariant point  $ospml$  in such an "accidental" isobaric section cutting the point cannot be determined directly by Schreinemakers' rules, but can be deduced, as done here, by merging the isobaric invariant points, each carrying its own configuration, into the truly invariant point. This discussion is amplified in somewhat more detail by Lindsley, Speidel, and Nafziger (1968).

As the pressure rises above 17 kbar, curve  $osp$  moves through the truly invariant point and begins to cut the curve  $osl$ , thus generating the isobaric invariant point  $ospl$ , Fig. 18.28c. Two other new isobaric invariant points also appear,  $opml$  and  $spml$ ; these are points on the univariant curves of the same names in Fig. 18.26, the  $T$ - $P$  projection. The geometry of all these new points is straightforward and can be derived, using care, from the usual rules.

With further rise in pressure, the  $osp$  curve intersects the other truly invariant point,  $ospi$  and eventually passes through it. This process eliminates the equilibrium  $osi$  from the isobaric sections, and produces instead a new equilibrium,  $psi$ , and two new isobaric invariant points,  $opil$  and  $spil$ .

Such isobaric sections are omitted from this book, but the reader may care to try his luck with them (taken at 17.5 kbar and a higher pressure) as a useful exercise. Those who do so may be rewarded by seeing the original versions, for comparison, in Lindsley, Speidel, and Nafziger (1968).

It may be noted in Fig. 18.28c that ferrosilite melts incongruently to quartz plus liquid (curve *psl*).

## MgO-FeO-SiO<sub>2</sub>

We will not explore this system in any detail at high pressures; an exposition is given by Speidel and Nafziger (1968), and it contains quantitative information on the compositions of coexisting olivine and pyroxene as a function of  $P$ ,  $T$ , and  $f_{O_2}$ . Oxidation drives both mineral compositions toward Mg, as Fe is used up as ferric iron in oxide minerals or liquid.

A few general remarks are pertinent. It may not have escaped the reader's notice that the invariant points *ospil* and *ospml* in Figs. 18.26 and 18.27 have identical counterparts at 1 atm in the system MgO-FeO-Fe<sub>2</sub>O<sub>3</sub>-SiO<sub>2</sub>, where they are named with capital letters (OSPIL and OSPML in Fig. 17.4). They are, of course, the same equilibria. As Mg is added to Fe-SiO<sub>2</sub>-O, the pressure required to stabilize pyroxene decreases, until it reaches 1 atm for pyroxene compositions near En<sub>15</sub>Fs<sub>85</sub>. The composition of pyroxene in equilibrium with olivine and silica is therefore a sensitive indicator of pressure in some crustal rocks. Wheeler (1965) recognized the breakdown of iron-rich orthopyroxene to olivine plus quartz in a Labrador adamellite, and Smith (1971) studied the reaction experimentally. Berg (1977) made use of this and similar assemblages in metamorphosed iron formation to estimate pressures in the contact metamorphic aureole of the anorthositic Nain Complex, Labrador.

## Summary

We have now ripped through the essential features of our earlier 1-atm phase diagrams at high pressures, omitting petrogeny's residua system and ternary feldspars. The main messages of high pressure are contained in the generally positive melting slopes, the frequent appearance of singular points as liquid compositions move past crystal compositions, the occurrence of cusps where solidi intersect solid reactions, and the geometrical analysis of reactions in intensive-variable space. Many phase diagrams are incompletely known at high pressure, but are sufficiently known for estimating behavior in the mantle to a first approximation. Our information on

temperatures is incomplete, but is gradually being improved by the many experimental studies recently made on selected compositions approaching natural peridotite.

The analysis of crystallization and melting paths proceeds at a given high pressure just as it does in isobaric diagrams at 1 atm, so it has not been discussed here. Further discussion of the implications of high pressure for basalt genesis will be undertaken in Chapter 20.

## Chapter 19

# Effects of Volatiles at High Pressure

### Introduction

Melting temperatures are lowered dramatically when  $\text{H}_2\text{O}$  is added under pressure to a system of anhydrous silicate crystals. This is because a silicate melt can readily dissolve  $\text{H}_2\text{O}$ , thereby reducing the volume of  $\text{H}_2\text{O}$  from that occupied by a gas to that occupied by a liquid. The silicate crystals can dissolve only minute amounts of  $\text{H}_2\text{O}$ . A system composed of an anhydrous phase plus  $\text{H}_2\text{O}$  gas has a large volume just below the melting point, and the formation of hydrous melt will lead to a smaller volume above the melting point, so high pressure favors the formation of melt.

At low to moderate pressures, carbon dioxide is much less soluble in silicate melts than  $\text{H}_2\text{O}$ , so it has a less pronounced effect on the lowering of melting temperatures.

Water and carbon dioxide are the chief volatiles of interest for the earth's mantle. Both are observed in substantial amounts in volcanic eruptions, but this cannot be taken as evidence that they originate with the magma, because the isotopic ratios of H, C, and O show that most of the volatiles come from meteoric (recycled) waters. The search for juvenile water, long frustrated by this overwhelming flux of meteoric water, has now been rewarded by recognition of the  $^3\text{He}/^4\text{He}$  ratio as the important tracer. This ratio can demonstrate the existence of unrecycled mantle water in volcanic emanations. But the primary evidence for water in the mantle comes from phenocrysts of the hydrous mineral phlogopite in kimberlites, and from primary hydrous amphibole in mantle xenoliths (although both these minerals probably contain a large oxy-component rather than their full comple-

ment of hydroxyl). Similarly, the primary (and impressive) evidence for  $\text{CO}_2$  in the mantle comes from the carbonate-rich composition of kimberlites. The composition of fluid inclusions in mantle minerals also shows the existence of  $\text{H}_2\text{O}$  and  $\text{CO}_2$ . Whether these are important components in the genesis of basalt magma depends on their concentration. They are important if present in sufficient amounts, as for example in subduction zones. Moreover, the presence of the hydrosphere and atmosphere require degassing of the planet through time, so the effect of volatiles in magmas plays an important role in planetary evolution.

If water is added to albite and the system heated at 1 atm, the water will soon turn to steam and escape, so no effect will be noted in the melting relations. In order for water or any volatile to have an observable effect on melting, the experimental system must be closed, and pressure must be applied to prevent the escape of steam. If albite plus 1%  $\text{H}_2\text{O}$  are contained at a pressure of 5 kbar at, say,  $500^\circ\text{C}$ , the system consists of crystals plus supercritical gas, and it is common parlance to say that the water pressure equals the total pressure ( $P_{\text{H}_2\text{O}} = P_{\text{T}}$ ), because the gas always fills the container and therefore bears the load, hydrostatically, with the crystals. Purists regularly and insistently decry the term "water pressure" or " $P_{\text{H}_2\text{O}}$ " in such cases, and they are, of course, right to do so, because the gas at these conditions is no longer composed of  $\text{H}_2\text{O}$  only, but is a solution of  $\text{H}_2\text{O}$  and some of the silicate material (mostly silica, as it turns out). Therefore the pressure is sustained not by pure  $\text{H}_2\text{O}$  gas but by an  $\text{H}_2\text{O}$ -silicate gaseous solution. If this is so, the partial pressure of the  $\text{H}_2\text{O}$  part of the gas is less than the total pressure, the rest being made up by the silicate component of the gas.

Numerous dodges have been resorted to in the interests of accuracy and clarity when talking about hydrous systems with a gas phase under pressure. Perhaps the best is to use the term "steam" and "steam pressure", for nobody knows or cares what steam is composed of, and in this way we tell no lies. Another helpful device is to use  $P_{\text{aq}}$ , meaning "the pressure of an aqueous fluid", likewise a guiltless phrase. The most common dodge, in some ways the most appealing, goes something like this: purists are tedious people, and everybody knows very well that the stuff is a complex solution, so let's just call it water pressure and assume that everybody will read this as a euphemism for whatever it really is.

Returning to the albite with 1%  $\text{H}_2\text{O}$ , if we now take the system to  $800^\circ\text{C}$  at 5 kbar, it will consist of a single phase, melt. The melt will consist of 99%  $\text{NaAlSi}_3\text{O}_8$  and 1%  $\text{H}_2\text{O}$  (as components, not as molecular species) in solution. Now no aqueous gas phase exists to bear the pressure load, so purists and dodgers alike are sure that the partial pressure of water vapor is less than the total pressure, i.e.  $P_{\text{H}_2\text{O}} < P_{\text{T}}$ . The criterion of *vapor* (gas) *saturation* is of crucial interest in petrology, and in common parlance, saturation is meant by the notation  $P_{\text{H}_2\text{O}} = P_{\text{T}}$  and undersaturation is meant  $P_{\text{H}_2\text{O}} < P_{\text{T}}$ . In the first case, a gas *phase* is present; in the

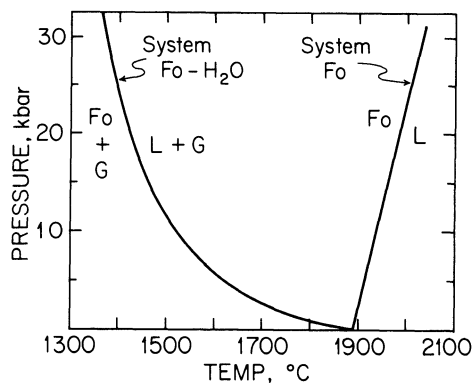
second case, it is absent. For the case of Ab-H<sub>2</sub>O, a gas phase would be present with melt at 800°C, 5 kbar if the system composition were 20% H<sub>2</sub>O, 80% Ab, because only about 9% H<sub>2</sub>O is needed to saturate the liquid with gas at 800°C, 5 kbar (see Burnham and Davis, 1974).

This chapter contains a selective review of the melting relations of common silicate systems with water, and a very limited discussion of the role of carbon dioxide in such systems. The subject of volatiles in magma genesis is vast in scope, and we can attempt here no more than an introduction. For an appreciation of the scope of the subject, interested readers may wish to consult the excellent (and somewhat divergent) reviews by Wyllie (Presidential Address, 1979), Eggler and Holloway (1977) and Mysen (1977).

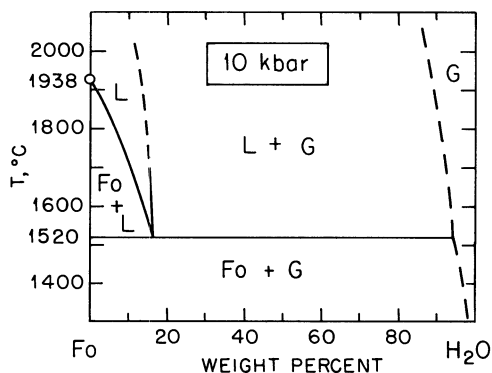
## Forsterite-H<sub>2</sub>O

Figure 19.1 shows by means of a *P-T* projection the dramatic effect on the melting point of forsterite when water is added at high pressures. The diagram shows the dry melting curve  $Fo = L$  on the right, and the H<sub>2</sub>O - saturated curve  $Fo + G = L + G$  running out to the left, to lower temperatures.

Figure 19.2 is an isobaric *T-X* section at 10 kbar showing the eutectic-like melting of the system Fo-H<sub>2</sub>O. (It is not truly eutectic because the gas phase contains much more silica than magnesia, so neither the gas nor the liquid lie in the Fo-H<sub>2</sub>O join, as shown by Nakamura and Kushiro, 1974.) The assemblage  $Fo + G$  melts at 1520°C, 418° lower than pure Fo at 10 kbar. The coexistence of  $Fo + G$  is interrupted by liquid at all higher temperatures. The “eutectic” liquid contains about 18% H<sub>2</sub>O in solution.



**Figure 19.1.** *P-T* projections showing the melting of forsterite, dry and with H<sub>2</sub>O in excess. Dry curve from Fig. 18.10; wet curve from Kushiro and Yoder (1968).



**Figure 19.2.** Isobaric 10 kbar  $T$ - $X$  section showing melting relations in the join  $\text{Fo}$ - $\text{H}_2\text{O}$ . Melting is not strictly eutectic because the gas and liquid compositions lie off the join. Temperatures from Fig. 19.1; liquid composition after Hodges (1974).

The  $\text{Fo}$  liquidus describes the composition of liquid in equilibrium with forsterite crystals at higher temperatures; this curve shows that the  $\text{H}_2\text{O}$  content of the liquid decreases to zero at the dry melting point,  $1938^\circ\text{C}$  at 10 kbar. A liquid field in the shape of a gore shows the range of bulk compositions that occur as gas-undersaturated liquid. This field is bounded to the left by the liquidus, and to the right by a saturation curve denoting saturation of the liquid with an aqueous gas phase. This curve is part of a solvus whose crest is beyond temperatures of interest and whose right-hand limb is seen in the right part of the diagram. The solvus curve delimits the two-phase  $L + G$  field from the  $L$  field on the left and the  $G$  field on the right. The gas phase contains a nontrivial amount of silicate component.

The fields  $L$  and  $\text{Fo} + L$  in Fig. 19.2 are those for which  $P_{\text{H}_2\text{O}}$  is clearly less than the total pressure, 10 kbar, because a gas phase is absent from those fields. Elsewhere in the diagram,  $P_{\text{aq}} = P_T$ .

The relation between Figs. 19.1 and 19.2 is shown in the perspective sketch of the  $P$ - $T$ - $X$  prism in Fig. 19.3. This figure shows the relationship between a *projection* and a *section*. Two isobaric  $T$ - $X$  sections are shown, at 10 and 20 kbar; these resemble Fig. 19.2 seen from the back of the page. The isobaric sections show the  $T$ - $X$  relations at single values of pressure. The actual trace of the first liquid composition with varying  $T$  and  $P$  is shown by the dashed curve within the prism; this trace connects the first liquids formed at all pressures. It is this trace, *projected* along the composition axis, which appears as the curve  $\text{Fo} + G = L + G$  in Fig. 19.1 and in the  $P$ - $T$  face of the prism in Fig. 19.3. Any isocompositional  $P$ - $T$  section could be used to collect this projected trace, but it is most convenient to use the anhydrous face of the prism for this purpose, since that face truly contains the dry melting curve. The same dashed curve tracing the liquid composition in equilibrium with  $\text{Fo} + G$  is projected, in Fig. 19.3, onto the  $P$ - $X$  face to give a  $P$ - $X$  projection. This projection shows the composition of the liquid, rather than the temperature, as a function of pressure.

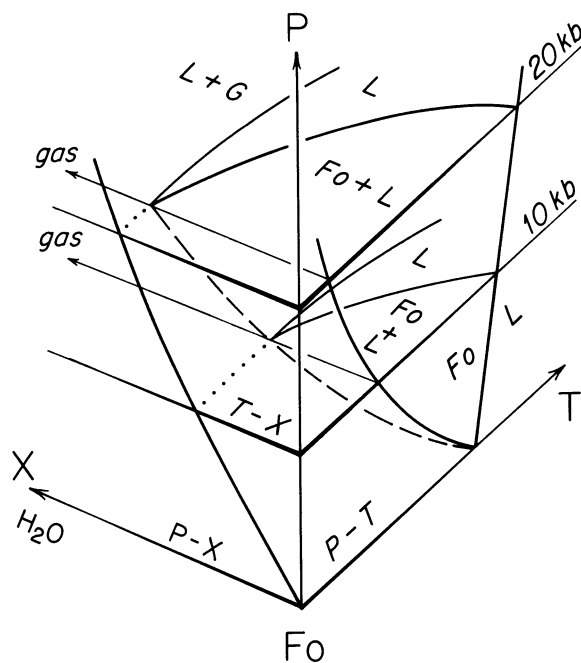


**Figure 19.3.**  $P$ - $T$ - $X$  prism for the system  $\text{Fo-H}_2\text{O}$ , showing isobaric sections at 10 and 20 kbar. Only the  $\text{H}_2\text{O}$ -poor compositions are shown; similar relations could be sketched for  $\text{H}_2\text{O}$ -rich compositions. The dashed line is the trace, within the prism, of the "eutectic" liquid composition. This trace is projected along  $X$  onto the  $P$ - $T$  plane, and along  $T$  onto the  $P$ - $X$  plane.

## SiO<sub>2</sub>-H<sub>2</sub>O

The wet and dry melting curves for silica are shown in  $P$ - $T$  projection in Fig. 19.4. The point labelled  $K$  is a *critical end point*, to be described. The same relations are shown schematically in Fig. 19.5. The dashed curve in this figure is the critical curve  $L = G$  running from  $K_{S-H}$ , the critical end point for  $\text{SiO}_2 - \text{H}_2\text{O}$ , to  $K_S$ , the critical point for  $\text{SiO}_2$ . The wet melting curve generates invariant points at its intersections with the tridymite field, and it terminates *without metastable extension* at the triple point for  $\text{SiO}_2$ . The absence of a metastable extension here is due to the fact that the hydrous melting reaction is undefined in the anhydrous system  $\text{SiO}_2$ . That the wet melting curve originates at the triple point for  $\text{SiO}_2$  can be deduced from the fact that gases of compositions  $\text{H}_2\text{O}$  and  $\text{SiO}_2$  are completely miscible in all proportions, and the resulting fact that the  $G$  field in the limiting system  $\text{SiO}_2$  must be continuous with the  $G$  field in  $\text{SiO}_2 - \text{H}_2\text{O}$ . All wet melting curves for silicates likewise originate at the triple point for the anhydrous silicate rather than at the 1-atm melting point, because of course there is nothing special about the pressure of 1 atm except that we love it. The wet and dry melting curves are commonly drawn to meet at 1 atm

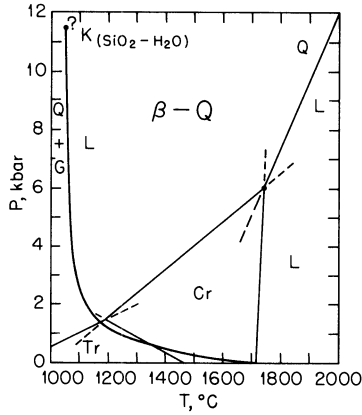


**Figure 19.4.** *P-T* projection of melting relations in the system  $\text{SiO}_2\text{-H}_2\text{O}$ . Point K is a critical end point. Data for  $\text{SiO}_2$  from Fig. 18.13, and for  $\text{SiO}_2 - \text{H}_2\text{O}$  from Kennedy *et al.* (1962) and Stewart (1967).

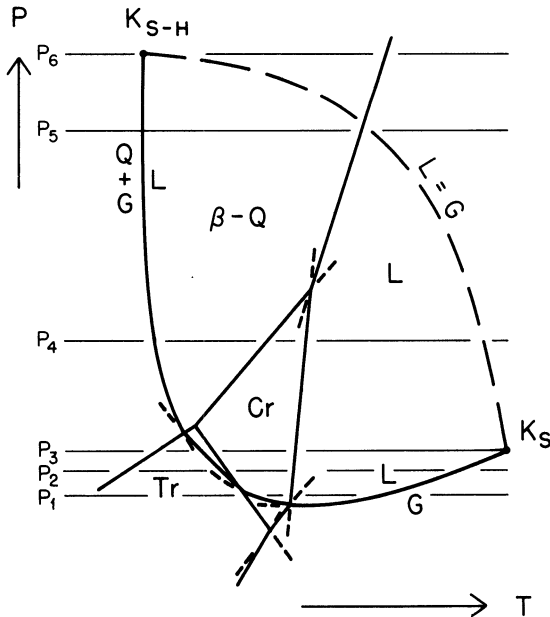


**Figure 19.5.** Schematic *P-T* projection for  $\text{SiO}_2\text{-H}_2\text{O}$  showing locations of isobaric sections  $P_1$  through  $P_6$  and the critical curve  $L = G$  connecting the two critical (end) points  $K_{S-H}$  (for the binary system) and  $K_S$  (for the unary system  $\text{SiO}_2$ ). The wet melting curve runs to the triple point in the system  $\text{SiO}_2$  and ends there without metastable extension.

simply because the difference between this case and the real one is experimentally undetectable in ordinary work.

A series of isobaric  $T$ - $X$  sections, corresponding to the pressures  $P_1$  through  $P_6$  in Fig. 19.5, is shown in Fig. 19.6 to illustrate the melting and critical relations for SiO<sub>2</sub> - H<sub>2</sub>O. The diagrams are valid in principle for all such systems, but are drawn in the book only for this one, in which enough data are available to make the relations qualitatively meaningful. The story told by these  $T$  -  $X$  sections requires little elaboration. Section  $P_3$  shows the nature of the critical point in the system SiO<sub>2</sub>, where the distinction between gas and liquid vanishes and the state of the system is described as that of a supercritical fluid. The following sections show the continued

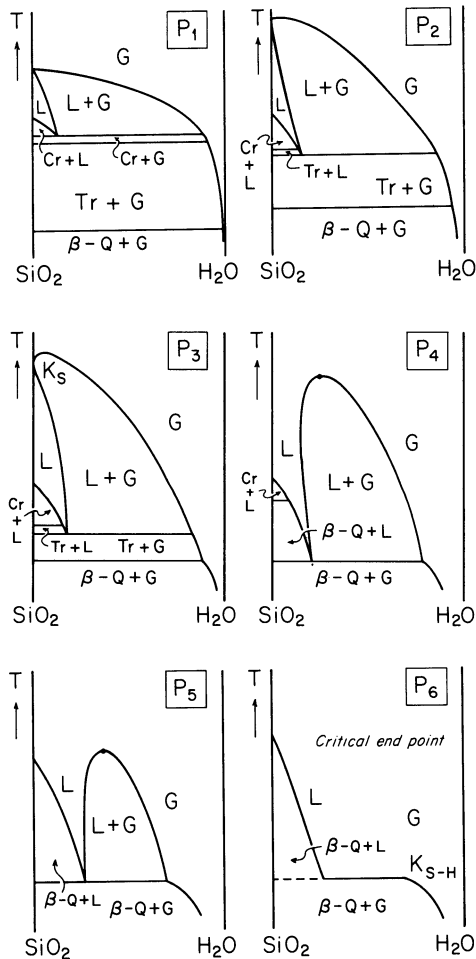


**Figure 19.6.** Schematic isobaric  $T$ - $X$  sections  $P_1$  through  $P_6$  for SiO<sub>2</sub>-H<sub>2</sub>O. Symbols:  $\beta$ -Q high quartz, Tr tridymite, Cr cristobalite, L liquid, G gas,  $K_S$  critical point, and  $K_{S-H}$  critical end point.

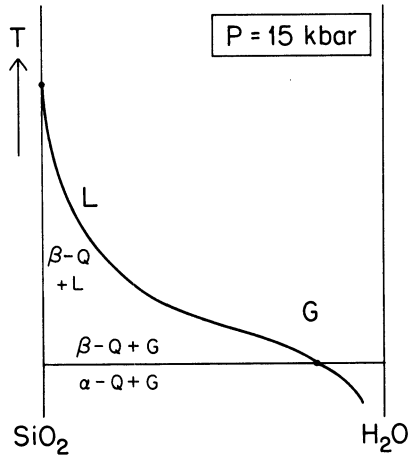


**Figure 19.7.** Isobaric  $T$ - $X$  section at 15 kbar for the system  $\text{SiO}_2$ - $\text{H}_2\text{O}$ . After Nakamura (1974).

diminution of the  $L + G$  field in the binary system  $\text{SiO}_2 - \text{H}_2\text{O}$  as the pressure is raised. Section  $P_6$  shows the nature of the critical end point  $K_{S-H}$  in the binary system. Fig. 19.7 shows the supercritical condition at 15 kbar in the binary system; this figure is based on actual data obtained by Nakamura (1974).

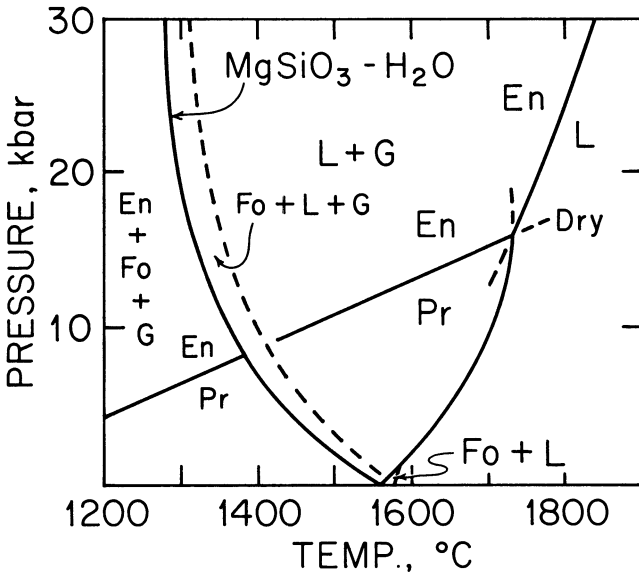


**Figure 19.8.**  $P$ - $T$  projection of the melting relations of  $\text{MgSiO}_3 - \text{H}_2\text{O}$ . After Kushiro, Yoder, and Nishikawa (1968) and Chen and Presnall (1975).

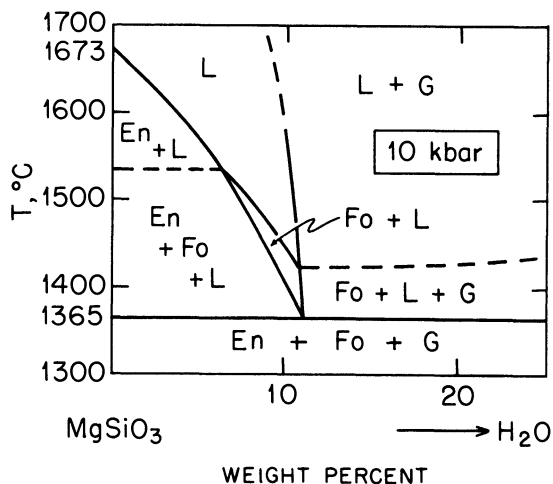


**Figure 19.9.** Isobaric 10 kbar  $T$ - $X$  section along the join  $\text{MgSiO}_3$ - $\text{H}_2\text{O}$ , after Kushiro, Yoder, and Nishikawa (1968).

### Enstatite-H<sub>2</sub>O

The  $P$ - $T$  projection for  $\text{MgSiO}_3$  -  $\text{H}_2\text{O}$  is shown in Fig. 19.8, and the melting behavior is further illustrated in Figs. 19.9 and 19.10. Fig. 19.10 shows that enstatite dissolves incongruently with  $\text{H}_2\text{O}$  at 10 kbar to  $\text{Fo} + \text{G}$ . It also melts incongruently to  $\text{Fo} + \text{L} + \text{G}$ , as shown by the transition from the 1300°C to the 1400°C isothermal, isobaric section in Fig. 19.10. The  $T$ - $X$  section of Fig. 19.9 can be understood by reference to the ternary sections of Fig. 19.10.

The wet melting of enstatite at 20 kbar is compared with the dry melting behavior, at the same pressure, in Fig. 19.11. The 20 kbar diagram emphasizes the fact that addition of  $\text{H}_2\text{O}$  at high pressure changes the melting behavior of enstatite from congruent to incongruent, thus destroying the thermal barrier present in the dry system. Ultramafic sills that show cotectic crystallization of olivine and bronzite must have crystallized from relatively dry liquids.

### Forsterite-Plagioclase-Silica-H<sub>2</sub>O

The liquidus relations at 15 kbar, projected from  $\text{H}_2\text{O}$  onto the anhydrous plane  $\text{Fo} - \text{An}_{50} - \text{SiO}_2$ , are shown in Fig. 19.12. Olivine and plagioclase do not coexist with liquid under these conditions, but react to form a pargasitic amphibole instead. This evidence can be used to argue that troctolites

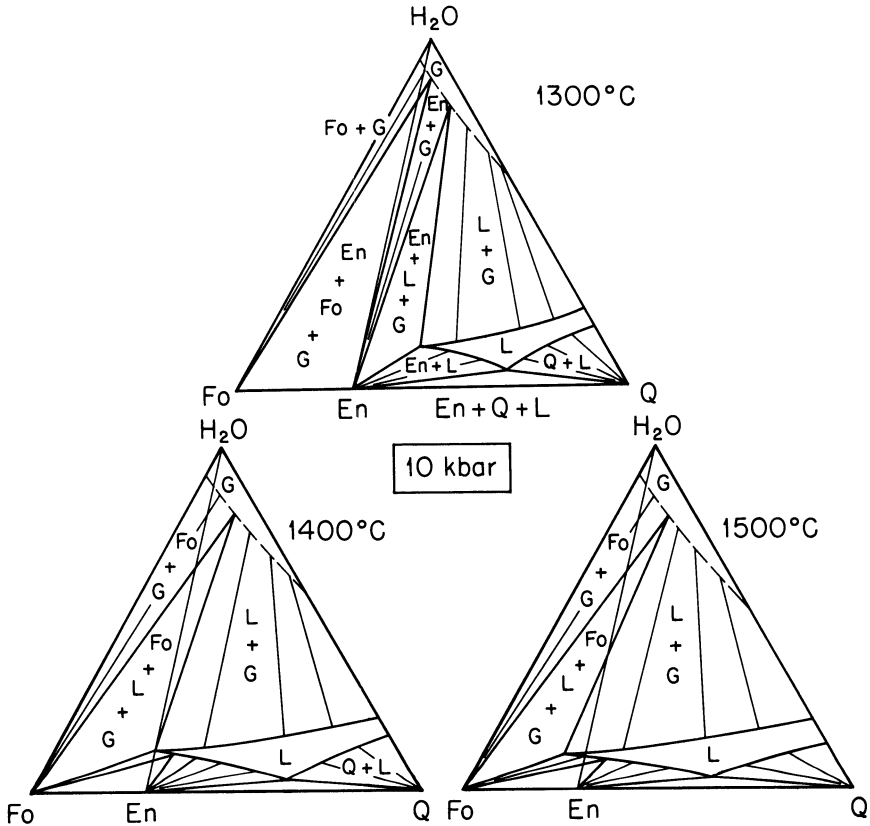


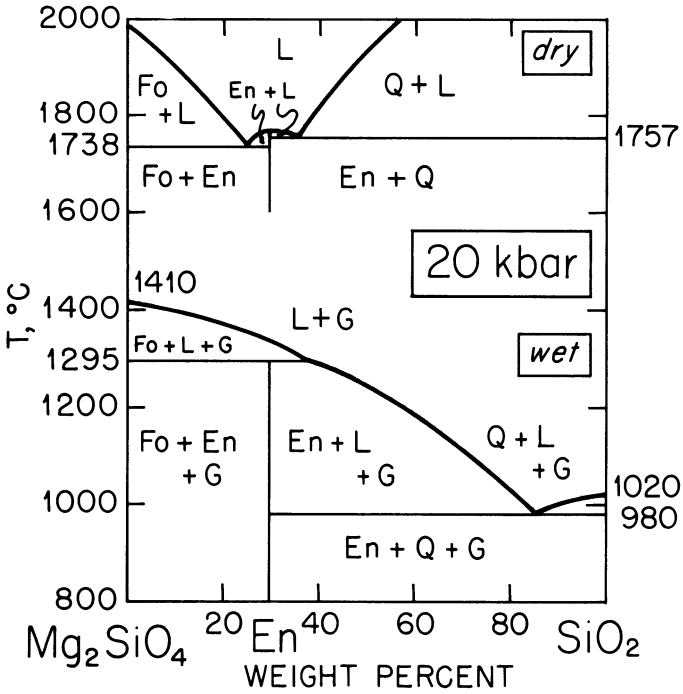
Figure 19.10. Isobaric (10 kbar) - isothermal sections for the system Fo-Q-H<sub>2</sub>O, after Kushiro, Yoder, and Nishikawa (1968).

crystallize from H<sub>2</sub>O - undersaturated or relatively dry melts. Enstatite and plagioclase do coexist with liquid, so high water pressure is, in principle, no bar to the crystallization of norites.

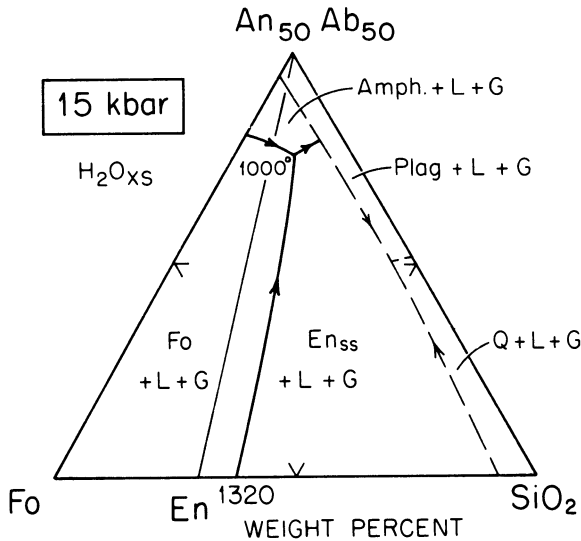
### Forsterite-Diopside-Silica-H<sub>2</sub>O

Figure 19.13 shows that the incongruent melting of enstatite - H<sub>2</sub>O extends far into the system Fo-Di-SiO<sub>2</sub>-H<sub>2</sub>O. Mantle-like compositions in the triangle Fo-Di<sub>ss</sub>-En<sub>ss</sub> will begin to melt, with H<sub>2</sub>O, to a liquid at the peritectic composition X, 1220°C. Such a liquid may be likened to a basaltic andesite; it is clearly silica-saturated in terms of its normative composition.

The shift of quartz-saturated equilibria toward the SiO<sub>2</sub> corner is remarkable. Yoder (1973) argued that the liquid composition Y was an adequate proxy for rhyolite, and used the 20 kbar diagram to explain the



**Figure 19.11.** Dry and wet melting relations of enstatite at 20 kbar. Dry diagram at top is an isobaric *T-X* section; wet diagram is a projection from H<sub>2</sub>O. After Kushiro (1969) and Chen and Presnall (1975).



**Figure 19.12.** Gas-saturated liquidus relations in the system Fo-An<sub>50</sub>-SiO<sub>2</sub> at 15 kbar, after Kushiro (1974). Amph. is pargasitic amphibole.

contemporaneous eruption of rhyolite and basalt from the same vent. The analysis requires a mantle source composed of two pyroxenes plus quartz. Such a composition would melt, with water, to a rhyolitic liquid Y at 960°C. If the melt were fractionally removed, or removed in a batch when the TSC reached the joint En-Di, no further melting would occur until the temperature rose to 1220°C, supposing a new supply of H<sub>2</sub>O to be added to replace that removed in the rhyolitic liquid. The basaltic liquid would be generated at 1220°C until the TSC reached the tie line En<sub>ss</sub> - Fo, at which point melting would cease unless the temperature rose above 1220°C.

Figure 19.13 shows a fractional fusion exercise for a bulk composition BC in the field En<sub>ss</sub> + Di<sub>ss</sub> + Q + H<sub>2</sub>O. The TSC moves from BC to C with extraction of the first melt (ILC) of composition Y. The TSC then moves from C to D, away from X, while the TLC moves on the mixing line XY, as shown by the dotted line and the sample lever at  $F_L = 0.38$ . When the total solid composition has reached D, diopside is used up, and the liquids move along XW, the peritectic boundary. The total liquid composition

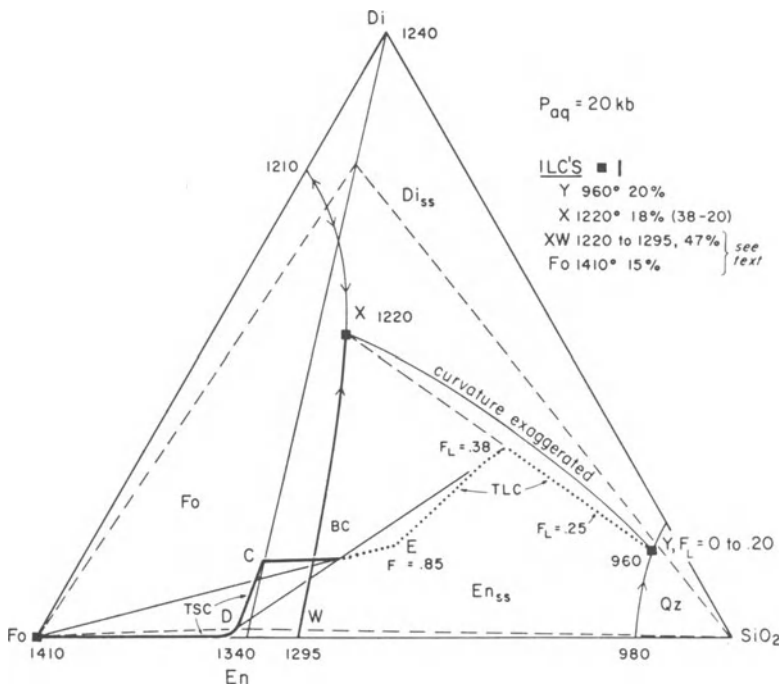


**Figure 19.13.** Liquidus diagram of the system Fo-Di-SiO<sub>2</sub>-H<sub>2</sub>O at 20 kbar, after Kushiro (1969). The boundary XY has an exaggerated curvature to show the mixing line used for the analysis of fractional fusion (Yoder, 1973; Morse, 1976). Dashed lines show the assumed limits of pyroxene solid solution, after Yoder (1973). Reproduced from Morse (1976) by permission.

moves toward this collection of liquids XW, sweeping rapidly toward W. The TLC path to E is constructed as follows. First, point E is located as the TLC when all En is exhausted and the TSC has reached Fo; point E is therefore a point on the line Fo-BC, extended. The location of E on this line is found to sufficient accuracy by determining  $F_L$  when the TSC has just reached Fo, as follows. Point D and the line XW are projected from diopside onto the base of the triangle, and the lever relation using D as a fulcrum gives 76% liquid of composition  $\overline{XW}$  and 24% Fo crystals. The total amount of the system previously present as a TSC composition D was 62%, i.e.,  $1 - 0.38 = 0.62$  as a fraction, and so the new fraction of solid forsterite is  $0.62 (0.24) = 0.15$ , and  $F_L = 0.38 + 0.47 = 0.85$ . These values locate point E as the last TLC before pure forsterite begins to melt. The TLC path to E is now constructed with the constraint that it must lie everywhere below the extension of the line W-E, which is the leading tangent to point E.

From this analysis, it quickly becomes apparent that the TLC vector toward X and related liquids is microscopically short, and that the liquids sweep rapidly toward W. This is reflected in the TSC path, which quickly approaches the sideline Fo-En.

This exercise is done with Yoder's bulk composition, which yields 20% liquid Y and 18% liquid X. The amount of liquid X is obtained by noting that  $F_L = 0.38$  when diopside is exhausted, and that this fraction represents the sum of liquids X and Y. Since  $F_Y = 0.20$ ,  $F_X = 0.38 - 0.20 = 0.18$ . An explicit solution for *equal* amounts of liquids X and Y is shown in Fig. 19.14. Lines of constant yield of liquid Y are rigorously parallel to the En - Di join as can easily be shown by similar triangles. Such a line for a yield of 20% liquid Y is plotted in Fig. 19.14 and marked 0.20Y. The desired bulk composition, supposing an initial liquid yield of 20 percent is desired, lies somewhere on this line. For an equal yield of Liquid X, we seek a bulk composition such that  $F_L$  (as TLC) = 0.40 when Di is exhausted in the solids. For any such bulk composition, all lines of constant  $F_L$  lie parallel to the mixing line XY as can be shown with similar triangles. The desired line can be found accurately enough by choosing two random bulk compositions near the desired one on the line 0.20Y and calculating  $F_L$  for the case when each of these has just lost all Di to liquid X. The examples chosen, A and C in Fig. 19.14, gave  $F_L = 0.303$  and  $0.537$ , respectively. Graphically, plotting distance from XY versus  $F_L$ , find by interpolation the distance required for  $F_L = 0.40$ . A line parallel to XY at this distance intersects 0.20Y in the desired bulk composition, point B in the figure. The lever through B from the TSC on Fo-En<sub>ss</sub> gives  $F_L = 0.40$ , as desired. Yoder's bulk composition, yielding 18% X, is shown as a circle near point B in Fig. 19.14. It lies very close to the bulk composition yielding equal amounts of liquids X and Y, thus showing that the relative amounts of liquid are quite sensitive to small changes in the bulk composition. This is so because liquids X and Y are both quite remote from the bulk composition.

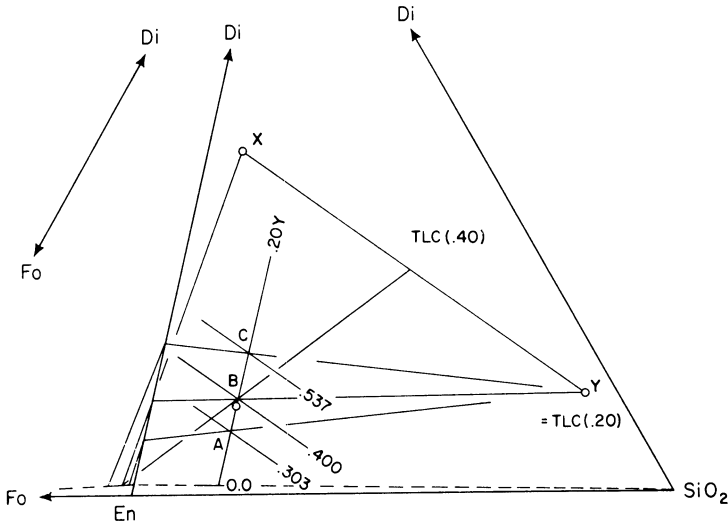


**Figure 19.14.** Explicit graphical solution for equal amounts of liquids Y and X on fractional melting. The line labelled 0.20Y is parallel to En-Di, and the lines labelled 0.303–0.537 are parallel to XY. Both sets are lines of constant  $F_L$ . Point B is the desired bulk composition for X = 0.20, Y = 0.20. The circle is point BC of Fig. 19.13. From Morse (1976), with permission.

**Albite-H<sub>2</sub>O**

The *P-T* projection for the melting of Ab-H<sub>2</sub>O is shown in Fig. 19.15. The figure also shows three *liquidus* curves for the cases where insufficient H<sub>2</sub>O is present to saturate the liquid at all pressures; these are curves for  $P_{aq} <$

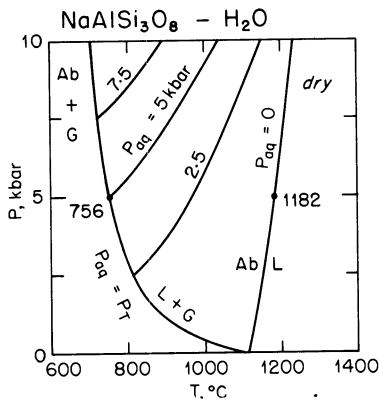


**Figure 19.15.** Melting of albite with water at high pressure, shown in a *P-T* projection. Dry melting curve from Fig. 18.7; wet melting curves after Burnham and Davis (1974). Curves labelled with  $P_{aq} < P_T$  show liquidus temperature in the absence of a gas phase. The curve Ab + G + L is the trace of the liquidus; the actual solidus lies at lower temperatures because of incongruent melting in Ab-H<sub>2</sub>O.

$P_T$ . The curve  $Ab + G + L$  is, in principle, the solidus curve for all compositions; it is also the liquidus curve for vapor-saturated conditions. (The actual solidus curve lies somewhat below the curve drawn, because Ab dissolves incongruently in H<sub>2</sub>O and melts over an interval of temperature.) Suppose the system contains just enough H<sub>2</sub>O to saturate the liquid with gas at 5 kbar. Then the system will melt completely at 756°C. Now transfer this liquid isothermally to 7.5 kbar. Crystals of Ab will now form until the liquid is again just saturated with gas. At 7.5 kbar, the temperature will have to be raised to 920°C in order to melt the new Ab crystals. At 920°C, the liquid will again be undersaturated with gas,  $P_{aq}$  being only 5 kbar while  $P_T$  is 7.5 kbar. If the liquid is now returned to 5 kbar, 756°C, it will be just saturated with gas again.

### Albite-Orthoclase-H<sub>2</sub>O

The entry of H<sub>2</sub>O into the liquid at high pressures so reduces the solidus temperature that it cuts into the Ab-Or solvus at 5 kbar, as shown in Fig. 19.16. The reaction  $Ab + Sa + G = L$  occurs at 701°C at 5 kbar. The solvus crest rises with pressure, at a rate we shall take to be 18°/kbar. The intersection of the solidus (trace of the minimum temperature for Ab-Or-H<sub>2</sub>O) and the solvus *critical line* (trace of  $T_c$  with pressure) occurs at about 4.2 kbar, 715°C (Morse, 1970). However, this is an *indifferent crossing* because nothing happens there. The reason for this may be seen with the aid of Figs. 19.17 and 19.18. The critical composition  $X_c$  on the solvus, and the minimum composition  $X_m$ , are not in general the same. This means that when  $T_c$  and  $T_m$  are the same, at the indifferent crossing, the melting loop still lies above the solvus crest  $X_c$  and the solidus and solvus are not in contact. The actual contact occurs, in the general case, at some pressure  $S_1$  where the solidus just kisses the solvus (Fig. 19.18a). This generates the reaction  $Ab + G = Sa + L$ , using simplified notation in which Ab and Sa are solid solutions near or at the solvus. The pressure  $S_1$  marks the first coexistence of two feldspars with liquid. The singular point  $S_1$ , caused by the collinearity of Ab, Sa, and L in projection, lies at a minimum pressure on the continuous equilibrium curve  $Ab + Sa + L$  (Fig. 19.17). At a pressure slightly higher than  $S_1$ , a field of  $Sa + L$  occurs in the  $T$ - $X$  projection, Fig. 19.18b. This field is bounded downward in temperature by the incongruent melting reaction  $Ab = Sa + L$ , and upward by the same reaction in reverse, i.e.  $Sa + L$  at a lower temperature going to Ab at a higher temperature. This geometry requires the curve  $Ab + Sa + L$  to be concave upward, as in Fig. 19.17. The composition of sanidine in equilibrium with liquid, without Ab, is not constrained to the solvus and therefore lies on a new sanidine-rich solidus outside the solvus (Fig. 19.18b).

When the pressure is increased to that of point A in Fig. 19.17, the Ab

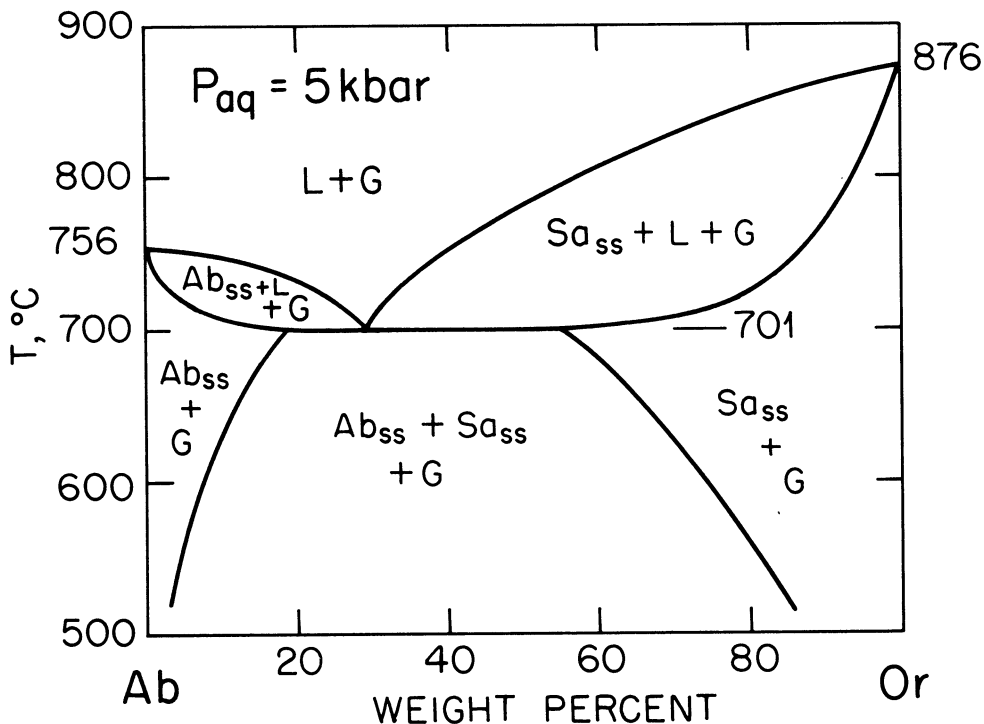


**Figure 19.16.** Melting of alkali feldspars at 5 kbar, shown in an isobaric  $T$ - $X$  projection from  $H_2O$  onto the Ab-Or join. After Yoder, Stewart, and Smith (1957) and Morse (1970). Solvus is that of Waldbaum and Thompson (1969) translated upward at a rate of  $18^\circ/\text{kbar}$ . Base of diagram measures 10 cm.

solidus and the Sa solidus have just united at the critical point on the solvus. At a slightly higher pressure (Fig. 19.18c), the solidus becomes totally detached from the solvus except at one point, and rapidly begins to change shape, moving away from the solvus. This change is shown schematically by two new lower bounds to the Sa + L loop in Fig. 19.18c. That the change in solidus shape is continuous and correct can be shown by constructing a series of  $G$ - $X$  diagrams for the sequence shown in Fig. 19.18.

Eventually the solidus becomes so deeply embedded in the solvus that the minimum composition  $X_m$  touches the Ab limb of the solvus, generating the singular point  $S_2$  (Figs. 19.18d and 19.17). Below the pressure of  $S_2$ , all melting involving two feldspars is peritectic, and above  $S_2$  it is eutectic.  $S_2$  is therefore a familiar type of singular point occurring where a reaction changes from odd to even. This singular point marks the upper limit in  $P$  of the minimum melting reaction  $F = L$  (where F stands for feldspar solid solution of minimum composition).

The above analysis has been made completely general, so that it applies to any system in which the projected trace of a solidus cuts a solvus at

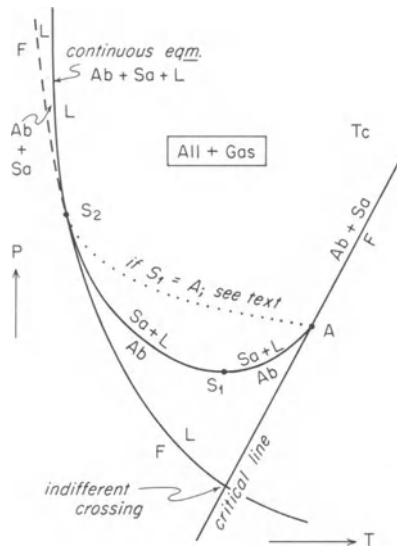


**Figure 19.17.** Geometrical relations of alkali feldspar melting in the presence of an aqueous gas phase, shown in a  $P$ - $T$  projection. Both Ab and Sa are solid solutions on or near the solvus. Dotted line shows the trace of the equilibrium  $Ab + Sa + L + G$  (i.e.  $Ab = Sa + L$ ) if the solidus first intersects the solvus at the critical point. Modified from Morse (1970).  $S_1$  and  $S_2$  are singular points.

some point away from the crest. In the alkali feldspar system, however,  $X_c$  and  $X_m$  are very close together, and therefore the solidus must have a slope near zero in  $T$ - $X$  projection near the critical composition. Moreover, it can be argued from experience and ideas about the structure of highly polymerized liquids that the solidus undergoes a premonitory flattening as it approached the solvus. In this case,  $dT/dX = 0$  for the solidus and the solvus simultaneously, and the first point of contact occurs at A in Fig.

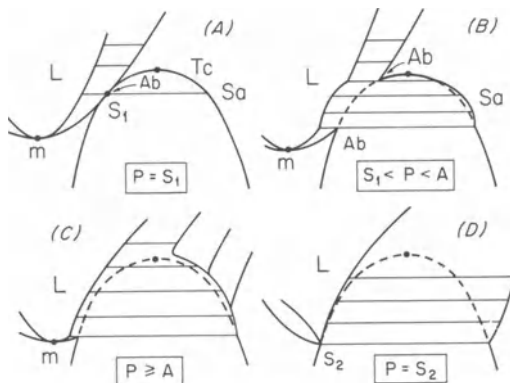


**Figure 19.18.** Schematic isobaric  $T$ - $X$  projections from  $H_2O$  onto the Ab-Or join, showing melting relations corresponding to those displayed in Figure 19.17.

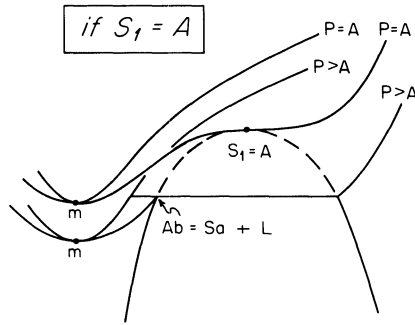


**Figure 19.19.** Polybaric  $T$ - $X$  projection from  $H_2O$  showing the case where the solidus first touches the solvus at the critical point. Motion of the solvus with pressure is ignored.

19.17, on the critical line. In such a case,  $S_1$  is a singular point by identity rather than by collinearity of composition, and it lies at  $A$ . The continuous equilibrium  $Ab + Sa + L$  then rises from  $A$  to  $S_2$ , as shown by the dotted line in Fig. 19.17. This is the geometry deduced by Morse (1970). It is illustrated here in a  $T$ - $X$  sketch, Fig. 19.19.

### Diopside- $H_2O$

The  $P$ - $T$  projection for  $Di-H_2O$  is shown in Fig. 19.20. The wet melting curve is unusual in showing a minimum near 20 kbar, implying that at higher pressures, the volume change on melting is positive.

### Diopside- $CO_2$ - $H_2O$

At low pressures carbon dioxide enters silicate liquids only in small quantity; it thus lowers the melting temperatures only moderately, as shown by the  $Di-CO_2$  curve in Fig. 19.20. When  $CO_2$  and  $H_2O$  are mixed in a molar ratio  $CO_2/(CO_2 + H_2O) = 0.8$  and added to diopside, the solidus lies as shown by the dashed line in Fig. 19.20. The effect of  $H_2O$ , even in small amounts, clearly dominates the slope of the melting curve. The solubilities of  $H_2O$  and  $CO_2$  in silicate melts are reviewed in detail by Mysen (1977).

### Phlogopite- $H_2O$

When a hydrous phase is heated under pressure, it will tend to decompose by dehydration to an assemblage of anhydrous crystals plus gas. The gas so released will tend to cause melting, leading to a water-poor melt which

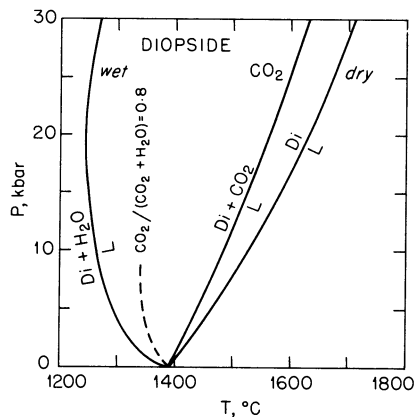


**Figure 19.20.** Melting of diopside dry, with CO<sub>2</sub>, and with water, shown in a *P-T* projection. Dry curve from Figure 18.2. Wet curve from Yoder (1965), Egger (1973), and Hodges (1974). CO<sub>2</sub> curves from Egger (1973) and Rosenhauer and Egger (1975).

absorbs all the released H<sub>2</sub>O and is therefore far from being saturated with a gas phase. The case of the magnesian mica phlogopite furnished the first demonstration of this important principle (Yoder and Kushiro, 1969). An isobaric 10 kbar *T-X* projection of the relevant system is shown in Fig. 19.21. In the absence of gas, the first liquid is generated at 1220°C from an assemblage of phlogopite with forsterite, leucite, and kalsilite. This liquid contains only about 2.5% H<sub>2</sub>O by weight. Moreover, the diagram shows that upon crystallization from melts poorer in H<sub>2</sub>O than the phlogopite composition, the phlogopite extracts H<sub>2</sub>O from the melt, causing the latter to become even poorer in H<sub>2</sub>O. The initiation of melting in a phlogopite-bearing mantle would presumably be like that on the H<sub>2</sub>O - poor side of phlogopite in the diagram. It is interesting to note that the H<sub>2</sub>O - poor melting temperature, 1220°C, is not very much higher than that of the gas-saturated melting reaction at 1185°C. These two temperatures, in fact, shift past one another as the pressure varies, as will now be shown.

## General P-T-X Relations for the Model System A-H<sub>2</sub>O

The melting behavior of phlogopite illustrates the general class of melting relations in a system A-H<sub>2</sub>O containing an anhydrous phase (or phases) A and a hydrous phase H. The generalized *P-T-X* relations for such a system have been reviewed in detail by Egger (1973b) and Egger and Holloway (1977). Fig. 19.22 illustrates such an analysis. The upper left part of the figure is a *P-T* projection containing two singular points *S* and two invariant points *I*. The *P* and *T* scales are arbitrary. The rest of the figure consists of

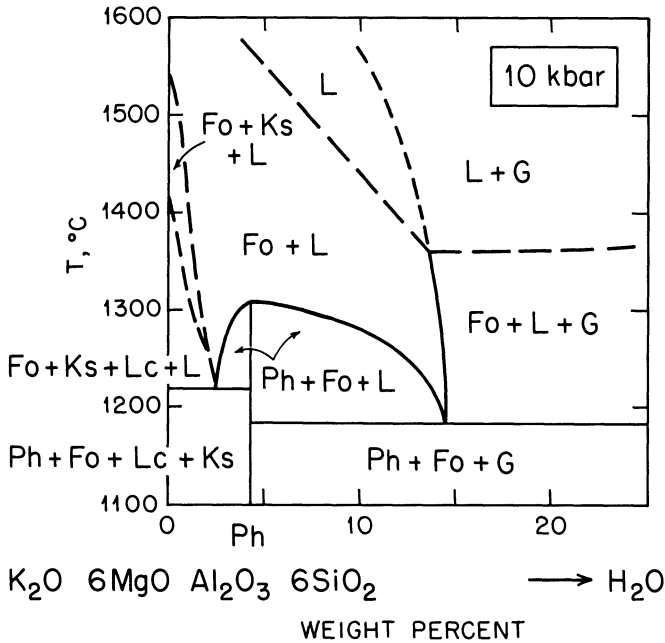


**Figure 19.21.** Melting of phlogopite,  $\text{K Mg}_3\text{AlSi}_3\text{O}_{10}(\text{OH})_2$ , at 10 kbar total pressure. After Yoder and Kushiro (1969).

a series of isobaric  $T$ - $X$  sections, arranged in sequence from the upper left corner. In the figure,  $L_1$  denotes the water-poor liquid, unsaturated with a gas phase, and  $L_2$  denotes the gas-saturated liquid. The conventional missing-phase notation is used in the  $P$ - $T$  projection to identify the reaction assemblage.

The two invariant points are each generated by the intersection of a dehydration curve ( $L$ ) and a solidus curve ( $H$ ). The two singular points are each generated by the coincidence of liquid composition with the hydrous phase composition. Below the pressure of  $I_1$  the hydrous phase dehydrates to  $A + V$  (vapor), and at a higher temperature  $A + V$  melts to a water-poor liquid  $L_1$ . These two reactions merge at  $I_1$ , and at a pressure just above  $I_1$ , the relations shown in the upper left corner of Fig. 19.22 occur. At this pressure, the hydrous phase melts incongruently to liquid plus vapor, while a eutectic  $A + H = L_1$  is formed at a lower temperature. At a pressure  $P = 1.8$ , the first singularity occurs when the liquid composition reaches  $H$ . At a higher pressure 2.3, the hydrous phase melts congruently and two eutectic liquids occur. Both liquids become progressively richer in  $\text{H}_2\text{O}$  as the pressure rises, and the solidus reaction switches to liquid  $L_2$  at  $P = 2.5$ . The shift toward more  $\text{H}_2\text{O}$ -rich compositions finally causes  $L_1$  to reach  $H$ , as in the section labelled  $P = 7.0$ , the pressure of singular point  $S_2$ . Above this pressure the hydrous phase again melts incongruently, now to  $A + L$ . Eventually this incongruent melting reaction occurs at the same temperature

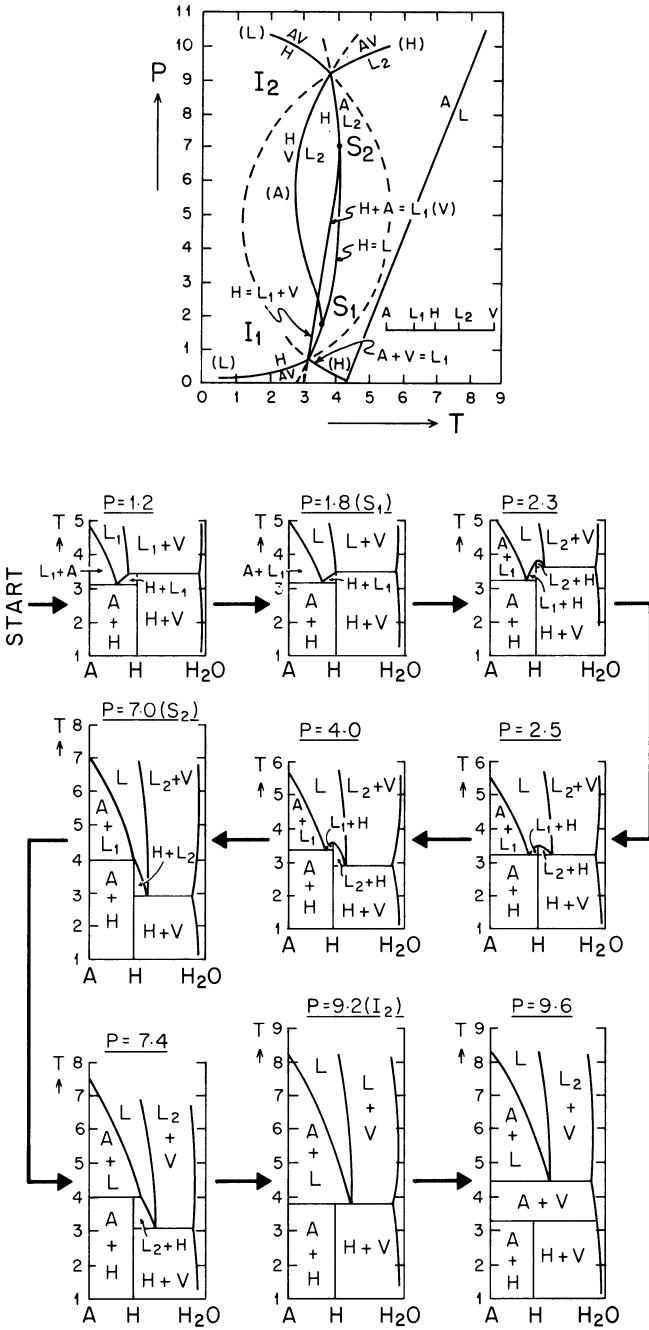


**Figure 19.22.** Phase relations in a model system A-H<sub>2</sub>O containing an anhydrous phase A and a hydrous crystalline phase H. The first diagram is a  $P$ - $T$  projection; others are isobaric  $T$ - $X$  sections, arranged in the sequence shown by the arrows. All scales are in arbitrary units. Adapted from Egglar and Holloway (1977).

as the reaction  $H + V = L$ , generating the invariant point  $I_2$  (section labelled  $P = 9.2$ ). At higher pressures than  $I_2$ , the hydrous phase again dehydrates to  $A + V$ , and the melting reaction is  $A + V = L_2$ . At such high pressures, the anhydrous phase  $A$  would crystallize directly from  $L_2$  on cooling, with release of gas.

The upper limit of stability of the hydrous phase  $H$  is given, in the  $P$ - $T$  projection, by the congruent melting curve  $H = L$ . This curve mimics the observed stability of amphibole, which recurves sharply to lower temperatures in the range 20-30 kbar (see Wyllie, 1979, for summary).

The relations illustrated in Fig. 19.22 have been extended to the ternary model system  $A$ - $B$ - $H_2O$  and the model system  $A$ - $H_2O$ - $CO_2$  by Egger and Holloway (1977), whose work should be consulted for a more complete appreciation of the principles involved. The application of dehydration-melting principles to crustal anatexis involving pelitic and granitic rocks is discussed in detail by Thompson and Algor (1977).

## Summary

The component  $H_2O$  drastically reduces the beginning-of-melting (solidus) temperature of silicate minerals if it is present in sufficient quantity to generate an aqueous gas phase. Even the merest trace of gas will cause melting at the solidus. The amount of liquid generated can be predicted from the lever rule: for example if the system contains 1%  $H_2O$  and the first liquid contains 10%  $H_2O$ , then 10% liquid will be generated at the isobaric invariant point involving  $S$ - $L$ - $G$ . This is generally accounted sufficient to cause magma separation by intergranular flow. If 0.1%  $H_2O$  is present in such a system, 1% melt will be generated. This is generally accounted insufficient for magma separation, but sufficient for seismic attenuation to yield the Low Velocity Zone (LVZ, asthenosphere) of the upper mantle (roughly 100–200 km deep). This interpretation of the LVZ must be viewed with caution, however, because the required grain-boundary relaxation may be an intrinsic property of unmelted mantle material at these depths (Anderson and Minster, 1979).

Studies of the role of  $H_2O$  and  $CO_2$  in magma genesis have reached a high degree of sophistication in recent years, including such tricks as  $\beta$ -track mapping of the  $CO_2$  content and distribution in quenched silicate melts (Mysen and Seitz, 1975). There has simultaneously arisen an increased understanding of silicate melt structure and the thermodynamic mixing properties of silicate melts (e.g. Burnham, 1979). The resulting payoff in terms of our theoretical and pragmatic understanding of magma generation has been enormous, even if large questions about the real processes in the earth remain. An elegant introduction to some of these questions is given in the treatise by Yoder (1976).

**G-X Diagrams for Ab-Or-H<sub>2</sub>O**

The system Ab - Or - H<sub>2</sub>O furnishes a useful example of G - X diagrams for a ternary system, projected onto a binary join. The crystalline phases lie rigorously (we assume) in the join Ab - Or, but the liquid composition is ternary, and must be projected from H<sub>2</sub>O. Fig. 19.23 shows that the result is similar to that obtained with a simple binary system, as previously shown in Figs. 12.26 and 15.23. The dashed lines in Fig. 19.23 refer to ternary equilibria in which the liquid composition is projected onto Ab - Or, and the solid lines refer to compositions in the join Ab - Or. The diagrams are schematic, and the relative positions of the minimum composition (or

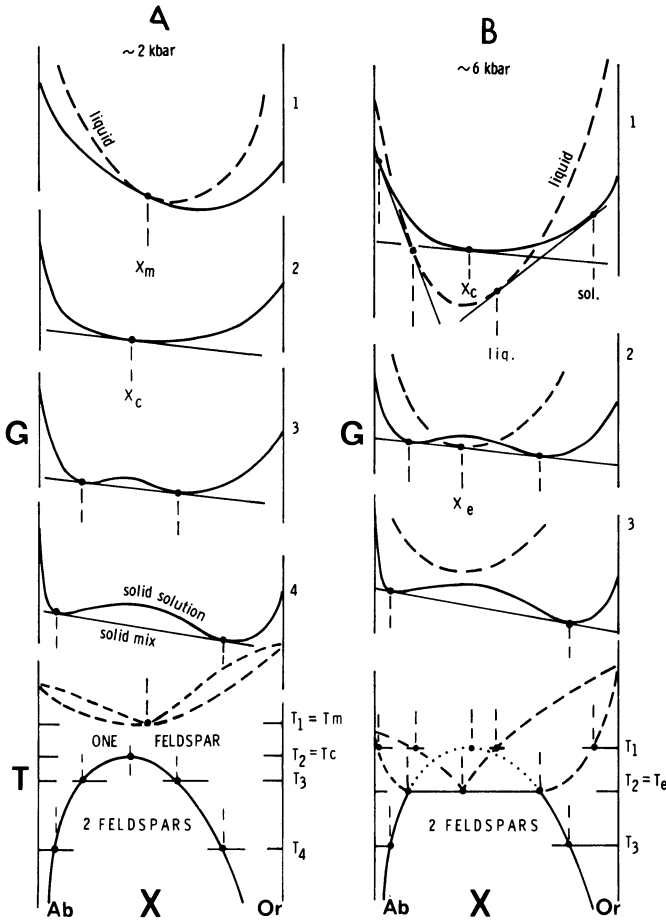


**Figure 19.23.** G- and T-X diagrams for the system albite-orthoclase at high pressures near 2 kbar in A and near 6 kbar in B. Melting (dashed lines) refers to a steam-saturated system.

eutectic composition) and the critical composition on the solvus are deliberately offset to avoid confusion.

Fig. 19.23a shows, schematically, the case for a total pressure near 2 kbar; four  $G$ - $X$  diagrams are superimposed on a  $T$ - $X$  diagram, and all are isobaric projections from  $H_2O$ . With falling temperature, the solvus limbs theoretically reach the pure end members at  $0^\circ K$ . At temperature  $T_4$ , the  $G$ - $X$  curve for the crystalline solution is composed of three segments, the outer two of which are concave up and the middle of which is concave down. A common tangent is drawn to the two nodes on this  $G$ - $X$  curve. This tangent, where it touches the  $G$ - $X$  curve, defines the stably coexisting compositions on the solvus; clearly at this temperature, a mechanical mixture of the two nodal compositions is minimized in  $G$  relative to homogeneous solid solution. At the higher temperature  $T_3$ , the picture is much the same, but the nodes have drawn closer together. At  $T_2$ , the critical temperature, the nodes have united at the critical composition  $X_c$ , and the solid solution is now described in  $G$ - $X$  space by a single concave-up curve. In Fig. 19.23a, it is assumed that steam (water vapor) is present at 2 kbar. Under these conditions, a minimum melting relationship obtains for alkali feldspars, as suggested by the dashed loops in the  $T$ - $X$  section. At temperature  $T_1$ , the system is at the minimum melting point, and the  $G$ - $X$  diagram has the form seen in Fig. 12.26. Note that the minimum composition  $X_m$  and the critical composition  $X_c$  are not, in general, the same. In reality,  $X_m$  probably lies to the left of  $X_c$ , as in Fig. 19.18.

Fig. 19.23b illustrates the case when a solidus is embedded in a solvus. This corresponds to the case of alkali feldspars in the presence of steam at about 6 kbar. Note that the  $G$ - $X$  curves for the solvus are defined completely, as before, despite the presence of liquid. At temperature  $T_3$ , liquid has a high  $G$  relative to any solids and is therefore metastable: the system is solid. At  $T_2 = T_e$ , the node of the liquid curve just touches the binodal tangent connecting the stable feldspar compositions, and this is the eutectic condition. At any temperature slightly above this, the binodal tangent is interrupted by two crystal-liquid tangents, which are minimized in  $G$  relative to feldspars on the solvus. The solvus is therefore metastable above  $T_2$ . It continues to be metastable up to the critical temperature, above which it does not exist. Section 1 depicts the  $G$ - $X$  relations at the critical temperature. Above this, the  $G$ - $X$  relations are essentially those of any eutectic diagram.

## Chapter 20

# Some Applications to Basalt Magma Genesis

### Mineral Facies of the Upper Mantle

Lherzolite is a rock composed essentially of olivine, orthopyroxene, and clinopyroxene. Such rocks occur in ultramafic complexes crystallized in the crust, or perhaps diapirically intruded into the crust from the mantle, but they also occur as xenoliths (nodules) in basalts and kimberlites (e.g. Boyd, 1973). The occurrence of abundant xenoliths of this rock type, combined with seismic evidence, meteorite compositions, and theoretical arguments, gives rise to the widely accepted idea that the upper mantle of the earth (and the source region for most basalt magma) has the composition and mineralogy of lherzolite. See Yoder (1976), Ch. 2, for discussion.

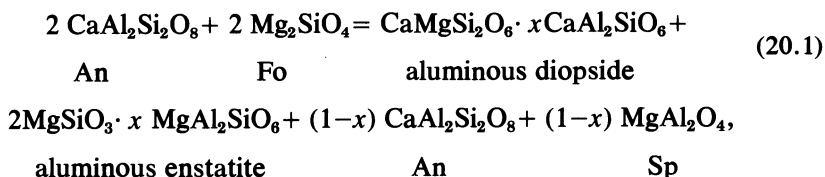
The mineral assemblage ol + opx + cpx is commonly regarded as a "barren" one because it has insufficient Al and alkalis to yield the plagioclase component of a basaltic magma, on melting. An additional requirement for a "fertile" source rock for basalt magma is the presence of an aluminous mineral. At low pressures, plagioclase itself may serve this purpose. Such a *plagioclase lherzolite*, if heated at high pressures, will, by subsolidus (metamorphic) reaction, transform to a *spinel lherzolite*, and at even higher pressures, to a *garnet lherzolite*. This fact has given rise to a tripartite division of the upper mantle into plagioclase, spinel, and garnet *facies*. (By analogy to the terminology of regional metamorphism, the word *zone* might be preferable to *facies*, as zones are usually defined by the appearance of a key mineral, whereas *facies* are best defined as sets of mineral assemblages that may comprise several zones. However, the word

facies is in vogue, and the word zone overworked, so a change in the names is not warranted.)

The fate of the plagioclase component when taken to high pressure has already been foreshadowed in some of the phase diagrams previously studied in this book. The existence of the spinel field at the *liquidus* of the system Fo-An (Chapter 9), for example, indirectly suggests the possibility of a subsolidus spinel-forming reaction, and this possibility is further enhanced by the closure of the spinel and diopside fields at high pressure in the system Fo-Di-An (Chapter 18). Of more direct significance are the subsolidus transformations of the plagioclase end members themselves: An to Gross + Ky + Q (grossular is a garnet end member) and Ab to Jd + Q (jadeite is a pyroxene end member).

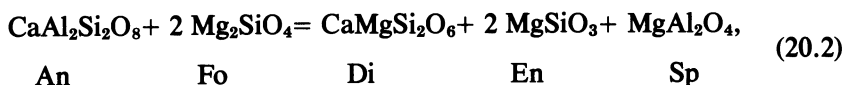
Kushiro and Yoder (1966) first documented experimentally the fate of plagioclase in the presence of olivine at high pressures. They studied the reactions of the end members Fo and An, and subsequent work with intermediate plagioclase and olivine compositions (e.g. Emslie, 1971) showed that the effects of adding Ab and Fa tend to cancel out, so that the positions of the spinel and garnet facies boundaries in the mantle must be quite similar to those determined for the high-temperature end members by Kushiro and Yoder.

The spinel-forming reaction was represented by Kushiro and Yoder as follows:



Where  $0 < x < 1$ .  $\text{CaAl}_2\text{SiO}_6$  and  $\text{MgAl}_2\text{SiO}_6$  are both ‘‘Tschermak components’’ involving the coupled tetrahedral Al substitution  $\text{AlAl} \rightleftharpoons \text{R}^{2+}\text{Si}$ , where  $\text{R}^{2+}$  denotes a divalent cation.

In model ultramafic rocks containing a larger ratio of Fo to An than 1:1, the residual An on the right-hand side of reaction (20.1) would disappear. An idealized spinel-forming reaction for the molar ratio An : 2Fo can be written (Kushiro and Yoder, reaction 4):



but this reaction obscures the highly important entry of Al into the pyroxenes. In fact, Kushiro and Yoder showed indirectly that the Al content of the pyroxenes increases with pressure, if enough An is initially present, by the reaction



As pressure is further increased within the spinel field, a limit is reached at which garnet is formed. The idealized reaction can be derived by noting that the right-hand side of reaction (20.1) is equal to  $2\text{CaMg}_2\text{Al}_2\text{Si}_3\text{O}_{12}$ , a garnet of composition  $\text{Py}_2\text{Gr}$ , where Py is pyrope and Gr is grossular.

In summary, the spinel-forming and garnet-forming reactions are conveniently (if loosely) remembered as “plagioclase + olivine = 2 pyroxenes + spinel” and “2 pyroxenes + spinel = garnet.” In normal ultramafic (hence plagioclase-poor) mantle rocks, there will always be an excess of olivine, orthopyroxene, and clinopyroxene, so the fundamental rock name will still be lherzolite for all three facies: plagioclase, spinel, and garnet.

The generalized  $P$ - $T$  boundaries of the three facies in the upper mantle are shown in Fig. 20.1, along with the solidus trace for an assumed average lherzolite composition. The *geotherms* shown as dashed lines in the figure are the estimated geothermal gradients for Precambrian shield areas (coldest mantle), ocean plate areas (intermediate temperatures), and ocean ridge areas or mantle upwellings (hottest mantle); these geotherms are assumed to converge at 200 km. The depth scale of Fig. 20.1 is calculated for oceanic regions, assuming a gradient of 100 km/32.5 kbar. The deeper part of the ocean ridge geotherm having a slope of  $0.5^\circ\text{C}/\text{km}$  is *adiabatic* (Greek derivation meaning “not passing through”), which is what you get if you decompress a parcel of material from depth to a shallower level *without gain or loss of heat*. Since entropy can be defined by  $dS = dQ_r/T$ , where  $Q_r$  is the heat content for a reversible process, an adiabat ( $dQ = 0$ ) is also

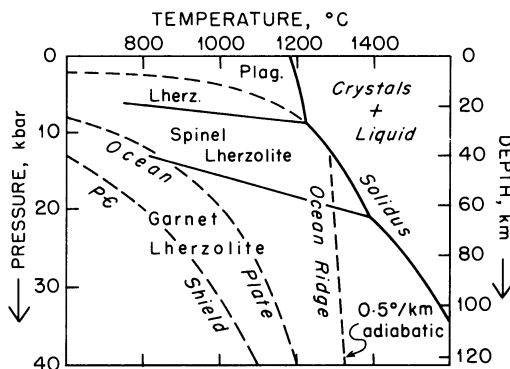


**Figure 20.1.** Mineral facies of the upper mantle, with geotherms (dashed) and solidus. Based on data and analysis of Presnall *et al.*: (1979), Kushiro and Yoder (1966), and Wyllie (1979). Geotherms from Solomon (1976), except that Ocean Ridge geotherm above 30 km is modified according to the ideas of Presnall *et al.* (1979) as revised by Presnall, (oral communication, 1979).

an isentrope ( $dS = 0$ ). Because the compressibility of mantle material is small, a mantle adiabat is nearly an isotherm. The part of the ocean ridge geotherm lying at shallow depths is schematic, and will be discussed on a later page.

## Mineral Facies of Basalt at Pressures

Eclogite is a metamorphic rock defined by the assemblage pyrope-rich garnet plus a jadeite-rich pyroxene called omphacite. Omphacite, as noted wryly by Appelman (1966), is commonly defined as the green pyroxene occurring in eclogite, so the definitions are completely circular. However, there is no doubt that omphacite is essentially  $(Jd-Di)_{ss}$ . And there is no doubt that most eclogites have the essential bulk composition of gabbro (or basalt), an equivalence first noted by Fermor (1913). The minor minerals of eclogite include hypersthene, kyanite, and quartz. Yoder and Tilley (1957, 1962) showed that basalt could be converted quantitatively to eclogite at high pressures, and concluded that any of the major classes of basalt would be converted to the appropriate type of eclogite at depth in the earth. The oceanic crust is composed of major amounts of abyssal basalt, plus sediments. When such a crust is subducted at plate margins, it must eventually transform in large part to eclogite, whose density is about  $3.5 \text{ g/cm}^3$  as compared to about  $2.9 \text{ g/cm}^3$  for basalt. Anderson (1979) has suggested that it is the fate of such material to accumulate in the mantle as a perched eclogite layer between 220 and 400 km deep in the earth. If so, eclogite would be the second most abundant silicate rock type in the earth, after peridotite.

The basalt-eclogite transformation arises primarily from the instability of plagioclase at high pressures. As noted in Chapter 19, both end members of plagioclase break down at pressures near 30 kbar. Albite will enter the pyroxene as jadeite, and anorthite will enter garnet as grossular and pyroxene as CaTs. The actual transition for natural basaltic material occurs over an interval between 10 and 20 kbar, as shown in Fig. 20.2.

In regionally metamorphosed terrains, it is often possible to trace basaltic rocks showing pillows and other features of volcanic origin into higher-grade zones where the same strata occur as amphibolites. The chemical equivalence of amphibolite and hydrated basalt has thus long been recognized in the field. Yoder and Tilley (1962) demonstrated this equivalence dramatically by quenching basaltic magma with excess water directly to amphibolite. The metamorphic transformation is assumed to occur readily in subducted slabs carrying ocean floor material into the mantle. As the material sinks deeper along a subduction zone, rising temperatures will cause partial dehydration, and rising pressures, conversion to eclogite. The resulting rock type will be amphibolite at shallow depths and eclogite at greater depths, as shown in Fig. 20.2. The wet solidus for olivine tholeiite

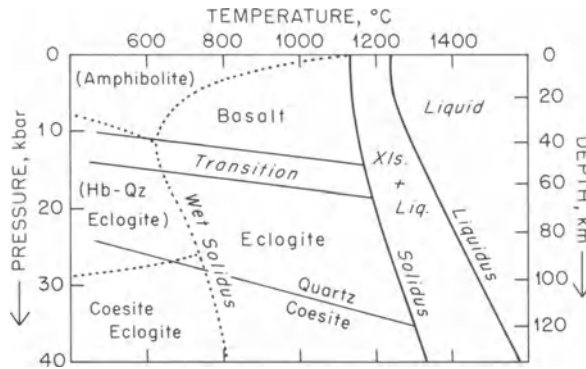


**Figure 20.2.** Mineral facies and melting relations for olivine tholeiite composition in the upper mantle. Dotted curves relate to system basalt-H<sub>2</sub>O. Basalt-eclogite transition after Yoder and Tilley (1963); melting relations and wet facies relations after Stern, Huang, and Wyllie (1975) and Wyllie (1979). Quartz-coesite curve from review by Weaver, Chipman, and Takahashi (1979).

is also shown in the figure. Basaltic melts cannot be generated at this solidus, because the source material *is* basaltic, and hence cannot be converted to basalt magma except at the liquidus. This objection holds for any source material of basalt composition; if total melting is required, the local amount of magma produced is likely to be too large to be consistent with geophysical evidence which implies an essentially solid (unmelted) mantle. Conceivably small nodules of eclogite distributed in a peridotite host, like raisins in a pudding, could become totally melted, but the relations of the dry solidus for lherzolite and the dry liquidus for eclogite at pressures less than 20 kbar (compare Figs. 20.1 and 20.2) give little support to such an idea, because the container might begin to melt before the liquid reached basalt composition.

Most schemes for basalt magma generation involve the partial melting of lherzolite, in greater or lesser degree according to the magma composition wanted. We shall consider briefly only a few of the central ideas about basalt magma genesis that involve phase diagrams.

### Melting at a Cusp for Abyssal Tholeiites

The so-called abyssal or ocean ridge tholeiites are the most voluminous basaltic rocks on earth, and apparently have been over most of geologic time. They are extruded at ridge crests and eventually carried away from the crests across the deeper ocean floor and perhaps ultimately down a subduction zone back into the mantle. In order to explain the localization of heat needed to produce basaltic magma with such high frequency at ocean ridges, it is usual to call upon a mantle “upwelling” or diapir under

the ridges, this being commonly identified as part of a mantle-wide convection system or else as a mantle plume. A central feature to be explained in any model for the origin of abyssal olivine tholeiite magma is the relatively constant major element chemistry combined with widely varying minor element and particularly large-ion lithophile (LIL) element chemistry. A fusion model which produces magma from a piercing point involving always the same mineral phases, but in which the amount of melt can vary between limits of, say, 5% to 30%, appears to meet most chemical requirements.

Melting of dry lherzolite at a cusp on the solidus was suggested by Presnall *et al.* (1979) as the major generator of abyssal tholeiite magma. Fig. 20.3, a reoriented blow-up of Fig. 20.1, shows the relevant  $T$ - $P$  projection. The heavy solidus curve is that determined experimentally to 20 kbar by Presnall *et al.*, for the system  $\text{CaO-Al}_2\text{O}_3\text{-MgO-SiO}_2$  (CAMS). The cusp on the solidus is a true invariant point involving the phases Fo, An, En, Di, Sp, and  $L$ ;  $\phi = 6$ ,  $c = 4$ ,  $W = 6 - 6 = 0$ . Three of the unvariant curves which meet at this point are drawn in the figure. The other three, i.e. (Fo), (Di), and (En), have not been located experimentally, but it is clear that their stable segments lie above the solidus. The cusp lies at 9 kbar, 1300°C.

Real lherzolite compositions are more complicated, of course, than the system CAMS. However, Presnall *et al.* were able to argue from the evidence of basalt chemistry and other types of experimental evidence that a similar cusp must control the natural melting relations, and that the ( $L$ ) curve will not move greatly as a function of composition. The principal

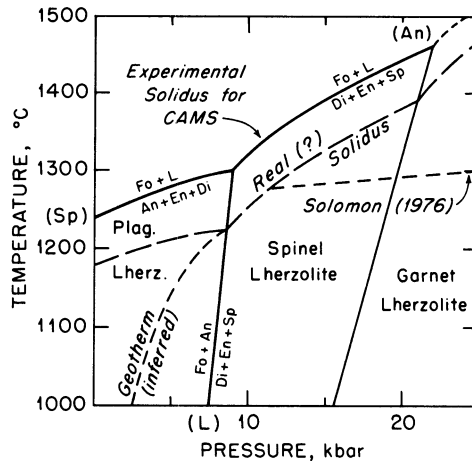


**Figure 20.3.** Experimental solidus for the system CAMS, showing cusp at invariant point, and estimated real solidus for natural lherzolite. Symbols in parentheses indicate phases missing from the reaction on the curve. Adiabatic part of ocean ridge geotherm is from Solomon (1976); geotherm below cusp is schematic. After Presnall *et al.* (1979).

effect of composition, they argued, would be to reduce the solidus temperatures to something like those shown by the dashed solidus in Fig. 20.3. They then argued that this geometry permits a relatively large range in the amount of melting  $F_L$  for a small range of temperature, thus allowing for LIL-rich magmas if  $F_L$  is small, and LIL-poor magmas (by dilution) if  $F_L$  is large.

The estimated cusp temperature (about 1225°C for natural lherzolite) is far above any normal geotherm for oceanic regions, and a thermal perturbation of some kind is needed to produce any melting beneath ocean ridges. The easiest (and perhaps the only) way to explain such a perturbation is to assume that hot mantle material rises from depth by plastic flow. How hot should such material be? The answer is, hot enough to cause the amount of melting we see, as volcanic products. The ocean ridge geotherm estimated by Solomon (1976) exactly suits the requirements of the model developed by Presnall *et al.*; it is shown as the adiabatic curve in Figs. 20.1 and 20.3. Fresh, undepleted (previously unmelted) garnet lherzolite would rise in the mantle-upwelling along this geotherm. At about 20 kbar, it would recrystallize to spinel lherzolite, and at about 11 or 12 kbar (near 40 km), it would begin to melt at the spinel lherzolite solidus. The heat absorbed in melting would prevent further adiabatic rise, and the partially melted source rock would tend to follow closely along the solidus, with further upwelling. At the cusp, the maximum amount of melting would occur for a given input of heat, because the cusp is a piercing point, resembling a eutectic except for its compositional freedom along solid solutions of the participating phases. At this point, magma would tend to separate from its residual crystals and to erupt. Note that if the eruption takes the magma to the surface adiabatically, it may cross the plagioclase lherzolite solidus and have the capacity to melt entrained crystals. If no crystals are entrained, the magma may become superheated (above the liquidus). Note that the average olivine tholeiite liquidus in Fig. 20.2 lies at about 1220°C, very near the assumed solidus temperature of lherzolite at the cusp. The remaining residual lherzolite from which the melt had been extracted, would now rise and cool along a steep geotherm, and then flow laterally, carrying the ocean floor piggyback.

An attractive consequence of melting at a cusp, as pointed out by Presnall *et al.*, is that the cusp may act as a thermal buffer that locks the geotherm in place. In Fig. 20.3, that part of the solidus between the cusp and the intersection with the adiabatic geotherm would play the role of thermal buffer. The action of such a buffer is as follows. Heat is absorbed during melting, and then is extracted from the mantle system by separation and eruption of magma. This cools the residual mantle, displacing it below the solidus. No further melting takes place until new, hot material is brought into place from below, sufficient to raise the geotherm once again to the cusp and the solidus. Thus the frequency and volume of eruption and magma removal are adjusted according to the delivery rate, from below, of

hot lherzolite. The ocean ridge geotherm oscillates into and out of the solidus with time, by the feedback or buffer effect, and averages out to a position like that in Fig. 20.3, for active spreading centers.

Presnall *et al.* have pointed out that volatiles such as  $H_2O$  and  $CO_2$  are not abundant enough in the source regions of abyssal tholeiites to be of importance to magma genesis, and this view is shared by Wyllie (1979, p. 470). The cusp-melting model permits the assumption that a continuous convection-driven upwelling occurs along the world-wide ocean ridge system, and that volcanism occurs only where and when the geotherm has risen to the solidus at or near the 9 kbar cusp. Thus all ocean ridge basalts are generated from about the same depth by about the same process, which accounts for their gross major-element similarity and yet allows for their differences in LIL abundances. No doubt fractional crystallization and magma mixing (Anderson, 1976; O'Hara, 1977; Rhodes *et al.*, 1979) also play important roles in modifying the final magma composition.

### Effect of Pressure on Silica Saturation

It has long been argued, on a variety of grounds, that alkali basalt magma is generated at greater depths than tholeiitic magma. It has also been argued, as discussed in Chapter 18, that alkali basalt represents smaller amounts of partial melting than tholeiite. Reasons for both these principles are clarified by reference to the system Fo-Ne-SiO<sub>2</sub>, the floor of the basalt tetrahedron, at high pressures (Kushiro, 1968). Fig. 20.4 shows the position of the field boundary  $L$  (Fo, Opx) at 1 atm and at several high pressures. This field boundary is cotectic at 10 kbar and above, and it terminates against a field for sodic minerals near the Ne-SiO<sub>2</sub> join. This termination (an isobaric invariant point) is where the first liquid forms, on melting of a model peridotitic composition consisting of Fo, En<sub>ss</sub>, and minor amounts of a sodic mineral. The invariant point shifts rapidly across the critical plane, into the *ne*-normative field, with pressure.

Consider the melting of bulk composition P, Fig. 20.5, at 20 kbar. (The principles involved are valid for all high pressures above a few kbar.) The first liquid forms at the invariant point (1). When all the sodic phase is used up, the liquid moves up in temperature along the cotectic toward (2). If it reaches (2), it has crossed the critical plane into *hy-ol* normative space, and is therefore akin to an olivine tholeiite. Even at this relatively large amount of melting,  $F_L$  is still around 0.2, so the amount of melt is reasonable by most criteria. A smaller amount of partial melt, between (1) and (2), would be *ne*-normative and akin to alkali basalt. This exercise illustrates how the degree of partial melting can profoundly affect the nature of the magma produced. The effect is very pronounced because the field boundary  $L$ (Fo,

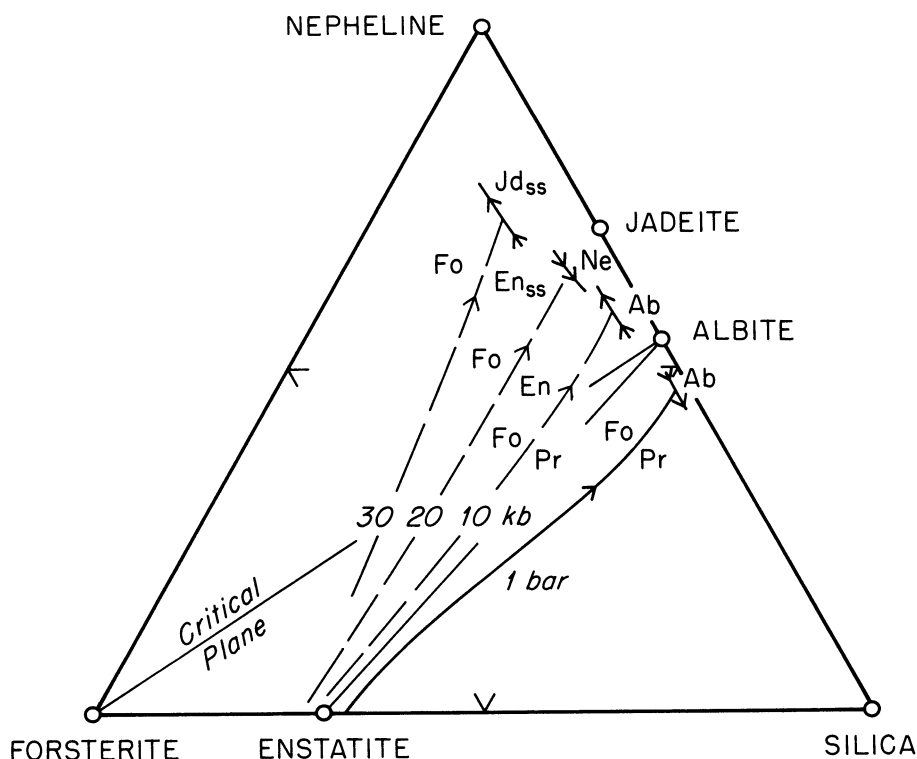


**Figure 20.4.** Floor of the basalt tetrahedron, Fo-Ne-SiO<sub>2</sub>, showing field boundaries at 10, 20, and 30 kbar compared to 1 atm. Trace of the critical plane of silica undersaturation is shown for reference. Main field boundary at each pressure is that for *L* (Fo, Opx); this is assumed to terminate against Ab at pressures up to 10 kbar, against Ne at 20 kbar, and against Jd<sub>ss</sub> at 30 kbar. High pressure boundaries are estimated by Kushiro (1968); 1 atm boundaries are from Schairer and Yoder (1961).

Opx) runs nearly towards the enstatite composition itself from the composition of the first melt.

By reference to Fig. 20.4, it can be seen that the higher the pressure, the more *ne*-normative (alkalic) the first melt will be. This illustrates the dependence of alkali basalt compositions on pressure.

## Wet Versus Dry Melting

Assuming anhydrous phases coexisting with an aqueous gas, the first melt will always be gas-saturated, but what happens with further melting depends on the H<sub>2</sub>O content of the system. Kushiro (1972) explored the effects of water content on magma composition, and by means of experiments on a

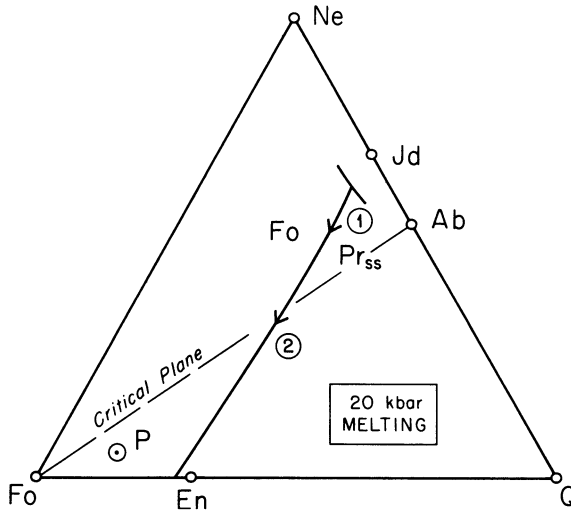


**Figure 20.5.** Melting of a model peridotite P containing crystals of Fo, En<sub>ss</sub>, and Ne or Jd at 20 kbar, dry. The first liquid formed at (1) is strongly nepheline-normative (silica undersaturated). With a large increase in the amount of melting, the liquid may reach a hypersthene normative composition (2) on the field boundary L (Fo, En<sub>ss</sub>). After Kushiro (1972).

few simple systems was able to make important generalizations that lend themselves nicely to a visual grasp of the matter. Although H<sub>2</sub>O may play a negligible role in the origin of magmas at ocean ridges, it must almost certainly play a role in downgoing slabs in subduction zones, as in the case of back-arc basins and in island arcs themselves.

It will be helpful to bear in mind several principles about the melting of mantle materials in the presence of an aqueous gas. The first is that incongruent *dissolution* occurs, well before melting, and that the gas tends to be very rich in silica. A review of Fig. 19.10 will illustrate the point in the case of Fo-SiO<sub>2</sub>-H<sub>2</sub>O. This effect means that the first *melt*, which effectively swallows up the gas phase, will also be rich in silica, even if it coexists with olivine. The process of melting in a ternary system containing H<sub>2</sub>O will now be reviewed with the aid of Figs. 20.6 and 20.7, which are isobaric 20 kbar X-X liquidus projections onto the composition base of the triangular T-X prism. The figures thus show the liquidus diagram for Fo-SiO<sub>2</sub>-H<sub>2</sub>O at 20 kbar. The field boundaries, with exaggerated curvature, are the gas-saturated boundaries L(Fo,G) and L(En,G) and the gas undersaturated cotectic boundary L(Fo,En). All bulk compositions within the triangle Fo - En - H<sub>2</sub>O yield, on melting, a eutectic liquid at 1295°C.

Bulk composition (1), Fig. 20.6, consists of Fo and En in the ratio of point P, and enough H<sub>2</sub>O to yield the plotted composition. For convenience, we will treat the gas component as part of the total "solid" composition, which for accuracy could be called the total *unmelted* composition. The

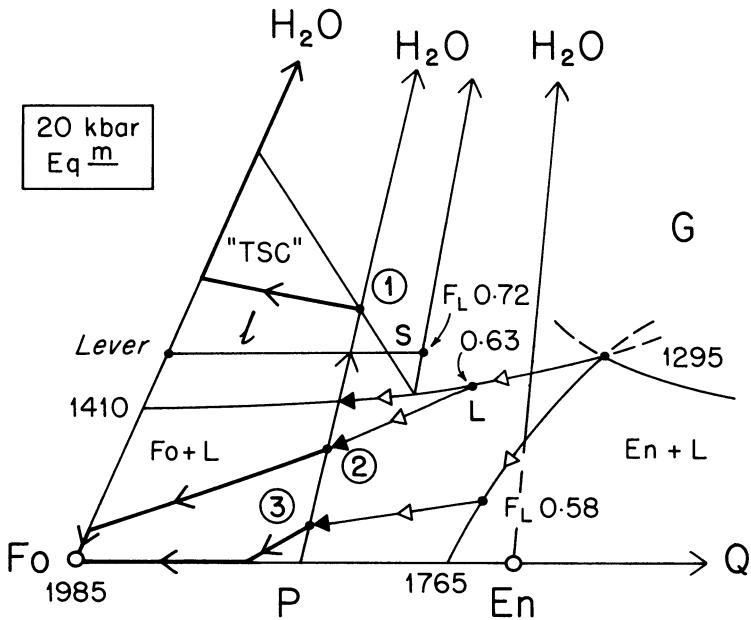


**Figure 20.6.** Equilibrium melting of three bulk compositions in the system  $\text{Fo-SiO}_2\text{-H}_2\text{O}$  at 20 kbar. The diagram is schematic. Heavy lines are "TSC" paths, all of which contain a gas component unless they lie on the sideline  $\text{Fo-Q}$ . Triangular arrowheads represent liquid compositions.

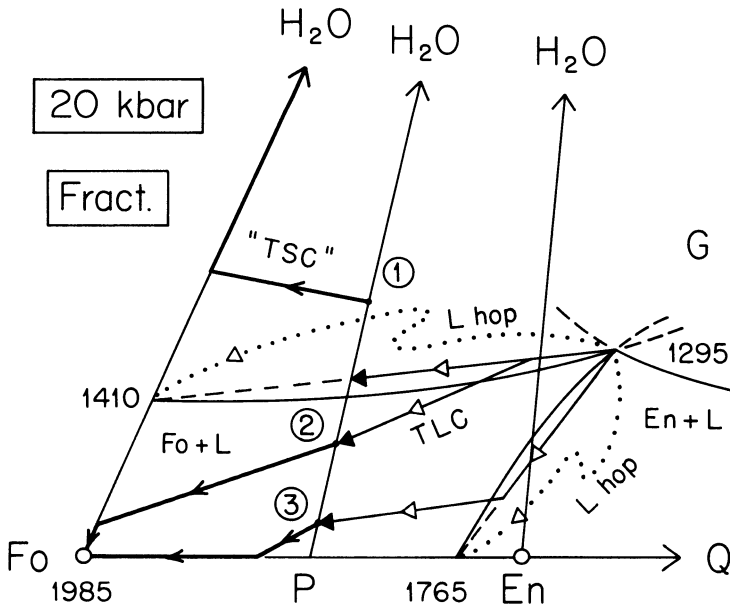


**Figure 20.7.** Fractional melting of the three bulk compositions shown in Figure 20.6. TLC paths follow mixing lines (dashed).

initial "TSC" contains more gas than the first liquid at 1295°C. As a result, the "TSC" becomes slightly enriched in H<sub>2</sub>O as it moves directly away from the isobaric eutectic. When the "TSC" reaches the sideline Fo-H<sub>2</sub>O, the crystals of En have been used up. The "TSC" now moves toward H<sub>2</sub>O, away from Fo, as the liquid moves along the boundary  $L(\text{Fo}, \text{G})$ . A sample "TSC" -  $L$  tie line is shown passing through BC (1). This tie line is a lever, but not the one desired for  $F_L$ . The desired gas-free lever is found by projecting the tie line from H<sub>2</sub>O, either onto the Fo-En join or an arbitrary line parallel to that join, as done in the figure. The illustration shows the case for  $F_L = 0.72$ . Melting is completed when the "TSC"-liquid tie line reaches the line P-H<sub>2</sub>O, at which point the liquid has the composition of P plus enough H<sub>2</sub>O to yield the plotted liquid composition shown by the black arrowhead. Throughout the process, gas has been present in excess of that needed to saturate the liquid.

For a lower H<sub>2</sub>O content, as in bulk composition (2), the system is gas-saturated only until the "TSC" reaches Fo. At this point, where  $F_L = 0.63$ , the gas phase disappears, because the liquid contains more H<sub>2</sub>O than the bulk composition and therefore must become more dilute in H<sub>2</sub>O as it approaches the bulk composition. It does this by moving directly toward Fo until it reaches the bulk composition.

For an even lower H<sub>2</sub>O content, as in bulk composition (3), the gas phase is exhausted while Fo and En both remain as crystals, and at this point the liquid leaves the eutectic to travel along the gas-absent curve  $L(\text{Fo}, \text{En})$ . This is the case most pertinent to melting in the mantle. When  $F_L = 0.58$ , En crystals are used up and the liquid moves directly toward Fo. At  $F_L = 0.58$ , the liquid is silica undersaturated (olivine-normative), whereas at certain smaller values of  $F_L$  it was quartz-normative. Thus we see that early hydrous liquids in equilibrium with Fo and En are *q*-normative whereas later, more dilute liquids obtained at higher temperatures are *ol*-normative. This result is *exactly the reverse* of that in the dry system Fo-Ne-SiO<sub>2</sub> (Fig. 20.5), so we see that H<sub>2</sub>O affects both the melting temperatures and the nature of silica saturation in early and late liquids. Fig. 20.7 shows the fractional melting paths for the same three bulk compositions treated in Fig. 20.6. In this case, the instantaneous liquids lie at discrete points (1295, 1410, 1765, and 1985°C) and the total liquid composition lies either at 1295 or along a mixing line to one of the other ILC's. The principles are familiar, and the melting histories should become evident with a bit of study. The same fundamental differences between wet and dry melting arise here as in the equilibrium case.

The behavior of wet versus dry melting in Fo-SiO<sub>2</sub>-H<sub>2</sub>O carries over into all systems based on this one; for example, Fo-Ne-SiO<sub>2</sub>-H<sub>2</sub>O, shown projected from the H<sub>2</sub>O apex at 20 kbar in Fig. 20.8. The dry boundary  $L(\text{Fo}, \text{En})$  is taken from Fig. 20.4. The wet (gas-saturated) boundary runs from Q to 1295. The region R-1765-1295-Q is the projected surface for  $L(\text{Fo}, \text{En})$  at varying water contents; it is the ternary extension of the gas-

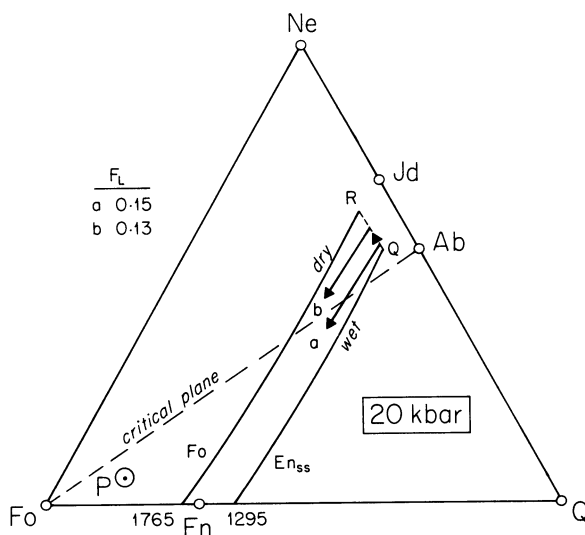


**Figure 20.8.** Projection from  $H_2O$  onto the anhydrous base of the basalt tetrahedron, showing contrasting melting paths for a relatively water-rich bulk composition (path *a*) and a relatively water poor one (path *b*) at 20 kbar total pressure. The anhydrous bulk composition is represented by the model peridotite P. The line 1765-R is the trace of the dry boundary *L* (Fo,  $En_{ss}$ ), whereas the line 1295-Q is its gas-saturated counterpart. After Kushiro (1972).

absent curve  $L(Fo, En)$  in Figs. 20.6 and 20.7. Melting of a model peridotite P containing a small amount of a free gas phase will always yield liquid Q at first. As melting continues, the liquid will begin to move toward R as soon as the free gas phase is used up, and will thereby become more alkalic. As soon as the sodic phase is consumed, the liquid will move, with further melting, along path *a*, and may eventually become *hy*-normative. If the initial composition contains an even smaller amount of  $H_2O$ , the liquid will depart point Q sooner and move further toward R before the sodic phase is consumed, thereafter following along path *b*. We therefore see that for roughly equivalent amounts of melting, the lower the  $H_2O$  content of the starting mixture, the more alkalic the final liquid. According to this principle, both alkali basalt and olivine tholeiite can be produced from the same source material, depending only on the  $H_2O$  content. Larger  $H_2O$  contents tend to produce more silicated melts, whereas smaller  $H_2O$  contents tend to produce more alkalic melts. For comparison, note that under  $H_2O$ -absent conditions, the transition from alkalic to silica saturated melts requires different degrees of partial melting.

The same principles of wet versus dry melting are seen in the system Fo-Di-SiO<sub>2</sub>-H<sub>2</sub>O at 20 kbar, Fig. 20.9. Here again, path *a* represents a higher initial  $H_2O$  content and path *b* a lower one. The initial liquid for all cases involving a free gas phase is X, which is *q*-normative. The liquid moves a variable distance toward W, depending on the  $H_2O$  content, before Di is

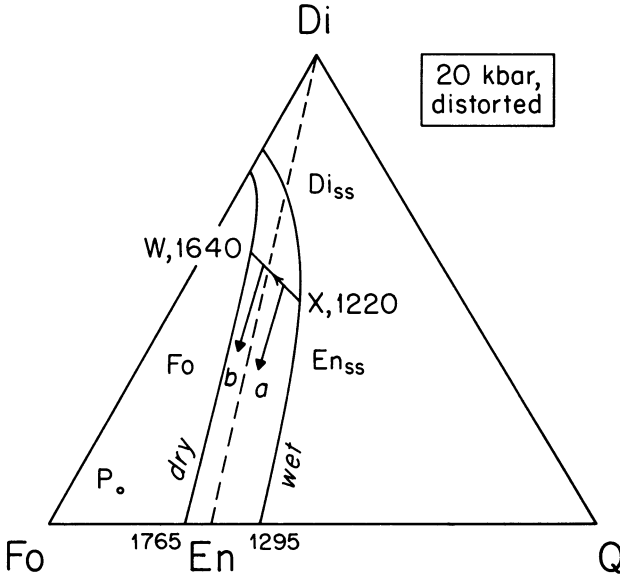


**Figure 20.9.** Projection from H<sub>2</sub>O onto the anhydrous base of the tetrahedron Fo-Di-Q-H<sub>2</sub>O at 20 kbar, showing contrasting melting paths for a peridotite P with a relatively large amount of water (path *a*) and relatively little water (path *b*). The line 1765-W is the dry boundary *L* (Fo, En<sub>ss</sub>); the line 1295-X is the corresponding gas-saturated boundary; and the line WX is the trace of the point *L* (Fo, Di<sub>ss</sub>, En<sub>ss</sub>), with H<sub>2</sub>O content of the system varying from zero at W to a maximum at X. Compare Figure 18.18 (10 kbar dry) and 19.13 (20 kbar wet) for approximately scale-free relations. Modified (by distortion) from Kushiro (1972).

consumed. The smaller the H<sub>2</sub>O content, the further toward W the liquid will move. Path *b* yields an *ol*-normative melt, and Kushiro (1972) showed that this is an adequate proxy for alkali basalt.

In summary, the initial liquids produced in dry melting are alkalic, the more so the higher the pressure. At higher pressures, more melting is required for the liquid to cross the critical plane toward higher silica saturation. In contrast, the first liquid produced in wet melting is always less alkalic and more silicic than in the dry case, and larger degrees of partial melting (or a lower water content) are required to produce alkalic liquids. The ultimate cause of the wet melting behavior is the sharply incongruent dissolution of silicates by H<sub>2</sub>O, to form a relatively silica-rich vapor which enters the first melt.

### Carbon Dioxide and the ZIVC Reaction

When CO<sub>2</sub> and H<sub>2</sub>O are mixed at low to moderate pressures the effect on melting is dominated by the H<sub>2</sub>O, which is more soluble than CO<sub>2</sub> in silicate melts (Fig. 19.20). Fig. 20.10 illustrates this principle in terms of a model

system A-CO<sub>2</sub>-H<sub>2</sub>O containing a hydrous crystalline phase H and an anhydrous phase (or assemblage) A. Fig. 20.10a is an isobaric, isothermal section showing a large field of liquid intervening between H and an H<sub>2</sub>O-rich gas. The smaller inset to this part of the figure, labelled T<sub>1</sub>, shows the relations where the liquid composition just touches the three-phase triangle AHG. This triangle is a *vapor buffer* (gas buffer) because at constant P, T, the composition of the gas phase is uniquely specified by the assemblage of the hydrous mineral breaking down to its reaction products. Such a geometry exists over a range of pressures and temperatures, within which the vapor composition changes over a certain range. The P-T-X region in which the AHG assemblage occurs was called by Eggler (1977, 1978) a *zone of invariant vapor composition*, or ZIVC. In such a region, all compositions within the ZIVC melt at a single temperature, as shown by the solidus in the section a-a', Fig. 20.10. Moreover, the liquid produced is always of the same composition. In the case where the hydrous phase is amphibole, the vapor has the composition X<sub>CO<sub>2</sub></sub> ≈ 0.8, and the solidus of the ZIVC is the upper stability limit of amphibole when gas is present. The first melt produced is judged to be nephelinitic, and more silicic melts are judged to arise only if the vapor composition is H<sub>2</sub>O-rich and the initial melting reaction takes place outside the ZIVC toward more gas-rich compositions (Eggler and Holloway, 1977).

The T<sub>2</sub> section of Fig. 20.10 shows the case where the temperature has risen above the ZIVC contact and the hydrous phase has been isolated from the gas by the tielines A + L. At this stage, both liquid and gas have become more CO<sub>2</sub>-rich, and the gas buffer no longer exists.

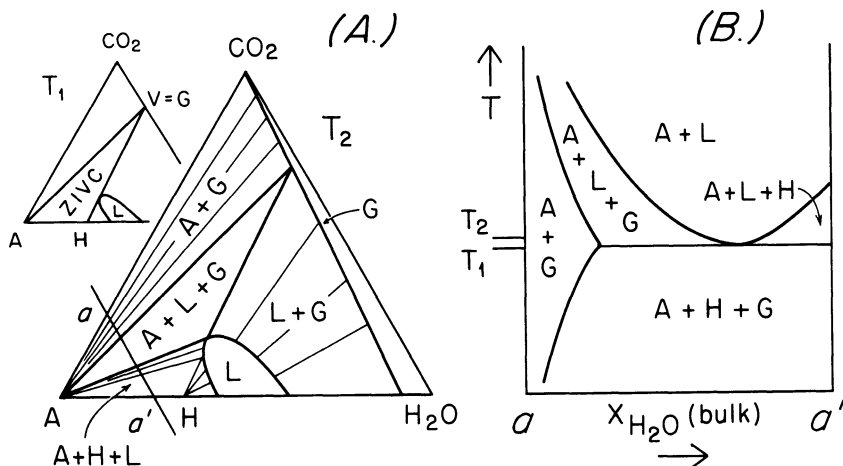


**Figure 20.10.** Model system A-CO<sub>2</sub>-H<sub>2</sub>O in two isobaric, isothermal sections (A) and in T-X section along line a-a' (B). A is an anhydrous phase, and V = G = gas. The conditions at temperature T<sub>1</sub> show Eggler's conception of a "ZIVC" (zone of invariant vapor composition). After Eggler and Holloway (1977).

The concept of the ZIVC appears to be experimentally valuable in helping to locate the gas composition and the limit of amphibole stability. The utility of the name ZIVC has been questioned, however, by Wyllie (1978, 1979), who finds that the range of isobarically invariant vapor compositions is extreme over a wide range of pressures. Hence, for our final example, we may take a brief look at Wyllie's view of mantle melting in subduction zones where H<sub>2</sub>O and CO<sub>2</sub> are important components.

### Peridotite-CO<sub>2</sub>-H<sub>2</sub>O Solids

Although H<sub>2</sub>O has the dominant effect on melting temperatures at low pressures, the solidus temperature of peridotite-H<sub>2</sub>O changes very little in the region 10–40 kbar, as shown by the H<sub>2</sub>O solidus trace in Fig. 20.11. In contrast, the effect of CO<sub>2</sub> on melting becomes large over the region 20–30 kbar, as shown by the CO<sub>2</sub> solidus in the figure. This effect occurs because dolomite peridotite melts more readily than the assemblage spinel peridotite-CO<sub>2</sub>. This matter needs a bit of explanation.

The carbonation of peridotite at high pressures was discovered by Wyllie and Huang (1975, 1976) and Eggler (1976). It occurs, for temperatures in the range 1000–1200°C, over a pressure range from about 15 to 40 kbar. By adding CO<sub>2</sub> to peridotite, at increasing pressure, one first obtains dolomite<sub>ss</sub>, then magnesite<sub>ss</sub> with orthopyroxene, then magnesite<sub>ss</sub> with quartz and coesite. By addition of about 23% CO<sub>2</sub>, a peridotite at 1100°C, 40 kbar can be completely transformed to a coesite - magnesite - garnet marble (Wyllie, 1979). The magnesite facies of peridotite, however, is of minor interest here, because it is the dolomite facies that undergoes melting in the region of interest. The dolomite carbonation reaction, which requires only about 5% CO<sub>2</sub> for completion, is reaction (6) of Wyllie's papers:



The location of the reaction curve is indicated in the *P-T* projection of Fig. 20.11. Since this is a carbonation reaction, it has a positive slope, so that pressure favors the smaller volume (CaMg(CO<sub>3</sub>)<sub>2</sub> crystals) and temperature favors the larger volume (CO<sub>2</sub> gas).

The intersection of the carbonation reaction with the solidus generates a cusp on the solidus, just as in the case of the plagioclase/spinel lherzolite cusp discussed earlier in this chapter. Such cusps are required by law (Schreinemakers' rules), as we have learned. The difference between this cusp and the others we have studied is in its magnitude, involving a recurvature of some 130°C from the maximum on the CO<sub>2</sub>-saturated spinel lherzolite solidus to the invariant point at about 26 kbar, 1200°C. Why should this effect be so large? The clue lies in the carbonation reaction itself, wherein pressure favors the aggregation of CO<sub>3</sub> groups around

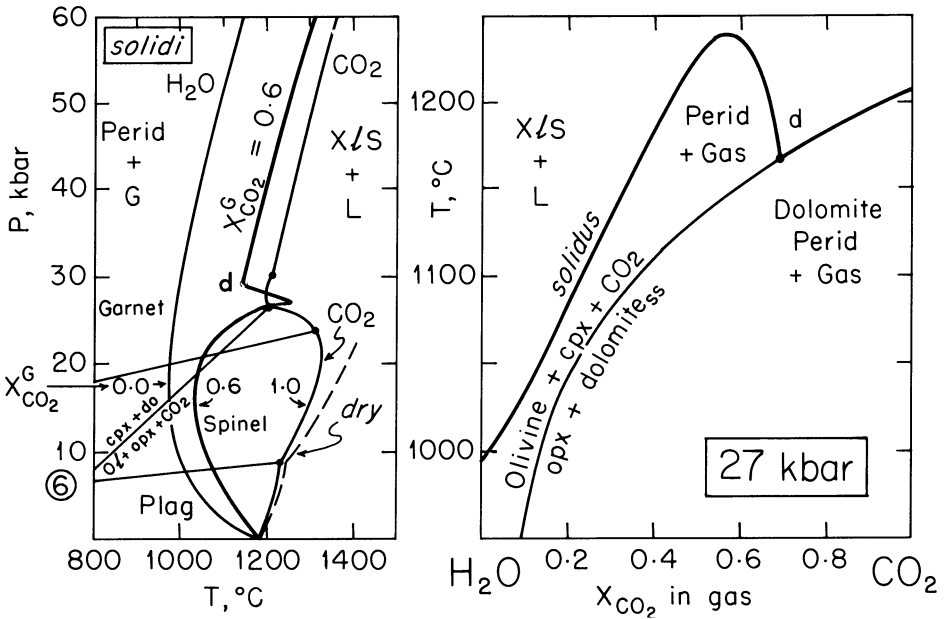


**Figure 20.11.** Model system peridotite-CO<sub>2</sub>-H<sub>2</sub>O in *P-T* and *T-X<sub>CO<sub>2</sub></sub>* projections, after Wyllie (1978, 1979). Fields of hornblende and phlogopite are omitted. The *P-T* projection shows the solidi for H<sub>2</sub>O, for CO<sub>2</sub>, and for a constant gas composition  $X_{CO_2} = CO_2 / (CO_2 + H_2O) = 0.6$  (molar). The dashed line is the dry solidus for an average peridotite (in part from Presnall *et al.*, 1979). A thermal maximum occurs at about 27 kbar on the solidus for  $X_{CO_2} = 0.6$ . This maximum is one of a family of maxima, near this pressure, for a range of  $X_{CO_2}$ . The same maximum appears in the *T-X* diagram, where the solidus is mapped at 27 kbar for the entire range of  $X_{CO_2}$ . The thermal maximum separates the region of basaltic magmas, at low pressures or low  $X_{CO_2}$ , from the region of kimberlitic magmas, at high pressures or high  $X_{CO_2}$ .

divalent cations rather than the alternative, CO<sub>2</sub> gas. If this happens in the solid state, why should it not also happen in the liquid? It does, as many experimental studies have shown: above 26 kbar, liquids become very carbonate-rich (Wyllie and Huang, 1975; other references in Egglar and Holloway, 1977, p. 25). The large scale of the melting cusp for carbonated peridotite arises from a large increase in the solubility of CO<sub>2</sub> in peridotitic melts over the range 20–30 kbar. This large increase in solubility, related to the subsolidus crystal structure, dramatically illustrates the connection between melt structure and crystal structure expounded by Ubbelohde (1965) and mentioned in Chapter 3 of this book.

When H<sub>2</sub>O and CO<sub>2</sub> are mixed with peridotite, the effect upon the solidus is intricate. At pressures below 20 kbar, the H<sub>2</sub>O effect is dominant (Fig. 19.20), but at higher pressures the CO<sub>2</sub> effect becomes dominant because in this region, the solubility of H<sub>2</sub>O in the melt changes only slightly, whereas the solubility of CO<sub>2</sub> changes radically. The heavy curve

in the  $P$ - $T$  projection of Fig. 20.11 illustrates the case for a constant gas composition  $X_{\text{CO}_2} = 0.6$ . Under this constraint, the solidus rises to a *thermal maximum* at about 27 kbar, and then changes to a new minimum near 29 kbar before rising with pressure thereafter. The thermal maximum is one of a family obtained over the whole range of  $X_{\text{CO}_2}$ , and this family of maxima generates a pronounced thermal ridge in  $P$ - $X_{\text{CO}_2}$  space, lying between pressures of 23 and 30 kbar for vapor compositions  $X_{\text{CO}_2} = 1.0$  to 0.2 (Wyllie, 1978, 1979).

The thermal maximum is illustrated by the heavy solidus curve in the 27 kbar, isobaric  $T$ - $X$  projection from peridotite -  $\text{CO}_2$  -  $\text{H}_2\text{O}$  with excess vapor in Fig. 20.11. From the maximum near  $X_{\text{CO}_2} = 0.6$ , the solidus drops steeply toward that for pure  $\text{H}_2\text{O}$ , and steeply also toward a local minimum  $d$  at  $X_{\text{CO}_2} = 0.7$ , where the solidus merges with the decarbonation reaction. The point  $d$  gives the isobaric invariant vapor composition corresponding to what Egger (1977) termed the ZIVC. The locus of  $d$  in  $P$ - $T$  projection gives the solidus curve for dolomite peridotite - vapor, with vapor composition buffered to values given by the locus of  $d$  in  $P$ - $X$  projection. The maximum to the left of point  $d$  in Fig. 20.11 separates the region where  $\text{H}_2\text{O}$  dominates (at  $X_{\text{CO}_2} < 0.6$ ) from the region where  $\text{CO}_2$  dominates (at  $X_{\text{CO}_2} > 0.6$ ) the melting process. A series of isobaric sections from 25 to 30 kbar would show this maximum moving across the diagram from  $X_{\text{CO}_2} \approx 0.9$  at 25 kbar to  $X_{\text{CO}_2} \approx 0.15$  at 30 kbar, with point  $d$  following along the decarbonation curve (Wyllie, 1979). The thermal maximum on the solidus is thus also a compositional divide in  $X_{\text{CO}_2}$ .

The thermal maximum on the peridotite -  $\text{CO}_2$  -  $\text{H}_2\text{O}$  solidus separates the region of basaltic (or andesitic) magmas at low pressures from the region of carbonatitic or kimberlitic magmas at high pressures (above about 27 kbar). As pressures rise toward 25 kbar, basaltic magmas will tend to contain more  $\text{CO}_2$  and have increasingly alkalic affinities. The carbonate-rich composition of melts produced at pressures above 30 kbar helps to explain the deep origin of kimberlitic magmas.

The wide range of gas compositions expressed by the locus of point  $d$  (Fig. 20.11) over the pressure range 25–30 kbar shows one reason why Wyllie (1978, 1979) questions the name ZIVC applied by Egger to a univariant assemblage including vapor: the vapor composition cannot usefully be described as invariant when it changes over nearly the whole range of  $X_{\text{CO}_2}$  in a small interval of pressure.

## Summary and Comment

Both Wyllie (1979) and Presnall *et al.* (1979) agree that  $\text{H}_2\text{O}$  and  $\text{CO}_2$  are of minor importance in the production of abyssal tholeiites at ocean ridges. Melting at a cusp on the solidus for dry spinel lherzolite, near 9 kbar, may

account for most of the earth's basaltic magma and, at the same time, fix the geotherm near 9 kbar under ocean ridges.

The work of Kushiro (e.g. 1972) on simple silicate systems with and without H<sub>2</sub>O provides a fundamental understanding of why high pressure favors more alkalic magmas, whereas low pressure favors more silicic magmas. It also shows why the presence of H<sub>2</sub>O generates first melts that are silica-rich, because H<sub>2</sub>O selectively dissolves silica out of the mantle minerals before melting occurs. Kushiro's work also nicely illustrates the dilution effect of partial melting, in which more alkalic initial liquids become more silicic by dilution as they incorporate more and more of the residual mantle minerals.

Eggler (1974) extended these principles by showing that high CO<sub>2</sub> pressure also favors alkalic magmas. To a limited extent, the addition of CO<sub>2</sub> can be regarded as simple dilution of the H<sub>2</sub>O content toward the dry condition at moderate pressures. This analogy breaks down at high pressures where CO<sub>2</sub> solubility rises markedly in the liquids.

The work of two major research groups led by Eggler and by Wyllie has shed much light on the generation of magmas in subduction zones or other parts of the earth where CO<sub>2</sub> and H<sub>2</sub>O play important roles. Both groups agree that magmas generated at pressures above 30 kbar are carbonate-rich, with either nephelinitic or kimberlitic affinities. It is perhaps worth suggesting, in this regard, that no *dry CO<sub>2</sub> free* magmas are known from the  $P > 30$  kbar range, and that they may not, indeed, occur in the earth at such pressures: note that the peridotite solidus and the geotherms diverge strongly above 30 kbar. At high pressures, CO<sub>2</sub> (and to a lesser extent H<sub>2</sub>O) are probably essential to melting. The generation of diamond-bearing, phlogopite-bearing, carbonate-rich kimberlite magmas beneath shield areas furnishes abundant evidence for the role of carbon, CO<sub>2</sub>, and H<sub>2</sub>O in the deeper parts of the upper mantle. Are these volatiles recycled from the earth's surface? If so, it would be nice to know how they get from the subduction zones to the subcratonic areas from which they reappear.

It seems to me that the carbonation of peridotite and the attendant increase in CO<sub>2</sub> solubility of peridotite melts represents a discovery of profound importance. Not only are the deep occurrence of carbonate-rich magmas and the shallow occurrence of hydrous magmas thereby clarified, but also the structural properties of silicate-carbonate melts are illuminated. The principle of melting at a cusp receives strong support from the work of Presnall *et al.* (1979) and Wyllie (1978), and it greatly strengthens the notion that the melt structure bears important resemblances to the crystalline structure of the materials being melted. Cusps always occur where subsolidus phase transformations or reactions intersect the solidus, and the large size of the carbonated peridotite cusp suggests that the correspondence between crystal and liquid structures is meaningfully large. An appreciation of this fact can improve our ability to predict melting behavior not readily

accessible to experiment or observation, for example in the core of the earth or in the deep mantle at earlier stages of earth history, or in other planetary bodies. The interrelation of crystal and liquid structures also receives important confirmation in the quasi-crystalline model for silicate melts being developed by Burnham (e.g. 1979), who has been able to predict phase diagrams accurately using the model.

This leads me to peroration on the value of experimentally determined phase diagrams in igneous petrology. It has long been a widely recognized goal in petrology to calculate phase diagrams from thermodynamic principles, knowing the ideal or non-ideal mixing properties of solid and liquid solutions in detail. Such efforts are highly valuable, as we have already seen, for example, in Waldbaum and Thompson's (1969) calculation of equilibria in the system Ab-Or (Chapter 15). And they are valuable in their predictive power, especially for regions inaccessible to easy experimentation, or as preparation for experimental work, to avoid making an excessive number of runs. But the extraction and extrapolation of thermodynamic data from calorimetry alone will always be beset with problems, in part related to disorder and unforeseen phase transformations, in part related to poorly understood pre-melting and pre-freezing phenomena, and in part related to the minuscule change in the Gibbs free energy of many geologically important reactions.

As an example of the latter problem, the latest tables of thermodynamic data (Robie, Hemingway, and Fisher, 1978) predict the stable coexistence of forsterite and silica at 1500°C, whereas we all know that protoenstatite is stable instead (Fig. 10.1) in experimental runs, and that enstatite is stable instead in nature. The trouble is caused in part by inadequate calorimetric data, and can be overcome by reevaluating the entropy of orthopyroxene from observed equilibria in a lava lake (Morse, 1979). But the experimental truth was simply arrived at with a few runs by Bowen and Andersen more than 65 years ago, and these experiments were vastly cheaper and easier to make than modern experiments by solution calorimetry. The phase equilibrium diagram is, in itself, a kind of calorimeter, as emphasized by Zen (1977).

The carbonation of peridotite at high pressures, discovered experimentally by Wyllie and Huang (1975, 1976) and Eggler (1976), represents a quantum leap in our understanding of physical chemistry and melt structure, and goodness knows how long it would take to reproduce the result from thermodynamic calculations alone. In fact, Ellis and Wyllie (1979) have once again turned the tables to derive thermodynamic data from the phase equilibria.

I therefore fail to foresee the end of productive experimental studies of phase equilibria at any time in the future. That we need continually improved thermodynamic data, from calorimetry as well as from phase equilibria studies, is also obvious. We also need improved crystallographic data, particularly for iron rich pyroxenes. The experimentalist is an empi-

ricist, and may often feel like the fellow who says, I know more than I realize about this thing. An experimentally reversed equilibrium curve, or experimentally produced carbonate mineral, represents an invaluable kind of knowledge, but it is the thermodynamic data and the theoretical analysis that help us realize what those experimental truths mean.

## Appendix 1

# Chemical Calculations

### Appendix 1A: CIPW Norm Calculation Procedures

**Note:** These rules have been abridged for the most common rocks. They omit certain contingent calculations which must be observed if the rock is unusual or if rigorous accuracy is required. See form on pp. 432–433 for guidance in the calculations

1. Determine for each oxide the *molecular number* (divide Wt.% by Mol. Wt.). Multiply by 1000 to clear of decimals. Throw away any result less than 2 unless it is  $K_2O$ .
2. Add  $MnO$  to  $FeO$  if  $MnO \geq 2$ .  
Make normative minerals as follows. Every time you use some of an oxide, enter it as debit against the analysis. Cross off all oxides when they are used up.
3. Apatite (*ap*) All  $P_2O_5$  + 3.33 times as much  $CaO$  as there was  $P_2O_5$ .
4. Magnetite (*mt*) All  $Fe_2O_3$  + equal amount of  $FeO$ .
5. Ilmenite (*il*) All  $TiO_2$  + equal amount of  $FeO$ .
6. Orthoclase (*or*) All  $K_2O$  + equal amount of  $Al_2O_3$ .
7. Albite (provisional) (*ab*) All  $Na_2O$  + equal amount of  $Al_2O_3$ .
18. Anorthite (*an*) All the remaining  $Al_2O_3$  + equal amount of  $CaO$ .

<sup>1</sup> If the  $CaO$  is gone before the  $Al_2O_3$ , the excess  $Al_2O_3$  is called corundum (*c*).

9. Assign  $\text{SiO}_2 = 6or, 6ab, 2an.$

In the following calculations,  $M = \text{all remaining MgO} + \text{FeO}, X_{Mg} = \text{MgO}/M$

$N = \text{initial Na}_2\text{O}, K = \text{initial K}_2\text{O}$

$XS = (\text{SiO}_2 \text{ used} - \text{SiO}_2 \text{ initial})$

10. *di*. Make remaining CaO into *di*, with  $M = \text{CaO}$ . Assign  $\text{SiO}_2 = 2\text{CaO}$ .

11. *hy*. Make remaining M into *hy*. Assign  $\text{SiO}_2 = M$  to *hy*.  
FIND XS.

12. *q*. If  $XS \leq 0$ , change the sign, call it *q*, and go to step 17.

13. *hy+ol*. Let  $ol = 2XS, hy = M - ol$ . Assign  $\text{SiO}_2 = 1hy, \text{SiO}_2 = ol/2$ .

14. *ol*. If  $hy < 0$ , let  $ol = M, hy = 0$  and proceed.

FIND XS AGAIN. (If  $XS = 0$  go to step 17.)

15. *ne*. Make  $ne = XS/4, ab = N - ne$ . Assign  $\text{SiO}_2 = 2ne, \text{SiO}_2 = 6ab$ .

If  $ab < 0$  let  $ne = N, ab = 0$  and proceed.

FIND XS AGAIN. (If  $XS = 0$  go to step 17.)

16. *lc*. Make  $lc = XS/2, or = K - lc$ . Assign  $\text{SiO}_2 = 4lc, \text{SiO}_2 = 6or$ .

$XS = 0 \pm 1$  IF NO ERROR.

17. Mg/Fe TREATMENT. Complete *di, hy, ol* as follows.

$$\begin{array}{lll} di: wo = \text{CaO} & hy: en = hy(X_{Mg}) & ol: fo = ol(X_{Mg}) \\ en = \text{CaO}(X_{Mg}) & fs = hy - en & fa = ol - fo \\ fs = \text{CaO} - en & & \end{array}$$

18. WEIGHT NORM. Multiply first molecular number for each molecule times the molecular weight/1000 in column III. Add up end members for *fsp, di, hy, ol*. Add "Rest" at bottom of column IV. Sum should equal analysis sum  $\pm 0.5\%$ .

## Selected chemical analyses from Macdonald and Katsura (1964).

Spec. no.	14 C-14	15 C-15	16 C-16	17 C-17	18 C-18
SiO <sub>2</sub>	50.22	50.80	49.50	49.70	49.90
TiO <sub>2</sub>	2.08	1.93	2.10	2.48	2.31
Al <sub>2</sub> O <sub>3</sub>	15.14	15.25	15.38	14.83	14.65
Fe <sub>2</sub> O <sub>3</sub>	3.64	2.91	4.51	4.47	5.69
FeO	8.27	7.23	6.99	7.52	6.88
MnO	0.17	0.16	0.17	0.17	0.16
MgO	7.18	8.27	7.23	6.17	6.57
CaO	10.07	9.83	10.44	10.34	10.25
Na <sub>2</sub> O	1.93	2.15	2.10	2.13	2.15
K <sub>2</sub> O	0.33	0.28	0.39	0.25	0.26
H <sub>2</sub> O <sup>-</sup>	0.55	0.32	0.36	0.47	0.50
H <sub>2</sub> O <sup>+</sup>	0.73	0.75	0.88	1.01	0.82
P <sub>2</sub> O <sub>5</sub>	0.25	0.25	0.28	0.27	0.26
Total	100.56	100.13	100.33	99.81	100.40
<i>Q</i>	5.88	4.56	4.68	7.14	7.80
<i>or</i>	1.67	1.67	2.22	1.67	1.67
<i>ab</i>	16.24	17.82	17.82	17.82	17.82
<i>an</i>	31.69	31.41	31.41	30.02	29.75
<i>di</i> { <i>wo</i>	6.84	6.50	7.77	8.12	8.00
{ <i>en</i>	4.30	4.40	5.40	5.40	5.70
{ <i>fs</i>	2.11	1.58	1.72	2.11	1.58
<i>hy</i> { <i>en</i>	13.70	16.30	12.70	10.00	10.70
{ <i>fs</i>	6.86	6.34	4.22	4.09	2.77
<i>ol</i> { <i>fo</i>	—	—	—	—	—
{ <i>fa</i>	—	—	—	—	—
<i>mt</i>	5.34	4.18	6.50	6.50	8.35
<i>il</i>	3.95	3.65	3.95	4.71	4.41
<i>ap</i>	0.67	0.67	0.67	0.67	0.67

GROUP 1. No olivine.

Selected chemical analyses from Macdonald and  
Katsura (*continued*)

Spec. no.	13 C-65	14 C-66	15 C-70	16 C-69
SiO <sub>2</sub>	43.49	48.72	47.48	45.54
TiO <sub>2</sub>	3.38	2.19	2.63	2.85
Al <sub>2</sub> O <sub>3</sub>	16.66	15.11	17.42	17.61
Fe <sub>2</sub> O <sub>3</sub>	3.69	1.79	3.59	3.56
FeO	11.05	9.50	8.10	8.25
MnO	0.18	0.17	0.18	0.17
MgO	6.74	8.70	6.74	6.42
CaO	8.93	10.69	8.54	10.82
Na <sub>2</sub> O	2.35	1.85	3.12	2.74
K <sub>2</sub> O	0.25	0.28	1.20	0.70
H <sub>2</sub> O <sup>-</sup>	1.29	0.12	0.22	0.10
H <sub>2</sub> O <sup>+</sup>	1.41	0.72	0.40	0.60
P <sub>2</sub> O <sub>5</sub>	0.33	0.23	0.36	0.34
Total	99.75	100.07	99.98	99.70
<i>Q</i>	—	—	—	—
<i>or</i>	1.11	1.67	7.23	3.89
<i>ab</i>	19.91	15.72	26.20	23.06
<i>an</i>	34.47	31.97	30.02	33.92
<i>ne</i>	—	—	—	—
<i>di</i> { <i>wo</i>	3.36	8.47	4.06	7.42
{ <i>en</i>	1.90	5.10	2.60	4.70
{ <i>fs</i>	1.32	2.90	1.19	2.24
<i>hy</i> { <i>en</i>	8.40	16.40	4.60	0.60
{ <i>fs</i>	5.94	9.50	2.11	0.26
<i>ol</i> { <i>fo</i>	4.55	0.21	6.72	7.49
{ <i>fa</i>	3.57	0.10	3.47	3.98
<i>mt</i>	5.34	2.55	5.34	5.34
<i>il</i>	6.38	4.26	5.02	5.32
<i>ap</i>	0.67	0.34	1.01	0.67

GROUP 2. Olivine & hypersthene.

Spec. no.	8	9	10
	C-72	C-73	C-79
SiO <sub>2</sub>	47.99	50.25	49.79
TiO <sub>2</sub>	2.62	2.12	2.51
Al <sub>2</sub> O <sub>3</sub>	19.36	19.03	18.37
Fe <sub>2</sub> O <sub>3</sub>	5.83	4.53	6.03
FeO	5.17	5.50	4.82
MnO	0.21	0.22	0.22
MgO	4.39	3.11	4.01
CaO	6.54	5.98	6.68
Na <sub>2</sub> O	4.58	5.30	4.58
K <sub>2</sub> O	1.82	2.20	2.08
H <sub>2</sub> O <sup>-</sup>	0.17	0.40	0.32
H <sub>2</sub> O <sup>+</sup>	0.33	0.54	0.24
P <sub>2</sub> O <sub>5</sub>	0.63	1.14	0.56
Total	99.64	100.32	100.21
<i>Q</i>	—	—	—
<i>or</i>	10.56	12.79	12.23
<i>ab</i>	36.15	42.97	37.73
<i>an</i>	26.97	21.68	28.91
<i>ne</i>	1.42	0.85	0.57
<i>di</i> {	<i>wo</i>	0.81	0.23
	<i>en</i>	0.60	0.20
	<i>fs</i>	0.13	—
<i>hy</i> {	<i>en</i>	—	—
	<i>fs</i>	—	—
<i>ol</i> {	<i>fo</i>	7.28	5.32
	<i>fa</i>	0.51	2.55
<i>mt</i>	8.35	6.50	8.82
<i>il</i>	5.02	3.95	1.34
<i>ap</i>	1.34	2.69	1.34

GROUP 3. Nepheline.

CIPW Norm Form

Oxide	Wt. %	Mol. Wt.	Mol. No. <sup>a</sup>	Analysis No. _____ Subtractions	Petrographer _____ Calculations
SiO <sub>2</sub>	_____	60	_____		M = MgO+FeO after <i>il</i> =
Al <sub>2</sub> O <sub>3</sub>	_____	102	_____		
Fe <sub>2</sub> O <sub>3</sub>	_____	160	_____		X <sub>mg</sub> = MgO/M =
FeO	_____	72	_____		N = Na <sub>2</sub> O =
MnO	_____	71	_____		XS = (SiO <sub>2</sub> used-SiO <sub>2</sub> initial)
MgO	_____	40	_____		q =  XS<O  =
CaO	_____	56	_____		
Na <sub>2</sub> O	_____	62	_____		ol = 2XS =
K <sub>2</sub> O	_____	94	_____		ne = XS/4 =
P <sub>2</sub> O <sub>5</sub>	_____	142	_____		lc = XS/2 =
TiO <sub>2</sub>	_____	80	_____		
Rest	_____	("Rest" = H <sub>2</sub> O etc)			Analysis sum _____

Normative Minerals

I	II	III	IV
	SiO <sub>2</sub>	Mol. Wt./1000	Weight Norm <sup>b</sup>
<i>ap</i> (P+[CaO=3.33P])		.336	<i>ap</i>
<i>mt</i> (Fe'''+Fe'')		.232	<i>mt</i>
<i>il</i> (Ti+Fe'')		.152	<i>il</i>
<i>or</i> (K+Al)	(6K)	.556	<i>or</i>
<i>ab</i> (Na+Al)	(6Na)	.524	<i>ab</i>
<i>an</i> (Al+Ca)	(2Ca)	.278	<i>an</i>
		Total feldspar	
		100 An/(An+Ab)	
<i>di</i> (Ca+MgFe)	(2Ca)	.116	
			(for Σdi)
		.100	
		.132	<i>di</i>
(Let M= M - <i>w</i> <i>o</i> )			
<i>hy</i> (Mg+Fe)	Σ SiO <sub>2</sub> = (1M)	.100	
		.132	<i>hy</i>
<i>ol</i> (Mg+Fe)	(.5M)	.140	
			Use
			Half
			MgO,FeO
<i>ne</i> (Na+Al)	(2Na)	.204	<i>ol</i>
<i>q</i> (Si)	(1Si)	.284	<i>ne</i>
	Σ SiO <sub>2</sub> =	.060	<i>q</i>
			Rest
			Σ

<sup>a</sup>10<sup>3</sup> Wt. %/Mol. Wt.

<sup>b</sup>Mol. No. of first oxide in Col. I × Col. III

### Appendix 1B: Cation and Oxygen Units

#### CATION UNITS

Cation equivalents are obtained from weight percentages of formula units as follows. The molecular weight of the formula unit is divided by the number of cations in the formula to obtain the average weight per cation. The weight percentage of the formula unit in question is then divided by this average weight per cation. When this is done for the two or more components representing the composition in question, the results (cation equivalent proportions) are summed and divided through by the sum to obtain normalized cation equivalents. An example follows.

Problem: find the cation equivalent composition of En on the join Fo - SiO<sub>2</sub> from the weight percent composition, Fo 70.1%, SiO<sub>2</sub> 29.9%. The molecular weight of Mg<sub>2</sub>SiO<sub>4</sub> is 140.71 and there are three cations in the formula; the cation-averaged weight is then 140.71 / 3 = 46.90. The molecular weight of SiO<sub>2</sub> is 60.09, which is already normalized to one cation. We therefore obtain the following:

Enstatite composition, MgSiO<sub>3</sub>

	Wt. %		Cation wt.		Cation prop.	Cation equiv. (%)
Mg <sub>2</sub> SiO <sub>4</sub>	70.1	/	46.9	=	1.4947	75.0
SiO <sub>2</sub>	29.9	/	60.09	=	0.4976	25.0
					1.9923	100

And En plots at Fo 3 SiO<sub>2</sub> 1, as it should from the cation formulation described in Ch. 13.

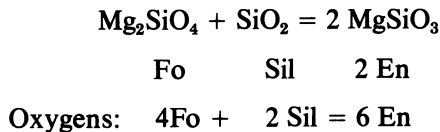
To obtain cation units from molecular units, simply multiply moles times the number of cations in the formula and normalize the results. Again using En as an example, we obtain the following table.

Enstatite composition MgSiO<sub>3</sub>

	Mole %		Cations		Cation prop.	Cation equiv. %
Mg <sub>2</sub> SiO <sub>4</sub>	50	×	3	=	150	75
SiO <sub>2</sub>	50	×	1	=	50	25

#### OXYGEN UNITS

Oxygen units are developed in an analogous way to cation units. We have



En therefore plots at  $\frac{2}{3}$  Fo,  $\frac{1}{3}$  Sil.

The oxygen-normalized molecular weights are as follows.

$$\text{Fo } 140.71/4 = 35.1775$$

$$\text{Sil } 60.09/2 = 30.045$$

$$\text{En } 100.40/3 = 33.467$$

Oxygen units are obtained from weight units as follows:

Enstatite composition $\text{MgSiO}_3$						
	Wt. %	/	Oxygen wt.	=	Oxygen prop.	Oxygen %
Fo	70.1	/	35.1775	=	1.9927	66.7
$\text{SiO}_2$	29.9	/	30.045	=	0.9952	33.3
					<u>2.9879</u>	<u>100</u>

From mole units, the calculation follows the previous example for cation units.

Enstatite composition $\text{MgSiO}_3$						
	Mole %		Oxygens	=	Oxygen prop.	Oxygen %
Fo	50	×	4	=	200	66.7
$\text{SiO}_2$	50	×	2	=	100	33.3
					<u>300</u>	<u>100</u>

## CATION NORM

Begin the calculation by obtaining a list of *cation numbers*: multiply each molecular number by the number of cations in the oxide formula, or better yet, use half molecular weights for oxides with two cations. Thus use 51 for  $\text{Al}_2\text{O}_3$ , 80 for  $\text{Fe}_2\text{O}_3$ , 31 for  $\text{Na}_2\text{O}$ , 47 for  $\text{K}_2\text{O}$ , and 71 for  $\text{P}_2\text{O}_5$ , and obtain the cation numbers directly by division. Now proceed as usual with the norm calculation, using the following rules:

$$\begin{array}{ll} \text{Ap} = \text{P} + 1.67\text{Ca} & \text{Hy} = \text{M} + \text{Si} \\ \text{Mt} = \text{Fe}''' + 0.5\text{Fe}'' & \text{Ol} = 2\text{XS} = \text{M} + 0.5\text{Si} \\ \text{Il} = \text{Ti} + \text{Fe}'' & \text{Ne} = \text{XS}/2 = \text{Na} + \text{Al} + \text{Si} \\ \text{Or} = \text{K} + \text{Al} + 3\text{Si} & \text{Lc} = \text{XS} = \text{K} + \text{Al} + 2\text{Si} \\ \text{Ab} = \text{Na} + \text{Al} + 3\text{Si} & \text{Q} = \text{Si} \\ \text{An} = \text{Al} + 0.5\text{Ca} + \text{Si} & \text{C} = \text{Al}/2. \\ \text{Di} = \text{Ca} + \text{M} + 2\text{Si} & \end{array}$$

Now add each row laterally to obtain the sum of each molecule, including Si. Then find the sum of all molecules (which should equal the original sum of the cation numbers  $\pm 1$ ), and divide each by the sum/100 to obtain the cation norm. Note that you can divide by the original cation sum/100 immediately to obtain the cation norm item by item. The results should add up to  $100 \pm 0.1\%$ . An example is shown in Table A1.1, after Barth (1962).

**Table A1.1.** Example of Cation Norm Calculation, Using Gough Island Olivine Basalt of Barth (1962, Table III-9)

Oxide	Wt. %	Equiv. Mol. Wt.	Cation No.	Normative Minerals	Normalized
SiO <sub>2</sub>	49.10	60	818	Ap = 8 + 1.67(8) = 21	1.18
TiO <sub>2</sub>	3.59	80	45	Mt = 36 + 18 = 54	3.04
Al <sub>2</sub> O <sub>3</sub>	16.21	51	318	Il = 45 + 45 = 90	5.06
Fe <sub>2</sub> O <sub>3</sub>	2.87	80	36	Or = 59 + 59 + 177 = 295	16.59
FeO	6.84	72	95	(Ab = 114 + 114 + 342 = 570)	
MnO	0.05	71	1	An = 73 + 145 + 145 = 363	20.42
MgO	5.04	40	126	Wo = 73 + 73 = 146	Di 16.42
CaO	8.90	56	159	Hy = 73 + 73 = 146	
Na <sub>2</sub> O	3.53	31	114	Ol = 86 + 43 = 129	7.26
K <sub>2</sub> O	2.76	47	59	Si 853	
P <sub>2</sub> O <sub>5</sub>	0.54	71	8	853 - 818 = 35; 35/2 = 18 for Ne	
H <sub>2</sub> O	0.47	—	—	Ab = 114 - 18 = 96	
				Ab = 96 + 96 + 288 = 480	27.00
			1778	Ne = 18 + 18 + 18 = 54	3.04
					1778
					100.01

The prescription for the cation norm given by Chayes and Métais (1964, p. 193) is erroneous and should not be used. However, the computer program used by Chayes (and many others) correctly calculates the cation norm as prescribed by Barth (F. Chayes, personal communication, 1980). The article by Chayes and Métais furnishes a useful comparison of cation and weight norms, and includes details of historical interest as well.

# Appendix 2

Annotated extract from *American Journal of Science*, Vol. 29, pages 151–217. Reproduced by permission of the Journal. Extract runs from p. 173–193 and p. 209–210 of the original.

## THE SYSTEM, MgO-FeO-SiO<sub>2</sub>.

N. L. BOWEN AND J. F. SCHAIRER.

### INTRODUCTION.<sup>1</sup>

In view of the great importance of ferromagnesian silicates as rock-forming minerals a study of equilibrium in the system, MgO-FeO-SiO<sub>2</sub>, may be expected to reveal facts and relations of much value in deducing the conditions of formation of many rocks. With these considerations in mind investigation of the system was undertaken. The procedure adopted and the results attained are here presented.

### A SERIES OF ISOTHERMAL PLANES.<sup>2</sup>

The salient features of the equilibrium relations of the metasilicate and of the orthosilicate solid solutions, individually, have now been pointed out. Although some aspects of the relations between the two series have been brought out by means of the metasilicate section, a complete picture of the composition of all the phases concerned in the equilibria is gained only with the aid of ternary figures. We shall therefore present a series of isothermal planes.<sup>15</sup>

<sup>15</sup> These figures, representing isothermal planes, are all drawn to true scale, the composition of all phases (including the solid solutions but excepting the magnesio-wüstites) being determined by the experimental results. Further information regarding these determinations is given under the head "Three Phase Triangles and Three Phase Boundaries."

<sup>1</sup>From *Bowen and Schairer* original, page 151.

<sup>2</sup>From *Bowen and Schairer* original, page 173.

The first to be discussed is that for 1550°, Fig. 9. At this temperature the liquid *a*, which is of orthosilicate composition, is in equilibrium with olivine whose composition lies at the point at the other end of the brace joining it with *a*. The equilibrium is binary, the brace being the device here adopted to indicate binary equilibrium. All the liquids *a-b* are in equilibrium with olivine, each with an olivine of different composition as indicated by the tie-lines. Any mixture whose composition is represented by a point in the triangle *aob* thus consists at 1550° of olivine and liquid, the composition of each of which is indicated by the ends of the tie-line passing through the point of composition of the mixture.

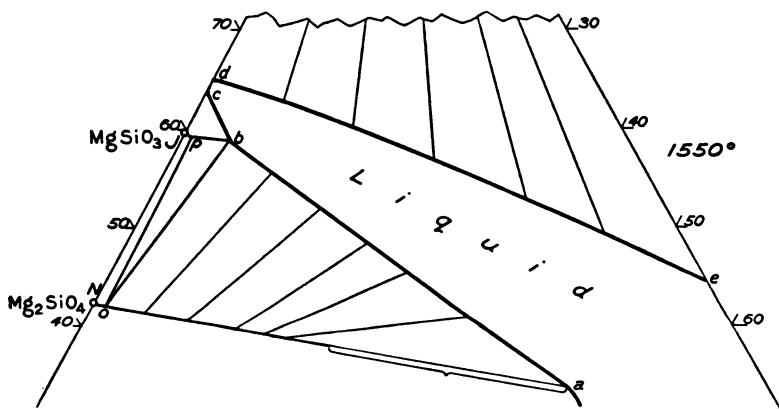


Fig. 9. Phase relations at 1550°. Truncated  $\text{SiO}_2$  apex = *T* in text. Cf. Fig. 11.

The liquid *b* is in equilibrium with both the olivine *o* and the pyroxene *p* and is therefore a point in the boundary curve *KL* of Fig. 5. All mixtures lying in the triangle *pbo* consist at 1550° of the three phases, liquid *b*, pyroxene *p*, and olivine *o*.

The liquids *b* to *c* are in equilibrium with clino-pyroxenes varying in composition from *p* to *J* and all mixtures in the area *cbpJ* thus consist at 1550° of liquid between *b* and *c* and pyroxene between *p* and *J*. Tie-lines are here omitted to avoid crowding.

The mixtures in the area *JpoN* are completely crystalline at 1550° and consist of pyroxene *p* to *J* and olivine *N* to *o*.

The liquids *d* to *e* are in equilibrium with cristobalite at 1550° and all mixtures in the triangle *deT* consist at 1550° of cristobalite and liquid whose composition is given by the tie-

<sup>3</sup>These folios are from Bowen and Schairer original.

line passing through the point indicating the total composition of the mixture. The tie-lines are thus lines radiating from the  $SiO_2$  apex here truncated to save space, but called  $T$  in this and subsequent figures.

The next isothermal plane (Fig. 10) is that for  $1527^\circ$ , the temperature of the point  $O$  of Fig. 5 at which the metasilicate join crosses the pyroxene-olivine boundary curve. The point is lettered  $O$  in Fig. 10 also. It is not an invariant point but is merely a limiting case of points having the properties of  $b$  in Fig. 9. The liquid  $O$  is in equilibrium with the pyroxene  $p$  (a binary relation indicated by a brace) and also

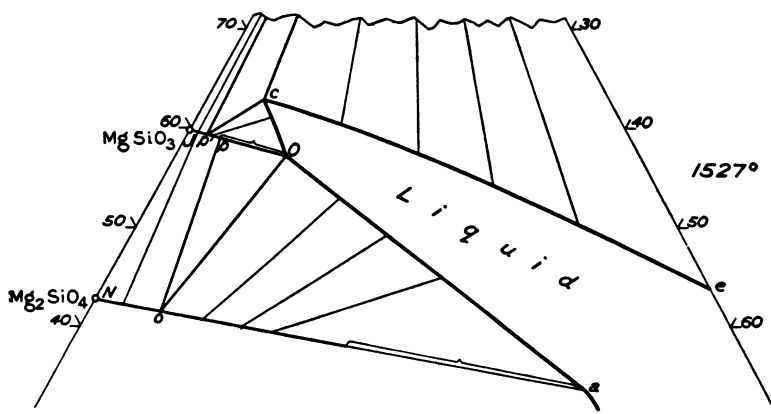


Fig. 10. Phase relations at  $1527^\circ$ . Truncated  $SiO_2$  apex =  $T$  in text.

with the olivine  $o$ . The liquids  $O$  to  $c$  are in equilibrium with pyroxenes  $p$  to  $p'$ . The liquid  $c$  is in equilibrium with the pyroxene  $p'$  and with cristobalite. All mixtures in the triangle  $cp'T$  consist of the three phases pyroxene  $p'$ , cristobalite, and liquid  $c$ . All mixtures in the triangle  $p'JT$  consist of the two phases cristobalite and a pyroxene between  $p'$  and  $J$ . All other areas have the same properties as their analogues in Fig. 9.

The next isothermal plane, Fig. 11, is that for  $1450^\circ$ . All other figures of this character have been limited on the low-silica side by the orthosilicate join and have been truncated on the high-silica side. In the present example the full triangle is shown in order to make clear the general appearance of the completed figures. This particular temperature is so treated because it is the only one at which the equilibrium involving magnesio-wüstite has been approximately determined.

The liquids *f* to *g* are in equilibrium with magnesio-wüstites and the liquid *f* is in equilibrium with both magnesio-wüstite *h* and olivine *o'*. The liquids *f* to *a* to *b* are in equilibrium with olivines.

One special feature may be pointed out. At 1527° (see Fig. 10) the pyroxene *p'*, which is in equilibrium with  $\text{SiO}_2$  and liquid, is more magnesian than the pyroxene *p*, which is in equilibrium with olivine and liquid. At 1400° (see Fig.

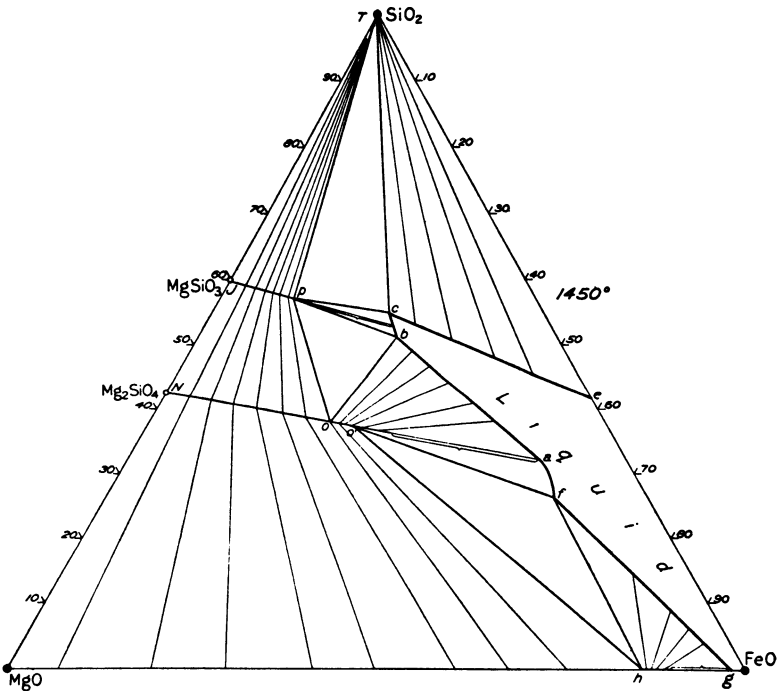


Fig. 11. Phase relations at 1450°.<sup>4</sup>

12) the opposite condition prevails, i.e., the pyroxene *S*, which is in equilibrium with  $\text{SiO}_2$  and liquid, is less magnesian than the pyroxene *p*, which is in equilibrium with olivine and liquid. At some intermediate temperature, therefore,  $\text{SiO}_2$  and liquid on the one hand and olivine and liquid on the other will be in equilibrium with the same pyroxene. Our determinations do not enable us to state definitely the temperature at which this condition prevails, but they indicate that it is probably not far from 1450°. In Fig. 11, therefore, the liquid *c* and  $\text{SiO}_2$

<sup>4</sup>See Notes on Appendix 2, page 459.

The System,  $MgO-FeO-SiO_2$ .

177

(tridymite) and also the liquid  $b$  and olivine  $o$  are shown in equilibrium with the same pyroxene  $p$ .

The next isothermal plane (Fig. 12) is that for the temperature  $1400^\circ$ , the temperature of the point  $R$  of Figs. 5 and 8, which is not an invariant point but merely the point of

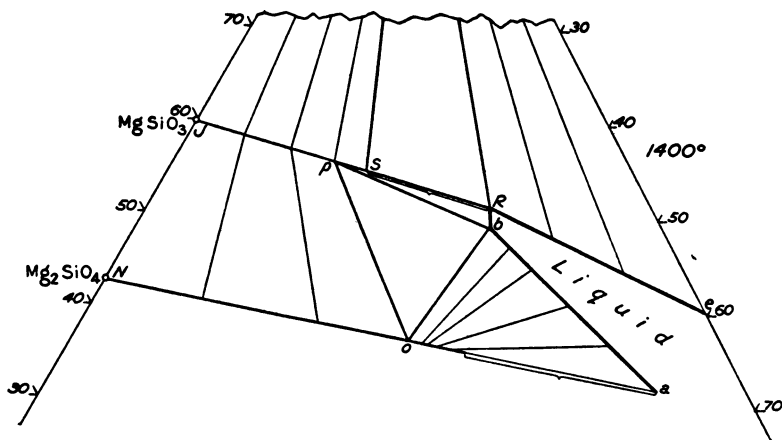


Fig. 12. Phase relations at  $1400^\circ$ . Truncated  $SiO_2$  apex =  $T$  in text.

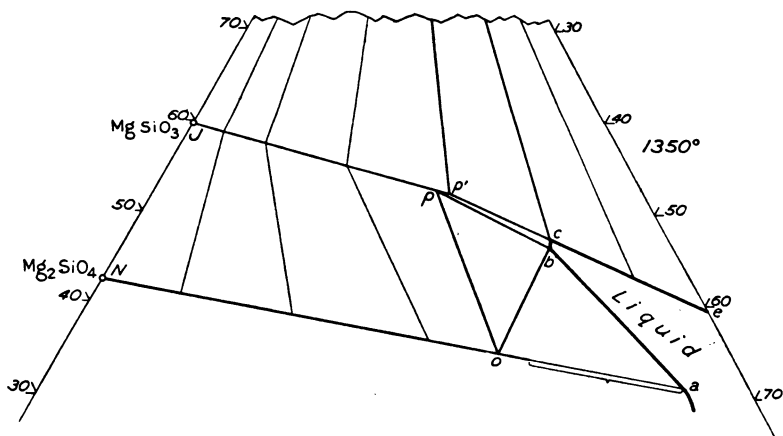


Fig. 13. Phase relations at  $1350^\circ$ . Truncated  $SiO_2$  apex =  $T$  in text.

intersection of the pyroxene-tridymite boundary curve with the metasilicate join. The liquid  $R$  is in equilibrium with the pyroxene  $S$  (the binary relation indicated by the same letters in Fig. 8) and with tridymite. All other areas have the properties of their analogues in former figures.

The next isothermal plane (Fig. 13) is that for  $1350^\circ$ , which

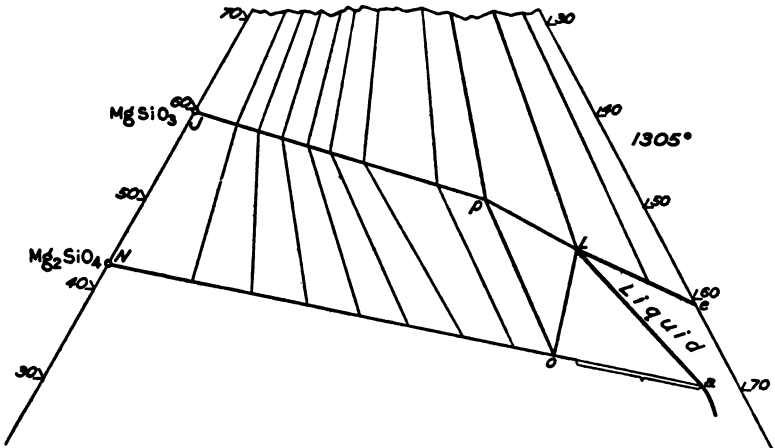


Fig. 14. Phase relations at 1305°. Truncated SiO<sub>2</sub> apex = T in text.<sup>5</sup>

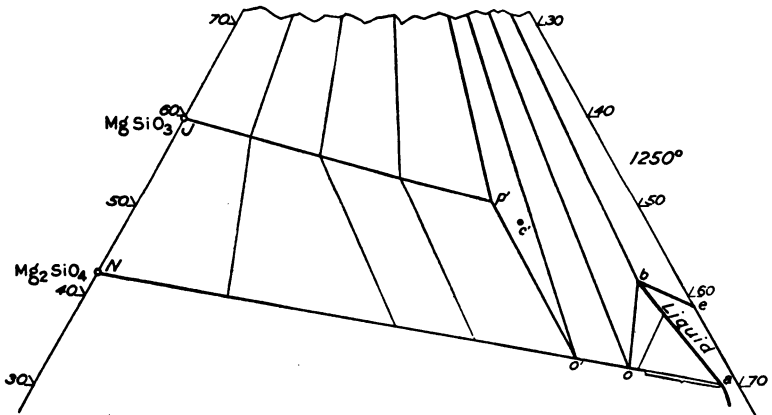


Fig. 15. Phase relations at 1250°. Truncated SiO<sub>2</sub> apex = T in text.

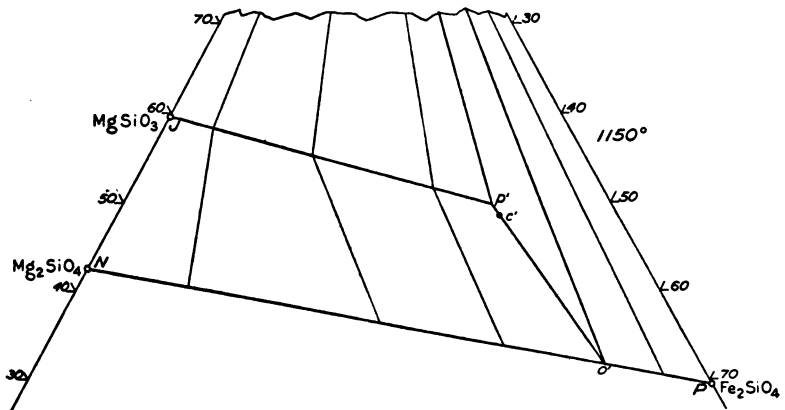


Fig. 16. Phase relations at 1150°. Truncated SiO<sub>2</sub> apex = T in text.

<sup>5</sup>See Notes on Appendix 2, page 459.

is typical of those temperatures between  $1400^\circ$  and  $1305^\circ$  where both the liquid  $c$ , in equilibrium with pyroxene  $p'$  and tridymite, and the liquid  $b$ , in equilibrium with the pyroxene  $p$  and olivine  $o$ , lie on the low-silica side of the metasilicate join. The areas require no special discussion.

The next isothermal plane (Fig. 14) is that for  $1305^\circ$ , the temperature of the invariant point  $L$  of Fig. 5 which is again lettered  $L$  in the present figure. The liquid  $L$  is in equilibrium with the three solid phases with which it is joined, viz., olivine  $o$ , pyroxene  $p$ , and tridymite  $T$ . At a temperature immediately below  $1305^\circ$ , pyroxene ceases to be stable in contact with liquid. The line  $pL$  therefore disappears and its place is taken by  $oT$ .

The next isothermal plane (Fig. 15) is that for  $1250^\circ$ , typical of those temperatures where only olivine and tridymite are in equilibrium with liquid. The liquid  $b$  is that in equilibrium with both these phases, the olivine having the composition  $o$ . The triangle  $boT$  includes the composition of all mixtures that consist of the three phases, liquid  $b$ , olivine  $o$ , and tridymite  $T$ . The adjacent triangle  $oo'T$  includes all mixtures that consist of only the two phases, tridymite  $T$  and an olivine between  $o$  and  $o'$ . The triangle  $o'p'T$  is again a three-phase triangle, in this instance all three phases being solid, the olivine  $o'$ , the pyroxene  $p'$ , and tridymite  $T$ .

The next isothermal plane (Fig. 16) shows the relations at  $1150^\circ$ , a temperature at which no liquid forms in any mixture of the system. There is only one three-phase triangle, the three-solid-phase triangle  $o'p'T$  which includes all mixtures that consist of the three phases, olivine  $o'$ , pyroxene  $p'$ , and tridymite  $T$ .

The next isothermal plane (Fig. 17) is that for  $1050^\circ$ , typical of temperatures where two different kinds of pyroxene co-exist in equilibrium. The triangle  $o''p''p'''$  is a three-solid-phase triangle which includes all mixtures that consist of olivine  $o''$ , ortho-pyroxene  $p''$ , and clino-pyroxene  $p'''$ . The three-solid-phase triangle  $p''p'''T$  includes all mixtures that consist of the same two pyroxenic phases and tridymite. The three-solid-phase triangle  $o'p'T$  has the same properties as its analogue in Figs. 15 and 16. All other areas are two-phase areas. Thus the area  $JNo''p''$  includes all mixtures that consist of the two phases, olivine between  $o''$  and  $N$  and ortho-pyroxene between  $p''$  and  $J$ . The area  $o''o'p'p'''$  includes all mixtures that consist of the two phases, olivine between

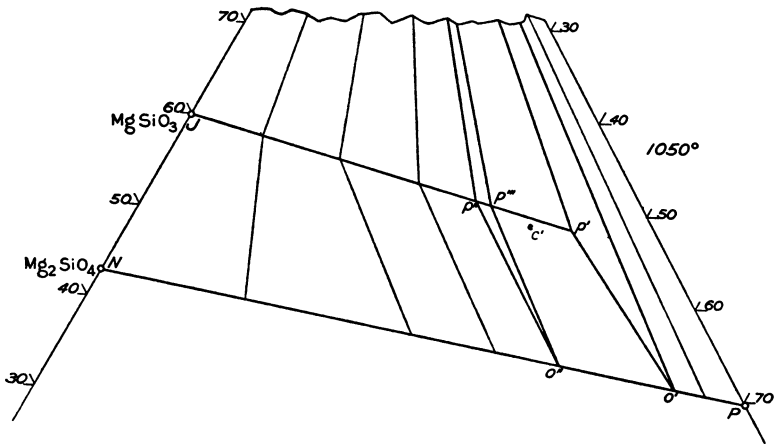


Fig. 17. Phase relations at 1050°. Truncated SiO<sub>2</sub> apex = T in text.

*o''* and *o'* and clino-pyroxene between *p'''* and *p'*. With this explanation no discussion of the other areas is necessary.

The next isothermal plane (Fig. 18) is that for 955°, which is the temperature of the invariant point at which four solid phases coexist, the horizontal XYZ of Fig. 8. The points X and Y of Fig. 18 correspond with the points similarly lettered in Fig. 8. The four solid phases in equilibrium are ortho-pyroxene X, clino-pyroxene Y, olivine *o*, and tridymite T. This temperature is the lowest temperature of stable existence of pure ferromagnesian clino-pyroxene. Immediately above 955° the triangle TY*o* represents the stable configuration. Immediately below 955° the triangle TX*o* represents the stable configuration.

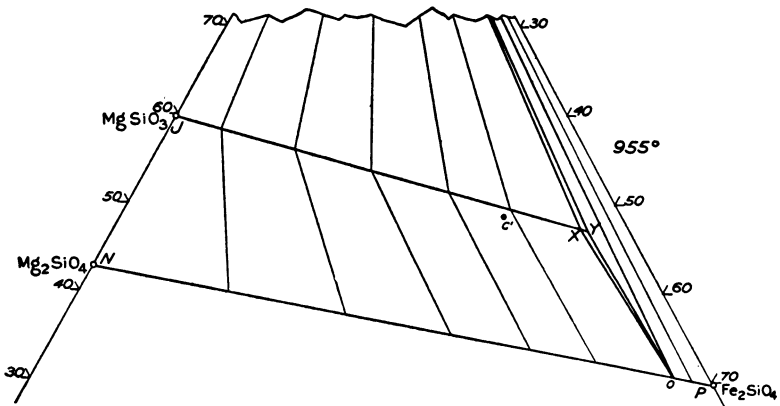


Fig. 18. Phase relations at 955°. Truncated SiO<sub>2</sub> apex = T in text.

## THREE-PHASE TRIANGLES AND THREE-PHASE BOUNDARIES.

In the isothermal figures there are numerous examples of liquids that are in equilibrium with two solid phases. The point indicating the composition of the liquid is the apex of a three-phase triangle, the two points at the ends of the base indicating the composition of the two solid phases. The sides of a three-phase triangle are called three-phase boundaries and are to be carefully distinguished from boundary curves. The three-phase triangles referring to the equilibrium between liquid, olivine, and pyroxene are of greatest interest in the present system. These are the triangles  $bop$  of Figs. 9-14.<sup>16</sup> It is important to note that any point in the three-phase boundary  $bo$  of any one of these figures represents a mixture which consists of liquid  $b$  and olivine at the temperature at which the individual diagram applies. Any such mixture cooled from the liquid state has therefore experienced separation of olivine and has just arrived at a temperature where separation of pyroxene begins. Similarly, any mixture represented by a point in the three-phase boundary  $bp$  consists of liquid and pyroxene and has just arrived at a temperature where separation of olivine begins. Moreover, any point in the three-phase boundary  $op$  (the base of the three-phase triangle) of these several figures represents a mixture consisting of pyroxene  $p$  and olivine  $o$  and, if cooling, has just reached that condition, i.e., the last trace of liquid has just disappeared. Obviously it is necessary to know the position of these three-phase boundaries in order to be able to describe accurately the course of crystallization of any mixture. One method of determining these three-phase boundaries is to hold a mixture at a temperature at which it consists of liquid with some olivine and pyroxene crystals and to determine optically the composition of both olivine and pyroxene. This gives the two points at the ends of the base of the three-phase triangle. Since the composition of the liquid lying on the boundary curve at all temperatures has been previously determined, the apex of the three-phase triangle for the temperature of the experiment is known and therefore the complete triangle. Such determinations have been made upon a number of mixtures at different temperatures. It is with these as basis and, of course, similar determinations for other types of

<sup>16</sup> There is no triangle  $bop$  in either Fig. 10 or Fig. 14, but the triangles  $Oop$  and  $Lop$  of these figures respectively are limiting cases of the triangle  $bop$  and have the same properties.



three-phase triangles, that the several isothermal figures 9-18 have been drawn. They are drawn to scale and solid-phase compositions may be read from them. No table of such compositions is given, since they do not lend themselves to presentation in such form.

A more extended discussion of the general properties of three-phase triangles is given in the paper on the system,  $CaO-FeO-SiO_2$ .<sup>17</sup>

#### COURSES OF CRYSTALLIZATION.

With this preliminary explanation of the method of determination and of the full significance of the three-phase boundaries of the isothermal figures, we may proceed to discuss the crystallization of typical liquids. For this purpose it is, in some instances, necessary to use a distorted diagram on account of the confusion of lines and points that would otherwise result. Fig. 19 is such a distorted diagram on which the several points and curves have been lettered in accordance with the plan used in the isothermal figures 9-18. A mixture of composition  $x$  (Fig. 19) begins to crystallize with separation of a highly magnesian olivine of composition represented by a point between  $o$  and  $N$ . The liquid follows the curved course  $xb$ ,<sup>18</sup> reaching the boundary curve  $KL$  at  $b$  when the olivine has attained the composition  $o$ , the line  $ob$  being the three-phase boundary (of the  $ob$  type of Figs. 9-14) which passes through  $x$ . At the temperature of  $b$  pyroxene of composition  $p$  begins to crystallize,  $bp$  being a three-phase boundary of the  $bp$  type of Figs. 9-14. With further cooling the liquid changes along the boundary curve  $KL$ , pyroxene separating and olivine being resorbed and both being changed continuously in composition. At  $b'$  the last trace of liquid disappears,  $o'p'$  being the base of the three-phase triangle or the three-phase boundary (of the  $op'$  type of Figs. 9-14) which passes through  $x$ , and  $b'$  being its apex. The mass then consists entirely of pyroxene  $p'$  and olivine  $o'$ . The pyroxene which forms directly from liquid is in all mixtures of this system, clino-pyroxene. Upon cooling it is transformed, at equilibrium, to ortho-pyroxene •but we shall not follow the majority of the mixtures discussed beyond the stage where they first become completely crystalline. On a later page the

<sup>17</sup> Bowen, N. L., Schairer, J. F., and Posnjak, E.: Op. cit., p. 233 ff.

<sup>18</sup> Necessarily curved because the composition of the olivine is continually moving along  $No$  towards  $o$ .

changes in the solid state will be followed for one mixture, by way of illustration of the use of three-solid-phase triangles.

The mixture  $x$  of Fig. 19 is typical of those that exhibit partial but incomplete resorption of olivine. We shall now discuss a mixture which is typical of those that exhibit complete resorption of olivine. The mixture  $x$  of Fig. 20 (also a distorted diagram) is of this latter character. Cooled from

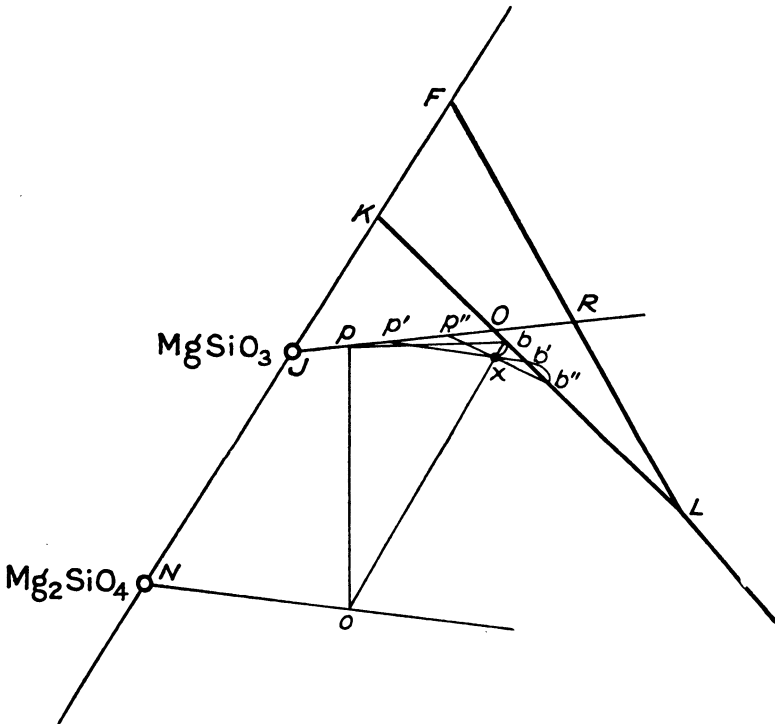


Fig. 21. Distorted diagram to illustrate courses of crystallization.<sup>6</sup>

the liquid state, it precipitates olivine first and the composition of the liquid follows a curved course to the boundary curve  $KL$  at  $b$ , at which time the olivine has the composition  $o$ . Pyroxene of composition  $p$  then begins to separate and the liquid moves along the boundary curve, pyroxene separating and olivine being resorbed. When the liquid has reached the composition  $b'$ , such that the three-phase boundary  $p'b'$  passes through  $x$ , the mixture now consists only of pyroxene  $p'$  and

<sup>6</sup>See Notes on Appendix 2, page 459.

liquid, i.e., the olivine has been completely resorbed. The liquid now crosses the pyroxene field on the curved course  $b'c$ . At  $c$  the pyroxene has the composition  $p''$ , the line  $p''c$  being a three-phase boundary of the type  $p'c$  of Figs. 10 and 11.<sup>19</sup> From the liquid  $c$  cristobalite begins to separate and the liquid changes along the boundary curve towards  $R$ , both pyroxene and cristobalite separating until the liquid is exhausted, at which time the liquid has a composition between  $c$  and  $R$  not far removed from  $c$ . The actual point and the construction lines that determine it are not given on account of the confusion of lines that results, but it is the apex of the three-phase triangle (of the type of  $cpT$  of Fig. 11) whose base (of the type  $Tp$  of Fig. 11) passes through  $x$ .

The liquid  $x$  of Fig. 21 is typical of a small area of liquids in the angle  $JOL$  of Fig. 5. Again a distorted diagram is necessary. Crystallization begins with separation of olivine and the liquid follows the curved course  $xb$ . When the liquid has the composition  $b$  the olivine has the composition  $o$  and pyroxene of composition  $p$  begins to separate. The liquid now moves along the boundary curve towards  $L$ , pyroxene separating and olivine being resorbed. When the liquid has reached the composition  $b'$ , whose position is determined by the three-phase boundary (of the  $pb$  type of Figs. 9 and 10) which passes through  $x$ , the pyroxene has the composition  $p'$  and the olivine is completely resorbed. The liquid now leaves the boundary curve and moves into the pyroxene field, pyroxene alone separating. The liquid follows the curved course  $b'b''$  which brings it back to the boundary curve at  $b''$ . The position of  $b''$  is determined by another three-phase boundary (also of the  $pb$  type of Figs. 9 and 10) which passes through  $x$ . Olivine now begins to crystallize again and separates together with pyroxene until crystallization is complete. The last minute quantity of liquid has the composition represented by a point on the boundary curve between  $b''$  and  $L$  (not indicated in the diagram), the position of the point being determined as the apex of the three-phase triangle (of the type  $bpo$ ) whose base (of the type  $po$ ) passes through  $x$ . Only a very small area of liquids represented by points in the angle  $JOL$  have two different three-phase boundaries of the  $pb$  type passing through them, and the range of liquids which show this precipitation, complete resorption, and reprecipitation of olivine is therefore much restricted. There is, however, a considerable range of composition of liquid, of which points

<sup>19</sup> In Fig. 11  $p$  and  $p'$  fall at one point which is lettered  $p$ .

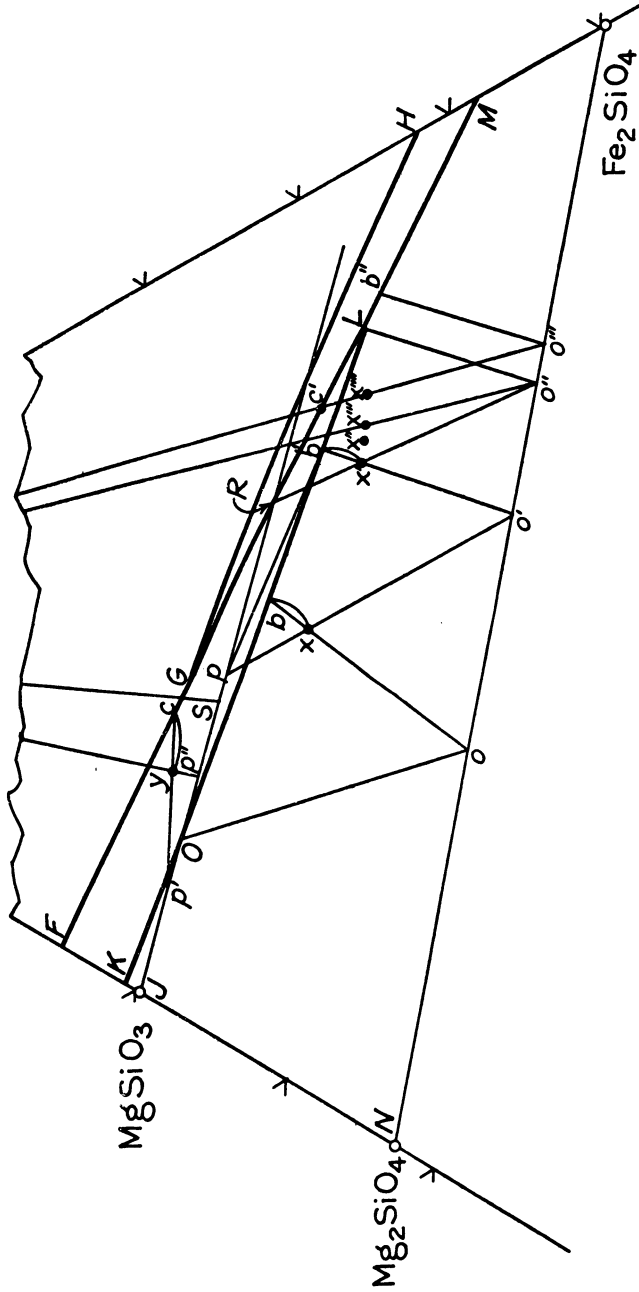


Fig. 22. True-scale diagram to illustrate courses of crystallization.

in  $bo$  between  $x$  and  $o$  are representative, that shows incomplete resorption of olivine followed by a period of renewed precipitation of olivine.

The crystallization of a great many liquids can be discussed satisfactorily with the aid of an undistorted or true-scale diagram. Fig. 22 is of this character. With its aid we may discuss the crystallization of a number of mixtures in the olivine field which have characteristics somewhat different from those of mixtures in that field that have already been discussed. The liquid  $x$  begins to crystallize with separation of olivine and follows the curve  $xb$ . When the liquid has the composition  $b$  the olivine has the composition  $o$  and pyroxene of composition  $O$  begins to crystallize. Not only pyroxene but olivine also continues to separate (no resorption of olivine) the liquid following the boundary curve to  $b'$  when the pyroxene has the composition  $p$ , the olivine the composition  $o'$ , and the last trace of liquid has just disappeared (since  $po'$  passes through  $x$ ). Mixtures lying in the three-phase boundary  $ob$  (of which  $x$  is typical) are the first mixtures that fail to show resorption of olivine, i.e., all mixtures to left of  $ob$  in the olivine field do show resorption of olivine whereas all mixtures to the right do not. The reason for this situation is that liquids to the right of  $b$  on the boundary curve are in equilibrium with olivine and with a pyroxene to the right of  $O$ , on the metasilicate join, that is, with two solid phases that lie on opposite sides of the boundary curve,<sup>20</sup> and movement along the boundary curve is accomplished by subtraction of both these solid phases. On the other hand, liquids to the left of  $b$  on the boundary curve are in equilibrium with olivine and with a pyroxene to the left of  $O$ , i.e., between  $J$  and  $O$ . They are thus in equilibrium with two solid phases that lie on the same side of the boundary curve and movement along the boundary curve can thus be accomplished only with resorption of the olivine and separation of pyroxene. Because all mixtures to the right of  $ob$  show only simple subtraction of both olivine and pyroxene from the liquid and all liquids to the left of  $ob$  show, at some stage, resorption of olivine, it is not to be assumed that liquids to the left of  $ob$  never show simple subtraction of both olivine and pyroxene. Some of them do in the final stages of their crystallization,

<sup>20</sup> Since the boundary curve is sensibly a straight line there is no need to speak of the tangent to it.

as we have seen in the discussion of mixtures referred to Fig. 21.

The mixture  $x'$  of Fig. 22 begins to crystallize with separation of olivine, and the liquid follows the curved course  $x'b'$ . At  $b'$  the olivine has the composition  $o'$ , pyroxene of composition  $p$  begins to separate, and the liquid moves along the boundary curve to  $L$ . At  $L$  the olivine has the composition  $o''$  and the pyroxene a composition, for all practical purposes, coincident with  $R$ . Since  $o''R$ , the base of the three-phase triangle, passes through  $x'$ , the mass consists entirely of the two solid phases, and the liquid, now of composition  $L$ , has vanished.

The mixtures  $x''$ ,  $x'''$  and  $x''''$  will, of course, still have some liquid of composition  $L$  when they reach the temperature  $L$  because they lie within the three-phase triangle  $Ro''L$ . The liquid  $L$  will then react with pyroxene to produce olivine and tridymite, the temperature remaining constant meanwhile. In the case of mixture  $x''$  the liquid will be consumed by this reaction and the completely crystalline mass will consist of olivine  $o''$ , pyroxene  $R$  and tridymite  $T$ . In the case of mixture  $x'''$  pyroxene and liquid are exhausted simultaneously and the mass consists of olivine  $o''$  and tridymite  $T$ . In the case of mixture  $x''''$  some liquid remains when the pyroxene is consumed. The liquid changes in composition along  $LM$ , olivine and tridymite separating. Crystallization is complete when the liquid has reached the composition  $b''$  and the olivine the composition  $o'''$ , the base  $o'''T$  of the three-phase triangle  $b''o'''T$  passing through  $x''''$ .

The olivine  $o''$  is plainly the most magnesian olivine that can form in equilibrium with free silica in the present system at atmospheric pressure. It has about 32 per cent  $Mg_2SiO_4$ .

We may now turn to the crystallization of liquids in the pyroxene field. The liquid  $y$  of Fig. 22 begins to crystallize with separation of pyroxene of composition between  $p'$  and  $J$  and the liquid follows the curved course  $yc$  to the boundary curve. When the liquid has the composition  $c$  the pyroxene has the composition  $p'$  and cristobalite begins to separate,  $p'c$  being the three-phase boundary of the type so lettered in Fig. 10. The liquid then moves along the boundary curve with separation of both pyroxene and cristobalite until the liquid has the composition  $G$ , when cristobalite changes to tridymite. The liquid then moves along the boundary curve  $GL$  and is finally consumed when it has a composition represented by a point not far from  $G$ . The position of the point

is determined as the apex of the three-phase triangle (of the  $pTc$  type of Fig. 11) whose base (of the  $pT$  type of Fig. 11) passes through  $y$ .

No other mixtures in the pyroxene field will be discussed except those that show features of particular interest. Among these are included all mixtures whose crystallization is such that at some stage the liquid moves along the portion  $RL$  of the boundary curve  $GRL$ . A distorted diagram, Fig. 23, is

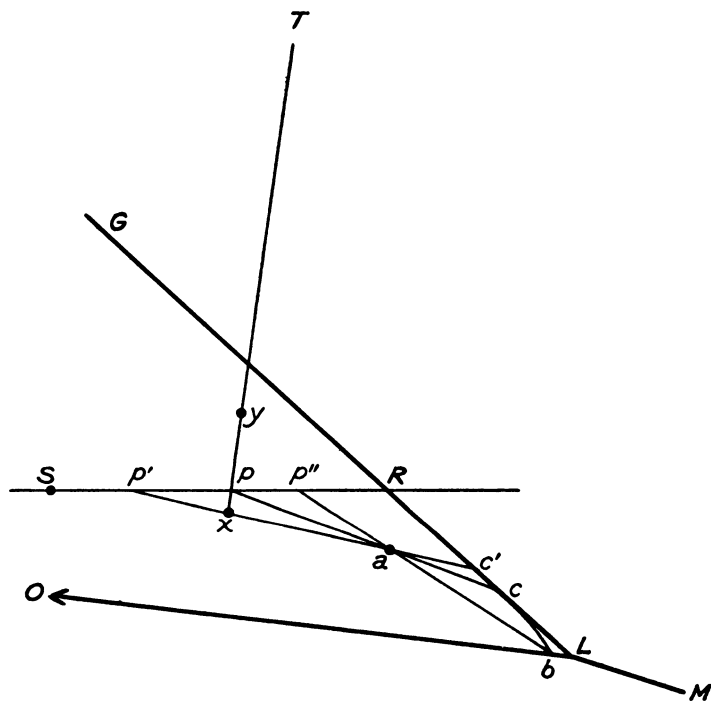


Fig. 23. Distorted diagram to illustrate courses of crystallization.

necessary for the discussion of these. In it curves are lettered to correspond with those in the undistorted diagram (Fig. 22) and the relations depicted are readily transferred mentally to the undistorted figure.

The mixture  $p$  of Fig. 23 is of metasilicate composition. Its crystallization can therefore be read from Fig. 8 but not in full detail, for at certain stages the equilibrium is ternary and the composition of some phases appearing at these stages is incapable of expression in Fig. 8. In Fig. 23, on the other

hand, all phases can be depicted. Thus the liquid  $p$  begins to crystallize with separation of clino-pyroxene somewhat more magnesian than  $S$  and the liquid, maintaining metasilicate composition, moves along  $pR$  to  $R$ , at which temperature the crystals have the composition  $S$ . Now crystallization of tridymite begins and the liquid follows the boundary curve  $RL$ . When the liquid has attained the composition  $c'$  the pyroxene has the composition  $p'$ ,  $c'p'$  being a three-phase boundary of the type  $cp'$  of Fig. 13. The proportions of the three phases, liquid  $c'$ , pyroxene  $p'$ , and tridymite  $T$  are determined by the position of the point  $p$  within the three-phase triangle  $p'c'T$ . In particular the proportion of tridymite is given by the ratio  $\frac{px}{Tx}$ ,  $x$  being the point of intersection of  $p'c'$  and  $Tp$  produced.<sup>7</sup> When the liquid has attained the composition  $c$ , the pyroxene has attained the composition  $p$ ,  $cp$  being again a three-phase boundary of the same type. But since  $p$  lies in the base  $pT$  of the three-phase triangle the liquid is reduced to zero when it has attained the composition  $c$  and, since  $p$  lies at the end of the base, the tridymite is likewise reduced to zero. Thus both tridymite and liquid are finally consumed when the liquid has the composition  $c$  and the whole mass then consists of the pyroxene  $p$ . As the liquid changes from  $R$  to  $c$  there is, then, at first an increase of tridymite from its initial value of zero, passage through a maximum value and then final return to zero. The maximum proportion of tridymite will obviously occur when the value of the intercept  $px$  and therefore of the ratio  $\frac{px}{Tx}$  passes through a maximum as the three-phase boundary passes from the position  $SR$ , through  $p'c'$ , to the position  $pc$ .

The crystallization of the liquid  $y$  is in some respects related to that of the liquid  $p$ . Crystallization begins with the separation of pyroxene somewhat more magnesian than  $S$ . The liquid follows a curved course to the boundary curve  $GR$  where crystallization of tridymite begins. The liquid then moves along the boundary curve with separation of both tridymite and pyroxene. When the liquid has the composition  $R$  (1400°) the pyroxene has the composition  $S$ , and the third phase is tridymite  $T$ . The proportion of tridymite at this temperature is given by the ratio  $\frac{yp}{Tp}$ . With further cooling

<sup>7</sup>See Notes on Appendix 2, page 459.

the liquid moves towards  $L$ . When it has attained the composition  $c'$ , the pyroxene has the composition  $p'$  and the proportion of tridymite is given by the ratio  $\frac{yx}{Tx}$ , which is greater than  $\frac{yp}{Tp}$ . When the liquid attains the composition  $c$ , the pyroxene has the composition  $p$ . The amount of liquid has therefore been reduced to zero and the mass consists entirely of tridymite  $T$  and pyroxene  $p$ . The proportion of tridymite is again  $\frac{yp}{Tp}$ , the same as it was at  $1400^\circ$ . During the fall of temperature and change of composition of liquid from  $R$  to  $c$  the proportion of tridymite plainly passes through a maximum and this maximum is at the same temperature as that for the liquid  $p$  already discussed, since it likewise depends on the maximum value of the changing intercept  $xp$ , or more specifically  $xy$ , which is  $xp$  plus the constant  $yp$ .

From the above discussion it will be clear that for all mixtures on the three-phase boundary  $Tp$  there is a certain temperature and composition of the liquid between  $R$  and  $L$  at which the proportion of tridymite passes through a maximum, i.e., separation of tridymite ceases and its resorption begins. Moreover, this is the same temperature (and composition of the liquid) for all these mixtures lying in  $Tp$ . For any other mixture such as  $p'$  or one lying in  $p'T$  there is likewise a temperature of maximum proportion of tridymite but it is a different temperature (and composition of the liquid) from that obtaining for mixtures lying in  $pT$ . Thus the reaction that takes place at any point in the curve  $RL$  may be different for different total compositions of the mixtures concerned, that is, for different proportions of the three phases concerned, the compositions of the individual phases being necessarily the same in all cases. At a certain temperature tridymite will be *subtracted from* the liquid if the total composition (in other words the relative proportions of the three phases) has a certain value, and at the same temperature tridymite will be *added to* (resorbed by) the liquid if the proportions have a certain different value.

There is yet another type of mixture whose course of crystallization falls, in part at least, along the portion  $RL$  of the boundary curve. The metasilicate mixture  $p$  and the mixture  $y$  with excess silica over the metasilicate ratio have been discussed. We shall now turn to a mixture with a lower proportion of silica. Such a mixture is represented by  $a$  (Fig.

23). A liquid of composition  $a$  begins to crystallize with separation of pyroxene of composition approaching  $S$  and follows a curved course which meets the boundary curve at  $c'$ , the pyroxene then having the composition  $p'$ . At  $c'$  tridymite begins to separate and the liquid moves along the boundary curve. After a short period of separation, tridymite begins to be resorbed and when the liquid has the composition  $c$  resorption is complete, the mass consisting entirely of pyroxene  $p$  and liquid  $c$ . The liquid now leaves the boundary curve and passes across the pyroxene field on the curved course  $cb$  with continued separation of pyroxene until the boundary curve  $OL$  is encountered at  $b$ . Here olivine begins to separate,  $bp''$  being a three-phase boundary of the  $bp$  type of Fig. 13. With separation of both olivine and pyroxene the liquid moves along the boundary curve toward  $L$ . Further crystallization need not be discussed since it depends upon factors already considered in connection with the points  $x'$ ,  $x''$ ,  $x'''$ , and  $x''''$  of the true-scale diagram, Fig. 22.

The liquid  $a$  (Fig. 23) is typical of those mixtures in the angle  $SRL$  through which pass two three-phase boundaries of the  $pc$  type.

It is to be noted that a liquid of the composition  $c'$ , when entirely free from crystals, moves along the boundary curve with separation of pyroxene and tridymite, passes through  $c$  still following the boundary curve, and effects resorption of tridymite which is not complete until the liquid has attained the composition  $L$ . The mass now consists of pyroxene  $R$  and liquid  $L$ , the ultimate three-phase boundary of the  $pc'$  type coinciding sensibly with  $RL$ . We may follow further crystallization of  $c'$  by referring back to the true-scale diagram, Fig. 22, upon which the composition  $c'$  has been marked. From this figure it is plain that the pyroxene  $R$  reacts with the liquid  $L$  to produce olivine  $o''$  and tridymite. In other words, tridymite, which had been completely resorbed, now reappears and the temperature remains constant at  $L$  until the pyroxene has disappeared. The liquid then moves along the boundary curve  $LM$  with separation of olivine and tridymite until the liquid has the composition  $b''$ , at which time crystallization is complete and the mass consists of olivine  $o'''$  and tridymite. Recapitulating, we find that tridymite appears, disappears, and reappears, pyroxene appears and disappears upon formation of olivine and tridymite from it, and if we follow the completely crystallized product to lower temperatures we find olivine and tridymite recombining to pyroxene. This is a

truly remarkable complexity of behavior for a mixture of only three components.

*Fractional Crystallization.*

209

The fractional crystallization of liquids of the system,  $MgO-FeO-SiO_2$ , is remarkable in the possible scope of its results, yet at the same time of rather simple character. In these respects it is not unlike the same process in liquids of the plagioclase system, anorthite-albite. Just as in this latter system the composition albite is the goal towards which all liquids strive during fractional crystallization, so in the present system all liquids strive to reach the composition of the point  $M$  (Fig. 22).<sup>37</sup> In detail the process is, of course, much more complicated than in the simple binary system of the plagioclases.

Some liquids of the system begin to crystallize with separation of highly magnesian olivine and reach the boundary curve  $KL$  at a point between  $K$  and  $O$  (again Fig. 22). All of these except those in the triangle  $KJO$  are liquids having a deficiency of silica below the metasilicate ratio (which we shall refer to as *undersilicated*) but upon encountering the curve  $KO$  they fail to follow it, as they would in non-fractional crystallization. Instead, they precipitate pyroxene only and cross the pyroxene field, acquiring a notable excess of silica over the metasilicate ratio (*oversilicated*) and reaching the boundary curve  $FGRL$  which they follow with separation of pyroxene and free silica (cristobalite or tridymite). If fractionation is limited (reaction between liquid and crystals only moderately restricted) the liquid may become completely exhausted when its composition is represented by some point between  $G$  and  $R$ . The final liquid is still oversilicated.

On the other hand, if the fractionation is stronger (reaction between liquid and crystals more restricted), some liquid may remain and continue to change composition along  $RL$ , thus becoming undersilicated once again. In the ideal case of perfect fractionation (complete lack of reaction between liquid and crystals) the liquid would continue past  $L$  and follow  $LM$ , olivine and tridymite now separating, until a final infinitesimal quantity of the liquid reached the composition  $M$ . The crys-

<sup>37</sup> We omit, as being of no importance in the present connection, all liquids of lower silica content than the orthosilicate ratio. It is to be noted also that pure olivine liquids fractionate not towards  $M$  but towards pure fayalite.

talline products of this last example would range all the way from highly magnesian olivine as the earliest crystals, through highly magnesian pyroxene accompanied by silica, then more ferri-ferrous pyroxene accompanied by silica, to highly ferri-ferrous olivine again accompanied by silica.

Most oversilicated liquids of the system will encounter and follow the curve *FL* during their fractional crystallization and may eventually proceed along *LM*, if fractionation is adequate, in exactly the same manner as the liquids just discussed. Some few oversilicated liquids first encounter the boundary curve *LM* and then proceed along it.

Those undersilicated liquids that reach the boundary curve *KOL* at points between *O* and *b* do not immediately follow that curve. They pass into the pyroxene field with separation of pyroxene but, never becoming oversilicated, follow a curved course that brings them back again to the boundary curve *KOL* which they then follow towards *L*. They attain *L* and pass on towards *M* if conditions permit an adequate degree of fractionation.

Those undersilicated liquids that reach the boundary curve *KOL* between *b* and *L* follow the curve to *L* during their fractional crystallization and may pass on towards *M* if fractionation is adequate, and, of course, some undersilicated liquids encounter *LM* directly.

The perfect equilibrium (non-fractional) type of crystallization discussed on earlier pages may be a very complex process but, when it is completed, the crystalline product is of simple constitution. At the other extreme the type of crystallization showing maximum fractionation is, in general, not so complex a process; but it is extended through a much wider range of temperatures and yields a crystalline product with a greater number of phases and a wide range of composition of the variable phases (solid solutions). These results grow out of the prevalence of incongruent melting and solid solution in the system. It is this principle of flexibility of crystallization introduced by the phenomena just mentioned that renders the course of crystallization and the products of it responsive to the conditions attending crystallization. The importance of this principle has been pointed out elsewhere,<sup>38</sup> but no apology is here offered for emphasizing it once again especially in connection with experimental results upon such important rock-forming minerals as pyroxenes and olivines.

<sup>38</sup> Bowen, N. L.: The reaction principle in petrogenesis, *J. Geol.*, 30, 177-198, 1922.

## Notes on Appendix 2

(Page numbers refer to *Bowen and Schairer* original.)

**Page 176, Figure 11.** Note that the Mg/Fe ratio decreases in the sequence: pyroxene-olivine-magnesiowüstite, i.e., away from SiO<sub>2</sub>. This is a convenient way of remembering the Mg fractionations.

**Page 178, Figure 14.** Note the reaction  $Px + L = Ol + Tr$ , described in the last sentence of paragraph 2, p. 179. Point *L* is a peritectic.

**Page 184, Figure 21 and associated text.** A sequence in which the reaction on the liquidus field boundary *KL* is first odd and then even (after the excursion  $b' - b''$ ) with equilibrium crystallization is described here. This behavior was described in Chapter 15 for the system Ne-Ks-SiO<sub>2</sub>, and as before, arises during equilibrium crystallization when the TSC lies for a time on a single-phase solid solution line. When the liquid returns to the field boundary at  $b''$ , the fictive extract lies on the pyroxene join and simultaneously on the tangent to  $b'b''$ . For liquid compositions between  $b''$  and *L*, the fictive extract lies between the pyroxene and olivine joins on the tangent to *KL* and the reaction is even.

**Page 190.** The authors have used a shortcut in determining the proportion of tridymite. In the notation of this book, the TSC may be found along  $p'T$  by drawing a line from  $c'$  through the bulk composition  $p$ ; this is the solid-liquid lever, and line  $p'T$  is the solid-solid lever geometrically similar to  $Tx$  of the original paper. The point being made in this and the next example is that the curve *GL*, representing the equilibrium *L* ( $Px$ ,  $Tr$ ), is in part even ( $L = Px + Tr$ ) and in part odd ( $L = Px - Tr$ ), depending on the circumstances. Tridymite first grows and is then resorbed (see p. 191).

## DISCUSSION

Melting exercises will not be undertaken here, but can be pursued by the student for himself, using the principles developed in earlier chapters. An excellent place to begin is with a solid mixture lying on *Oo* in Fig. 22 of the original paper. Such a mixture of olivine and pyroxene first yields melt of composition *b*. In fractional melting, the TSC path will curve downward toward the olivine join while the fractional liquids move along the olivine-pyroxene field boundary. Examples are given by Presnall (1969).

# References

- Akimoto, S.I., Komada, E., and Kushiro, I. (1967): Effect of pressure on the melting of olivine and spinel polymorphs of  $\text{Fe}_2\text{SiO}_4$ . *J. Geophys. Res.*, vol. **72**, pp. 679–686.
- van Alkemade, A.C. van Rijn (1893): Graphische Behandlung einiger thermodynamischen Probleme über Gleichgewichtszustände von Salzlösungen mit festen Phasen. *Z. Phys. Chem.*, vol. **11**, pp. 289–327.
- Anderson, A.T. (1976): Magma mixing: petrological process and volcanological tool. *J. Volcan. Geotherm. Res.*, vol. **1**, pp. 3–33.
- Anderson, D.L. (1979): The upper mantle transition region: eclogite? *Geophys. Res. Letters*, vol. **6**, pp. 433–436.
- Anderson, D.L. and Minster, J.B. (1979): (abs) The physical mechanism of subsolidus creep and its relation to seismic wave attenuation. *EOS Trans. Am. Geophys. Union*, vol. **60**, pp. 378.
- Andersen, O. (1915): The system anorthite-forsterite-silica. *Am. J. Sci.*, 4th ser., vol. **39**, pp. 407–454.
- Appleman, D.E. (1966): Crystal chemistry of the pyroxenes in *Short Course Notes on Chain Silicates*, American Geological Institute, Palo Alto, Calif., p. 10.
- Atkins, F.B. (1968): Pyroxenes of the Bushveld intrusion, South Africa. *J. Petrol.*, vol. **10**, pp. 222–249.
- Bachinski, S.W., and Müller, G. (1971): Experimental determinations of the microcline-low albite solvus. *J. Petrol.*, vol. **12**, pp. 329–356.
- Bailey, E.B., Clough, C.T., Wright, W.B., Richey, J.E. and Wilson, G.V. (1924): Tertiary and post-tertiary geology of Mull, Loch Aline, and Oban. *Mem. Geol. Surv. Scot.*
- Barth, T.F.W. (1962): *Theoretical petrology*. Wiley, New York.

- Bell, P.M., and Roseboom, E.H. Jr. (1969): Melting relationships of jadeite and albite to 45 kilobars with comments on melting diagrams of binary systems at high pressures. *Mineral. Soc. Am., Spec. Pap. 2*, pp. 151–162.
- Bence, A.E., and Papike, J.J. (1972): Pyroxenes as recorders of lunar basalt petrogenesis: chemical trends due to crystal-liquid interaction. *Proc. Third. Lunar Sci. Conf., Geochim. Cosmochim. Acta. Supp. 3*, vol. 1, pp. 431–469.
- Berg, J.H. (1977): Regional geobarometry in the contact aureoles of the anorthositic Nain complex, Labrador. *J. Petrol.*, vol. 18, pp. 399–430.
- Bollmann, W., and Nissen, H.u. (1968): A study of optimal phase boundaries: the case of exsolved alkali feldspars. *Acta Crystallogr.*, vol. A24, pp. 546–557.
- Bowen, N.L. (1913): Melting phenomena in the plagioclase feldspars. *Am. J. Sci.*, vol. 35, pp. 577–599.
- \_\_\_\_\_ (1914): The ternary system diopside-forsterite-silica. *Am. J. Sci.*, 4th ser., vol. 33, pp. 551–573.
- \_\_\_\_\_ (1915): The crystallization of haplobasaltic, haplodioritic, and related magmas. *Am. J. Sci.*, vol. 40, pp. 161–185.
- \_\_\_\_\_ (1928): *The evolution of the igneous rocks*. Princeton University Press, Princeton, N.J.
- \_\_\_\_\_ (1941): Certain singular points on crystallization curves of solid solutions. *Proc. N.A.S.*, vol. 27, pp. 301–309.
- \_\_\_\_\_ (1945): Phase equilibria bearing on the origin and differentiation of alkaline rocks. *Am. J. Sci.*, vol. 243A, pp. 75–89.
- Bowen, N.L., and Andersen, O. (1914): The binary system MgO-SiO<sub>2</sub>. *Am. J. Sci.*, 4th ser., vol. 37, pp. 487–500.
- Bowen, N.L., and Schairer, J.F. (1932): The system FeO-SiO<sub>2</sub>. *Am. J. Sci.*, 5th Ser., vol. 24, pp. 177–213.
- \_\_\_\_\_ (1935): The system, MgO-FeO-SiO<sub>2</sub>. *Am. J. Sci.*, 5th Ser., vol. 29, pp. 151–217.
- Boyd, F.R. (1973): A pyroxene geotherm. *Geochim. Cosmochim. Acta*, vol. 37, pp. 2533–2546.
- Boyd, F.R., and England, J.L. (1963): Effect of pressure on the melting of diopside, CaMgSi<sub>2</sub>O<sub>6</sub>, and albite, NaAlSi<sub>3</sub>O<sub>8</sub>, in the range up to 50 kilobars. *J. Geophys. Res.*, vol. 68, pp. 311–323.
- Boyd, F.R., England, J.L., and Davis, B.T.C. (1964): Effects of pressure on the melting and polymorphism of enstatite, MgSiO<sub>3</sub>. *J. Geophys. Res.*, vol. 69, pp. 2101–2109.
- Burnham, C.W. (1979): The importance of volatile constituents, in Yoder, H.S. Jr., ed., *The evolution of the igneous rocks*, Princeton University Press, Princeton, N.J., pp. 439–482.
- Burnham, C.W., and Davis, N.F. (1974): The role of H<sub>2</sub>O in silicate melts: II. Thermodynamic and phase relations in the system NaAlSi<sub>3</sub>O<sub>8</sub>-H<sub>2</sub>O to 10 kilobars, 700° to 1100°C. *Am. J. Sci.*, vol. 274, pp. 902–940.

- Carmichael, I.S.E., Turner, F.J., and Verhoogen, J. (1972): *Igneous petrology*. McGraw-Hill, New York.
- Chayes, F. (1963): On pyroxene molecules in the CIPW norm. *Geol. Mag.*, vol. 100, pp. 7–10.
- \_\_\_\_\_ (1969): Curve fitting in the ternary diagram. *Carnegie Inst. Washington Yearb.*, vol. 67, pp. 236–239.
- \_\_\_\_\_ (1972): Silica saturation in Cenozoic basalt. *Philos. Trans. R. Soc. London. A*, vol. 271, pp. 285–296. (Data extracted from computer output for this paper, with permission.)
- Chayes, F., and Métais, D. (1964): On the relation between suites of CIPW and Barth-Niggli norms. *Carnegie Inst. Washington Yearb.*, vol. 63, pp. 193–195.
- Chen, C.H., and Presnall, D.C. (1975): The system  $Mg_2SiO_4 - SiO_2$  at pressures up to 25 kilobars. *Am. Mineral.*, vol. 60, pp. 398–406.
- Clark, S.P. Jr. (1959): Effect of pressure on the melting points of eight alkali halides. *J. Chem. Phys.*, vol. 31, pp. 1526–1531.
- \_\_\_\_\_ (ed.) (1966): *Handbook of physical constants*. *Geol. Soc. Am. Mem.*, vol. 97.
- Clark, S.P. Jr., Schairer, J.F., and de Neufville, J. (1962): Phase relations in the system  $CaMgSi_2O_6 - CaAl_2SiO_6 - SiO_2$  at low and high pressure. *Carnegie Inst. Washington Yearb.* vol. 61, pp. 59–68.
- Cohen, L.H., and Klement, W. Jr. (1967): High-low quartz inversion: determination to 35 kilobars. *J. Geophys. Res.*, vol. 72, pp. 4245–4251.
- Cross, W., Iddings, J.P., Pirsson, L.V., and Washington, H.S. (1903): *Quantitative classification of igneous rocks*. Univ. Chicago Press, Chicago.
- Czamanske, G.K., and Wones, D.R. (1973): Oxidation during magmatic differentiation, Finnmarka complex, Oslo area, Norway: part 2, the mafic silicates. *J. Petrol.*, vol. 14, pp. 349–380.
- Davis, B.T.C., and England, J.L. (1964): The melting of forsterite up to 50 kilobars. *J. Geophys. Res.*, vol. 69, pp. 1113–1116.
- Day, A.L., and Allen, E.T. (1905): *The isomorphism and thermal properties of the feldspars*. *Carnegie Inst. Washington Publ.*, vol. 31.
- Eggler, D.H. (1973a): Role of  $CO_2$  in melting processes in the mantle. *Carnegie Inst. Washington Yearb.*, vol. 72, pp. 457–467.
- \_\_\_\_\_ (1973b): Principles of melting of hydrous phases in silicate melt. *Carnegie Inst. Washington Yearb.*, vol. 72, pp. 491–495.
- \_\_\_\_\_ (1974): Effect of  $CO_2$  on the melting of peridotite. *Carnegie Inst. Washington Yearb.*, vol. 73, pp. 215–224.
- \_\_\_\_\_ (1975):  $CO_2$  as a volatile component of the mantle: the system  $Mg_2SiO_4 - SiO_2 - H_2O - CO_2$ . *Phys. Chem. Earth*, vol. 9, pp. 869–881.
- \_\_\_\_\_ (1976): Does  $CO_2$  cause partial melting in the low-velocity layer of the mantle? *Geology*, vol. 4, pp. 69–72.
- \_\_\_\_\_ (1977): The principle of the zone of invariant vapor composition: an example in the system  $CaO - MgO - SiO_2 - CO_2 - H_2O$  and implications for the mantle solidus. *Carnegie Inst. Washington Yearb.*, vol. 76, pp. 428–435.

- Eggler, D.H. (1978): The effect of CO<sub>2</sub> upon partial melting of peridotite in the system Na<sub>2</sub>O-CaO-Al<sub>2</sub>O<sub>3</sub>-MgO-SiO<sub>2</sub>-CO<sub>2</sub> to 35 kb, with an analysis of melting in a peridotite-H<sub>2</sub>O-CO<sub>2</sub> system. *Am. J. Sci.*, vol. **278**, pp. 305-343.
- Eggler, D.H., and Holloway, J.R. (1977): Partial melting of peridotite in the presence of H<sub>2</sub>O and CO<sub>2</sub>: Principles and review, in Dick, H.J.B., ed., *Magma genesis. Oreg. Dep. Geol. Miner. Ind. Bull.* **96**, pp. 15-36.
- Ellis, D.E., and Wyllie, P.J. (1979): Carbonation, hydration, and melting relations in the system MgO-H<sub>2</sub>O-CO<sub>2</sub> at pressures up to 100 kbar. *Am. Mineral.*, vol. **64**, pp. 32-40.
- Emslie, R.F. (1971): Liquidus relations and subsolidus reactions in some plagioclase-bearing systems. *Carnegie Inst. Washington Yearb.*, vol. **69**, pp. 148-155.
- Engel, A.E.J., Engel, C.G., and Havens, R.G. (1965): Chemical characteristics of oceanic basalts and the upper mantle. *Geol. Soc. Am. Bull.*, vol. **76**, pp. 719-734.
- Eskola, Pentti (1954): A proposal for the presentation of rock analyses in ionic percentage. *Ann. Acad. Sci. Fenn.*, Ser. A, III, vol. **38**, pp. 2-15.
- Eugster, H.P. (1959): Reduction and oxidation in metamorphism: in Abelson, P.H., ed., *Researches in geochemistry*, Wiley, New York, pp. 397-426.
- Eugster, H.P., and Wones, D.R. (1962): Stability relations of the ferruginous biotite, annite. *J. Petrol.*, vol. **3**, pp. 82-125.
- Fenner, C.N. (1929): The crystallization of basalts. *Am. J. Sci.*, 5th Ser., vol. **18**, pp. 225-253.
- Fermor, L.L. (1913): Preliminary note on garnet as a geological barometer and on an infra-plutonic zone in the earth's crust. *Rec. Geol. Surv. India*, vol. **43**, pt. 1, pp. 41-47.
- Ford, W.E. (1932): *Dana's textbook of mineralogy*. Wiley, New York, p. 559.
- Franco, R.R., and Schairer, J.F. (1951): Liquidus temperatures in mixtures of the feldspars of soda, potash, and lime. *J. Geol.*, vol. **59**, pp. 259-267.
- Fudali, R.F. (1963): Experimental studies bearing on the origin of pseudoleucite and associated problems of alkalic rock systems. *Geol. Soc. Am. Bull.*, vol. **74**, pp. 1101-1126.
- Gast, P.W. (1965): Terrestrial ratio of potassium to rubidium and the composition of the earth's mantle. *Science*, vol. **147**, pp. 858-860.
- \_\_\_\_\_ (1968): Trace element fractionation and the origin of tholeiitic and alkaline magma types. *Geochim. Cosmochim. Acta.*, vol. **32**, pp. 1057-1080.
- Goldsmith, J.R. (1980) Melting and breakdown reactions of anorthite at high pressures and temperatures. *Am. Mineral.*, vol. **65**, pp. 272-284.
- Greenland, L.P. (1970): An equation for trace element distribution during magmatic crystallization. *Am. Mineral.*, vol. **55**, pp. 455-465.
- Greig, J.W. (1927): Liquid immiscibility in silicate melts. *Am. J. Sci.*, 5th ser., vol. **13**, p. 15.
- Greig, J.W., and Barth, T.F.W. (1938): The system Na<sub>2</sub>O·Al<sub>2</sub>O<sub>3</sub>·2SiO<sub>2</sub> (nephelite, carnegieite)-Na<sub>2</sub>O·Al<sub>2</sub>O<sub>3</sub>·6SiO<sub>2</sub> (albite). *Am. J. Sci.*, 5th ser., vol. **35A**, pp. 93-112.

- Grout, F.F. (1928): Anorthosites and granite as differentiates of a diabase sill from Pigeon Point, Minnesota. *Geol. Soc. Am. Bull.*, vol. **39**, pp. 555–578.
- Guthrie, Frederick (1884): On eutexia. *Philos. Mag.* **17**, vol. **5**, pp. 462–482.
- Hess, H.H. (1939): Extreme fractional crystallization of a basaltic magma; the Stillwater igneous complex. *Trans. Am. Geophys. Union*, Pt. 3, pp. 430–432.
- \_\_\_\_\_ (1960): Stillwater igneous complex, Montana: a quantitative mineralogical study. *Geol. Soc. Am. Mem.*, vol. **80**.
- Hodges, F.N. (1974): The solubility of H<sub>2</sub>O in silicate melts. *Carnegie Inst. Washington Yearb.*, vol. **73**, pp. 251–255.
- Hytönen, Kai, and Schairer, J.F. (1961): The plane enstatite-anorthite-diopside and its relation to basalts. *Carnegie Inst. Washington Yearb.*, vol. **60**, pp. 125–134.
- Irvine, T.N. (1970): Crystallization sequences in the Muskox intrusion and other layered intrusions. *Geol. Soc. S. Afr., Spec. Publ. 1*, pp. 441–476.
- \_\_\_\_\_ (1975): Olivine-pyroxene-plagioclase relations in the system Mg<sub>2</sub>SiO<sub>4</sub>-CaAl<sub>2</sub>Si<sub>2</sub>O<sub>8</sub>-KAlSi<sub>3</sub>O<sub>8</sub>-SiO<sub>2</sub> and their bearing on the differentiation of stratiform intrusions. *Carnegie Inst. Washington Yearb.*, vol. **74**, pp. 492–500.
- Irvine, T.N., and Smith, D.H. (1967): The ultramafic rocks of the Muskox intrusion, Northwest Territories, Canada, in Wyllie, P.J., ed., *Ultramafic and related rocks*, Wiley, New York, pp. 38–49.
- Jackson, E.D. (1961): Primary textures and mineral associations in the ultramafic zone of the Stillwater Complex, Montana. *U.S. Geol. Surv., Prof. Pap.*, vol. **358**.
- \_\_\_\_\_ (1967): Ultramafic cumulates in the Stillwater, Great Dyke, and Bushveld intrusions. in Wyllie, P.J., ed., *Ultramafic and related rocks*, Wiley, New York, pp. 20–38.
- \_\_\_\_\_ (1970): The cyclic unit in layered intrusions—a comparison of repetitive stratigraphy in the ultramafic parts of the Stillwater, Muskox, Great Dyke, and Bushveld complexes. *Geol. Soc. S. Afr., Spec. Publ. 1*, pp. 391–424.
- Kennedy, G.C. (1955): Some aspects of the role of water in rock melts, in Poldervaart, A., ed., *Crust of the Earth. Geol. Soc. Am., Spec. Pap. 62*, pp. 489–503.
- Kennedy, G.C., Wasserburg, G.J., Heard, H.C., and Newton, R.C. (1962): The upper three-phase region in the system SiO<sub>2</sub>-H<sub>2</sub>O. *Am. J. Sci.*, vol. **260**, pp. 501–521.
- Kennedy, W.Q., and Anderson, E.M. (1938): Crustal layers and the origin of magmas. *Bull. Volcanol.*, 2nd ser., vol. **3**, pp. 23–82.
- Kracek, F.C. (1953): Polymorphism: *Encyclopedia britannica*.
- Kracek, F.C. and Clark, S.P. Jr. (1966): Melting and transformation points in oxide and silicate systems at low pressure, in Clark, S.P. Jr., ed., *Handbook of physical constants, Geol. Soc. Am. Mem.*, vol. **97**, pp. 301–322.
- Kuno, H. (1959): Origin of Cenozoic petrographic provinces of Japan and surrounding areas. *Bull. Volcanol.*, 2nd ser., vol. **20**, pp. 37–76.
- \_\_\_\_\_ (1960): High-alumina basalt. *J. Petrol.*, vol. **1**, pp. 121–145.
- Kushiro, I. (1968): Composition of magma formed by partial zone melting of the earth's upper mantle. *J. Geophys. Res.*, vol. **73**, pp. 619–634.

- Kushiro, I. (1969): The system forsterite-diopside-silica with and without water at high pressures. *Am. J. Sci.*, vol. 267-A (Schairer Volume), pp. 269–294.
- \_\_\_\_\_ (1972a): Determination of liquidus relations in synthetic silicate systems with electron probe analysis: the system forsterite-diopside-silica at 1 atmosphere. *Am. Mineral.*, vol. 57, pp. 1260–1271.
- \_\_\_\_\_ (1972b): Effect of water on the composition of magmas formed at high pressures. *J. Petrol.*, vol. 13, pp. 311–334.
- \_\_\_\_\_ (1973): The system diopside-anorthite-albite: determination of compositions of coexisting phases. *Carnegie Inst. Washington Yearb.*, vol. 72, pp. 502–507.
- \_\_\_\_\_ (1974): Melting of hydrous upper mantle and possible generation of andesitic magma: an approach from synthetic systems. *Earth Planet. Sci. Letters*, vol. 22, pp. 294–299.
- Kushiro, I., and Fujii, T. (1977): Flotation of plagioclase in magmas at high pressures and its bearing on the origin of anorthosite. *Proc. Jpn. Acad.*, vol. 53, Ser. B, pp. 262–266.
- Kushiro, I., and Schairer, J.F. (1963): New data on the system diopside-forsterite-silica. *Carnegie Inst. Washington Yearb.*, vol. 62, pp. 95–103.
- \_\_\_\_\_ (1970): Diopside solid solutions in the system diopside-anorthite-albite at 1 atm. and at high pressures. *Carnegie Inst. Washington Yearb.*, vol. 68, pp. 222–226.
- Kushiro, I., and Yoder, H.S. Jr. (1966): Anorthite-forsterite and anorthite-enstatite reactions and their bearing on the basalt-eclogite transformation. *J. Petrol.*, vol. 7, pp. 337–362.
- \_\_\_\_\_ (1969): Melting of forsterite and enstatite at high pressures under hydrous conditions. *Carnegie Inst. Washington Yearb.*, vol. 67, pp. 153–158.
- \_\_\_\_\_ (1970): Stability of field of iron-free pigeonite in the system  $MgSiO_3$ - $CaMgSi_2O_6$ . *Carnegie Inst. Washington Yearb.*, vol. 68, pp. 226–229.
- Kushiro, I., Yoder, H.S. Jr., and Nishikawa, M. (1968): Effect of water on the melting of enstatite. *Geol. Soc. Am. Bull.*, vol. 79, pp. 1685–1692.
- Lindsley, D.H. (1966a): *P-T* projection for part of the system kalsilite-silica. *Carnegie Inst. Washington Yearb.*, vol. 65, pp. 244–247.
- \_\_\_\_\_ (1966b): Pressure-temperature relations in the system  $FeO$ - $SiO_2$ . *Carnegie Inst. Washington Yearb.*, vol. 65, pp. 226–230.
- \_\_\_\_\_ (1968): Melting relations of plagioclase at high pressure, in Isachsen, Y.W., ed., *Origin of anorthosite and related rocks*, N.Y. State Mus. Sci. Serv. Mem. vol. 18, pp. 39–46.
- Lindsley, D.H., Brown, G.M., and Muir, I.D. (1969): Conditions of the ferrowollastonite-ferrohedenbergite inversion in the Skaergaard intrusion, East Greenland. *Mineral. Soc. Am. Spec. Pap.* 2, pp. 193–201.
- Lindsley, D.H., and Emslie, R.F. (1968): Effect of pressure on the boundary curve in the system diopside-albite-anorthite. *Carnegie Inst. Washington Yearb.*, vol. 66, pp. 479–480.
- Lindsley, D.H., and Munoz, J.L. (1969): Subsolidus relations along the join

- hedenbergite-ferrosilite. *Am. J. Sci.*, vol. 267-A (Schairer Volume), pp. 295–324.
- Lindsley, D.H., and Smith, D. (1971): Chemical variations in the feldspars. *Carnegie Inst. Washington Yearb.*, vol. 69, pp. 274–278.
- Lindsley, D.H., Speidel, D.H., and Nafziger, R.H. (1968): P-T- $f_{O_2}$  relations for the system Fe-O-SiO<sub>2</sub>. *Am. J. Sci.*, vol. 226, pp. 342–360.
- Lipin, B.R. (1978): The system Mg<sub>2</sub>SiO<sub>4</sub>-Fe<sub>2</sub>SiO<sub>4</sub>-CaAl<sub>2</sub>Si<sub>2</sub>O<sub>8</sub>-SiO<sub>2</sub> and the origin of Fra Mauro basalts. *Am. Mineral.*, vol. 63, pp. 350–364.
- Longhi, J., and Hays, J.F. (1979): Phase equilibria and solid solution along the join CaAl<sub>2</sub>Si<sub>2</sub>O<sub>8</sub>-SiO<sub>2</sub>. *Am. J. Sci.*, vol. 279, pp. 876–890.
- Macdonald, G.A. (1949): Petrography of the Island of Hawaii. *U.S. Geol. Surv., Prof. Pap.*, vol. 214D, pp. 51–96.
- Macdonald, G.A., and Katsura, T. (1964): Chemical composition of Hawaiian lavas. *J. Petrol.*, vol. 5, pp. 82–133.
- Michot, Jean (1960): La palingenèse basique. *Acad. R. Belg. Bull. 1. sci.* 5, vol. 46, pp. 257–268.
- Morey, G.W. (1964): Phase-equilibrium relations of the common rock-forming oxides except water. *U.S. Geol. Surv., Prof. Pap.* 440-L.
- Morse, S.A. (1961): The geology of the Kiglapait layered intrusion, coast of Labrador, Canada. Unpub. Ph.D. thesis, McGill Univ.
- \_\_\_\_\_ (1968): Layered intrusions and anorthosite genesis, in Isachsen, Y.W., ed., *Origin of anorthosite and related rocks*, N. Y. State Mus. Sci. Serv. Mem., vol. 18, pp. 175–187.
- \_\_\_\_\_ (1969): *The Kiglapait layered intrusion, Labrador*. *Geol. Soc. Am. Mem.*, vol. 112.
- \_\_\_\_\_ (1969a): Syenites. *Carnegie Inst. Washington Yearb.*, vol. 67, pp. 112–120.
- \_\_\_\_\_ (1969b): Ternary feldspars. *Carnegie Inst. Washington Yearb.*, vol. 67, pp. 124–126.
- \_\_\_\_\_ (1970): Alkali feldspars with water at 5 kb pressure. *J. Petrol.*, vol. 11, pp. 221–251.
- \_\_\_\_\_ (1976): The lever rule with fractional crystallization and fusion. *Am. J. Sci.*, vol. 276, pp. 330–346.
- \_\_\_\_\_ (1979): Reaction constants for En-Fo-Sil equilibria: an adjustment and some applications. *Am. J. Sci.*, vol. 279, pp. 1060–1069.
- Morse, S.A., Lindsley, D.H., and Williams, R.J. (1980): Concerning intensive parameters in the Skaergaard intrusion. *Am. J. Sci.*, vol. 280-A (Jackson Volume), pp. 159–170
- Muan, A., and Osborn, E.F. (1956): Phase equilibria at liquidus temperatures in the system MgO-FeO-Fe<sub>2</sub>O<sub>3</sub>-SiO<sub>2</sub>. *J. Am. Ceram. Soc.*, vol. 39, pp. 121–140.
- Murphy, W.M. (1977): An experimental study of solid-liquid equilibria in the albite-anorthite-diopside system. Unpublished manuscript thesis, Univ. of Oregon, Eugene.
- Mysen, B.O. (1977): Solubility of volatiles in silicate melts under the pressure and temperature conditions of partial melting in the upper mantle, in Dick, H.J.B., ed., *Magma genesis*. *Oreg. Dep. Geol. Miner. Ind. Bull.*, 96, pp. 1–14.

- Mysen, B.O., and Kushiro, I. (1977): Compositional variations of coexisting phases with degree of partial melting of peridotite in the upper mantle. *Am. Mineral.*, vol. **62**, pp. 843–865.
- Mysen, B.O., and Seitz, M.G. (1975): Trace element partitioning determined by beta-track mapping—an experimental study using carbon and samarium as examples. *J. Geophys. Res.*, vol. **80**, pp. 2627–2635.
- Nakamura, Y., (1974): The system  $\text{SiO}_2\text{-H}_2\text{O-H}_2$  at 15 kbar. *Carnegie Inst. Washington Yearb.*, vol. **73**, pp. 259–262.
- Nakamura, Y., and Kushiro, I. (1974): Composition of the gas phase in  $\text{Mg}_2\text{SiO}_4\text{-SiO}_2\text{-H}_2\text{O}$  at 15 kbar. *Carnegie Inst. Washington Yearb.*, vol. **73**, pp. 255–258.
- Neuman, H., Mead, J., and Vitaliano, C.J. (1954): Trace element variation during fractional crystallization as calculated from the distribution law: *Geochim. Cosmochim. Acta.*, vol. **6**, pp. 90–100.
- Niggli, P. (1936): Molekularnormen zu Gesteinsberechnung. *Schweiz. Mineral. Petrogr. Mitt.*, vol. **16**, p. 295.
- O'Hara, M.J. (1977): Geochemical evolution during fractional crystallization of a periodically refilled magma chamber. *Nature*, vol. **266**, pp. 503–507.
- Osborn, E.F. (1942): The system  $\text{CaSiO}_3\text{-diopside-anorthite}$ . *Am. J. Sci.*, vol. **240**, pp. 751–788.
- \_\_\_\_\_ (1959): Role of oxygen partial pressure in the crystallization and differentiation of basaltic magma. *Am. J. Sci.*, vol. **257**, pp. 609–647.
- Osborn, E.F., and Schairer, J.F. (1941): The ternary system pseudowollastonite-akermanite-gehlenite. *Am. J. Sci.*, vol. **239**, pp. 715–63.
- Osborn, E.F., and Tait, D.B. (1952): The system diopside-forsterite-anorthite. *Am. J. Sci.*, Bowen vol., pp. 413–433.
- Ostrovsky, I.A. (1967): On some sources of errors in phase-equilibria investigations at ultra-high pressures; phase diagram of silica. *Geol. J.*, vol. **5**, pp. 321–328.
- Paster, T.P., Schauwecker, D.S., and Haskin, L.A. (1974): The behavior of some trace elements during solidification of the Skaergaard layered series. *Geochim. et Cosmochim. Acta*, vol. **38**, pp. 1549–1577.
- Peck, D.L., Wright, T.L., and Moore, J.G. (1966): Crystallization of tholeiitic basalt in Alae lava lake, Hawaii. *Bull. Volcanol.*, vol. **29**, pp. 629–656.
- Presnall, D.C. (1966): The join forsterite-diopside-iron oxide and its bearing on the crystallization of basaltic and ultramafic magmas. *Am. J. Sci.*, vol. **264**, pp. 753–809.
- \_\_\_\_\_ (1969): The geometric analysis of partial fusion. *Am. J. Sci.*, vol. **267**, pp. 1178–1194.
- Presnall, D.C., Dixon, S.A., Dixon, J.R. O'Donnell, T.H., Brenner, N.L., Schrock, R.L., and Dycus, D.W. (1978): Liquidus phase relations on the join diopside-forsterite-anorthite from 1 atm to 20 kbar: their bearing on the generation and crystallization of basaltic magma. *Contr. Mineral. Petrol.*, vol. **66**, pp. 203–220.
- Presnall, D.C., Dixon, J.R., O'Donnell, T.H., and Dixon, S.A. (1979): Generation of mid-ocean ridge tholeiites. *J. Petrol.*, vol. **20**, pp. 3–36.

- Rankin, G.A., and Wright, F.E. (1915): The ternary system  $\text{CaO-Al}_2\text{O}_3\text{-SiO}_2$ . *Am. J. Sci.*, vol. **39**, pp. 1–79.
- Rayleigh, J.W.S. (1896): Theoretical considerations respecting the separation of gases by diffusion and similar processes. *Phil. Mag.*, vol. **42**, pp. 493–498.
- Rhodes, J.M., Dungan, M.A., Blanchard, D.P., and Long, P.E. (1979): Magma mixing at mid-ocean ridges: evidence from basalts drilled near 22°N on the Mid-Atlantic ridge. *Tectonophysics*, vol. **55**, pp. 35–61.
- Robie, R.A., Hemingway, B.S., and Fischer, J.R. (1978): Thermodynamic properties of minerals and related substances at 298.15 K and 1 bar ( $10^5$  pascals) pressure and at higher temperatures. *US Geol. Surv. Bull.* 1452.
- Roeder, P.L. (1974): Paths of crystallization and fusion in systems showing ternary solid solution. *Am. J. Sci.*, vol. **224**, pp. 48–60.
- Roeder, P.L., and Emslie, R.F. (1970): Olivine-liquid equilibria. *Contrib. Mineral. Petrol.*, vol. **29**, pp. 275–289.
- Ronov, A.B., and Yaroshevsky, A.A. (1969): Chemical composition of the earth's crust, in *The earth's crust and upper mantle*, P.J. Hart, ed., *Am. Geoph. Union Monograph*, vol. **13**, pp. 37–57.
- Rosenhauer, M., and Eggler, D.H. (1975): Solution of  $\text{H}_2\text{O}$  and  $\text{CO}_2$  in diopside melt. *Carnegie Inst. Washington Yearb.*, vol. **74**, pp. 474–479.
- Schairer, J.F. (1950): The alkali feldspar join in the system  $\text{NaAlSi}_3\text{O}_8\text{-KAlSi}_3\text{O}_8\text{-SiO}_2$ . *J. Geol.*, vol. **58**, pp. 512–517.
- \_\_\_\_\_ (1951): Phase transformations in polycomponent silicate systems, in *Phase transformations in solids*, R. Smoluchowski, ed., Wiley, New York, pp. 278–295.
- Schairer, J.F., and Bowen, N.L. (1955): The system  $\text{K}_2\text{O-Al}_2\text{O}_3\text{-SiO}_2$ . *Am. J. Sci.*, vol. **253**, pp. 681–746.
- \_\_\_\_\_ (1956): The system  $\text{Na}_2\text{O-Al}_2\text{O}_3\text{-SiO}_2$ . *Am. J. Sci.*, vol. **254**, pp. 129–195.
- Schairer, J.F., and Kushiro, I. (1964): The join diopside-silica. *Carnegie Inst. Washington Yearb.*, vol. **63**, pp. 130–132.
- Schairer, J.F., and Yoder, H.S. Jr. (1960): The nature of residual liquids from crystallization, with data on the system nepheline-diopside-silica. *Am. J. Sci.*, vol. **258A**, pp. 273–283.
- \_\_\_\_\_ (1962): The system diopside-enstatite-silica. *Carnegie Inst. Washington Yearb.*, vol. **61**, pp. 75–82.
- \_\_\_\_\_ (1971): The joins  $\text{Na}_2\text{O} \cdot 5\text{MgO} \cdot 12\text{SiO}_2$ -sodium disilicate and  $2\text{Na}_2\text{O} \cdot 3\text{MgO} \cdot 5\text{SiO}_2$ -sodium disilicate in the system  $\text{Na}_2\text{O-MgO-SiO}_2$ . *Carnegie Inst. Washington Yearb.*, vol. **69**, pp. 157–160.
- Schreinemakers, F.A.H. (1915–1925): In- mono- and di-variant equilibria: 29 papers in vols. 18–28 of *Proc. K. Akad. Wet.*, Amsterdam, and reproduced by the College of Earth and Mineral Science, Penn. State Univ., University Park, Pa.
- Seck, H.A. (1971): Koexistierende Alkalifeldspäte und Plagioclase im System  $\text{NaAlSi}_3\text{O}_8\text{-KAlSi}_3\text{O}_8\text{-CaAl}_2\text{Si}_2\text{O}_8\text{-H}_2\text{O}$  bei Temperaturem von 650°C bis 900°C. *Neues Jahrb. Mineral. Abh.*, vol. **115**, pp. 315–345.

- Smith, C.H. (1962): Notes on the Muskox intrusion, Coppermine River area, District of MacKenzie. *Geol. Surv. Can., Pap.* 61-25.
- Smith, C.H., Irvine, T.N., and Findlay, D.C. (1966): Geologic maps of the Muskox intrusion. *Geol. Surv. Can. Maps* 1213-A and 1214-A.
- Smith, C.H., and Kapp, H.E. (1963): The Muskox intrusion, a recently discovered layered intrusion in the Coppermine River area, Northwest Territories, Canada. *Miner. Soc. Amer., Spec. Pap. 1*, pp. 30-35.
- Smith, D. (1971): Stability of the assemblage iron-rich orthopyroxene-olivine-quartz. *Am. J. Sci.*, vol. 271, pp. 370-382.
- Solomon, S.C. (1976): Geophysical constraints on radial and lateral temperature variations in the upper mantle. *Am. Mineral.*, vol. 61, pp. 788-803.
- Sosman, R.B. (1952): Temperature scales and silicate research. *Am. J. Sci.*, Bowen volume, pp. 517-528.
- Speidel, D.H., and Nafziger, R.H. (1968): P-T- $f_{O_2}$  relations in the system Fe-O-MgO-SiO<sub>2</sub>. *Am. J. Sci.*, vol. 266, pp. 361-379.
- Stern, C.R., Huang, W.-L., and Wyllie, P.J. (1975): Basalt-andesite-rhyolite H<sub>2</sub>O: crystallization intervals with excess H<sub>2</sub>O and H<sub>2</sub>O-undersaturated liquidus surfaces to 35 kilobars, with implications for magma genesis. *Earth Planet. Sci. Lett.*, vol. 28, pp. 189-196.
- Stewart, D.B. (1967): Four-phase curve in the system CaAl<sub>2</sub>Si<sub>2</sub>O<sub>8</sub>-SiO<sub>2</sub>-H<sub>2</sub>O between 1 and 10 kilobars. *Schweiz. Mineral. Petrogr. Mitt.*, vol. 47, pp. 35-59.
- Stewart, D.B., and Roseboom, E.H. (1962): Lower temperature terminations of the three-phase region plagioclase-alkali feldspar-liquid. *J. Petrol.*, vol. 3, pp. 280-315.
- Tammann, G. (1903): *Kristallisieren und Schmelzen*: J.A. Barth, Leipzig. English translation in *States of aggregation* (1925) D. Van Nostrand.
- Thompson, A.B., and Algor, J.R. (1977): Model systems for anatexis of pelitic rocks I. Theory of melting reactions in the system KAlO<sub>2</sub>-NaAlO<sub>2</sub>-Al<sub>2</sub>O<sub>3</sub>-SiO<sub>2</sub>-H<sub>2</sub>O. *Contr. Mineral. Petrol.*, vol. 63, pp. 247-269.
- Tilley, C.E. (1950): Some aspects of magmatic evolution. *Quart. J. Geol. Soc.*, Lond., vol. 106, pp. 37-61.
- Tilley, C.E., Yoder, H.S. Jr., and Schairer, J.F. (1963): Melting relations of basalts. *Carnegie Inst. Washington Yearb.*, vol. 62, pp. 77-84.
- Tomita, T. (1935): On the chemical compositions of the Cenozoic alkaline suite of the circum-Japan sea region. *J. Shanghai Sci. Inst.*, sect. III, pp. 227.
- Tuttle, O.F., and Bowen, N.L. (1950): High temperature albite and contiguous feldspars. *J. Geol.*, vol. 58, pp. 572-583.
- \_\_\_\_\_ (1958): Origin of granite in the light of experimental studies in the system NaAlSi<sub>3</sub>O<sub>8</sub>-KAlSi<sub>3</sub>O<sub>8</sub>-SiO<sub>2</sub>-H<sub>2</sub>O. *Geol. Soc. Am. Mem.*, vol. 74.
- Tuttle, O.F., and Smith, J.V. (1958): The nepheline-kalsilite system II. Phase relations. *Am. J. Sci.*, vol. 256, pp. 571-589.
- Ubbelohde, A.R. (1965): *Melting and crystal structure*. Clarendon Press, Oxford.
- \_\_\_\_\_ (1979): *The molten state of matter. Melting and crystal structure*. Wiley-Interscience, New York.

- Ulmer, G.C., ed. (1971): *Research techniques for high pressure and high temperature*. Springer-Verlag, New York.
- Wager, L.R. (1960): The major element variation of the layered series of the Skaergaard intrusion and a reestimation of the average composition of the hidden layered series and of the successive residual magmas. *J. Petrol.*, vol. 1, pp. 364–398.
- Wager, L.R., and Brown, G.M. (1968): *Layered igneous rocks*. W.H. Freeman and Co., San Francisco.
- Wager, L.R., Brown, G.M., and Wadsworth, W.J. (1960): Types of igneous cumulates. *J. Petrol.*, vol. 1, pp. 73–85.
- Wager, L.R., and Deer, W.A. (1939): Geological investigations in East Greenland, Pt. III. The petrology of the Skaergaard intrusion, Kangerdlugssauq, East Greenland. *Medd. Groenl.*, vol. 105, No. 4, pp. 1–352.
- Waldbaum, D.R. (1969): Some observations on preparing glass for compositions on the alkali feldspar join. *Am. J. Sci.*, vol. 267, pp. 1249–1253.
- Waldbaum, D.R., and Thompson, J.B. Jr. (1969): Mixing properties of sanidine crystalline solutions. IV. Phase diagrams from equations of state: *Am. Mineral.*, vol. 54, pp. 1274–1298.
- Weaver, J.S., Chipman, D.W., and Takahashi, T. (1979): Comparison between thermochemical and phase stability data for the quartz-coesite-stishovite transformations. *Am. Mineral.*, vol. 64, pp. 604–614.
- Wheeler, E.P. 2nd (1965): Fayalitic olivine in northern Newfoundland-Labrador. *Canad. Mineral.*, vol. 8, pp. 339–346.
- Whittaker, E.J.W., and Muntus, R. (1970): Ionic radii for use in geochemistry. *Geochim. et Cosmochim. Acta.*, vol. 34, pp. 945–956.
- Wiebe, R.A. (1979): Fractionation and liquid immiscibility in an anorthosite pluton of the Nain complex, Labrador. *J. Petrol.*, vol. 20, pp. 239–270.
- Williams, R.J. (1971a): Reaction constants in the system Fe-MgO-SiO<sub>2</sub>-O<sub>2</sub>: I. Experimental results. *Am. J. Sci.*, vol. 270, pp. 334–360.
- \_\_\_\_\_ (1971b): Reaction constants in the system Fe-Mg-SiO<sub>2</sub>-O<sub>2</sub>: intensive parameters in the Skaergaard intrusion, East Greenland. *Am. J. Sci.*, vol. 271, pp. 132–146.
- \_\_\_\_\_ (1972): Activity-composition relations in the fayalite-forsterite solid solution between 900° and 1300°C at low pressure. *Earth Planet. Sci. Lett.*, vol. 15, pp. 296–300.
- Windom, K.E., and Boettcher, A.L. (1977): (abs) Melting of albite at high pressure: a redetermination. *EOS Trans. Am. Geophys. Union*, vol. 58, p. 1243.
- Wood, B.J. (1978): Reactions involving anorthite and CaAl<sub>2</sub>SiO<sub>6</sub> pyroxene at high pressures and temperatures. *Am. J. Sci.*, vol. 278, pp. 930–942.
- Wyllie, P.J. (1978): Mantle fluid compositions buffered in peridotite-CO<sub>2</sub>-H<sub>2</sub>O by carbonates, amphibole, and phlogopite. *J. Geol.*, vol. 86, pp. 687–713.
- \_\_\_\_\_ (1979): Magmas and volatile components. *Am. Mineral.*, vol. 64, pp. 469–500.
- Wyllie, P.J., and Huang, W.L. (1975): Peridotite, kimberlite, and carbonatite explained in the system CaO-MgO-SiO<sub>2</sub>-CO<sub>2</sub>. *Geology*, vol. 3, pp. 621–624.

- \_\_\_\_\_ (1976): Carbonation and melting reactions in the system CaO-MgO-SiO<sub>2</sub>-CO<sub>2</sub> at mantle pressures with geophysical and petrological applications. *Contr. Mineral. Petrol.*, vol. 54, pp. 79–107.
- Yoder, H.S. Jr. (1950): High-low quartz inversion up to 10,000 bars. *Trans. Am. Geophys. Union*, vol. 31, pp. 827–835.
- \_\_\_\_\_ (1973): Contemporaneous basaltic and rhyolitic magmas. *Am. Mineral.*, vol. 58, pp. 153–171.
- \_\_\_\_\_ (1976): *Generation of basaltic magma*: National Acad. Sci., Washington, D.C.
- Yoder, H.S. Jr., and Kushiro, I. (1969): Melting of a hydrous phase; phlogopite: *Am. J. Sci.*, vol. 267-A (Schairer Volume), pp. 558–582.
- Yoder, H.S. Jr., Stewart, D.B., and Smith, J.V. (1957): Ternary feldspars. *Carnegie Inst. Washington Yearb.*, vol. 56, pp. 206–214.
- Yoder, H.S. Jr. and Tilley, C.E. (1957): Basalt magmas. *Carnegie Inst. Washington Yearb.*, vol. 56, pp. 156–161.
- \_\_\_\_\_ (1962): Origin of basalt magmas: an experimental study of natural and synthetic rock systems. *J. Petrol.*, vol. 3, pp. 342–532.
- Yund, R.A. (1975): Microstructure, kinetics, and mechanisms of alkali feldspar exsolution. Ch. 6 in Ribbe, P.H. (ed.) *Feldspar Mineralogy*, M.S.A. Short Course Notes 2, Mineral. Soc. Am., Washington, D.C.
- Zavarizskii, A.N. and Sobolev, V.S. (1964): *The physiochemical principles of igneous petrology*. Israel Program for Scientific Translations, Jerusalem.
- Zen, E-an. (1963): Components, phases, and criteria of chemical equilibrium in rocks. *Am. J. Sci.*, vol. 261, pp. 929–942.
- \_\_\_\_\_ (1966): Construction of pressure-temperature diagrams for multi-component systems after the method of Schreinemakers—a geometric approach. *U.S. Geol. Surv., Bull.* 1225.
- \_\_\_\_\_ (1977): The phase-equilibrium calorimeter, the petrogenetic grid, and a tyranny of numbers. *Am. Mineral.*, vol. 62, pp. 189–204.

# Author Index

- Akimoto, S. I. 371, 372  
Algor, J. R. 402  
Allen, E. T. 61, 73  
Andersen, O. 130, 152, 153, 161, 162, 329, 424  
Anderson, A. T. 412  
Anderson, D. L. 402, 408  
Anderson, E. M. 4  
Appleman, D. E. 408  
Atkins, F. B. 340
- Bachinski, S. W. 293  
Bailey, E. B. 4  
Barth, T. F. W. 10, 63, 244, 246, 437  
Bell, P.M. 349, 355, 366, 368  
Bence, A. E. 341  
Berg, J. H. 378  
Blanchard, D. P. 412  
Boettcher, A. L. 355  
Bollman, W. 293  
Bowen, N. L. 4, 7, 41, 42, 61, 62, 63, 70, 72, 77, 90, 108, 118, 125, 126, 130, 152, 153, 162, 182, 184, 185, 244, 245, 246, 249, 256, 257, 263, 264, 274, 277, 278, 284, 297, 298, 299, 303, 325, 326, 327, 328, 330, 331, 357, 369, 424, 439  
Boyd, F. R. 346, 350, 351, 355, 358, 362, 405
- Brenner, N. L. 354, 357, 358, 359  
Bridgman, P. W. 346, 348  
Brown, G. M. 178, 220, 223, 226, 239, 340, 343  
Burnham, C. W. 383, 394, 402, 424
- Carmichael, I. S. E. 343  
Carnegie, A. 244  
Chayes, F. 9, 10, 12, 233, 340, 437  
Chen, C. H. 358, 361, 362, 363, 388, 391  
Chipman, D. W. 361, 409  
Clark, S. P. Jr. 26, 234, 350, 360, 361  
Clough, C. T. 4  
Cohen, L. H. 360  
Cross, W. 10  
Czamanske, G. K. 304, 339
- Day, A. L. 61, 73  
Davis, B. T. C. 130, 357, 358, 362  
Davis, N. F. 383, 394  
Deer, W. A. 219, 303  
De Neufville, J. 234  
Dixon, J. R. 346, 354, 357, 358, 359, 363, 364, 365, 368, 407, 410, 411, 412, 421, 422, 423  
Dixon, S.A. 346, 354, 357, 358, 359, 363, 364, 365, 368, 407, 410, 411, 412, 421, 422, 423

- Dungan, M. A. 412  
 Dycus, D. W. 354, 357, 358, 359
- Eggler, D. H. 383, 399, 401, 402, 419,  
 420, 421, 422, 423, 424  
 Ellis, D. E. 424  
 Emslie, R. F. 222, 298, 356, 357, 406  
 Engel, A. E. J. 3  
 Engel, C. G. 3  
 England, J. L. 130, 346, 350, 351, 355,  
 357, 358, 362  
 Eskola, P. 10  
 Eugster, H. P. 303, 304
- Fenner, C. N. 303  
 Fermor, L. L. 4, 408  
 Findlay, D. C. 230  
 Fisher, J. R. 342, 424  
 Ford, W. E. 54  
 Franco, R. R. 283  
 Fudali, R. F. 264, 271, 284, 285, 287  
 Fujii, T. 357
- Gast, P. W. 3, 111, 369  
 Goldsmith, J. R. 352  
 Greenland, L. P. 111  
 Greig, J. W. 63, 130, 184, 185, 246  
 Grout, F. F. 357  
 Guthrie, F. 43
- Haskin, L. A. 241  
 Havens, R. G. 3  
 Hays, J. F. 162, 361  
 Heard, H. C. 386  
 Hemingway, B. S. 342, 424  
 Hess, H. H. 227, 239  
 Hodges, F. N. 384, 399  
 Holloway, J. R. 383, 399, 401, 402, 419,  
 421  
 Huang, W. L. 409, 420, 421, 424  
 Hytönen, K. 231
- Iddings, J. P. 10  
 Irvine, T. N. 161, 162, 178, 213, 230,  
 231, 233, 235, 236, 237, 329
- Jackson, E. D. 161, 178, 227, 228, 229,  
 230  
 Jaffe, H. W. 293
- Kapp, H. E. 230  
 Katsura, T. 12, 432  
 Kennedy, G. C. 303, 343, 386  
 Kennedy, W. Q. 4  
 Klein, C. Jr. 293  
 Klement, W. Jr. 360  
 Komada, E. 371, 372  
 Kracek, F. C. 360, 361  
 Kuno, H. 3, 4  
 Kushiro, I. 37, 54, 80, 84, 90, 130, 131,  
 181, 182, 183, 184, 185, 186, 187,  
 203, 204, 212, 351, 357, 365, 369,  
 371, 372, 383, 388, 389, 390, 391,  
 392, 399, 400, 406, 407, 412, 413,  
 414, 417, 418, 423
- Lindsley, D. H. 279, 280, 283, 284, 309,  
 321, 322, 328, 337, 341, 343, 352,  
 356, 357, 369, 370, 371, 372, 373,  
 374, 375, 376, 377, 378  
 Lipin, B. R. 223, 328, 330, 331  
 Long, P. E. 412  
 Longhi, J. 162
- Macdonald, G. A. 4, 12, 432  
 McBirney, A. R. 220  
 Mao, H. K. 349  
 Mead, J. 111  
 Métais, D. 233, 437  
 Michot, J. 116, 179  
 Minster, J. B. 402  
 Morey, G. W. 178  
 Morse, S. A. 71, 72, 94, 121, 122, 218,  
 219, 220, 221, 222, 241, 247, 264,  
 278, 284, 328, 337, 340, 343, 357,  
 392, 394, 395, 396, 397, 398, 424
- Moore, J. G. 94  
 Muan, A. 300, 301, 331  
 Muir, I. D. 343  
 Müller, G. 293  
 Munoz, J. L. 341  
 Muntus, R. 9, 255  
 Murphy, W. M. 57  
 Mysen, B. O. 369, 383, 398, 402
- Nafziger, R. H. 309, 321, 322, 331, 332,  
 336, 337, 373, 374, 375, 376, 377,  
 378  
 Nakamura, Y. 383, 388  
 Neuman, H. 111  
 Newton, R. C. 386

- Niggli, P. 10  
Nishikawa, M. 388, 389, 390  
Nissen, H. U. 293
- O'Donnell, T. H. 346, 357, 358, 359,  
363, 364, 365, 368, 407, 410, 411,  
412, 421, 422, 423  
O'Hara, M. J. 412  
Osborn, E. F. 39, 41, 42, 57, 63, 90, 130,  
133, 301, 303, 329, 331, 338, 339,  
343  
Ostrovsky, I. A. 360
- Papike, J. J. 341  
Paster, T. P. 241  
Peck, D. L. 94  
Pirsson, L. V. 10  
Presnall, D. C. 112, 120, 122, 123, 124,  
125, 127, 202, 252, 328, 338, 339,  
346, 354, 357, 358, 359, 361, 362,  
363, 364, 365, 368, 388, 391, 407,  
410, 411, 412, 421, 422, 423, 481
- Rankin, G. A. 162  
Rayleigh, J. W. S. 111  
Rhodes, J. M. 412  
Richardson, S. W. 322  
Richey, J. E. 4  
Robie, R. A. 342, 424  
Robinson, P. 186, 293  
Roeder, P. L. 125, 283, 298  
Ronov, A. B. 9  
Roozeboom, B. H. W. 73  
Roseboom, E. H. Jr. 284, 355, 366, 368  
Rosenhauer, M. 399  
Ross, M. 293
- Schairer, J. F. 38, 39, 54, 62, 63, 78, 82,  
83, 84, 90, 130, 131, 162, 182, 184,  
186, 226, 231, 234, 244, 245, 246,  
249, 256, 257, 258, 259, 262, 263,  
283, 284, 289, 297, 298, 299, 325,  
326, 327, 328, 330, 331, 357, 369,  
413, 439  
Schauwecker, D. S. 241  
Schreinemakers, F. A. H. 309  
Schrock, R. L. 354, 357, 358, 359  
Seck, H. A. 284  
Seitz, M. G. 402  
Shaw, H. R. 2
- Smith, C. H. 213, 230  
Smith, D. 279, 280, 283, 284, 378  
Smith, J. R. 283, 395  
Smith, J. V. 263, 264  
Sobolev, V. S. 59  
Solomon, S. C. 407, 410, 411  
Sosman, R. B. 37  
Speidel, D. H. 309, 321, 322, 331, 332,  
336, 337, 373, 374, 375, 376, 377,  
378  
Stern, C. R. 409  
Stewart, D. B. 283, 386, 396
- Tait, D. B. 90, 130, 133, 329  
Takahashi, T. 361, 409  
Tammann, G. 21  
Thompson, A. B. 402  
Thompson, J. B. Jr. 258, 260, 288, 289,  
290, 291, 292, 369, 396, 402, 424  
Tilley, C. E. 4, 12, 13, 83, 145, 151, 226,  
248, 249, 250, 251, 252, 408, 409  
Tomita, T. 4  
Turner, F. J. 343  
Tuttle, O. F. 263, 264, 274, 347
- Ubbelohde, A. R. 21, 23, 27, 28, 62, 421  
Ulmer, G. C. 296, 346
- van Alkemade, A. C. van Rijn 73  
Verhoogen, J. 343  
Vitaliano, C. J. 111
- Wager, L. R. 178, 219, 220, 223, 226,  
239, 303, 340, 343  
Waldbaum, D. R. 256, 258, 260, 288,  
289, 290, 291, 292, 369, 396, 424  
Wadsworth, W. J. 223, 239  
Washington, H. S. 10  
Wasserburg, G. J. 386  
Weaver, J. S. 361, 409  
Wheeler, E. P. 378  
Whittaker, E. J. W. 9, 255  
Wiebe, R. A. 357  
Williams, R. J. 337, 342, 343, 344  
Wilson, G. V. 4  
Windom, K. E. 355  
Wones, D. R. 304, 339  
Wood, B. J. 352, 353  
Wright, F. E. 162  
Wright, T. L. 94

- Wright, W. B. 4
- Wyllie, P. J. 94, 120, 383, 402, 407, 409,  
412, 420, 421, 422, 423, 424
- Yaroshevsky, A. A. 9
- Yoder, H. S. Jr 4, 12, 13, 38, 62, 78, 82,  
83, 90, 118, 145, 151, 184, 186,  
226, 248, 249, 250, 251, 252, 283,
- 348, 360, 383, 388, 389, 390, 392,  
393, 396, 399, 400, 402, 405, 406,  
407, 408, 409, 413
- Yund, R. A. 293
- Zavaritskii, A. N. 59
- Zen, E-an 33, 323, 424

# Subject Index

- absent phase (*see* missing-phase notation)
  - acid liquid 77, 84
  - activity, definition 342
  - activity coefficient, definition 342
  - accumulate theory 239–241
  - accumulus growth 239–241
  - adiabat 407–408
  - åkermanite 182
  - albite
    - basalt classification and 8
    - Ca entry into 77
    - high pressure melting 354–355, 365–369
    - melting point 62–63
    - in Ne-SiO<sub>2</sub> system 244, 245, 246, 247
    - in Ne-SiO<sub>2</sub>-X ternary systems 248–250
    - reaction with water at high pressure 382
    - superheating and 62
    - synthesis 62
    - thermal barrier 365
    - viscosity 62
  - albite-jadeite system
    - high pressure melting
      - behavior 365–369
      - negative melting slope 369
  - albite-orthoclase join 258–262
  - binodal solvus 292–293
  - coherent solvus 293
  - equilibrium crystallization 260–261
  - fractional crystallization 261–262
  - G-X diagrams 288–293
  - incongruent melting 258, 259
  - metastable melting 260
  - minimum melting 258, 261, 264, 292
  - in Ne-Ks-SiO<sub>2</sub> system 269–278
  - piercing point 261
  - singular point 261
  - spinodal solvus 292–293
  - T-X diagram 259, 260
  - variance 261
- albite-orthoclase-water system, high pressure melting 395–398
  - continuous equilibrium 395–398
  - G-X diagrams 403–404
  - melting loop 395–396
  - peritectic and eutectic regions 396
  - singular point 396, 397, 398
  - solidus 395, 397
  - solvus 395–398
- albite solid solution
    - in Ab-Or system 259, 260
    - in Ne-Ks-SiO<sub>2</sub> system, 266, 268, 269
    - in Ne-SiO<sub>2</sub> system 246–247
  - albite-water system
    - high pressure melting 394–395
    - incongruent melting 394
  - alkali basalt
    - basalt classification and 8
    - basalt tetrahedron and 16, 17
    - definition 2

- alkalai basalts [*cont.*]  
 fractional crystallization 278  
 high pressure fractionation 359  
 mineralogy 7–9  
 parent 253  
 petrography 17  
 sources 4
- alkali basalt magma, source region 412
- alkali excess 77
- alkali exchange 256
- alkali feldspar 255–293  
 high pressure melting 371  
 melting behavior 288–293  
 wet high pressure melting 395–398,  
 403–404
- alkali feldspar join (*see* albite-orthoclase  
 join)
- alkalic melt 368
- Alkemade line 161
- allivalite 137, 139
- alumina (*see also* corundum)  
 abundance in earth's crust 9  
 in synthesis of anorthite 39–40
- aluminum, incorporation into  
 diopside 53–54, 77, 81
- amphibole 381, 389, 391, 402, 408
- anatexis 402
- andalusite 55
- andesite 390
- anorthite  
 continuous equilibrium with  
 corundum 351–353  
 high pressure melting 351–353  
 incongruent melting at high  
 pressure 351–352  
 melting point 39–40  
 metastable melting 353  
 singular point at high pressure 351–353  
 in solid solution 56–57, 61–75  
 synthesis 39
- anorthite-albite system 61–75  
 assimilation of crystals in 69–71  
 equilibrium crystallization 65–67  
 equilibrium melting 68  
 fractional crystallization 67–68, 71–73  
 fractional melting 68, 71–73  
*G-X* diagrams, 73–75  
 instantaneous solid composition 67  
 lever rule application 64–75, 70–73  
 liquidus curve 63–64, 66  
 partition ratio during crystallization 65  
 solid solutions 73–75  
 solidus curve 63–64, 66  
 TLC path 68, 71–73  
 TSC path 67–68, 71–73
- T-X* plot 63, 66, 72, 74  
 variance 64
- anorthite-albite-orthoclase  
 system 279–284
- equilibrium crystallization 281–283  
 fractional crystallization 280–282  
 ISC path in fractional  
 crystallization 280–281  
 liquid path 280–281
- anorthite-nepheline-silica system, thermal  
 barrier 248–250
- anorthoclase 250
- anorthosite 94, 112, 116, 220, 357, 364
- apatite 11, 221, 224
- apparatus, high pressure  
 cold-seal 347, 348  
 diamond anvil 349  
 gas 348–349  
 single-stage 346–347
- aqueous pressure 382
- assemblage  
 metastable 312, 315  
 stable 312, 314
- assimilation, in An-Ab system 69–71
- asthenosphere 402
- asymmetrical solutions 291
- atmosphere 382
- atmosphere (pressure unit), conversion to  
 bars 26
- augite  
 basalt classification and 7, 17  
 in CMFS system 339–344  
 definition 54  
 exsolution lamellae of 198  
 in Fo-Di-SiO<sub>2</sub> system 181, 182, 184,  
 198, 212, 213  
 in Kiglapait intrusion 220, 221, 222  
 in Skaergaard intrusion 224, 227
- augite-ferroaugite-ferrohedenbergite  
 series 7, 296
- bar (pressure unit), definition 26, 345
- basalt (*see also* alkali basalt; tholeiitic  
 basalt)  
 abyssal 408  
 chemistry 9–10  
 critically undersaturated 251–253  
 definition 1  
 high alumina, definition 3  
 mineralogy 7–9  
 petrography 17–18  
 research problems 1–4  
 undersaturated 253

- basalt tetrahedron 12–13, 16–17, 54–57,  
81–83, 85, 253–254  
critical plane in 13, 151, 251, 327  
plane of silica saturation in 151, 158,  
161, 186, 327  
thermal barriers and 248, 251
- basanite 8
- beer 186
- beginning-of-melting curve (*see solidus*)
- binary eutectic system 43  
An-SiO<sub>2</sub> as 162  
definition 32  
Di-An system 37–60  
Di-SiO<sub>2</sub> as 182  
Fo-Di system 130, 131  
Fo-SiO<sub>2</sub> and 155  
idealized 52–53
- binary join, *G-X* projections onto 403–404
- binary loop  
lever rule in 65  
in olivine series 298
- binodal tangent 404
- boiling point curve 25
- Bowen trend 303, 304, 338–339
- bronzite, in Fo-Di SiO<sub>2</sub> system 184
- bronzitite  
in Fo-Di-SiO<sub>2</sub> system 199, 200  
in Ol-An-SiO<sub>2</sub> system 330–331  
in Stillwater complex 227
- bulk composition 45
- Bushveld complex 227, 340, 341
- CaCO<sub>3</sub> 38
- calc-alkali series 303, 304, 339
- calcic sanidine 220
- calcium  
in albite 77, 81, 118, 119  
in Di-An-Ab system 94, 118, 119  
in forsterite 131
- calcium Tschermak's molecule 18,  
54–57, 79–82, 119, 134, 144, 408  
definition 54  
high pressure melting and 356
- calorimetry 424
- CAMS system 18, 54–57, 131–133,  
146–149, 410
- CAMSN system 79–83, 85
- CaO 38
- CaO-MgO-FeO-SiO<sub>2</sub> system 339–344
- carbonation reaction 420
- carbon dioxide  
in Di-CO<sub>2</sub>-H<sub>2</sub>O system 398, 399  
effect on magma type 422–424  
occurrence in mantle 382  
solubility in silicates 381, 421  
ZIVC reaction and 418–420, 422
- carnegieite 244, 245, 249, 262–267
- cation equivalent (*see cation unit*)
- cation norm 233, 436
- cation unit 233, 235, 236, 328, 329, 330,  
435
- CaTs (*see calcium Tschermak's molecule*)
- chemical potential 306  
activity and 342  
definition 35, 58
- chemographic analysis 58  
of Fo-Di-SiO<sub>2</sub> system 189–191  
of Mg-Fe-Si system 333–338  
principles of 190–193
- chemographic diagram 196 (*see also*  
compositional polygon; compositional  
triangle)  
in analysis of olivine melting 311–316  
of Fe-SiO<sub>2</sub>-O system 373  
of Fo-Di-SiO<sub>2</sub> system 189–196  
oxygen projection and 316
- chemographic space 81
- CIPW norm 233  
calculation 10–12, 14–15, 427–434  
common normative mineral molecules  
in 11  
nepheline in 243–244
- Clausius-Clapeyron equation 28, 307, 345
- clinoenstatite 152
- clinopyroxene 220, 221, 231, 233, 234,  
235
- clinopyroxene series 296 (*see also*  
augite-ferroaugite-ferrohedenbergite  
series)
- CMFS system (*see CaO-MgO-FeO-SiO<sub>2</sub>*  
system)
- coesite 361, 368, 420
- comendite 77
- component, definition 32
- composition, critical 395, 404
- composition, minimum 395, 404
- composition space 81
- compositional polygon; 189
- compositional triangle) 191
- compressibility, of mantle material 408
- concentration, as intensive variable 34
- condensed phase 22
- condensed system 360
- conjugation line 161
- contamination 69
- contamination hypothesis 339
- continuous equilibrium  
Ab + Jd + L 365–366

- continuous equilibrium [*cont.*]  
 Ab + Sa + L 395–398  
 An + Cor + L 351–353  
 Fo + Pr + L 362  
 San + Lc + L 370  
 convection 218–219, 410  
 cordierite 248, 249  
 core-mantle boundary 345  
 corundum 39, 40, 351–353, 355  
 cotectic 57, 109–110, 120–124, 193, 228  
 (*see also* field boundary)  
 cristobalite 153, 154  
 in Fo-An-SiO<sub>2</sub> system 329  
 in Fo-Di-SiO<sub>2</sub> system 182, 185, 186  
 in Fo-SiO<sub>2</sub> system 155  
 in high pressure systems 360, 361, 362, 364  
 in Ks-SiO<sub>2</sub> system 256–257  
 melting point 256  
 in Ne-Ks-SiO<sub>2</sub> system 262, 265  
 in Ne-SiO<sub>2</sub> system 245  
 in Ne-SiO<sub>2</sub>-X ternary systems 248–250  
 in Ol-An-SiO<sub>2</sub> system 330  
 in silica-water system 386–388  
 synthesis 38  
 critical curve 386  
 critical end point 384, 385, 386, 388  
 critical line 395  
 critical plane 13, 151, 251–253, 278, 327  
 as model system 251–253  
 critical point 23, 24, 25, 26, 292–293  
 critical temperature, of solvus 292–293  
 cryptic layering 219  
 cryptic variation 219  
 crystal 21–29  
 melt structure and 421, 424  
 premonitory phenomena 27, 363, 397, 424  
 structure, definition 22  
 crystalline solution, mixing properties 289, 424  
 crystallization (*see also* equilibrium crystallization; fractional crystallization)  
 isothermal 47–48, 136  
 principles of 27  
 crystal path (*see* TSC path)  
 crystal settling  
 in cooling magma 218  
 Fo-Di-SiO<sub>2</sub> system and 213  
 in Muskox intrusion 232  
 cumulate 219  
 cumulus minerals  
 in Kiglapait intrusion 220  
 in Skaergaard intrusion 224
- cuspidal  
 abyssal tholeiite melting at 409–412  
 carbonation reaction and 420–422  
 in fayalite melting curve 371  
 on melting curve 363, 367, 368  
 cyclic units 227–229, 230, 232
- dacite 2  
 degeneracy 205, 301, 317, 377  
 degenerate equilibrium, definition 205  
 degrees of freedom 36 (*see also* variance)  
 diamond 423  
 diffusion  
 adcumulus growth and 240  
 in albite-orthoclase join 293  
 in cooling magma 218  
 intracrystalline, during crystallization 65, 67  
 dilution 368, 411, 423  
 dimension, variance and 45  
 diopside  
 Al entry into 53–54, 77, 81  
 glass, synthesis 38  
 high pressure melting 350–351  
 melting point determination 38–39  
 in pyroxene quadrilateral 296, 340  
 synthesis 37–38  
 diopside-albite system 77–84  
 components 79–83  
 liquid trends 79–83  
 melting intervals 83  
 solid solutions 81–83  
 thermal barrier 83  
 diopside-anorthite system 37–60  
 as binary system 42–43  
 equilibrium crystallization 50  
 equilibrium melting 50  
 fractional crystallization 50–51  
 fractional melting 51–52  
 G-X diagrams 58–60  
 high pressure melting 353–354  
 lever rule application 47–49  
 mixture preparation 40  
 as model system 57–58  
 solid solutions 53–57  
 T-X plot 41  
 variance 43–46  
 diopside-anorthite-albite system 85–128  
 equilibrium crystallization 91–104  
 equilibrium melting 114  
 fractional crystallization 104–112  
 fractional melting 114–117

- fractionation paths in 106–109,  
 123–126  
 high pressure melting 356–357  
 ILC paths 122  
 ISC paths 112–114, 121  
 lever rule application 120–123  
 non-ternary nature 117–118, 119  
 plagioclase loop in 93–94  
 plane on basalt tetrahedron 82, 85  
 ternary *T-X* projection for 87–90  
 TLC path 122  
 TSC path 101–105, 111, 114,  
 115–117, 121, 126–128  
 variance 91, 98–99, 106  
 diopside-carbon dioxide-water system, high  
 pressure melting 398, 399  
 diopside-enstatite join  
   in Fo-Di-SiO<sub>2</sub> system 182–184, 185,  
   186  
   plane of silica saturation and 186  
   *T-X* diagram 184  
 diopside-nepheline-silica system, thermal  
 barrier 248–250  
 diopside-pigeonite boundary, in Fo-Di-SiO<sub>2</sub>  
 system 206–207  
 diopside-silica system 182  
 diopside solid solution 55–56, 82, 85  
   Di-rich compositions and 202–206  
   in Fo-Di-SiO<sub>2</sub> system 182–190,  
   195–200, 203–206  
   projections 209–211  
   Mg entry into 131  
 diopside-water system, high pressure  
 melting 398, 399  
 diorite 220  
 Disko Island 305  
 disorder 27  
 dissociation, of volatiles in magma 305,  
 339  
 dissociation reaction, in incongruent  
 melting 151  
 divariant region 44  
 divariant surface, in ternary eutectic  
 system 134  
 divariant system 36, 44  
 dolomite, carbonation reaction 420–422  
 dunite 139, 140, 197, 198, 199, 200,  
 227  
 eclogite 408, 409  
 electron probe 185, 187  
 enantiomorph 313, 335  
 energy, internal 35  
 enstatite 55, 79, 152 (*see also*  
   diopside-enstatite join;  
   protoenstatite)  
   on basalt tetrahedron 151  
   high pressure melting 358, 361–363  
   incongruent melting 152–154,  
   157–158, 248, 326, 389, 390  
   in Fo-Di-SiO<sub>2</sub> system 182–203  
   in pyroxene quadrilateral 296  
   thermal barrier at high pressures 363,  
   364  
 enstatite-water system 388, 389, 390,  
 391  
 enthalpy 33  
 entropy 28, 33, 35, 407  
 equilibrium  
   chemical, definition 34  
   continuous (*see* continuous equilibrium)  
   local 34  
   metastable, definition 34  
   stable, definition 34  
 equilibrium crystallization 50, 68  
   bulk composition and path of 119  
   completion in ternary system 99  
   equilibrium path, derivation 123,  
   126–128  
 eutectic melting reaction, as temperature  
 buffer 307  
 eutectic point (*see also* binary eutectic  
 system)  
   characteristics 45, 47–49  
   definition 43, 134  
   even reaction at 153  
   silica saturation and 57  
   ternary 57, 133  
 eutectic temperature, crystallization  
   at 49–50  
 even curve, in Fo-Di-SiO<sub>2</sub> system 207  
 even reaction 153  
   of An + Cor at high pressure 351  
   in Fo-Di-SiO<sub>2</sub> system 196, 204, 205  
   in high pressure Ne-SiO<sub>2</sub> system 366  
   in Ne-Ks-SiO<sub>2</sub> system 270, 284–286  
   in Ol-An-SiO<sub>2</sub> system 330  
   in olivine melting 320  
 exsolution 198  
 extensive variables 33  
   phase rule and 35  
 fayalite 11, 296–298, 303–304  
   high pressure melting 370–372  
   incongruent melting 297–298,  
   301–302, 321–322

- fayalite [*cont.*]  
   melting 309–311  
   oxidation 303–304  
   stability, limit of 321  
   synthesis 296  
 fayalite granite 326  
 fayalite-nepheline-silica system, thermal  
   barrier in 248–250  
 FDS (*see* forsterite-diopside-silica system)  
 FE (*see* fictive extract)  
 feedback effect 412  
 feldspar fractionation 279–284  
 feldspar minimum 278  
 feldspar solid solution in Ne-Ks-SiO<sub>2</sub>  
   system 262, 263, 264, 284–286,  
   287  
 feldspathoid 3  
 Fenner trend 303, 304, 339  
 FeO-Fe<sub>2</sub>O<sub>3</sub>-SiO<sub>2</sub> system 301  
 ferrosilite 11  
   as barometer 300  
   high pressure melting 373–378  
   instability at low pressure 327  
   in pyroxene quadrilateral 296  
 ferrosyenite 139, 220  
 Fe-SiO<sub>2</sub>-O system 297, 300, 309–322,  
   376–377  
   degeneracy 377  
   divariant surfaces 377  
   fayalite melting 297  
   Schreinemakers analysis 309–322  
   singular points 376  
   T-X projection 310–311  
   variance 309  
 Fe-Ti oxide minerals 328  
 fictive extract  
   definition 166, 207, 285  
   in Di-An-Ab system 96  
   in Fo-Di-An system 137  
   in Fo-Di-SiO<sub>2</sub> system 189, 191, 197,  
   207  
   in MgO-FeO-SiO<sub>2</sub> system 481  
   in Ne-Ks-SiO<sub>2</sub> system 285–286  
 fictive mean composition (*see* total liquid  
   composition)  
 field boundary  
   definition 88  
   in Di-An-Ab system 88–89, 93, 95,  
   105  
   in Fo-Di-An system 138, 142  
   in ternary eutectic system 135  
 first melt 368, 370  
   gas phase and 413–418  
 fluid inclusions 382  
 FMQ oxygen buffer reaction 304, 305,  
   306–308  
   in olivine melting 314, 322  
 forsterite 11, 182, 183  
   Ca entry into 131  
   in enstatite melt 152  
   in enstatite-water system 388, 389  
   high pressure melting 357–358  
   melting point 130  
   in phlogopite-water system 399, 400  
   plane of silica saturation and 151  
   synthesis 130  
 forsterite-anorthite system  
   properties 130–133  
   spinel and 130–133  
   variance 131  
 forsterite-anorthite-silica system 161–180  
   application to basalts and related  
   rocks 176–180  
   binary joins 162  
   comparison to O1-An-SiO<sub>2</sub>  
   system 328–331  
   cotectic crystallization 163–164  
   equilibrium crystallization 164–171  
   equilibrium melting 174  
   fractional crystallization 171–174  
   fractional melting 174–176  
   high pressure melting 363–365  
   liquidus diagram in cation units 329  
   peritectic point, high pressure 364  
   phase diagram 162  
   primary phase regions 162–163  
 forsterite-diopside system 130–131  
 forsterite-diopside-albite system 83, 251  
 forsterite-diopside-anorthite  
   system 129–149  
   basalt tetrahedron and 146–149  
   equilibrium crystallization 135–138  
   equilibrium melting 140  
   eutectic liquid produced on melting 144  
   fractional crystallization 138–140  
   fractional melting 140–143  
   high pressure melting 358–360  
   lever rule application in equilibrium  
   crystallization 137  
   in fractional melting 142–143  
   melting hiatus 140  
   as model of Kiglapait intrusion 223  
   of Muskox intrusion 231  
   of Skaergaard intrusion 224–227  
   non-ternary effects 144–145  
   ternary eutectic point in 133, 134,  
   143–144, 145  
   three-phase triangle analyses 136–144

- TSC path in equilibrium crystallization 137
  - in equilibrium melting 140
  - in fractional crystallization 139
  - in fractional melting 140–143
- forsterite-diopside-anorthite-albite system 145, 251–253
- forsterite-diopside-anorthite-silica system
  - as model of Muskox intrusion 233–235
  - pigeonite field in 237–239
- forsterite-diopside-anorthite-spinel system, components 146
- forsterite-diopside-silica system 181–215
  - bounding joins 182
  - chemographic analysis 189–196
  - cotectic boundary 193, 196, 197, 199–200, 206
  - diopside-pigeonite boundary in 206–207
  - Di-rich compositions 202–206
  - Di-rich region, *T-X* section 211
  - equilibrium crystallization 186–196, 202–206
  - even reaction 196, 204, 205, 206
  - fictive extract 189, 191, 207
  - fractional crystallization 196–200
  - fractional melting 200–202
  - high pressure melting 365
  - ILC path in fractional melting 201–202
  - ISCs, in fractional crystallization 197, 198, 199, 213
  - lever rule application 197, 201, 202
  - maximum 186, 203, 204, 205, 206
  - melting loop 183–184
  - minimum 186, 196, 203, 206
  - as model 254
    - for basalts and granites 212–213
    - of Muskox intrusion 231
    - of Skaergaard intrusion 224–225
    - of Stillwater complex 228–229
  - odd reaction 189, 191, 204, 205, 206, 213
  - olivines and pyroxenes in 182–184
  - peritectic 186, 189, 191, 193, 195, 210, 211
  - phase diagram 185
  - reactions in four-phase region 189–196
  - solidus curves 183–184
  - three-phase triangle 188
  - tie lines and bulk compositions 187, 188, 189, 190
  - tie line template 187, 188
  - TLC path, in fractional melting 201–202
  - TSC paths, in equilibrium crystallization 189–196
    - in fractional crystallization 197–200
    - in fractional melting 201–203
    - two-liquid field 184–186
    - variance 189, 191, 192, 193, 194, 195, 197
- forsterite-diopside-silica-water system
  - high pressure melting 390–393
  - TLC path, in fractional fusion 392–394
  - TSC path, in fractional fusion 392
- forsterite-fayalite series, binary loop 298–299
- forsterite-nepheline-silica system, thermal barrier 248–250
- forsterite-plagioclase-silica-water system, high pressure melting 389–390
- forsterite-protoenstatite system, melting 157
- forsterite-silica system 151–159, 424
  - binary eutectic region 155, 158, 159
  - equilibrium crystallization 154–156
  - fractional crystallization 156
  - fractional melting 157
  - G-X* diagrams 158–159
  - liquid hop, in fractional melting 157
  - high pressure melting 361–363
  - incongruent melting 156–157
  - phase diagram 158
  - rock path, in fractional melting 157
  - silica oversaturated reaction 154
  - singular point 362
  - TSC path, in equilibrium crystallization 154
  - variance 154
- forsterite solid solution
  - in Di-Fo system 131
  - in Fo-Di-SiO<sub>2</sub> system 182–211
- forsterite-water system
  - gas phase 384
  - high pressure melting 383–385
  - P-T-X* prism 384, 385
  - solvus 384
- fractional crystallization 50–51
  - accumulates and 240
  - in binary system 261–262
  - bulk composition and path of 119
  - lever rule and 71–73, 120–123
  - of magma 219
  - magma variation and 3
  - natural basalts and 112
  - simplified rock compositions from 142
  - in ternary system 104–112
  - completion 108–109

- fractional crystallization [*cont.*]  
 by zoning 67, 68  
 fractional fusion (*see* fractional melting)  
 fractional melting 114–117, 121–126,  
 392  
 fractionation path  
 definition 106  
 derivation 123  
 tie lines and 95  
 free energy (*see* Gibbs free energy)  
 free lunch 317  
 freezing point depression 43  
 fugacity  
 definition 306  
 parameters of 306–307  
 fundamental axiom of Schreinemakers 312  
 furnace, in high pressure apparatus 346
- gabbro** 140  
**gabbroic anorthosite** 94, 112, 116, 220,  
 357, 364  
**gabbroic rock, plagioclase content** 94,  
 105, 112  
**garnet** 356, 406–408, 420  
**garnet lherzolite** 410, 411  
**gaseous state** 22 (*see also* vapor)  
**gas mixing, for syntehsis of**  
 fayalite 296–297  
**gas phase** 382–383, 400–402  
 in magma genesis 413–418, 420–424  
**Geophysical Laboratory** 37  
 temperature scale 328, 358, 359  
**geotherm** 367, 368, 407, 411  
**Gibbs energy of mixing** 290  
**Gibbs free energy** 35, 58, 424  
 activity and 342  
 fugacity and 306  
 in *G-X* diagrams 58–70, 73–75,  
 158–159, 213–215, 288–293,  
 403–404  
**glass** 24  
**granite** 322  
**Great Dyke** 227  
**grossular** 352  
*G-X* diagram (*see* Gibbs free energy)
- harzburgite** 227, 330–331, 337  
**heat capacity of rock** 143  
**hedenbergite, in pyroxene**  
 quadrilateral 296, 340  
<sup>3</sup>He/<sup>4</sup>He ratio 381  
**hematite** 300  
**hematite-magnetite buffer** 322  
**hercynite, in Ne-SiO<sub>2</sub>-X ternary**  
 system 249  
**heteronuclei** 28  
**HM buffer** (*see* hematite-magnetite buffer)  
**hydrogen, in FMQ oxygen buffer**  
 reaction 304  
**hydrosphere** 382  
**hypersthene** 7, 11, 151, 181, 184, 198,  
 328  
**hypersthene basalt** 8, 16, 253
- ice, polymorphs** 26  
**ideal solution, definition** 342  
**ILC** (*see* instantaneous liquid composition)  
**ilmenite** 8, 11, 328  
**incongruent dissolution** 395, 413  
**incongruent melting**  
 in binary system 151–159  
 definition 151, 152  
 of diopside 203  
 of diopside-enstatite 183–186  
 of fayalite 297–298, 301–302  
 pressure and 326, 351–352  
 of sanidine 256–258  
 in ternary system 161–180  
**indifferent crossing** 395  
**indifferent phase** 318  
**instantaneous liquid composition**  
 definition 52  
**instantaneous solid composition**  
 definition 51  
 hop (*see* rock hop)  
**intensive variables** 34–36  
**intensive variable space** 373  
**intercumulus liquid** 220, 227, 231, 239,  
 240–241  
**interior phase, pigeonite (example)** 191  
**invariant by restriction** 197, 261  
**invariant point** 45, 131, 244, 312–319  
**invariant system, definition** 36  
**iron** 295–304  
 oxidation 378  
 in olivines 298–299  
 olivine melting and 309–311  
 in silicates 296  
**iron crucible** 297, 322  
**iron enrichment** 303  
**iron oxidation, silica saturation**  
 and 250–251  
**iron oxide, basalt classification and** 17  
**iron silicate liquids, oxygen**  
 content 327–328  
**iron-wüstite buffer** 304, 305

- ISC (*see* instantaneous solid composition)
- isentrope 408
- isobaric sections 376
- isotherm 43, 125–126, 408
- isothermal section  
 definition 96  
 for Di-An-Ab system 96–98
- IW buffer (*see* iron-wüstite buffer)
- jadeite 264, 354, 355, 365–369, 406
- join, binary 161, 162  
 definition 55
- kalsilite 11, 256, 399, 400
- kalsilite-silica system 256–258, 369–370  
 continuous equilibrium 370  
 crystallization 256–257  
 high pressure melting 369–370  
 melting 256–258  
 metastable melting point 369  
 singular point 369–370  
 variance 256–257
- kalsilite solid solution, in Ne-Ks-SiO<sub>2</sub>  
 system 262–267
- katanorm 223 (*see also* cation norm)
- Kiglapait intrusion 139, 220–223, 225,  
 241, 283  
 pyroxene quadrilateral and 340–344
- Kilauea 235, 236
- kimberlite 381
- kimberlitic magma 421–423
- Kipp generator 304
- kyanite 55, 352, 356, 408
- large ion lithophile elements 369, 410
- latent heat of crystallization 48, 218
- latent heat of fusion 48, 70, 143
- lattice 22
- lava, temperature 1, 57, 94
- lava lake  
 equilibria in 424  
 olivine hiatus in 326
- layered intrusions 217–241, 326  
 Fo-Di-SiO<sub>2</sub> system and 213  
 magnetite and Ca-poor pyroxene in 338  
 olivine hiatus in 326  
 pyroxene quadrilateral and 339–344
- LeChatelier's principle 341
- leucite 11  
 high pressure melting  
 behavior 369–370  
 in Ks-SiO<sub>2</sub> system 256, 257  
 melting point 256  
 in phlogopite-water system 399, 400
- leucite-nepheline-silica system, thermal  
 barrier 248–250
- leucite-silica system 256–258, 261
- leucite solid solution  
 in Ab-Or system 259, 260  
 in Ne-Ks-SiO<sub>2</sub> system 262–266,  
 270–272, 284–286
- lever rule 46–47  
 An-Ab system and 64–65, 71–73  
 application to A-H<sub>2</sub>O systems 402  
 in binary loop 64–65  
 in Di-An system 46–47  
 with fractional crystallization and  
 melting 71–73, 120–123  
 in ternary system with equilibrium  
 crystallization 99–104, 119  
 with fractional crystallization 110,  
 119, 120–123
- lherzolite 405, 407
- LIL elements (*see* large ion lithophile  
 elements)
- liquid  
 definition 22  
 interface with vapor 23
- liquid field  
 definition 96
- liquid hop 52, 116, 141, 157
- liquid path 113–114, 280, 281
- liquid state 25
- liquidus  
 definition 42  
 eutectic point and 43, 45  
 lever rule and 47
- liquidus curve 78
- liquid fractionation line 120, 121  
 derivation of 125–126  
 in derivation of equilibrium liquid  
 path 127  
 in Ne-Ks-SiO<sub>2</sub> system 273–274
- liquidus maximum (*see* maximum)
- liquidus minimum (*see* minimum)
- liquidus surface 87–89
- local equilibrium 34
- Low Velocity Zone 402
- magma  
 definition 1  
 fractional crystallization 219  
 genesis 405–425  
 lunar 305  
 mixing 412

- magma [*cont.*]  
   primary types 254  
   rate of cooling 218  
   source region 129, 346, 405  
 magnesite 420  
 magnetite 8, 11, 220, 224, 300, 301, 304,  
   309–311, 328, 373, 375, 376  
   basalt classification and 8  
   in high pressure systems 373, 375, 376  
   in Kiglapait intrusion 220  
   olivine melting and 309–311  
   in Skaergaard intrusion 224  
 magnetite-wüstite buffer 318–319, 322  
 magnesiowüstite 327, 332  
 magnesium Tschermak's molecule 79–80  
 mantle xenoliths 381  
 marble 420  
 mass 33  
 maximum  
   in Fo-Di-SiO<sub>2</sub> system 186, 203,  
   207–212  
   G-X diagrams and 213–215  
 maximum, thermal, on solidus 421–422  
 mean plagioclase composition 110–112,  
   118, 119  
 melt 21–29  
   definition 22  
   premonitory phenomena 27, 363, 397,  
   424  
   supercooling in 28  
 melting (*see also* minimum melting)  
   beginning of  
     curve (*see* solidus)  
     definition 40  
   equilibrium 50, 51  
   fractional 51–52  
     lever rule and 71–73, 120–123  
   as function of pressure 28–29  
   high pressure 350–378  
   incongruent (*see* incongruent melting)  
   isothermal 47–48, 143–144  
   in model system A-H<sub>2</sub>O 399–402  
   principles of 27  
   retrograde 317  
   ternary eutectic 143–144  
 melting hiatus 116, 140  
 melting interval 43, 83  
 melting loop 63, 64, 183–184  
 melt structure 27, 363  
   crystal structure and 421, 424  
 membrane equilibrium 338  
 mesocumulate 240  
 mesostasis 158  
 metastable extension 34, 153, 312–323,  
   385–386  
 metastable melting 260, 353, 361–362  
 metastability, limit of 293  
 Mg-Fe-Si-O system  
   crystallization paths 336–337  
   invariant points, analysis  
     about 331–338  
 MgO, in synthesis 38  
 MgO-FeO-SiO<sub>2</sub> system  
   high pressure melting 378  
   iron effects 325–327  
   oxygen effects 331–338  
 MgO-Fe-O-SiO<sub>2</sub> system 302–303  
 micropegmatite 2, 224  
 microsyenite 3  
 mineral facies 405–409  
 mineral variation 219  
 minimum 404  
   in Ab-Or system 258, 261  
   in Fo-Di-SiO<sub>2</sub> system 186, 196, 203,  
   207–212  
   G-X diagrams and 213–215  
   invariant by restriction 197  
   in Ne-Ks-SiO<sub>2</sub> system 262, 263–264,  
   272, 273, 274, 275, 278  
 minimum-melting system 208–209,  
   213–215  
 miscibility gap 339  
   definition 53  
 missing-phase notation 309–310, 314,  
   322–323  
 modal composition, definition 7  
 molar volume 28  
 molecular norm (*see* cation norm)  
 molecular percent 41  
 mole fraction 41  
 monticellite 182  
 monzonite 220, 338, 341  
 mullite, in Ne-SiO<sub>2</sub>-X ternary system 249  
 Muskox intrusion 213, 227, 230–237, 240  
 MW buffer (*see* magnetite-wüstite buffer)
- Nain complex 378  
 nepheline 3, 11  
   basalt classification and 8, 17  
   CIPW norm and 243–244  
   synthesis 244  
 nepheline-silica system 243–247,  
   365–369  
   crystallization 246  
   cusp 367  
   high pressure melting 365–369  
   invariant point 367, 368  
   inversion point 244

- melting 244–246
- odd and even reactions 366
- singular point 366, 367, 368
- solidus 245, 246
- solvus 245, 246
- T-X* diagram 245
- variance 244
- nepheline-kalsilite-silica system 262–279
  - equilibrium crystallization 270–271, 284–288
  - fractional crystallization 272–274, 288
  - fractional melting 274–277, 288
  - isothermal sections 263, 265–269
  - lever rule application 284–285
  - liquidus diagram 262–264
  - liquidus fractionation lines 273–274
  - minima 262–263
  - odd and even reactions 269–270, 284–286
  - peritectic point 262, 264, 275–277, 285, 286, 288
  - solidus fractionation lines 274–277
  - variance, complex changes in 287
- nepheline solid solution
  - in Ne-Ks-SiO<sub>2</sub> system 262–267, 271
  - in Ne-SiO<sub>2</sub> system 244, 245
- norite 116, 330–331, 338, 364, 365, 405
- normative composition, definition 7
- nucleation 24, 28, 218, 229
  
- ocean ridge geotherm 407–408, 411–412
- odd curve, in Fo-Di-SiO<sub>2</sub> system 207
- odd reaction 153, 157 (*see also* peritectic reaction)
  - in An-Cor high pressure system 351
  - in Fo-Di-SiO<sub>2</sub> system 189, 191, 193, 204, 205
  - in high pressure Ne-SiO<sub>2</sub> system 366
  - in Lc-SiO<sub>2</sub> system 261
  - in Ne-Ks-SiO<sub>2</sub> system 269, 270, 284–286
  - in Ne-SiO<sub>2</sub> system 245
  - in Ol-An-SiO<sub>2</sub> system 331
  - in olivine melting 314, 320
- olivine 11
  - basalt classification and 7–8
  - crystallization from Fo-Di-SiO<sub>2</sub> system 188, 189, 190
  - in Fo-SiO<sub>2</sub> crystallization 157
  - high pressure melting loops 371–372
  - iron-bearing 296–323, 325–338
  - iron-free (*see* forsterite)
  - melting 298–303
  - Schreinemakers analysis of 308–322
  - T-f*O<sub>2</sub> analysis 308–322
  - in Muskox intrusion 231–236
  - orthopyroxene reaction rim around 155–156, 158
  - oxidation 328, 343
  - pyroxene quadrilateral and 339–344
  - reaction relations 212–213
  - reaction with plagioclase at high pressure 389
  - silica activity and 342
  - in Skaergaard intrusion 224
- olivine-anorthite-silica system
  - even and odd reactions 330–331
  - iron effects 328–331
- olivine basalt, basalt tetrahedron and 16
- olivine gabbro 139, 220–221
- olivine hiatus 224, 326, 340
- olivine join 326–327
- olivine pyroxenite 140
- olivine tholeiite
  - basalt tetrahedron and 16
  - formation 253–254
  - wet solidus 408–409
- omphacite 408
- optimal phase boundary 293
- order 27
- orthoclase 11, 250, 255, 256, 258 (*see also* albite-orthoclase system)
- orthocumulate 240
- orthopyroxene
  - Ca-poor, in CMFS system 339–344
  - in Fo-SiO<sub>2</sub> crystallization 157–159
  - incongruent melting 155–159, 161
  - in Ol-An-SiO<sub>2</sub> system 330
  - reaction relation to olivine plus liquid 212
  - in reaction rim around olivine 155–156, 159
- orthopyroxene series 296, 326
- orthopyroxenite 198, 200, 231–236
- Oslo Province 304
- oxygen 8, 9, 303–323
  - dissolved 327–328
  - in Fo-Fa system 298
  - fugacity 306–308, 331, 338–339
  - in iron silicate liquids 327–328
  - magnetite formation and 304
  - in melts 305–306
  - partial pressure 306–307
  - retrograde melting and 317
- oxygen buffer 304–308, 315, 338 (*see also* FMQ oxygen buffer reaction; iron-wüstite buffer; magnetite-wüstite buffer)

- oxygen projection 311, 332–333  
oxygen unit, calculation 435–436  
oxysymplectite 328
- pantellerite** 77, 248  
parameters of state 33  
partial melt, during magma genesis 412, 417  
partial pressure of gas, definition 306  
partitioning 255  
partition ratio  
  calculation in ternary system 120–123  
  in plagioclase system 65, 66  
pascal 345  
peralkaline liquid 77, 84, 118  
peridotite 129, 408, 409  
  carbonation 420  
  model for magma genesis 417  
  in Muskox intrusion 231, 232  
peridotite-carbon dioxide-water  
  solidi 420–422  
peritectic point  
  definition 131  
  in Fo-Di system 130, 131  
  in Fo-Di-SiO<sub>2</sub> system 186  
  in Fo-SiO<sub>2</sub> system 153, 154  
  in Ks-SiO<sub>2</sub> system 256, 257  
  in Ne-Ks-SiO<sub>2</sub> system 262, 264, 288  
  odd reaction at 153  
phase  
  absent 314 (*see also* missing-phase notation)  
  definition 33  
  indifferent 318  
phase diagram, principles 4–6  
phase rule 31–36  
  application to Fo-An system 130–131  
  to Fo-Di-An system 133  
  definition 35–36, 43–44  
  isobaric 44  
  in pseudobinary system 78  
  ternary eutectic system and 57  
  variance and 35–36  
phase transition loop 244  
phlogopite 381  
phlogopite-water system, high pressure melting 398–399, 400  
phonolite 3  
  critically undersaturated basalt system and 253  
  in Ne-Ks-SiO<sub>2</sub> system 264, 278  
  Ne-SiO<sub>2</sub> system and 247  
phonolite minimum 278
- phosphorus  
  in basalts 295  
  in intercumulus liquid determination 241  
picritic basalt 235  
Picture Gorge 279, 280  
piercing point 134, 144, 261, 329, 330, 360  
pigeonite  
  in CMFS system 339–344  
  in Fo-Di-SiO<sub>2</sub> system 181–212  
  in high pressure system 365  
  as interior phase 191  
  reaction relation to olivine 212  
  reaction relation to Pr<sub>SS</sub> 212  
  in Skaergaard intrusion 224  
pigeonite, inverted 198  
pigeonite field  
  clinopyroxene and olivine projections in 238–239  
  in Fo-Di-An-SiO<sub>2</sub> system 233–234, 237–239  
  Muskox intrusion and 235–236  
pigeonite series 296  
piston, in high-pressure single stage apparatus 346–347  
plagioclase  
  basalt classification and 7–8, 17  
  crystal setting and 218  
  equilibrium crystallization 91–104  
  fractional crystallization 104–112  
  high pressure melting 355–356, 357  
  in Kiglapait intrusion 220, 221  
  in Muskox intrusion 231, 234, 235, 236  
  reaction time in crystal formation 91–92  
  reaction with olivine at high pressure 389  
  in Skaergaard intrusion 224  
plagioclase composition  
  mean 110–112, 118, 119  
  variability of, in ternary system 118  
plagioclase effect 77, 113, 118, 248–250  
plagioclase feldspar, *T-X* plot 72 (*see also* anorthite-albite system)  
plagioclase lherzolite 410, 411  
plagioclase loop 63, 64, 75, 93–94  
plagioclase solid solution 82  
plagioclase system (*see* anorthite-albite system)  
platinum 38, 39  
pore liquid (*see* intercumulus liquid)  
porosity 239  
potassium 255–293  
  first melts and 370

- occurrence in minerals 255  
 potassium feldspar (*see* orthoclase; sanidine)  
 premonitory phenomena 27, 363, 397, 424  
 pressure (*see also* aqueous pressure; vapor pressure; water pressure)  
   as function of depth 345  
   as intensive variable 34  
   total 382  
   units 26  
   variable in energy equation 35  
 pressure, high  
   apparatus 346–349  
   effects of 345–379  
   effects of volatiles at 381–404  
   melting curves at 350–378  
 pressure projection 374–378  
 primary magma 254  
 primary phase field 88  
 projection (*see also* oxygen projection)  
   in analysis of Muskox intrusion 234  
   for Fe-SiO<sub>2</sub>-O system 373–378  
   pressure 374–378  
   *P-T* 386  
   relation to section 384  
 protoenstatite 152, 153, 154, 424  
   from equilibrium crystallization of Fo-SiO<sub>2</sub> system 154–155  
   in Fo-An-SiO<sub>2</sub> system 329  
   in high pressure systems 358, 362, 364  
   metastable melting point 361, 362  
   reaction relation to pigeonite 212  
 protoenstatite-cristobalite, melting 156–157  
 protoenstatite solid solution 182–203, 211, 212  
 pseudobinary diagram 78  
 pseudobinary section, in Fo-Di-SiO<sub>2</sub> system 183, 184  
 pseudobinary sideline, in Fo-Di-An system 140–141  
 pseudoleucite 271  
 pyroxene 11 (*see also* augite; hypersthene; pigeonite)  
   anorthite and 54  
   basalt classification and 7–8, 17  
   Ca-poor, in layered intrusion 338  
   Di-En join 182–184  
   iron-bearing 339–344  
   role of Al in 53–54  
   silica activity and 342  
 pyroxene join 326–327  
 pyroxene quadrilateral 296, 339–344  
 pyroxene solid solution 186  
 QFM oxygen buffer reaction (*see* FMQ oxygen buffer reaction)  
 quartz 2, 11, 79  
   basalt classification and 8  
   in eclogite 408  
   in high pressure systems 352, 354–356, 360–362, 364  
   metastable melting point 361  
   olivine melting and 309–311  
   in silica-water system 386–388  
   in Skaergaard intrusion 224  
 quartz basalt 253  
 quartz diorite 198  
 quartz monzonite 198, 341  
 quaternary system, definition 32  
 quenching method 39  
  
 reaction  
   in Fo + An + Sp crystallization 148, 149  
   in Fo-Di-SiO<sub>2</sub> system 189–196, 204–206, 212  
   intracrystalline, during crystallization 66, 133  
   in Ne-Ks-SiO<sub>2</sub> system 287  
 reaction constant, in determination of silica activity 343  
 reaction point, in Fo-SiO<sub>2</sub> crystallization 154–159  
 reaction relation, olivine 155, 212, 326, 365  
 rectilinear diameter 291, 292  
 residual liquid, in Fo-Di-SiO<sub>2</sub> system 200  
 residua system 262–279 (*see also* nepheline-kalsilite-silica system)  
 residuum 51, 58, 69, 158  
 resorption 148  
 retrograde melting 317  
 reversible path 67  
 rhyolite 2, 253, 254  
   critically undersaturated basalt system and 253  
   granite and 322  
   formation 254  
   in Ne-Ks-SiO<sub>2</sub> system 264, 269, 278  
   Ne-SiO<sub>2</sub> system and 247  
   in wet high pressure systems 390, 392  
 rhyolite minimum 278  
 rhythmic layering 219, 227  
 Richardson's rule 322–323, 332, 334, 335, 373  
 rock hop 52, 139, 140, 156  
   definition 51, 113

- rock path (*see* instantaneous solid composition path)
- ruled surface 375
- rule of moments 46–47 (*see also* lever rule)
- rule of V's 89
- sanidine 256  
 in high pressure systems 369–370, 395–398  
 incongruent melting 250, 256, 259  
 in Ks-SiO<sub>2</sub> system 256–258  
 in Lc-Ne-SiO<sub>2</sub> system 249–250  
 melting properties 288–293  
 mixing properties of solutions of 291  
 synthesis 256
- sanidine solid solution  
 in Ab-Or system 258–261  
 in Ne-Ks-SiO<sub>2</sub> system 266–272
- Schreinemakers analysis  
 of olivine melting 308–322  
 of MgO-FeO-Fe<sub>2</sub>O<sub>3</sub>-SiO<sub>2</sub> system 332–338
- Schreinemakers' rules 312–313, 360, 363, 373, 420
- section, relation to projection 384
- silica  
 abundance in earth's crust 9  
 activity 342–344  
 in basalts 2  
 first melts and 370  
 high pressure melting 360–361  
 pyroxene trends and 341–342  
 vapor pressure 360
- silica excess 77
- silica saturation 8, 58  
 basalt tetrahedron and 13  
 CIPW norm calculation 12  
 effect of pressure on 412–413  
 eutectic and 57  
 in Fo-SiO<sub>2</sub> system 154–156, 157  
 in natural analogs of Fo-Di-An system 145  
 in spinel + L field 148–149
- silica saturation, plane of 13, 83, 151, 159, 161, 186, 327  
 iron oxidation and 250–251  
 Kiglapait intrusion and 220  
 orthopyroxene series and 326
- silicate  
 crystal growth 24  
 crystalline densities 23  
 gas phase 360  
 glass, synthesis 40
- iron in 296  
 liquid structure 24  
 melting curves 29  
 physical properties 23–24  
 vapor state 42  
 viscosity 23
- silica-water system 385–389  
 critical curve 386  
 critical end point 384, 385, 386, 388  
 triple point 385, 386
- sillimanite 55
- Simon equation 371, 372
- singular point  
 in Ab-Or system 261  
 in An-Cor high pressure system 351–353  
 in FeO-Fe<sub>2</sub>O<sub>3</sub>-SiO<sub>2</sub> system 301, 319–322  
 in Ne-Ks-SiO<sub>2</sub> system 274  
 in Ne-SiO<sub>2</sub> high pressure system 366  
 olivine melting analysis and 301, 319–322
- Skaergaard intrusion 219–220, 224–227, 240  
 iron enrichment 303  
 pyroxene quadrilateral and 340–344
- S-L curve (*see* melting curve)
- S+L region 64
- soda leucite 264, 271
- sodium disilicate 62, 79, 244
- solid-solid leg, of three-phase triangle 92, 96, 101, 119
- solid solution 29, 42, 143  
 in An-Ab system 73–75  
 of anorthite in CAMS system 56–57  
 binary 52–53, 326  
 CaTs and 55–57  
 in Di-Ab system 81–83  
 effect on TSC path in fractional melting 140  
 in Fo-Di system 131  
 near solvus 396, 397  
 non-binary 53–54
- solid state 25
- solidus  
 cusp on 409–412, 420–422  
 definition 42, 52  
 effect of water on 402  
 embedded in solvus 395, 404  
 in equilibrium melting of ternary system 114  
 eutectic point and 43, 45  
 in peridotite-CO<sub>2</sub>-H<sub>2</sub>O system 420–422
- solidus fractionation lines  
 derivation 123–124

- in derivation of equilibrium TSC
  - path 126–128
  - in Ne-Ks-SiO<sub>2</sub> system 274–277
- liquid (see also solid solution)
  - liquid 29
  - mixing properties 289, 424
- solvus
  - alkali feldspar 371
  - binodal 291–292
  - coherent 293
  - critical line 395, 397, 398
  - critical temperature of 292
  - definition 53, 183
  - in Fo-Di-SiO<sub>2</sub> system 183–185, 191, 205
  - in Ne-SiO<sub>2</sub> system 245, 246
  - in pyroxene quadrilateral 339–344
  - sanidine, in Ab-Or system 290
  - spinodal 293
  - ternary feldspar 283–284
- source region, of basaltic magma 129, 346
- space group 182
- spinel 18
  - Fo-An system and 130–133
  - in Fo-An-SiO<sub>2</sub> system 329
  - in Fo-Di-An system 146–149
  - in high pressure systems 359, 364, 372
  - in mantle 406–407
  - in Ol-An-SiO<sub>2</sub> system 330
- spinel lherzolite 410, 411, 420, 422
- spinel-nepheline-silica system, thermal barrier 248–250
- spinodal point 293
- state of matter 33
- statistical mechanics 31
- steam pressure 263, 278
- Stillwater Complex 227–230
- subalkaline basalt 156
- subduction zone 382, 408
- sublimation curve 25
- subsolvus reaction 308, 334, 359, 363
- supercooling 28
- supercritical fluid, definition 387
- superheating 28
- syenite 119, 220, 247
- syenite problem 247, 279
- system
  - closed, definition 31–32
  - component of, classification 32
  - definition 31–32
  - degenerate 206, 297, 301, 302, 320
  - extensive variables of 33
  - open, definition 32
- tangent rule 285
  - for fictive extract 166, 206–207, 285
  - for ISC path 106, 112
  - for odd and even reactions 166, 206–207, 285
  - for TSC path 112, 123
- temperature
  - as intensive variable 34
  - variable in energy equation 35
- temperature buffer, eutectic melting reaction as 307
- temperature contours 89, 90
- temperature scale 37, 328, 358, 359
- ternary eutectic system
  - melting in 143–144
  - properties 133, 134–135
- ternary feldspar 279–284
- ternary system
  - definition 32
  - graphical analysis of 86–91
  - variance in 91, 98–99
- T-fO<sub>2</sub> sections, of Fe-SiO<sub>2</sub>-O system 375
- thermal barrier 83, 242
  - absence of, in enstatite-water system 389
  - albite and 247, 365
  - enstatite and, at high pressures 363, 364
  - in high pressure systems 359, 363, 364, 365
  - in Ne-SiO<sub>2</sub> system 247
  - principle of 251
  - in ternary systems 247–251
- thermal buffer, cusp on melting curve 368, 411
- thermal divide (see thermal barrier)
- thermal maximum (see maximum)
- thermal ridge 422
- thermal valley 264, 278, 279
- thermocouple, in high pressure apparatus 347
- thermodynamic data 31, 424
- tholeiite
  - abyssal
    - definition 3
    - melting at cusp 409–412
  - basalt tetrahedron and 16
  - definition 2
  - formation 156
    - at high pressure 359
  - fractional crystallization 278
  - magma source 412
  - mineralogy 7–9
  - oceanic (see tholeiite, abyssal)
  - olivine, basalt classification and 8
  - parent 253
  - petrography 17

- Q-bearing, basalt classification and sources 4
- tholeiitic basalt  
 characteristics 212–213  
 formation 253  
 in MgO-FeO-SiO<sub>2</sub> system 326
- three-phase triangle  
 in analysis of Di-An-Ab system 91–92, 95–96, 98, 100–104  
 of Fo-Di-An system 136–144  
 Fe-Ol-L 302–303  
 in Fo-Di-SiO<sub>2</sub> system 188, 192  
 TSC from 92, 100–104
- tie line 45  
 bulk composition and, in Fo-Di-SiO<sub>2</sub> system 187, 188, 189, 190, 192  
 in derivation of liquidus fractionation lines 125  
 in Di-rich region of Fo-Di-SiO<sub>2</sub> system 204–205  
 plagioclase-liquid 91–95, 99–102, 104, 105, 118  
 in ternary system 89, 90, 91, 92
- tie line template, for Fo-Si-SiO<sub>2</sub> system 187, 188, 189, 192
- titanomagnetite 328
- TLC (*see* total liquid composition)
- total liquid composition  
 in An-Ab system 71–73  
 definition 52
- total liquid composition path 73  
 in ternary system 122
- total solid composition  
 in An-Ab system 67–68, 71–73  
 definition 50  
 in equilibrium crystallization 92, 100–104, 109  
 in fractional crystallization 109–112  
 from three-phase triangle 92, 100–104
- total solid composition path 71–73 (*see also* individual systems)  
 in ternary system 101–105, 111, 114, 115–117, 119
- trachyte 3  
 critically undersaturated basalt system and 253  
 in Ne-Ks-SiO<sub>2</sub> system 264, 273, 278  
 Ne-SiO<sub>2</sub> system and 247
- trachyte minimum 278
- triangle plot, properties 86–87
- tridymite  
 in Di-SiO<sub>2</sub> system 182, 183  
 in FeO-Fe<sub>2</sub>O<sub>3</sub>-SiO<sub>2</sub> system 301  
 in Fo-Di-SiO<sub>2</sub> system 182–208, 211  
 in high pressure SiO<sub>2</sub> system 360–361  
 in Ks-SiO<sub>2</sub> system 256–258  
 melting 257  
 in Ne-Ks-SiO<sub>2</sub> system 262, 266, 272, 275  
 in Ne-SiO<sub>2</sub> system 245, 246  
 in Ne-SiO<sub>2</sub>-X ternary systems 248–250  
 in Ol-An-SiO<sub>2</sub> system 330  
 olivine melting and 309–311  
 in silica-water system 386–388
- triple point  
 definition 25  
 for silica 385, 386  
 for silicates 360  
 for water 26
- troctolite 139, 363, 389  
 in Kiglapait intrusion 220, 221, 222
- TSC *see* total solid composition
- T-X plot 40–42  
 of binary system 41–42  
 melting maxima and minima and ternary 87–91 (*see also* T-X projection)
- T-X projection  
 deduction of 87–90  
 experimental 90–91
- unary system, definition 32
- unit cell 22
- univariant curve 64, 133
- univariant lines 133, 134
- univariant system  
 definition 36, 45  
 example 45
- unsupported area seal, in high pressure apparatus 348
- vapor  
 definition 22–23  
 interface with liquid 23
- vapor buffer 419
- vapor saturation 382
- vapor state, of silicates 42
- variance 36  
 dimension and 45  
 phase rule and 35–36  
 restricted 44, 197, 261, 391  
 in ternary system 91, 98–99, 106
- viscosity 23
- volatiles, effects of high pressure 381–404
- volume 33  
 variable in energy equation 35

- water (*see also* ice; volatiles)
  - carbonation of peridotite and 420–424
  - crystal growth 24
  - effect on melting curves of silicates 29
  - juvenile 381
  - melting and crystallization 23–27
  - meteoric 381
  - occurrence in mantle 381
  - phase diagrams 24–26
  - physical properties 23–27
  - solubility in silicates 381, 421
- water-poor melt 398, 400
- water pressure 382
- websterite 200, 231, 232, 233
- weight percent 41
- wollastonite 11, 18, 55, 182
- wüstite 300, 301, 331 (*see also* iron-wüstite buffer; magnetite-wüstite buffer)
  - olivine melting and 309–311
- xenolith 405
- X-X plot, for ternary system 86–87, 88
- X-X space (*see* composition space)
- ZIVC (*see* zone of invariant vapor composition)
- zone of invariant vapor composition 418–420, 422
- zoning 67